

Impedance-based Analysis of Adherent Cells using Interdigitated Electrodes of Subcellular Dimensions

DISSERTATION

zur Erlangung des Doktorgrades der
Naturwissenschaften (Dr. rer. nat.)
der Fakultät für Chemie und Pharmazie
der Universität Regensburg



vorgelegt von **Maria Zinkl** aus Tännesberg, 2021

Diese Doktorarbeit entstand in der Zeit von März 2016 bis Mai 2020 am Institut für Analytische Chemie, Chemo- und Biosensorik der Fakultät Chemie und Pharmazie der Universität Regensburg.

Diese Arbeit wurde angeleitet von Prof. Dr. Joachim Wegener.

Promotionsgesuch eingereicht am: 28.05.2021

Kolloquiumstermin: _____

Prüfungsausschuss:

Vorsitzender:	Prof. Dr. Oliver Tepner
Erstgutachter:	Prof. Dr. Joachim Wegener
Zweitgutachter:	PD Dr. Hans-Heiner Gorris
Drittprüfer:	Apl. Prof. Dr. Rainer Müller

*Bilbo: „Mir ist ein schöner Schluss für mein Buch eingefallen:
Und so lebte er vergnügt bis ans Ende seiner Tage.“*

Der Herr der Ringe, J. R. R. Tolkien

Meiner Familie

Contents

1	Introduction	1
1.1	Cell-based assays	1
1.2	Whole cell-based transducers	6
1.3	Electric cell-substrate impedance sensing (ECIS)	12
1.4	Interdigitated electrodes	16
2	Objective	23
3	Theoretical background	25
3.1	Electrochemical impedance spectroscopy	25
3.1.1	Electric cell-substrate impedance sensing (ECIS)	28
3.1.2	Data representation	32
3.1.2.1	Impedance spectra	32
3.1.2.2	Normalized impedance	35
3.1.2.3	Error calculation	36
3.1.2.4	High time-resolved measurement	37
3.2	COMSOL Multiphysics	38
3.2.1	Finite element method	39
3.2.2	The AC/DC module of COMSOL Multiphysics	40
4	Materials and methods	43
4.1	Cell culture techniques	43
4.1.1	Common cell culture conditions	43
4.1.2	Cell lines	43
4.1.3	Subcultivation of the different cell lines	48
4.1.3.1	Standard protocol for subcultivation of the cell lines	48
4.1.3.2	Protocol for cultivation of the Cor.At® cell line	49
4.1.4	Cryopreservation and recultivation	50
4.1.5	Preparation of a monolayer of the cells for experiments	51
4.1.6	Preparation of Spheroids of U373 cells	52
4.2	Microscopic techniques	52
4.2.1	Applied microscopes	52

4.2.2	Cytochemical staining	54
4.2.2.1	Fixation and permeabilization	54
4.2.2.2	Live/Dead staining	54
4.2.2.3	Unspecific staining with carbol fuchsin	55
4.2.2.4	Staining of the cell nuclei with DAPI	56
4.2.2.5	Tight junction staining with ZO-1 immunostaining .	56
4.2.2.6	Staining of the actin cytoskeleton with phalloidin .	56
4.3	Interdigitated electrodes for impedance analysis	58
4.3.1	Layout of the interdigitated electrodes	58
4.3.1.1	Preparation of IDEs by photolithography	59
4.3.1.2	Fabrication of different window sizes	61
4.3.2	Layout of the commercially available ECIS arrays	63
4.4	Impedance-based measurements	64
4.4.1	Basic measurement setup	64
4.4.2	Different impedance recording parameter	66
4.4.3	Specific assay conditions	67
4.4.3.1	Characterization of cell-free electrodes	67
4.4.3.2	Spectral characterization of different cell types	67
4.4.3.3	Phenotypic assays	68
4.4.3.4	Emerging impedance-based assays	72
4.4.4	Simulation with COMSOL Multiphysics	73
5	Characterization of cell-free electrodes	75
5.1	Spectra of cell-free electrodes	75
5.2	Spectra of cell-free electrodes with different window sizes	79
5.3	Simulation of cell-free electrodes by finite element techniques	82
5.4	Discussion	93
6	Impedance-based comparison of different mammalian cell lines grown on various electrode layouts	99
6.1	Simulating the dielectric properties of adherent cells grown on interdigitated electrodes	101
6.2	Spectra of cell-covered electrodes with different electrode layouts and their analysis	111
6.2.1	Spectra of cell-covered electrodes with different electrode layouts	111
6.2.2	Analysis of different aspects of the impedance spectra	119
6.3	Frequency spectra of cell-covered IDEs with different window sizes . .	127
6.4	Micromotion measurement of different cell types grown on various electrodes	132
6.5	Discussion	136

7	Phenotypic assays	153
7.1	Monitoring the time course of cell adhesion	154
7.1.1	Three-dimensional representation of time- and frequency-dependent impedance analysis of cell adhesion	154
7.1.2	Time-dependent analysis of cell spreading by single frequency impedance readings	159
7.1.3	Impedimetric monitoring cell adhesion using IDEs: dependence on active electrode area	169
7.1.4	Discussion	172
7.2	Monitoring cell proliferation using different electrode layouts	177
7.2.1	Discussion	180
7.3	Monitoring the impact of non-isotonic media	182
7.3.1	Monitoring the impact of non-isotonic pressure on MDCK II cells	183
7.3.2	Monitoring the impact of non-isotonic pressure on NRK cells	186
7.3.3	Discussion	189
7.4	Monitoring signal transduction cascades	193
7.4.1	Impedance-based analysis of the stimulation of the H_1 receptor with histamine	193
7.4.2	Monitoring the stimulation of U373 cells with calcimycin	197
7.4.3	Discussion	199
7.5	Analysis of the time course of the impedance during adhesion and beating of cardiomyocytes	203
7.5.1	Monitoring the time course of the cell adhesion of cardiomyocytes on different electrode types	203
7.5.2	Impedance-based analysis of the beating of the cardiomyocytes cultured on different electrodes	203
7.5.3	Manipulation of the beating rate with isoprenaline	208
7.5.4	Discussion	211
7.6	Impedance-based analysis of the cytotoxicity of BPA	215
7.6.1	Analysis of the metabolic activity with a PrestoBlue assay	216
7.6.2	Impedance-based analysis of the acute toxicity	218
7.6.3	Concentration-dependend micromotion	222
7.6.4	Impedance-based analysis of cell migration after wounding	224
7.6.5	Time-dependent capacitance change during proliferation	227
7.6.6	Staining of the cells after incubation with BPA	229
7.6.7	Summary of the cytotoxicity of BPA	231
7.6.8	Discussion	232

8	Use of interdigitated electrodes in emerging impedance-based assays	239
8.1	<i>In situ</i> electroporation	239
8.1.1	<i>In situ</i> electroporation using commercial electrode layouts . .	240
8.1.2	<i>In situ</i> electroporation using IDEs	242
8.1.3	Discussion	247
8.2	Impedance-based analysis of U373 spheroids	253
8.2.1	Adhesion of spheroids on different electrode types	253
8.2.2	Stimulating cell-surface receptors	260
8.2.3	Discussion	262
9	Summary	269
10	Zusammenfassung	271
11	Outlook	273
	References	275
A	Appendix	301
A.1	Supplementary information	301
A.1.1	Simulation of cell-free electrodes by finite element techniques using COMSOL simulations	301
A.1.2	Measurement of the cell size	303
A.1.3	Impedance-based comparison of different mammalian cell lines grown on various electrode layouts	304
A.1.4	Micromotion measurement of different cell types grown on var- ious electrode layouts	315
A.1.5	Monitoring the time course of cell adhesion measurement . . .	316
A.1.6	Analysis of the time course of the impedance during adhesion and beating of cardiomyocytes	317
A.1.7	Impedance-based analysis of the cytotoxicity of BPA	324
A.2	Abbreviations and symbols	325
A.3	Materials and instrumentations	331
A.4	Curriculum Vitae	336
A.5	Danksagung	337
A.6	Eidesstattliche Erklärung	339

1 Introduction

1.1 Cell-based assays

There is a wide range of opportunities to use cell-based assays in various applications. These applications can range from analyzing whether a chemical or material is toxic to cells, ensuring that biological products are properly manufactured or to proof-of-principle studies *in vitro*, and many more. These *in vitro* studies have increased in recent years to reduce and avoid animal testing. The *in vitro* situations inside animals and humans are imitated and conclusions about the conditions and reactions *in vivo* can be gained. In particular, the assays to be mentioned here are cytotoxicity assays, cell viability assays, cell reporter gene assays and cell signaling assays, among others. In general, cell-based assays include all assays that measure whole cells or cell aggregates. This broad definition clearly shows that there exist many different types of assays and applications.

Cell-based assays can also be integrated very well into biosensors. A biosensor is defined as a device which transforms information into an analytical signal, whereas the device can use different recognition systems. It consists of three components: i) the biological recognition system (receptor), ii) the physico-chemical transducer and iii) a signal processing system (Thévenot et al., 2001) (see fig. 1.1).

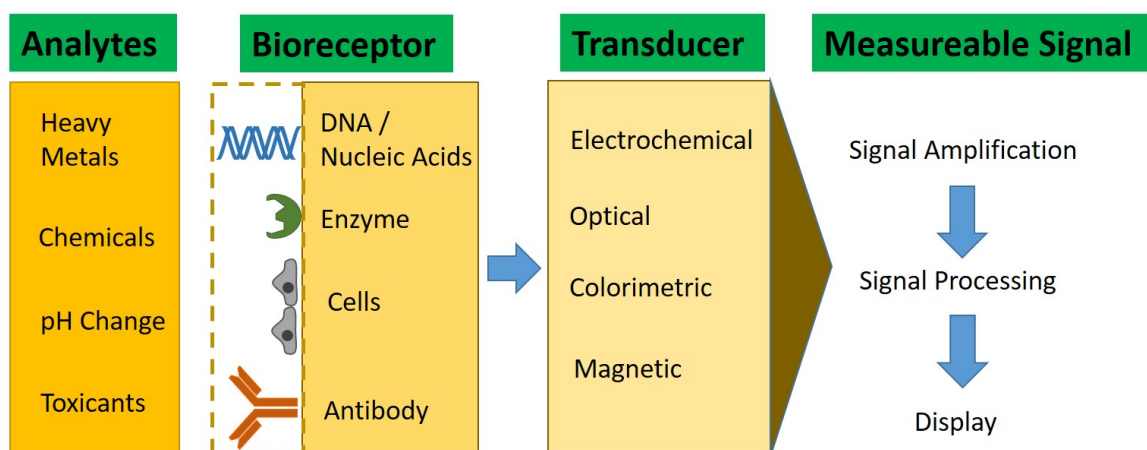


Figure 1.1: Schematic principle of the different parts of a biosensor with generic examples of different analytes, bioreceptors and transducers.

In the case of the cell-based assays the biological recognition system are whole cells, whereas the transducer can vary widely (see chapter 1.2). The cell-based assays have the advantage that it is possible to obtain functional information of a living component, like the effect of a stimulus, a toxic substance or the apoptosis of cells using whole cells. Nearly all kind of cell types can be obtained, for instance from the German cell bank *Deutsche Sammlung von Mikroorganismen und Zellkulturen* and the *American type culture collection*. Many research groups are working on the development of an organ- or even a body-on-a-chip with many different cultured cell types which are connected via a microfluidic channel. With this, the influence of a substance or drug can be analyzed with close attention to a special cell type and to the interrelation of the different cell types. Furthermore, these assays help to reduce and replace animal testing which would be conducted for this purpose otherwise. These *in vitro* models are a huge step to decrease the gap between *in vivo* and *in vitro* researches.

Due to the distinct objects of the analyzed results and the multiple possibilities of using different transducers and various cell types, there is a wide range of applications for which cell-based assays can be used. Some examples of the use of cell-based assays are briefly explained in the following.

Cell-based assays are used, for instance, in the **food industry** at different manufacturing steps and during storing at consumer side. The applications are focused on the detection of bacteria arising from fermentation processes.

The presence of the bacterial cells *E.coli* O157:H7 and *Salmonella typhimurium* were analyzed in a whole chicken bought in a supermarket. The anti-*E.coli* and anti-*Salmonella* antibodies were immobilized on the detection electrodes, whereby the anti-*Salmonella* antibodies were immobilized through covalent bounding via crosslinker and the anti-*E.coli* via physisorption. The impedance-based cell assay was able to differentiate live from dead bacteria and had a detection limit of *Salmonella* of 10 cells/mL and of *E.coli* of 13 cells/mL in less than 1 hour (Abdullah et al., 2019). The detection of these bacteria was further researched with other assays, for instance from Guo et al. who used magnetic nanoparticle which were conjugated with monoclonal antibodies against *Salmonella typhimurium* resulting in a magnetic bacteria. The formed magnetic bacteria conjugated to a nanocluster of polyclonal antibodies and glucose oxidase. These nanoclusters catalyze glucose into gluconic acid and hydrogen peroxid. The latter can be measured with a peroxide test strip and analyzed with smartphone images. The authors revealed a limit of detection of 16 CFU/mL (Guo et al., 2019). Other bacteria like *Salmonella enteritidis* and *Listeria monocytogenes* were analyzed in drinking water, tomato and pork samples. A chromatography assay was used to stain the bacteria with crystal violet. The stained bacteria were detected in a novel lateral flow strip with anti-bacteria

monoclonal antibodies. The authors were able to detect gram-negative and gram-positive bacteria in one device and they could exclude interference with biological stains like rhodamine B, comassie brilliant blue or malachite green. A detection limit up to 80 CFU/mL in 11 min was achieved (Bu et al., 2019).

Additional to bacteria cells in the food industry, there is an enormous field of possibilities to use cell-based assays with adherent cells in **medical** applications.

For instance, the authors in the lab of Becerra analyzed various methods to prevent the cell death of two retinal cell lines. They performed assays measuring the cell death after photo-oxidation stress due to the quantification of ATP levels with luciferase over time, the cytotoxicity of sodium iodate due to the measurement of the extracellular lactate dehydrogenase or the growth factor depletion due to microscopic inspection. The aim of the work was to use these assays as simple methods in high-throughput screening in order to invent novel therapeutics for retinal disorders (Bullock et al., 2020). As a further assay the imaging of lectin was examined to stain glycocalyx in a three-dimensional microfluidic cell culture. Endothelial glycocalyx is important in the progressing and occurrence of microvascular illnesses. Into a microfluidic device with a central gel region with a height of 120 μm , HUVEC cells were seeded resulting in a microvascular three-dimensional network which was built through spontaneous vasculogenesis. The human mammary adenocarcinoma cells were added to one side of the microfluidic device and were driven to the three-dimensional microvascular network on the 6th day after seeding of the HUVEC cells using a slight hydrostatic pressure difference. For the immunocytochemistry the cells were stained with phalloidine and the lectin was stained with lectin tetramethylrhodamine isothiocyanate conjugate. The glycocalyx defects were made visible through the lectin staining at the site of cancer cells. The authors showed the suitability of the lectin staining in a high resolved image to reveal the role of glycocalyx in cancer cell extravasation (Beyer et al., 2021).

A further topic of cell-based assays in medicine has occurred over the past year due to the global pandemic. Many research groups analyzed drugs or treatments against the **SARS-CoV-2 virus** which causes the Corona disease. In the following only some examples are named.

One of these groups used African green monkey kidney epithelial (Vero E6) cells and the human hepatocellular carcinoma (Huh-7) cells to analyze the antiviral activity of Lianhuaqingwen (LH) against the SARS-CoV-2 virus. The cells were inoculated with the coronavirus strains for 2 h and afterwards with LH for 72 h. The treatment with LH resulted in an inhibition of the replication of SARS-CoV-2 virus with an IC_{50} value of 411.2 $\mu\text{g/mL}$. Furthermore, the cells were infected with 50 plaque-forming units of SARS-CoV-2 and were covered with agar overlay after 2 h. After 48 h the agar was removed and the cells were stained with crystal violet and the

plaques were counted. The incubation with LH had a dose-dependent inhibition effect on the building of plaque of the virus. The authors were able to show an inhibition of the virus replication and a reduction of the cytokine release from the cells after inoculation with the SARS-CoV-2 virus using LH (Runfeng et al., 2020). Mavrikou et al. invented a portable and ultra-sensitive cell-based sensor to detect the SARS-CoV-2 S1 spike protein which is expressed on the surface of the virus. Their goal was, among other aspects, to assess early-stage patients as quickly as possible. The assay is based on green monkey kidney cells (Vero cells) into whose cell membrane the SARS-CoV-2 spike S1 antibody was introduced using electroinjection. These membrane-engineered kidney cells were added to the measurement wells on a strip with eight gold screen-printed electrodes. After addition of the samples to be tested, the actual binding of the SARS-CoV-2 S1 spike protein antigen to the antibody could be measured immediately through changes in the membrane potential as a time-series of the potentiometric signal. It was possible to perform this measurement in a rapid, reproducible, highly sensitive and high-throughput manner. The authors managed to discriminate different concentrations of the SARS-CoV-2 S1 spike protein within 3 min with a limit of detection of 1 fg/mL (Mavrikou et al., 2020). Furthermore, the pharmacological activity of chloroquine and hydroxychloroquine was analyzed with Vero cells from the green monkey kidney which were infected with the SARS-CoV-2 virus. They used two different approaches: i) the confluent cells were inoculated with a multiplicity of infection of 0.01 and after 2 h the washed cells were treated with chloroquine or hydroxychloroquine in a concentration range of 0.032-100 μ M for 24 and 48 h. ii) The cells were pretreated with the substances for 2 h before the virus-containing medium was added. In the case of both approaches the supernatant was collected for the extraction and analysis of the RNA. This *in vitro* study revealed a good antiviral activity of both chloroquine and hydroxychloroquine which decreased the viral replication. Nevertheless, hydroxychloroquine showed a smaller EC_{50} value resulting in a more potent antiviral activity (Yao et al., 2020). The cells of the green monkey kidney were also used in the work of Hattori et al.. They analyzed two small-molecule-compounds (named GRL-1720 and 5h) for their specific antiviral characteristics for the SARS-CoV-2 infection. The cells were incubated with the SARS-CoV-2 virus for 1 h and after washing they were cultured for three days in the presence of the tested compounds in various concentrations. Then the supernatant was analyzed to the viral copy numbers with a quantitative RNA-qPCR assay. Furthermore, immunocytochemistry with primary antibodies of COVID-19-convalescent patient were used to monitor the cellular cytoskeleton filamentous actin. Cells, which were exposed to the virus show a lost F-actin structure and a high number of infected cells. The incubation with the compounds GRL-1720 and 5h resulted in a significantly reduced

number of infected cells and no virus breakthrough could be seen. The authors concluded that both substances were able to block the infectivity and cytopathicity of SARS-CoV-2 virus without viral breakthrough or detectable cytotoxicity (Hattori et al., 2021). Further, 22 small molecules were analyzed due to their activity against SARS-CoV-2 virus using a novel luciferase complementation reporter assay. For this assay, plasmids with two luciferase fragments encoding a wild-type of SARS-CoV-2 virus were used to infect 293T cells. 4 h after transfection, the cells were seeded in a 96-well plate with the various tested compounds in a range of 0.1 to 100 μ M. The luciferase activity was then measured 30 h after transfection. The authors found out that boceprevir (FDA-approved protease inhibitor), Z-FA-FMK (preclinical compound, originally an inhibitor of cellular cysteine proteases), calpain inhibitor XII (preclinical compound, originally an inhibitor of cellular cysteine proteases) and GRL-0496 (preclinical compound, originally an inhibitor of SARS-CoV) can inhibit SARS-CoV-2 virus (Rawson et al., 2021).

Another application in which cell-based assays can be used is the development of **cosmetic**.

Figueiredo et al. investigated cell biomarkers for their use as parameters to measure sunscreen efficiency. These biomarkers have to change during the exposure to ultraviolet radiation (UV). For this assay they seeded fibroblast cells (L929 cells) and keratinocytes cells (HaCaT cells), radiated them with different doses of UVA (350 nm) and UVB (309 nm) light through a quartz plate and measured the cell viability with resazurin, the lipid peroxidation with the TBA-test (thiobarbituric acid), and the cellular oxidant stress with the measurement of the intensity of the fluorescence of 2',7'-dichlorodihydrofluorescein diacetate after incubation. The authors concluded from these results that the cell viability and the lipid peroxidation were promising parameters for the detection of photoprotective characteristics of sunscreens because they undergo a dose-dependent change during exposure of UVB light. Afterwards, the quartz plate, superimposed above the measurement wells containing the cells, was covered with samples of different sunscreens with a SPF value from 15-60 and the radiation was repeated. Using the previously mentioned parameter the authors proved that the sunscreens prevented the loss of the cell viability and the formation of lipid peroxides (Figueiredo et al., 2021). Furthermore, for the development of novel hair dyes a cytotoxicity assay is necessary. Venkatesan et al. tried to invent a hair dye which did not include p-phenylenediamine (PPD) because it is known for cutaneous reactions and allergic contact dermatitis. The authors introduced large side chains to the PPD molecule to reduce the skin permeability and the corresponding skin irritation. After the synthesis of the novel molecule, it had to be analyzed for its cytotoxicity, among others. For this, keratinocytes cells (HaCaT cells) were cultivated in a 96-well plate and after 24 h the substances to be

tested were added in a concentration range of 500 μM to 1.9 μM . After further 72 h the cells were washed and the cell viability was monitored using a MTT assay. They generated an IC_{50} value of 160 μM for the novel molecule, which corresponds to a 6-7 times less cytotoxicity compared to the PPD. The authors concluded that the novel compound paves the way toward a less hazardous cosmetic product (Venkatesan et al., 2021). A further application with a cosmetic and dermatological background was the analysis of ayurvedic plant extracts. Three different plant extracts were examined: i) extract of *Centella asiatica* L., ii) extract of *Clitoria ternatea* L. and iii) extract of *Epilobium angustifolium* L.. The authors investigated that those extracts have strong antioxidant, anti-inflammatory and anti-aging properties. Further, the cell viability was tested with normal human keratinocytes (HaCaT) cells and fibroblasts (BJ) cells which were cultured in a 96-well plate and the extracts in a concentration range of 10-1000 $\mu\text{g/mL}$ were added. After 24 h of incubation three assays were performed: i) the Neutral Red uptake assay, ii) the Alamar Blue assay with resazurin, and iii) lactate dehydrogenase (LDH) assay. In none of these assays a cytotoxic effect of the tested extracts were measured. The authors concluded that all three analyzed plants show promising results for a further application in care and treatment of skin diseases (Zagórska-Dziok et al., 2021).

In this chapter, only a few examples of the applications of cell-based assays are enumerated. Nevertheless, it was possible to give a small impression about the wide range of the applications and the currency of these assays. As mentioned earlier, this diversity is made possible by the enormous amount of cell types available, the use of many different transducers, and the completely different objects of the assays. In the following some transducers are further explained.

1.2 Whole cell-based transducers

Hulanicki et al. defined an extract of the different transducer devices as followed: The **optical transducers** transform changes in absorbance, reflectance, luminescence, fluorescence or refractive index to an analytical signal. The **electrochemical ones** are divided into four parts: i) voltammetric sensors including chemically inert electrodes and modified electrodes, ii) potentiometric sensors which measure the potential difference between an indicator electrode and the reference electrode, ii) chemically sensitized field effect transistors and, iv) potentiometric solid electrolyte gas sensors. The **electrical transducers** measure the change of electrical properties caused by the interaction of the analyte. It can be distinguished between metal oxide semiconductor sensors like gas phase detectors, organic semiconductor sensors,

electrolytic conductivity sensors and electric permittivity sensors. The **magnetic ones** use the change of paramagnetic properties (Hulanicki et al., 1991).

In the following some of these transducers are explained shortly: i) ion-sensitive field-effect transistor (ISFET), ii) light-addressable potentiometric sensor (LAPS), iii) quartz crystal microbalance (QCM), iv) surface plasmon resonance (SPR), v) impedance-based transducer. A schematic drawing is shown in fig. 1.2.

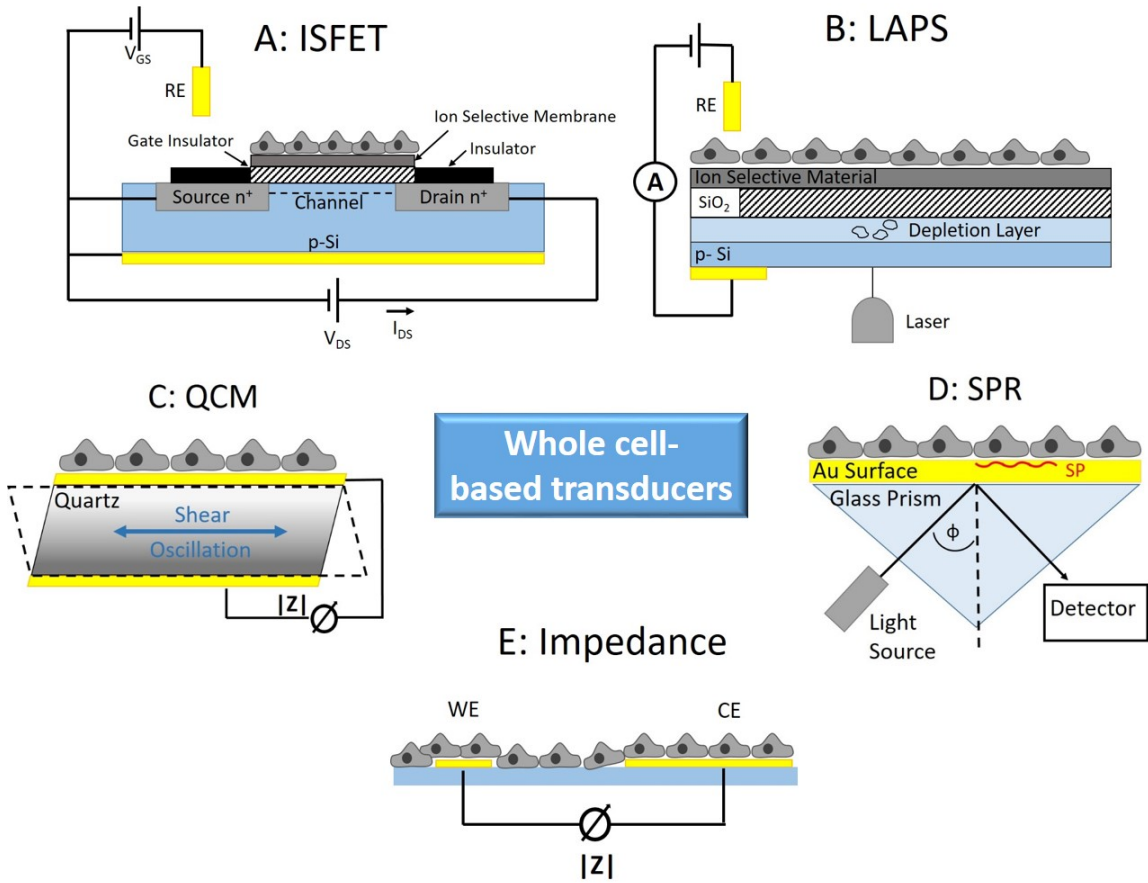


Figure 1.2: Schematic principle of different whole cell-based transducers. **A:** ion-sensitive field-effect transistor (ISFET), **B:** light-addressable potentiometric sensors (LAPS), **C:** quartz crystal microbalance (QCM), **D:** surface plasmon resonance (SPR), **E:** impedance-based transducer with the working (WE) and the counter electrode (CE).

Ion-sensitive field-effect transistor (ISFET)

The ion-sensitive field-effect transistor (ISFET) was first invented in 1970 by Bergveld (Bergveld, 1970) and measures the ion concentration in solutions. The functional principle of this transducer is the usage of an ion selective membrane. Cations from the analyte will adsorb to the membrane switching the n-channel enhancement FET to a conductive mode.

It is a combination of a conventional ion selective electrode and an insulated gate field-effect transistor. Instead of the use of a metal gate like in the MOSFET (metal oxide silicon field-effect transistor) device a chemically sensitive membrane, an electrolyte solution and a reference electrode (RE) are necessary (Yuqing et al., 2003). The silicon substrate of a p-type silicon with two n-doped regions are used, the source and the drain, which are separated by a short channel covered with the gate insulator (Bergveld, 1970). This gate insulator consists in the scenario of a pH-ISFET of ion sensing layers (SiO_2 or a double layer insulator $\text{SiO}_2\text{-Si}_3\text{N}_4$). This upper layer is used as the sensitive material and the reference electrode to apply the gate voltage (Schöning and Pogossian, 2002). The hydroxyl groups at the gate surface can donate or accept a proton and consequently, a change of the pH in the electrolyte can influence the insulator surface potential which can be measured. During cellular metabolism the pH value can be changed through acidic products like CO_2 , H^+ and lactic acid. This impact can be monitored and allows conclusions about the cell vitality (Matsuo and Esashi, 1981; Schöning and Pogossian, 2002). ISFET has many advantages like robustness, rapid response, small size, low output impedance and depending on the fabrication the detection of several ion species (Bergveld, 2003).

Light-addressable potentiometric sensor (LAPS)

A potentiometric transducer which can be used for analyzing whole cells is the light-addressable potentiometric sensor (LAPS) which was first explained in 1988 by Hafeman et al. (Hafeman et al., 1988). It is a part of the group of semiconductive transducers which change the carrier distribution with the different potentials on the insulator/electrolyte interface. With distinct modifications of the insulator layer it is possible to measure changes in pH caused by the extracellular acidification, redox or transmembrane potential.

The basic measurement setup is comparable with the aforementioned ISFET device. While the ISFET is sensitive to charges trapped all over the ion selective membrane, the LAPS sensor principle requires a spot illuminated by a laser. The LAPS device consists of a semiconductor with a thin layer for the insulation and an ohmic contact on the back side. The thin flat insulating layer comprises of n- or p-type silicon which is in contact with the electrolyte (Yoshinobu et al., 2005). The potential is fixed with a reference electrode (RE) of Ag/AgCl (Hafeman et al., 1988) and after illumination of the substrate the amplitude of the ac photocurrent is measured for the detection of the capacitance changes of the depletion layer (Miyamoto et al., 2011; Yoshinobu et al., 2005). When the measurement is started, a double layer is built on the insulator surface which varies the potential with the change of the pH of the electrolyte or with the concentration of other tracer molecules depending on the

modification of the surface (Miyamoto et al., 2011; Owicki et al., 1994; Yoshinobu et al., 2005). The substrate is illuminated with light, which is modulated, and the amplitude of the emerged AC photocurrent is monitored in dependence of the illumination (Yoshinobu et al., 2005). Due to this illumination hole-electron pairs are generated at the depletion layer which are separated in an electric field (Owicki et al., 1994). The holes are collected at the silicon-insulator interface, whereas the electrons move to the silicon bulk. This leads to a migration of the charges in the external circuit which can be detected (Owicki et al., 1994). The wavelength of the light source is chosen carefully depending on the absorption coefficient and the thickness of the semiconductor (Yoshinobu et al., 2005). With the different spatial regions of illumination it is possible to measure more analytes with one device (Hafeman et al., 1988).

Quartz crystal microbalance (QCM)

A further transducer is the quartz crystal microbalance (QCM) which can be used to study the cellular response and cell-substrate interactions without any labels. The basic principle of the QCM is the inverse piezoelectric effect in quartz crystals what was first discovered in 1880 by the Curie brothers (Curie and Curie, 1880). Piezoelectric materials deform, when an electric field is applied, and vice versa. The generated charges in a crystal can be explained with the shift of dipoles because of the displacement of the atoms in the piezoelectric material. This is only possible with an acentric material (Buttry and Ward, 1992).

For the QCM measurement two metal electrodes (often gold) are plated on each side of a thin quartz crystal. This crystal plate has to be cut in a specific orientation with respect to the axis (AT-cuts) (Deakin and Buttry, 1989). Due to the piezoelectric characteristic and the orientation of the crystal shear vibrations occur which changes the potential of the electrodes (Wegener et al., 1998). This generates a synchronously oscillating potential difference between the electrodes, which can stabilize this shear vibration at the resonance frequency of the crystal (Wegener et al., 1998). This resonance frequency at which the electrical and mechanical oscillations center and reach a maximum, depends on the thickness of the wafer and lies between 2 and 20 MHz (Deakin and Buttry, 1989). Depositing a foreign mass onto the crystal alters the frequency. Within certain limits the change of this frequency is dependent on the mass which is accumulated on the crystal. This was described by the Sauerbrey equation (O'Sullivan and Guibault, 1999). The attachment and the spreading of cells can be measured by monitoring the time-dependent change of the resonance frequency during cell adhesion (Redepenning et al., 1993). With this, cells in close contact with the quartz surface can be detected (Wegener et al., 1998).

Surface plasmon resonance (SPR)

With the optical technique surface plasmon resonance (SPR) it is possible to monitor processes at metal interfaces and thin films with a high sensitivity. Whole cells can be analyzed because of the non-invasive and label free measurement setup. SPR was first used for gas detection and biosensing in 1982 (Liedberg et al., 1983).

The basis of the surface plasmons (SP) in metals, like gold or silver, is an electron density that can be made to oscillate by light under certain conditions at the interface of the metal and the liquid with dielectric constants of opposite signs (Homola et al., 1999). The photons are coupled into the electron gas at the metal surface (Brockman et al., 2000). The prerequisite for this coupling is that the light of a certain wavelength impinges on the surface at a given angle of incidence through a prism with a higher refractive index than air, usually a glass prism in the Kretschmann geometry (Englebienne et al., 2003; Frutos and Corn, 1998; Nguyen et al., 2015). This electron oscillation propagates then parallel to the interface (Nguyen et al., 2015) and decays into both materials in an exponentially form (Guo, 2012; Brockman et al., 2000). At a special angle of total internal reflection of the incident light the surface plasmon resonance will occur with a maximum. This resonance angle is very sensitive to changes of the refractive index close to the metallic surface because of the small penetration depth of the evanescent field of 200 nm (Frutos and Corn, 1998). It is possible to measure the angle of minimum reflectivity of the light (angle scan mode) and the reflected light intensity with a fixed angle (kinetic measurement type) during cell stimulation or adhesion (Homola et al., 1999).

Impedance-based transducers

The impedance-based transducers are widely used in electrochemical measurements of cells due to the label free, non-invasive and quantitative setup. Depending on the flexible electrode design and fabrication many different applications can be realized, from cell counting, cancer research, drug screening to food and environmental safety monitoring. Fricke was one of the first who used impedance spectroscopy to calculate the electric conductivity and capacitance of cell suspensions in 1924 (Fricke, 1924). Afterwards, Cole and Curtis, and Cole and Guttman analyzed the impedance of marine eggs and frog eggs (Cole and Curtis, 1938; Cole and Guttman, 1942). The basis of these interpretations was to analyze the paths of the current flow at different frequencies. In 1956 the Coulter counter was invented which was used for blood analysis and cell volume measurements (Xu et al., 2016). Another impedance-based setup is the electric cell-substrate impedance sensing (ECIS) invented in the 1980s by Giaever and Keese (Giaever and Keese, 1984), which is of major importance for

the current elaboration and will be explained in detail later on in section 3.1.1.

Usually for measuring the complex impedance, small AC voltages are used and the corresponding current response is measured (see chapter 3.1). Cells are acting as insulating particles and can change the measured impedance depending on their number, behavior, vitality and metabolism. A lot of different measurement setups are realizable due to the possibility to adapt the electrode structures to the individual use. Due to this, the cells can be measured among others in flow systems, grown on porous filter membranes or directly on the electrodes. This chapter concentrates only on the most important sensor applications.

Weng et al. for instance invented a microfluidic chip with interdigitated electrodes in the measurement chamber to measure the ratio of blood cells in venous blood samples, which had been drawn freshly. It was possible to analyze the number of leukocytes and erythrocytes separately. The more cells attached on the electrodes, the higher was the impedance (Weng et al., 2018). Also Petchakup et al. have demonstrated that healthy and activated leukocytes can be detected using whole blood samples with an impedance-based sensor (Petchakup et al., 2018). Additionally, the impedance of whole cells were measured with the invented chip of Cho et al.. The micro electrical impedance spectroscopy device was able to trap single cells between two electrodes, to measure the impedance and to distinguish between highly metastatic and poorly metastatic cells due to the higher phase part of the electrical impedance spectra of the highly metastatic cells (Cho et al., 2009). Also Huerta-Nuñez et al. showed that low concentrations of cancer cells can be analyzed with an impedance sensor. Three different breast cancer cells were coupled to nanoparticles with magnetic properties by antibodies to position them between two electrodes (Huerta-Nuñez et al., 2019). Bohrn et al. seeded hamster lung cells onto a sensor chip to measure the influence of gaseous chemicals. They used carbon monoxide as a model gas and measured the impedance change resulting from the morphological reaction of the cells, the oxygen consumption and the acidification (Bohrn et al., 2011). Han et al. invented a sensor which analyzed the endothelial barrier dysfunction of cells after addition of inflammatory substances. As a model inflammatory substance they used bacterial lipopolysaccharide and histamine which were added on a confluent grown monolayer of human umbilical vein endothelial cells and the changes in the impedance spectra were shown (Han et al., 2018). A different setup of an impedance-based sensor is the cultivation of cells on a filter which is placed between two electrodes. Rutten et al. for instance measured with this device the influence of the chemokine *stromal cell-derived factor-1* on bone marrow mononuclear cells and peripheral blood mononuclear cells on filter (Rutten et al., 2015).

1.3 Electric cell-substrate impedance sensing (ECIS)

In the last years the *electric cell-substrate impedance sensing*, ECIS, has been established more and more as a multimodal technique to monitor cell behavior and cell signals of adherent cells in a non-invasive and time resolved manner. As mentioned in the previous chapter, this impedance-based technique was first described in 1984 by Giaever and Keese (Giaever and Keese, 1984). A huge advantage of this technique is the possibility to profile phenotypic changes in real time and not only cell death as the final biological response. It is sensitive for two generic aspects of adherent cells: i) cell number or ii) changes in cell shape. The theory of this technique will be explained in chapter 3.1.1 in detail. Therefore, only a short explanation will be given now. The cells are grown on two planar gold electrodes: a working and a counter electrode. The cells act as insulating particles forcing the current to flow through the narrow clefts underneath and between the cell bodies. The number of grown cells on the electrode corresponds to the level of the measured impedance. When cells in a confluent monolayer change their shape due to certain stimuli or phenotypic responses, the current pathway around the cells is affected, resulting in a change in the measured impedance. Consequently, the measured impedance is a parameter for the coverage of the electrodes and the change in cell shape (Reiss and Wegener, 2015).

ECIS has recently been used to study a broad range of different phenotypic reactions of the cells, like necrosis and apoptosis, micromotion, migration or adhesion and proliferation to the exposure of xenobiotics (see fig. 1.3).

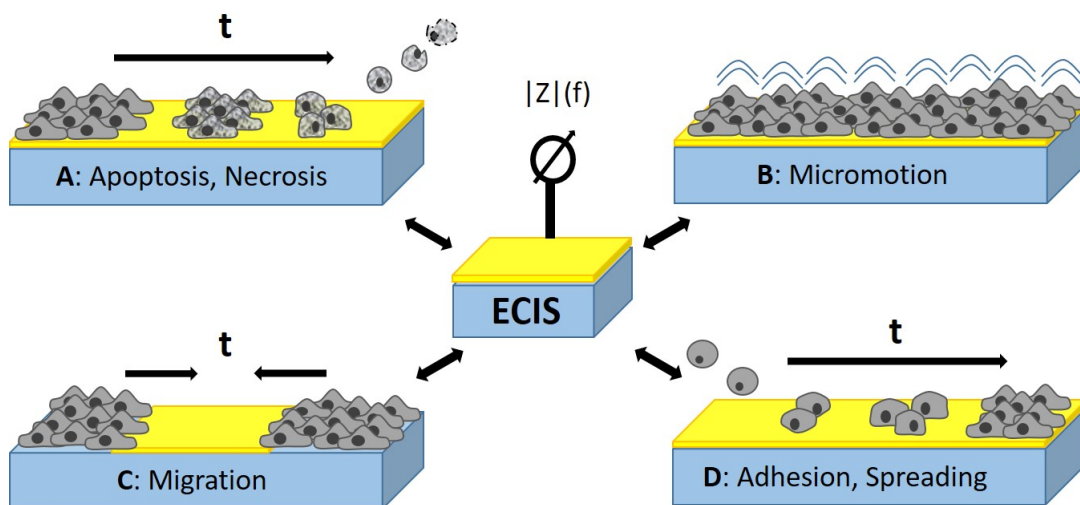


Figure 1.3: Scheme of the phenotypic functional assays monitored by ECIS measurement upon exposure to xenobiotics. **A:** apoptosis and necrosis, **B:** micromotion, **C:** migration, **D:** adhesion and spreading.

A review was given from the author of this thesis which serves as a basis for the following short exemplarily overview of the richness of applications of ECIS relating to xenobiotics (Zinkl and Wegener, 2019).

Apoptosis and necrosis

The most widely used phenotypic assay is measuring the time course of the impedance of a confluent monolayer during exposure to a suspicious substance. The cells' reaction to the impact of the xenobiotics (swelling or shrinking) can be monitored continuously with ECIS. This yields a huge advantage in comparison to corresponding end point assays. With one single run a dose-response curve for different exposure times can be established. In recent years many studies applying ECIS have been performed to analyze the impact of nanomaterial on various cell types. In table 1.1 an incomplete selection of different studies examine the impact of nanomaterials on different cells is shown with the measured cell line and the lowest cytotoxic concentration (Zinkl and Wegener, 2019).

Table 1.1: Incomplete selection of studies monitoring the influence of different nanomaterials on cell monolayers of various tissues measured with a time resolved impedance assay. The cytotoxicity is expressed as the lowest cytotoxic concentration. QD = quantum dot; SWCNT = single-walled carbon nanotube; NP = nanoparticles.

nanomaterial	cell type	lowest toxic concentration	reference
Kaempferol-based ruthenium complex	A549 HDFa	10 μ M 125 μ M	Thangavel et al., 2018
CdSe/ZnS core/shell QD	MDCK II	50 nM	Breus et al., 2015
SWCNTs	BEAS-2B	25 μ g/mL	Eldawud et al., 2015
Mesoporous ruthenium NP	HEMA	100 μ g/mL	Ramasamy et al., 2015
Silver NP	A549	10 ppm	Sambale et al., 2015
Superparamagnetic ion oxide NP	HMEC-1	0.2 mM	Astanina et al., 2014
Silica nanotubes	HeLa HMEC	750 μ g/mL 7.5 μ g/mL	Tran et al., 2013
Carbon nanotubes gold NP	BSC BSC	10 μ g/mL nontoxic	Kandasamy et al., 2010

Apart from the influence of nanomaterials on cells, an impedance-based device to detect pollutants in drinking water was invented. To develop a portable device it was necessary to have a cell type that enables long-term growth and storage in mobile devices (Curtis et al., 2009b). Many typical water pollutants like ammonia, phenol, nicotine, herbicide, aldicarb or pentachlorophenol were tested with several different cell types (Brennan et al., 2012; Curtis et al., 2009a; Widder et al., 2015). The detected concentrations were compared with the human lethal concentration and the military exposure guidelines. Curtis et al. selected four cell lines (HUVECs, Vero cells, IgH-2 cells and BLMVECs) and compared the results of the influence of aldicarb and pentachlorophenate, among others, with the one of a monolayer of bovine pulmonary artery endothelial cells (BPAEC). The authors reveal a higher sensitivity to these toxicants for the BLMVEC and IgH-2 cells in comparison to the BPAEC monolayer (Curtis et al., 2009a).

Furthermore, different studies were analyzing the time course of the impedance change in the presence of isolated food ingredients like anthocyanins from red wine or blackberries (Évora et al., 2017), complex materials like extracts of milk thistle, propolis, and birchbark (Fallarero et al., 2015), or particulate and soluble components of cigarette smoke (An et al., 2019).

Motility of the cell body: micromotion

Even in a confluent layer cells are moving in a horizontal and vertical direction and consequently, are changing their cell shape which is monitored with impedance changes. These fluctuations, called micromotion, are metabolically driven and can be used as indicator for cell viability (Giaever and Keese, 1991). This measurement setup is very sensitive because cell shape changes of around 1 nm can be detected (Giaever and Keese, 1991). The micromotion measurements are monitored with a time resolution of around 1 data point/s or even less. When xenobiotics were added, the cells responded sensitively to this impact and changed their micromotion. Compared to the viability test MTT (3-(4,5-Dimethylthiazol-2-yl)-2,5-diphenyltetrazoliumbromide), which is routinely used, it was proven that the micromotion assay was more sensitive for the impact of low concentrations of the metal and semiconductor nanoparticles on MDCK II cells (Tarantola et al., 2009). With the micromotion assays it was even possible to distinguish the cytotoxic effect of spherical gold particles in comparison to rod-shaped ones. Surprisingly, the spherical gold particles were more toxic than the rod-shaped ones. This effect was affiliated to different uptake rates of the particles (Tarantola et al., 2011). Another important aspect is the choice of the proper cell culture for toxicity measurements. The micromotion was decreasing nearly to zero after incubation of A549 human lung epithelial

cells with a MnO-based core of the nanoparticles whereas particles with a Fe₂O₃ core were stimulating the cell reaction. Repeating this experiment with CaKi1-cells, no toxicity of MnO particles was shown anymore (Rother et al., 2013).

Cell migration: wound healing assays

Another common assay is the measurement of the ability of the cells to migrate in a cell-free area. When a confluent monolayer is grown, the cells on the electrodes are killed with a short high-amplitude voltage or current pulse. Cells not covering the electrode are not harmed and can migrate in the open space. This repopulation of the electrodes and the needed time can be monitored using impedance measurements (Keese et al., 2004). Xenobiotics can prolong and shorten the time it takes for the cells to repopulate the electrodes. On the one hand it was shown, that polydesoxyribonucleotides (Koo and Yun, 2016) and anthocyanins isolated from red wine and blackberries (Évora et al., 2017) can accelerate the wound closure and therefore the cell migration. On the other hand, the cell migration could be slowed down, shown with the use of ionizing radiation which influenced the cytoskeleton (Young and Smilenov, 2011). The same effect was seen after incubation of tracheal epithelial cells with organic dust extracts taken from a swine confinement feeding operation (Poole et al., 2015).

Adhesion and spreading

Adherent cells are dependent on the possibility to spread on biocompatible substrates. The prevention of spreading leads to an apoptotic effect on the cells because of the missing cell-matrix contacts. Consequently, it is important to study the interference of suspicious substances with the cells' spreading processes. The less toxic a substance is, the better is the adhesion onto the electrodes and the measured impedance is increasing more and more. With this assay different types of potentially toxic materials were mixed with the suspended cells and were analyzed for their biological activity, like heavy metals, such as cadmium chloride, sodium arsenate and mercury chloride (Xiao and Luong, 2003; Xiao and Luong, 2005). Besides heavy metals, the impact of various nanomaterials on the spreading ability was studied and the concentration for the half maximum effect (EC₅₀) was calculated. For instance, graphene/graphene-derived nanostructures (Male et al., 2012), gold nanoparticles (EC₅₀ < 45 µM) and CdTe/CdS-based quantum dots (EC₅₀ = 0.25-6.0 µM) (Male et al., 2008) or titanium dioxide nanoparticles (EC₅₀ = 158 ppm) (Male et al., 2013) were measured. All in all it was possible to determine an imme-

diate cytotoxicity of the suspicious substances with the suspended cells.

Besides the aforementioned assays many different aspects of cells can be monitored with ECIS. Among others, the barrier function of endothelial or epithelial cells can be analyzed. Furthermore, it is possible to electroporate cells to introduce substances into cells as well as to monitor the cell response to receptor stimulation, like G-protein-coupled receptors. With this richness of impedance-based phenotypic assays many various substances or cell stimuli can be analyzed. The range of possible applications goes from pH values to medical substances, anti-cancer drugs, food or water contaminants to many more.

1.4 Interdigitated electrodes

The basis of this thesis is to explore the benefits of using interdigitated electrodes (IDEs) in monitoring cell-based assays in comparison to the commercially available ECIS electrodes. IDEs are often used as transducers in biochemical or pharmaceutical applications. With the possibility to vary the layout of IDEs with respect to the width of the electrode fingers and the gap between the electrode fingers, and the material of the electrodes or the substrates a wide range of applications is possible. The most common material is gold, whereas silver, and many other materials also can be used. Due to different penetration depth of the electric field into the electrolyte, dependent on the gap between the fingers, different aspects of cells or of the measurement volume can be analyzed. In the following a short overview of different applications of IDEs is shown. They vary from measurements without cells, to bacterial and mammalian cells.

First, some of the recently invented applications of interdigitated electrodes as a transducer **without cells** are explained.

Among others, an electronic tongue was created based on paper with interdigitated carbon electrodes with a width of 10 mm and a spacing of 1 mm. It was able to distinguish between different sugars (glucose, fructose and sucrose) using capacitance measurements. The measurement channels were defined with melted wax and were filled with hydrogels containing phenyl boronic acid which could bind saccharides. Known concentrations of sugars were analyzed as well as the sugar concentrations in six brands of different commercially available apple juices (Daikuzono et al., 2019). A further application was the use of interdigitated gold electrodes with a width and gap of 1.5 mm and 0.75 mm, respectively, to measure the pH value. Multi-walled carbon nanotubes were coated onto the electrodes and acted as an H^+ ion sensing layer. The proof-of-principle was done with five different pH values from 4 to 9

and the impedance, the capacitance and the resistance of the sensor, which was immersed in the solution, were measured. With the coating the resistance of the sensor is increasing with increasing pH value (Stojanović et al., 2019). To use interdigitated gold electrodes as a transducer it is often necessary to functionalize the electrodes with a self-assembled monolayer (SAM) of alkanethiols with a functional head group. This enables the immobilization of antibodies. Chinnadayya et al. invented a sensor with SAM on the interdigitated gold electrodes (width and spacing of 7 μm) to detect the IgM rheumatoid factor in human serum. A model antigen was immobilized onto the electrodes and different concentrations of the IgM rheumatoid factor were measured as well as human serum. In the presence of redox probes a major change in the impedance spectrum due to a change in the charge transfer resistance could be detected upon binding of the IgM rheumatoid factor. Therefore, it was possible to distinguish the concentration of the IgM rheumatoid factor in human serum (Chinnadayya et al., 2019). A SAM was also used to analyze a prostate cancer's biomarker - the prostate-specific antigen (PSA) - in human serum. For this, an anti-PSA DNA aptamer was bound by the use of SAM to the interdigitated gold electrodes with a width and spacing of 10 μm , respectively. It was possible to get a limit of detection of 0.510 ng/mL of the prostate-specific antigen in undiluted human serum (Ibaw et al., 2019). Another possibility to immobilize antibodies on electrodes was a layer of silk fibroin to develop an immunosensor for an early diagnostic of autoimmune hemolytic anemia. By immersion of the substrate a monoclonal antibody against human immunoglobulin was immobilized on interdigitated gold electrodes with a width and gap of 10 μm , respectively. Normal and sick red blood cells were added to the electrodes and the measured impedance response was used to obtain the dielectric loss and the capacitance values by modeling. The authors concluded out of the shift of the relaxation peak that only sick red blood cells bound to the antibody and changed the impedance. Consequently, a high sensitivity was achieved (Moraes et al., 2019).

Secondly, IDEs are often used in the detection of **bacteria** with a highly diversified range of different setups. *Salmonella* and *E.coli* bacteria are the most common food borne pathogens which can cause infectious diseases. Consequently, it is important to detect even small concentrations of those very quickly in food samples to avoid human infections. In recent days IDEs are often used for this detection.

The group of Almasri M. invented a biosensor to detect three different types of *Salmonella* with very low concentrations. The first generation of the sensor consisted of one channel with a focusing area with interdigitated electrodes forcing the bacteria in the center of the channel with electrophoresis. Furthermore, the sensor had a sensing region with three interdigitated gold electrodes with a width of 10 μm and a gap of 10 μm . Each of these electrodes was functionalized with specific anti-

Salmonella antibodies with different serotypes, respectively. It was possible to distinguish between live and dead *Salmonella* cells with a detection limit of 8 cells/mL (Liu et al., 2018). The next generation of this sensor was changed to use three microchannels in which every *Salmonella* serotype could be detected individually. They tested different samples of raw chicken and ready-to-eat turkey, whereby a limit of detection of 7 cells/mL in 40 min and a high selectivity was achieved (Jasim et al., 2019). Wen et al. analyzed the concentration of *Salmonella Typhimurium* in chicken carcass samples which was bought from a supermarket. The interdigitated electrodes on the portable impedance immunosensing system had a width of 15 μm , a gap of 15 μm and a length of 3 mm. After preparation of the electrodes a biotinylated antibody was dropped onto them and after further washing steps, the electrodes were ready to use. In the presence of $[\text{Fe}(\text{CN})_6]^{-3/-4}$ the faradaic impedance was measured. Out of the change of the electron-transfer resistance after attaching of bacterial cells the number of bacterial cells bound to the antibodies can be calculated. It was possible to reach a limit of detection of 100 CFU/50 μL (Wen et al., 2017). A further opportunity to detect bacteria in food samples was invented by Wilson et al.. They used silver screen-printed interdigitated electrodes with a gap and width of 180 μm and magnetic nanoparticles which were functionalized with the peptide melittin. The bacterial cells were conjugated to the nanoparticles and deposited onto the electrodes placed over a magnetic support. It was possible to detect *E.coli* in a concentration of 1 CFU/mL in water and 3.5 CFU/mL in apple juice without any further preparation of the samples in 25 min (Wilson et al., 2019). IDEs can also be used in a three-dimensional manner to detect bacteria. A simulation of Courniot et al. clarified that the geometry of the electrodes, the surface coverage and the bacteria diameter can significantly change the signal-to-noise ratio and the sensitivity. They showed that the measured impedance is dependent on the number of bacteria as well as on their position on the electrodes. It was calculated among others that the optimal gap between the fingers is four times the bacteria diameter (Courniot et al., 2013). Brosel-Oliu et al. invented a three-dimensional sensor for the analysis of the response of bacteria to ampicillin. The interdigitated fingers had a width of 3 μm and a gap of 3 μm and consisted of a highly conductive tantalum silicide. The three-dimensional effect was achieved with a 4 μm high insulating barrier which separated the electrode digits. The walls in the measurement chamber and the electrodes were covered with a polyethyleneimine polycation as an assembling layer for the *E.coli* bacteria which were immobilized on the electrodes. To evaluate the approach 10 mg/L ampicillin was added and the impedance change was monitored for 24 h (Brosel-Oliu et al., 2019). Another three-dimensional device to detect bacterial metabolism was invented from Butler et al.. They used a 10 nm/100 nm layer of Cr/Au layer and a 10 μm thick layer of nickel which were etched to define the

interdigitated electrodes (with a width of 15 μm and a gap of 35 μm). To increase the sensor area self-assembled gold nanostructures were deposited onto the nickel layer and consequently, a three-dimensional sensor was fabricated. The sensor was completely covered with an agar layer and the sample of the *E.coli* bacteria suspended in the same broth of the agar was added. After a certain incubation time the authors were able to detect the released ions from the cells during cell metabolism using the non-Faradaic impedance. It was possible to detect the metabolic activity of 10-1000 *E.coli* cells/ μL in 1 μL sample volume in one hour (Butler et al., 2019).

The detection of bacteria can also be a great issue in medical applications. Huiszoon et al. utilized a platform to monitor the *Escheria coli* biofilm formation on a biomedical device with interdigitated gold electrodes with a width and spacing of 300 μm , respectively. This flexible sensor was integrated into a urinary catheter and it was characterized in a custom-developed flow system. To perform a proof-of-principle measurement, a known concentration of *Escheria coli* bacteria was added and the impedance was measured before the addition, during seeding, 5 h after addition and 24 h after, to monitor the growth of the bacterial film on the electrodes in real-time (Huiszoon et al., 2019). A comparable application was invented in form of a flexible sensor with interdigitated gold electrodes with a gap and width of 10 μm , respectively to measure the thickness of undesired deposits on the surfaces of water pipes and tanks. It was proven that the sensor could be applied inside of pipes and tanks because of the thickness of the slime in a range of 2 μm to 10 μm (Turolla et al., 2019). In a further application interdigitated gold electrodes were used to measure the microbiological alteration during sterilization processes with hydrogen peroxide vapor sterilization which was adapted from industrial standards. The electrodes had a width of 4 μm and a spacing of 3 μm . The impedance was measured of a blank sensor, of one with bacterial biofilm and after sterilization (Jildeh et al., 2018). Jeong et al. started first experiments to integrate an interdigitated electrode into a PCR system to avoid fluorescence labeling as proceeded in conventional real-time detection. They used gold electrodes with a gap of 0.5 mm and a width of 5.7 mm to measure the genomic DNA region (180 bp length, 10 ng/ μL) of *Escheria coli* during 30 cycles. Furthermore, they made sure that the impedance measurement had no damaging influence on the probes (Jeong et al., 2019).

Except of bacteria it is possible to monitor **mammalian cells** and their behavior with interdigitated electrodes.

As early as over 20 years ago impedance-based measurements with IDEs and mammalian cells were performed. In 1997 interdigitated platinum electrodes with a width and spacing of 50 μm were used to monitor impedimetrically the adhesion of kidney cells of a male adult African green monkey and cells from a human colon adenocarci-

noma. Furthermore, the effect of Triton X-100 and Cadmium Chloride was analyzed with eight electrodes in parallel (Ehret et al., 1997). This sensor was further used to characterize the cellular growth of five different cell lines during adhesion for four days. The end-point of the measurement was set with the addition of Triton X-100 (Ehret et al., 1998). In later years interdigitated gold electrodes with a width of 8 μm and a gap of 8 μm were used to monitor the proliferation of L929 mouse fibroblast cells with a impedance measurement. The authors invented a portable impedance monitoring device which showed the different stages of growth caused changes in the electrical impedance after certain time points (Chen et al., 2012). The cell cycles of human cervical carcinoma cells were analyzed with interdigitated gold electrodes with a width of 15 μm and a spacing of 60 μm . The cells were synchronized using the double thymidine block protocol and the cellular impedance of the synchronized cells was measured for 5 days in a frequency range of 5-250 kHz. The measured impedance clarified the degree of synchronicity of the cell population and showed the progression in real time (Wang et al., 2010). Reitingner et al. examined human bone marrow-derived multipotent stem cells with interdigitated electrodes with a gap and a width of 50 μm , respectively. The cell adhesion and spreading were measured as well as cell viability and usability of the sensor for the osteogenic and adipogenic differentiation caused by specific media (Reitingner et al., 2012).

Moreover, it is possible to manipulate mammalian cells with interdigitated electrodes. Jen et al. for instance electroporated osteoblast-like cells with interdigitated electrodes to introduce DNA plasmids into the cells. The cells were cultivated on the interdigitated gold electrodes with a width and gap of 100 μm , respectively. A gold plate was placed on top of the culture cavity to be used as the cathode. When additional to the cathode above the cavity one comb of the interdigitated structure was connected to the anode, the attraction of the electric field drove the negatively charged DNA plasmids to accumulate at the electrode fingers with positive polarity and consequently, the DNA concentration was enriched on top of the cells. Afterwards, the cathode was reconnected to the other comb of the interdigitated structure and with a short electric impulse transient pores in the cell membrane were created and the DNA plasmids were able to enter the cells (Jen et al., 2004). A different device to electroporate adherent cells was invented by García-Sánchez et al. who managed to use electrodes without direct contact to the cells. The interdigitated electrodes with a width and spacing of 75 and 150 μm were patterned on a substrate with the same dimensions as the measurement chamber and was placed above the cell monolayer. To ensure an in situ application small microseparations were added to hinder a direct contact of the cells and the electrodes. Due to the applied electric field pulse, pores in the membrane were created and fluorescein isothiocyanate-dextran with a molecular weight of 20 kDa could enter the

cells which could be analyzed with fluorescence microscopy (García-Sánchez et al., 2012). Further, interdigitated electrodes were used for characterization of oral cancer cells. The electrode fingers had a width and gap of 15 μm , respectively and were made of gold. With the measurement of the impedance spectra they managed to analyze the adhesion of cancer and non-cancer cells. The authors observed that the impedance magnitude in a frequency range of 10 kHz to 100 kHz was several times higher for the cancer cells in comparison to the non-cancer cells. Furthermore, a higher resistance and smaller capacitance magnitude was measured for the cancer cells. Based on these different magnitudes the authors concluded that it is possible to differentiate between cancerous and non-cancerous cells with their device (Mamouni and Yang, 2011). Adipose tissue-derived stem cells were analyzed with a 100 nm thick nanocrystalline diamond film with built-in interdigitated gold electrodes with a width and gap of 100 μm , respectively. The authors compared two different sensors: i) one with the nanocrystalline layer on the gold electrodes and ii) one without the diamond layer. The human adipose tissue-derived stem cells were seeded on both sensors and the adhesion and the cell growth were measured. After impedance measurement the cells were stained whereby a polygonal morphology was more pronounced on the diamond covered electrodes and a spindle-shaped one on the gold sensors. They proved that there was no significant difference between the sensors in the microscopic observation but during adhesion the diamond-based sensor seemed to be more sensitive in the first 15 h (Procházka et al., 2019).

The interdigitated electrodes were also used recently in the medical application to detect cells which expressed the human leukocyte antigen (HLA-B*57:01). Cells expressing this antigen are more sensitive to abacavir, an anti-HIV drug. It is important to enumerate these cells to prevent a hypersensitivity reaction which can lead to life threatening side reactions. The interdigitated electrodes with a width and gap of 8 μm , respectively, were functionalized with an antibody which was targeted against this antigen expressed on the cell surface. It was possible to distinguish between cell lines with and without the HLA-B*57:01 expression in 20 min and to measure the number of captured expressing cells in ten different human peripheral blood samples (Chan et al., 2019). A different application of interdigitated electrodes was the invention of an implantable electrical stimulator which promoted the attachment, proliferation and differentiation of osteoblasts with electrical stimulation. A great practical advantage of this device was the self-powered system due to the connected triboelectric nanogenerator. The flexible gold electrodes had a width of 100 μm and a spacing of 300 μm and were covered with a polydimethylsiloxane layer of 50 μm thickness. The attachment and spreading of murine calvarial preosteoblasts were measured and the promoted reaction of the cells to electrical stimulation was monitored. These cells were chosen as a model for bone tissue regeneration applications.

The whole device was further implanted into a rat on a bone surface for *in vivo* experiments. It was proven that the device could be implanted and that the daily movement of the rat generated energy (Tian et al., 2019).

This short overview shows that in recent days the usage of interdigitated electrodes were focused on bacterial measurements and not on mammalian ones. This is one of the reasons that this thesis is characterizing interdigitated electrodes with adherent cells in different measurement setups and different electrode dimensions in order to close the gap and to pave the way to novel applications of the interdigitated electrodes in cell-based assays.

2 Objective

In recent years, applications of cell-based assays for medical or environmental problems have increased to avoid animal testing. These *in vitro* approaches are imitating the *in vivo* situation and provide conclusions about the conditions inside the animals and humans. To advance the reduction of animal testing, it is necessary to constantly develop novel and improved techniques. Interdigitated electrodes (IDEs) were often used as electrodes in these techniques, but only few devices with IDEs exist detecting and analyzing adherent mammalian cells and cell reactions to a certain stimulus. The aim of this thesis is to explore and characterize interdigitated electrodes and to analyze the benefits of their use as electrodes in impedance-based cell assays for novel applications.

The focus of this thesis is on interdigitated electrodes with subcellular dimensions. The previous master thesis of this author (*“Impedanz-basierte Analyse von adhärennten Zellen mit Hilfe interdigitierter Elektroden subzellulärer Dimensionen”*, Zinkl, 2015) has given an indication that the dimension (width and gap of the electrode fingers) of the electrodes has a significant influence on the results of the impedance-based cell assays. With the same preconditions of the experiments, different results were revealed with the ECIS electrodes and with the IDEs with subcellular dimension. Two types of interdigitated electrodes were used in the master thesis: i) type I with an electrode finger width of $4\mu\text{m}$ and a gap between the electrode fingers of $3\mu\text{m}$ and ii) type II with a finger width of $7\mu\text{m}$ and a gap of $5\mu\text{m}$. The measurements, like the impedance spectra of MDCK I, MDCK II and NKR cells, the time-dependent impedance change during proliferation of NRK cells or during adhesion measurement of NRK and MDCK II cells, have proven that with a subcellular dimension of the electrodes other information of the cell reaction can be gained than with electrodes with a size much larger than the cells.

These initial observations need to be further investigated and the extent to which the subcellular dimension has an impact on the results has to be demonstrated. The dependence of the dimension of the electrodes on the measurement results can be analyzed by varying the dimensions of the interdigitated structure. For the interpretation of the results, it is important to repeat all measurements with commercially available electrodes with a large electrode area, in this work ECIS electrodes, under the same conditions for each setup.

First, the properties of the various cell-free electrode layouts have to be analyzed and compared to provide a good foundation for the cell-based assays. Data collection of further basic measurements, such as impedance, resistance and capacitance spectra as a function of the frequency, should be performed with as many cell types as possible in order to obtain an impression of the electrophysical differences of the various electrode layouts as comprehensive as possible. These characteristics of the electrodes can better be understood and interpreted when the electric potential and the electric field is simulated. Different results of the various cell types measured with the individual electrodes can probably be explained by such simulations. When a solid understanding of the individual electrical characteristics of the electrode layouts is established, further experiments with adherent cells can be performed. Basic phenotypic assays like the time-dependent impedance change during the adhesion and proliferation of well established cell lines are to be thought of here first. Information about the advantages or disadvantages of the IDEs with subcellular dimension compared to the commercially available electrodes (ECIS electrodes) can further be provided by the impedance-based analysis of the effects of strongly varying stimuli on the established cell monolayer, measured with the different electrode layouts. The stimulus can initiate distinct mechanisms of cellular responses and can vary from the addition of certain substances to the change of the physical characteristics of the electrolyte. Furthermore, it can be analyzed whether the use of IDEs with a subcellular dimension has advantages in emerging assays. As such an assay the analysis of three-dimensional cell aggregates or the manipulation of the monolayer with electrical pulses can be considered.

Independently of the various assays, it is important to repeat all measurements with the commercially available and well established electrodes, in this case ECIS electrodes, which have a larger dimension. This enables an interpretation and determines in which kind of cell reaction the IDEs with subcellular dimensions show an additional or more sensitive signal change in comparison to commercially available electrodes. The important question is whether there is a different type of information that can be obtained by using IDEs with subcellular dimensions compared to the commercially established larger electrodes. The resulting advantages and disadvantages of the IDEs for impedance-based analysis of adherent cells can pave the way for further applications of these electrodes in the medical or environmental research.

3 Theoretical background

In this chapter fundamental information about the theory of the techniques used in this work and the routinely applied data representation is given. In the first part, the physical basis of the electrochemical impedance spectroscopy is explained. As mentioned before, this technique provides a label free, non-invasive and time resolved approach which can be used in many diverse applications. In the second subchapter the *electric cell-substrate impedance sensing* (ECIS) model is explained which is able to analyze the measured impedance of cell-free and cell-covered electrodes with a physical model (Giaever and Keese, 1984). In the following part the different data representations, like the impedance spectra and the normalization of the measured impedance are given. It is also explained how the data analysis of a high time-resolved measurement (called rapid time collection) works. As a last part, the basis of the simulation software COMSOL Multiphysics is shortly clarified.

3.1 Electrochemical impedance spectroscopy

The impedance of a system is measured in dependence of the frequency of the alternating current or voltage. By measuring the impedance over a wide range of frequencies, usually over several decades, an impedance spectrum can be received. The complex impedance comprises the information about the capacitance, the resistance and the inductive elements of the system. Small amplitudes are chosen to guarantee a non-invasive measurement with a minimum disturbance of the biological sample (Franklin et al., 1991). Consequently, electrochemical impedance spectroscopy (EIS) enables the analysis of the smallest changes of the cell morphology during adhesion, spreading or in a confluent monolayer. In combination with the high time resolution it is considered as an important tool for cell-based assays from all fields of biomedical research *in vitro* (Wegener, 2010). The derivations of the following equations were adapted to Muñoz-Berbel et al., 2008 and Wegener, 2010.

On the basis of Ohm's law, the resistance R in an electric system with an applied direct current (DC) is defined as the ratio of the applied voltage U to the corresponding current I as described in equation 3.1:

$$R = \frac{U}{I} \quad (3.1)$$

In a typical EIS experiment sinusoidal AC voltage is used. As a consequence, the complex impedance Z becomes time-dependent (see equ. 3.2).

$$Z = \frac{U(t)}{I(t)} \quad (3.2)$$

$U(t)$, the AC voltage, is a function of the time t and the frequency ω :

$$U(t) = U_0 \sin(\omega \cdot t) \quad (3.3)$$

with U_0 as the applied voltage amplitude, $\omega = 2\pi f$ as the angular frequency and f as the AC frequency.

The measured AC current $I(t)$ is dependent on the applied voltage and is also sinusoidal with the same frequency ω as $U(t)$, labeled as $I(t)$. Nevertheless, if inductive or capacitive elements are present, a phase shift by the angle φ of the current relative to the voltage occurs (see equ. 3.4).

$$I(t) = I_0 \sin(\omega t - \varphi) \quad (3.4)$$

It is possible to convert the current and the voltage into a complex notation with the Euler's formula with $i^2 = -1$:

$$U(t) = U_0 \cdot e^{i\omega t} \quad (3.5)$$

$$I(t) = I_0 \cdot e^{i(\omega t - \varphi)} \quad (3.6)$$

A combination of equation 3.2, 3.5 and 3.6 shows the complex impedance in polar coordinates:

$$Z = \frac{U(t)}{I(t)} = \frac{U_0 \cdot e^{i\omega t}}{I_0 \cdot e^{i(\omega t - \varphi)}} = \frac{U_0}{I_0} \cdot e^{i\varphi} = |Z| \cdot e^{i\varphi} \quad (3.7)$$

Consequently, it is possible to depict the impedance signal at each frequency with two magnitudes: i) the impedance quantity (the ratio of the amplitudes of I_0 and U_0) and ii) the phase angle φ between current and voltage (Wegener, 2010).

As a different representation of the complex impedance in place of the polar coordinates, the Cartesian coordinates can be used as described in equation 3.8. Therefore, the impedance is described with an imaginary (X) and a real (R) component:

$$Z = R + iX \quad (3.8)$$

The two components are called *resistance* R and *reactance* X and can be defined by the following equations:

$$\begin{aligned} R &= \operatorname{Re}(Z) = |Z|\cos\varphi \\ X &= \operatorname{Im}(Z) = |Z|\sin\varphi \end{aligned} \quad (3.9)$$

Plotting this in a complex Gaussian plane shows the coherence of the two components. As the abscissa the real part ($\operatorname{Re}(Z)$) is used and as the ordinate the imaginary part ($\operatorname{Im}(Z)$). The amount of the impedance ($|Z|$) is shown as a vector (see fig. 3.1).

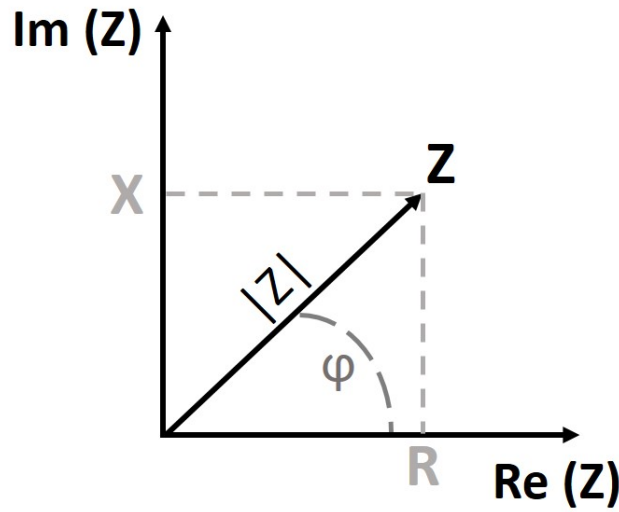


Figure 3.1: Schematic vector illustration of the complex impedance Z in a Cartesian Gaussian coordinate system with the real part $\operatorname{Re}(Z)$ as abscissa and the imaginary part $\operatorname{Im}(Z)$ as ordinate. The length of the vector represents the amount of the impedance magnitude $|Z|$. The angle between the abscissa and the vector describes the phase shift φ between the voltage and the current.

The length of the vector corresponds to the magnitude of the impedance $|Z|$, while the angle φ between the vector and the abscissa represents the phase shift between the voltage and the current. The vector and the angle can be depicted as in the following equations:

$$|Z| = \sqrt{R^2 + X^2} \quad (3.10)$$

$$\varphi = \arctan\left(\frac{X}{R}\right) \quad (3.11)$$

The resistance R , the real part of the complex impedance, results from the fact that the current is in-phase with the applied voltage. In the case of biological samples the measured resistance can be influenced by two different aspects: i) the ion concentration in the samples which is available for the current flow or ii) the

reduced migration of ions due to the limitation of the aqueous space caused by the insulated cell membranes or cell junctions. This geometric aspect hinders the current to flow without restriction. Hence, the magnitude of the resistance is dependent on the ion concentration in biological fluids and their geometric dimensions. The reactance X , the imaginary part, shows the impedance contribution arising from the current which is 90° out-of-phase with the voltage. The reactance results from the storage elements of electrical charges, for instance capacitors or inductors, like the cell membrane of a biological sample (Wegener, 2010).

3.1.1 Electric cell-substrate impedance sensing (ECIS)

The basis of the theory in chapter 3.1 can also be applied for the analysis of cells *in vitro*. For this, the aforementioned electric cell-substrate impedance sensing (ECIS) model of Giaever and Keese enables an analysis and gives the possibility for the interpretation of the measured impedance as a function of the frequency. This physical model of Giaever and Keese was derived in 1991 (Giaever and Keese, 1991; Giaever and Keese, 1986).

This model is based on the impedance of a cell-free electrode, the specific impedance through the cell layer and the resistivity of the culture medium. ECIS uses small working electrodes (WE) with a diameter of $250\text{ }\mu\text{m}$ (total area of $5 \cdot 10^{-4}\text{ cm}^2$ (8W1E electrode) and $5 \cdot 10^{-3}\text{ cm}^2$ (8W10E electrodes)) and a counter electrode (CE) which is at least 100 times larger. Due to this size difference the voltage drop and current density of the counter electrode can be neglected and the measured impedance is determined by the working electrode. For modeling the cell layer the following approximations were defined by Giaever and Keese (Giaever and Keese, 1991).

The cells which are growing directly on planar gold electrodes in a distance h (between 25 and 150 nm) (Reiss and Wegener, 2015) are approximated as circular disks with a radius r_c and have an insulating character (see 3.2). Depending on the AC frequency two different current pathways across the cells are possible: i) the extracellular pathway of the current starts from the electrode radially underneath the cells in the cleft between the electrode and the basal side of the cell membrane. The current is then entering the bulk electrolyte through the intercellular cleft between adjacent cells (see fig. 3.2 A). This resistive pathway occurs at a lower frequency range (approximately between $0\text{ Hz} \leq f \leq 10\text{ kHz}$). ii) At higher frequencies ($30\text{ kHz} \leq f$) the capacitive transcellular pathway through the plasma membranes and the cytoplasm dominates. This all can lead to a complex electrical configuration with a frequency and position dependency (Giaever and Keese, 1991, Reiss and Wegener, 2015).

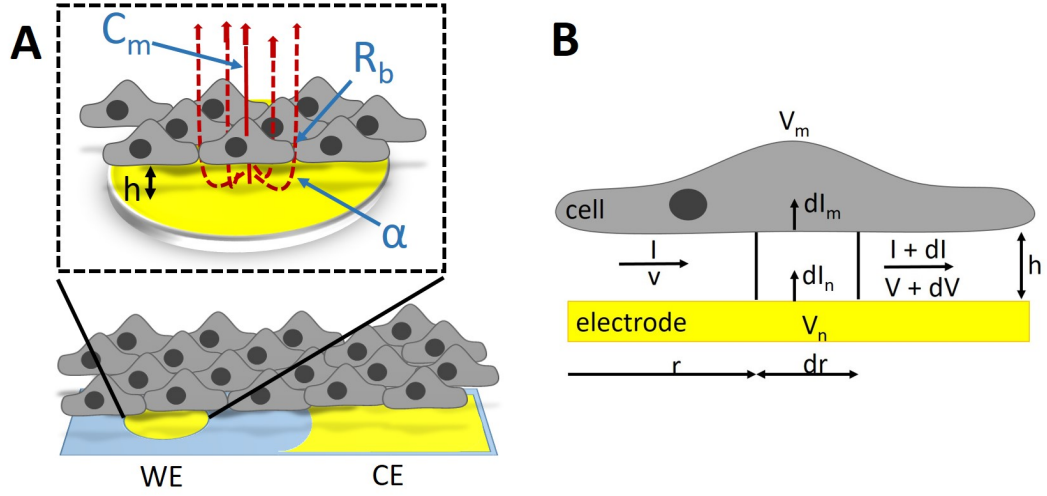


Figure 3.2: Scheme of the model of a cell-covered electrode proposed by Giaever and Keese (Giaever and Keese, 1991) with the working electrode (WE) and the counter electrode (CE). **A:** Schematic presentation of the ECIS measurement principle. The cells are seen as insulating disks at a distance h above the electrode. The current can pass the layer on two different pathways: transcellular (dashed lines) and paracellular (solid line). The parameters α , R_b and C_m show the impedance contribution of the space between cell and electrode, the specific resistance of the cell-cell contacts and the capacitance of the cell membrane, respectively. **B:** Scheme for creating the differential equation. V_n and V_m are defined as the potential of the electrode and the potential of the bulk electrolyte outside of the cells and dI_n and dI_m represent the current coming out of the electrode and the part of the current which escapes through the cell layer. I and V display the current and the potential in the cleft between the basolateral cell membrane and the electrode. dI and dV are changes in current and potential as a result from the infinitesimal cell radius increase of the segment dr .

Giaever and Keese used differential equations to model the current flow between electrode and cell layer (see fig. 3.2 B) (Giaever and Keese, 1991). The basis of the calculations for the differential equations is that the current underneath the cells is not changing in z -direction. Dividing the space under the cells in lateral direction into infinitesimal small parts, the current itself changes with infinitesimal small steps (dI). This change is the difference between the current from the electrode dI_n and the current escaping through the cell layer dI_m (see eq. 3.12).

$$dI = dI_n - dI_m \quad (3.12)$$

The change of the potential dV is influenced by the resistivity of the electrolyte ρ in the cleft between cell and electrode and the distance h between those and the cell radius r . It can be calculated with the following equation:

$$-dV = \frac{\rho dr}{h \cdot 2\pi r} \cdot I \quad (3.13)$$

According to Ohm's law, the potential differences between electrode and the cleft (eq. 3.14), and cleft and electrolyte outside the cell layer (eq. 3.15) can be calculated as following:

$$V_n - V = \frac{Z_n}{2\pi r dr} dI_n \quad (3.14)$$

$$V - V_m = \frac{Z_m}{2\pi r dr} dI_m \quad (3.15)$$

with Z_n as the specific impedance of the cell-free electrode and Z_m as the specific impedance of the cell layer. Combining the equation 3.12 - 3.15 it is possible to define the specific impedance for a cell-covered electrode Z_{total} (Giaever and Keese, 1991; Reiss and Wegener, 2015):

$$Z_{total} = \left(\frac{1}{Z_n} \left[\frac{Z_n}{Z_n + Z_m} + \frac{\frac{Z_m}{Z_n + Z_m}}{\frac{1}{2} \gamma r_c \frac{I_0(\gamma r_c)}{I_1(\gamma r_c)} + R_b \left(\frac{1}{Z_n} + \frac{1}{Z_m} \right)} \right] \right)^{-1} + R_{bulk} \quad (3.16)$$

with:

$$\gamma \cdot r_c = \sqrt{\frac{\rho}{d} \cdot \left(\frac{1}{Z_n} + \frac{1}{Z_m} \right)} \cdot r_c = \alpha \cdot \sqrt{\left(\frac{1}{Z_n} + \frac{1}{Z_m} \right)} \quad (3.17)$$

I_0 and I_1 are modified Bessel functions of the first kind of order zero and one, respectively. In this calculation it is not possible to distinguish the apical and basal membrane because they are in series. C_m is the average membrane capacitance of both membranes, even though in reality both membranes can differ in their surface area and consequently, in their capacitance. The parameter α is linked to the current flow in the cleft between the cells and the substrate. It is interpreted to describe cell-substrate interactions and is dependent of the cell radius r_c , the resistivity of the electrolyte in the cleft ρ and the distance between cell and substrate h (eq. 3.18).

$$\alpha = r_c \sqrt{\frac{\rho}{h}} \quad (3.18)$$

The parameter R_b describes the influence of the cell-cell contacts and consequently, the strength of the tight junctions (Reiss and Wegener, 2015).

An overview of the parameter used for electrical modeling of a two-dimensional cell layer can be seen in table 3.1.

Table 3.1: Parameters of the electrical modeling of a cell layer with the symbols used in this thesis and the respective units.

modeling parameter	symbol	unit
specific cell membrane	C_m	$\mu\text{F}\cdot\text{cm}^{-2}$
cell-substrate interaction	α	$\Omega^{0.5}\cdot\text{cm}$
resistance of cell-cell contacts	R_b	$\Omega\cdot\text{cm}^2$

In fig. 3.3 the three modeling parameters are varied and the change in the simulated impedance spectra can be seen.

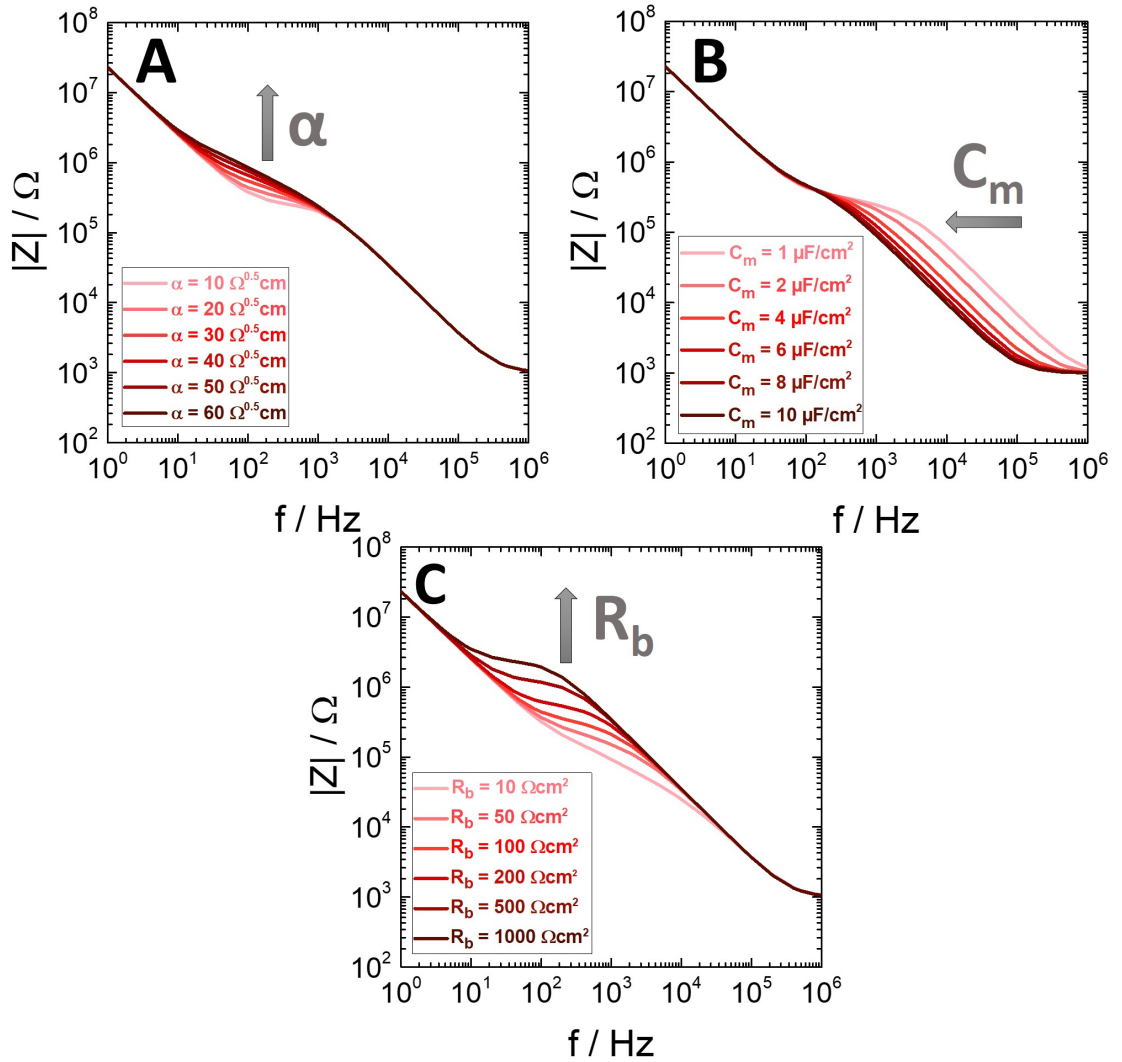


Figure 3.3: Simulated impedance spectra for a cell-covered electrode with alteration of just one parameter while the others were kept constant. **A:** variation of the impedance of the cleft beneath the cells α , **B:** change of the specific cell membrane C_m or **C:** increasing of the barrier function R_b . For the simulation the following parameter were used except the one under study: $\alpha = 20 \Omega^{0.5}\text{cm}$; $R_b = 100 \Omega\text{cm}^2$; $C_m = 2 \mu\text{F}/\text{cm}^2$; $R_{bulk} = 1000 \Omega$; $A_{El} = 5 \cdot 10^{-4} \text{cm}^2$; $n_{CPE} = 0.96$; $A_{CPE} = 15 \cdot \mu\text{Fs}^{n-1} / \text{cm}^2$.

During variation of one parameter the other parameters were kept constant. The changes occur in a range of 10 Hz to 500 kHz where a plateau of the adherent cells can be monitored. With increasing α the slope of the cell plateau is increasing (fig. 3.3 A). Higher cell membrane capacitances lead to a reduced plateau width (fig. 3.3 B). The parameter R_b influences the height of the plateau (fig. 3.3 C).

In the higher frequency range the overall impedance is dominated of the impact of R_{bulk} . This acts as a frequency-independent Ohmic resistor and therefore, can be monitored as a horizontal line (Reiss and Wegener, 2015). R_{bulk} is defined as the sum of the solution resistance R_s and the constriction resistance R_{cs} (eq. 3.19). R_{cs} dominates the equation as long as there is a small distance between CE and WE.

$$R_{bulk} = R_s + R_{cs} \approx R_{cs} \quad (3.19)$$

By fitting the impedance parasitic resistive elements can occur, like the lead resistance R_{lead} or the contact resistance R_{cont} . Those are ohmic elements and influence the whole spectra. Furthermore, dependent on the electrode type the stray capacitance can influence the measured capacitance from 100 kHz to higher frequencies.

3.1.2 Data representation

In the following chapter the representation of the impedance spectra and the calculation of the different types of normalization of the measured impedance are explained. Furthermore, the detrended variance analysis for the interpretation of the micromotion measurements is shown.

3.1.2.1 Impedance spectra

In routine measurements the complex impedance is measured as a function of frequency over several decades (normally from 1 Hz to 1 MHz). Consequently, it is necessary to use a specialized method to represent the whole data. There are two established types of data representation in impedance spectroscopy: i) the *Nyquist* plot and ii) the *Bode* plot (Muñoz-Berbel et al., 2008; Wegener, 2010).

The first type for the representation of the impedance data is the *Nyquist* plot (see fig. 3.4 A). Therefore, the imaginary part is plotted against the real part of the complex impedance. In the case of biological samples the imaginary part is negative due to the absence of inductive elements, consequently $-\text{Im}(Z)$ is shown on the ordinate. With this representation it is not possible to draw conclusions directly about the frequency domain. Normally, an arrow is drawn to monitor the direction in which the frequency is increasing (shown in gray). This plot has the advantage that the

shape of the curve can give information about the electrical structure and which parts of the system differ from an ideal electrical network. Furthermore, it is possible to draw conclusions about the resistance and the capacitance directly from the center and the radius of the semicircle (Muñoz-Berbel et al., 2008; Wegener, 2010). The second data representation method is the most frequently used *Bode* diagram (see fig. 3.4 B). In this diagram the impedance $|Z|$ and the phase shift φ between the current and the voltage are plotted in dependence of the frequency. To obtain an informative spectrum, a logarithmic or semi-logarithmic scale is used, respectively (Muñoz-Berbel et al., 2008; Wegener, 2010).

In fig. 3.4 both simulated plots are shown exemplarily for a cell line with strong tight junctions (here MDCK I cells) and the spectrum of the cell-free electrode (here 8W10E electrodes). The parameters are explained in the following chapters.

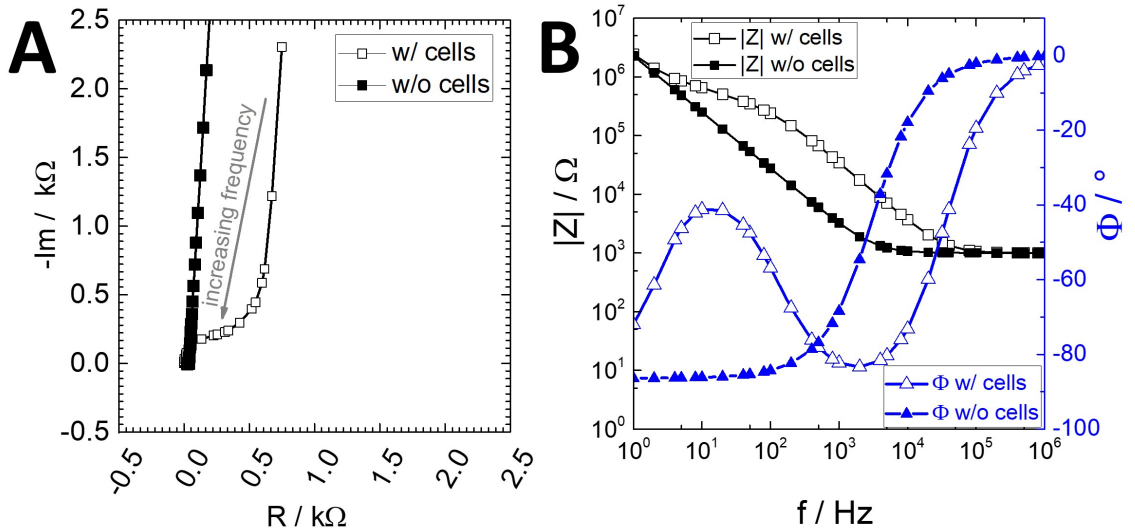


Figure 3.4: An exemplary scheme of a simulated Nyquist plot (A) and a simulated Bode plot (B) with commercially available ECIS electrodes (8W10E). The filled symbols represent the simulated curve of a cell-free electrode and the empty symbols display the simulated curve of a cell-covered electrode with MDCK I cells. The parameter for the simulation are defined as the following: $\alpha = 120 \Omega^{0.5} \text{cm}$; $R_b = 1250 \Omega \text{cm}^2$; $C_m = 2 \mu\text{F}/\text{cm}^2$; $R_{\text{bulk}} = 1000 \Omega$; $A_{\text{El}} = 5 \cdot 10^{-3} \text{cm}^2$; $n_{\text{CPE}} = 0.96$; $A_{\text{CPE}} = 15 \cdot \mu\text{Fs}^{n-1}/\text{cm}^2$.

Although the *Nyquist* plot has many advantages, the most commonly used method of presentation and analyzing is the *Bode* plot. Basis of both presentations is the description of the electrical structure of a biological system by means of an electrical network. The equivalent circuit of the system is a combination of serial or parallel connections of impedance elements like resistors \mathbf{R} , capacitors \mathbf{C} or inductors \mathbf{L} (Wegener, 2010). For example, a simple equivalent circuit model for a cell monolayer is a capacitor in parallel with a resistor. Furthermore for predicting the impedance

of biomaterials, other impedance elements have to be added for ionic phenomena, like adhesion and diffusion (Wegener, 2010). They are derived from empirical experiments, such as the constant phase elements (CPE) or the Warburg impedance. Those are often non-ideal elements and are themselves frequency-dependent (Barsoukov and Macdonald, 2005). The CPE is defined as a non-ideal capacitor and was introduced to describe the interface between the electrolyte and noble metals. The CPE arises from the surface roughness and the specific ion adsorption to interfaces (Wegener, 2010). It is defined by two parameter: i) n_{CPE} and ii) A_{CPE} and the complex impedance is given as followed:

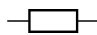
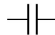

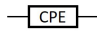
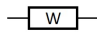
$$Z_{CPE} = \frac{1}{(i2\pi f)^n A} \quad (3.20)$$

For the value of the n_{CPE} two different boundary conditions can be defined: i) the element behaves like an ideal capacitor ($n_{CPE} = 1$) and ii) the CPE resembles a pure resistor ($n_{CPE} = 0$). According to the resistive and capacitive properties of the electrode-electrolyte interface, n_{CPE} ranges between 0 and 1 (Reiss and Wegener, 2015).

The Warburg impedance describes the impedance which arises from the diffusion to an electrode or from an electrode and the related diffusion limitations (Muñoz-Berbel et al., 2008).

Once an appropriate model for an equivalent circuit is found, then the frequency-dependent impedance or so-called transfer function arises from the components by means of Kirchhoff's law and Ohm's law. The impedance contribution of the individual elements of the system is quantified due to iteratively adjusting the data to match the experimental data. This adjustment of the parameter is computed by ordinary least-squares algorithms (Levenberg-Marquardt) (Wegener, 2010). In table 3.2 the most important circuit elements with their corresponding impedance contribution and phase shift are shown to describe biomaterials.

Table 3.2: Overview of the different circuit elements with the corresponding impedance contribution, the phase shift and the symbols used in a circuit circle. $\omega = 2\pi f$ (Wegener, 2010).

circuit element	parameter	impedance Z	phase shift φ	symbol
resistor	R	R	0	
capacitor	C	$1/(i \cdot \omega \cdot C)$	$-\pi/2$	
inductor	L	$i \cdot \omega \cdot L$	$+\pi/2$	
constant phase element	CPE	$1/(i \cdot \omega)^n \cdot A$	$-n \cdot \pi/2$	
Warburg impedance	σ	$\sigma \cdot (1-i) \cdot \omega^{-0.5}$	$-\pi/4$	

Complicated and complex equivalent circuits have to be simplified to prevent a redundant system (too many parameter). It can happen that different circuit models give equally good fits to the experimental data. Therefore, it is necessary to perform independent experiments like microscopic or other spectroscopic methods to have a closer look at the electrical structure of the sample and to approximate the circuit the most appropriate model. Consequently, it is necessary to find the balance between a possible exact equivalent circuit and to avoid a redundant model (Wegener, 2010).

3.1.2.2 Normalized impedance

A different possibility to represent and interpret impedance data is to normalize the impedance. In this thesis two different types of normalized impedance were used: i) the normalized impedance spectra (seen in fig. 3.5 A) and ii) the normalized impedance time course (seen in fig. 3.5 B).

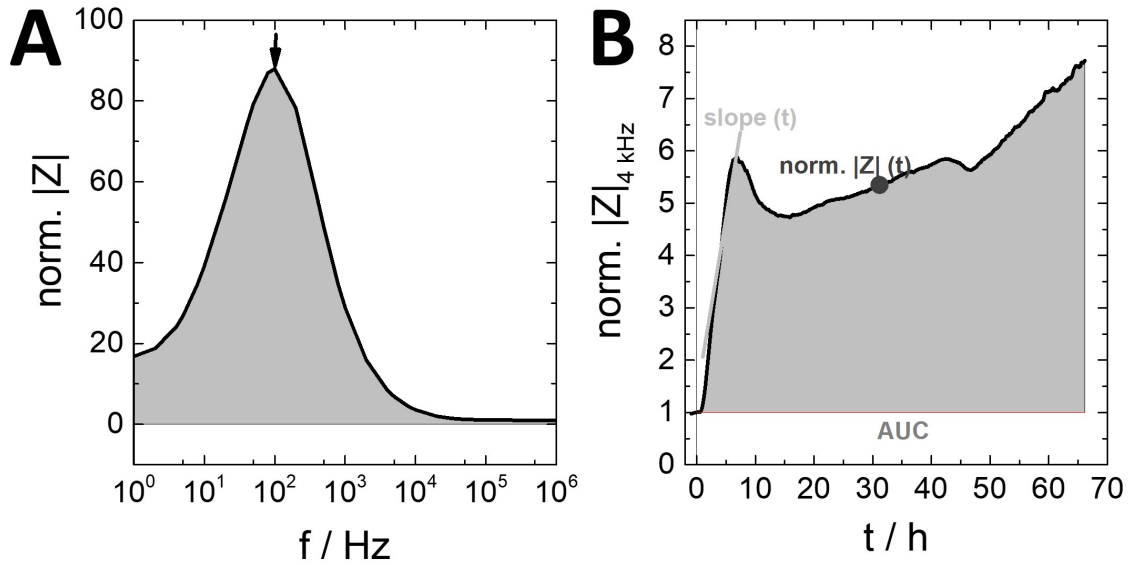


Figure 3.5: Scheme of the two possibilities for normalized impedance representations. The gray area shows the calculated area under the curve (AUC). **A:** Normalized impedance spectra calculated with the simulated spectra of the *Bode* plot in fig. 3.4. The black arrow symbolizes the frequency with the highest impedance magnitude (f_{max}). **B:** Time resolution of the normalized impedance of an adhesion measurement of MDCK I cells at 4 kHz on a commercially available ECIS electrodes (8W10E).

The normalized impedance spectra is defined as the ratio of the spectra of cell-covered electrodes to the spectra of cell-free electrodes. The calculated normalized impedance is plotted against the frequency in a semi-logarithmic manner and as clarified in fig. 3.5 A a frequency dependency can be seen. As an example, the simulated spectra of the *Bode* plot in fig. 3.4 B were used for this calculation and the

representation. There are different aspects of this normalized impedance spectrum which can be analyzed and compared between the different electrode types or even between the different cell lines. The black arrow in fig. 3.5 **A** symbolizes the maximum of the normalized impedance which represents the frequency of the highest sensitivity (f_{max}) which is varying for every cell or electrode type. A further aspect for comparing the data is the area under the curve (AUC). If the same baseline is determined in every spectra, the integrated absolute area between the curve and the baseline can be calculated and compared between the different measurements. This data analysis is also possible for the resistance and the capacitance of a system. The second type of normalization is seen in fig. 3.5 **B**. It is also feasible to monitor the time-dependent change of the impedance, the resistance or the capacitance at different frequencies which can be chosen dependent on the cell line or the interested parameter. For all three parameters most commonly the frequency at which the magnitude of the corresponding parameter is the highest (f_{max}) is chosen, respectively. With regard to the selected frequency of the capacitance care must be taken to avoid inductive and parasitical influences. The time curve is usually normalized to the last value before adding a substance or the cell suspension depending on the experimental setup. There are two possibilities of normalization: i) the difference of the impedance of the last point before addition and each point of the curve ($\Delta|Z|$) or ii) the ratio of the impedance of every single point of the curve to the impedance of the last point before addition (norm. $|Z|$). Normally, the time line on the abscissa is also normalized to the time point of the addition. It is possible to compare the different curve shapes, the area under the curve (in gray), the impedance value at a specific time point (norm. $|Z|$ (t)) or even the slope of the impedance change (slope (t)) (see fig. 3.5 **B**).

3.1.2.3 Error calculation

In this work the errors of the measurements and calculations were expressed by three options: i) the standard deviation (SD), ii) the standard error of the mean (SEM) and iii) the maximum error (max. error).

The standard deviation is defined with the following relation:

$$SD = \sqrt{\frac{1}{N-1} \sum_{i=1}^N (x_i - \bar{x})^2} \quad (3.21)$$

with the number of measurements N , the individual data points x_i and the mean of the sample \bar{x} . Dividing the SD by the square root of the number of measurements results in the standard error of the mean (SEM) (see eq. 3.22).

$$SEM = \frac{SD}{\sqrt{N}} \quad (3.22)$$

The maximum error (max. error) is used in the case of the division or multiplication of two error afflicted data series, for example the normalized impedance spectra (see chapter 3.1.2.2). The normalized impedance spectra is defined as the ratio of the spectra of cell-covered electrodes to the spectra of cell-free electrodes, whereas the spectra were afflicted with errors, respectively. For the calculation of the maximum error, the relative errors of the spectra were added up and the absolute error results from the multiplication of the sum of the relative errors and the calculated ratio of the mean values of the spectra. This absolute error is defined as the maximum error (max. error) in the following work.

3.1.2.4 High time-resolved measurement

Using a high time resolution for the data recording, the micromotion of the cells can be monitored. In this thesis this is measured with the rapid time collection mode (RTC) (described in chapter 4.4.2). To enable the analysis and interpretation of the high time-resolved measurement the detrended variance analysis (DVA) was used. The basis of this straightforward method is to estimate the fluctuation intensity of the data in given time segments by calculating the related variance after detrending for the complete measurement. All parts of the calculation can be performed with a LabView based software (Prof. Wegener, University Regensburg). For each RTC measurement a value for the variance of the data set can be calculated and compared between the different measurements. An example for the calculation is displayed in fig. 3.6 with the distinct calculation steps (raw data were measured with A549 cells at 4 kHz and a commercially available ECIS electrodes (8W1E)).

The time course was monitored with a time resolution of around 1 data point / s (see fig. 3.6 **A**). For the interpretation it is possible to use the impedance or the resistance which is then normalized. Two different types of normalization are available: i) dividing all data points by the mean of the complete measurement (norm. $|Z|$ or rather norm. R) (see fig. 3.6 **B**) or ii) subtract the mean of the complete measurement from every data point ($\Delta |Z|$ or rather ΔR) (not shown). In the next step the time course is divided into small time segments of 4 s, 16 s, 32 s or 64 s (depicted in fig. 3.6 **B** as the dotted lines). In this work only the time segments with 32 s were analyzed. Afterwards, the local trend in each segment is calculated using linear functions (seen in fig. 3.6 **C** as the gray line). These local trends were subtracted from the normalized values in each segment leading to the detrended time series

norm. R_d (fig. 3.6 **D**). The variance of the detrended time series was used as a measure for the intensity of the micromotion.

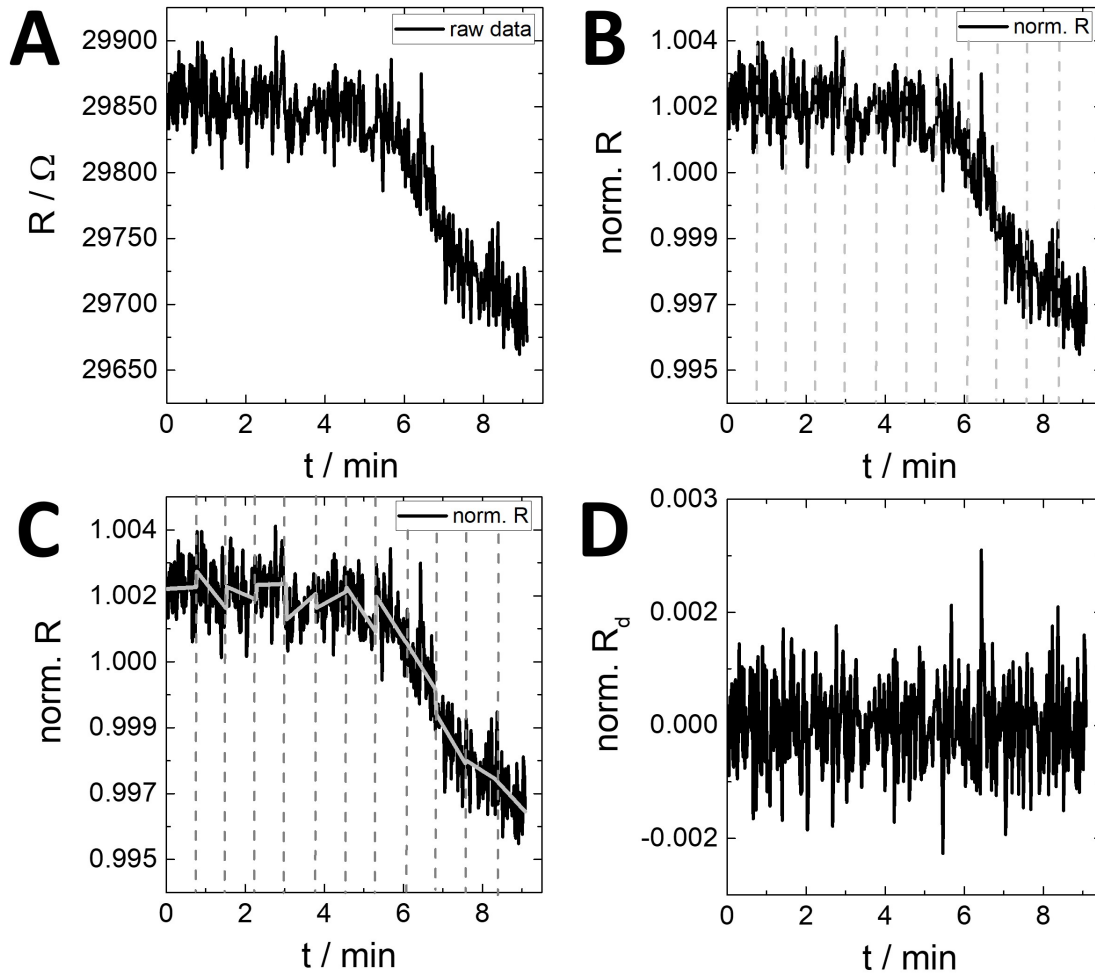


Figure 3.6: Scheme of the calculation of the variance for the RTC measurements by means of the detrended variance analysis (A549 cells, 4 kHz, 8W1E electrode). **A:** time course of the raw data of the resistance, **B:** the normalized resistance (by means of division) with time segments of 32s (dotted lines), **C:** normalized resistance with the local trend in each segment (gray line), **D:** detrended time series by means of the subtraction of the local trend in each segment from the normalized values.

3.2 COMSOL Multiphysics

COMSOL Multiphysics is a software package which is broadly used for modeling and solving physical problems and tasks using partial differential equations. It enables a combination of multiple physics and can therefore be widely used in research, teaching or development. Electrical, mechanical, fluid, acoustic and chemical applications can be simulated and visualized. For each problem a different module

can be used as the AC/DC, semiconductor, molecular flow, heat transfer or electrochemistry module, just to name some. In this thesis the AC/DC module was used for the simulations. The coupling of different physics and modules can be solved simultaneously and simplifies the solution of complex physical questions. All of these modules are based on the finite element method which will be explained shortly.

3.2.1 Finite element method

To analyze complex engineering problems a numerical model was invented to enable a more simplified description of this system. This is based on differential equations and given conditions. For solving these in many cases very difficult equations, the finite element method is used as the major numerical solution technique. The basis of this method is the division of the problem domain into many subdomains, called *finite elements*. As a consequence, the problem domain consists of many small finite element subdomains (Young and Hyochoong, 2000). Those physical properties are more easily calculated due to their simple geometry. The simulation of the whole problem domain is then calculated with respect to the change of the physical properties of one subdomain during the influence of different elements, like forces or boundary conditions. With the propagation of these influences into the adjacent subdomains with the given continuity conditions of the engineered problem, each finite element can be calculated and can be combined for the whole domain (Babuska, 1973). For a better visualization of the division of the problem domain into subdomains an example was simulated in COMSOL Multiphysics (see fig. 3.7).

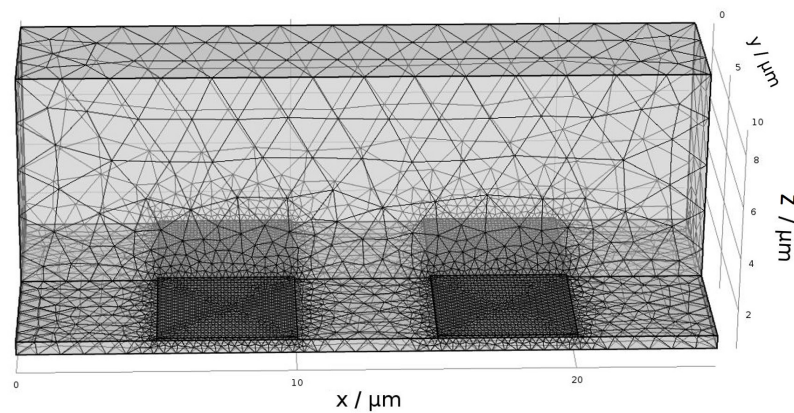


Figure 3.7: Simulated example of two interdigitated electrodes in COMSOL Multiphysics. The simulated gold electrodes have a height of 100 nm and a width and a gap of 5 μm , respectively. They are shown on a substrate with a height of 0.5 μm . The medium is symbolized as a cuboid with a height of 8 μm , a length of 25 μm and a width of 5 μm . The sequence type of the mesh is a physics-controlled one with a fine element size.

In fig. 3.7 two interdigitated electrodes with a gap and a width of 5 μm , respectively, on a substrate can be seen. In this example only half of the medium is shown to provide a better overview. The whole object is covered with a fine physics-controlled mesh symbolizing the division into the subdomains. This mesh was calculated automatically with the software. It can be seen that the closer the subdomains are to the electrodes, the smaller they are. In these areas the changes of the physical properties, for example the electric field or the electric potential, are much higher than in the medium too far away to have a strong influence of the electrodes underneath. As a consequence the subdomains near the electrodes have to be chosen smaller than the ones in the medium to simulate the physical properties as realistic and simple as possible.

3.2.2 The AC/DC module of COMSOL Multiphysics

In this thesis the optional add-on AC/DC module of the COMSOL Multiphysics software version 5.2 a was used. This module is available for simulation of electromagnetics in two-dimensional or three-dimensional studies. It is possible to select between the following types of physics interfaces:

- Electric currents
- Electrical circuit
- Electrostatics
- Magnetic fields
- Rotating machinery
- Particle tracing

In this thesis the interface of the electric currents was used and will consequently be explained shortly in the following. With this module it is further possible to choose between a frequency domain, small-signal analysis, stationary or time-dependent study among others. (COMSOL, 2018).

To use this interface different constitutive relations to describe the macroscopic properties of the medium, the material properties and the relative permittivity have to be defined (COMSOL, 2018). The relative permittivity is defined as followed:

$$\epsilon_r = \frac{D}{\epsilon_0 E} \quad (3.23)$$

with the electric displacementfield D and the electric field E . The relative permittivity ϵ_r is specific for every material, whereas the permittivity of vacuum ϵ_0 is given in

eq. 3.24 with the permeability of vacuum μ_0 and the velocity of an electromagnetic wave in a vacuum c_0 .

$$\epsilon_0 = \frac{1}{c_0^2 \mu_0} = 8.854 \cdot 10^{-12} F/m \approx \frac{1}{36\pi} \cdot 10^{-9} F/m \quad (3.24)$$

The polarization P is defined with the following relation:

$$P = D - \epsilon_0 \epsilon_r E \quad (3.25)$$

The electric polarization vector P is based on the space dimension and describes the polarization of a material when an electric field is present. As a further parameter the remanent electric displacement has to be defined, seen in eq. 3.26, whereas D_r symbolizes the remanent displacement when no electric field is present.

$$D = \epsilon_0 \epsilon_r E + D_r \quad (3.26)$$

In this thesis the stationary study was used. In the case of the stationary electric alternating current it is necessary to consider the stationary equation of continuity. The point form of the Ohm's law shows:

$$J = \sigma E + J_E \quad (3.27)$$

with the current density J , the electrical conductivity σ and an externally generated current density J_E . Consequently, the static form of the equation of continuity is then defined as:

$$\nabla \cdot J = -\nabla \cdot (\sigma \nabla V - J_E) = 0 \quad (3.28)$$

with the scalar electric potential V . This equation can be generalized to handle current sources with the point current source Q_j , as following:

$$-\nabla \cdot (\sigma \nabla V - J_E) = Q_j \quad (3.29)$$

This equation is combined with a Maxwell equation (see eq. 3.30) to:

$$\nabla \cdot D = \rho \quad (3.30)$$

and generalized to handle current sources:

$$-\nabla \cdot ((\sigma + j\omega\epsilon_0)\nabla V - (J_e + j\omega P)) = Q_j \quad (3.31)$$

Repeatedly this equation is generalized to handle current sources yielding the following equation:

$$-\nabla \cdot \frac{\delta}{\delta t}(\epsilon_0 \nabla V - P) - \nabla \cdot (\sigma \nabla V - J_e) = Q_j \quad (3.32)$$

Simulating in a three-dimensional planar manner requires the consideration of the thickness d in the z -direction:

$$-\nabla \cdot d \frac{\delta}{\delta t}(\epsilon_0 \nabla V - P) - \nabla \cdot d(\sigma \nabla V - J_e) = dQ_j \quad (3.33)$$

All equations and derivation in this chapter were adapted to COMSOL, 2018.

4 Materials and methods

4.1 Cell culture techniques

The work with mammalian cells was performed using standard protocols and requirements for standard cell culture laboratory. The following chapter shows an overview of the cell lines used in this thesis, the cultivation protocols and the preparation of the cells for experimental use.

4.1.1 Common cell culture conditions

Sterile conditions are essential for the work with mammalian cells to avoid bacterial contamination. Therefore, all cell culture work was performed in a laminar flow hood. All used material were either sent sterile by the material supplier or were sterilized via heating for 20 min at 120 °C in an autoclave or via sterile filtration with a pore diameter of 0.2 µm.

The cultivation of the cells was executed in cell culture flasks made of polystyrene with a growth area of 25 cm² with 4 mL culture medium. These flasks were stored in a humidified atmosphere in a cell culture incubator at 37 °C and 5 Vol.-% CO₂. The medium was exchanged every third day and 24 h before the beginning of the experiment, and the subcultivation was done once a week according to the standard protocol (see chapter 4.1.3.1). For the Cor.At® a different protocol was used (see chapter 4.1.3.2).

4.1.2 Cell lines

In this thesis ten different adherently growing cell lines were used. Each cell line needed a specific medium with different additives, as shown in table 4.1. On the following pages the different characteristics and references of the cell lines used in this work will be explained shortly.

A549

The A549 cells are a lung tumor cell line from a human alveolar carcinoma (Giard et al., 1973). The tumor cells were removed from a 58-year-old Caucasian male in 1972 for the first time. The cells synthesize desaturated lecithin which utilizes the cytidine diphosphocholine pathway. They grow in a regular epithelial-like and flat monolayer with a doubling time of 48 h (Lieber et al., 1976). The cells were kindly obtained from Prof. Dr. Heilmann (Institute of Pharmacy, University of Regensburg, Germany).

BAEC

The BAEC cell line (*Bovine Aortic Endothelial Cells*) was isolated from a bovine aorta and grow in a cobblestone-like endothelial morphology. It is only possible to replicate the cells *in vitro* for a finite number of times before they undergo a morphological change and a loss of the ability to replicate (Schwartz, 1978). Furthermore, they express the β_1 - and β_2 -adrenoceptors (Zink et al., 1993). The BAEC cells were kindly provided by Dr. Zink and Prof. Rösen from the DDZ (*Deutsches Diabetes Zentrum, Düsseldorf, Germany*).

CHO_D2R

The CHO_D2R cells (*Chinese Hamster Ovary*) were CHO-K1 cells which were isolated from a hamster ovary (Puck et al., 1958). They were transfected with the human dopamine₂ receptor in the long variant (D2_LR) which couples to guanine nucleotide regulatory protein (G-proteins) and to several intracellular second messenger pathways. The CHO_D2R cells are growing in an epithelial-like morphology (Hayes et al., 1992; Stolwijk et al., 2019). The cells were originally provided from the Garvan Institute of Medical Research (Darlinghurst, Australia) and were kindly supplied from the lab of Prof. Dr. Gmeiner (Department of Chemistry and Pharmacy, Erlangen, Germany).

Cor.At® cardiomyocytes

The Cor.At® cardiomyocytes were purchased from Axiogenesis AG. They were primary-like cardiomyocytes derived from mouse embryonic stem cells and were developed for academic and industrial cardiovascular research applications. According to Axiogenesis the cells are highly standardized with a fully functional cardiac phenotype. They exhibit a limited proliferation capacity and consequently cannot be subcultured.

NRK-52E

The NRK cells (*Normal Rat Kidney, epithelioid clone 52 E*) were isolated from the kidney of a normal rat of the species *rattus norvegicus*. They were cloned from a mixed culture in 1966 and studied for the binding of epidermal growth factor, whereby NRK-52E cells are supposed to be more stable. They are flat polyhedral cells which build an epithelial-like monolayer and grow in a cobblestone-like morphology (Duc-Nguyen et al., 1966; de Larco and Todaro, 1978). The NRK-52E cells have a very low transepithelial electrical resistance (TEER) of $(13 \pm 1) \Omega \cdot \text{cm}^2$ (Prozialeck et al., 2006) due to the lack of several tight junctions proteins (Limonciel et al., 2012). Nevertheless, the NRK-52E cells express the cell adhesion molecules occludin, E-cadherin and ZO-1 (zonula occludens-1) (Prozialeck et al., 2006). The cells were purchased from DSMZ (*Deutsche Sammlung von Mikroorganismen und Zellkulturen*). For simplification the NRK-52E cells are named “NRK” cells in the following thesis.

MCF-7

The MCF-7 cell line (*Michigan Cancer Foundation-7*) is a human breast adenocarcinoma cell line which was isolated from a 69-year-old Caucasian woman with a metastatic mammary carcinoma in 1970 (Soule et al., 1973). They grow in an epithelial-like monolayer with a polygonal morphology and express estrogen receptors (Levenson and Jordan, 1997). They possess the adhesion molecule E-cadherin and can form tightly packed, rounded spheroids (Lee et al., 2010). The cells were kindly provided by the research group of Prof. Göpferich (Institute of Pharmacy, University of Regensburg, Germany).

MDCK I and MDCK II

The MDCK (*Madin-Darby canine kidney, Strain I and II*) cell line was isolated from the kidney of a female cocker spaniel in 1958 (Fuller et al., 1984). Two different cell subtypes were cultivated with different characteristics. Strain I was obtained at an early passage (60 serial passages) and Strain II at a later passage (109 serial passages) (Richardson et al., 1981). Strain I grows to a very tight epithelium with a TEER in a range of $(4.16 \pm 0.24) \text{ k}\Omega \cdot \text{cm}^2$, whereas Strain II forms a leaky epithelial monolayer with lower resistance of $(71 \pm 6) \Omega \cdot \text{cm}^2$ (Richardson et al., 1981). The cells grow in a cuboidal epithelial monolayer and the apical cell surface of both strains is covered with microvilli, with the MDCK Strain II having longer and more densely packed ones (Stevenson et al., 1988). Both strains were purchased from the

DSMZ. In the following thesis the low-passage Strain I is defined as “MDCK I”, and the high-passage Strain II is named “MDCK II”.

SK-Mel-28

The SK-Mel-28 cell line is a human malignant melanoma cell line which was isolated from the axillary lymph node of a 51-year-old man. The cell line was isolated by Lloyd J. Old and Toshitada Takahashi in 1975. The cells have a polyglonal morphology and build an adherent monolayer (Carey et al., 1976; Fogh et al., 1977; Xing et al., 2012). The cell line was purchased by the *Cell Lines Service* (CLS).

U373 MG

The U373 MG cell line was initiated by J. Pontén and B. Westermark at the University of Uppsala in 1968. It is a human glioblastoma astrocytoma cell line originated from the malignant brain tumor tissue of a 50-year old man. The cells are growing in a glial morphology with a variable pattern produced by large, flat cells. The cells express the human histamine 1 receptor (H₁R) (Bigner et al., 1981; Ponten and Magintyre, 1968). Furthermore, it is possible to build tightly packed, rounded spheroids. The cell line was kindly provided by Prof. Buschauer (Institute of Pharmacy, University of Regensburg, Germany). In the following thesis the cell line is abbreviated to “U373”.

Table 4.1: All cell lines used in this thesis with the corresponding culture medium and the necessary additives. DMEM: dulbecco's modified eagle's medium; MEM-Eagle: Minimum essential medium eagle; FCS: fetal calf serum. In each medium 100 µg/mL penicillin and streptomycin were added, respectively.

Cell Line	Culture Medium	L-Glutamine	FCS	further additives
A549	DMEM/F-12 (1:1) 1.2 g/L NaHCO ₃ 3.15 g/L D-Glucose	-	5 %	
BAEC	DMEM 3.7 g/L NaHCO ₃ 1.0 g/L D-Glucose	4 mM	10 %	
CHO_D2R	DMEM/F-12 (1:1) 1.2 g/L NaHCO ₃ 3.15 g/L D-Glucose	2 mM	10 %	1 mg/mL G418 250 mg NaHCO ₃
Cor.At®	Cor.At® culture medium			10 µg/mL puromycin
NRK	DMEM 3.7 g/L NaHCO ₃ 4.5 g/L D-Glucose	2 mM	5 %	
MCF-7	MEM-Eagle 2.2 g/L NaHCO ₃ 1 g/L D-Glucose	2 mM	10 %	1 mM Pyruvat
MDCK I	MEM-Eagle 2.2 g/L NaHCO ₃ 1 g/L D-Glucose	4 mM	5 %	
MDCK II	MEM-Eagle 2.2 g/L NaHCO ₃ 1 g/L D-Glucose	4 mM	5 %	
SK-Mel-28	DMEM 3.7 g/L NaHCO ₃ 4.5 g/L D-Glucose	2 mM	10 %	
U373	MEM-Eagle 2.2 g/L NaHCO ₃ 1 g/L D-Glucose	2 mM	5 %	

4.1.3 Subcultivation of the different cell lines

In this work two different protocols for subcultivation were used: i) The standard protocol was applied to nine individual cell lines. The subcultivation for the different cell lines differed in various incubation times, the use of EDTA (ethylenediaminetetraacetic acid) and different centrifugation parameters. ii) For the Cor.At® a specific protocol had to be used.

4.1.3.1 Standard protocol for subcultivation of the cell lines

Once a week the cells were cultivated according to the standard cultivation protocol (see table 4.2). An exception were the CHO_D2R cells which were cultivated twice per week with the same protocol[†]. The individual steps of the subcultivation of the different cell lines were similar except for different incubation times with EDTA and trypsin (see table 4.2).

Table 4.2: The standard protocol of the subcultivation of different cell lines. The main differences of the subcultivation of the individual cell lines were the incubation with EDTA, the incubation time of trypsin and the centrifugation. In the case of MDCK I trypsin with a five times higher concentration was used*.

cell line	incubation time with EDTA / min	incubation time with trypsin / min	centrifugation at RT	seeding for one week
A549	only washing	8-10	110 g, 10 min	1:10
BAEC	only washing	5	110 g, 10 min	1:10
CHO_ D2R	only washing	3-5	110 g, 10 min	1:25 [†]
NRK	10	10	110 g, 10 min	1:20
MCF-7	only washing	5	200 g, 5 min	1:25
MDCK I	2 x 10	10*	110 g, 10 min	1:20
MDCK II	10	10	110 g, 10 min	1:20
SK-Mel-28	only washing	3-5	200 g, 5 min	1:15
U373	only washing	3	110 g, 10 min	1:10

All solutions used had to be heated in a 37°C warm water bath for 10 min. As a first step of the cultivation, all cell lines were washed twice with 4 mL pre-heated PBS⁻⁻ (phosphate buffered saline without additives of Ca²⁺ and Mg²⁺) to remove dead cells and divalent cations. They would disturb the detachment of the cells from the cell flask. Only NRK and MDCK II cells needed 10 min of incubation

with EDTA (1 mM in PBS⁻⁻), whereas it was necessary in the case of MDCK I cells to incubate twice for 10 min with EDTA. Afterwards the cells were incubated with a trypsin solution (0.05 % (w/v) in PBS⁻⁻) with different incubation times. For the detachment of MDCK I cells a higher concentration of the trypsin solution (0.25 % (w/v) in PBS⁻⁻)* was necessary. To accelerate the cell detachment the culture flask were carefully tapped on a solid substrate. After dilution with 10 mL of the corresponding culture medium the cell suspension was centrifuged at room temperature (RT) with 110 g for 10 min or 200 g for 5 min. The supernatant was removed and the cell pellet was resuspended with the corresponding culture medium. As the last step, the cells were seeded in the cell specific density in a new culture flask. The CHO_D2R cells were seeded 1:25 for three to four days[†]. In table 4.3 the composition of all used basic buffers were listed. Buffers were stored at 4°C until usage and if necessary filtrated sterile.

Table 4.3: Composition of the phosphate buffered saline (PBS), the earle's balanced salt solution (EBSS) and the L-15 medium.

	PBS ⁻⁻	PBS ⁺⁺	EBSS ⁺⁺	EBSS ⁺⁻	L-15 medium
NaCl	140 mM	140 mM	140 mM	140 mM	138 mM
KCl	2.7 mM	2.7 mM	5.3 mM	5.3 mM	5.3 mM
Na ₂ HPO ₄	8.1 mM	8.1 mM	-	-	1.3 mM
NaH ₂ HPO ₄	-	-	1.0 mM	1.0 mM	-
KH ₂ PO ₄	1.5 mM	1.5 mM	-	-	0.44 mM
Ca ²⁺	-	0.9 mM	1.8 mM	-	1.26 mM
Mg ²⁺	-	0.5 mM	0.8 mM	0.5 mM	0.99 mM
NaHCO ₃	-	-	26.2 mM	26.2 mM	-
D-Glucose	-	-	5.6 mM	5.6 mM	-

4.1.3.2 Protocol for cultivation of the Cor.At® cell line

The Cor.At® mouse embryonic stem cell-derived cardiomyocytes were obtained from Axiogenesis as frozen cryovials and were stored in the gas phase of the liquid nitrogen tank until use. Every vial contained 1 million cells. The day before subcultivation, the culture medium and the stock solution of puromycin (10 mg/mL) were thawed at 4°C over night protected from light. For the selection 50 mL culture medium was supplemented with 50 µL of the selection antibiotic (puromycin, stock solution (10 mg/mL)) and stored at 4°C. The next day the vial with the cardiomyocytes was removed from the liquid nitrogen tank and immediately thawed for 2.5 min at

37°C in the water bath. Then, the cell suspension was carefully added drop by drop to 7 mL culture medium. The cryovial was rinsed once with 1 mL culture medium to ensure that all cells were transferred to the 50 mL tube. The cells were centrifuged with 200 g for 5 min at RT and the pellet was resuspended with 4 mL puromycin containing culture medium resulting in a cell concentration of 250,000 cells/mL.

For the experiments with the cardiomyocytes the growing area of the electrodes was reduced with glass rings (inner diameter 4 mm) which were glued onto the electrodes, as shown in chapter 4.3. A day before thawing the cells the 8W1E arrays and the IDEs were sterilized for 30 s and 1 min, respectively, in the argon plasma and incubated over night with DMEM without supplements at 34°C and 5% CO₂. After removing DMEM every electrode was incubated with a fibronectin solution (10 µg/mL in PBS⁻⁻) for 3 h at 34°C. Afterwards, the cells were seeded in the glass ring of the coated electrodes in a density of 100,000 cells/cm². To guarantee a uniform distribution of the cells on the electrodes, the electrodes were put in the laminar flow hood for 30 min before they were stored in the cell incubator (34°C, 5% CO₂). After 1 h the complete electrode chambers surrounding the small glass rings were filled with 400 µL culture medium to avoid the liquid to vaporize. Four electrodes were connected to the measurement setup to trace the adhesion of the cells, the other electrodes were stored in the incubator until they were measured (34°C, 5% CO₂). All electrodes were fed after 24 h with puromycin containing medium. 48 h after seeding the medium was replaced with Cor.At® culture medium without puromycin.

4.1.4 Cryopreservation and recultivation

For storing the cells for a longer time it is necessary to deep-freeze them in a cryogenic tank. The almost confluent cell layer on the culture flask was treated with the same steps as the subcultivation (see chapter 4.1.3.1). After centrifugation the cells were resuspended in a freezing medium (90% FCS (v/v) and 10% (v/v) DMSO). DMSO acted as a cryoprotective agent and prevented the formation of ice crystals which would harm the cells. Afterwards, the cell suspension was filled in cryovials and cooled down to -80°C. It was important to achieve a constant cooling rate of -1°C /min using an isopropanol bath. After 24 h the cells were stored in liquid nitrogen at -196°C.

To recultivate the frozen cells the cryovials were taken from the cryogenic tank and stored at -20°C for 1-2 h. Afterwards, the cell suspension was carefully thawed in a 37°C warm water bath and filled into a 50 mL tube. 10 mL of a prewarmed medium was dropped slowly to the cells and the suspension was centrifuged with the respective setting of the cell line (see table 4.2). The resuspended cell suspension

was added to the culture flask in the appropriate dilution of the original cell density depending on the growth area and the medium was exchanged after 24 h. Then the cells were cultivated with the standard protocol.

4.1.5 Preparation of a monolayer of the cells for experiments

In order to be able to repeat the experiments, the cells had to be seeded in a defined ratio on electrodes or respective measurement arrays. Therefore, the cell number was counted with a hemocytometer after resuspension and diluted with the respective culture medium. For all measurements the cell densities in table 4.4 were used. The only exception was the proliferation measurement at which the cells were seeded with a density of 10,000 cells / cm².

Table 4.4: Seeding densities of the different cell lines and the necessary coating. The cultivated cells were measured during spreading or after 72 h.

cell line	cell seeding density / (cells / cm ²)	coating
A549	320,000	none
BAEC	200,000	0.5 % gelatine in H ₂ O
CHO_D2R	100,000	none
NRK	450,000	none
MCF-7	80,000	none
MDCK I	450,000	none
MDCK II	450,000	none
SK-Mel-28	50,000	none
U373	100,000	none

Before adding the diluted cell suspension the corresponding substrate was sterilized (argon plasma for 1 min (IDEs) or 30 s (ECIS array)). Afterwards, the electrodes were incubated with a 10 mM cysteine solution (87 mg cysteine, 430 mg NaCl, 50 mL H₂O) for 10 min at RT. The electrodes were washed three times with water and one time with culture medium before the cell suspension was added. For the ECIS electrodes, Fraunhofer EMFT and self fabricated electrodes a volume of 400 µL and for the Metrohm DropSens electrodes a volume of 160 µL was used. Seeding the BAEC cells required a coating of the electrodes. The corresponding electrodes were sterilized with the argon plasma and incubated with 200 µL of a 0.5 % gelatin solution. After 30-45 min the solution was removed and the BAEC cell suspension was added.

4.1.6 Preparation of Spheroids of U373 cells

The spheroids were formed with U373 cells using the liquid overlay technique. The cells were detached and centrifuged with the standard protocol (see table 4.2). The resuspension was done with culture medium with an addition of 20 mM HEPES (4-(2-hydroxyethyl)-1-piperazineethane-sulfonic acid) to enable the incubation overnight in an incubator without CO₂. Then, 200 μ L of the cell suspension with a concentration of 26,000 cells/well were added to a 96-well microtiter plate. This plate was filled one day before with 50 μ L/well of 1.5 % (w/v) agarose gel in serum-free U373 culture medium without additives. To support the forming of the spheroids the 96-well plates were hermetically closed with a parafilm and put in an incubator (0 % CO₂, 37°C) on an orbital shaker. This shaker was moving with 120 rpm for 4 h directly after seeding and then overnight with 50 rpm. On the next day the plates were stored in the cell incubator (5 % CO₂, 37°C) without shaking until the spheroids were used. In this work the spheroids were three days old.

4.2 Microscopic techniques

This chapter focuses on the two different microscopes used in this study: i) phase contrast microscope and ii) confocal laser scanning microscope. Furthermore, the cytochemical staining of living and dead cells, the cell nuclei, the tight junctions, the actin cytoskeleton and the unspecific staining of the cell membrane is explained in addition to the corresponding preparation of the samples.

4.2.1 Applied microscopes

Phase contrast microscope

Thin biological samples have a small contrast when they are examined with standard bright-field light microscopy; they appear almost invisible due to a poor light absorption. With a phase contrast microscope a contrast of the sample can be achieved and visualized without staining the cells. The working principle of the phase contrast microscopy is that the phase of the light is shifted passing through the transparent sample depending on its refractive index or the thickness of the structures. The phase shift can be factored into the amplitude change which can be recognized as a difference in image contrast. In a standard bright-field microscope a phase ring and a condenser annulus can be introduced to convert it into a phase contrast microscope. Those convert the phase difference in an amplitude difference

and segregate the undiffracted and diffracted light (Köhler and Loos, 1941, Zernike, 1942).

In this work an inverted phase contrast Nikon Diaphot microscope was used to take images of adherent cells. Two different magnifying objectives were available: i) PLAN 4x / 0.13 and ii) PLAN 10x / 0.25 with a four and tenfold magnification and a numerical aperture (NA) of 0.13 and 0.25. The images were recorded with a digital camera attached to the microscope.

Confocal laser scanning microscope

All fluorescent images in this study were recorded with a *confocal laser scanning microscope* (CLSM). The principle of the CLSM is shown in fig. 4.1 and will be explained in the following.

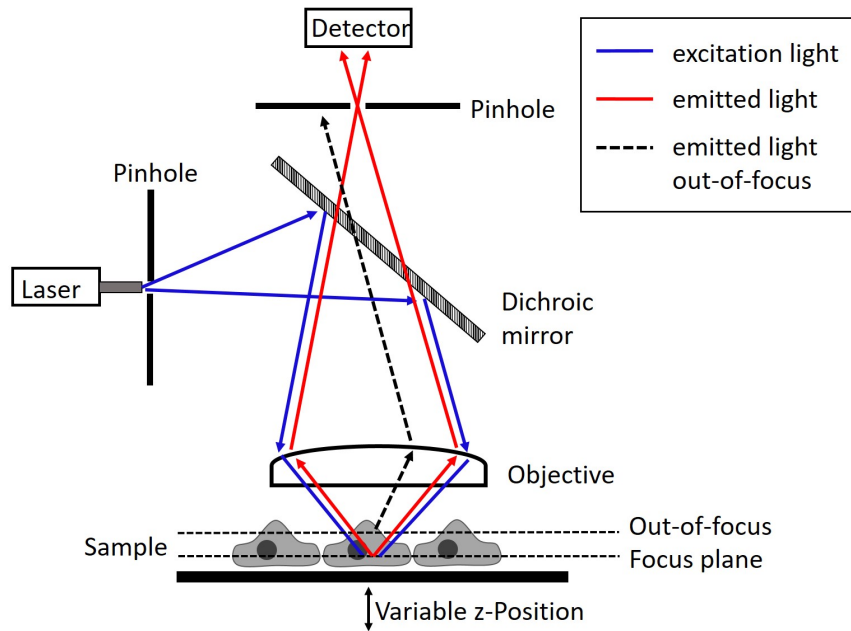


Figure 4.1: Schematic principle of a confocal laser scanning microscope (CLSM).

The CLSM utilizes the light of a monochromatic laser (seen in blue), which is confined by a pinhole and reflected at a dichroic mirror. An objective is used to focus the laser beam on the focus plane of the sample to excite the dye. The emitted light (depicted as the red line) is directed via the objective through the dichroic mirror where it can pass without reflection. After passing the pinhole the emitted light is monitored by the detector. The emitted light which was out-of-focus (black dotted line) can pass the dichroic mirror but is blocked by the pinhole to hit the detector. This microscope setup guarantees that only the emitted light from the dyes in the focus plane is detected. To increase the resolution the sample in the focus plane is scanned sequentially point-by-point. Varying the z-position of the focus plane (in

steps of 0.1 to 1 μm) makes it possible to generate a three-dimensional model of the sample.

The confocal laser scanning microscope used in this work had three different lasers and three different detectors (shown in table 4.5).

Table 4.5: Summary of different lasers, detectors and objectives of the Nikon Eclipse 90i confocal laser scanning microscope used in this thesis. BP: band pass, LP: long pass; NA: numerical aperture.

Laser	Detector	Objectives/ Magnification / NA
408 nm	450 / 35 nm BP (blue)	PLAN / 10 x / 0.25
488 nm	515 / 30 nm BP (green)	PLAN / 20 x / 0.40
543 nm	650 nm LP (red)	PLAN / 60 x / 1.0 water

4.2.2 Cytochemical staining

Different cell characteristics, like cell nuclei or the actin filaments, were stained specifically using protocols which are shortly explained in the following chapter. Some staining needed a fixation and a permeabilization step. In this thesis the Live/Dead, carbol fuchsin, phalloidin, DAPI and ZO-1 staining were applied. All solutions with dye and the washing solutions containing remains of the dye had to be disposed of as hazardous waste.

4.2.2.1 Fixation and permeabilization

It is often necessary to fix the cells to exclude changes of the structural characteristics because of the different staining steps. The confluent cell layers were carefully rinsed twice with PBS⁺⁺ and fixed with 4 % (w/v) PFA (*paraform aldehyde*) in PBS⁺⁺ for 10 min at RT. Then, the cell layers were washed repeatedly two times with PBS⁺⁺ before they were permeabilized to enable the dyes to enter the cell. This was done by addition of 0.5 % (v/v) triton-X-100 in PBS⁺⁺ for 10 min at RT. Finally, the cell layers were washed twice with PBS⁺⁺ to remove the detergent. These cell layers could be used immediately for staining or were stored in the fridge under PBS⁺⁺ for later use.

4.2.2.2 Live/Dead staining

Living and dead cells can be stained simultaneously with a Live/Dead viability/cytotoxicity kit without permeabilization or fixation. This kit contains a mixture of

two dyes: i) Calcein Acetoxymethylester (CaAM) is used to image living cells. This non-fluorescent molecule is highly membrane permeable. After entering a healthy cell the acetoxymethylester group is cleaved by intracellular esterases. The resulting molecule has a high affinity for binding of Ca^{2+} which increases the green fluorescence. This detectable green fluorescence marks living cells. ii) Dead cells can be visualized with Ethidium homodimer (EthD-1) which is an indicator for the loss of integrity of the cell membrane. EthD-1 can only enter heavily damaged or dead cells where it intercalates in the DNA. After intercalation the dye shows a bright red fluorescence which can be monitored with an excitation of 543 nm. In conclusion, damaged or dead cells appear red in the microscopic image whereas living cells show a green fluorescence.

The Live/Dead staining was used for visualization of spread spheroids on the electrodes, cell monolayers on the electrodes and the changes in a confluent monolayer after the influence of different concentrations of bisphenol A. First, a 4 μM solution of EthD-1 (stock solution: 2 mM in DMSO) and a 2 μM solution of CaAM (stock solution: 1 mM in DMSO) in PBS^{++} was prepared. The samples were washed once with PBS^{++} and the staining solution was added in an appropriate volume to cover all the cells. The incubation was done for 30 to 40 min in a dark incubator (0 % CO_2 , 37°C). Afterwards, the stained samples were either washed twice with PBS^{++} or microscopied directly with the confocal laser scanning microscope using the 10x and 60x magnification. EthD-1 was excited at 543 nm and the red emission was detected with a 650 LP detector. CaAM was excited at 488 nm and the green fluorescence was recorded with a 515 / 30 nm detector.

4.2.2.3 Unspecific staining with carbol fuchsin

Carbol fuchsin consists of a mixture of phenol and basic fuchsin and is a component of the Ziehl-Neelsen stain which is commercially used for bacterial staining. It binds unspecifically to components of the cell membrane.

In this work spheroids were stained with carbol fuchsin. The spheroids were allowed to settle to electrodes until they adhere and spread centrosymmetrically outwards and built a three-dimensional cell aggregate. After three days of adhesion the medium was aspirated and 200 μL undiluted carbol fuchsin solution was added for 5 min at RT. Excess dye in the solution was removed by washing the spheroids at least five times with 300 μL warm PBS^{++} until the supernatant showed no red coloring anymore. Images of the stained spheroids were taken with a phase contrast microscope and the integrated digital camera.

4.2.2.4 Staining of the cell nuclei with DAPI

It was further possible to stain the cell nuclei with DAPI (4', 6-diamidino-2-phenylindole dihydrochloride). DAPI can pass permeabilized cell membranes and binds to the adenine-thymine rich areas. This binding increases the blue fluorescence of the molecule.

The DAPI stock solution (100 ng/mL) was stored at -20°C and diluted with a factor 1:10 with PBS⁺⁺ resulting in a concentration of 10 ng/mL. The fixed and permeabilized cells were incubated with the DAPI solution (10 ng/mL) for 2 min at RT. After three times rinsing with PBS⁺⁺ the stained cells could be imaged with the CLSM. DAPI was excited with a laser of 408 nm and recorded with the 450 / 35 nm BP detector.

4.2.2.5 Tight junction staining with ZO-1 immunostaining

Tight junctions are the seal between neighboring cells and define the diffusion barrier of the paracellular pathway. They can be detected via an immunostaining of the ZO-1 protein which is located on the cytoplasmatic side of the membrane. Among others it is important for endothelial barrier formation and cell-cell tension (Tornavaca et al., 2015).

The tight junctions were stained with the following protocol. The fixed and permeabilized samples were incubated with 3% (w/v) BSA (*bovine serum albumine*) in PBS⁺⁺ for 20 min at 37°C to block unspecific binding of the antibodies. After removing the BSA, the monoclonal anti-ZO-1 antibody from mouse (stock solution: 500 µg/mL) with a dilution of 1:200 in 0.5% (w/v) BSA in PBS⁺⁺ was added and incubated for 1 h at 37°C. To remove the unbound antibodies the sample was washed three times with PBS⁺⁺. Afterwards, the second polyclonal anti-mouse antibody (stock solution: 2 mg/mL) which was labeled with ALEXA fluor 546 was diluted with a factor of 1:250 in PBS⁺⁺ supplemented by 0.5% (w/v) BSA. The cells were incubated for 40 min at 37°C protected from light. After removing the unbound antibodies via washing for three times with PBS⁺⁺ the samples could be imaged at the CLSM. The fluorophore was excited at 543 nm and detected with a 650 nm LP detector.

4.2.2.6 Staining of the actin cytoskeleton with phalloidin

The actin cytoskeleton was stained with fluorescently labeled phalloidin. Phalloidin is a fungal phallotoxin, isolated from the death cap mushroom (*Amanita phalloides*). It binds strongly to all variants of actin filaments which can be used for cellular

imaging applications.

In this work two different labeled phalloidin were used: i) TRITC phalloidin (red) with a stock solution with a concentration of 0.3 mg/mL, and ii) phalloidin alexa-fluor 488 (green) with a stock solution with a concentration of 8.7 mg/mL. The protocol is identical for both labels. Both solutions were stored at -20 °C. First, the phalloidin stock solution was diluted with a factor of 1:100 with PBS⁺⁺. The fixed and permeabilized samples were incubated with the respective solution for 40 min at 37 °C in a dark incubator. After three times of rinsing with PBS⁺⁺ the sample could be analyzed with the CLSM. The samples labeled with TRITC phalloidin were excited with 543 nm and recorded with a 650 LP detector. Samples with phalloidin alexa-fluor 488 were excited with 488 nm and detected at 515 / 30 nm.

4.3 Interdigitated electrodes for impedance analysis

In this thesis different electrode layouts were used to record the impedance of adherent cells. The gold IDEs were either provided from Metrohm DropSens (Filderstadt, Germany) and Fraunhofer EMFT (Munich, Germany) or were self fabricated with a photolithographical process. To compare the obtained results commercially available ECIS electrode arrays from Applied BioPhysics (Troy, NY) were used. The following chapter describes the different layouts and the process of photolithography.

4.3.1 Layout of the interdigitated electrodes

In this work six different layouts of interdigitated gold electrodes were used. They consist of two electrodes with interdigitating fingers and a defined width (w) and gap (g) (see fig. 4.2). Those differ between every electrode types which are named after the respective pitch (p), defined as the sum of the width of one electrode and one gap.

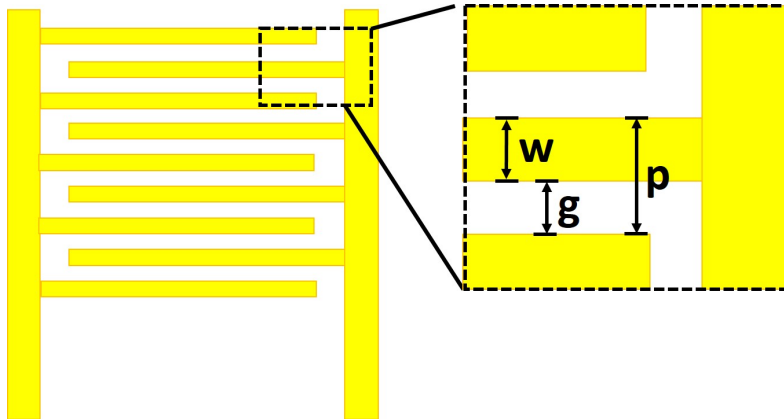


Figure 4.2: Schematic layout of the interdigitated gold electrodes. The straight fingers of the two electrodes form a comb-like structure which interdigitate in a given gap (g). Every finger has a defined width (w). The sum of the width of one electrode and the respective gap is defined as the pitch (p) of an electrode, according to which the individual electrode types are named.

The different IDEs used in this work are summarized in table 4.6 with the respective producers and names. The substrates of the electrodes provided by Fraunhofer EMFT (Munich, Germany) and Metrohm DropSens (Filderstadt, Germany) consist of glass, whereas the self-fabricated electrodes were sputtered onto a LEXAN® plate.

The provided electrode types from Fraunhofer EMFT (Munich, Germany) and Metrohm DropSens (Filderstadt, Germany) can be seen in fig. 4.3. To use those it was necessary to insulate the leads which is explained in the next chapter.

Table 4.6: Summary of the interdigitated electrodes used in this thesis. The electrodes differ in the width of each finger (w) and the gap between the electrodes (g). The respective pitch defines the naming of each type. The electrodes were provided from Fraunhofer EMFT (Munich, Germany) and Metrohm DropSens (Filderstadt, Germany) or were produced at the University of Regensburg (UR) by photolithography.

naming	width (w) / μm	gap (g) / μm	pitch (p) / μm	producer
IDE 7	4	3	7	Fraunhofer EMFT
IDE 10	5	5	10	Metrohm DropSens
IDE 12	6	6	12	Fraunhofer EMFT
IDE 20	10	10	20	Metrohm DropSens
IDE 300	150	150	300	UR
IDE 400	200	200	400	UR

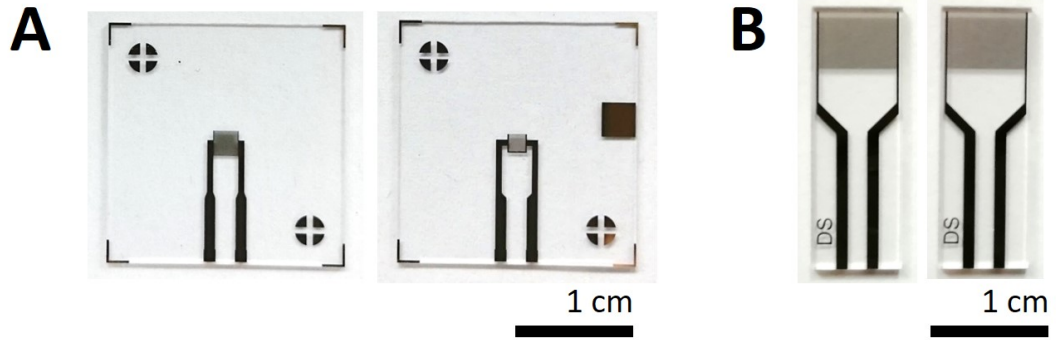


Figure 4.3: Photographs of the provided electrodes. **A:** Image of the two electrode types supplied by Fraunhofer EMFT: (*left*) IDE 7 and (*right*) IDE 12. **B:** Image of the electrodes from Metrohm DropSens: (*left*) IDE 10 and (*right*) IDE 20.

4.3.1.1 Preparation of IDEs by photolithography

The process of photolithography was the method of choice for structuring the IDE 300 and IDE 400 and for insulating the leads of every electrode type. Additionally, it was used to define various electrode areas which were not covered with photoresist: i) $(0.5 \times 0.5) \text{ mm}^2$, ii) $(1.1 \times 1.1) \text{ mm}^2$ and iii) $(2.0 \times 2.0) \text{ mm}^2$. These non-insulated electrode areas are defined as *windows* in the following thesis.

The complete process can be seen in fig. 4.4. The fabrication of the self designed electrodes is shown in step (1) to (6), whereas the insulation of the leads and the variation of the window sizes are schematically drawn in step (7)-(9).

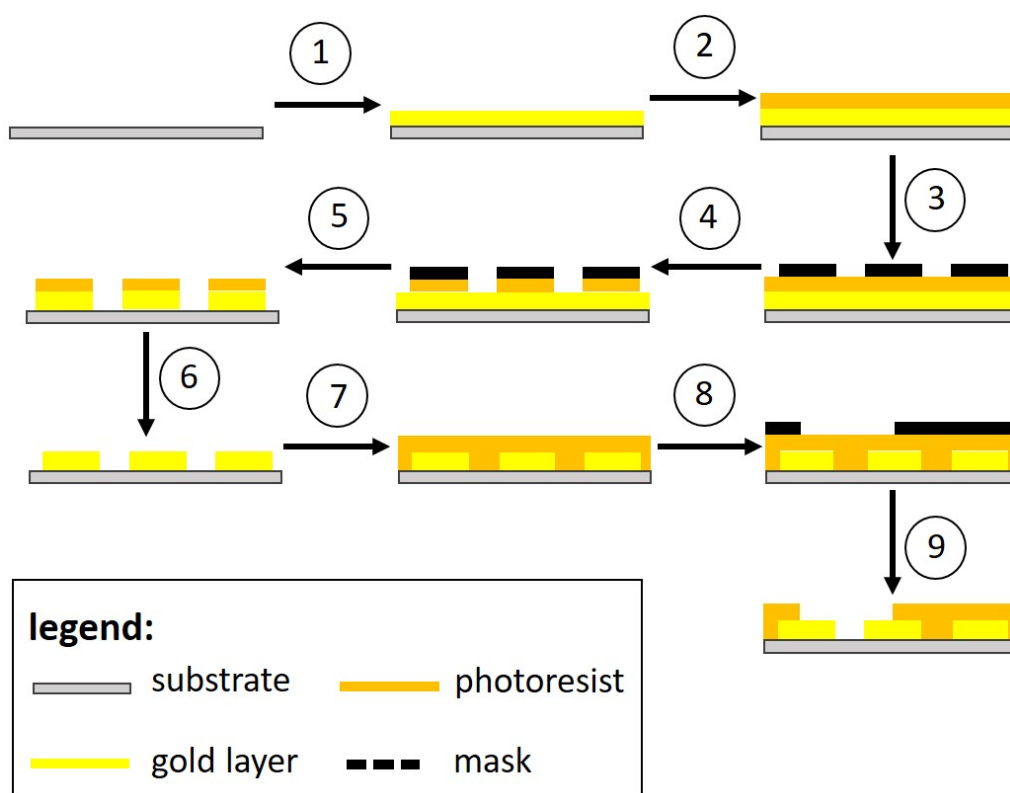


Figure 4.4: Schematic of the photolithographical process to fabricate IDE 300 and IDE 400 used in this work and the following steps to insulate the leads and to create different active electrode areas. The gold layer and photoresist layer are not drawn to scale.

The self fabricated IDE 300 and IDE 400 were prepared by a photolithographical method seen in fig. 4.4 step (1)-(6).

LEXAN® plates served as substrates and were cleaned and hydrophilized in the first step in argon plasma for 1 min and afterwards, they were coated with a 100 nm thick gold layer with a sputter coating device (fig. 4.4 (1)). The sputtered substrates were coated uniformly with a positive photoresist by means of a spin coater with 2,000 rpm for 1 min (fig. 4.4 (2)). The photoresist was cured via a soft-bake step (100°C, 30 min). Then the photoresist was exposed 2 min to UV light through a self designed mask (fig. 4.4 (3)). The masks were printed in an UV blocking black dye on a transparent foil with a foil printer (see fig. 4.5 A). The mask protected the polymer at the specific positions that determined the later gold structure. The irradiated photoresist was developed for 20 s with a solution of sodium hydroxide (7 g/L) in double distilled water. It was removed leading to a free gold layer (fig. 4.4 (4)). In the next step the uncovered gold layer was etched for 30 s under constant agitation (fig. 4.4 (5)). As an etching reagent an aqueous solution of KI (0.265 mM) and I₂ (0.499 mM) was used. The dissolved gold was removed by washing the substrate two times with double distilled water. The rest of the photoresist was removed via irradiation with UV light without mask for 2 min and further development with a sodium

hydroxide solution (7 g/L) (fig. 4.4 (6)). The masks used for the photolithography and an image of the self fabricated IDEs can be seen in fig. 4.5.

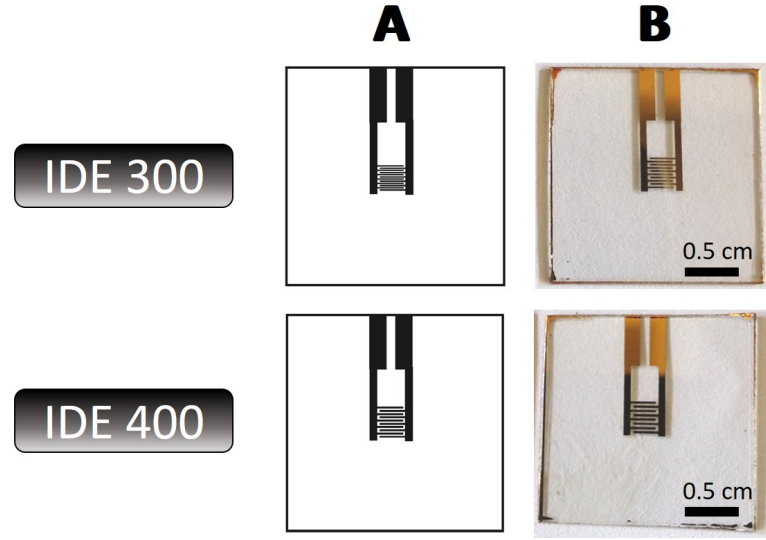


Figure 4.5: Images of the self fabricated IDEs. IDE 300 (width 150 μm , gap 150 μm (*top*)) and IDE 400 (width 200 μm , gap 200 μm)(*bottom*) were fabricated. The masks used for the photolithographical process can be seen in **A**. The photographic image is shown in **B**.

4.3.1.2 Fabrication of different window sizes

It is necessary to insulate the leads of the IDEs to avoid undefined electrode areas and consequently different influences on the capacitance. As an additionally experimental setup, the non-insulated electrode areas were varied. These active electrode areas are defined as *windows* in the following work. The individual steps for the process of the preparation of the windows are schematically shown in fig. 4.4 step (7)-(9).

First, the substrates with the electrodes have to be cleaned with different steps to ensure a clean and dry surface of the substrate. Every electrode type needed a different cleaning procedure:

Fraunhofer electrodes The electrodes provided by Fraunhofer EMFT (Munich, Germany) were covered with a protective film. This film was removed in several steps. The first step was to treat the substrates with acetone for 3 min in an ultrasonic bath. Secondly, the acetone was exchanged and the step was repeated for 1 min. As third step, the substrates were immersed into isopropanole and treated 1 min in the ultrasonic bath. After three times washing with double distilled water the substrates were dried for 30 min at 120 $^{\circ}\text{C}$ in an oven.

Metrohm DropSens electrodes The electrodes supplied by Metrohm DropSens (Filderstadt, Germany) were immersed for 3 min in acetone and treated with isopropanole for 1 min. After three times washing with double distilled water the substrates were dried for 30 min at 120 °C in an oven.

self fabricated electrodes The self fabricated electrodes were washed 1 min with isopropanole. After washing with double distilled water the substrates were dried for 30 min at 120 °C in an oven.

The cleaned substrates were spin-coated with the adhesion promoter TI-Prime with 3,000 rpm and 20 s. This promoter improves the adhesion of polymer layers on substrates like silicone or glass. The solvent was evaporated at 120 °C for 10 min and the promoter was activated during the drying step. The photolithography was continued with coating of the electrodes with photoresist via spin coater for 2,000 rpm and 1 min (see fig. 4.4 (7)). The photoresist was dried with a soft-bake step at 100 °C for 30 min. The windows were created with irradiation of the photoresist through a UV blocking black mask with UV light for 2 min defining the later non-insulated electrode areas (see fig. 4.4 (8)). The black mask had different dimensions: i) $(0.5 \times 0.5) \text{ mm}^2$, ii) $(1.1 \times 1.1) \text{ mm}^2$, and iii) $(2.0 \times 2.0) \text{ mm}^2$ (see fig. 4.6 A). Due to the various fabrication steps the effective non-insulated electrode areas, which were limited by the photoresist, deviated from the original mask as follows: i) $(0.5 \times 0.5) \text{ mm}^2$ with a measured side length of $(460 \pm 60) \mu\text{m}$, ii) $(1.1 \times 1.1) \text{ mm}^2$ with a measured side length of $(950 \pm 40) \mu\text{m}$, and iii) $(2.0 \times 2.0) \text{ mm}^2$ with a measured side length of $(1790 \pm 20) \mu\text{m}$ seen in fig. 4.6 B.

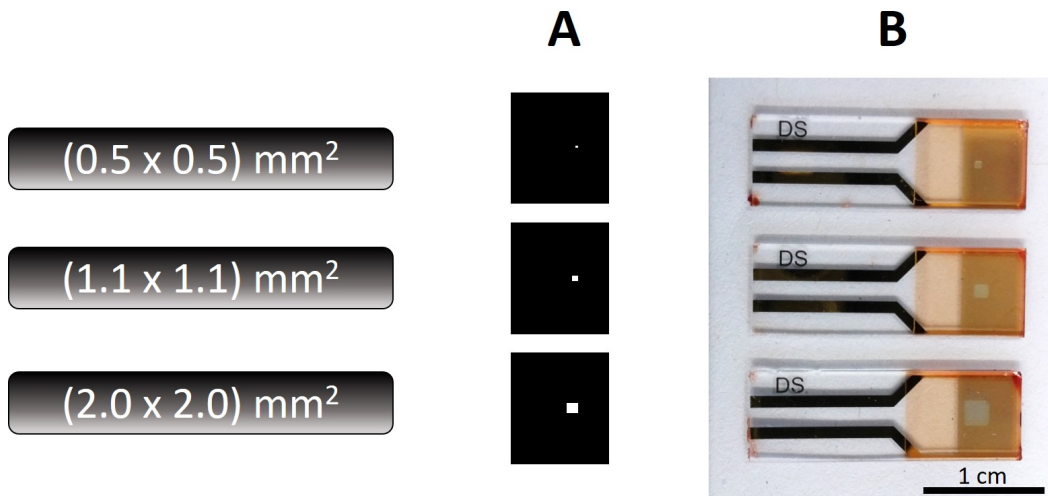


Figure 4.6: Images of the electrodes from Metrohm DropSens with the varying window sizes. Windows size of $(0.5 \times 0.5) \text{ mm}^2$ (*top*), $(1.1 \times 1.1) \text{ mm}^2$ (*center*) and $(2.0 \times 2.0) \text{ mm}^2$ (*bottom*) were fabricated. The masks used for the photolithography can be seen in A. The photographic images of the Metrohm DropSens electrodes with the three different window sizes are shown in B.

In this work all three windows sizes were implemented for IDE 10 and IDE 20, whereas only the two small window sizes could be realized for the IDE 12.

The exposed photoresist could be dissolved by immersion into a sodium hydroxide solution (7 g/L in double distilled water) for 20 s leading to an uncovered area of the gold electrode with a defined size (see fig. 4.4 (9)). The substrates were washed three times with double distilled water and were dried in a stream of nitrogen. The photoresist was hardened in a hard-bake step for 2 h at 118°C in the oven. The fabricated electrodes had to be stored protected from light and temperature until they were used.

For experimental use it was necessary to create a measurement chamber. For this purpose, planar glass rings were glued onto the sterilized electrodes. These glass rings were treated for 15 min in a solution with detergent in the ultrasonic bath. After three times rinsing with double distilled water the rings were repeatedly treated in the ultrasonic bath for 15 min. Afterwards, the rings were incubated for 10 min in ethanol. Until required for use, the rings were stored in ethanol. The dried rings were sterilized with argon plasma and glued onto the sterilized electrodes. The glue was hardened for 37°C over night. In this work three different sizes of rings were used. For the self fabricated electrodes and the one from Fraunhofer, rings with an inner diameter of 1 cm with a maximum volume of 400 μ L were used. For the Metrohm DropSens electrodes rings with an inner diameter of 5 mm and a maximum volume of 200 μ L were applied. To minimize the area for cultivation of the Cor.At® cells rings with an inner diameter of 4 mm and a maximum volume of 60 μ L were glued onto the electrodes into the big rings.

4.3.2 Layout of the commercially available ECIS arrays

For a comparison of the measured data commercially available ECIS electrodes from Applied BioPhysics (Troy, NY) were used. In this work three different electrode layouts were applied: i) 8W1E, ii) 8W10E, and iii) 8W10E+ (see fig. 4.7).

All electrode arrays have eight independent measurement chambers with a maximum volume of 400 μ L, whereas the individual layouts differ in number and arrangement of the electrodes. The 8W1E and 8W10E arrays have a big counter electrode in the center and various numbers of working electrodes per well. Each working electrode has a diameter of 250 μ m and an area of 5×10^{-4} cm². 8W1E arrays have one working electrode in the center of each well. 8W10E exhibit ten working electrodes per well which results in a complete electrode area of 5×10^{-3} cm². In the case of the 8W10E+ arrays the working and the counter electrodes were arranged in an interdigitated manner. The electrodes in each individual well comprise 40 electrodes

with a diameter of $250\text{ }\mu\text{m}$, respectively, resulting in a complete electrode area of 0.02 cm^2 .

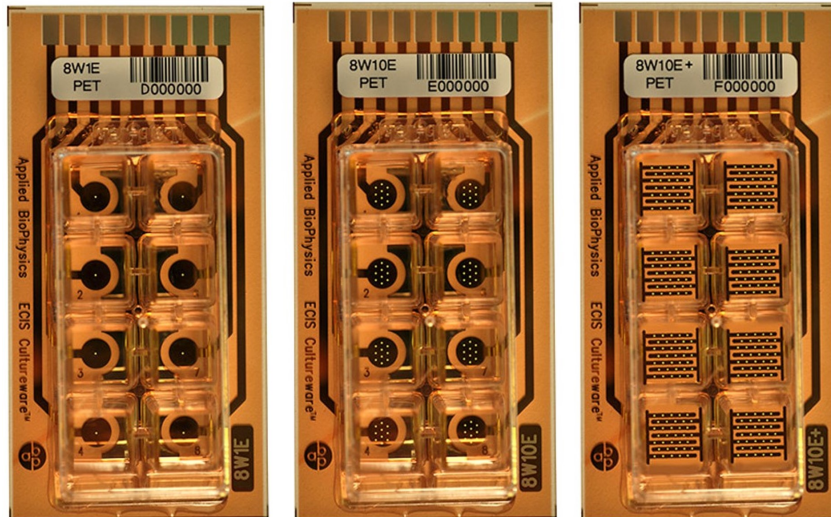


Figure 4.7: Images of electrode arrays provided by Applied BioPhysics (Troy, NY). In this work three different electrode arrays were used: i) 8W1E (*left*), ii) 8W10E (*center*), and iii) 8W10E+ (*right*). The photographs were taken from <http://www.biophysics.com/cultureware.php>.

4.4 Impedance-based measurements

All experiments were conducted in an incubator with humidified atmosphere at 37°C and 5% or for special measurements with 0% CO_2 . These incubators were cleaned and sterilized with ethanol before starting the experiments. Changes in cell morphology were monitored in a non invasive manner and with a high time resolution technique. Because of the applied weak sinusoidal ac voltage of 10 mV (rms) the cells are not harmed.

4.4.1 Basic measurement setup

The basic setup of the measurement devices are shown in fig. 4.8 - the standard self-made device in fig. 4.8 **A** and the device used for electroporation in fig. 4.8 **B**. Inside of the incubator the electrodes were mounted on a holder. For the IDEs a customized holder (fabricated by the workshop of the University of Regensburg) (seen in fig. 4.8 **A**) was used and for the ECIS arrays a manufactured holder (Applied BioPhysics, Troy, NY) (seen in fig. 4.8 **B**). It is possible to connect four IDEs with one holder and two 8-well ECIS arrays in parallel. These holders are connected to a relay which enables switching between the different electrodes. This relay

is linked with the impedance analyzer which contains an oscillator which uses a sinusoidal alternating voltage. The relay and the impedance analyzer are connected to an ordinary computer for data storage and recording, which is done by a self-written LabView-based software (Prof. Dr. J. Wegener, University of Regensburg, Germany).

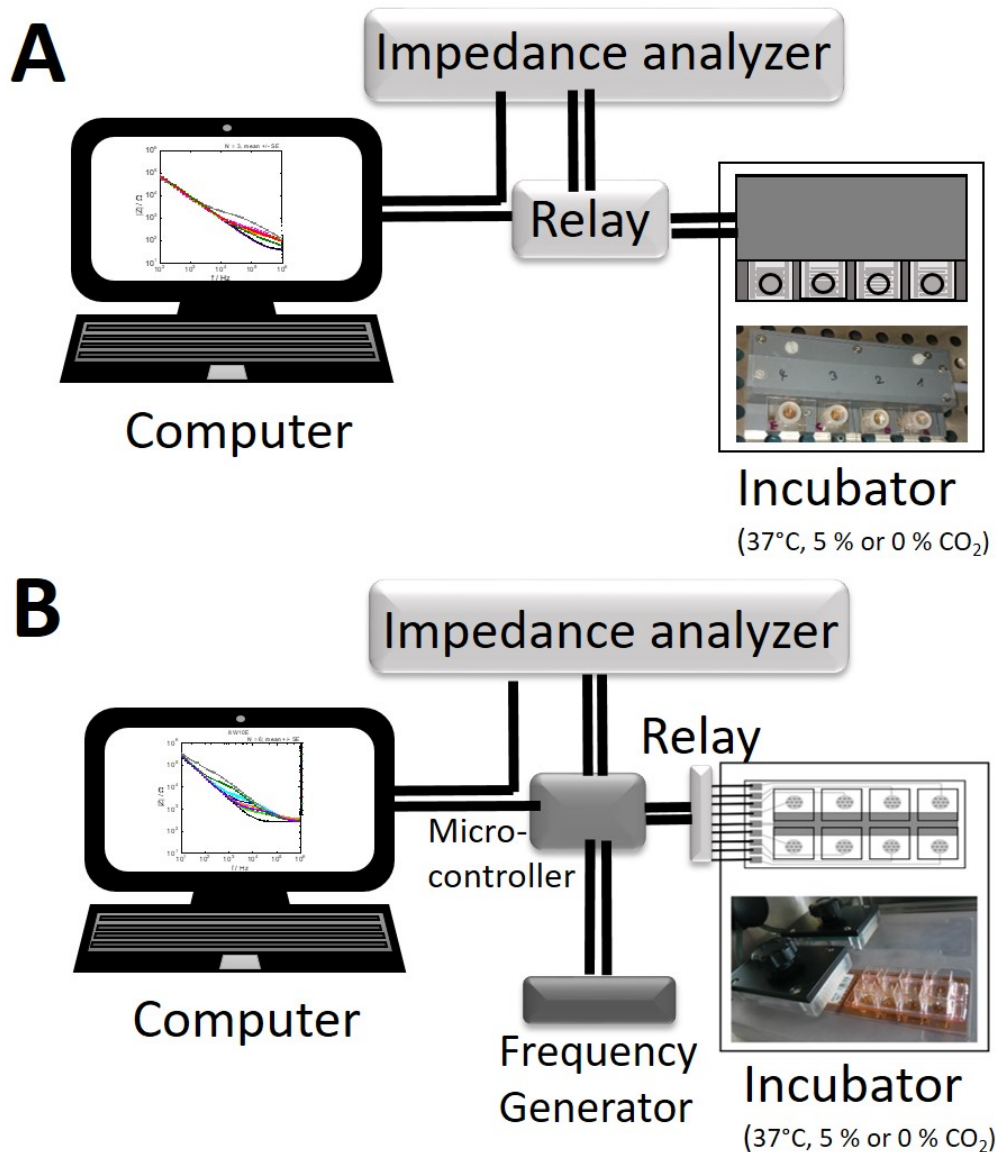


Figure 4.8: Scheme of the basic measurement setup. The electrodes inside the incubator are connected via a relay to an impedance analyzer. The latter is connected to an ordinary computer. **A:** Scheme of a self made setup with a drawing and image of the IDE holder. **B:** Scheme of the device for electroporation, which includes a micro-controller and a frequency generator, with a drawing and an image of a holder purchased from Applied BioPhysics (Troy, NY).

Using this device for electroporation a micro-controller and a frequency generator have to be added (see fig. 4.8 B). The micro-controller enables the switch between

the impedance analyzer and the frequency generator, which applies a short pulse at a special frequency with variable amplitudes between 1 V and 7 V and a pulse duration of 125 ms and 250 ms.

The commercially available devices (ECIS1600R or ECIS Z Θ (Applied BioPhysics (Troy, NY))), which were also used in this work, contain the impedance analyzer, the frequency generator and the relay in one device.

4.4.2 Different impedance recording parameter

With the commercial software as well as with the customized LabVIEW software (Prof. Dr. J. Wegener, University Regensburg, Germany) different ways of collecting data are available. On the one hand it is possible to measure the complex impedance over time at different frequencies with the Multi-Frequency/Time mode (MFT mode), on the other hand smallest micromotions of the cells can be monitored with a high time resolution at one discrete frequency (RTC mode). In the following the two different modes are described in more detail.

Multi-Frequency/Time (MFT) mode

In the Multi-Frequency/Time (MFT) mode different AC frequencies are applied. The commercial software can use flexible frequency ranges. In this work a range from 62.5 to 96,000 Hz with fifteen different frequencies was chosen, which results in a time resolution of 4 min between two data points by measuring 16 wells of an ECIS array. With the customized LabVIEW software data acquisition in a frequency range of 10^1 to 10^6 Hz with 51 equidistantly distributed frequencies on a logarithmic scale was used. The frequency spectrum for every electrode is monitored in sequence. Consequently, the time resolution is defined with the quantity of measured electrodes and frequencies, and ranges from 9.7 min between two data points (16 wells of the ECIS array) and 3.5 min (four IDEs). The time-dependent change of the impedance can be analyzed for every discrete frequency.

Rapid time collection (RTC) mode

Rapid time collection (RTC) was used to monitor the small fluctuations of a confluent cell layer, called micromotion. Cells in a confluent monolayer are not completely calm, they move in horizontal and vertical direction. The extent of this micromotions is cell type-dependent and can be an indicator of toxic influences. RTC is measured at one discrete frequency depending on the electrode type. The data acquisition was performed with a time resolution of 0.7 points per second and a data set of 10 min

per well or electrode. The data were analyzed using an increment analysis software customized by Prof. Dr. J. Wegener. This LabVIEW-based software is explained in chapter 3.1.2.4. The calculated variances can be used for a comparison of different measurement setups.

For analyzing the beating of the cardiomyocytes the time resolution was further improved. In chapter 4.4.3.3 the details can be seen.

4.4.3 Specific assay conditions

All experiments were performed under sterile conditions and were measured in the incubator in humidified atmosphere at 37 °C and 5 % or 0 % CO₂. Before starting the measurement all electrodes were sterilized with argon plasma for 30 s (ECIS arrays) or 1 min (IDEs) and were then immediately incubated with 10 mM cysteine solution for 10 min at RT (see chapter 4.1.5). After three times washing with PBS⁺⁺ and one time with serum-containing medium the electrodes could be used for measurements.

4.4.3.1 Characterization of cell-free electrodes

Measurement of the spectra of cell-free electrodes

The prepared electrodes were filled with warm medium (400 µL for ECIS arrays, Fraunhofer IDEs and self fabricated IDEs and 160 µL for Metrohm DropSens electrodes) and were contacted in the holder of the measurement device. To avoid temperature or CO₂ influences the spectra of the cell-free electrodes were measured with the MFT mode after half an hour of incubation.

4.4.3.2 Spectral characterization of different cell types

Frequency spectra of different cell types

After measuring the spectra of the cell-free electrodes the medium was aspirated and the cell suspension in the calculated cell concentrations per cm² were added, pursuant to table 4.4 in chapter 4.1.5. Before storing the electrodes in the cell incubator at 37 °C and 5 % CO₂ the cells were allowed to settle down on the electrodes by leaving the electrodes standing in the laminar flow hood for 20 min. 48 h after seeding, the medium was exchanged to ensure the supply of fresh nutrients. On the third day after seeding, the electrodes were mounted into the incubator with the specific holder and were incubated at least for 1 h to avoid temperature effects and influences of a fluctuating CO₂ concentration. The spectra were measured with the MFT mode.

Rapid time collection measurement of different cell types

After the measurement of the spectra of the cell-covered electrodes the measurement mode was changed to RTC mode. For every electrode type and window size a specific frequency was chosen and the cycles per frequency were adapted to the frequency, with the result that a time resolution of 1.5 s can be achieved. The micromotion was measured for 10 min for every electrode.

4.4.3.3 Phenotypic assays

Time-dependent adhesion measurement

The adhesion of the NRK, MDCK II, MDCK I and one time the U373 cells was measured nearly continuously during the addition of the cell suspension. The baseline recording was paused to add the cell suspension in a concentration of 450,000 cells/cm² (and 100,000 cells/cm² for U373 cells) in the laminar flow hood. After 20 min of leaving the electrodes standing in the laminar flow hood, the electrodes were mounted into the holders and the measurement was continued for at least 50 h without disturbance.

Time-dependent proliferation measurement

The measurement of the proliferation was performed in a similar manner as the adhesion. It differs from the seeding density: 10,000 cells/cm² were seeded subconfluently. Furthermore, the proliferation was measured for at least 90 h.

Monitoring the impact of non-isotonic media

For the stimulation two different hypertonic, but iso-conductive buffers were used with different osmotic pressure. The solutions of the different osmolalities were prepared in a double concentration because of the dilution in a 1:1 ratio on the electrodes during addition. The osmolalities were varied with addition of sucrose to a PBS⁺⁺/glucose (1g/L) buffer. The conductance γ was adjusted to the one of PBS⁺⁺/glucose (1g/L) with 1.5 M NaCl in double distilled water and the pure PBS⁺⁺/glucose buffer served as a control (0 mM sucrose). The osmolality π was measured after the experiment with a cryoscopic osmometer for each well. The final sucrose concentrations, conductances and osmolalities are listed in table 4.7.

For the hyperosmolar stimulation of NRK and MDCK II cells, the prepared and seeded electrodes after measuring of the spectra were used. The medium was

aspirated and 200 μL (ECIS arrays, Fraunhofer EMFT and self fabricated IDEs) or 80 μL (Metrohm DropSens electrodes) prewarmed PBS^{++} /glucose (1 g/L) were added. The electrodes were connected via the holder and a baseline was measured at least for 1.5 h until a stable signal was monitored. Afterwards, 200 μL or 80 μL warm PBS^{++} /glucose (0 mM sucrose) were added as a control. After nearly 2.5 h 200 μL or 80 μL were removed and the same warm volume of different sucrose concentrations was added. The measurement was stopped 2 h after addition.

Table 4.7: List of the hypertonic buffers. The conductivity γ at 37°C, osmolalities π and the difference between the various osmolalities $\Delta\pi$ of the used hypertonic buffers are shown. The solution with 0 mM sucrose consists of PBS^{++} /glucose. The osmolalities were measured after the experiment.

c (sucrose)	γ	π	$\Delta\pi$
/ mM	/ mS/cm	/ mOsmol/kg	/ mOsmol/kg
0	15.84	316 ± 3	0
100	15.85	454 ± 7	138 ± 10
200	15.85	573 ± 10	257 ± 13

Monitoring signal transduction cascades

- **Stimulation of H_1 receptors with histamine**

U373 cells were stimulated with a 10 μM histamine solution in L-15 medium. The complete volume of the medium of the confluent U373 monolayer was exchanged on the third day after seeding and afterwards the electrodes were filled with half of the volume with serum-free L-15 medium. The monolayer was incubated for 3 h at 37°C and 0 % CO_2 . After the incubation the electrodes were connected in the incubator at 0 % CO_2 and the RTC mode was started at a designated frequency. After 5 min, 200 μL or 80 μL of the histamine solution in double concentration in L-15 medium was added, leading to a concentration of 10 μM histamine on the electrodes. As a control the same volume of L-15 medium was added instead of histamine. The measurement was stopped after further 35 min.

- **Stimulation of U373 cells with calcimycin**

Another signal transduction pathway measurement was the stimulation of U373 cells with calcimycin. This is an ion-carrier which increases the intracellular Ca^{2+} level. The confluent cell layer was treated similarly to the histamine stimulation, whereas only the IDE10 electrodes were used. After 3 h incubation with 80 μL serum-free L15-medium at 0 % CO_2 , the electrodes

were connected with the holder in the incubator and a 5 min baseline in the RTC mode at 316 kHz at 0 % CO₂ was recorded. 80 µL calcimycin solution in the double concentration was added, leading to a final concentration of 10 µM on the electrodes. To exclude influences of the solvent of the stock solution (DMSO), it was necessary to add DMSO to the solvent control in the same ratio as calcimycin. After 35 min the measurement was finished.

Analysis of the time course of the impedance during adhesion and beating of cardiomyocytes

The adhesion of the cardiomyocytes is described in chapter 4.1.3.2. 24 and 48 h after seeding the beating of the cardiomyocytes was recorded. To monitor the beating the RTC mode had to be improved. Every measurement was limited to 29 s and had a different time resolution. The IDE 12 and IDE 7 were measured at a frequency of 4 kHz, 40 kHz and 80 kHz. It was possible to generate a time resolution of 128 points per second with the commercially available devices. To exclude instrumental noise the cell-free electrodes were measured before seeding under the same conditions and measurement parameter. The 8W1E electrodes were measured at 1 kHz, 4 kHz and 40 kHz and a resolution of 64 points per seconds could be achieved with the commercial devices.

The beating rate can be increased with isoprenaline, which is a β -adrenoreceptor selective agonist. The increased beating was monitored 72 h after seeding at 20 kHz for the IDEs and at 4 kHz for the ECIS electrodes with the time resolution aforementioned. 100 nM isoprenaline in medium was added and the beating was recorded at defined time points: just before addition, just after addition, 5 min after, 10 min after, 30 min after and 60 min after addition.

Analysis of the cytotoxicity of BPA

A cytotoxicity study with NRK cells was performed with different concentrations of bisphenol A (BPA) and related with it, with different concentrations of ethanol as a solvent control. The stock solution of BPA (20 mM in ethanol (96 %)) was diluted with serum-free L-15 medium (BPA: 0, 30, 60, 80, 100, 150, 200 and 300 µM). The concentration range of ethanol was chosen to exclude a solvent impact independently of the used BPA concentration. They were diluted with serum-free L-15 medium (ethanol: 0, 0.1, 0.3, 0.5, 0.8, 1, 1.5 and 2 %). For the impedimetric measurements the control concentration of 0 µM BPA contained 1.5 % ethanol, with the exception of the proliferation, in which 1 % ethanol was added to the 0 µM BPA control.

The range of the concentrations of BPA was defined with respect to the cytotoxic

index and the corresponding EC_{50} value determined by a PrestoBlue assay. This resazurin-based assay monitors the metabolic activity of cells after incubation with different concentrations of bisphenol A (BPA). Resazurin can enter the cells through the membrane and is then reduced by enzymes in viable cells to the pink colored and red fluorescent resorufin which can be detected by fluorescence spectroscopy.

- **PrestoBlue assay**

NRK cells were seeded in a density of $450,000 \text{ c/cm}^2$ in a 96-well-plate (area per well: $A = 0.32 \text{ cm}^2$). 24 h after seeding, the medium was exchanged and after 72 h the cells were washed twice with L-15 medium. Afterwards, two columns of the 96-well-plate were filled with L-15 medium as negative control, two columns with 0.5 % (v/v) triton-X-100 as a positive control, and the remaining ones were filled with different BPA concentrations in a range of 0-300 μM . After inoculation at 0 % CO_2 for 20 h the cells were washed with PBS^{++} /glucose (1 g/L), the PrestoBlue solution was added and the fluorescence was measured with a Tecan reader after an incubation time of 2 h.

Four different impedance-based assays were performed: i) acute toxicity, ii) rapid time collection (RTC), iii) migration and iv) proliferation.

In the case of the first three measurements the NRK cells were seeded with a density of $450,000 \text{ cells/cm}^2$ and the medium was exchanged after 24 h. 48 h after seeding the medium was aspirated, L15-medium was added and the CO_2 concentration was lowered to 0 %. After 5 h of incubation the different measurements started.

- **Acute toxicity**

For the measurement of the acute toxicity the incubation with L-15 medium was used as a baseline. BPA and ethanol solutions were added in different concentrations to the cells on the 8W10E electrodes and the IDE12 and the impedance changes were monitored over time.

- **Concentration-dependent micromotion**

After 5 h of incubation with L-15 medium the cells on the 8W1E electrodes and the IDE12 were incubated with the different BPA or ethanol concentrations for 20 h. Afterwards, the RTC mode was started and each electrode was measured successively for 10 min at 4 kHz (8W1E electrodes) and 400 kHz (IDE12). Variance analysis of these time profiles was calculated with the LabView-based software (Prof. Dr. J. Wegener) seen in chapter 3.1.2.4.

- **Analysis of cell migration after wounding**

After the measurement of RTC the cells on the 8W1E electrodes were wounded with a pulse of 5 V at 40 kHz for 30 s. Thus, the cells were incubated with BPA or ethanol for around 24 h before wounding. The time-dependent repopulation of the electrode area was monitored for at least 20 h.

The seeding process differed for the proliferation in comparison with the three others assays. A baseline without cells was measured before the NRK cells were seeded in a density of 10,000 cells/cm² on a 8W10E+ electrodes.

- **Time-dependent capacitance change during proliferation in the presence of BPA**

24 h after seeding, the medium was aspirated and the BPA and ethanol solutions in different concentrations were added. In the control of 0 μ M BPA 1 % ethanol was added as a solvent control. After a total of 100 h the measurement was stopped.

To further analyze the influence of BPA on the cells, they were stained by vital stains (Calcein Acetoxymethylester (CaAM), Ethidium homodimer (EthD-1), 4', 6-diamidino-2-phenylindole dihydrochloride (DAPI)).

The cells were seeded for the stainings with 450,000 cells/cm² in glued glass rings into a petri dish. 24 h after inoculation the medium was exchanged and after 48 h the cells were incubated with L-15 medium for 5 h. Afterwards, BPA (0, 30, 80, 100, 200 and 300 μ M) solutions were added and incubated for 20 h at 0 % CO₂. To visualize the influence, the cells were stained according to the protocol shown in chapter 4.2.2 and imaged with the CLSM.

4.4.3.4 Emerging impedance-based assays

Impedance-based analysis of U373 spheroids

The adhesion, micromotion and the histamine stimulation of spheroids were measured in this work. For this purpose, the electrodes had to be sterilized and incubated with cysteine as explained in chapter 4.1.5. A baseline of the IDEs and the 8W1E electrodes with prewarmed medium was measured before the spheroids were placed centrally on the electrodes. Only spheroids which were three days old and had a round shape were used. The spheroids were allowed to settle down on the electrodes for 20 min in the laminar flow hood. Afterwards, the electrodes were connected with the holder carefully in the incubator and the adhesion was measured for 60 h. Then, the RTC mode was started and the micromotion was recorded for 10 min as aforementioned. Subsequently, the medium was aspirated and the spheroids were incubated with L-15 medium for 3 h before they were stimulated with 10 μ M histamine in the same way like the monolayer (see chapter 4.4.3.3).

To image the adhesion and the centrosymmetrical spreading of the spheroids, they were stained following the protocols in chapter 4.2.2. Different dyes were used: i) carbol fuchsin, ii) CaAM and EthD-1 and iii) DAPI and three-dimensional images were taken with CLSM.

***In situ* electroporation**

For the electroporation the self-made setup shown in fig. 4.8 **B** with the frequency generator and the micro-controller was used. The IDE 10, IDE 12, IDE 20 and the 8W1E electrodes were prepared as aforementioned (see chapter 4.1.5) and the NRK cells were seeded with a density of 450,000 cell/cm². The medium was exchanged after 48 h and the measurement started on the third day after seeding. The medium was aspirated and the cells were incubated with EBSS⁺⁺ for at least 3 h before the baseline impedance was measured. After a stable signal was established FITC-dextran (fluorescein isothiocyanate) with a size of 2 MDa and a final concentration of 2 mg/mL in EBSS⁺⁺ was added. After 10 min the cells were electroporated with different voltage values (1, 2, 3, 4, 5, 6, 7 V) for 125 ms. The frequency was chosen electrode specific: 8W1E array at 40 kHz, IDE 10 and IDE 20 at 200 kHz, and IDE 12 at 400 kHz. The cell reaction was monitored for further 20 min before they were washed twice with prewarmed PBS⁺⁺. The efficiency of the dye uptake was verified with CLSM images which were taken with a 60x magnification. The green fluorescence of the FITC-dextran inside of the cells was detected with the 488 nm laser and the 515/30 detector, whereas the fluorescence of the photoresist was excited with the 543 nm laser and was recorded with the 650 LP detector.

4.4.4 Simulation with COMSOL Multiphysics

The software “COMSOL Multiphysics 5.2a” was used for the simulation of the electric potential and the electric field for various electrode types modeled as cell-free and cell-covered electrodes. For the simulation it is necessary to define the electrical conductivity and the relative permittivity of the individual materials which are listed in tab. 4.8.

Representing the interdigitated electrodes IDE 7, IDE 10, IDE 20, IDE 40, IDE 100 and IDE 300 were simulated in order to draw conclusions about the distribution of the electric potential and the penetration depth of the electric field. The electrode fingers of the IDEs have the following width and gap: i) IDE 7: width: 4 μm , gap: 3 μm , ii) IDE 10: width and gap: 5 μm , iii) IDE 20: width and gap: 10 μm , iv) IDE 40: width and gap: 20 μm , v) IDE 100: width and gap: 50 μm , vi) IDE 300: width and gap: 150 μm , respectively. For a direct comparison the 8W10E and 8W1E electrodes were simulated with the same preconditions as in the case of the IDEs. The radius of each working electrode amounted to $r = 125 \mu\text{m}$. The shape of the counter electrode (CE) could be compared with an angular horseshoe with the semi-circle open to the working electrodes (WE). For the only WE of the 8W1E electrode the distance to the CE amounted to 3 mm. The 8W10E electrodes had 10 WEs with

a distance to each other of 1 mm. The nearest WEs were 2.5 mm apart from the CE. A precise scheme of the ECIS arrays can be seen in fig. 5.4. The material of every electrode was set to be gold with a thickness of 100 nm.

Table 4.8: Characteristics of the materials used in the simulation with COMSOL Multiphysics. The electrical conductivity and the relative permittivity of the individual materials are listed.

material	electrical conductivity / S/m	relative permittivity / -	references
medium	1.38	78	(Kenchetty et al., 2019)
glass substrate	$1 \cdot 10^{-12}$	4.2	(Procházka et al., 2019)
gold electrode	$4.9 \cdot 10^7$	1	(Hering et al., 2014)

From the AC/DC module of the COMSOL Multiphysics software the physical interface “electric currents” was selected. All boundaries were assigned to the electric insulation and the initial value of the electric potential was set to be $V = 0.05$ V. The CEs were defined as ground and the WE as terminal. A physics-controlled mesh with a “finer element size” was used for the calculation of the simulation. For a simplified analysis a stationary study was used and a filled contour representation was chosen for monitoring the results.

The simulation of cell-free electrodes in chapter 5 was calculated with the medium as a rectangle on the electrodes. The representation was a combination of three-dimensional and two-dimensional images of the whole geometry or only a plane of this.

In the case of the simulations of cell-covered electrodes in chapter 6 the cells were added to the simulations of the cell-free electrodes. The cells were monitored as completely insulated rectangles with a varying height of $h = 0.5 \mu\text{m}$, $h = 1.0 \mu\text{m}$, $h = 3.0 \mu\text{m}$ and $h = 5.0 \mu\text{m}$ and a length of $l = 7.0 \mu\text{m}$ with an intercellular cleft of 100 nm. The distances of the cells to the electrodes differ from: i) $d = 25$ nm to ii) $d = 500$ nm. The borders of the cells were defined as completely insulating.

5 Characterization of cell-free electrodes

The basis of this work is the comparison of different electrode types prepared in various interdigitated layouts of subcellular pitches and the commercially available electrodes that are commonly used in impedance-based cell assays. To enable interpretations of advantages of disadvantages of the electrodes used in the assays, the cell-free electrodes have to be measured and characterized first.

5.1 Spectra of cell-free electrodes

For the characterization of the cell-free electrodes the spectra of the impedance $|Z|$, the resistance R and the capacitance C were recorded as a function of frequency. For these spectra 8W1E, 8W10E, IDE 400, IDE 300, IDE 20, IDE 12, IDE 10 and IDE 7 were measured and plotted in fig. 5.1.

The impedance spectra (fig. 5.1 **A**) show clear differences between the various electrode types. In the frequency range $< 10^4$ Hz all electrodes reveal a linear characteristic with various slopes s for the impedance. The steepest slope of the impedance can be seen for the 8W1E electrodes with a value of $s = (-15.9 \pm 0.4) \Omega/\text{Hz}$ ($n = 4$) and the flattest slope for the 8W10E electrodes with a slope of $s = (-1.76 \pm 0.02) \Omega/\text{Hz}$ ($n = 15$). The slopes of the IDE 400 and IDE 300 lie between and show similar values (IDE 400: $s = (-3.0 \pm 0.4) \Omega/\text{Hz}$ ($n = 4$) and IDE 300: $s = (-3.5 \pm 0.2) \Omega/\text{Hz}$ ($n = 7$)). The slopes of the smaller IDEs are even steeper but still far below the slope of the 8W1E (IDE 20: $s = (-4.5 \pm 0.2) \Omega/\text{Hz}$ ($n = 13$); IDE 12: $s = (-5.7 \pm 0.4) \Omega/\text{Hz}$ ($n = 5$); IDE 10: $s = (-5.9 \pm 0.2) \Omega/\text{Hz}$ ($n = 15$); IDE 7: $s = (-5.0 \pm 0.4) \Omega/\text{Hz}$ ($n = 3$)). All slopes were calculated for a range of $200 \text{ Hz} \leq f \leq 8 \text{ kHz}$. It can be concluded that the slopes are similar for the smaller IDEs and similar for the IDE 300 and IDE 400, respectively. Nevertheless, the 8W1E and 8W10E electrodes show significantly different values. A further difference between the various electrode layouts in the range $< 10^4$ Hz is a shift in y-direction which depends on the various electrode areas and the corresponding various $|Z|_{CPE}$. The highest impedance value can be seen for the 8W1E electrodes (at 10^4 Hz: $|Z| = (3330 \pm 60) \Omega$; $n = 4$) and the

smallest one for the 8W10E electrodes (at 10^4 Hz: $|Z| = (437 \pm 5) \Omega$; $n = 15$). The IDEs are lying between these values, whereas IDE 20, IDE 12, IDE 10 and IDE 7 (at 10^4 Hz: $|Z| = (1100 \pm 200) \Omega$; $n \geq 3$) and also IDE 400 and IDE 300 (at 10^4 Hz: $|Z| = (800 \pm 80) \Omega$; $n \geq 4$) can be pooled, respectively.

In a frequency range $> 10^4$ Hz the impedances flatten out to a constant value. In this frequency range R_{bulk} dominates the spectra which will be explained in the discussion. The frequency at which the constant value occurs and the value itself are dependent on the electrode type. The earliest saturation can be observed for the 8W10E electrodes at 25 kHz ($|Z| = (300 \pm 6) \Omega$; $n = 15$), followed by IDE 400 at 32 kHz ($|Z| = (460 \pm 20) \Omega$; $n = 4$), IDE 300 at 50 kHz ($|Z| = (360 \pm 20) \Omega$; $n = 7$) and 8W1E electrodes also at around 50 kHz ($|Z| = (1410 \pm 20) \Omega$; $n = 4$). The impedance for the IDEs with the smaller pitches achieves a saturation only at much higher frequency ranges. The IDE 20 and IDE 10 display a constant value at around 316 kHz ($|Z| = (86 \pm 3) \Omega$; $n \geq 13$), whereas the IDE 12 and IDE 7 only reveal a slight flattening of the impedance at 630 kHz ($|Z| = (42 \pm 3) \Omega$; $n \geq 3$).

The curves of the resistance spectra (fig. 5.1 B) reveal a similar pattern for the electrode layouts. In lower frequency ranges ($< 10^3$ Hz) the resistance shows a linear course with various slopes of the different electrodes. These slopes were calculated in a frequency range of $100 \text{ Hz} \leq f \leq 800 \text{ Hz}$. Parallel to the impedance spectra, the 8W1E electrodes obtain the highest value (at 10^3 Hz: $R = (3060 \pm 70) \Omega$; $n = 4$) with a slope of $s = (-17 \pm 2) \Omega/\text{Hz}$ and the 8W10E electrodes the lowest one (at 10^3 Hz: $R = (442 \pm 8) \Omega$; $n = 15$) with a slope of $s = (-1.7 \pm 0.1) \Omega/\text{Hz}$. The values of the IDE 400 and IDE 300 lie between the ECIS electrodes (at 10^3 Hz: $R = (830 \pm 80) \Omega$; $s = (-4.2 \pm 0.9) \Omega/\text{Hz}$; $n \geq 4$). In comparison, the IDEs with smaller pitches show higher resistance values (at 10^3 Hz: $R = (1100 \pm 200) \Omega$; $n \geq 3$) and have a different averaged slope ($s = (-12 \pm 3) \Omega/\text{Hz}$). Increasing the frequency leads to a saturation of the resistance change, which is strongly dependent on the electrode layout. 8W10E electrodes achieve a constant value at 4 kHz ($R = (323 \pm 6) \Omega$; $n = 15$), IDE 400 and IDE 300 at 63 kHz (IDE 400: $R = (520 \pm 30) \Omega$; $n = 4$; IDE 300: $R = (440 \pm 20) \Omega$; $n = 7$) and 8W1E electrodes at 13 kHz ($R = (1340 \pm 20) \Omega$; $n = 4$). The IDEs with smaller pitches show a constant value only in higher frequency ranges. The IDE 20 and IDE 10 reach a saturation at 80 kHz ($R = (86 \pm 3) \Omega$; $n \geq 13$), whereas IDE 12 and IDE 7 achieve a minimum at 316 kHz ($R = (42 \pm 3) \Omega$; $n \geq 3$).

As a third parameter, the capacitance as a function of the frequency was measured (fig. 5.1 C). In the frequency range $< 10^4$ Hz the capacitance shows an individual constant value for all electrodes dependent on the layout and the corresponding electrode area. The 8W10E electrodes reveal the highest value with $C = (49.4 \pm 0.5) \text{ nF}$ ($n = 15$), followed by IDE 400 and IDE 300 with the averaged $C = (23 \pm 4) \text{ nF}$ ($n \geq 4$) and IDE 20, IDE 12, IDE 10 and IDE 7 which are pooled, resulting in a value of

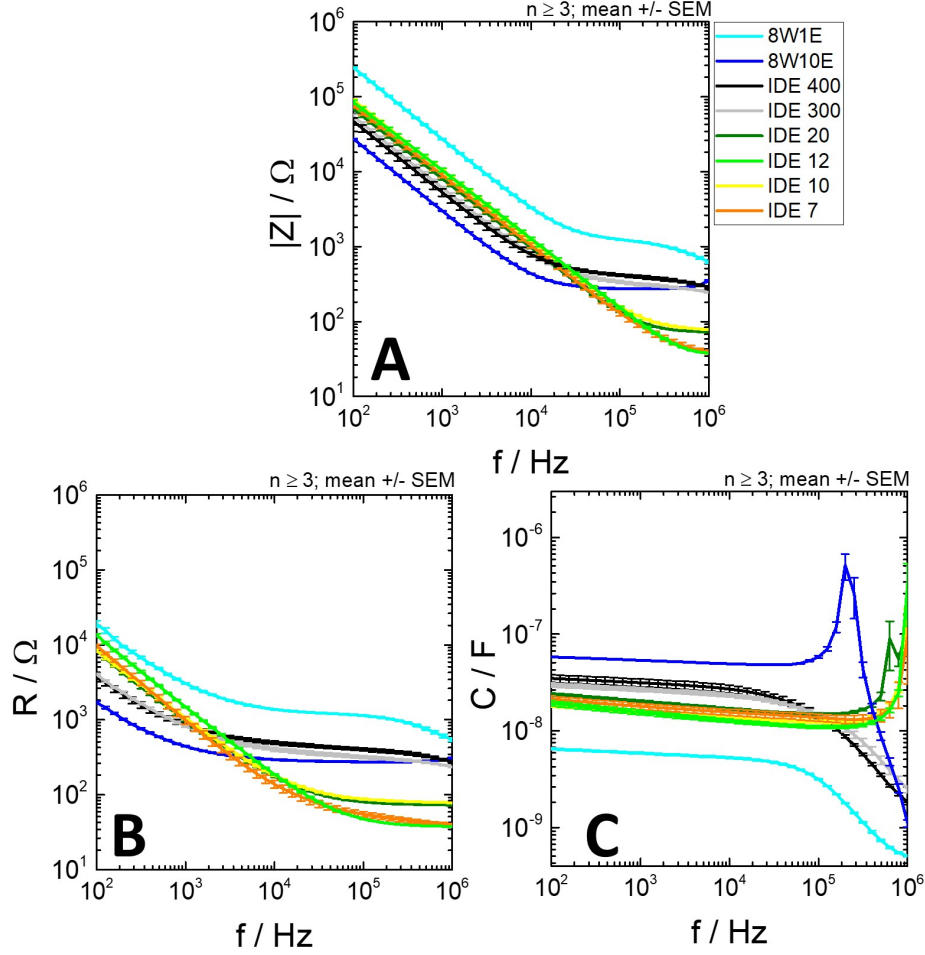


Figure 5.1: Frequency-dependent impedance, resistance and capacitance of the various cell-free electrode layouts. The spectra of 8W1E, 8W10E, IDE 400, IDE 300, IDE 20, IDE 12, IDE 10 and IDE 7 are shown. **A:** impedance $|Z|$, **B:** resistance R , **C:** capacitance C . The legend in **A** corresponds to all spectra. ($n \geq 3$).

$C = (15 \pm 3) \text{ nF}$ ($n \geq 3$). The smallest value can be seen for the 8W1E electrodes with $C = (5.3 \pm 0.1) \text{ nF}$ ($n = 4$). In higher frequency ranges ($> 10^4 \text{ Hz}$) the measured capacitance is changing significantly. On the one hand, the capacitance of the 8W1E electrodes, IDE 400 and IDE 300 is decreasing at $\approx 50 \text{ kHz}$ to values at 1 MHz for 8W1E electrodes: $C = (0.51 \pm 0.01) \text{ nF}$ ($n = 4$), IDE 400: $C = (1.8 \pm 0.1) \text{ nF}$ ($n = 4$) and IDE 300: $C = (2.5 \pm 0.2) \text{ nF}$ ($n = 7$). On the other hand, the capacitance is increasing for the other electrodes. In the case of the 8W10E electrodes the capacitance stays constant until a frequency of 79 kHz , before it increases to a value of $C = (500 \pm 200) \text{ nF}$ at 200 kHz ($n = 15$). With higher frequencies the capacitance is decreasing to a value of $C = (1.11 \pm 0.09) \text{ nF}$ at 1 MHz ($n = 15$). The IDEs with smaller pitches show a delayed increase at 500 kHz until a value of $C = (400 \pm 300) \text{ nF}$ ($n \geq 3$) is reached. This individual course of the capacitance at this frequency range ($> 10^5 \text{ Hz}$) is not directly dependent on the electrode layout. At this frequencies

stray capacitances influence the measured capacitance which can lead to high deviations.

In summary, it can be said that the electrode layout has a significant influence on the frequency-dependent impedance, resistance and capacitance. The variations of the linear characteristics of the impedance and the resistance in a frequency range $< 10^4$ Hz for the impedance and $< 10^3$ Hz for the resistance can be attributed to the impedance of the CPE which is related to the electrode area (see eq. 3.20 in chapter 3.1.2). This influence of the electrode area is also seen in the capacitance spectra in the various values for the individual electrodes ($< 10^4$ Hz). In the impedance and resistance spectra the influence of R_{bulk} is dominating in the frequency range of $> 10^4$ Hz for the impedance and $> 10^3$ Hz for the resistance which leads to a flattening of the values. Through the experience with IDEs with subcellular dimension it is known that the cell-dependent increase of the impedance and resistance is monitored in a higher frequency range. For this reason, the flattening of the impedance and the resistance is a restricting factor for the cell measurement with these IDEs. Overall it has to be emphasized that some electrode layouts show the same frequency-dependent courses. The exceptions are the 8W1E electrodes and the 8W10E electrodes which differ in all three spectra from the other electrodes. The 8W1E electrodes have significantly higher impedance and resistance values and much smaller capacitance values in the whole measured frequency range compared to all the other electrode layouts. The 8W10E electrodes show the reversed course with lower impedance and resistance values and higher capacitance values. For the IDEs some similarities between the layouts can be observed. The IDE 400 and IDE 300 can be pooled in the impedance spectra as well as in the resistance and capacitance spectra. They show the similar slopes of the linear part of the impedance and resistance spectra and amount to the same values of the flattening of the impedance and the resistance. Also in the capacitance spectra the same frequency-dependent course can be seen. The same similarity can be observed for the IDEs with smaller pitches (IDE 7, IDE 10, IDE 12, IDE 20). The various frequency-dependent courses are similar in all three cases (impedance, resistance and capacitance) with the difference of the flattening of the impedance and resistance in the high frequency range ($> 10^5$ Hz for the impedance and $> 10^4$ Hz for the resistance). In this range both IDE 12 and IDE 7 can be pooled as well as the IDE 10 and IDE 20, respectively. From this it can be concluded that these respective electrode pairs resemble each other and that the influence in this high frequency range is not linearly related to the dimension of the electrode layout.

5.2 Spectra of cell-free electrodes with different window sizes

A further experiment in this thesis was to change the sizes of the non-insulated electrode areas (see chapter 4.3.1.2), which were not covered with photopolymer and were called “window”. It was possible to vary the sizes of these windows for the IDE 10, IDE 12 and IDE 20. Apart from the generally used size of $(1.1 \times 1.1) \text{ mm}^2$ two additional window sizes were tested: i) $(0.5 \times 0.5) \text{ mm}^2$ (for IDE 10, IDE 12, IDE 20) and ii) $(2.0 \times 2.0) \text{ mm}^2$ (only for IDE 10 and IDE 20 possible). If nothing else is mentioned, the size of $(1.1 \times 1.1) \text{ mm}^2$ is used for all assays in this work. The influence of the different windows on the measured signals was analyzed with respect to the impedance $|Z|$, resistance R and capacitance C . For all three parameters the change in dependence of the frequency was recorded (see fig. 5.2).

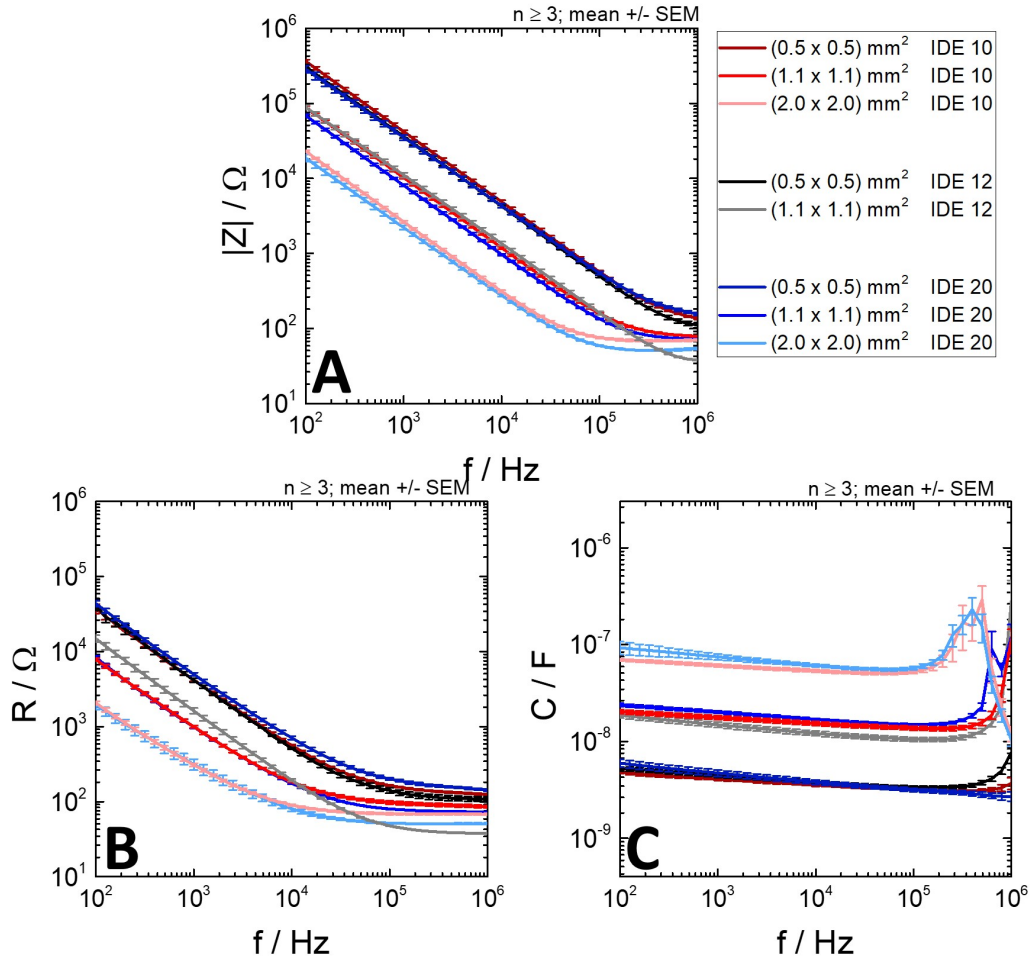


Figure 5.2: Spectra of different cell-free electrodes with various non-insulated electrode areas (windows). Different spectra are revealed: **A:** impedance $|Z|$, **B:** resistance R , **C:** capacitance C . The legend in **A** corresponds to all spectra. The mean with SEM is plotted ($n \geq 3$).

The impedance spectrum (fig. 5.2 A) monitors a strong influence of the window size on the signal, independent of the electrode type. Below a frequency of 32 kHz all impedances are decreasing linearly. The slopes in the range of $100 \text{ Hz} \leq f \leq 10 \text{ kHz}$ differ from $s = (-32 \pm 2) \Omega/\text{Hz}$ ($n \geq 4$) for the electrodes with the small window size over $s = (-8.2 \pm 0.4) \Omega/\text{Hz}$ ($n \geq 5$) for the electrodes with the middle window size to $s = (-2.1 \pm 0.3) \Omega/\text{Hz}$ ($n \geq 4$) for the electrodes with the big window. Consequently, the bigger the window size is, the flatter is the slope. A further difference between the windows is the shift in y-direction which is dependent on the impedance of the CPE which is inversely proportional to the electrode area. The smaller the windows, the higher are the impedance values. Hence, the averaged impedances show the following values at 32 kHz for the electrodes: i) the smallest window with $(0.5 \times 0.5) \text{ mm}^2$ reveals an average of $|Z| = (1500 \pm 200) \Omega$ ($n \geq 4$), ii) the window with $(1.1 \times 1.1) \text{ mm}^2$ a mean value of $|Z| = (400 \pm 50) \Omega$ ($n \geq 5$) and iii) the biggest window monitors a calculated value of $|Z| = (115 \pm 7) \Omega$ ($n \geq 4$). Increasing the frequency leads to a flattening of the curve and to the achievement of a constant value. With greater window size, this constant value is obtained at lower frequencies. Therefore, the electrodes with the biggest window reach the constant value ($|Z| = (73 \pm 2) \Omega$ ($n = 4$) for IDE 10 and $|Z| = (55 \pm 1) \Omega$ ($n = 6$) for IDE 20) at 126 kHz and 158 kHz, respectively. The electrodes with the middle window show a saturation of $|Z| = (86 \pm 3) \Omega$ ($n \geq 13$) at 316 kHz for the IDE 20 and IDE 10 and a slight flattening of $|Z| = (42 \pm 3) \Omega$ at 630 kHz ($n = 5$) for the IDE 12. This leveling off can also be seen for all curves of the smallest window from 400 kHz without reaching a constant value. The flattening of the impedance can be traced back to the growing influence of R_{bulk} with higher frequencies ($> 10^4 \text{ Hz}$) which is further explained in the discussion.

Analyzing the resistance as a function of the frequency, similar observations can be made (fig. 5.2 B). The resistance of all electrodes shows a linear course in the lower frequency range ($< 10^4 \text{ Hz}$) before a constant value is reached. The slopes of these linear parts differ between the windows in the range of $100 \text{ Hz} \leq f \leq 2 \text{ kHz}$. The electrodes with the smallest window show a slope of $s = (-21 \pm 3) \Omega/\text{Hz}$ ($n \geq 4$), whereas the slope of the electrodes with the biggest window is flatter ($s = (-1.0 \pm 0.2) \Omega/\text{Hz}$ ($n \geq 4$)). The values for the slope of the electrodes with the middle window lie between the others ($s = (-4.0 \pm 0.2) \Omega/\text{Hz}$ ($n \geq 13$) for the IDE 10 and IDE 20, and $s = (-7.4 \pm 0.9) \Omega/\text{Hz}$ ($n \geq 5$) for IDE 12). Repeatedly, the biggest difference between the frequency-dependent resistance courses of the various window sizes is seen in a y-shift. The electrodes with the smallest window show the highest averaged resistance value in comparison to the other window sizes (at $f = 10^4 \text{ Hz}$: $(0.5 \times 0.5) \text{ mm}^2$: $R = (600 \pm 70) \Omega$ ($n \geq 4$); $(1.1 \times 1.1) \text{ mm}^2$: $R = (180 \pm 20) \Omega$ ($n \geq 5$); $(2.0 \times 2.0) \text{ mm}^2$: $R = (85 \pm 9) \Omega$ ($n \geq 4$)). Over 10^4 Hz the resistance achieves constant values. Again the electrodes with the smallest window show the highest averaged

value ($R = (146 \pm 3) \Omega$; $n \geq 4$) from a frequency of 158 kHz. The values for the electrodes with the middle window match exactly with the impedance values. In the case of the electrodes with the biggest window the resistance varies from $R = (68 \pm 2) \Omega$ ($n = 4$) for IDE 10 to $R = (51 \pm 1) \Omega$ ($n = 6$) for IDE 20 starting from a frequency of 25 kHz.

The third parameter which was monitored was the capacitance. The data of the capacitance spectra (fig. 5.2 C) show a significant correlation of the electrodes with the same window sizes which enables the calculation of the average of the capacitances for each window. This average is further normalized to the areas of the windows which are calculated from the measured side lengths in chapter 4.3.1.2. The highest capacitance can be seen for the electrodes with the biggest window ($C = (55 \pm 5) \text{ nF}$; $n \geq 4$ at 100 kHz) with an area-normalized capacitance of $C_{norm} = (17 \pm 2) \text{ nF/mm}^2$, followed by the middle window ($C = (13 \pm 2) \text{ nF}$; $n \geq 5$ at 100 kHz) with $C_{norm} = (14 \pm 3) \text{ nF/mm}^2$ to the smallest capacitance for the smallest window ($C = (3.2 \pm 0.3) \text{ nF}$; $n \geq 4$ at 100 kHz) with $C_{norm} = (15 \pm 6) \text{ nF/mm}^2$. The values of the area-normalized capacitance are in a comparable range within the error. Nevertheless it can be seen that the smaller the window, the larger the error. In the range of higher frequencies the capacitances are increasing, for the $(2.0 \times 2.0) \text{ mm}^2$ window at 158 kHz, for the $(1.1 \times 1.1) \text{ mm}^2$ at 316 kHz and for the $(0.5 \times 0.5) \text{ mm}^2$ window at 500 kHz. Due to the high errors it is obvious that the increase is individual for every single electrode.

In summary, it has to be emphasized that the frequency-dependent courses of the impedance, resistance and capacitance show similarities for the individual window sizes. The course of the electrodes with the smallest window ($(0.5 \times 0.5) \text{ mm}^2$) obtains for the impedance as well as for the resistance the highest slopes and values across the whole frequency spectra. The flattening of the impedance and the resistance occurs at higher frequencies and higher values than for the electrodes with other windows. In the case of the capacitance the smallest values are reached for this window size. Furthermore, the increase of the capacitance is at higher frequencies. The reversible trend can be observed for the measurements with the electrodes with the highest window ($(2.0 \times 2.0) \text{ mm}^2$) with the lowest impedance and resistance values and the highest capacitance values over the whole frequency spectra. The flattening of the impedance and the resistance as well as the increase of the capacitance occurs at smaller frequencies than for the other windows. The courses for the electrodes with the middle window ($(1.1 \times 1.1) \text{ mm}^2$) lie between the other two windows and were further explained in the chapter before. No significant differences can be observed for different electrodes with the same window size. Consequently, the influences on the spectra are dependent on the window sizes and not only on the dimensions of the IDEs.

5.3 Simulation of cell-free electrodes by finite element techniques

To complete the characterization of the cell-free electrodes the dielectric properties like the potential and the electric field are simulated by finite element techniques using the software COMSOL Multiphysics 5.2a (see chapter 3.2.2).

It was decided to simulate various layouts of the IDEs and the 8W10E and 8W1E electrodes. For the simulation the frequency with the highest impedance magnitude of each electrode layout (f_{max} , explained in chapter 6.2.2) and an initial electric potential of $V = 0.05$ V are chosen.

Simulation of the electric potential

As a first aspect the electric potential was calculated (in V). In fig. 5.3 a three-dimensional representation of the distribution of the electric potential simulated for the IDE 10 is shown from different perspectives.

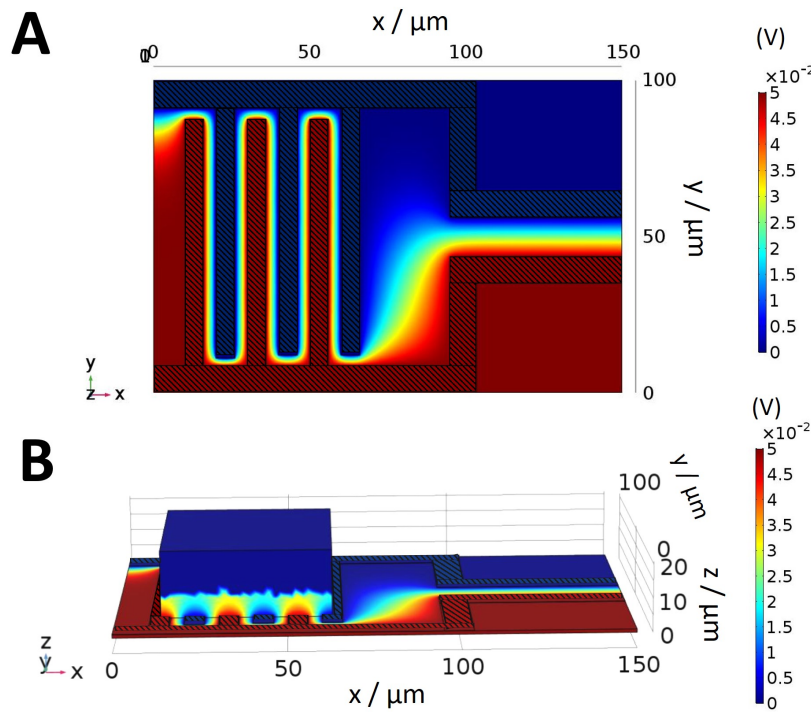


Figure 5.3: Representation of the simulated distribution of the electric potential in V of a cell-free IDE 10 (width and gap 5 μm , respectively) at a frequency $f = 251$ kHz and an initial electric potential of $V = 0.05$ V. The medium is modeled as a homogeneous cuboid on the electrodes (dashed with black lines) and is not shown in **A**. Two various perspectives are chosen: **A**: from the top in z -direction, **B**: from the side in y -direction.

Figure 5.3 shows the outcome of an electric potential simulation for a complete substrate with the cell-free IDE 10 with an electrode finger width and gap of $5\text{ }\mu\text{m}$, respectively. One electrode is defined as the ground, the other as the terminal. For the simulation a frequency of $f=251\text{ kHz}$ and an initial electric potential of $V=0.05\text{ V}$ was chosen. The electric potential can be seen at the whole area of the substrate, but only within the medium (modeled as the cuboid) a distribution in z -direction is obtained. The penetration into the medium reveals as a semicircle above the electrodes. The radius of the semicircle is simulated to be $5\text{ }\mu\text{m}$ which corresponds to the width of one finger. The electric potential does not spread further into the medium. This calculation will be further analyzed in the two-dimensional representation (see fig. 5.6).

For a complete comparison the electric potential of the ECIS electrodes is simulated under the same conditions as for the IDE 10 with the exception of the different frequency of $f=4\text{ kHz}$ for the ECIS electrodes. For a better overview only one measurement chamber (well) of each ECIS array was simulated with the corresponding working and counter electrodes (explained in chapter 4.3.2). Each well of the 8W1E arrays (fig. 5.4 A) comprises one small working electrode with a diameter of $250\text{ }\mu\text{m}$ and a big counter electrode with a shape of an angular horseshoe. In addition to the same counter electrode as the 8W1E arrays, one well of the 8W10E arrays (fig. 5.4 B) has ten working electrodes, each with a diameter of $250\text{ }\mu\text{m}$.

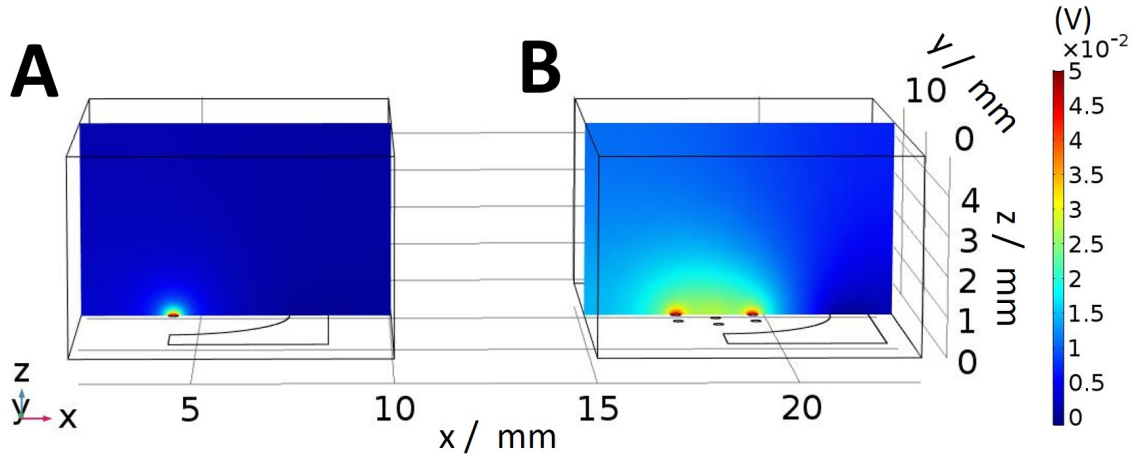


Figure 5.4: Three-dimensional scheme of the simulated electric potential in V of two wells of the ECIS arrays. The simulation was performed at a frequency of $f=4\text{ kHz}$ and with an initial electric potential of $V=0.05\text{ V}$. The medium is mapped as a cuboid above the electrodes, whereas only one xz plane is monitored. The electrodes are modeled as holes in the passivation. The electrodes in two wells of various ECIS array types are analyzed: **A:** well of the **8W1E** array with one working and one counter electrode and **B:** well of the **8W10E** array with ten working and one counter electrode.

In fig. 5.4 the half area of the counter electrode with a shape similar to an angular horseshoe in both simulations as well as the half of the working electrode in the case of the well of the 8W1E array (fig. 5.4 **A**) and five working electrodes in the well of the 8W10E array (fig. 5.4 **B**) can be seen. Since the electrodes were modeled as holes in the passivation of the well, it was not necessary to draw the leads. For a better overview the potential within the medium is only displayed with one xz plane. The counter electrode is defined as the ground, whereas the working electrodes are representing the terminal. The simulated electric potential is seen as a semicircle above the WEs. To achieve a better resolution of the distribution of the electric potential, fig. 5.4 has been enlarged with the focus on the working electrodes (see fig. 5.5).

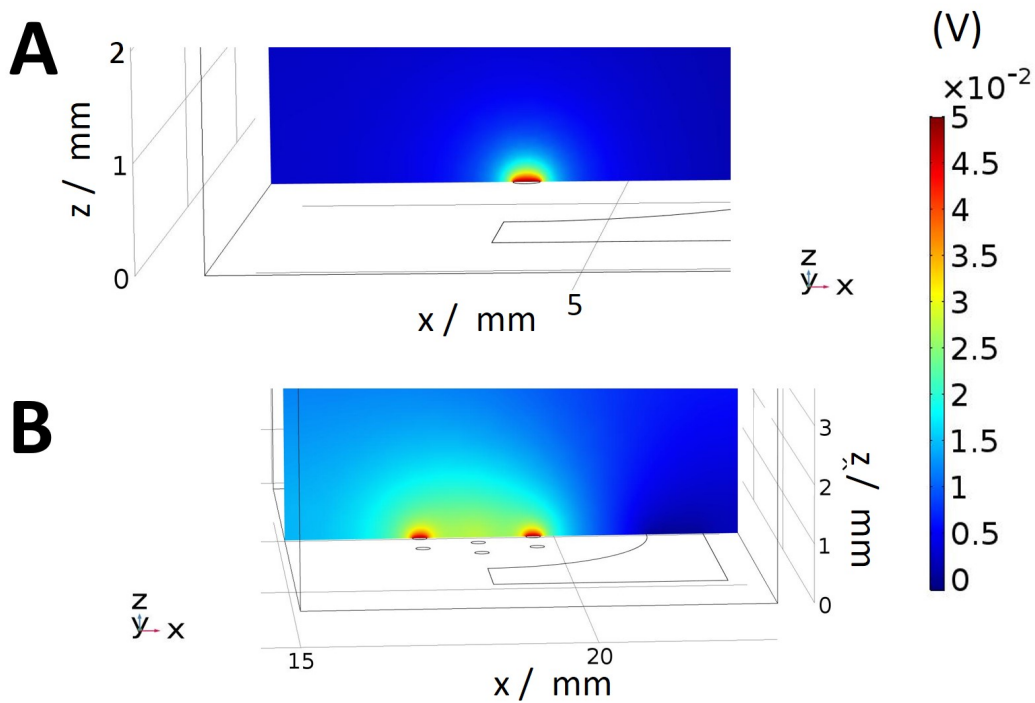


Figure 5.5: Magnification of the three-dimensional scheme of the calculated electric potential in V of the wells of the ECIS arrays seen in fig. 5.4. For the simulation a frequency of $f = 4$ kHz and an initial electric potential of $V = 0.05$ V was used. The medium is monitored with only one xz plane and the electrodes are simulated as holes in the passivation. Two different wells of the ECIS electrodes are used and enlarged with focus on the distribution around the working electrodes: **A**: excerpt of the well of the **8W1E** array and **B**: excerpt of the well of the **8W10E** array.

In fig. 5.5 the magnification of the two modeled wells (**A**: well of 8W1E array, **B**: well of 8W10E array) can be seen with focus on the distribution of the electric potential around the working electrodes. Due to the fact that only one working electrode is used in the well of the 8W1E array the spatial expansion of the potential is much lower than in the case of the ten working electrodes in the well of the 8W10E array.

With this array a significant greater spatial extension of the potential can be seen due to the higher number of electrodes.

This propagation of the electric potential into the electrolyte can better be shown in a two-dimensional representation (see fig. 5.6). For the wells of the 8W1E and the 8W10E array the xz planes, shown in the three-dimensional representation in fig. 5.4, were used and renamed into a xy dimension. Therefore, only two working electrodes are displayed in the case of the well of the 8W10E array (fig. 5.6 C).

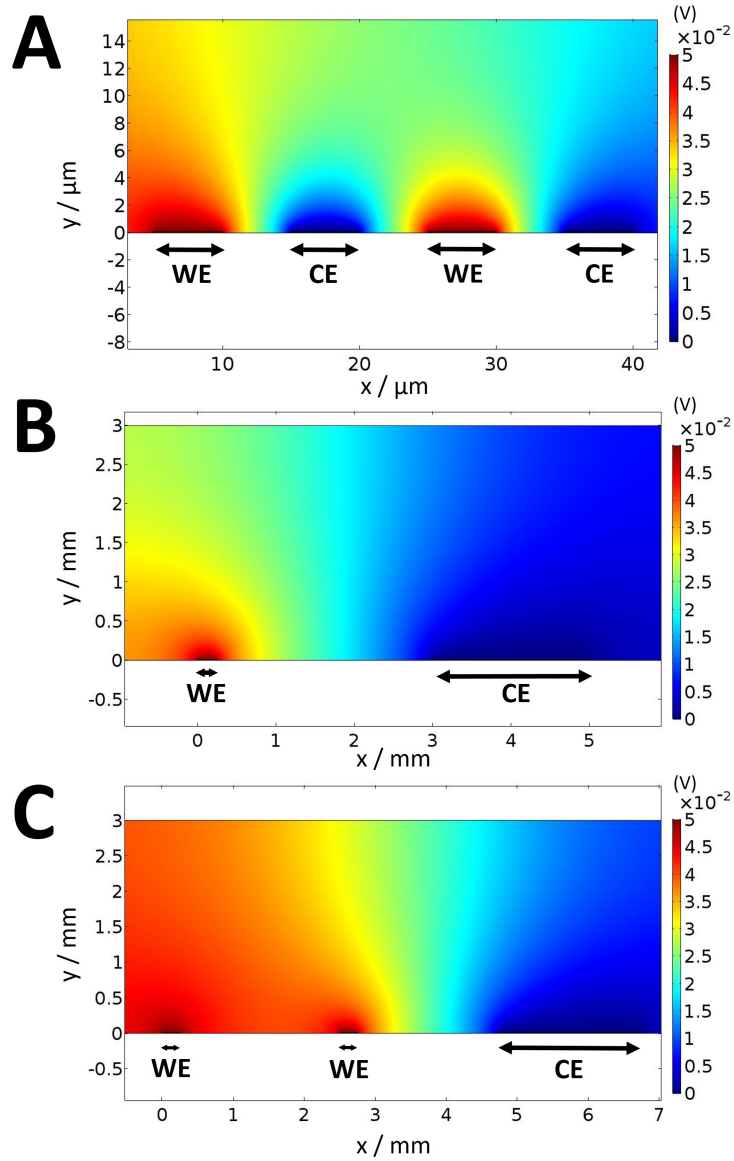


Figure 5.6: Two-dimensional cross section of the simulated electric potential of various cell-free electrode types in V with an initial electric potential of $V = 0.05$ V. For a better understanding the dimensions and the location of the electrodes are marked with arrows. For this simulation the **A:** IDE 10 at $f = 251$ kHz, **B:** electrodes of one well of the 8W1E array at $f = 4$ kHz and **C:** electrodes of one well of the 8W10E array at $f = 4$ kHz were modeled. CE: counter electrode, WE: working electrode.

The two-dimensional representation of the simulation (fig. 5.6) clarifies that the spatial expansion of the electric potential into the electrolyte is strongly dependent on the dimensions of the working and the counter electrode. In the case of the IDE 10 (fig. 5.6 **A**) the width of the fingers is $5\text{ }\mu\text{m}$ and it can be seen that the maximal expansion of the potential into the electrolyte is in a range of $5\text{ }\mu\text{m}$. Within this distance the electric potential arises to $V \approx 0.02\text{ V}$ (CE) and decreases to $V \approx 0.03\text{ V}$ (WE), respectively. More than $5\text{ }\mu\text{m}$ away from the electrode in the electrolyte, the electric potential settles to the value of $V \approx 0.025\text{ V}$. The exceptions are the electrodes at the rim of the medium where the less defined boundary conditions lead to this side-effect of the simulation which can be neglected. Looking at the electrodes in the ECIS arrays (fig. 5.6 **B** and **C**) it is important to note that the spatial dimension is changing from μm (IDE 10) to mm (ECIS arrays) because of the distance between WE and CE. Furthermore, the side-effects of the simulation at the rim of the medium can also be seen for the wells of the ECIS arrays. The simulated electric field in the well of the 8W1E array (fig. 5.6 **B**) shows values of $V \approx 0.03\text{ V}$ in a distance of 1.5 mm from the WE, whereas values of $V \approx 0.01\text{ V}$ can be seen in a distance of 1.5 mm above the CE. In fig. 5.6 **C** a cross section of the whole well of the 8W10E array is observed which only shows two WEs and the CE. The expansion of the electric field in the y-direction does not show any borders. In a distance of 2 mm above the WEs values of $V \approx 0.0375\text{ V}$ and $V \approx 0.035\text{ V}$ can be simulated. In this distance above the CE values of $V \approx 0.01\text{ V}$ are reached. Comparing these simulations it is obvious that the dimensions of the electrodes have a huge influence on the distribution of the electric field into the electrolyte. This dependence was further confirmed with a two-dimensional simulation of cell-free IDEs with various layouts (see fig. A.1 in the appendix). The electric field simulated with the IDE 7 (width: $4\text{ }\mu\text{m}$, gap: $3\text{ }\mu\text{m}$) shows a distribution in y-direction which is mainly seen in a distance of $3.5\text{ }\mu\text{m}$ above the electrodes. In this distance values of $V \approx 0.025\text{ V}$ (CE) and $V \approx 0.0325\text{ V}$ (WE) are reached. This expansion is increasing with increasing electrode dimension, like seen with the IDE 20 (width $10\text{ }\mu\text{m}$, gap: $10\text{ }\mu\text{m}$). With this electrode layout the main fraction of the electric potential is simulated in a semicircle above the electrodes with a radius of $\approx 8\text{ }\mu\text{m}$. To complete the simulation the IDE 300 (width: $150\text{ }\mu\text{m}$, gap: $150\text{ }\mu\text{m}$) are modeled. This electrode follows the trend and shows a distribution of the electric field of $\approx 150\text{ }\mu\text{m}$ above the electrodes into y-direction.

In summary, the dimensions of the electrodes have a significant influence on the distribution of the potential into the electrolyte. With the interdigitated layout a extension of the potential in the form of a semicircle with the radius of the electrode width above the electrodes into the electrolyte can be simulated. The electrodes of

the wells of the ECIS arrays have a larger distribution in the electrolyte due to their much greater dimensions of the width and spacing of WE and CE.

Simulation of the electric field

The second parameter which was simulated was the electric field in V/m.

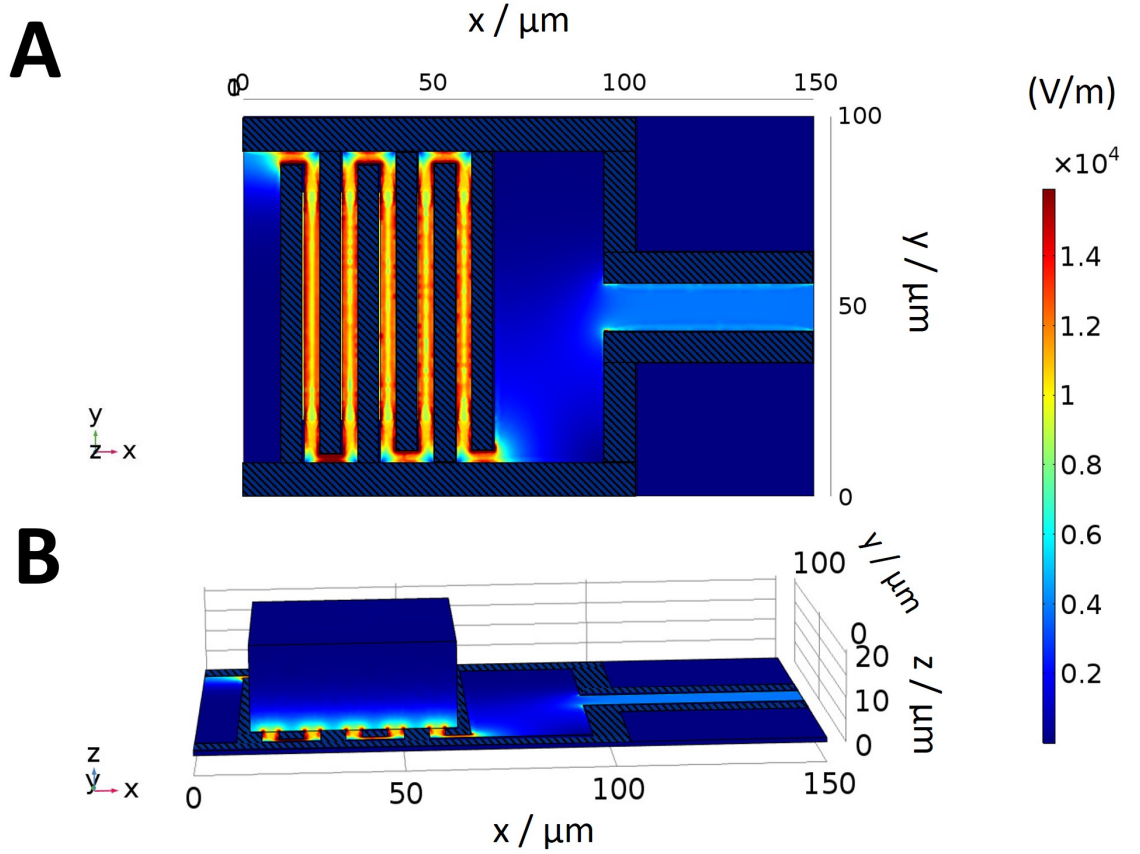


Figure 5.7: Three-dimensional scheme of the simulated electric field of an IDE 10 in V/m at a frequency of $f = 251$ kHz and an initial electric potential of $V = 0.05$ V. The medium is modeled as a cuboid on the electrodes but is not shown in **A**. The electrodes are dashed with black lines. For a better representation various perspectives are chosen: **A**: from the top in z-direction without the medium, **B**: from the side in y-direction.

In fig. 5.7 the electric field simulated for the IDE 10 at a frequency of $f = 251$ kHz and an initial electric potential of $V = 0.05$ V is monitored in a three-dimensional representation with various angles of view. The highest intensities of the electric field are seen at the areas where the electrodes are close to each other, in particular at the edges of the electrodes ($E \geq 1.5 \cdot 10^4$ V/m). At the leads a low intensity is observed, whereas between the interdigitated fingers the electric field is more significant ($E \approx 1.1 \cdot 10^4$ V/m). An expansion in z-direction is only monitored within the

medium. For a better analysis of the distribution of the electric field into the electrolyte, a magnification of the three-dimensional scheme (fig. 5.7 B) was performed in fig. 5.8.

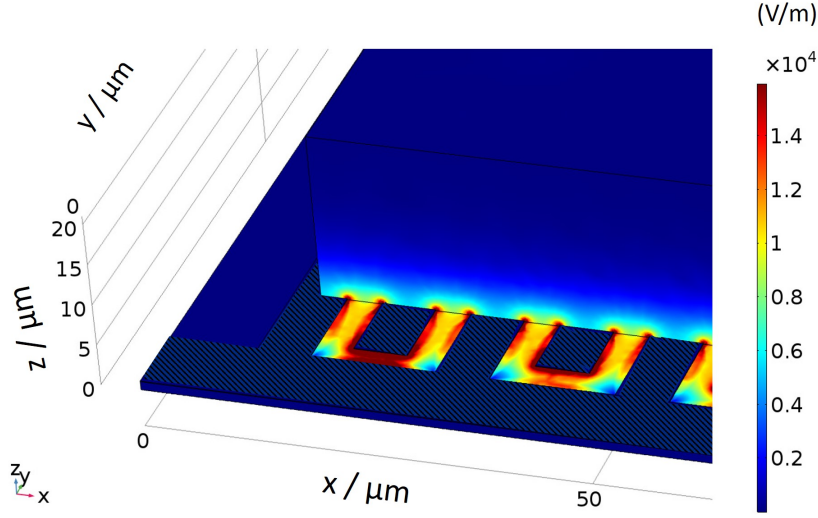


Figure 5.8: Magnification of the three-dimensional scheme of the simulated electric field of a cell-free IDE 10 in V/m at a frequency of $f = 251$ kHz and an initial electric potential of $V = 0.05$ V. The electrodes were highlighted with black dashes and the medium is modeled as a cuboid on the electrodes.

In fig. 5.8 it can be seen that the distribution of the electric field into the electrolyte is restricted to a volume close to the electrodes. The highest values of the electric field are simulated at the edges of the electrodes with a value of $E \geq 1.5 \cdot 10^4$ V/m. Between the electrodes in the electrode gap values of $E \approx 0.9 \cdot 10^4$ V/m can be reached near the substrate. Increasing the distance from the substrate in the electrolyte the electric field is strongly decreasing. In a distance of $\approx 3 \mu\text{m}$ above the electrode gap the electric field is simulated with values of $E \approx 0.7 \cdot 10^4$ V/m. At a distance of $\approx 5 \mu\text{m}$ an electric field of $E \approx 0.3 \cdot 10^4$ V/m is seen which continues to decrease sharply to a distance of $\approx 10 \mu\text{m}$. At a greater distance $> 10 \mu\text{m}$ the values of the electric field are negligibly small. With this it can be assumed that the penetration depth has a correlation with the gap between the electrodes. This assumption will be further analyzed with the two-dimensional simulations in fig. 5.10.

To further examine the distribution of the electric field into the electrolyte the three-dimensional simulations for the electrodes of one well of the 8W1E (fig. 5.9 A) and for the electrodes of one well of the 8W10E array (fig. 5.9 B) is simulated at a frequency $f = 4$ kHz and with an initial electric potential of $V = 0.05$ V. For simplification, the electrodes are modeled as holes in the passivation. Similar to the representation of the electric potential only one xz plane of the medium is shown to enable a better overview and the look onto half of the electrode structure. In

fig. 5.9 it is obvious that the electric field shows the highest values at the working electrodes (WE) ($E \geq 4 \cdot 10^4 \text{ V/m}$). In both wells of the ECIS arrays a semicircle distribution of the electric field in the electrolyte can be seen. In a distance of 0.5 mm above the WE of the well of the 8W1E array (fig. 5.9 A) the electric field amounts to $E \approx 1.75 \cdot 10^4 \text{ V/m}$, whereas in a distance of 1 mm it decreases to a value of $E \approx 1.0 \cdot 10^4 \text{ V/m}$. Increasing the distance to the WE no significant value of the electric field is seen. In this well the electric field at the counter electrode (CE) is comparatively small and shows higher values ($E \geq 4 \cdot 10^4 \text{ V/m}$) only at the edges of the electrode in a very small volume above it. The distribution of the electric field in the well of the 8W10E array shows differences (see fig. 5.9 B). Because of the chosen xz plane only two of the ten working electrodes can be seen in this representation. Similar to the 8W1E electrodes the electric field is distributed in a semicircle shape into the electrolyte. In a distance of $\approx 0.5 \text{ mm}$ above the WEs the values of the electric field amounts to $E \approx 1.75 \cdot 10^4 \text{ V/m}$. As a difference to the electrodes of the 8W1E array an electric field of $E \approx 1.2 \cdot 10^4 \text{ V/m}$ in a distance of 2 mm above the WEs can be simulated. This is the double penetration depth of the electric field in the electrolyte in comparison to the electrodes of the 8W1E array. Consequently, with more WE more parts of the electrolyte can be analyzed.

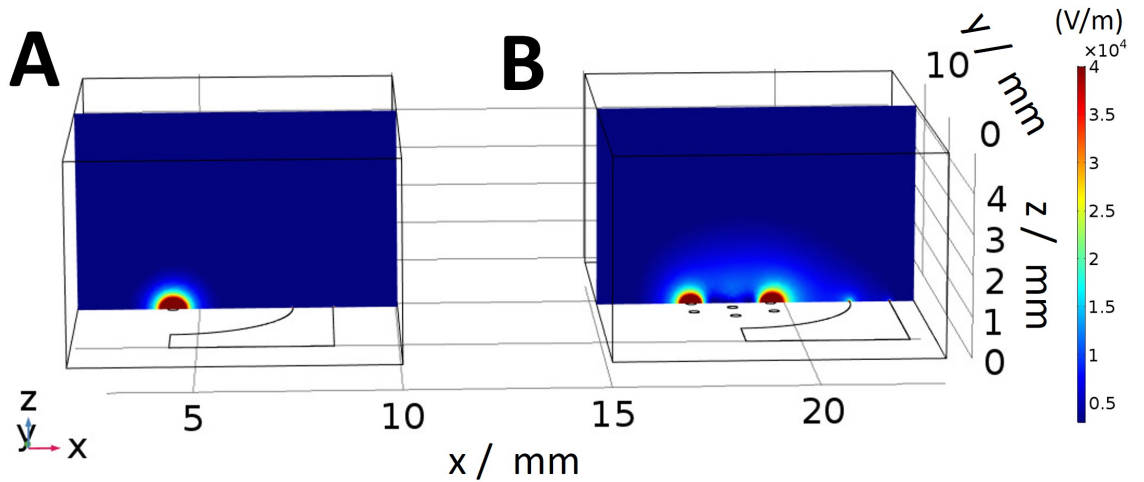


Figure 5.9: Three-dimensional representation of the simulated electric field for the cell-free electrodes in the wells of the ECIS arrays in V/m at a frequency $f = 4 \text{ kHz}$ and with an initial electric potential of $V = 0.05 \text{ V}$. The medium is shown as a cuboid above the electrodes, whereas only one xz plane is displayed. The simulation was proceeded for the electrodes in one well of **A**: the 8W1E array and **B**: the 8W10E array.

In the three-dimensional simulations a dependence of the layout of the electrodes to the distribution of the electric field into the electrolyte is seen. To confirm and to further analyze this dependence different electrode layouts are modeled to simulate the electric field in two dimensions.

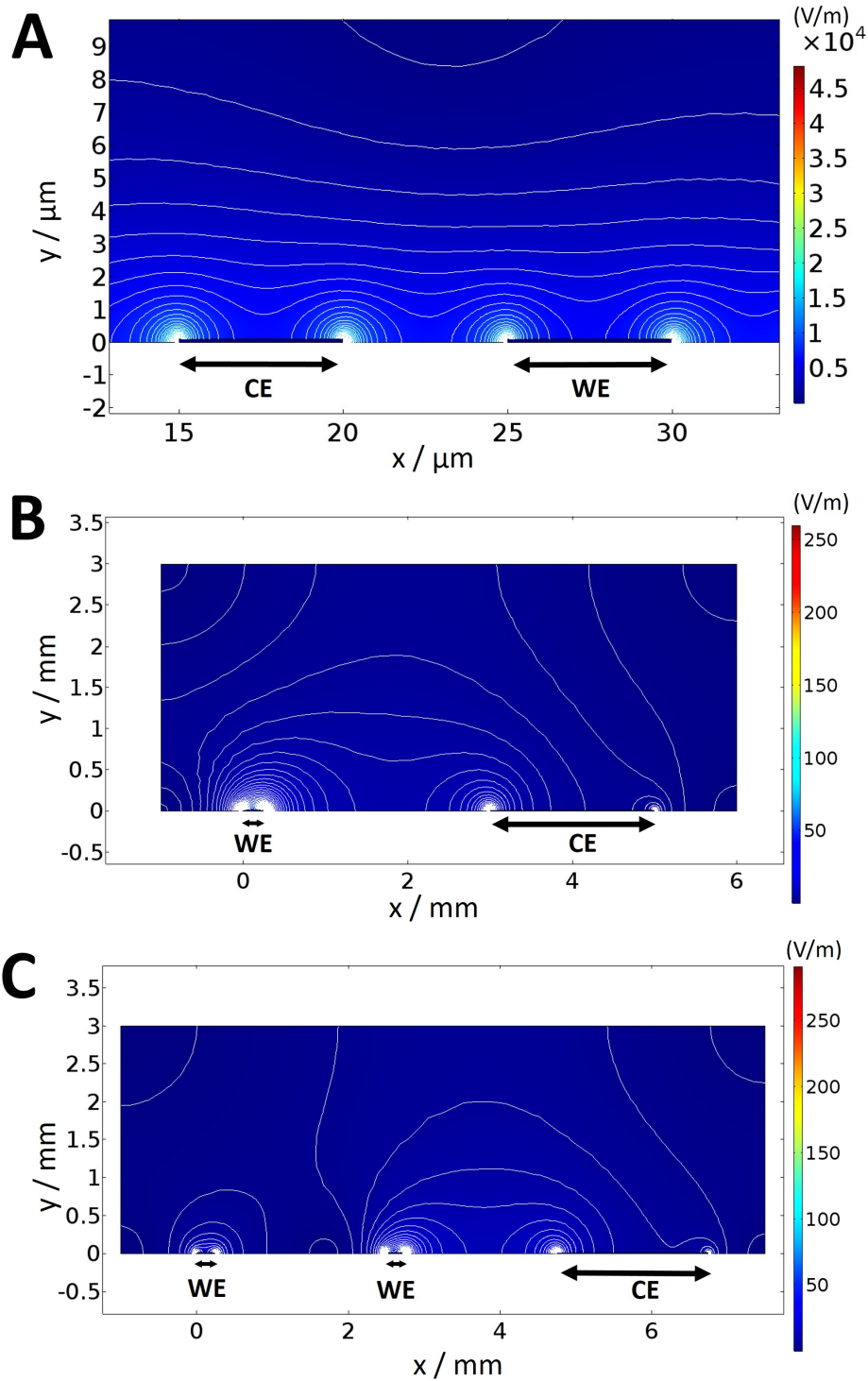


Figure 5.10: Two-dimensional image of the simulated electric field of various electrode layouts. A filled contour representation was displayed. For a better understanding the dimensions and the location of the electrodes are marked with arrows. For this simulation an initial electric potential of $V = 0.05$ V was used and various electrodes were modeled: **A:** IDE 10 at $f = 251$ kHz, **B:** electrodes of one well of the 8W1E array at $f = 4$ kHz, **C:** electrodes of one well of the 8W10E array at $f = 4$ kHz. CE: counter electrode, WE: working electrode.

In fig. 5.10 the electric field of the IDE 10 (fig. 5.10 **A** at a frequency of $f = 251$ kHz), the electrodes of one well of the 8W1E array (fig. 5.10 **B** at a frequency of $f = 4$ kHz) and the electrodes of one well of the 8W10E array (fig. 5.10 **C** at a frequency of $f = 4$ kHz) are modeled with an initial electric potential of $V = 0.05$ V, respectively. In order to achieve a better overview, the electric field was represented by contour levels which are filled in. It must be emphasized that the dimensions are changing from μm (IDE 10) to mm (ECIS arrays). For the IDE 10 (fig. 5.10 **A**) an enlarged display of only two electrode fingers is monitored, whereas the xz planes seen in the three-dimensional representation of the wells of the ECIS arrays are used to show the individual distribution of the electric field (8W1E: fig. 5.10 **B**, 8W10E: fig. 5.10 **C**). Furthermore, the electrodes were modeled as holes in the passivation and no leads can be seen. For all three electrode types the working (WE) and the counter electrode (CE) are labeled and highlighted by arrows for a better understanding of the dimensions and the location of the electrodes.

The individual simulations show an inhomogeneous intensity distribution of the electric field of the various electrode types. Analyzing the electric field of the IDE 10 (fig. 5.10 **A**) some observations have to be emphasized. The electric field is strongest at the edges of the individual electrodes ($E \approx 4 \cdot 10^4$ V/m), whereas the overall electrode surface represents smaller field strengths. It is obvious that the penetration of this field into the medium is not very spatially extended. In a distance of $0.3 \mu\text{m}$ above the electrode edges values up to $E \approx 2 \cdot 10^4$ V/m are simulated. Increasing the distance to the electrode edges in y-direction the electric field is strongly decreasing. $1 \mu\text{m}$ above the electrode edges only values of $E \approx 1 \cdot 10^4$ V/m can be seen, whereas $2 \mu\text{m}$ above the electrode edges the electric field is decreased to $E \approx 0.8 \cdot 10^4$ V/m. In a distance of $5 \mu\text{m}$ above the electrode edges the values are comparably small ($E \approx 0.5 \cdot 10^4$ V/m). With a higher distance the electric field becomes negligible. Consequently, most of the electric field is seen in a range under $3 \mu\text{m}$ above the electrodes, whereas the greatest intensities are monitored in a distance under 500 nm. This leads to the assumption that the current flow of IDEs with a small pitch has its main part within some hundred nanometer above the electrodes.

In the case of the electrodes of one well of the 8W1E array (fig. 5.10 **B**) it also can be observed that the electric field is the highest at the edges of the working electrodes ($E \approx 250$ V/m). The electric field decreases as a function of the distance to the electrodes, similar to the IDE 10. The higher the penetration depth into the medium, the smaller the values of the electric field. In a distance of 0.5 mm above the WE values up to $E \approx 60$ V/m are reached. In the electrode gap a value of $E \approx 50$ V/m in a distance of 1 mm above the substrate is gained. Within a distance of 1.5 mm the electric field is $E \approx 40$ V/m in this electrode gap, whereas it is negligible in a larger distance. Consequently, the main distribution of the electric field can be seen in a

distance of ≈ 1 mm above the electrode gap in the case of the 8W1E electrodes. The penetration depth is consequently strongly dependent on the distance between the WE and CE which is much higher for the 8W1E electrodes than for the IDE 10.

This is in agreement with the simulation of the electrodes of the well of the 8W10E array (fig. 5.10 C). The electric field is repeatedly the highest at the edges of the electrodes ($E \approx 270$ V/m) and is decreasing with the penetration into the medium. Due to the chosen cross section of the well only two working electrodes are monitored. Between the WE which is the nearest to the CE a semicircle distribution of the electric field in this electrode gap can be seen. In a distance of 0.5 mm the electric field arises to $E \approx 60$ V/m and to $E \approx 50$ V/m in a penetration depth of 1 mm. Up to a distance of 2 mm the electric field amounts to $E \approx 40$ V/m, whereas with a greater distance the electric field is negligibly small. Due to the fact that only two WEs are modeled the distribution of the electric field is slightly under determined. In a well of the commercially available 8W10E arrays there are several WEs between the two shown in this image. Consequently, the electric field is stronger in the range of these WEs as it overlaps which can clearly be observed in fig. 5.9 in the three-dimensional representation. This simulation also strengthens the assumption that the distance of the electrodes have a clear influence on the penetration depth of the electric field into the electrolyte.

To further substantiate this assumption, IDEs with various dimensions were simulated (see fig. A.2 in the appendix). For this, IDE 7 (width: $4\text{ }\mu\text{m}$, gap: $3\text{ }\mu\text{m}$), IDE 20 (width: $10\text{ }\mu\text{m}$, gap: $10\text{ }\mu\text{m}$) and IDE 300 (width: $150\text{ }\mu\text{m}$, gap: $150\text{ }\mu\text{m}$) were chosen. The highest values of the electric field can repeatedly be seen at the edges of the electrodes (IDE 7: $E \approx 5.5 \cdot 10^4$ V/m, IDE 20: $E \approx 3 \cdot 10^4$ V/m, IDE 300: $E \approx 8 \cdot 10^3$ V/m). Starting from these edges the electric field propagates into the medium in these simulations. The most revealing part of the simulations is the distribution of the electric field between the electrodes above the electrode gap. Looking at the IDE 7 a value of $E \approx 1.8 \cdot 10^4$ V/m is simulated in a distance of $0.5\text{ }\mu\text{m}$ to the substrate above the electrode gap. In a distance of $1.5\text{ }\mu\text{m}$ to the substrate values of $E \approx 1.5 \cdot 10^4$ V/m can be seen, whereas the electric field is more decreasing the greater the distance to the substrate is (at $2.5\text{ }\mu\text{m}$: $E \approx 0.9 \cdot 10^4$ V/m and at $4\text{ }\mu\text{m}$: $E \approx 0.5 \cdot 10^4$ V/m). Increasing the distance to the substrate $> 5\text{ }\mu\text{m}$ the electric field is negligible small. A similar distribution is revealed for the IDE 20. In the electrode gap an electric field of $E \approx 0.8 \cdot 10^4$ V/m is simulated in a distance of $2\text{ }\mu\text{m}$ above the substrate. This electric field is further reduced to $E \approx 0.4 \cdot 10^4$ V/m in a distance of $5\text{ }\mu\text{m}$, whereas only $E \approx 0.15 \cdot 10^4$ V/m is reached at a distance of $9\text{ }\mu\text{m}$ to the substrate. Above a distance of $12\text{ }\mu\text{m}$ to the substrate no significant electric field can be seen anymore. For the IDE 300 the distribution is similar but with different values. Overall smaller values by a factor of ten of the electric field are simulated for this

layout. As with the other IDEs the electric field is decreasing with a higher distance from the substrate. In a distance of 25 μm the value of the electric field amounts to $E \approx 0.9 \cdot 10^3 \text{ V/m}$. Up to a distance of 60 μm an electric field of $E \approx 0.6 \cdot 10^3 \text{ V/m}$ is simulated, till a distance of 160 μm with a value of $E \approx 0.4 \cdot 10^3 \text{ V/m}$ is reached. With greater distance to the substrate the electric field can be neglected. The main part of the electric field can consequently be simulated in a distance to 60 μm to the substrate.

Comparing all these simulations a clear dependence of the distance to the electrodes on the distribution of the electric field into the electrolyte can be seen. The smaller the gap between the electrodes is, the smaller is the penetration of the electric field into the electrolyte. Even with small differences of the dimensions, like the IDE 7 and IDE 10, clear variations of the penetration are detectable. In a distance in y-direction according to the size of the electrode gap the electric field displays only a fraction of the highest values at the electrode edges: i) IDE 7: 10.9 % at a distance of 3 μm , ii) IDE 10: 12.5 % at a distance of 5 μm , iii) IDE 20: 5 % at a distance of 5 μm , and iv) IDE 300: 6.2 % at a distance of 150 μm . This proves that for the IDEs the main part of the electric field is simulated in a volume very close to the electrodes which is strongly increasing with a higher distance to the electrodes depending on the size of the electrode gap. For very high gap sizes, like in the wells of the 8W1E and 8W10E array, a penetration depth of several mm results.

These simulations can be considered as evidence that the electrode layout has a great influence on the distribution of the electric field and that various layouts can be used to force a different focus of the studied part of the electrolyte in a cell-free arrangement.

5.4 Discussion

The impedance spectra of a cell-free electrode can be expressed in an equivalent circuit with just two elements: i) the impedance of the electrode/electrolyte interface and ii) the resistance of the bulk electrolyte R_{bulk} (Reiss and Wegener, 2015; Mamouni and Yang, 2011) which are connected in series (see fig. 5.11 A).

In general, for a noble electrode with almost no charge transfer across the interface, a capacitive charge due to the ions of the electrolyte is present. This initiates an electrical structure of the metal analogous to a capacitor (Muñoz-Berbel et al., 2008). Nevertheless, no interface behaves as an ideal capacitor and it is necessary to depict the interface of a noble metal electrode in an impedance spectra with the constant phase element (CPE) (Wegener, 2010). The impedance of the CPE represents the electrode/electrolyte interface resulting from the electrical double layer and scales with the inverse of the area of the electrode (see eq. 3.20 in chapter 3.1.2) (Reiss

and Wegener, 2015; Xiao and Luong, 2010). Further, due to the eq. 3.19 in chapter 3.1.2, the R_{bulk} is defined as the sum of the solution resistance and the constriction resistance (Lo et al., 1995). The solution resistance is a result of the current which has to flow through the electrolyte solution. The associated length of the way through the solution is dependent on the electrode geometry and influences the magnitude of the solution resistance (Muñoz-Berbel et al., 2008). The constriction resistance is initiated from the constriction of the electric field from the electrolyte to the size of the electrode and is related with $1/r$ to the radius of the electrode (Wegener, 2010). R_{bulk} dominates the impedance spectrum in the higher frequency range ($> 10^4$ Hz) (Mamouni and Yang, 2011) and acts as a frequency-independent Ohmic resistor, leading to a horizontal line in the spectrum (Lo et al., 1995). In lower frequency ranges ($< 10^4$ Hz) the total impedance is determined by the $|Z|_{CPE}$. In the capacitance spectrum the slope of the capacitance reveals that the electrode is not a perfect capacitor (Wegener, 2010). Due to the equivalent circuit of IDEs (fig. 5.11 B) (Mamouni and Yang, 2011) the working and the counter electrode are equivalent. Consequently in comparison to an individual set of electrodes, the slope accords only to half the capacitance (Muñoz-Berbel et al., 2008).

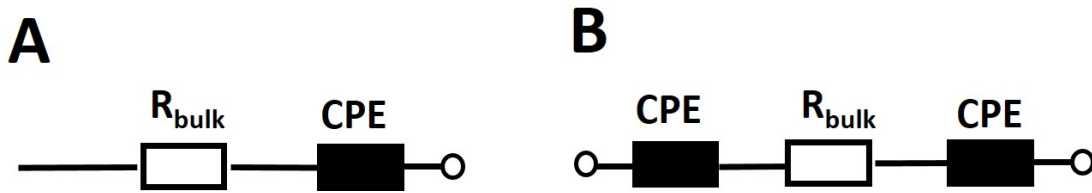


Figure 5.11: Equivalent circuit for cell-free electrodes. **A:** electrodes in a well of the ECIS array, **B:** electrodes of an IDE layout. CPE: constant phase element, R_{bulk} : resistance of the bulk.

Cell-free spectra measured with different electrode types

On the basis of these definitions the spectra of the cell-free electrodes can be explained. The shift in y-direction in the impedance and the resistance spectrum of the different electrode types is due to the different electrode areas, because in this frequency range $< 10^4$ Hz the $|Z|_{CPE}$ dominates the signal which is inversely proportional to the electrode area (see eq. 3.20 in chapter 3.1.2). 8W1E electrodes have a much smaller electrode area ($A_{El} = 5 \cdot 10^{-4} \text{ cm}^2$) than the 8W10E electrodes ($A_{El} = 5 \cdot 10^{-3} \text{ cm}^2$) which is seen in the shift to higher impedance values. All the interdigitated electrodes were insulated with photopolymer leading to a defined non-insulated electrode area of $(1.1 \times 1.1) \text{ mm}^2$ for every pitch resulting in an electrode area of one electrode comb independent of the pitch of $A_{El} = 3.0 \cdot 10^{-3} \text{ cm}^2$. The self-made IDE 400 and IDE 300 show a small difference to the other electrodes, which can be explained with the photolithography process. Due to the unique steps of the

process, the gold fingers are not completely straight and the electrode area can be slightly different. This is also revealed in the capacitance spectra. The capacitance is proportional to the electrode area (Xiao and Luong, 2010) and shows different values for the various electrode types depending on the electrode area. The smaller the electrode area, the smaller is the capacitance value.

The flattening of the impedance and resistance with higher frequencies can be explained with the influence of R_{bulk} . As aforementioned, this resistance is a frequency-independent Ohmic resistor and is indicated by a horizontal line. The solution resistance which is a part of this resistance, is dependent on the distance between the electrodes. The greater the gap between the electrodes, the longer is the way of the current through the solution and consequently, the higher is the solution resistance. The other part of R_{bulk} is the constriction resistance which scales with $1/r$ (r : radius of the electrode). Consequently, the constriction resistance is higher, the smaller the electrode radius. The seen R_{bulk} is then a combination of both resistances.

8W1E electrodes have the longest way between the working electrode to the counter electrode and show therefore the highest solution resistance. In addition, the working electrode of the 8W1E electrode has a diameter of $250\text{ }\mu\text{m}$, which is one tenth of the value for the ten working electrodes in one well of the 8W10E array, resulting in a much higher constriction resistance. These comparatively high solution and constriction resistances are the explanation for the higher R_{bulk} value of the electrodes of the 8W1E electrode compared to the 8W10E electrodes. The values for R_{bulk} of the 8W10E electrodes and the IDE 300 and IDE 400 are comparable. The electrodes of the 8W10E array have a high averaged solution resistance due to the distance between the WEs and the CE and a high constriction resistance due to the ten round WEs. The distance of the WE and CE is smaller in the case of the IDE 300 and IDE 400 but the individual finger length of the non-insulated electrode area is comparatively long ($\approx 1100\text{ }\mu\text{m}$), which leads to an overall high solution resistance. The constriction resistance of IDE 300 and IDE 400 is smaller than for the 8W10E electrodes because of the comparatively large window size. These different resistance variables can cancel each other out, resulting in a comparable value for R_{bulk} for these electrodes. The IDEs with smaller gaps show a much smaller R_{bulk} , due to the smaller way of the current through the electrolyte and the corresponding smaller solution resistance. Due to the same window size of the IDEs, the constriction resistance should not show big differences between the IDEs with these small pitches. Nevertheless, the higher R_{bulk} for the IDE 10 than for IDE 12 is noticeable. It is possible to observe the same values of R_{bulk} for the IDE 20 and IDE 10, and the same for the IDE 12 and IDE 7, respectively. This contradicts the explanation of the different solution resistances due to the distance of the electrodes and the same constriction resistance because of the same window size. It follows that the differences

of R_{bulk} of the small electrodes must be due to something else. A possible explanation for this is the influence of leads and the contact pins of the electrodes (R_{lead} and $R_{cont.}$) which can change the measured signal at higher frequencies. IDE 20 and IDE 10 were provided from Metrohm DropSens, and IDE 12 and IDE 7 from Fraunhofer EMFT. Due to the different producers of the electrodes the leads and contact pins can have slightly different sizes and associated with this distinct resistances resulting in an influence of the measured resistance in the higher frequency ranges. These parasitic resistive elements can be seen massively in the strong fluctuation of the measured capacitance with high frequencies. Depending on the electrode type those can influence the capacitance from 100 kHz to higher frequencies leading to individual impacts. The capacitance of the ECIS electrodes and the IDE 400 and IDE 300 is influenced at lower frequencies than the other IDEs.

Cell-free spectra of different window sizes of IDEs

The spectra of the cell-free electrodes with different window sizes can be explained in parallel to the aforementioned spectra (see fig. 5.1). The different windows are leading to distinct non-insulated electrode areas resulting in individual values of $|Z|_{CPE}$ which is inversely proportional to the electrode area. This is shown in the highest impedance and lowest capacitance values for the electrodes with the smallest window. In general it can be said that with a smaller electrode area higher impedance values and greater fluctuations are revealed (Lo et al., 1993). These fluctuations result from the parasitic influences. Normalizing the capacitance to the area of the individual window similar values for all window sizes could be calculated. This proves that the various capacitance values are only dependent on the electrode size. Furthermore, the electrodes with the smallest window show the highest constriction resistance compared to the bigger ones because of the smaller dimensions of the non-insulated electrode area. This results in higher values for R_{bulk} . The biggest window ((2.0 x 2.0) mm²) has on the one side the highest solution resistance and on the other side the lowest constrictions resistance, resulting in a comparable smaller value for R_{bulk} .

Simulation of the cell-free electrodes by finite element techniques using COMSOL Multiphysics

The electric potential is defined as the work per unit of charge which is required to transfer a charge from a reference to a specified point. Due to the fact that the CEs are determined as ground and the WEs as the terminals, opposite values can be obtained at the various electrodes. Between the electrodes a spreading of the potential occurs. These different values and the distribution within the medium can also be seen in literature, when interdigitated electrodes are simulated. For example, the three-dimensional representation of the IDEs in this work resembles the electric potential colormap in the study of Jun et al. (Jun et al., 2018). The potential between

the electrodes is distributed in the same way as in this work. In the two-dimensional representation the same semicircle expansion of the electric potential is revealed in MacKay et al., 2015a with a maximal distribution of the electric potential into the electrolyte in the range of the electrode width. In all of these simulations the electrodes are side by side to each other. Consequently, there is a big local difference of the electric potential because of the various distances to the electrode with opposite polarity. This spatial dependence is observed in the comparison of the electrodes of the 8W1E and the 8W10E arrays. The electrodes of the 8W10E array have a greater distribution of the electric potential into the electrolyte because of the further distance of most of the WE to the CE.

The second simulated parameter was the electric field strength created when two opposite charges are facing each other. The static electric field is the negative of the gradient of the electric potential. Due to the unit of V/m, it is obvious that the electric field is strongly dependent on the distance between the two electrodes and can be seen as a distant force of individual charges which has a certain field strength and direction at each point in space. With the simulation in this work it can be observed that the electric field is the highest at the edges of the electrodes. This compares favorably with the literature. Bujong et al. and Kenchetty et al. measured the maximal electric field at the edges of the electrodes (Bujong et al., 2015, Kenchetty and Uno, 2020) and Procházka et al. observed high current density peaks at the electrode edges (Procházka et al., 2019). One explanation for this is that the electric field is distorted at the edges because of the boundary effect that the plane does not continue. Another explanation is the spacing of the electrodes to each other. Like aforementioned, the electric field is strongly dependent on the distance between the electrodes (MacKay et al., 2015b). The electrodes in this work have a height of 100 nm. The two lateral sides of the electrodes are facing each other and can be assumed as plane parallel condensators which are the closest parts of the individual electrodes. Consequently, the highest electric field is revealed here. This spatial dependence of the electric field to the electrode dimensions has been frequently analyzed in the development of interdigitated electrodes, particularly the influence of the electrode gap and the electrode width. In general it was demonstrated that a smaller electrode gap size generates a higher average electric field (Bujong et al., 2015; Jun et al., 2018; MacKay et al., 2015a; Singh et al., 2010). An essential condition for this observation is the same potential for the electrodes which are compared. This could also be seen in the simulations of the IDEs in this work which were all proceeded with the same initial electric potential. The average of the electric field is the highest simulated with the IDE 7 and the smallest for the IDE 300. Simulated for the electrodes of the ECIS arrays only a fraction of these values are seen, since there is a much larger distance between the WE and CE. Furthermore,

the influence of the width of the electrode fingers was analyzed in literature. On the one hand, a significant change of the width of the electrode on the IDE performance was reported. It was shown that with decreasing width the average of the electric field becomes higher (Jun et al., 2018). On the other hand, it was revealed that the increasing width of the electrode is not drastically changing the field strength (Singh et al., 2010). This observation was not simulated in this work, because the IDEs used in this thesis vary in gap and width and no measurement was proceeded using electrodes with the same gap but different widths. In summary it can be said that the variance of the gap has the highest effect on the measured electric field and the distinct dimensions of the width of the fingers can be neglected.

This strong dependence of the penetration depth of the electric field on the distance between the electrodes can be confirmed with the simulations in this work. In general it was found that the smaller the gap, the lower is the penetration depth of the electric field into the medium. Van Gerwen et al. calculated that 80 % of the current flows in a layer which is not higher than the spacing between two electrodes (van Gerwen et al., 1998). With the simulation of the electric field in this work this assumption can even be reduced modeling the IDEs. The percentage ratio of the values of the electric field at a distance from the substrate equal to the electrode gap to the highest values at the electrode edges is calculated. Values of 10.9 % (IDE 7, at a distance of 3 μm), 12.5 % (IDE 10, at a distance of 5 μm), 5 % (IDE 20, at a distance of 10 μm) and 6.2 % (IDE 300, at a distance of 150 μm) of the highest value for the electric field can be calculated at this distances to the substrate. Consequently, more than 87 % of the current flows in a range close to the electrodes which is not larger than the size of the electrode gap. Increasing the gap between the WE and the CE to several mm, 16 % (for the electrodes of the well of the 8W1E array) and 14.8 % (for the electrodes of the well of the 8W10E array) of the highest values of the electric field at the electrode edges can be found in the electrolyte at a distance of 1.5 mm to the substrate. This proves that with a much larger electrode gap the penetration depth of the electric field is increasing strongly. Thus, with the dimensions of the electrode layouts the electric field can be focused to various layers near the electrode or on a larger area of the electrolyte.

This chapter revealed different characteristics of the cell-free electrodes used in this work. Even without cells it can be proven that due to the individual penetration depth of the electric field various results can be obtained for the electrode types. The IDEs owe a high sensitivity due to the high electric field and the current density at the electrode vicinity (Singh et al., 2010). On the basis of this observation it is important to analyze in which cell assays a higher sensitivity of the IDEs with various layouts can be obtained because of their different penetration depth of the electric field and in which assays this is a disadvantage.

6 Impedance-based comparison of different mammalian cell lines grown on various electrode layouts

As a first impression the influence of insulating cells on the distribution of the electric field is simulated by finite element techniques using the software COMSOL Multiphysics. Different influencing criteria are varied and the results are compared. In addition, cell lines grown on different electrode layouts are analyzed with impedance-based methods. The measured impedance, resistance and capacitance spectra as well as the micromotion data are used for comparison.

The special characteristic of the interdigitated electrodes used in this work is the smaller dimension of the gold fingers compared to the size of the cells and the related advantages and disadvantages. To prove these subcellular dimensions of the IDEs the size of the cells must be determined first.

The area of the cells was determined for MDCK I, MDCK II, NRK and U373 cells which were cultivated with the same seeding densities as in the following experiments. On the third day after seeding the cells were stained with phalloidin and DAPI and images with the CLSM were taken (see fig. A.3). With the phalloidin staining the borders of the individual cells could be seen and the areas of the cells were measured with the software ImageJ. Apart from this, the radius and the diameter were calculated from the area assuming circular cells (see tab. 6.1).

The smallest area with a value of $(26.0 \pm 0.9) \mu\text{m}^2$ was determined for the MDCK I cells, followed by the size of the MDCK II and NRK cells which could not be distinguished. The biggest area is revealed for the U373 cells. With the assumption of a round shape the radius and the diameters of each cell type were calculated out of the measured area. The resulting radii and diameter show the same trend as the measured areas with the smallest values for the MDCK I cells, the higher ones for the MDCK II and NRK cells and the greatest radius and diameter for the U373 cells. Looking at the images of the stained cells (see fig. A.3) it is obvious that the cells do not have a circular shape and that consequently, the calculation of the radius and the diameter is not very meaningful.

To prove the subcellular dimension of the IDEs, a three-dimensional image of MDCK I

cells cultivated on IDE 12 is shown in fig. 6.1. The tight junction associated ZO-1 protein was stained on the third day after seeding and a three-dimensional stack was taken. The tight junctions are localized at the borders of adjacent cells and consequently, the shape and the associated size of the cells can be seen. Due to the reflection of the fluorescence the gold fingers of the interdigitated structure appear as lines in this image. With this side-effect it is possible to monitor the ratio of the smallest cells used in this work (MDCK I cells) to the width and gap of the gold fingers (here IDE 12). Even with these cells the interdigitated fingers have a smaller dimension. Consequently, it can be demonstrated that the interdigitated electrodes used in this work (with the exception of the IDE 300 and IDE 400) have a subcellular dimension.

Table 6.1: Determination of the cell size of MDCK I (seeding density: 450,000 cells/cm²), MDCK II (seeding density: 450,000 cells/cm²), NRK (seeding density: 450,000 cells/cm²) and U373 cells (seeding density: 100,000 cells/cm²). The cultivated cells were stained with phalloidin and DAPI on the third day after seeding and the area of the individual cells was measured with ImageJ. Following the assumption of circular cells the radius and the diameter were calculated. The mean with the SEM is listed with the number of cells that have been counted.

	MDCK I	MDCK II	NRK	U373
	(n = 216)	(n = 235)	(n = 206)	(n = 192)
area / μm^2	26.0 ± 0.9	39 ± 1	38 ± 1	45 ± 1
radius / μm	2.9 ± 0.5	3.5 ± 0.6	3.5 ± 0.6	3.8 ± 0.6
diameter / μm	6 ± 1	7 ± 1	7 ± 1	8 ± 1

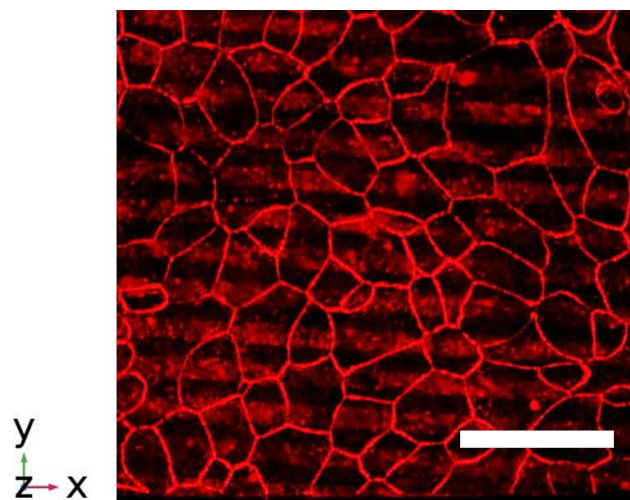


Figure 6.1: MDCK I cells cultivated on IDE 12 with a density of 450,000 cells/cm². On the third day after seeding the tight junction associated ZO-1 protein was stained and a three-dimensional stack with the CLSM (60x) was performed. The scale bar represents 50 μm .

6.1 Simulating the dielectric properties of adherent cells grown on interdigitated electrodes

For a better understanding of the impedance magnitude, cells were simulated on the IDEs by finite element techniques using the software COMSOL Multiphysics 5.2a. The focus was on the distribution of the electric field across the cell bodies with special emphasis on the cell-electrode junction. For simplification a two-dimensional simulation was chosen under the assumption of symmetry of the whole cell-covered electrode. The cells were monitored as rectangles (highlighted by the white dotted lines) with various distances to the electrode surface and with an intercellular gap of 100 nm. The height of the cells (h) was assumed to be 5 μm and the side length to be 7 μm , respectively, with exception of the variation of the cell height in fig. 6.3. In all cases the cells were simulated as completely insulating. For the simulations the frequency f_{max} (explained in chapter 6.2.2) of the individual electrodes (IDE 10: $f_{max} = 251$ kHz; IDE 20: $f_{max} = 200$ kHz, IDE 40: $f_{max} = 100$ kHz, IDE 100: $f_{max} = 4$ kHz, IDE 300: $f_{max} = 4$ kHz) and the electric potential of $V = 0.05$ V was used. The other parameters used for the simulation can be seen in chapter 4.4.4.

In fig. 6.2 cells are simulated with a cell height of $h = 5$ μm in a distance (d) of $d = 25$ nm above the electrodes of the IDE 10, as a representative for the IDEs with smaller pitches. The simulation was performed at $f = 251$ kHz and with the electric potential of $V = 0.05$ V. For a better understanding the intercellular cleft and the location of the electrodes are marked and labeled (with the black arrows and the blue dashes). In fig. 6.2 **A** two complete electrodes (**CE**: counter electrode; **WE**: working electrode) with two whole and two half cells are shown, whereas in fig. 6.2 **B** and **C** two enlarged excerpts of the space underneath the cells are provided. Since the cells are defined as completely insulating at this frequency ($f = 251$ kHz), the electric field has to distribute around the cells. It is obvious that the main part of the electric field is seen underneath the cells between the two electrodes. In this representation a colormap with the unit of V/m is chosen which does not undergo the value of $E \approx 1.0 \cdot 10^4$ V/m in the gap between the electrodes underneath the cells (seen in green). The highest value can be obtained at the edges of the electrodes. Furthermore, it is obvious that depending on the distance to the electrode edge the electric field can also expand through the intercellular cleft. However, the maximal value seen there is $E \approx 0.7 \cdot 10^4$ V/m in one cleft, whereas in the other clefts the values decrease to $E \approx 0.5 \cdot 10^4$ V/m and to $E \approx 0.2 \cdot 10^4$ V/m. The average of the electric field in these clefts is significantly smaller than the electric field underneath the cells. Consequently, with a cell-electrode distance of $d = 25$ nm the main part of the electric field is distributed underneath the cells and a small part can expand through the intercellular cleft.

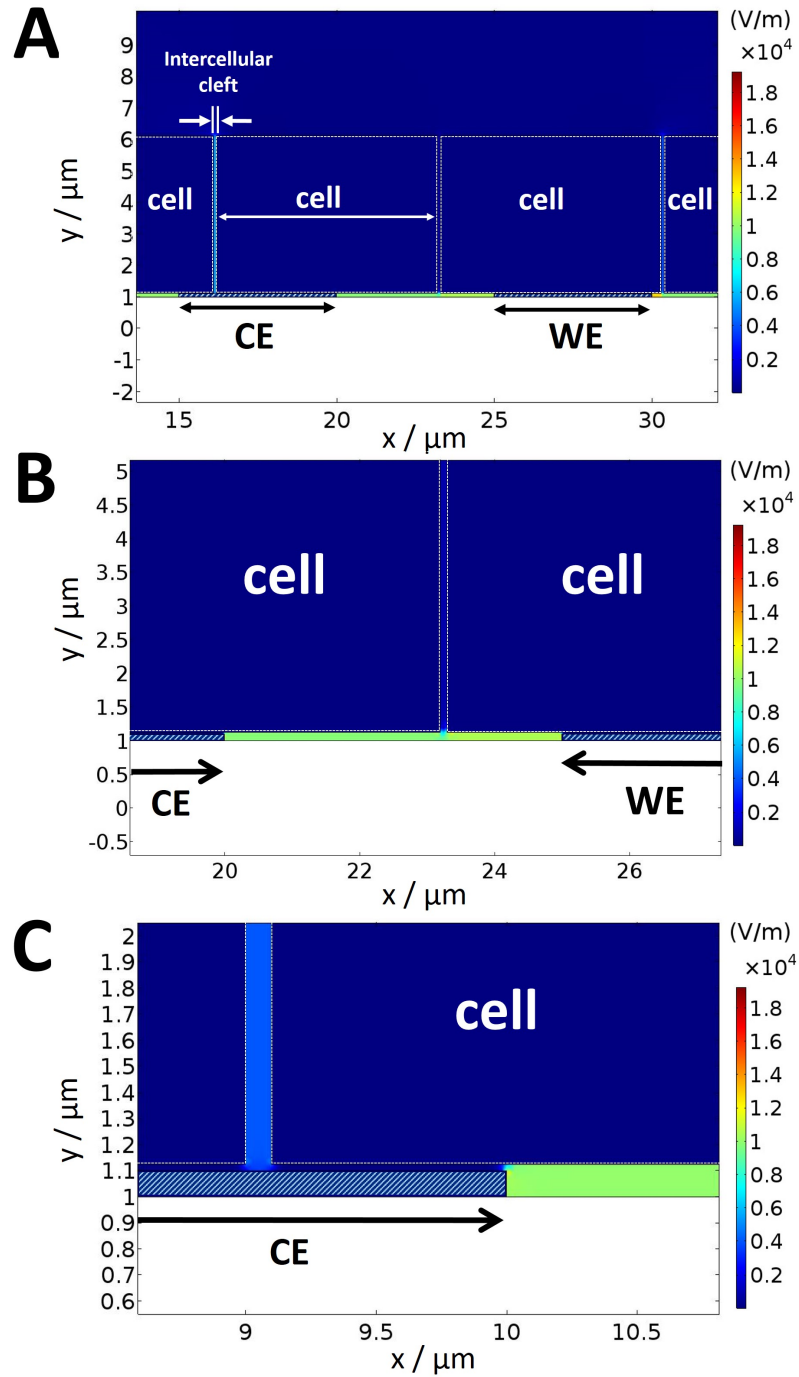


Figure 6.2: Two-dimensional representation of the simulated distribution of the electric field in V/m with cells ($h = 5 \mu\text{m}$) on the IDE10 simulated with an electric potential of $V = 0.05 \text{ V}$ and at a frequency of $f = 251 \text{ kHz}$. The gap and width of the electrodes is $5 \mu\text{m}$, respectively. The insulated cells are modeled as rectangles with a white dotted border. The distance between the cells and the electrode surface amounts to 25 nm and the intercellular cleft to 100 nm . For a better overview the electrodes were highlighted with blue dashes and the width and the location of the electrodes are monitored with black arrows. **A:** simulated cells on IDE10, **B:** zoom of the simulation, **C:** enlarged excerpt. **CE:** counter, **WE:** working electrode.

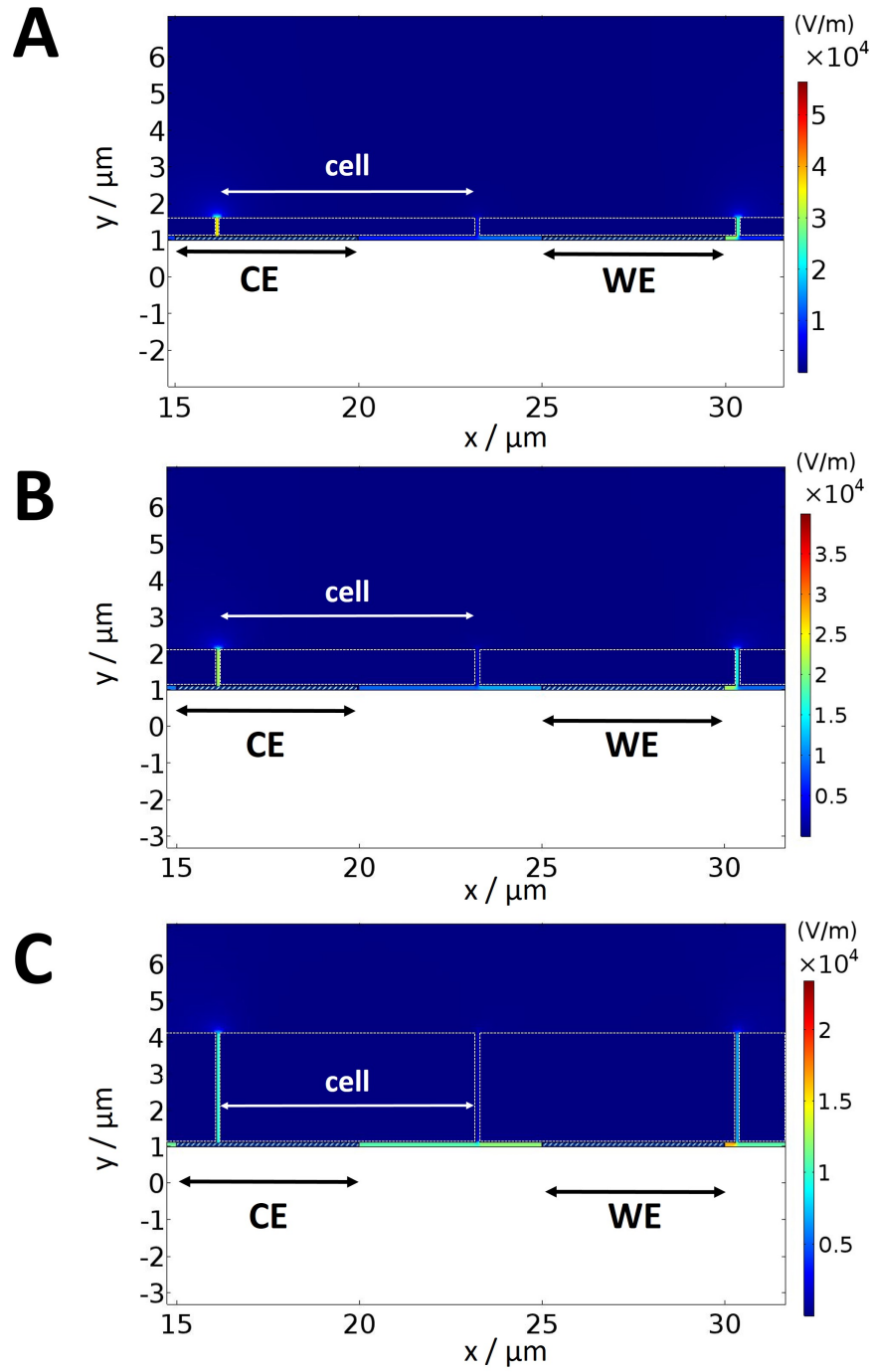


Figure 6.3: Representation of the simulated distribution of the electric field in V/m on the IDE 10 simulated with an electric potential of $V = 0.05$ V and at a frequency of $f = 251$ kHz with a varying height of the cells: **A:** cell height $h = 0.5$ μm , **B:** cell height $h = 1$ μm , **C:** cell height $h = 3$ μm . The gap and width of the electrodes amounts to 5 μm , respectively. The insulated cells are modeled as rectangles with a white dotted border. The distance between the cells and the electrode surface is simulated with 25 nm and the intercellular cleft with 100 nm. The electrodes were highlighted with blue dashes and the width and the location of the electrodes are shown with black arrows. **CE:** counter electrode, **WE:** working electrode.

To further analyze the distribution of the electric field on the IDE 10 the cell height is varied (see fig. 6.3). The dimensions of the electrodes (gap: $5\text{ }\mu\text{m}$, width: $5\text{ }\mu\text{m}$), the cell-electrode distance (25 nm), the intercellular cleft (100 nm) and the other parameter ($V=0.05\text{ V}$, $f=251\text{ kHz}$) were kept the same as in the simulation in fig. 6.2. The only variations are the cell heights: i) $h=0.5\text{ }\mu\text{m}$ (fig. 6.3 **A**), ii) $h=1\text{ }\mu\text{m}$ (fig. 6.3 **B**), iii) $h=3\text{ }\mu\text{m}$ (fig. 6.3 **C**). It should be emphasized that a different color legend is generated for each simulation. In fig. 6.3 it is seen that these various cell heights have a significant influence on the distribution of the electric field. With the simulation of very flat cells ($h=0.5\text{ }\mu\text{m}$) (see fig. 6.3 **A**) the main part of the electric field is distributed across the intercellular cleft. The values arise to $E \approx 3.5 \cdot 10^4\text{ V/m}$ and $E \approx 2.5 \cdot 10^4\text{ V/m}$ looking at the clefts near the electrode edges. An electric field of $E \approx 1.0 \cdot 10^4\text{ V/m}$ is simulated in the electrode gap underneath the cells, which is only a small fraction of the total simulated values. With the increase of the cell height to $h=1\text{ }\mu\text{m}$ (see fig. 6.3 **B**) the ratio of the distribution of the electric field changes. The fraction of the electric field in the electrode gap underneath the cells increases. With the cell height of $h=1\text{ }\mu\text{m}$ the electric field underneath the cells arises to $E \approx 1.2 \cdot 10^4\text{ V/m}$, whereas the fraction across the intercellular cleft is in a comparable order of magnitude than in **A** ($E \approx 2.5 \cdot 10^4\text{ V/m}$ and $E \approx 1.5 \cdot 10^4\text{ V/m}$). This observation is reinforced by a greater cell height of $h=3\text{ }\mu\text{m}$ (see fig. 6.3 **C**). The values of the simulated electric field underneath the cells ($E \approx 1.2 \cdot 10^4\text{ V/m}$) exceed the values in the intercellular cleft ($E \approx 0.9 \cdot 10^4\text{ V/m}$ and $E \approx 0.8 \cdot 10^4\text{ V/m}$). If the cell height is increased to $h=5\text{ }\mu\text{m}$ (see fig. 6.2 **A**), this trend is further strengthened. The electric field underneath the cells arises to $\approx 1.1 \cdot 10^4\text{ V/m}$ in comparison to the averaged simulated values of $E \approx 0.4 \cdot 10^4\text{ V/m}$ in the intercellular clefts.

The result of these simulations of the IDE 10 is that the distribution of the electric field depends on the cell height. With a cell height of $h=5\text{ }\mu\text{m}$ the main part of the electric field is simulated in the space underneath the cells between the electrodes. The flatter the cells are, the more the main part of the electric field shifts to the intercellular cleft. Consequently, the cell height has a clear influence on the measured signal.

Another aspect that can be explained with the simulation is how the distribution of the electric field changes when the cell-substrate distance becomes larger. In fig. 6.4 a distance between the cells ($h=5\text{ }\mu\text{m}$) and the electrode surface of $d=500\text{ nm}$ is simulated using the layout of IDE 10. Two whole and two half cells are monitored in fig. 6.4 **A** and a magnification of this image is shown in fig. 6.4 **B**. For this simulation an electric potential of $V=0.05\text{ V}$ and a frequency of $f=251\text{ kHz}$ were used. With a cell-electrode distance of $d=500\text{ nm}$ the distribution of the electric field is focused repeatedly underneath the cells between the electrodes. Depending

on the distance of the cleft to the electrodes a part of the electric field can distribute in the intercellular cleft. Values of $E \approx 0.7 \cdot 10^4 \text{ V/m}$, $E \approx 0.4 \cdot 10^4 \text{ V/m}$ and $E \approx 0.1 \cdot 10^4 \text{ V/m}$ are revealed in the different clefts in fig. 6.4 **A**. The main part of the electric field is displayed as a semicircle between the electrodes with an average value of $E \approx 1.0 \cdot 10^4 \text{ V/m}$, whereas the highest values can again be seen at the edges of the electrodes ($E \approx 2.2 \cdot 10^4 \text{ V/m}$). This shows that also with a higher cell-electrode distance the main part of the electric field arises underneath the cells.

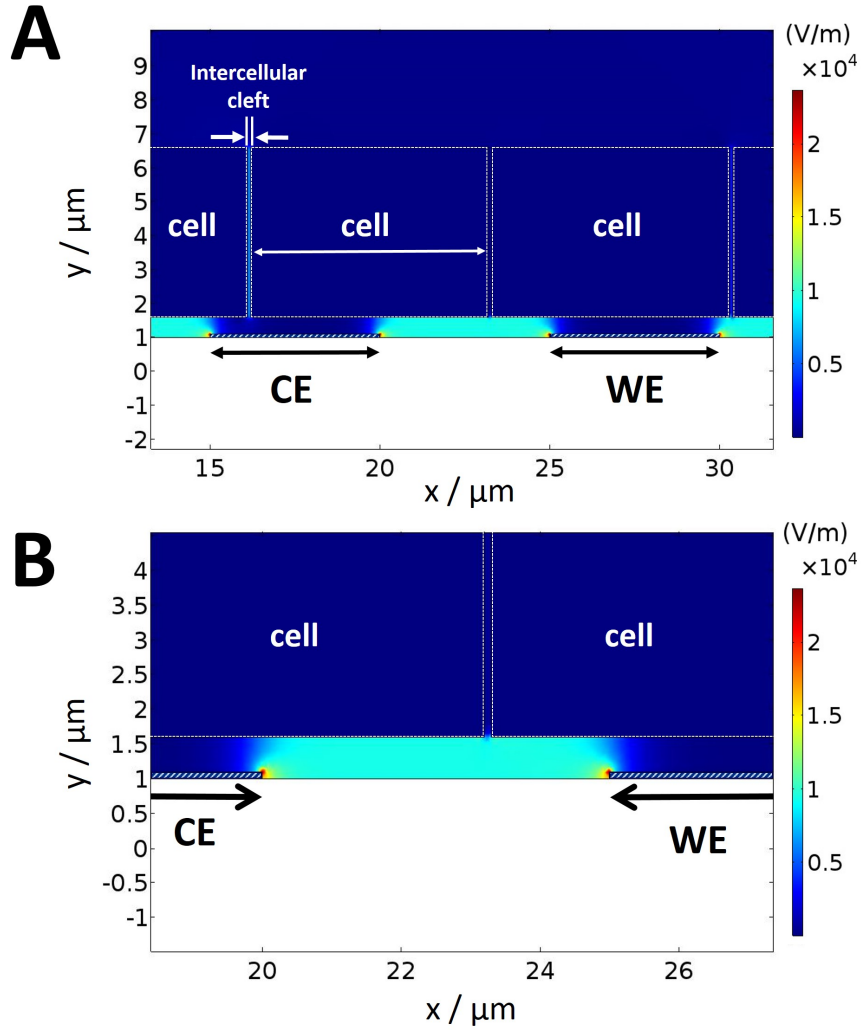


Figure 6.4: Simulated expansion of the electric field in V/m with cells grown on the IDE10 in a two-dimensional manner simulated with an electric potential of $V = 0.05 \text{ V}$ and at a frequency of $f = 251 \text{ kHz}$. The gap and width of the electrodes is defined to be $5 \mu\text{m}$, respectively. The insulated cells are modeled as rectangles with a white dashed border. The height of the cell-electrode distance amounts to 500 nm and the intercellular cleft to 100 nm . This cleft is marked and labeled in the image. For a better overview the electrodes were highlighted with blue dashes and the width and the location of the electrodes are monitored with black arrows. **A:** simulated cells on IDE10, **B:** zoom of the simulation. **CE:** counter electrode, **WE:** working electrode.

Comparing the three simulations of the IDE 10, it is obvious that the cell height has an influence on the distribution of the electric field as well as the cell-electrode distance. With a cell height of $h = 5 \mu\text{m}$ the main part of the electric field is distributed underneath the cells. Nevertheless, depending on the distance of the intercellular cleft to the edges of the electrode it is possible that a fractional part of the electric field is distributed across the intercellular cleft. The average of this part is in both simulations ($d = 25 \text{ nm}$ and $d = 500 \text{ nm}$) with the cell height of $h = 5 \mu\text{m}$ significantly smaller than the part of the electric field underneath the cells in the electrode gap. With a cell-substrate distance of 500 nm it can even be assumed that the intercellular cleft has almost no influence on the measured signal. Consequently, the values of the electric field below the cells ($h = 5 \mu\text{m}$) dominate the simulated total values. Furthermore, the cell height relocates the main part of the electric field. The flatter the cells are, the greater is the fraction of the electric field in the intercellular cleft and the smaller is the fraction underneath the cells. This leads to the result that for flatter cells the measured impedance is dominated more by the intercellular space than by the space between the cells and the substrate. For bigger cells the impedance of the space underneath the cells dominates the signal.

The results explained above apply to IDE 10 as a representative example for interdigitated electrodes with a subcellular dimension. In this work a series of interdigitated electrodes with different spacing of the electrode fingers were used, which are also non-subcellular. To understand the results of these electrodes IDEs with various gaps were simulated.

First, the IDE 300 with a width and a gap of $150 \mu\text{m}$, respectively, was simulated at a frequency $f = 4 \text{ kHz}$ and with an electric potential of $V = 0.05 \text{ V}$ (fig. 6.5). The dimensions of the cells ($h = 5 \mu\text{m}$, cell-electrode distance of $d = 25 \text{ nm}$) and electric parameters of the simulation are identical to the one of the IDE 10 with the exception of the frequencies used in the simulation: i) 251 kHz (IDE 10), ii) 4 kHz (IDE 300), which are oriented to f_{max} of the individual electrodes. Fig. 6.5 **A** shows a representation of two complete electrode fingers (highlighted by arrows, **CE**: counter electrode, **WE**: working electrode). The cells on the electrodes are difficult to identify and therefore a magnification of two smaller excerpts of the image can be seen in fig. 6.5 **B** and **C** with the marking of the cells ($h = 5 \mu\text{m}$) and the intercellular cleft. With the representation of the colormap it is obvious that the electric field has a different distribution than with the IDE 10. In contrast to the IDE 10 with a cell height of $h = 5 \mu\text{m}$ a very clear location dependency of the distribution of the electric field can be seen. Looking at the cells growing directly on the electrodes, the electric field is almost completely distributed across the intercellular cleft and arises to $E \approx 3.3 \cdot 10^3 \text{ V/m}$ (shown in the appendix fig. A.4 **A**). This electric field in the intercellular cleft becomes stronger the closer the cleft is to the edge of the

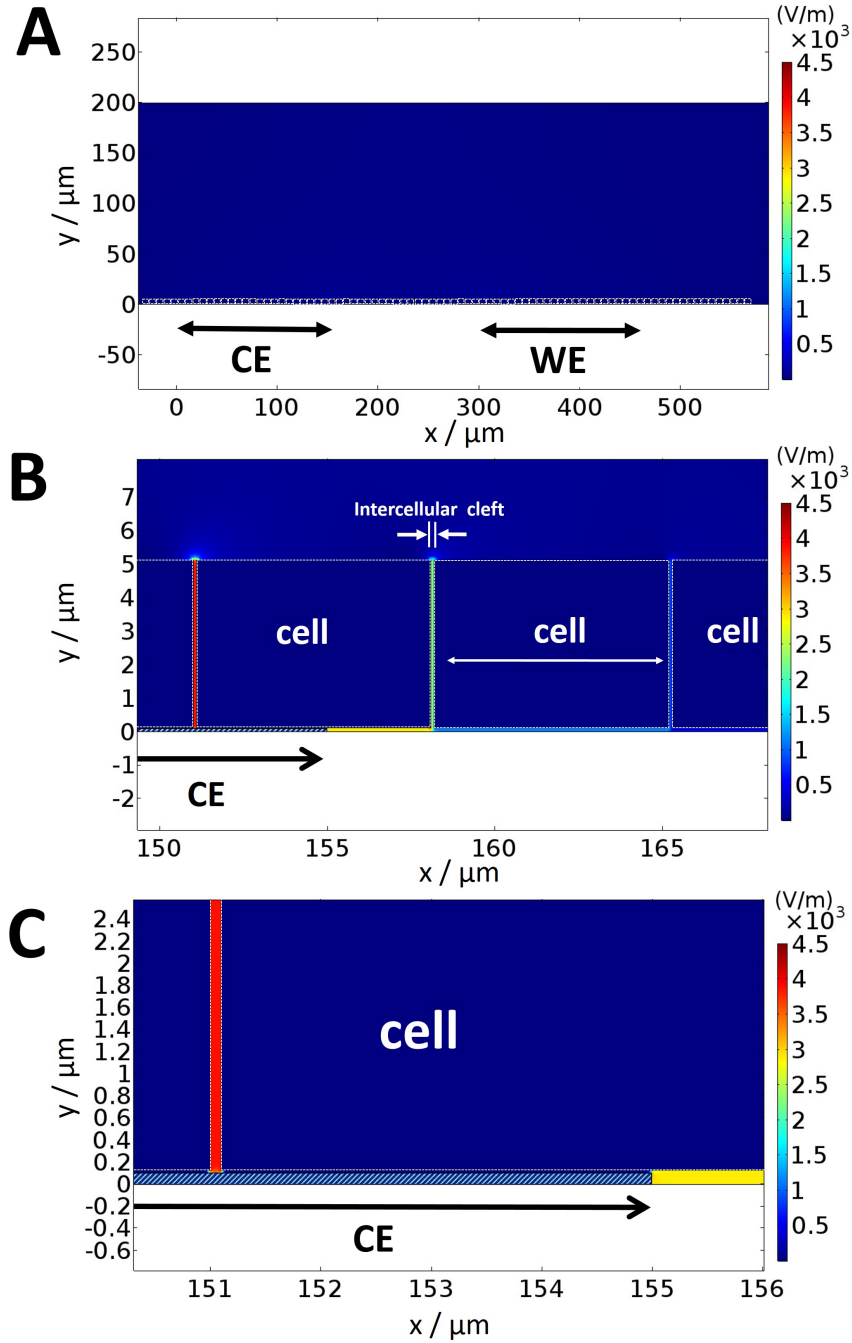


Figure 6.5: Simulation of the distribution of the electric field in V/m with cells on the IDE300 in a two-dimensional representation. For the simulation an electric potential of $V = 0.05$ V and a frequency of $f = 4$ kHz was used. The gap and width of the electrodes are set to be $150 \mu\text{m}$, respectively. The insulated cells with a height $h = 5 \mu\text{m}$ are shown as rectangles with a white dashed border. The distance of the cell-electrode amounts to 25 nm and the intercellular cleft to 100 nm , which is marked and labeled in the image. The electrodes were highlighted with blue dashes and the width and the location of the electrodes are symbolized with black arrows. **A:** simulated cells on IDE300, **B:** zoom of the image, **C:** enlarged excerpt of B. **CE:** counter electrode, **WE:** working electrode.

electrode. In fig. 6.5 **B** the electric field arises to $E \approx 3.9 \cdot 10^3 \text{ V/m}$ in the intercellular cleft of cells grown on the electrode near the electrode edge, while values of $E \approx 2.3 \cdot 10^3 \text{ V/m}$ are simulated in the intercellular cleft of the cells grown on the substrate near the electrode edge. Underneath the cells a relatively high electric field close to the electrode ($E \approx 2.8 \cdot 10^3 \text{ V/m}$) is monitored until the next intercellular cleft of the cells grown on the substrate. After this cleft the value of the electric field decreases to $E \approx 1.3 \cdot 10^3 \text{ V/m}$. Looking at the cells grown on the gap between the electrodes farther away from the electrode edge, it is seen that the electric field cannot be detected anymore underneath the cells or in the intercellular cleft because values of $E \approx 0 \text{ V/m}$ are simulated (seen in the appendix in fig. A.4 **B**). Nevertheless, the electric field above the cells grown on the gap assumes values up to $E \approx 0.1 \cdot 10^3 \text{ V/m}$. This means that for the electrodes with a large gap, the electric field is mainly distributed across the intercellular cleft of the cells grown directly on the electrodes and only a small value of the electric field is seen underneath the cells near the electrode. In the largest part of the electrode gap and in the intercellular space of the cells grown in this gap the electric field is negligibly small. Here the distribution of the electric field arises in the space above the cells in the electrolyte.

To understand the big differences in the distribution of the electric field calculated for the IDEs with subcellular dimensions (IDE 10) and for the IDEs with a very high pitch (IDE 300), additional IDEs with various pitches were simulated. The cells are modeled with a height of $h = 5 \text{ }\mu\text{m}$ and at a distance $d = 25 \text{ nm}$ to the electrodes. For all simulations an initial electric potential of $V = 0.05 \text{ V}$ and individual frequencies are used. IDE 20 (width: $10 \text{ }\mu\text{m}$, gap: $10 \text{ }\mu\text{m}$; $f_{max} = 200 \text{ kHz}$), IDE 40 (width: $20 \text{ }\mu\text{m}$, gap: $20 \text{ }\mu\text{m}$; $f_{max} = 100 \text{ kHz}$) and IDE 100 (width: $50 \text{ }\mu\text{m}$, gap: $50 \text{ }\mu\text{m}$; $f_{max} = 4 \text{ kHz}$) are modeled and are shown in fig. 6.6. It should be emphasized that each image has a different color legend. Nevertheless, it can be seen that the ratio of the distribution of the electric field in the intercellular cleft to the space underneath the cells is changing for the individual pitches. For the IDE 20 (fig. 6.6 **A**) values of $E \approx 0.5 \cdot 10^4 \text{ V/m}$, $E \approx 0.4 \cdot 10^4 \text{ V/m}$ and $E \approx 0.3 \cdot 10^4 \text{ V/m}$ are simulated for the electric field in the intercellular clefts, leading to an averaged value of $E \approx 0.4 \cdot 10^4 \text{ V/m}$ in the intercellular cleft. Underneath the cells a value of $E \approx 0.45 \cdot 10^4 \text{ V/m}$ and $E \approx 0.65 \cdot 10^4 \text{ V/m}$ close to the electrodes can be monitored. This shows that for this pitch the ratio of the electric field in the intercellular cleft to the space underneath the cells is nearly comparable. For the measurements with these electrodes this means that the intercellular cleft as well as the space underneath the cells influence the measured impedance. Increasing the gap to $20 \text{ }\mu\text{m}$ (IDE 40 seen in fig. 6.6 **B**) this ratio is clearly changing. Values up to $E \approx 4.5 \cdot 10^3 \text{ V/m}$, $E \approx 4.0 \cdot 10^3 \text{ V/m}$, $E \approx 2.0 \cdot 10^3 \text{ V/m}$ and $E \approx 1.5 \cdot 10^3 \text{ V/m}$ are simulated in the intercellular clefts depending on the distance to the electrode edges.

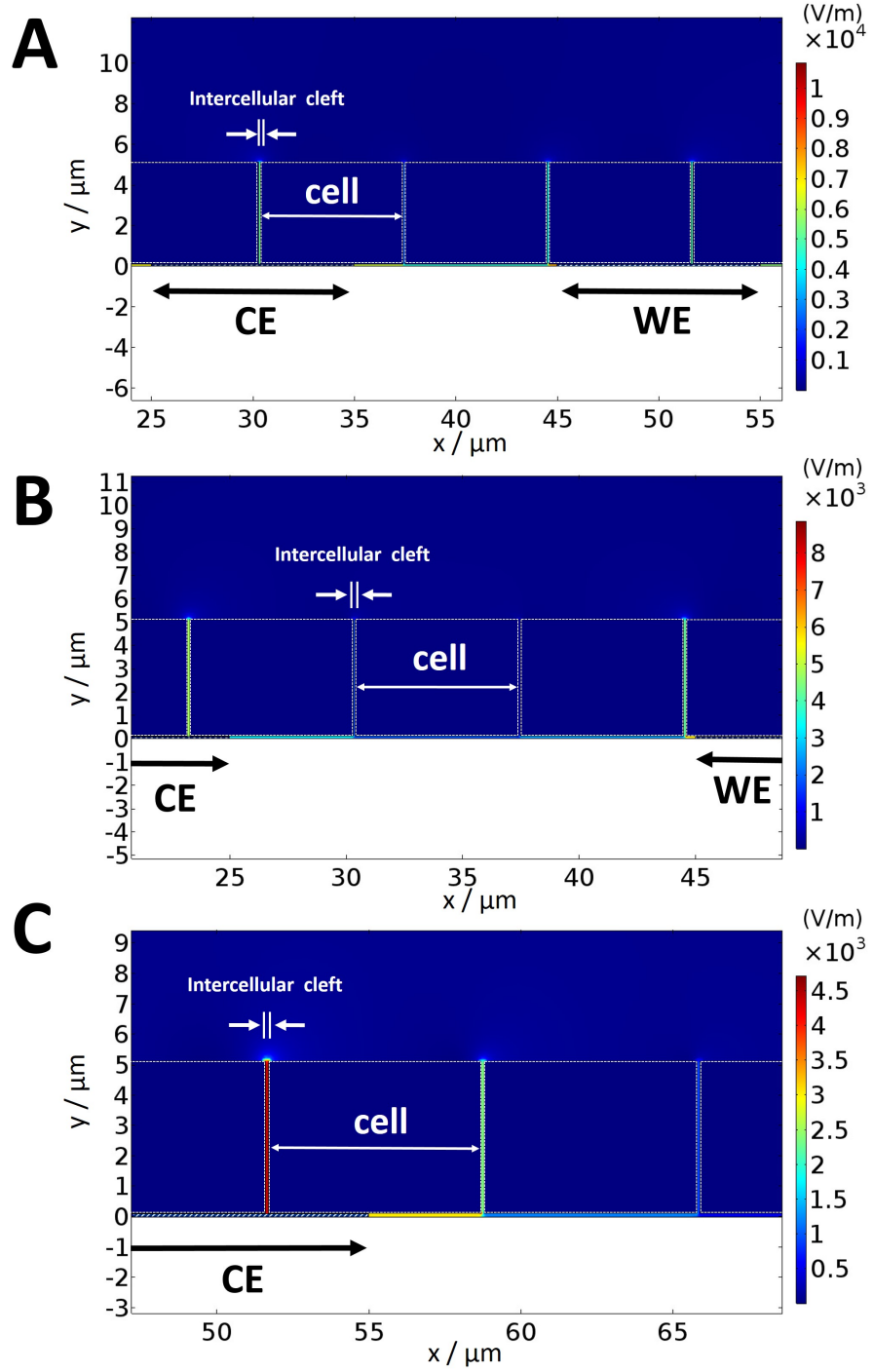


Figure 6.6: Simulation of the distribution of the electric field in V/m with cells on various IDEs in a two-dimensional representation. For the simulation an electric potential of $V = 0.05$ V and different frequencies were used. The insulated cells with a height $h = 5 \mu\text{m}$ and a distance to the electrodes of $d = 25$ nm are shown as rectangles with a white dashed border. The intercellular cleft (100 nm) is marked in the image and the electrodes are highlighted with blue dashes. The width and the location of the electrodes are symbolized with black arrows. **A:** simulated cells on **IDE 20**, $f = 200$ kHz, **B:** simulated cells on **IDE 40**, $f = 100$ kHz, **C:** simulated cells on **IDE 100**, $f = 4$ kHz. **CE:** counter electrode, **WE:** working electrode.

Underneath the cells the electric field varies from $E \approx 2.5 \cdot 10^3 \text{ V/m}$, $E \approx 2.9 \cdot 10^3 \text{ V/m}$ to $E \approx 3.2 \cdot 10^3 \text{ V/m}$ resulting in a smaller fraction of the electric field in this space than in the intercellular cleft. This shows a shift of a big part of the distribution of the electric field into the intercellular clefts. In measurements this space has a bigger influence on the results than the cell-substrate cleft. With an even greater gap of $50 \mu\text{m}$ (IDE 100, see fig. 6.6 C) this focusing of the electric field to the intercellular cleft is getting more clearly. The electric field in the intercellular cleft between the cells grown on the electrodes arises to $E \approx 4.3 \cdot 10^3 \text{ V/m}$ and is decreasing in every cleft which is farther away from the electrode edge above the electrode gap to $E \approx 2.2 \cdot 10^3 \text{ V/m}$ and $E \approx 1.2 \cdot 10^3 \text{ V/m}$. The electric field underneath the cells amounts values of $E \approx 3.0 \cdot 10^3 \text{ V/m}$ near the electrode gap and $E \approx 1.2 \cdot 10^3 \text{ V/m}$ until the next cleft. $10 \mu\text{m}$ away from the electrode edge the electric field decreases to $E \approx 0.7 \cdot 10^3 \text{ V/m}$. This simulation shows that the space underneath the cells has only a small influence on the results measured with IDEs with a great gap. This is in agreement with the simulations for the IDE 300 (fig. 6.5 and fig. A.4) which confirm this ratio of the distribution of the electric field with the focus on the intercellular clefts. In conclusion, the variation of the gap has a significant influence on the ratio of the distribution of the electric field in the intercellular cleft to the part underneath the cells. The larger the gap, the more clearly the focus of the electric field is on the intercellular cleft. Consequently, with IDEs with a small gap the electric field is focused below the cells.

This chapter clarifies that the electric field is distributed significantly differently with various cell heights, cell-electrode distances and with changing electrode gaps. This distribution of the electric field determines which space around the cells dominates the measured impedance. The simulation of different cell heights showed that the smaller the cell height is, the higher becomes the fraction of the electric field in the intercellular cleft until the cell-cell contacts dominate the total measured values. With a small electrode gap the main part of the electric field is focused below the cells in the electrode gap. With these small gaps it is possible to measure basal responses of the cells more precisely. Simulating larger gaps between the electrodes the main fraction of the electric field distributes over the intercellular cleft of the cells grown directly on the electrodes. In the space underneath the cells in the electrode gap the electric field is negligibly small. This connection is independent of the interdigitated structure, it depends only primarily on the size of the electrode gap. In the case of the 8W10E and 8W1E electrodes this gap is even larger and it can be concluded that the electric field for these electrodes (not shown) has almost the same distribution as the simulation of the IDE 300. Consequently, the gap between the electrodes changes the spatial distribution of the electric field significantly and not only the use of an interdigitated structure.

6.2 Spectra of cell-covered electrodes with different electrode layouts and their analysis

For a direct comparison of the various electrode types nine different cell lines were cultivated on the 8W10E electrodes, IDE 12 and IDE 7 in the first part of this chapter. In the second part MDCK I, MDCK II, NRK and U373 cells grown on electrodes with various layouts are analyzed to extend the informative value. Further information regarding all cell lines can be seen in chapter 4.1.2. The data were collected on the third day after seeding (following the individual seeding protocol seen in tab. 4.4 in chapter 4.1.5) and the same time points for the medium changes were chosen for all cell types and electrodes to ensure comparable conditions. In the third part of this chapter different parameters like the frequencies f_{max} or the area under the curve of the measured spectra are defined more precisely. The shown error bars represent the SD, SEM or the max. error. The calculation of these errors is explained in chapter 3.1.2.3.

6.2.1 Spectra of cell-covered electrodes with different electrode layouts

First, nine different cell types were cultivated on 8W10E electrodes, IDE 12 and IDE 7 and were measured with impedance-based methods. In fig. 6.7 the impedance spectra (**A**) and the norm. $|Z|$ (**B**) as a function of the frequency of these measurements are shown.

In the impedance spectra and the norm. $|Z|$ of the 8W10E electrodes (fig. 6.7 **a**)) different impedance magnitudes can be monitored for the individual cell types. The biggest impedance value over the whole frequency range used in this work is revealed for the MDCK I cells (10^1 Hz - 10^5 Hz), followed by the MDCK II cells ($> 10^2$ Hz). However, in a range $> 10^4$ Hz the MCF-7 cells show a higher magnitude than the MDCK II cells. The next smaller impedance is the one of the NRK and then of the A549 cells ($> 2,000$ Hz). The nearly identical impedance for the CHO_D2R and the BAEC cells ($> 2,500$ Hz) is even smaller. The lowest impedance is monitored for the SK-Mel-28 and the U373 cells ($> 3,000$ Hz). The exact frequency of the maximum impedance magnitude and the values for the maxima of the norm. $|Z|$ can be seen in chapter 6.2.2.

The data of the IDE 12 (fig. 6.7 **b**)) show many differences in the order of the impedance magnitudes for the individual cell lines. The only similarity to the 8W10E electrodes is that the MDCK I cells obtain the highest impedance magnitude, whereas it is shifted to a much higher frequency range ($> 3,000$ Hz). The

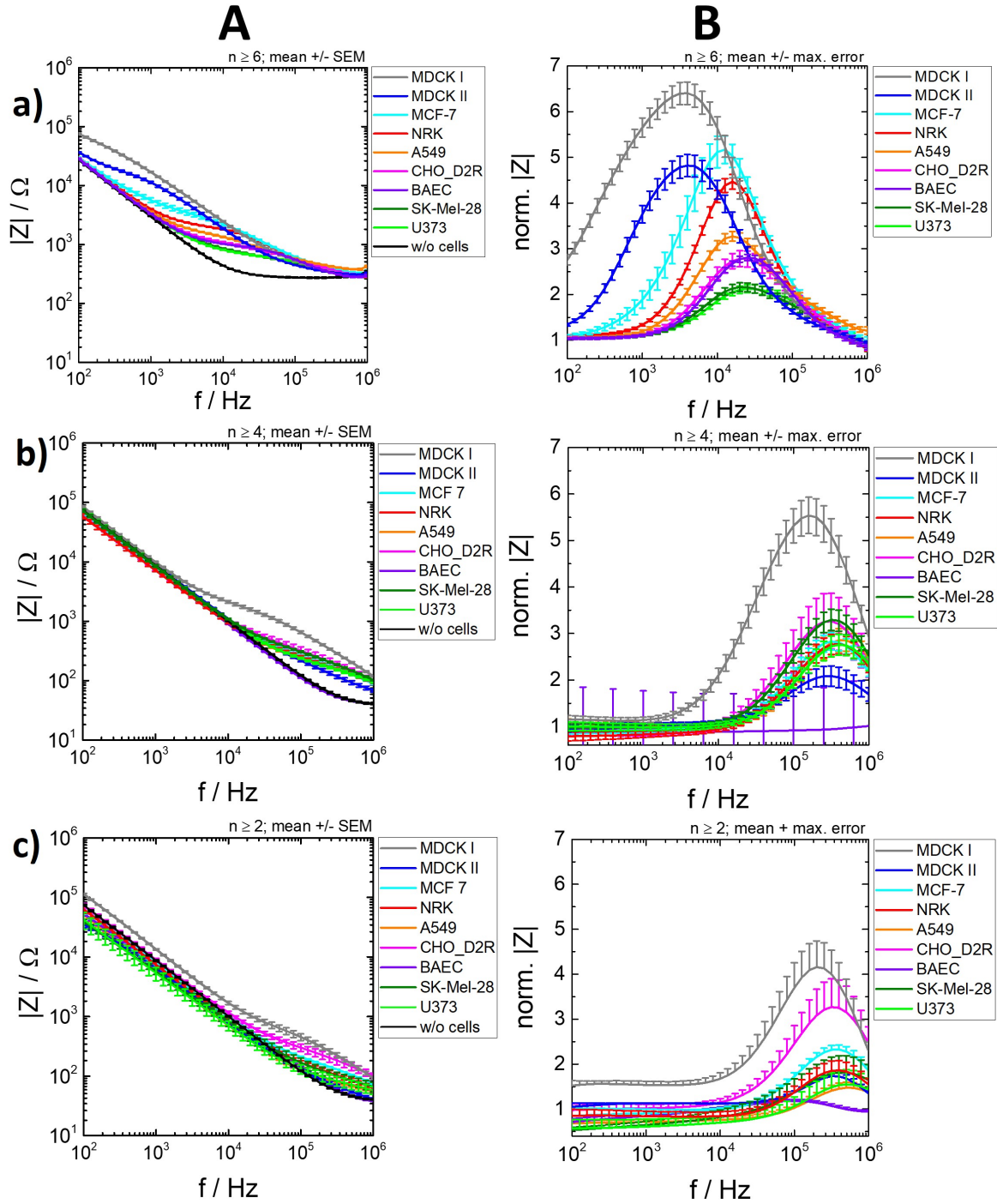


Figure 6.7: Impedance spectra in dependence of the frequency of nine different cell lines cultivated on various electrode layouts. The spectra were measured on the third day after seeding. The impedance (**A**) and the norm. $|Z|$ (**B**) are monitored for the individual electrode layouts: **a**): 8W10E electrodes ($n \geq 6$), **b**): IDE12 ($n \geq 4$) and **c**): IDE7 ($n \geq 2$). The mean with the SEM ($|Z|$) and with the max. error (norm. $|Z|$) is plotted.

following smaller impedance signal is a mixture of MCF-7, NRK, A549, CHO_D2R, SK-Mel-28 and U373 cells ($> 16,000$ Hz). In the graph of the norm. $|Z|$ (fig. 6.7 **B**, **b**)) norm. $|Z|$ for CHO_D2R and SK-Mel-28 cells is slightly higher than for the

other cell lines, but due to the data scattering it is difficult to draw precise conclusions. The biggest difference between the two electrode layouts (8W10E electrodes and IDE 12) is the impedance magnitude of the MDCK II and of the BAEC cells. The MDCK II cells show a significantly smaller value than the other cell lines and the impedance of the BAEC cell is not distinguishable from the one of the cell-free electrode. In the representation of norm. $|Z|$ (fig. 6.7 **B**, **b**)) the error bars for the BAEC cells are comparatively large due to the fact that the impedance spectra of the cell-covered and the cell-free electrodes are very close together and thus, the errors are greater after the normalization.

The impedance of the BAEC cells is also not visible with the IDE 7 (fig. 6.7 **c**)). It is indiscernible from the one of the cell-free electrode and the norm. $|Z|$ monitors no clear signal over the frequency range. For the other cell lines only some aspects can be noted. The highest impedance is obtained for the MDCK I cells ($> 32,000$ Hz). Nevertheless, the impedance magnitude is much smaller in comparison to the other electrode types. The next higher impedance signal is seen for the CHO_D2R cells followed by the one of the MCF-7 ($> 60,000$ Hz). For the other cell types no clear trend can be revealed within the error range.

Similar observations can be made analyzing the resistance (fig. A.5) and the capacitance spectra (A.6) in the appendix. For all three electrode types the MDCK I cells show the biggest increase of the resistance and the capacitance relative to the cell-free electrode. In the case of the 8W10E electrodes the resistance (fig. A.5 **a**)) and capacitance (fig. A.6 **a**)) magnitudes of the MDCK II cells are clearly higher than for the MCF-7 and NRK cells in the range of lower frequencies ($< 10^3$ Hz). With higher frequencies the MDCK II cells show a much smaller value than these two cell lines. The resistance and capacitance magnitudes of the other cell lines follow the same order as in the impedance spectra, with the highest magnitude of the A549, before the CHO_D2R and BAEC cells. The smallest value is the one of the SK-Mel-28 and the U373 cells. The resistance (fig. A.5 **b**)) and the capacitance spectra (fig. A.6 **b**)) of the IDE 12 show the same ratios as the impedance spectra. The MDCK I cells have the highest signal and the one of the MDCK II cells is lower than for all the other cell types, with the exception of the BAEC which cannot be distinguished from the cell-free electrode. Additionally, with the resistance and the capacitance spectra of the IDE 7 (fig. A.5 **c**) and fig. A.6 **c**)) no further insights can be gained. The resistance and the capacitance show high errors and it is difficult to draw clear conclusions.

Consequently, it is obvious that the cells grown on IDE 12 and IDE 7 show a significantly different impedance, resistance and capacitance magnitude than the same cells grown on the 8W10E electrodes.

A further analysis of the data is the fitting of the impedance spectra of the 8W10E electrodes with a LabView-based software (provided by Prof. Dr. Joachim Wegener). The curves can be fitted on the basis of the ECIS model (explained in chapter 3.1.1) and the parameters R_b , α and C_m are determined (see tab. 6.2).

Table 6.2: Fitted parameters of the impedance spectra of the 8W10E electrodes. The ECIS model is the basis for the fit and the parameters R_b : resistance of the cell-cell contacts, α : impedance in the cell-electrode junction and C_m : specific cell membrane capacitance are determined. The mean with the SD is listed with $n \geq 6$.

	R_b	α	C_m
cell type	/ Ωcm^2	/ $\Omega^{0.5}\text{cm}$	/ $\mu\text{F}/\text{cm}^2$
MDCK I	121 ± 9	71 ± 6	3.1 ± 0.3
MDCK II	30 ± 10	17 ± 2	4.4 ± 0.5
MCF-7	5 ± 1	10 ± 3	1.6 ± 0.1
NRK	5.1 ± 0.2	4.1 ± 0.3	2.0 ± 0.2
A549	2.3 ± 0.3	5.1 ± 0.4	1.9 ± 0.2
CHO_D2R	1.8 ± 0.4	4.3 ± 0.2	1.2 ± 0.2
BAEC	2.46 ± 0.06	2.8 ± 0.2	1.4 ± 0.1
SK-Mel-28	0.9 ± 0.2	4.0 ± 0.2	0.70 ± 0.04
U373	0.9 ± 0.2	3.1 ± 0.2	1.0 ± 0.3

In tab. 6.2 it can be seen that MDCK I cells show a significantly higher value for the resistance of the cell-cell contacts (R_b) and the impedance in the cell-electrode junction (α) than all the other cell types. Otherwise, the value for the specific cell membrane capacitance (C_m) of the MDCK I cells is smaller than for the MDCK II cells. The other parameters of this cell line lay between the MDCK I and all the others. The values for R_b and α are high looking at the other cell lines, whereas they are much smaller than the ones of the MDCK I cells.

Some of the other cell lines show similar values for the fit parameters. For instance, the values for R_b of the MCF-7 and NRK cells are in the same range as well as the values for R_b of the A549, CHO_D2R and BAEC cells. The SK-Mel-28 and U373 cells show both very low R_b values. The values for α also display some similarities. The lower values of α of the BAEC and U373 cells and the higher one of NRK, A549, CHO_D2R and SK-Mel-28 cells are comparable, respectively, whereas the one of the MCF-7 is appreciably greater. In the case of the C_m values MDCK II and MDCK I cells show the highest values and SK-Mel-28 and U373 cells the smallest. The values for the other cell lines are in a comparable range in between.

These fit data will later be used to understand the influence of the different cell

lines on the measured impedance of the 8W10E electrodes. It is possible to analyze the resulting impedance and to draw conclusions about the corresponding cell characteristics. Further, these cell characteristics can serve as a basis to explain the various impedance signals measured with the IDEs and in particular the difference of the focus of the measured impedance.

Fitting the data of the IDEs on the basis of the ECIS model was not possible because it has already been shown in the simulations in chapter 6 that the electric field of the IDEs with a small pitch has a completely different distribution around the cells than of the 8W10E electrodes. This leads to the result that the ECIS model is not appropriate for the IDEs with small pitches. To underline this result a simulation (with a LabView-based software provided by Prof. Dr. Joachim Wegener) of four different cell lines on the IDE 12 were proceeded (see fig. A.7 B) and compared with the measured data (see fig. A.7 A). For the simulation, the fit parameters for the cells grown on the 8W10E electrodes seen in tab. 6.2 and the parameter of the fit of a cell-free IDE 12 (electrode area = 0.003 cm^2 , A of CPE = $2.10 \cdot 10^{-5} \text{ cm}^2$, n of CPE = 0.94 and $R_{bulk} = 38 \Omega$) were used. It can be seen that the simulated impedances of the cells on the IDE 12 (see fig. A.7 B) are significantly different than the measured ones (see fig. A.7 A). All simulated impedance magnitudes are shifted to lower frequencies and span a wide frequency range. Furthermore, the order of the maxima of the cell lines are different for the simulated data. It can clearly be said that there is a huge difference between the simulated and the measured data. Due to the simulations of the electric field it is understood that the impedance underneath the cells have a much higher influence measured with the IDEs with a smaller pitch than for the 8W10E electrodes. To show whether the difference between the simulated and the measured data is due only to this different weighting of the impedance underneath the cells, α is varied in the simulation of the MDCK I cells on the IDE 12 (see fig. A.7 C). Even with a tenth part of α the simulated spectra is completely different to the measured one. α has only an influence on the impedance at a frequency range $< 10^3 \text{ Hz}$. The simulated spectra is clearly different to the measured one. This clarifies that for the IDEs with a small pitch not only α is different, but that the total ECIS model is not appropriate for these electrodes.

To enable a further explanation of the various electrode types four different cell lines were analyzed with distinct IDE layouts. For this purpose, MDCK I, MDCK II, NRK and U373 cells were chosen and the impedance, the resistance and the capacitance as a function of the frequency were measured with the IDE 300, IDE 20 and IDE 10. For all electrodes the window size of $(1.1 \times 1.1) \text{ mm}^2$ was used. In fig. 6.8 the impedance spectra (A) and the norm. $|Z|$ (B) in dependence of the frequency can be seen.

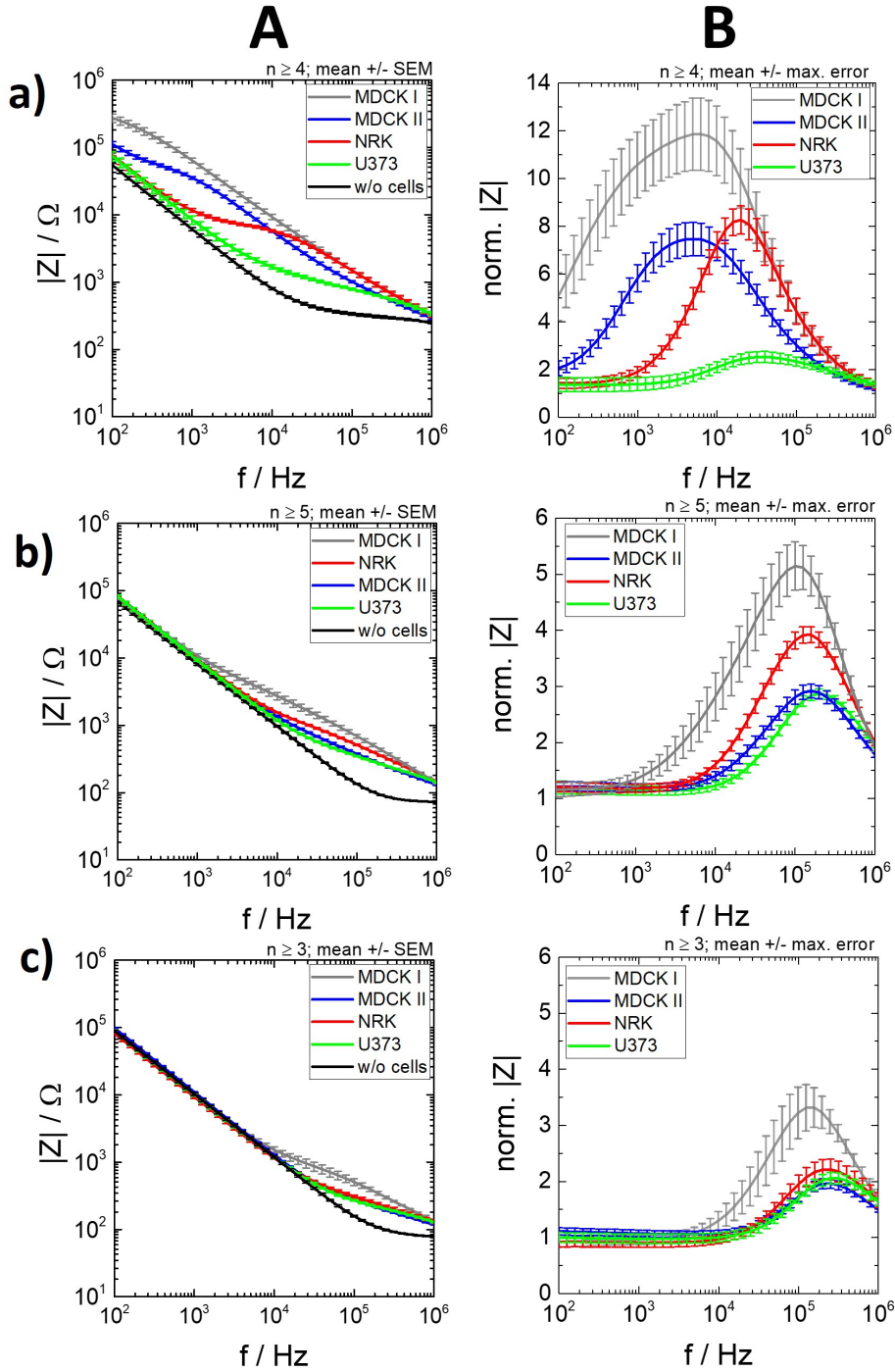


Figure 6.8: Impedance spectra of four distinct cell types cultured on three different IDE layouts in dependence of the frequency. The data were measured on the third day after cultivation. The IDE layouts used in this experiments were **a)**: IDE 300 ($n \geq 4$), **b)**: IDE 20 ($n \geq 5$) and **c)**: IDE 10 ($n \geq 3$). The impedance spectra (**A**) and the norm. $|Z|$ (**B**) are presented. The mean with the SEM is plotted in **A** and with the max. error in **B**.

The different electrode types obtain the similarity that the MDCK I cells give the highest impedance magnitude. The impedance spectrum of the MDCK I cells measured with the IDE 300 (fig. 6.8 **A a**)) can be seen nearly in the whole frequency

range measured in this work (10^2 - 10^6 Hz). It significantly dominates the results of the norm. $|Z|$ (fig. 6.8 **B**, **a**). For the IDE 20 (fig. 6.8 **b**) and IDE 10 (fig. 6.8 **c**) the MDCK I cells also show the highest impedance magnitude, whereas the maximum occurs in higher frequency ranges (IDE 20: $> 10^3$ Hz, and IDE 10: $> 10^4$ Hz). The other three cell lines provide different impedance magnitudes for the various electrode types. The MDCK II cells show a high impedance measured with the IDE 300 (fig. 6.8 **a**). This impedance can be seen in a broad frequency range similar to the MDCK I cells (**A**). In contrary to the MDCK I cells, the impedance of the MDCK II cells approaches the value of a cell-free electrode in the range $< 10^2$ Hz. In the norm. $|Z|$ (**B**) the MDCK II cells show the second highest impedance magnitude $< 10^4$ Hz, whereas it is smaller than the one of the NRK cells at higher frequencies ($> 10^4$ Hz). This magnitude change can also be seen in the impedance spectra, in which the signal of the NRK cells is smaller at smaller frequencies ($< 10^4$ Hz) until it is not distinguishable from the cell-free electrode ($< 10^3$ Hz). In the frequency range $> 10^4$ Hz the impedance spectra of the NRK cells is higher than the one of the MDCK II cells and overlaps with the impedance of the MDCK I cells. The fourth cell line, U373 cells, provides a much smaller impedance in the range $> 10^4$ Hz. The impedance magnitude is only a fractional ratio of the other cell lines which also can be seen with the low values of norm. $|Z|$.

For the IDE 20 (fig. 6.8 **b**) the impedance magnitudes are significantly different. In the frequency spectra (**A**) the impedance signal of the NRK cells occurs in the range $> 10^4$ Hz and shows a higher value than the one of the MDCK II and U373 cells, which cannot be clearly distinguished from each other. The norm. $|Z|$ (**B**) underlines this observations. The maxima are in the same frequency range for all four cell types but the NRK cells obtain significantly the second highest value after the MDCK I cells. The maxima of norm. $|Z|$ of the MDCK II and the U373 cells are much smaller and have a comparable value within the error range.

The IDE 10 (fig. 6.8 **a**) does not show such a significant difference between the cells. The impedance of the MDCK I cells can be seen in a range $> 10^4$ Hz but with a smaller magnitude in comparison to the other IDEs. For the other cell lines the impedance magnitude is monitored in a range > 40 kHz. Here, the NRK cells reveal a slightly higher impedance but within the error range it is not clearly distinguishable from the one of the MDCK II and the U373 cells.

It has to be emphasized that a clear difference between the IDE 300 and the IDEs with a smaller pitch can be seen. The magnitude of the impedance measured with the IDE 300 is about twice the size of the values of the smaller IDEs. Those measured with the IDE 300 are even bigger than the ones of the 8W10E electrodes (see fig. 6.7 **a**). The magnitudes of the impedance show a clear gap between the IDE 300 and the smaller IDEs. Furthermore, the maxima of the normalized impedance of

the individual cell lines measured with the IDE 300 are shifted significantly to lower frequency ranges. Comparing the frequency spectra and the normalized spectra of the IDE 300 (fig. 6.8 **a**)) with the other spectra, a bigger similarity to the spectra of the 8W10E electrodes (fig. 6.7 **a**)) can be seen than for the spectra of the other IDEs (IDE 7, IDE 10, IDE 12, IDE 20, fig. 6.7 **b**), **c**) and fig. 6.8 **b**), **c**)). It can be concluded that the distribution of the electric field of the IDE 300 is similar to the one of the 8W10E electrodes resulting in a similar measured impedance.

The previous simulations (see chapter 6.1) showed that the electric field is distributed differently for the electrodes with a smaller pitch than for the 8W10E electrodes. Consequently, the ECIS model is not appropriate for these IDEs (IDE 20, IDE 10) and it was not possible to fit these spectra on the basis of the ECIS model.

In the resistance (fig. A.8) and in the capacitance (fig. A.9) spectra seen in the appendix the same trends can be determined. For all three electrodes the MDCK I cells obtain the highest resistance and capacitance magnitudes, whereas the maxima are shifted to a higher frequency range with smaller pitch of the IDEs. Further, the MDCK II cells reveal a greater resistance and capacitance magnitude than the NRK and U373 cells in the case of the IDE 300 (fig. A.8 **a**) and fig. A.9 **a**)). For the IDE 20 the difference of the higher signal of NRK to the smaller one of MDCK II cells is more pronounced in the resistance and the capacitance spectra (fig. A.8 **b**) and fig. A.9 **b**)). Additionally, it can be observed that the MDCK II cells have a greater resistance magnitude than the U373 cells. Nevertheless, the resistance and the capacitance of the U373 cells is much higher measured with the IDE 20 and IDE 10 as in comparison with the IDE 300. For the IDE 10 no further information can be gained from the resistance and capacitance spectra (fig. A.8 **c**) and fig. A.9 **c**)). The MDCK I cells show the highest resistance and capacitance magnitude, whereas the smaller values of the MDCK II, NRK and U373 cells cannot be distinguished significantly. Repeatedly it is seen that there is a significant gap between the results of the IDE 300 and the one of the IDE 20. The ones of the IDE 300 are similar to the ones of the 8W10E electrodes.

To sum it up, the IDE 300 resembles with the 8W10E electrodes in the impedance spectra and the intensities of the measured magnitudes (impedance, resistance, capacitance). The data of IDE 20 can be compared with the IDE 12 with the exception of the higher impedance magnitude for MDCK II cells which is in the same range as the one of U373 cells. The IDE 10 is similar to the IDE 7 which does not differentiate between the different cell lines except for the strong magnitudes of MDCK I cells.

In this chapter significant differences were found in the measurements of various cell types grown on different electrode layouts. The conditions for each cell type were kept the same to allow direct comparison. It is evident that for the same cell line various impedance magnitudes are generated for the 8W10E electrodes compared

to the IDEs. An exception is the IDE 300 which has similar impedance magnitudes as the 8W10E electrodes. For the other IDEs with smaller pitches the impedance magnitudes, the order of the maxima of the impedance and the frequency with the maximum magnitude, among others, are different. This illustrates that the electric field for each electrode layout is different and the measured impedance results from other influences of the cells, depending on the electrode type.

6.2.2 Analysis of different aspects of the impedance spectra

The measured impedance spectra were analyzed with regard to different parameters. The evaluation of the frequency at the highest magnitude of the impedance (f_{max}), the maximum of the normalized impedance (norm. $|Z|_{max}$), the area under the curve of the frequency spectra ($AUC_{log(|Z|)}$) and of the norm. $|Z|$ ($AUC_{norm. |Z|}$) are determined for different cell lines measured with the various electrode types. This enables a comparison of the 8W10E electrodes and the five various interdigitated layouts.

f_{max} of the impedance spectra

As a first parameter the frequency at which the magnitude of the impedance is the highest is determined. It can be seen at the maximum of the norm. $|Z|$ (fig. 6.7 **B** and fig. 6.8 **B**) and will be shortened to f_{max} in the following work. All f_{max} of the various cell types on the electrodes are listed in tab. 6.3.

Table 6.3: f_{max} for all cell lines cultivated on 8W10E, IDE 300, IDE 20, IDE 12, IDE 10 and IDE 7. The frequency can be determined in the graph of norm. $|Z|$.

	8W10E	IDE 300	IDE 20	IDE 12	IDE 10	IDE 7
cell type	/ kHz	/ kHz	/ kHz	/ kHz	/ kHz	/ kHz
MDCK I	4	6	100	200	158	251
MDCK II	4	5	158	316	251	316
MCF-7	13	-	-	316	-	400
NRK	16	20	158	400	251	501
A549	16	-	-	400	-	501
CHO_D2R	20	-	-	316	-	316
BAEC	25	25	-	1,000	-	1,000
SK-Mel-28	20	-	-	316	-	400
U373	25	40	200	400	251	500

Analyzing the frequencies f_{max} some trends are seen. In general, all the maxima of the 8W10E electrodes and the IDE 300 are in a much lower frequency range (≤ 40 kHz) than the ones of the IDEs with smaller pitches (≥ 100 kHz). Another obvious aspect is that the MDCK I cells have a maximum at lower frequencies than the other cell lines, independently of the electrode type. Due to the fact that the cell types are sorted by descending magnitudes of the impedance of the 8W10E electrodes, a shift to higher frequencies is obtained along with lower impedance magnitudes of the cells in the case of the 8W10E electrodes (4 kHz (MDCK I cells) to 25 kHz (U373 cells)). The same trend can be observed for the IDE 300 (6 kHz (MDCK I cells) to 40 kHz (U373 cells)) and for the IDE 20 (100 kHz (MDCK I cells) to 200 kHz (U373 cells)). In the case of the IDE 12, IDE 10 and IDE 7 the maxima are in a similar range within the electrode type with the exception of the MDCK I and the BAEC cells. f_{max} for MDCK I cells is lower in all cases, whereas the BAEC cells show a much higher value. The maxima of the other cell types fluctuate around $f_{max} = (350 \pm 40)$ kHz for the IDE 12, $f_{max} = 251$ kHz for the IDE 10 and $f_{max} = (420 \pm 80)$ kHz for the IDE 7.

The IDE 12 and IDE 7 show on average higher values of f_{max} than the IDE 20 and IDE 10. Furthermore, it has to be emphasized that the IDE 300 resembles more the 8W10E electrodes than the IDEs with a smaller pitch. There is a clear cleft between the IDE 300 and the IDE 20 showing that the electrode gap has an essential influence on the measured impedance.

Area under the curve of the impedance spectra

Furthermore, the area under the curve ($AUC_{\log(|Z|)}$) of the impedance spectra is calculated. The borders of these areas are defined as the curves of the cell-free and the cell-covered electrodes. In order to avoid overestimation it is necessary to plot the $\log(|Z|)$ against the $\log(f)$ (not pictured) and to calculate the $AUC_{\log(|Z|)}$ in this representation. The obtained $AUC_{\log(|Z|)}$ is consequently a direct parameter for the magnitude of the impedance and provides an integral value for a direct comparison of the different electrode types.

In fig. 6.9 the calculated $AUC_{\log(|Z|)}$ of the impedance spectra of the nine different cell lines can be seen. For this direct comparison the 8W10E electrodes (**A**), the IDE 12 (**B**) and the IDE 7 (**C**) are shown. For all three electrode types the cell lines are sorted by the descending magnitude of the $AUC_{\log(|Z|)}$ of the 8W10E electrodes. The 8W10E electrodes (fig. 6.9 **A**) provide the highest $AUC_{\log(|Z|)}$ for the MDCK I cells followed by the MDCK II and MCF-7 cells which are very close together. The $AUC_{\log(|Z|)}$ for the NRK, A549, CHO_D2R and BAEC cells decreases in this order until the smallest values of $AUC_{\log(|Z|)}$ are reached for the SK-Mel-28 and the U373

cells. The analysis of the IDE 12 (fig. 6.9 **B**) shows a different order of the individual cell types. The only accordance to the 8W10E electrodes is the highest $AUC_{\log(|Z|)}$ for the MDCK I cells. The most noticeable differences are the very small $AUC_{\log(|Z|)}$ for the BAEC cells and the comparatively small $AUC_{\log(|Z|)}$ for the MDCK II cells. The $AUC_{\log(|Z|)}$ for the other cell types show similar values within the errors and lie in the middle of the value range. Comparing this with the calculation of the $AUC_{\log(|Z|)}$ for the IDE 7 (fig. 6.9 **C**) some similarities can be seen: i) the $AUC_{\log(|Z|)}$ of BAEC is by far the smallest one, ii) the MDCK II cells reveal comparable small values, and iii) the $AUC_{\log(|Z|)}$ for the MDCK I cells is relatively high. A huge difference to the 8W10E electrodes and to the IDE 12 is the $AUC_{\log(|Z|)}$ of the SK-Mel-28 cells which amounts to the highest values for all cell types. The other cell types show similar values within the error.

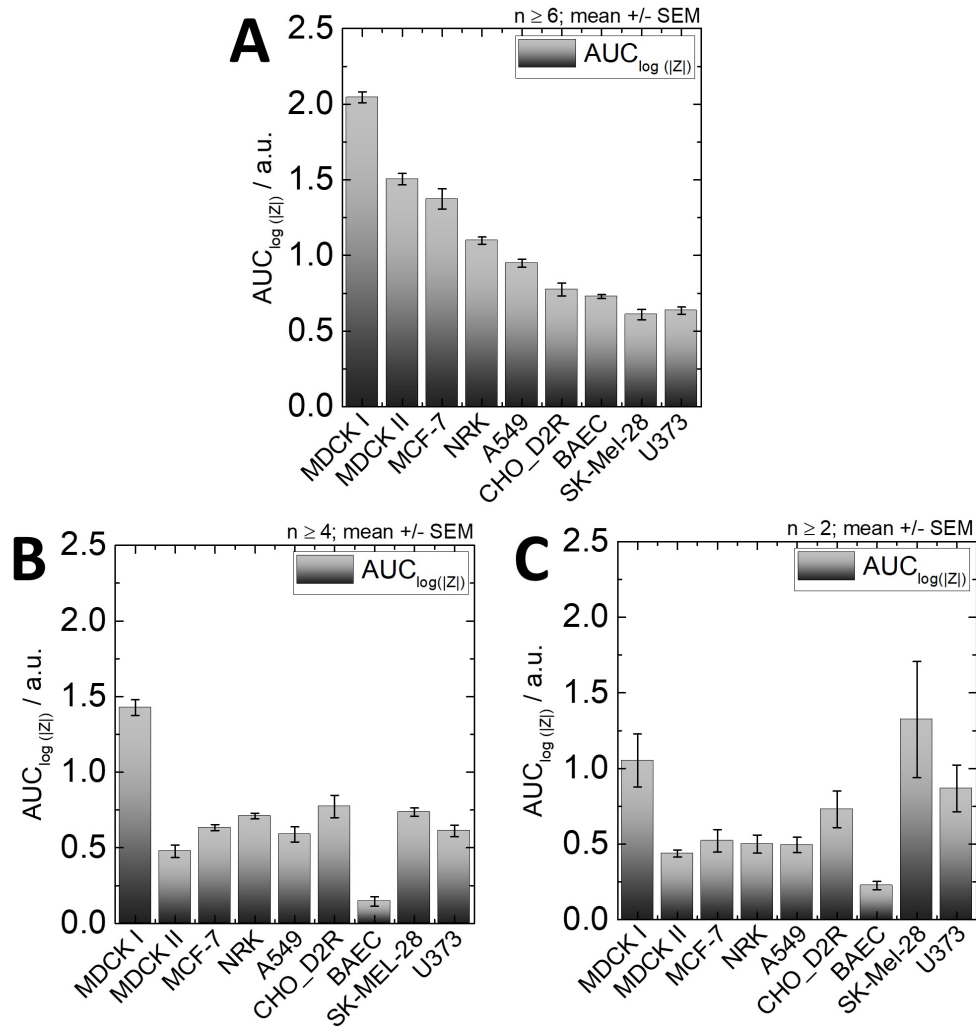


Figure 6.9: Area under the curve ($AUC_{\log(|Z|)}$) of the impedance spectra. The $\log(|Z|)$ against the $\log(f)$ was plotted and the area between the cell-free and cell-covered spectra was calculated. The $AUC_{\log(|Z|)}$ is shown for nine different cell lines on the third day after seeding, cultivated on 8W10E (**A**) with $n \geq 6$, on IDE 12 (**B**) with $n \geq 4$ and on IDE 7 (**C**) with $n \geq 2$. The mean with the SEM is plotted.

This representation of the $AUC_{\log(|Z|)}$ underlines the observations in the frequency spectra (see fig. 6.7) that with the IDE 12 and IDE 7 different impedance magnitudes of the cells can be measured compared to the 8W10E electrodes. Consequently, the penetration depth of the electric field must be different for the IDE 12 and IDE 7 than for the 8W10E electrodes resulting in the measurement of various aspects of the cells.

To complete the comparison of the various cell lines the $AUC_{\log(|Z|)}$ of the MDCK I, MDCK II, NRK and U373 cells grown on five different interdigitated layouts and on the 8W10E electrodes are presented in fig. 6.10.

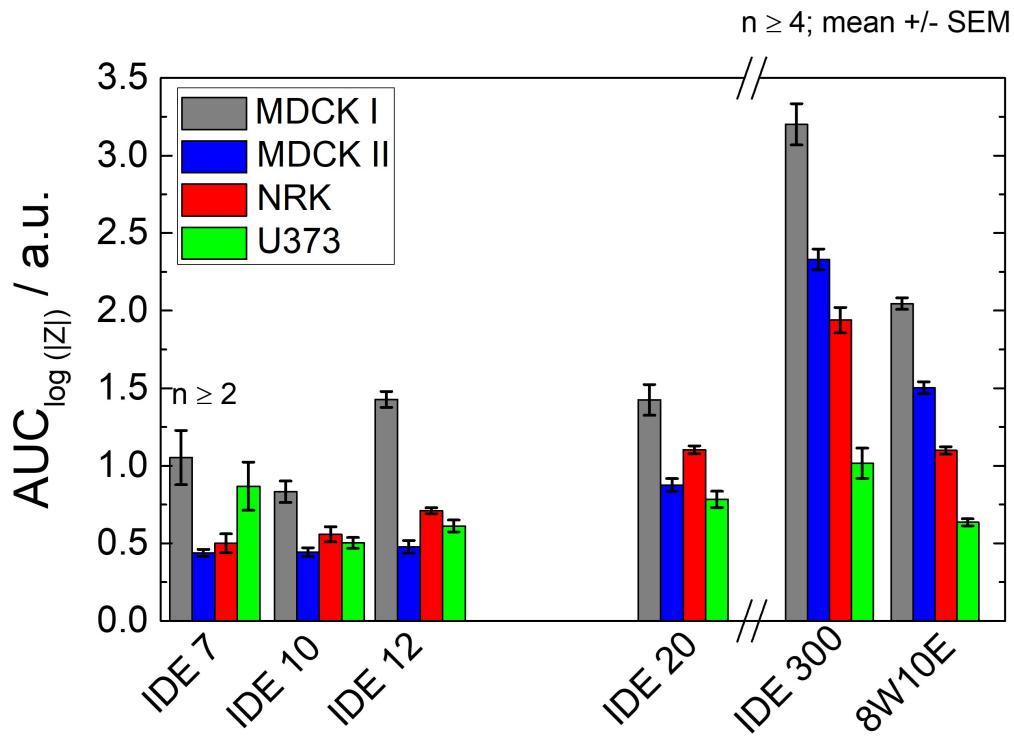


Figure 6.10: Area under the curve ($AUC_{\log(|Z|)}$) of the impedance spectra of various electrode types. The $\log(|Z|)$ was plotted against the $\log(f)$ and the area between the cell-free and cell-covered electrode was calculated. The $AUC_{\log(|Z|)}$ was determined for MDCK I, MDCK II, NRK and U373 cells grown on IDE 7, IDE 10, IDE 12, IDE 20, IDE 300 and 8W10E electrodes. The measurement was conducted on the third day after cultivation. The mean with the SEM is plotted with $n \geq 4$, with the exception of IDE 7 with $n \geq 2$.

Comparing the individual electrode types (see fig. 6.10) the order of the magnitude of the $AUC_{\log(|Z|)}$ is of particular interest. With all six electrode layouts the MDCK I cells show the highest $AUC_{\log(|Z|)}$, but the MDCK II, NRK and U373 cells have a different magnitude measured with the various electrode types. The IDE 300 and the 8W10E electrodes have the same order of these cell lines. In both cases the

MDCK II cells reveal the second highest $AUC_{\log(|Z|)}$, followed by NRK cells and by the smallest signal of the U373 cells. For the IDE 20 it is seen that the NRK cells have the second highest signal and the U373 the smallest one, whereas the $AUC_{\log(|Z|)}$ of the MDCK II cells lays in between. The order for the IDE 12 and IDE 10 differs from this. Here, the signal of the MDCK I cells is followed by the one of the NRK and afterwards of the U373 cells. The smallest $AUC_{\log(|Z|)}$ is obtained for the MDCK II in both cases. In the case of the IDE 7 the second highest $AUC_{\log(|Z|)}$ is revealed for the U373 cells, whereas the signal of the NRK cells is only slightly higher than the MDCK II cells.

Consequently, it can be seen that the $AUC_{\log(|Z|)}$ for the MDCK I cells is the highest one independently of the electrode layout, even if the total values of the IDEs with a small pitch are lower than for the IDE 300 and 8W10E electrodes. Overall, with the magnitude of $AUC_{\log(|Z|)}$ and the order of the individual cells the IDE 300 is more similar to the 8W10E electrodes than to the other IDEs. A noticeable gap between the data of the IDE 20 and the IDE 300 can be seen. This suggests that the distribution of the electric field and the corresponding measured impedance is strongly dependent on the electrode layout and is changing with a larger electrode gap.

Maxima of norm. $|Z|$ at f_{max}

As a next parameter the values for the maxima of the norm. $|Z|$ at f_{max} individually for each cell type and each electrode layout are determined.

In fig. 6.11 the values for the maxima of the norm. $|Z|$ at f_{max} for the 8W10E electrodes (**A**), the IDE 12 (**B**) and the IDE 7 (**C**) can be seen. The norm. $|Z|_{max}$ of the MDCK I cells reveals the highest value for all three electrode types. In the case of the 8W10E electrodes (fig. 6.11 **A**) the next highest value is obtained for the MCF-7, the MDCK II and the NRK cells, whereas within the error range the MCF-7 cells have a slightly higher value than the MDCK II and the NRK cells with the smallest signal of the three. Afterwards, the A549 cells are listed before the CHO_D2R and the BAEC cells with a similar value. The smallest norm. $|Z|_{max}$ is observed for the SK-Mel-28 and the U373 cells. For the IDE 12 (fig. 6.11 **B**) the values do not differ as strongly as for the 8W10E electrodes. The MDCK I cells reveal the highest and the BAEC cells the smallest norm. $|Z|_{max}$. All the other values are in the same range within the errors, with the exception of the MDCK II cells. These cells have a value between the BAEC cells and the others. The IDE 7 (fig. 6.11 **C**) cannot show a significant trend of the individual cell lines. The norm. $|Z|_{max}$ of the MDCK I and CHO_D2R cells is higher than for the MCF-7 cells which monitor the second highest signal. All the other cell lines fluctuate within the error tolerance in the same range.

The values for the BAEC cells of the IDE 12 and IDE 7 are over determined in the calculation of the norm. $|Z|_{max}$. The fact that the cell-covered impedance spectra are not significantly distinguishable from the cell-free spectra leads to higher errors and to higher values for the division.

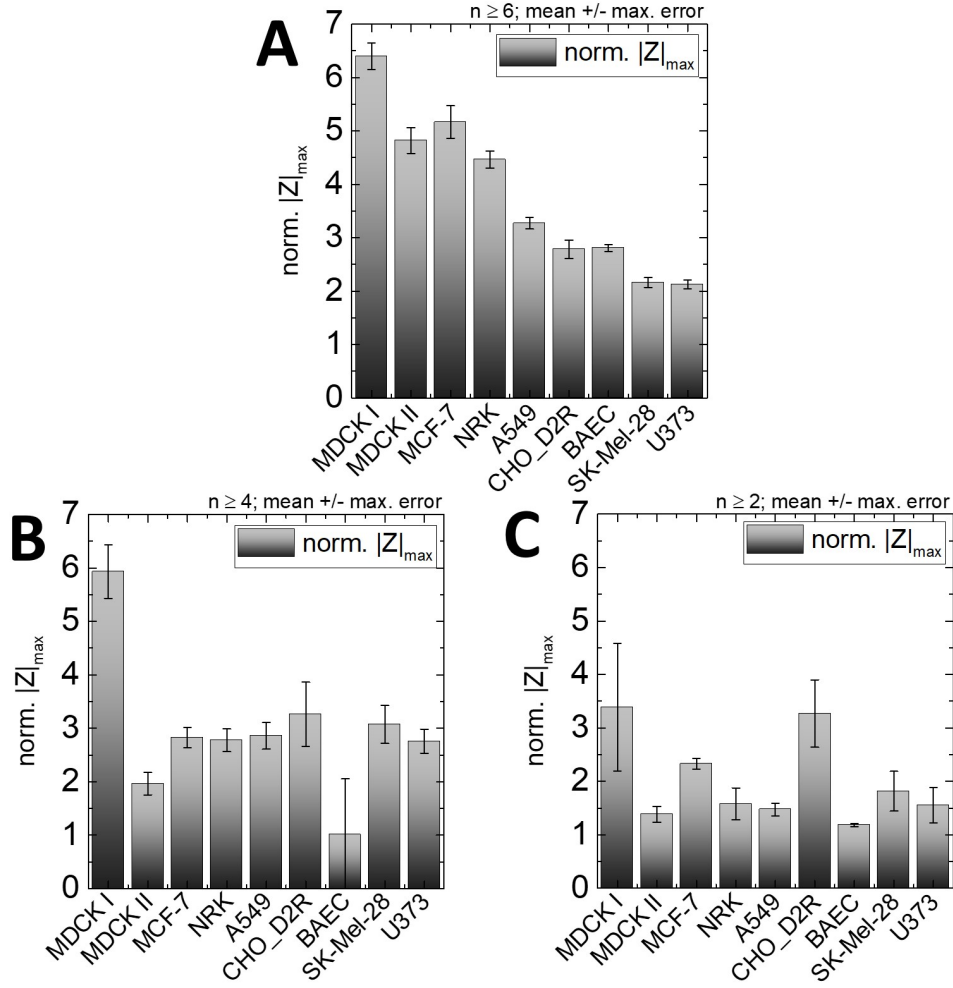


Figure 6.11: Maxima of the norm. $|Z|$ of nine individual cell lines. The data of the **A:** 8W10E electrodes ($n \geq 6$), **B:** IDE 12 ($n \geq 4$) and **C:** IDE 7 ($n \geq 2$) at f_{max} are analyzed. The mean with the max. error is plotted.

This representation of norm. $|Z|_{max}$ clarifies again that the high signal of the MDCK I cells are independently of the electrode type. The major difference of the IDE 12 and IDE 7 to the 8W10E electrodes is beside the order of the values for norm. $|Z|_{max}$ the small value of the BAEC cells and the comparatively smaller value of the MDCK II cells. Again it is demonstrated that different impedance magnitudes can be obtained for IDEs with a small pitch than for the 8W10E electrodes.

To complete the comparison of the individual maxima of the norm. $|Z|_{max}$ the values of the MDCK I, MDCK II, NRK and U373 cells on five different IDE structures and on the 8W10E electrodes are monitored in fig. 6.12. For the interdigitated structures

IDE 300, IDE 20, IDE 12, IDE 10 and IDE 7 were chosen.

Comparing the maximal values of norm. $|Z|$ of the different electrode types it is seen that the value of the MDCK I cells is the highest for every individual electrode type (fig. 6.12). Furthermore, it is obvious that the IDE 300 monitors the highest values for the MDCK I, MDCK II and NRK cells of all the measured electrodes.

The differences between the individual electrodes is the order of the magnitudes. For the IDE 7 and IDE 10 the maxima of norm. $|Z|$ of the MDCK II, NRK and U373 cells cannot be distinguished within the error tolerance. However, the NRK and the U373 cells show a higher signal than the MDCK II cells measured with the IDE 12. The IDE 20 and IDE 300 reveal a higher value for the norm. $|Z|_{max}$ of the NRK cells than of the MDCK II and U373 cells, whereas the IDE 300 obtains an even smaller value for the U373 cells. On the contrary, the 8W10E electrodes show the second highest signal for the MDCK II cells followed by the one for the NRK. The smallest norm. $|Z|_{max}$ is obtained for the U373 cells.

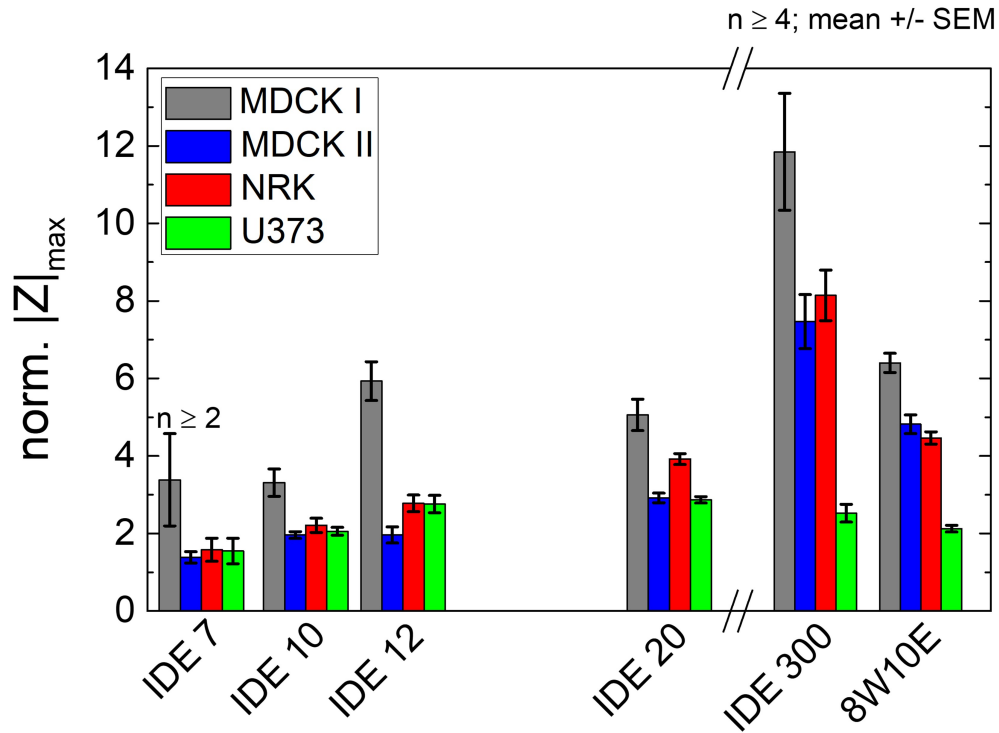


Figure 6.12: Maxima of norm. $|Z|$ of MDCK I, MDCK II, NRK and U373 cells cultivated on five different interdigitated structures and on the 8W10E electrodes. As IDEs the IDE 7, IDE 10, IDE 12, IDE 20 and IDE 300 were chosen. The data were obtained on the third day after seeding. The mean with the SEM is plotted with $n \geq 4$, with the exception of IDE 7 with $n \geq 2$.

The highest values of norm. $|Z|_{max}$ for the MDCK I cells show that this signal is not dependent on the electrode type. Furthermore, a gap between IDE 20 and IDE 300 can be seen which again indicates that the electrode gap has an essential influence on the measured impedance.

Area under the curve of the norm. $|Z|$

As a last parameter the area under the curve of the norm. $|Z|$ ($AUC_{norm. |Z|}$) was calculated. The numerical values of the nine different cell lines on the various electrode types can be seen in the appendix in tab. A.1. For the calculation the $\log(f)$ was used and a baseline of $y = 0$ was chosen.

For all electrodes a comparable order of the intensities as for the maximum of the norm. $|Z|$ can be obtained. The MDCK I cells show for all electrode types the highest magnitude, whereas the order of $AUC_{norm. |Z|}$ for the other cell lines changes dependent on the electrode types. It should be emphasized that the $AUC_{norm. |Z|}$ of the MDCK II can be counted among the lowest values of the interdigitated structures, whereas it belongs to the second highest signals in the case of the 8W10E electrodes.

In summary it is noteworthy that the analysis of the individual parameters of the impedance spectra and of norm. $|Z|$ has some advantages and disadvantages.

The frequency f_{max} of the impedance spectra only provides the frequency at the maximal impedance magnitude in comparison to the cell-free electrode and does not gain more information about the cell spectra. Nevertheless, this frequency is essential to enable a comparison between the different electrode layouts. In the following work most of the time courses of the impedance (for example the adhesion, proliferation or the stimulation) are shown at the specific f_{max} of the individual electrode. The calculation of the area under the curve of the impedance spectra ($AUC_{\log(|Z|)}$) provides a useful tool to analyze the proportion of the impedance magnitude for the various cell types, whereas no further information can be gained about the frequency range. The graph of the norm. $|Z|_{max}$ shows clearly the frequency range at which the individual cell signals and the proportion of the cell types to each other are visible. This is essential for the analysis of the frequency spectra. The calculation of $AUC_{norm. |Z|}$ does not gain additional information.

Consequently, for further analysis of the spectra, there is no unique parameter which contains all information. The maximum information can be obtained with a combination of the different parameters. Nevertheless these various parameters of the spectra and norm. $|Z|$ clarify that the MDCK I cells have the highest magnitude independently of the electrode layout. Furthermore, it is obvious that the IDE 300 is more similar to the 8W10E electrodes than to the IDEs with a small pitch. This can be traced back to the different distribution of the electric field and will be further explained in the discussion.

In this chapter the differences of the measured impedance, resistance and capacitance of cells grown on 8W10E electrodes to IDEs with various pitches were analyzed. It is obvious that with the IDEs with a small pitch (IDE 7, IDE 10, IDE 12, IDE 20) different impedance magnitudes are gained compared to the 8W10E electrodes, even

if the cultivated cells had the same preconditions. This shows that the measured impedance of the IDEs has a different focus than the one of the 8W10E electrodes. This goes along with the fact that the ECIS model is not appropriate for those IDEs with a smaller pitch. A huge exception are the IDE300 which resemble more the 8W10E electrodes than the other IDEs.

6.3 Frequency spectra of cell-covered IDEs with different window sizes

The characteristics of the IDEs were further determined with the variation of the non-insulated electrode area, called window. The aim of this variation was a change in sensitivity of the individual electrodes. For this purpose, the window size of $(0.5 \times 0.5) \text{ mm}^2$ and of $(2.0 \times 2.0) \text{ mm}^2$ was chosen and they were applied for the IDE10 and IDE20. For the IDE12 it was only possible to use the smaller window size. Analogous to the previous chapter the spectra of the MDCK I, MDCK II, NRK and U373 cells were analyzed.

In fig. 6.13 the impedance spectra of the electrodes with the small window with $(0.5 \times 0.5) \text{ mm}^2$ (fig. 6.13 **A**) and with the big one with $(2.0 \times 2.0) \text{ mm}^2$ (fig. 6.13 **B**) can be seen. For the small window of the IDE10 (fig. 6.13 **A, a**)) the impedance is clearly different to the known spectra of the electrodes with the middle window with $(1.1 \times 1.1) \text{ mm}^2$ in fig. 6.8. The impedance spectrum does not differentiate between the four distinct cell types. The signal can be seen in a range $> 20 \text{ kHz}$, but within the error tolerance no difference can be determined. This is different for the small window of the IDE12 (fig. 6.13 **A, b**)). The impedance of the MDCK I cells dominates the spectrum ($> 4 \text{ kHz}$), whereas the U373 cells show the smallest signal. The impedance of the MDCK II and NRK cells starts to change from 25 kHz and lies between the other two cell lines. Furthermore, a slightly higher impedance magnitude is shown for the NRK than for the MDCK II cells. The impedance for the $(0.5 \times 0.5) \text{ mm}^2$ of the IDE20 (fig. 6.13 **A, c**)) monitors also a difference between the various cell types. The impedance of the MDCK I cells starts at $\approx 10^3 \text{ Hz}$ but has huge variations. The next impedance magnitude can be seen for the NRK cells ($> 10^4 \text{ Hz}$) which seems to exceed the impedance of the MDCK I in the range $> 10^5 \text{ Hz}$. The smaller signal of the MDCK II and U373 cells starts $> 20 \text{ kHz}$ but cannot be distinguished.

In the case of the big window ($(2.0 \times 2.0) \text{ mm}^2$) of the IDE10 (fig. 6.13 **B, a**)) the impedance of the MDCK I cells obtains the highest value ($> 10^4 \text{ Hz}$), whereas the smaller impedances of the other three cell lines overlay each other and cannot be distinguished. The same window on the IDE20 (fig. 6.13 **B, c**)) reveals the identical

impedance magnitude for the MDCK I and the NRK cells (> 7 kHz). The smaller values of the MDCK II and U373 cells can be seen in the range $> 10^4$ Hz and shows more or less the same course.

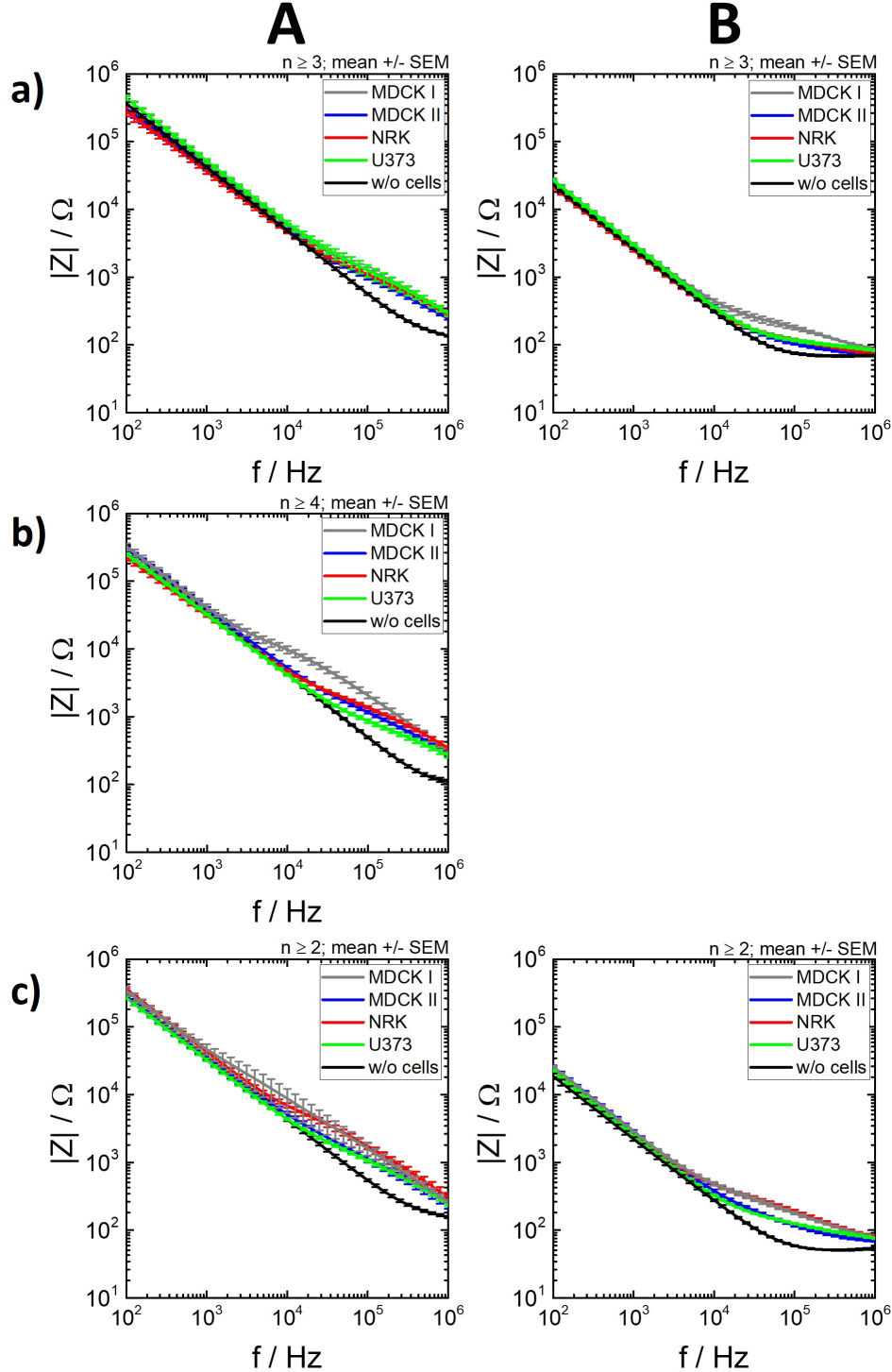


Figure 6.13: Impedance spectra of MDCK I, MDCK II, NRK and U373 on interdigitated electrodes with various window sizes in dependence of the frequency on the third day after seeding. The window size of **A**: window $(0.5 \times 0.5) \text{ mm}^2$ and **B**: $(2.0 \times 2.0) \text{ mm}^2$ were used for the IDEs of the type **a)**: IDE 10 ($n \geq 3$), **b)**: IDE 12 ($n \geq 4$) and **c)**: IDE 20 ($n \geq 2$). The mean with the SEM is plotted

With the resistance (fig. A.10) and capacitance spectra (fig. A.12) no more information can be gained. The spectra for the IDE 10 (fig. A.10 **A, a**) and fig. A.12 **A, a**) show the same course for all the cells on the $(0.5 \times 0.5) \text{ mm}^2$ window, whereas only the MDCK I cells obtain a higher signal on the electrodes with the $(2.0 \times 2.0) \text{ mm}^2$ window (fig. A.10 **B, a**) in the case of the resistance. With the measurement of the capacitance spectrum a higher capacitance change for the NRK than for the MDCK II and the U373 cells is revealed, additionally to the signal of the MDCK I cells (fig. A.12 **B, a**). For the IDE 12 (fig. A.10 **A, b**) and fig. A.12 **A, b**) the difference of the higher NRK signal to the MDCK II cells is monitored more clearly in the resistance and capacitance measurement as with the impedance spectrum. In the case of the IDE 20 (fig. A.10 **c**) and fig. A.12 **c**) the difference between the MDCK I and NRK cells is more pronounced. In the resistance spectra $< 10^4 \text{ Hz}$ the MDCK I cells have a higher signal than the NRK for both windows of $(0.5 \times 0.5) \text{ mm}^2$ (fig. A.10 **A, c**) and $(2.0 \times 2.0) \text{ mm}^2$ (fig. A.10 **B, c**), whereas with higher frequencies these signals converge to each other. Otherwise, the capacitance spectrum for the IDE 20 with the big window (fig. A.12 **B, c**) reveals a higher signal for the MDCK I than for the NRK cells in the complete frequency range $< 10^4 \text{ Hz}$. Furthermore, the MDCK II have a higher signal than the U373 cells. Consequently, with the analysis of the resistance and capacitance spectra no additional information can be generated.

To complete the description of the spectra for the individual windows the norm. $|Z|$ is monitored (fig. 6.14).

The IDE 10 with a window of $(0.5 \times 0.5) \text{ mm}^2$ (fig. 6.14 **A, a**) shows only a small difference between the various cell types. The MDCK I and U373 cells have a slightly higher value for the norm. $|Z|$ followed by the NRK and MDCK II cells. Nevertheless, the size of the error bars prevents a clear interpretation. The norm. $|Z|$ for the small window of the IDE 12 (fig. 6.14 **A, b**) reveals the same order of magnitudes as the frequency spectra. The additional information which is gained in comparison to the impedance spectra is the greater spreading of the individual magnitudes. The NRK cells show a significantly higher value than the MDCK II cells and an even smaller value for the U373 cells. In the case of the small window $((0.5 \times 0.5) \text{ mm}^2)$ of the IDE 20 (fig. 6.14 **A, c**) the large error bars prevent any statement about the exact order of the impedance magnitudes. It can only be assumed that the NRK cells have a slightly higher signal than the MDCK I cells. The MDCK II and U373 cells seem to have a smaller magnitude in the same range.

Furthermore, no additional information can be gained for the norm. $|Z|$ of the IDE 10 with the big window (fig. 6.14 **B, a**). It is only seen that the MDCK I cells have the highest magnitude for norm. $|Z|$, whereas the other three cell lines provide a value for norm. $|Z|$ in the same range. The IDE 20 shows for the big window (fig. 6.14 **B,**

c)) that the MDCK I and NRK cells have a similar value of norm. $|Z|$ with a slightly higher value for the NRK cells. The MDCK II and U373 cells reveal as well the same magnitude which is significantly lower.

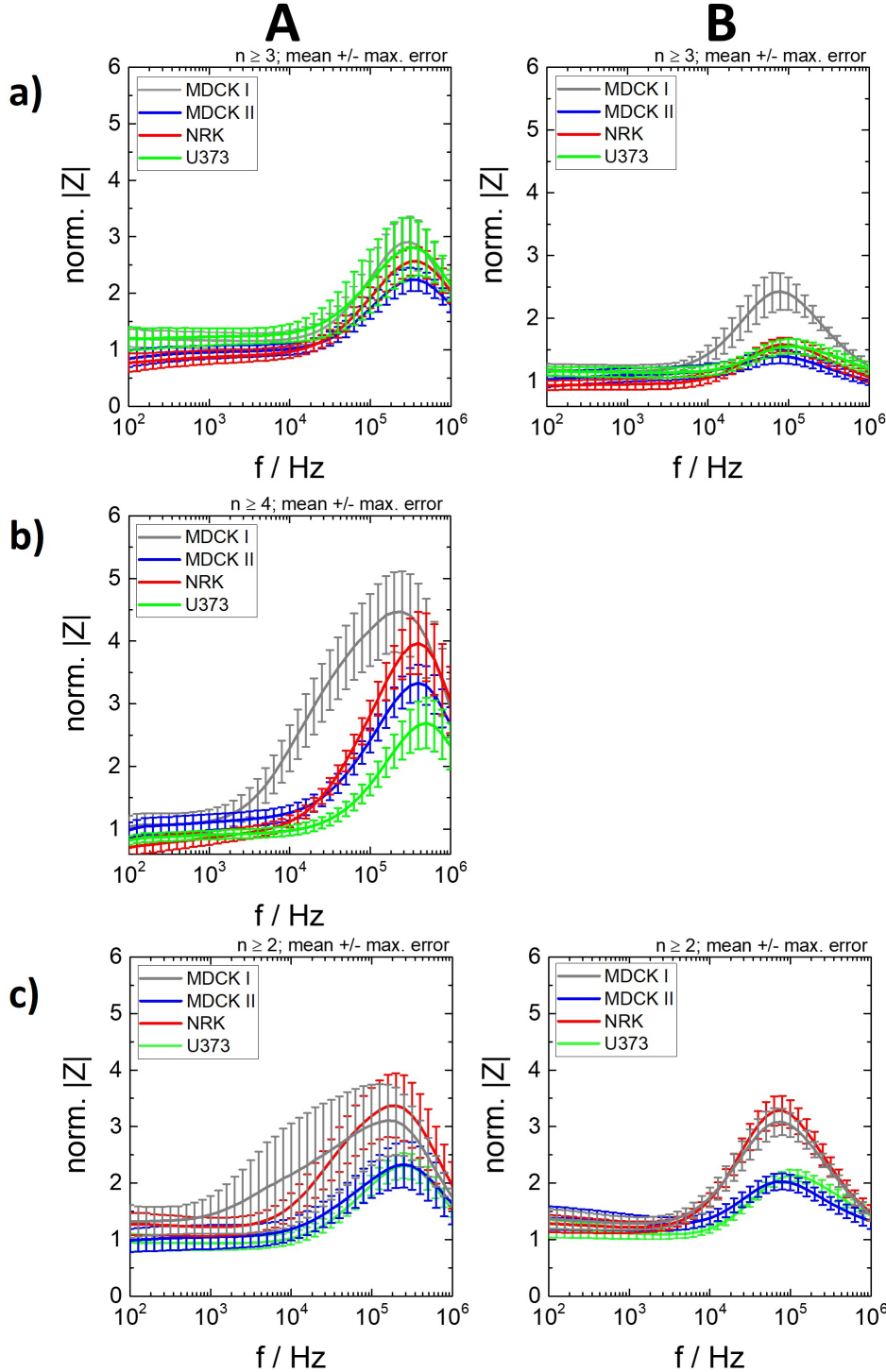


Figure 6.14: Norm. $|Z|$ of MDCK I, MDCK II, NRK and U373 cells cultivated on different interdigitated electrodes with various window sizes. The measurement was proceeded on the third day after seeding. The window size of **A**: $(0.5 \times 0.5) \text{ mm}^2$ and **B**: $(2.0 \times 2.0) \text{ mm}^2$ was used for the IDEs **a**): IDE 10 ($n \geq 3$), **b**): IDE 12 ($n \geq 4$), and **c**): IDE 20 ($n \geq 2$). The mean with the max. error is plotted.

The normalized resistance (fig. A.11) and the normalized capacitance (fig. A.13) provide even less information due to the high error bars. For the small window of the IDE 10 (fig. A.11 **A, a**) and fig. A.13 **A, a**) no differences between the cell lines can be detected in terms of both resistance and capacitance, whereas for the big window (fig. A.11 **B, a**) and fig. A.13 **B, a**) only the MDCK I cells differ from the other cells. For the small window of the IDE 12 (fig. A.11 **A, b**) the norm. R reveal a higher difference between the cell types leading to significant higher values for the NRK cells than for the MDCK II, whereas the MDCK I cells have the highest and the U373 cells have the lowest magnitude. On the contrary, no difference between MDCK II and NRK can be seen for the norm. C (fig. A.13 **A, b**). In the case of the IDE 20 (fig. A.11 **c**) the values for the norm. R of the MDCK I and NRK cells have big error bars for both window sizes leading to the assumption that the signal for the MDCK I and NRK is in the same range. However, different f_{max} of the cell types measured with the small window (fig. A.11 **A, c**) are observed. Furthermore, the norm. R of the MDCK I cells is clearly higher than the one of the NRK cells for the big window (fig. A.11 **B, c**). In both cases, for the small and big window, the values for the MDCK II and U373 cells are very low and cannot be distinguished from each other. The norm. C of the IDE 20 with the small window has too high error bars to enable a clear interpretation (fig. A.13 **A, c**). For the IDE 20 with the big window it can be seen that the NRK cells have the second highest norm. C after the small signal for the MDCK I cells, and the MDCK II and U373 cells cannot be distinguished (fig. A.13 **B, c**).

In summary it can be said, that with the variation of the window size the signal fluctuates more and that the error bars increase. It is more difficult to distinguish the signals of the different cell types. Consequently, it was not possible to gain a higher sensitivity with the variation of the non-insulated electrode areas.

6.4 Micromotion measurement of different cell types grown on various electrodes

Another aspect of the characterization of the different cell types grown on the various electrode layouts is the analysis of the cell motility, referred as micromotion. Cells in a confluent monolayer do not behave static, they move in a horizontal and vertical way which can be associated with the fluctuation of the measured impedance. These fluctuations can be seen as a direct measurement of the cell motion (Giaever and Keese, 1991). The sensitivity of the impedance measurement enables a monitoring of an average motion of the cells in the scale of nanometer (Lo et al., 1993). The evaluation of the various micromotions was proceeded with the detrended variance analysis which is explained in chapter 3.1.2.4.

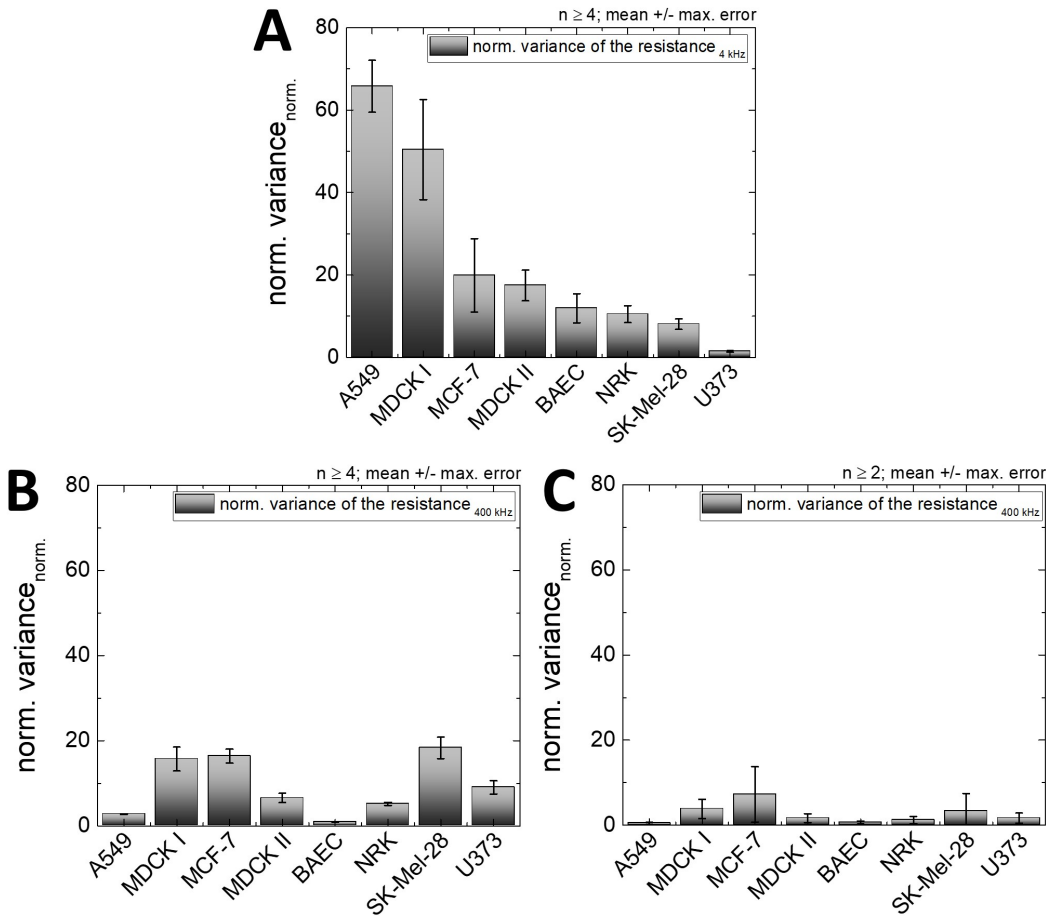


Figure 6.15: Normalized data of the detrended variance analysis of the resistance of the micromotion measurement. Eight different cell types were measured on the third day after seeding. The data were normalized to the data of the cell-free electrodes: $(15.9 \pm 0.9) \cdot 10^{-8}$ (8W1E), $(0.0711 \pm 0.0002) \cdot 10^{-8}$ (IDE 12), $(0.16 \pm 0.07) \cdot 10^{-8}$ (IDE 7). For the experiment **A**: 8W1E ($n \geq 4$) at 4 kHz, **B**: IDE 12 ($n \geq 4$) at 400 kHz and **C**: IDE 7 ($n \geq 2$) at 400 kHz were chosen. The mean with the max. error is plotted.

In fig. 6.15 the evaluation of the micromotion of the resistance of eight different cell lines grown on the 8W1E electrode (**A**), the IDE12 (**B**) and the IDE7 (**C**) measured on the third day after seeding can be seen. The 8W1E electrodes were used because they are more sensitive for micromotion than the 8W10E electrodes. For the measurement the frequency f_{max} was chosen individually for each electrode type: i) 8W1E at 4 kHz, ii) IDE12 at 400 kHz and iii) IDE7 at 400 kHz. All data are normalized to the data of the micromotion of the individual cell-free electrodes, whereas the original data can be seen in fig. A.14 in the appendix. The resulting $norm.variance_{norm.}$ is sorted by descending magnitude of the micromotion of the cells measured with the 8W1E electrodes.

Comparing the individual normalized variances of the electrodes it is obvious that the values of the $norm.variance_{norm.}$ measured with the 8W1E electrodes are higher than the one measured with the interdigitated electrodes. The smallest magnitudes of the 8W1E electrodes are in a comparable size like the highest ones of the IDE12. The variances measured with the IDE7 are even smaller and represent only a small fraction of the values of the 8W1E electrodes. Nevertheless, it is possible to compare the order of the various intensities of the variances measured with the electrodes.

For the 8W1E electrodes (fig. 6.15 **A**) the highest normalized variance is revealed for the A549 followed by the MDCK I cells. The next highest variance is the one of the MCF-7 and the MDCK II which are within the error tolerance in the same range. The smaller values for the BAEC and the NRK cells can also not be differentiated from each other and are only slightly higher than the variance of the SK-Mel-28 cells. The smallest value is monitored for the U373 cells which cannot be distinguished from the cell-free electrode (see fig. A.14 **A**).

In the case of the IDE12 (fig. 6.15 **B**) the order of these intensities changed significantly. The highest normalized variance is revealed for the SK-Mel-28 cells which is only slightly higher than the one of the MCF-7 and MDCK I cells. Considerably smaller is the variance of the U373 cells, followed by the MDCK II cells and the NRK cells with an even smaller variance. The second smallest variance is monitored for the A549 cells, whereas the variance of the BAEC cells cannot be distinguished from the cell-free electrode (see fig. A.14 **B**).

For the IDE7 (fig. 6.15 **C**) a comparable order of intensities can be seen. The highest normalized variance is monitored for the MCF-7 cells, followed by the MDCK I and SK-Mel-28 cells. However, the error tolerance of the MCF-7 and SK-Mel-28 is very high which makes a clear sorting more difficult. The next higher variance is revealed for the U373 and MDCK II cells which are in the same range, followed by the slightly smaller NRK cells. The smallest variances are monitored for the A549 and the BAEC cells which are difficult to differentiate within the error tolerance. Those cannot be distinguished from the cell-free electrode (see fig. A.14 **C**).

In summary some differences of the individual electrode types should be emphasized. The normalized values of the micromotion measured with the interdigitated electrodes are significantly lower than those of the 8W1E electrodes. The values of the IDE 7 represent even a small fraction of the normalized variance of the 8W1E electrodes. Big differences are also seen in the order of the intensities. On the one hand, the A549 cells have the highest normalized variance in the case of 8W1E electrodes, whereas it can be observed as the second lowest (IDE 12) or even the lowest one (IDE 7) for the interdigitated structures. On the other hand, in the case of the IDEs the MCF-7 and SK-Mel-28 cells have a much higher variance in comparison to the other cell types than with the 8W1E electrodes. Furthermore, it has to be underlined that the variance of the U373 cells which is not distinguishable from the cell-free 8W1E electrodes has a significant higher value measured with the IDEs. Furthermore, the normalized variance of the BAEC cells is not detectable with the IDEs compared to the high value of the 8W1E electrodes.

To complete the micromotion measurement, the variance of the MDCK I, MDCK II, NRK and U373 cells were analyzed on various interdigitated electrode layouts and were compared with the 8W1E electrodes (fig. 6.16).

The calculated variances of the resistance were measured at the frequency f_{max} specifically for the individual electrode type. For the normalization the division was used (explained in chapter 3.1.2.4). In fig. 6.16 the calculated normalized variance is shown without further normalization (with the cell-free data). The focus is on the order of the variances of the cell types in comparison between the electrode types. The data of the 8W1E electrodes, the IDE 12 and IDE 7 are identical to the one in fig. A.14 and are shown here for a complete comparison.

The similarity which can be seen for all electrodes is that the MDCK I cells monitor significantly the highest variance. The order of the values of the other three cell lines differ between the electrode types. The second highest variance can be seen for the MDCK II and the U373 cells in the case of the IDE 7, whereas only the MDCK II cells are following directly after the MDCK I for the IDE 10, IDE 300 and 8W1E electrodes. In the case of the IDE 12 and IDE 20 the second normalized variance can be recognized for the U373 cells, followed by the value of the MDCK II cells. For all the IDEs with lower pitches (IDE 7, IDE 10, IDE 12 and IDE 20) the smallest variance can be obtained for the NRK cells. In contrary to this, the U373 cells reveal the lowest variance measured with the IDE 300 and 8W1E electrodes.

Consequently, it is noteworthy that the IDE 300 resembles the 8W1E electrodes more than the other interdigitated electrodes in the order of descending variance intensities. In addition, the values of the cell motility are less pronounced measured with the interdigitated electrodes with a smaller dimension than those of the IDE 300 and 8W1E electrodes. Another difference is that the order of the variances is changed

for the smaller IDEs. The variance of the U373 cell is not the smallest as it can be seen for the IDE 300 and 8W1E electrodes.

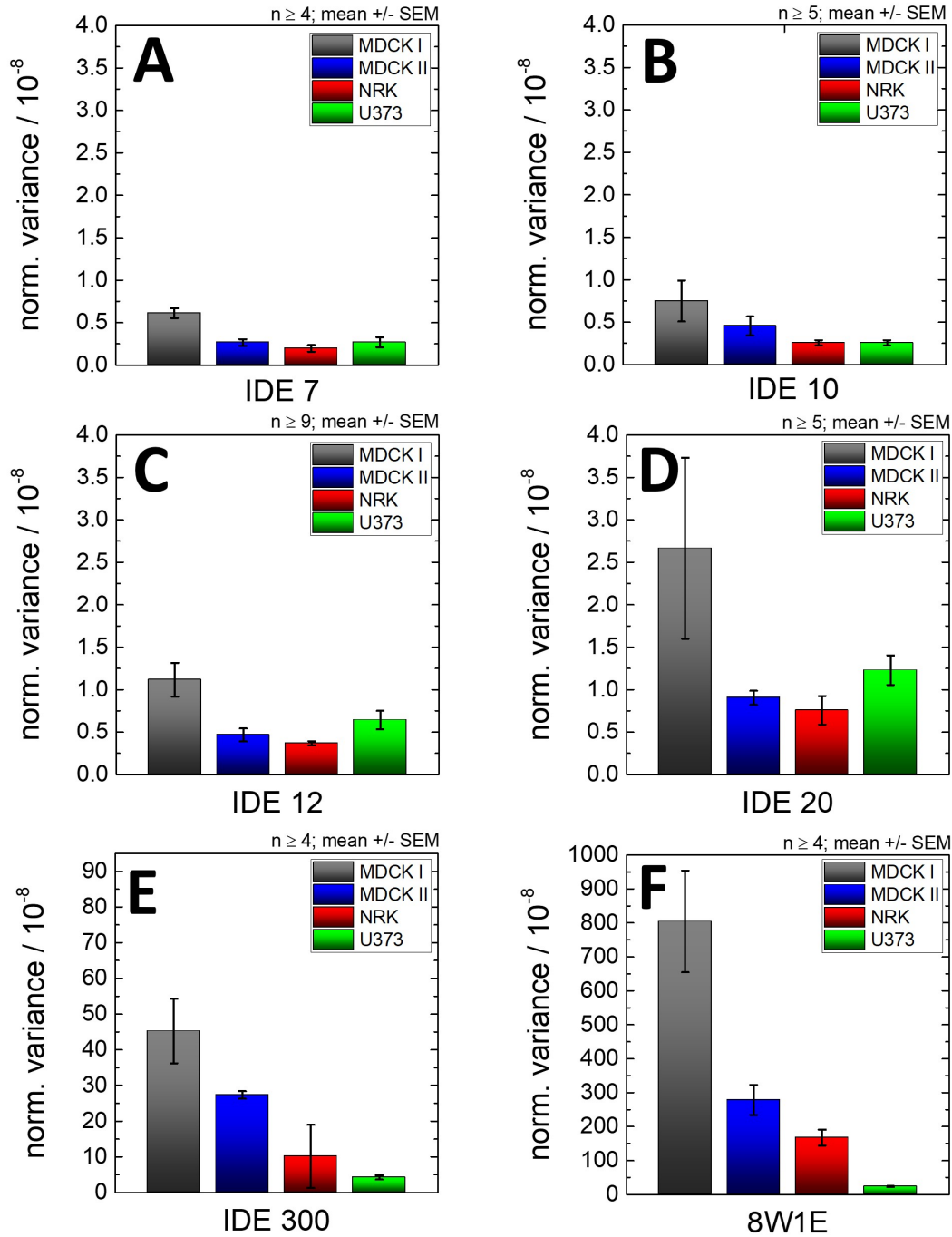


Figure 6.16: Data of the micromotion measured with various electrode types. The detrended variance analysis was proceeded for the resistance at a fixed frequency. The electrode types used in this experiment on the third day after seeding are **A**: IDE 7 at 400 kHz ($n \geq 4$), **B**: IDE 10 at 251 kHz ($n \geq 5$), **C**: IDE 12 at 400 kHz ($n \geq 9$), **D**: IDE 20 at 200 kHz ($n \geq 5$), **E**: IDE 300 at 4 kHz ($n \geq 4$) and **F**: 8W1E at 4 kHz ($n \geq 4$). The mean with the SEM is plotted.

6.5 Discussion

When cells are growing on the electrodes their insulating character restricts the current flow and the impedance is increasing. To allow the comparison with the cell-free electrode in chapter 5 the equivalent circuit is first briefly explained, even though the physical model from Giaever and Keese was used to understand the various impedance magnitudes of the cells. The impedance of the presence of the cell body on the electrode surface has to be added in the equivalent circuit in series to the cell-free electrode discussed in chapter 5. The impedance Z_{cl} can be described with two additional elements for the resistive and capacitive characteristics of the cell monolayer: i) a capacitor C_{cl} and ii) a resistor R_{cl} which are arranged in parallel (see fig. 6.17 A) (Wegener et al., 1999). Due to the big difference of the electrodes sizes in the case of the ECIS electrodes, the voltage drop and current density of the counter electrode can be neglected and the measured impedance is determined by the working electrode. Consequently, the equivalent circuit with one CPE, one Z_{cl} and one R_{bulk} in series clarifies the impedance magnitude the best (see fig. 6.17 A). In contrary to this, the IDEs have two same-sized electrodes which both contribute the same amount to the impedance measurement. For the correct equivalent circuit two CPEs and two Z_{cl} are necessary, whereas the current only flows once through the electrolyte, resulting in one R_{bulk} . The equivalent circuit for an interdigitated electrode layout can be seen in fig. 6.17 B.

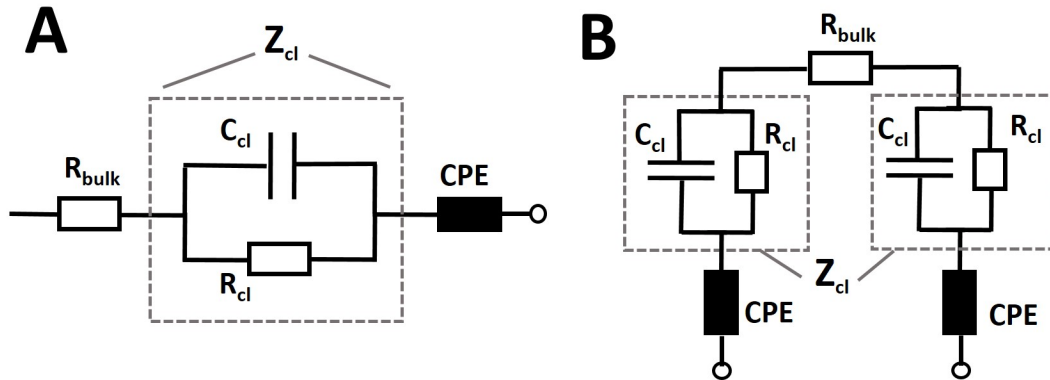


Figure 6.17: Equivalent circuit of cell-covered electrodes. **A:** ECIS electrode, **B:** IDE. CPE: constant phase element, R_{bulk} : resistance of the bulk, Z_{cl} : impedance of the cell, C_{cl} : capacitor of the cell, R_{cl} : resistor of the cell.

Comparing the impedance spectra of the cell-free and the cell-covered electrodes the impact of Z_{cl} can clearly be distinguished (see for instance fig. 6.7). To further understand the influence of the cells on the measured impedance the frequency-dependent current flow across the cell layer has to be analyzed (Wegener, 2010). The individual frequency range in which different parts of the cell influence the signal is strongly dependent on the electrode type and the cell line. Nevertheless, the

various frequency dependencies can be applied for all the electrode types used in this work.

In the very low frequency range the impedance of the electrode/electrolyte interface dominates the signal which can be seen in a straight curve with a linear slope. The impedance of the cells is not decisive in this range and cannot be distinguished from the cell-free electrode.

With increasing frequency the impedance of the membrane becomes more and more present and the current is forced to flow around the cells. The current has to flow through the narrow cleft of the basolateral membrane of the cells and the electrode surface before it passes the cell-cell junctions and escapes into the bulk electrolyte. Consequently, the electrical properties of the cell-matrix and cell-cell junctions influence the impedance in this range and can further be used to monitor these characteristics (Wegener, 2010).

At high frequencies the cell membranes react electrically as capacitors. The current can flow straight through these cell membranes as a displacement current. Consequently, at high frequencies information about the capacitance of the cell membranes C_m can be gained. This is revealed in the capacitance spectra in fig. A.6 with the decreasing capacitance at higher frequencies.

Simulation of the dielectric properties of adherent cells by finite element techniques

To understand the order of the signal magnitudes of the different cell lines measured with the IDEs it is important to explain first the various simulations of the adherent cells on the interdigitated electrodes. With the simulations by finite element techniques using COMSOL Multiphysics three main influences on the measured signal can be explained: i) the cell height, ii) the cell-electrode distance, and iii) the size of the electrode gap. These influences change the distribution of the electric field. This various penetration depth of the electric field is generally essential for the analysis of biological samples (MacKay et al., 2015a). In the case of a low penetration depth the main focus of the analysis lies in the near distance to the electrodes. Consequently, it is possible to detect phenomena close to the surface. With a larger distance between the electrodes (as with the ECIS electrodes) the electric field will be less sensitive for these changes close to the surface. Such electrodes are advantageous in the monitoring of larger species, like whole cells or cell aggregates (MacKay et al., 2015a). To simplify matters, the cell-cell contacts were omitted and the cells were assumed to be completely insulating. This insulating character of the cells occurs at the frequency f_{max} which was chosen for the individual electrodes: i) 251 kHz for IDE 10, ii) 200 kHz for IDE 20, and iii) 4 kHz for IDE 300. For the IDE 40 a f_{max} of 100 kHz and for the IDE 100 a f_{max} of 4 kHz was assumed and chosen.

First, the influence of the various cell heights on the distribution of the electric field

is explained. In fig. 6.2 **A** and 6.3 it is obvious that the electric field is distributed differently with various cell heights (from $h = 5 \mu\text{m}$ to $h = 0.5 \mu\text{m}$). With the precondition that all parameter of the various simulations are equal a clear trend for measuring with IDEs with a small pitch is emerging. With very flat cells the main part of the electric field is distributed across the intercellular cleft, whereas the electric field underneath the cells is comparably small. As the cell height increases, the electric field underneath the cells becomes more focused and the fraction of the electric field in the intercellular cleft decreases. This distribution in the clefts show a high local resolution depending on the distance of the cleft to the electrode edge. Due to the fact that only a small excerpt of the simulation is shown which is performed in two dimensions only some clefts are simulated. The measurement includes the electric field in the intercellular clefts as an averaged value. Nevertheless, the distribution in the intercellular clefts are overestimated in the simulation because for simplicity no cell-cell contacts were simulated. For the measured impedance the distribution of the electric field means that the cell height determines which space around the cell body dominates the signal. With cells, like for example with the MDCK cells ($h = 5 \mu\text{m}$ (Lo et al., 1995)), the focus of the measured signal is underneath the cells on the basal cell membrane. Measuring flatter cells, like the NRK cells ($h = (3.6 \pm 0.6) \mu\text{m}$ (Parak et al., 1999)), the intercellular cleft with the cell-cell contacts have a greater influence on the measured impedance. Consequently, the cell height influences significantly the focus of the measured signal when using IDEs with a small pitch. This knowledge is later used to explain the impedance magnitude measured with the IDEs.

Another influence on the distribution of the electric field which can be explained with the simulations of the IDE 10 is the cell-electrode distance. The cell height for this comparison was adjusted to the one of the MDCK cells: $h = 5 \mu\text{m}$ (Lo et al., 1995). The cell-electrode distance displayed on the one hand the MDCK cells with a value of $d = 25 \text{ nm}$ (Wegener, 2010) and on the other hand the BAEC cells with an average distance of $d = 500 \text{ nm}$ (Wegener et al., 1999). The simulations (see fig. 6.2 and fig. 6.4) show that with distances of $d = 25 \text{ nm}$ and $d = 100 \text{ nm}$ the electric field is focused underneath the insulating cells and only a small fraction of the electric field is distributed across the intercellular clefts. The difference between the two distances is that with the small distance ($d = 25 \text{ nm}$) the ratio of the electric field in the intercellular cleft is greater than with the larger distance. Consequently, the intercellular cleft has a higher influence on the measured signal with the smaller distance. With a larger cell-electrode distance ($d = 500 \text{ nm}$) the electric field spreads almost exclusively underneath the cells and has comparatively small values in the intercellular cleft. Consequently, the focus of the measured impedance is more on the basal side of the cells. Comparing the simulation of the cell-free IDE 10 (fig. 5.10 **A**)

and the cells in a distance $d = 500$ nm simulated on the IDE 10 (fig. 6.4) this observation can even be intensified. The electric field underneath the cells arises to a value of $E \approx 1.0 \cdot 10^4$ V/m and in the cell-free simulation to a value of $E \approx 0.8 \cdot 10^4$ V/m between the two electrodes in the gap. These similar values of the electric field in the electrode gap clarifies that the cells in a distance of $d = 500$ nm have nearly no influence on the electric field simulated between the electrodes and the penetration of the electric field into the electrolyte underneath the cells is almost not restricted. This results in a low measured impedance of the cells with a higher cell-electrode distance than of the cells with a smaller cell-electrode distance. This argument will later be used for the explanation of the missing impedance signal of the BAEC cells grown on the IDEs with a small pitch.

As a last aspect, which can influence the distribution of the electric field, the size of the electrode gap was analyzed. The distribution of the electric field changes drastically with the enlargement of the electrode gap. To draw conclusions to the measured signal the IDE 300 was simulated with cells ($h = 5$ μ m and $d = 25$ nm). With this simulation a very concrete local restriction can be seen. The main part of the electric field distributes across the intercellular cleft of the cells grown directly on the electrodes. Underneath the cells nearly no electric field is obtained in the electrode gap. Here the main part of the electric field is in the electrolyte above the cells. It is obvious that with this electrode layout the entire cells and the complete cell-cell contacts of the cells grown directly on the electrodes are monitored and dominate the measured signals, comparable to the ECIS model (explained in chapter 3.1.1). With the distribution of the electric field for this IDE 300 it is obvious that the signals of the IDE 300 resemble more the ones of the 8W10E electrodes than the ones of the IDEs with smaller pitches. To explain the differences of the distribution of the electric field simulated for the IDE 10 and the IDE 300, IDEs with pitches between these two were simulated (IDE 20, IDE 40, IDE 100). It can be seen that the ratio of the part of the electric field in the intercellular cleft to the part underneath the cells is changing with the gap size. With the IDE 20 it is shown, that the intercellular cleft as well as the space underneath the cells have an influence on the measured signal, whereas with the IDE 40 the electric field underneath the cells gets comparably small, until it can be neglected like in the simulation of the IDE 100. The distribution of the electric field of this IDE is very similar to the one of the IDE 300. This clarifies that the larger the gap is, the more the focus of the electric field is shifted to the intercellular cleft. Consequently, with IDEs with a small pitch the electric field can be focused on the space between the basolateral cell membrane and the substrate between the electrodes. As a result the basolateral responses of the cells are monitored more accurately with IDEs with a smaller gap as with IDEs with a larger gap.

In summary, the simulations of the cells grown on the electrodes are a big step towards understanding the measured impedance. The simulations showed that when IDEs with a small gap are used, the cell height and the distance of the cells to the electrode surface have a huge impact on the associated results. Increasing this gap the interdigitated electrodes resemble more and more the commercially available ECIS electrodes, like it was seen with the simulated IDE300. This in turn proves that the ECIS model is not appropriate for the IDEs with a small pitch. Based on these simulations, many differences of the measured impedance of the IDEs and the ECIS electrodes can be explained in the following thesis.

Evaluation of the fitted ECIS parameters of the 8W10E electrodes and the associated spectra

To enable an interpretation of the impedances of the cell-covered electrodes the physical model of ECIS was developed (Giaever and Keese, 1991), described in chapter 3.1.1. For the fitting of the spectra of the 8W10E electrodes three different parameters were used to describe the impact of the cell layer: i) α which monitors the electrical tightness of the cell-electrode junction, ii) R_b which defines the resistance of the cell-cell contacts and iii) C_m which is the specific cell membrane capacitance. The impact of the individual parameters on the impedance course was simulated in chapter 3.1.1 in fig. 3.3. It can be said that R_b and α are correlated due to the fact that the cleft of the cell membrane and the substrate is directly connected to the intercellular space which is filled with electrolyte. Cells with tight paracellular barriers also reveal a reduced conductivity underneath the cells (Reiss and Wegener, 2015). A further parameter for the tightness of the barrier function is the transepithelial electrical resistance (TEER), which represents a combination of the resistance of the cell-cell contacts, dominated by the tight junctions, (R_b) and the cell-electrode junctions (α). For this, a high value of R_b goes along with a high TEER value and can allow conclusions about strong cell-cell contacts. In general, epithelial cells from a kidney have a stronger occlusion of the paracellular diffusion barriers because they take part in the reabsorption of different metabolites from the urine (Reiss and Wegener, 2015).

This can be seen in the fitted data of the individual cell lines on the 8W10E electrodes (see tab. 6.2). The MDCK I cells have by far the highest values for R_b and α followed by the MDCK II cells for which the values are lowered by a factor of four. The differences of these two cell lines can be explained with the distinct barrier functions which are structurally associated with the formation of epithelial tight junctions (Wegener and Galla, 1996). The MDCK I cells grow to a very tight epithelia with very high resistances (TEER: $(4.16 \pm 0.25) \text{ k}\Omega \cdot \text{cm}^2$), whereas the MDCK II cells build a leaky epithelial monolayer with lower resistance (TEER: $(71 \pm 6) \text{ k}\Omega \cdot \text{cm}^2$)

(Balcarova-Ständer et al., 1984; Richardson et al., 1981). These high resistances explain the broad impedance signal over nearly the whole frequency range measured in this work for the 8W10E electrodes. The MDCK I cells dominate the spectra in all electrode types (except IDE 10 with a window size of $(0.5 \times 0.5) \text{ mm}^2$). Even the more leaky MDCK II cells show a very high magnitude within a broad frequency range in the case of the 8W10E electrodes and the IDE 300. The difference in the measurement with the other IDEs, in which the impedance spectra of the MDCK II cells reveal smaller impedance values, will be explained later. The impedance values of the MDCK II cells for the 8W10E electrodes are shifted to smaller impedance values than for the MDCK I cells. Due to the simulated data this can be explained with the higher C_m value. In general, the value for C_m is in the range of $1 \mu\text{F}/\text{cm}^2$, if the membranes do not form microvilli, invaginations or protusions (Reiss and Wegener, 2015). If the value for C_m is $> 1 \mu\text{F}/\text{cm}^2$, the membrane topography is convoluted (Reiss and Wegener, 2015). The MDCK II cells have more microvilli than the MDCK I cells (Balcarova-Ständer et al., 1984; Richardson et al., 1981) which are more expressed on the apical than on the basal membrane (Lo et al., 1995). With the fitting of the impedance data on the second day after seeding on a different electrode layout with an area of 0.33 cm^2 a C_m value of $3 \mu\text{F}/\text{cm}^2$ could be measured (Reiss and Wegener, 2015). This value is comparable with the one of this work. Due to this higher ratio of folds the value for C_m of the MDCK II is significantly higher than for the other cell lines. The fitted values of C_m for the other cell lines are very similar and lay in between 1 to $2 \mu\text{F}/\text{cm}^2$, with the exception of the SK-Mel-28 cells which will be explained later. The next highest impedance value can be seen for the MCF-7 cells. R_b is in the same range as for the NRK cells but α is much higher than for the other cells, with the exception of the MDCK cells. The TEER value for the MCF-7 cells was measured to be $(81.2 \pm 0.4) \Omega \cdot \text{cm}^2$ (Wu et al., 2010). Due to the fitting of the MCF-7 cells on an 8W1EDD electrode with an electrode diameter of $250 \mu\text{m}$ the fit data resembles with the one in this work ($R_b = (3.7 \pm 0.9) \Omega \cdot \text{cm}^2$, $\alpha = (6.2 \pm 1.0) \Omega^{0.5} \cdot \text{cm}$, $C_m = (3.1 \pm 0.2) \mu\text{F}/\text{cm}^2$) (Lai et al., 2019). The transmembrane protein claudin-6 is expressed on the cell membrane of the MCF-7 cells whose expression level and location is important for the organization and function of the tight junctions. When the expression of this protein is upregulated, the TEER values are increasing (Wu et al., 2010). MCF-7 cells can form tightly packed spheroids which need high physical strength to be disintegrated (Lee et al., 2010). This shows that the cell-cell contacts of the MCF-7 can be formed very tightly which is reflected in the strong impedance signal of the 8W10E electrodes. The next lower impedance signal is monitored for the NRK cells. This cell line has a smaller TEER value of $(13 \pm 1) \Omega \cdot \text{cm}^2$ which can be explained with the fact that occludin was found to be the only tight junction protein (Limonciel et al., 2012; Prozialeck et al., 2006). This

smaller TEER value results in the smaller impedance signal in comparison to the MDCK and MCF-7 cells in the case of the 8W10E electrodes and the IDE 300. The higher signal of the NRK cells with the IDEs with smaller pitches will be explained later. For the A549 cell line different results were obtained in literature. On the one hand, a TEER value of $< 25 \Omega \cdot \text{cm}^2$ (Geys et al., 2006) or $< 40 \Omega \cdot \text{cm}^2$ (George et al., 2015) can be measured, on the other hand it was shown that A549 cells have a less organized cortical actin cytoskeleton (George et al., 2015). Further, it was discovered that A549 cells were not able to form an efficient barrier (Forbes and Ehrhardt, 2005). This can be the explanation for the lower impedance signal of the A549 cells in comparison to the NRK, although they have a higher TEER value. The measurements of the TEER values in literature were provided on a later day after seeding which can also explain the smaller R_b values of the A549. As the next higher signal the impedance of the CHO_D2R and BAEC cells are revealed for the 8W10E electrodes. R_b has a higher value for the BAEC cells in comparison to the CHO_D2R cells, whereas with α it is reverse. The values for C_m are in the same range for both cell lines. The CHO cells do not form tight junctions (Bazzoni et al., 2000) as well as the BAEC which are known to express no significant barrier, resulting in a paracellular current pathway, which is very leaky (Reiss and Wegener, 2015; Wegener et al., 1999). Consequently, they have negligible barrier properties (Stannes et al., 1997) resulting in a low TEER value of $\approx 5 \Omega \cdot \text{cm}^2$ with a transwell setup (Santaguida et al., 2006). These low cell-cell contacts can be seen as the explanation of the low impedance value measured with the 8W10E electrodes. The lowest impedance signals were obtained for the SK-Mel-28 and U373 cells. The fit data of these cell lines do not differ much. On the one hand, R_b is identical for both cell types, on the other hand α shows a slightly higher value for the SK-Mel-28. A noticeable characteristic of the fit is the small C_m value compared to all the other cell lines. This can be explained by the fact that the cells cannot only build a monolayer but also grow over each other. Both cell lines are malignant tumor cells and are known to build three-dimensional spheroids. In this case the ECIS model would no longer work. Furthermore, both cell lines have a huge, more elongated shape during cultivation (not shown here). The ECIS model is based on the assumption of a circular shape of the cells (Giaever and Keese, 1991). In the case of the elongated shape of the SK-Mel-28 and U373 cells this model comes to its limit and the fit data (especially α) can be incorrect due to an overestimation of the path length of the current flow underneath the cells (Lo and Ferrier, 1998). If the cells were assumed to have a rectangular shape with two half semicircles at each end, α would be smaller than for the circular shape (Lo and Ferrier, 1998). As a combination of these assumptions the fit parameter of the 8W10E electrodes can be overrated

and the data for these cell lines can be much lower which can be observed with the impedance data of the 8W10E electrodes and the IDE 300.

The different resistance and capacitance magnitudes of the various cell lines on the 8W10E electrodes can be related to the explanation of the impedance spectra. In every case the whole network of the individual parts of the equivalent circuit is analyzed. For instance, high R_b values influence also the resistance and the capacitance measurement. This is proven with the fact that the order of the signal change of the individual cell lines measured with the 8W10E electrodes is the same for the impedance, resistance and capacitance.

Explanation of the order of signal magnitudes of the different cell lines measured with the IDEs

For the IDEs with smaller pitches (IDE 7, IDE 10, IDE 12 and IDE 20) the order of the magnitude of the various cell lines is different than for the IDE 300 and the 8W10E electrodes. The greatest distinction is that the BAEC spectrum is not distinguishable from the cell-free electrode and that the MDCK II cells have a proportionately small signal compared to the other cells except the U373 cells.

Basically, the simulation of the adherent cells on IDE 10 (see chapter 6.1) showed that the cell height has a huge influence on the distribution of the electric field when electrodes with a small electrode gap were used. The flatter the cells are, the more prominent is the fraction of the electric field in the intercellular cleft. A result of this is that the measured impedance of flatter cells can be dominated more from the intercellular cleft than from the space underneath the cells. Furthermore, it was proven that the distance of the cells to the electrodes has also a huge influence on the electric field.

The most promising results for an explanation of the differences are the spectra of the BAEC cells measured with the IDE 12 and IDE 7 which were not distinguishable from the cell-free electrode. Due to microscopic control (not shown here) it was proven that the cells were grown to a confluent monolayer on the electrodes. The cell-cell interactions of these cell lines are well developed but attach rather weakly on the growth substrate (Wegener et al., 1999). This could also be seen in the practical part of this work in which it was necessary to coat the electrodes with 0.5 % gelatin to ensure an attachment of the cells on the electrodes. Due to this weak cell-substrate interactions it can be concluded that the distance between the cells and the substrate is very high. An average distance of the cells and the substrate was measured to be larger than 500 nm (Wegener et al., 1999). Furthermore, the measurement with the SPR could not obtain any change in reflectivity or resonance wavelength during the monitoring of the BAEC cells. The penetration depth of the evanescent electric field of the SPR is in a range of 100-200 nm and the authors draw the conclusion from

this that the BAEC cells cannot be measured due to the high distance of the cells to the surface (Lieb et al., 2016b). This assumption could also be validated with the measurement of a confluent BAEC monolayer on a QCM quartz which is hard to detect due to the high cell-substrate distance (Wegener et al., 1999). On the basis of these observations and the undetectable impedance signal of the BAEC cells in the measurement with IDEs it can be concluded that the BAEC cells are growing too far away from the interdigitated electrode to be detected. This explanation is also proven with the COMSOL simulations (see fig. 6.4). The simulation shows that the electric field is not strongly restricted when the cells grow in such a distance like the BAEC cells. Consequently, the measured impedance does not change significantly in comparison to a cell-free electrode. On the contrary, with bigger electrodes like the 8W10E or 8W1E electrodes a clear impedance signal of the measured BAEC cells can be observed (see fig. 6.7 and fig. 6.9). This leads to the conclusion that the main amount of the measured impedance is originated in the area around some hundred nanometer above the subcellular interdigitated electrodes underneath the cells.

In general, it is difficult to make clear statements about the resistance in the cleft between the cells and the substrate because the different cell lines have individual ways to attach to the surface of the substrate resulting in individual specific resistivities of the cleft between the cells and the substrate (Reiss and Wegener, 2015). Consequently, each attachment can generate unique impedance data (Mamouni and Yang, 2011).

The fit of the ECIS parameters showed that the resistance of the cell-cell contacts (R_b) is connected with the impedance in the cleft between the basal membrane and the electrode surface (α). High R_b values also lead to high values for α . Strong tight junctions affect the diffusion of ions through these cell-cell contacts and influence the concentration in the cleft because the intercellular space and the cleft are spatially connected. Consequently, tight paracellular barriers result in a reduced conductivity in the cleft (Reiss and Wegener, 2015). This can be seen as one explanation of the high impedance signal of the MDCK I cells on every interdigitated structure. They have by far the strongest tight junctions of the cell lines used in this work and influence the resistance of the cleft underneath the cells the most. Nevertheless, this assumption cannot be the only explanation of the different impedance signals because the MDCK II cells which have strong tight junctions show lower impedance signals than the NRK cells and most of the other cell lines used in this work.

In general, the plasma membrane of adherent mammalian cells is in a range of $d = 25 \text{ nm}$ to 200 nm above the electrode surface (Reiss and Wegener, 2015; Wegener, 2010). For the MDCK cells an average distance of $d = 25 \text{ nm}$ between the basal membrane and the substrate was found under control conditions (Wegener,

2010). A difference of the two strains of the MDCK cells is that the MDCK II cells have more densely packed microvilli on the apical side in comparison to the MDCK I cells and that the MDCK II cells are larger and taller than the smaller MDCK I cells (Richardson et al., 1981). It was also monitored that the MDCK cells have a cell height of $h = 5 \mu\text{m}$ (Lo et al., 1995). Due to the fact that the tight junctions are located at the apical side of the cell (Stevenson et al., 1988; Wegener, 2010), it is decisive for the distribution of the electric field of the IDEs how thick a cell is which was proven with the simulation in chapter 6.1. With the greater cell height ($h = 5 \mu\text{m}$) the main part of the electric field is distributed underneath the cells and only a very small fraction could be seen in the intercellular cleft. The flatter the cells are, the higher is the influence of the intercellular cleft. The MDCK I are smaller than the MDCK II cells resulting in a smaller distance of the tight junctions to the IDEs which can enable a greater influence of the tight junctions of the MDCK I cells with those electrodes. A further explanation for the low impedance signal of the MDCK II cells measured with the IDEs is that the cell height of the MDCK II cells is too high so that the electric field in this cleft is comparably small. Consequently, the tight junctions do not affect the measured impedance so much. Furthermore, the plasma membrane invaginations of the basal membrane of the MDCK II can significantly influence the signal of the IDEs. The NRK cells which show a higher impedance signal are flat cells (de Larco and Todaro, 1978) with a cell height on average of $(3.6 \pm 0.6) \mu\text{m}$ (Parak et al., 1999). These lower cell heights lead to a more pronounced influence of the cell-cell contacts because of the higher fraction of the electric field in the intercellular cleft (see simulation in fig. 6.3). As a result the impedance signal of the NRK cells shows higher values in comparison to the MDCK II cells measured with the IDEs with a smaller pitch. This explanation can be underlined due to the fact that the signal of the MDCK I and the difference between the MDCK II and NRK cells are decreasing with decreasing pitch of the IDEs until nearly no difference can be seen anymore in the case of the IDE 7. Consequently, with a smaller electrode gap the part of the electric field underneath the cells is more dominating the total values.

The signals of the other cell lines are in the same range as the NRK cells (IDE 12 and IDE 7) which can be explained with a combination of the cell-cell contacts and the associated ion exchange of the electrolyte in the intercellular space and the cleft underneath the cells. Furthermore, the distance of the cells from the electrode surface has a strong influence on the impedance of the cell-substrate cleft, as α is inversely proportional to the square root of the cell-electrode distance (see eq. 3.18 in chapter 3.1.1). In this equation it can also be seen that the radius of the cells have an influence on α . The bigger the cell radius is, the higher is α . Consequently, for bigger cells the impedance of the cell-substrate cleft is more dominant as for smaller

cells. The U373 cells are larger than the MDCK I, MDCK II and NRK cells (see tab. 6.1) which results in a higher influence of α to the measured impedance. For the IDEs with a small pitch this influence of α is anyway higher than for the 8W10E electrodes because of the small electrode gap. With bigger cells this influence is even strengthened which can be seen in the comparatively high impedance of these cells measured with the IDEs (with the exception of the IDE 300). The same trend occurs for the SK-Mel-28 cells which are also very big cells (seen in the seeding density in tab. 4.4). This cell line shows a comparatively high impedance magnitude measured with the IDE 12 and IDE 7 compared to the 8W10E electrodes, for the same reasons as mentioned before. On the other side, these two cell lines are elongated. The ECIS model assumes cells with a circular shape (see chapter 3.1.1) and is therefore not suitable for elongated cells which have more a rectangular shape. With those cells an overestimation of the path length of the current flow underneath the cells occurs by using the ECIS model (Lo and Ferrier, 1998). Lo et al. were able to calculate α by the assumption of the cell shape as rectangle with two semicircles on each end of the cells and could show that α is smaller for the rectangular shape than for the circular one (Lo and Ferrier, 1998). For the IDEs with smaller pitch (IDE 7, IDE 10, IDE 12, IDE 20) the focus of the electric field is mainly underneath the cells and the part of α is dominating the measured impedance. The aspect of the elongated cells is not so prominent for these electrodes due to the fact that the size of the cells heightens the impedance underneath the cells significantly. The IDE 300 shows the same distribution of the electric field as the 8W10E electrodes. Consequently, the elongated shape resulting in the lower part of α has a strong influence on the impedance, which can be seen in the small impedance magnitude of the U373 cells measured with IDE 300.

To sum up this subchapter it has to be emphasized that the different intensities of the impedance magnitude of the individual cell lines measured with the IDEs and the 8W10E electrodes can be explained by the fact that the IDEs with a small gap have a smaller fraction of the electric field in the intercellular cleft than underneath the cells. Consequently, the prominent part of the impedance arises in a range of some hundred nanometer above the electrode surface underneath the cells. The individual distance of the cells to the electrode surface influence strongly the signal, as it is seen with the missing impedance signal of the BAEC cells. Furthermore, the height of the cells plays a role because the flatter a cell is, the higher is the ratio of the electric field in the intercellular cleft. As a result, the cell-cell contacts have a higher influence on the measured impedance with flatter cells than with larger ones. These two explanation were proven with the simulations. A further aspect is the influence of the cell-cell contacts on the resistivity of the cleft between the basal membrane and the electrode, seen in the high signal of the MDCK I cells. With stronger cell-cell

contacts the ion concentration in the cleft is more influenced which has a greater impact on the impedance of the IDEs than on the ECIS electrodes. This claim is supported by the result that the different signals of the measured cells become more and more similar, the smaller the pitches of the IDEs are. Furthermore, it was proven that the IDE 300 has the same order of impedance magnitudes than the 8W10E electrodes. The simulations confirm that the distance between the electrode fingers and the associated distribution of the electric field is decisive for the individual cell signals and not the interdigitated structure alone.

In summary, the difference in the impedance signal is a combination of various aspects. An interesting question now is to what extent this conclusion can be used and what advantages or disadvantages can be observed when using the IDEs. In the following work different assays were carried out with the individual IDEs to underline the aforementioned assumptions and to evaluate the benefits of the IDEs in these assays.

Analysis of the spectra of different adherent cells grown on IDEs with various window sizes

For the impedance, resistance and capacitance spectra of the MDCK I, MDCK II, NRK and U373 cells grown on different IDEs with various sizes of the non-insulated electrode area (window) less distinctions between the individual cell lines can be seen. The curves of the cell-free electrodes were already explained in chapter 5.

For the electrodes with the small window of $(0.5 \times 0.5) \text{ mm}^2$ no difference is monitored for cell lines measured with the IDE 10 and only a small distinction for the IDE 12 and IDE 20. The slope of the impedance spectra in a frequency range $< 10^4 \text{ Hz}$ is dependent on the impedance of the CPE which in turn is influenced by the electrode size (see chapter 5). With the smaller electrode area the impedance is shifted to higher impedance values. In general, a small electrode has higher impedance values and greater fluctuations (Lo et al., 1993). These fluctuations result from parasitic influences and lead to a high noise of the measurement which is revealed in the error bars in the calculated norm. $|Z|$. Another explanation for the high error bars is that during the photolithographical process huge differences of the side length of the small window can occur. The measured length of the small window of $(460 \pm 60) \mu\text{m}$ has a relative error of 13.8%. Due to this high variation of the side length of the window the non-insulated electrode area has different sizes for each individual electrode which can lead to great deviations of the impedance of the CPE. Deviations in the side length have greater effects with a smaller area than with a larger area. This is the explanation for the high error bars of the normalized data and the capacitance spectra. In spite of this, it is not possible at the present state to explain the low signal of the MDCK I measured with the IDE 10. Also for the IDE 20 the difference of MDCK I and NRK cells is becoming smaller.

With the higher electrode area of the electrodes with the big window of $(2.0 \times 2.0) \text{ mm}^2$, the resistance of the solution is increasing and can dominate the measured signal (Giaever and Keese, 1991). Furthermore, more resistances of the cell-cell contacts affect the total impedance. As the total resistance declines with more parallel connected resistors, the total impedance decreases. Consequently, the strong tight junctions of the MDCK I cells have less impact on the measured impedance and the signal for them is declining. In combination with the low penetration depth of the electric field no difference of the MDCK II, NRK and U373 cells can be obtained for the IDE 10 with the big window. However, the IDE 20 with the big window cannot differentiate between the MDCK I and NRK cells. The side length of the big window of $(1790 \pm 20) \mu\text{m}$ has only a relative error of 1.3 % which is by a factor of 10 less than for the small window. This results in the smaller error tolerance of the normalized data.

Comparing the data of the individual window sizes, it can be seen that no information gain can be achieved with either the smaller or the bigger window. In the ECIS theory it is essential that the electrode area is small so that the measured impedance results from this electrode (Lo et al., 1993). With small electrodes the influence of various resistance, like the one of solution resistance or the wires, can be minimized and the measured impedance is dominated by the electrode-electrolyte interface (Giaever and Keese, 1991). This impedance is inversely proportional to the area of the electrode (Xiao and Luong, 2010). With this connection it is possible to ensure the domination of the impedance of the electrode-electrolyte interface by reducing the electrode diameter (Giaever and Keese, 1991). It follows that the smaller the electrode, the more sensitive it is. Based on this, the window of $(0.5 \times 0.5) \text{ mm}^2$ should have the highest sensitivity of the measured impedance. As already mentioned, the influences of the parasitic elements increase with smaller electrodes and provide the larger scattering of the measured impedance. Furthermore, the high variance of the exact size of the small window also leads to a high noise of the measured data. These two reasons distort the measured data and prevent a clear impedance signal of the cells grown on the electrodes. Consequently, the highest sensitivity of the three chosen window sizes can be gained for the window of $(1.1 \times 1.1) \text{ mm}^2$. This assumption is further analyzed with an adhesion assay (chapter 7.1) and the detection of the stimulation with histamine (chapter 7.4.1) measured with the different window sizes.

Evaluation of the micromotion of the various cell lines

Cells in a confluent monolayer are moving in a horizontal and vertical direction which can be measured with the impedance. It is possible to monitor fluctuations in the range of 1 nm which are not recognizable with an optical microscope (Giaever and Keese, 1991; Lo et al., 1993). In general it can be said that the higher the micromotion of one cell type, the greater is the number of living cells (Das et al.,

2015). These micromotions arise from a chain of complex cellular reactions associated with dynamic structural changes in an ongoing rearrangement of actin filaments (Das et al., 2015; Parekh et al., 2018) and are dependent on the functionality of the cell type. The impedance fluctuations can be traced back to variations of only two parameter: i) α and ii) R_b (Giaever and Keese, 1991; Lo et al., 1993). Subnanometer changes of the cell-substrate cleft can have effects on the measured impedance (Lo et al., 1993) and even variations of the cell radius in a nanometer size can significantly influence the impedance change (Giaever and Keese, 1991). Important for the analysis of the micromotion is a control with a cell-free electrode to ensure that the measured signals arise from the cell motility and not from electric noise of the electrode. This is made sure in this thesis due to the low values of the variance of the cell-free electrodes.

The explanation of the values of the individual cell motility is the influence of the tightness of the cell-cell contacts and the associated influence of α on the measured micromotion. If the cell-cell contacts are very strong, even small changes have significantly high consequences on the micromotion. The general rule is that the higher the variance, the stronger is the micromotion.

A proof of this explanation is the order of intensities of the micromotion of the 8W1E electrodes which is in agreement with the order of the intensities of the impedance spectra with some exceptions. The order of the micromotions can consequently be explained with a combination of the strength of the cell-cell contacts and the cell-substrate interactions (seen in tab. 6.2). The exception in the order can be traced back to the higher micromotion of cancerous cells. Cancerous cell lines with their individual inter- and intracellular interactions on the basis of their unregulated and uncontrolled division and metabolism can show a higher micromotion than comparable noncancerous cell lines (Das et al., 2015). It is even possible to obtain notable differences between cancerous and noncancerous cells and to differentiated the cells from each other (Lovelady et al., 2007). With this explanation, the highest value of the micromotion of the A549 cells grown on the 8W1E electrodes can be understood. These cells are adenocarcinomic human alveolar basal epithelial cells and were isolated from cancerous tissues. For the reasons mentioned above, these cells show the highest value of the variance. The MDCK I cells have the next highest variance which agrees with the order of the intensities of the impedance spectra. The MDCK I cell grown on the 8W1E electrodes show the strongest cell-cell contacts and cell-substrate interactions (seen in tab. 6.2). The next highest variance signal after the MDCK I cells is the micromotion of the MCF-7 cells, a human breast cancer cell line. MCF-7 cells show a higher distribution of the impedance than normal epithelial cells which can be traced back to higher cellular movement (Das et al., 2015). This higher cellular movement can be revealed with the higher variance of the MCF-7

than with the MDCK II cells which have stronger tight junctions. The next signals of the BAEC, NRK and SK-Mel-28 cannot clearly be distinguished. These three cell lines have different functionalities because they are aortic, kidney or melanoma cells. The NRK cells have the highest TEER values of these three cell lines but are known to have a relative low motility in comparison to the MDCK cells. This can also be seen for the aortic endothelial cells (BAEC). Surprisingly the cancerous SK-Mel-28 cells have a comparable low micromotion. The reason for this is that the membranes are overlapping (see the value of C_m) and consequently, not the whole motility of the cells can be monitored with the 8W1E electrodes. Furthermore, due to the big size of the SK-Mel-28 cells less cell-cell contacts are monitored over the whole electrode which also can lead to an underestimated variance value. The same side-effect can also influence the micromotion of the big U373 cells which is not distinguishable from the cell-free electrode. A different explanation is that the glioblastoma cells do not move much in general.

The analysis of the micromotion measured with the IDEs shows much smaller values of the variances of the IDEs compared to the 8W1E electrodes (see fig. 6.15). Due to the non-insulated electrode area of $(1.1 \times 1.1) \text{ mm}^2$, IDEs measure with a higher electrode area than the 8W1E electrodes with an electrode diameter of $250 \text{ }\mu\text{m}$. Experience has shown that the micromotion increases with a smaller electrode area, as the fluctuations even out over time for large electrodes. This is also the reason why 8W1E electrodes with a smaller electrode area were used to measure cell motility rather than the 8W10E electrodes with the tenfold electrode area. Consequently, smaller electrodes are more sensitive to micromotion measurement than the larger electrodes. A further influence is the electrode layout. Looking at various IDE layouts it can be seen that the variance is getting higher, the greater the pitch is. The lowest variance is revealed for the IDE 7, increasing with the pitches until the highest value for the IDE 300 is reached. It was shown in the simulation in chapter 5.3 that with this small electrode gap of the IDE 7 the main part of the electric field is focused in a volume of several hundred nanometer above the electrodes. Consequently, it is not possible to analyze the complete cell movement with such a small electrode gap. With bigger distances of the electrode fingers, the fraction of the electric field in the intercellular cleft is raising and more aspects of the cells can be monitored which was proven with the simulations in chapter 6.1. As a result it can be said that with a gap of $10 \text{ }\mu\text{m}$ of the IDE 20 more movement of the cells is monitored than with a gap of $3 \text{ }\mu\text{m}$ of the IDE 7. Due to this explanation it is obvious that the micromotion measured with the IDEs has much lower values because: i) the IDEs are measuring with a bigger electrode area, and ii) the penetration depth of the IDEs with a smaller pitch is too small to detect all movement of the cells because the electric field is focused in the space underneath the cell.

Nevertheless, differences in the order of the magnitudes of the micromotion of the cells measured with the IDEs in comparison to the 8W1E electrodes can be seen. This is easily understandable looking at the explanation of the spectra. The signal of the IDEs is dominated by the various distributions of the electric field and cell parts or reactions cannot be monitored completely. If a cell is moving more in the vertical direction, it results in a higher variance value than if it is moving in the horizontal way. Furthermore, the distance of the cells and the electrode is decisive for the part of the monitored cell part. A proof for this explanation is repeatedly the small value of the BAEC cells which are growing too far away from the IDEs to be monitored. The further big difference of the IDEs and the 8W1E electrodes is the much smaller variance of the A549 cells. This is one of the lowest values for the IDEs, in contrast to the highest signal in the case of the 8W1E electrodes. The reason is that these cancerous cells are moving rather in a horizontal way which is not so strongly influencing the resistance measured with the IDEs. In contrast, the variance of the cancerous cell lines MCF-7 and SK-Mel-28 is much higher with the IDEs. They are part of the highest measured variances leading to the assumption that they are growing more closely to the electrode surface and are moving strongly in vertical direction.

Consequently, many different aspects play a role in the measurement of the micromotion. Among others, the tightness of the cell-cell contacts and the impedance of the cleft underneath the cells can influence the results. Furthermore, with the choice of the electrode layout various aspects of the cells can be monitored.

To sum up this chapter many different aspects and conclusions have to be emphasized for further experiments and explanations.

- The simulations by finite element techniques using COMSOL Multiphysics prove that the distribution of the electric field is strongly influenced by various aspects: i) the cell height, ii) the cell-electrode distance, and iii) the size of the electrode gap. Consequently, the measured impedance of the various electrode layouts is a mixture of numerous influences.
- Due to the analysis of the frequency spectra it is obvious that the time-dependent changes of the impedance cannot be monitored at the same frequency for all electrode types. Every layout and every cell line has a distinct frequency at which the maximum of the impedance magnitude can be revealed (f_{max}). In the following thesis f_{max} individually for each electrode type is chosen to enable a comparison of the time-dependent changes of the measured signals.

- The measurement of the impedance, resistance and capacitance in dependence of the frequency revealed a different order of the magnitudes of the individual cell lines for the electrode types. It is obvious that the IDEs are monitoring distinct aspects of the cell lines and the cell-cell or cell-substrate interactions than the commercially available ECIS electrodes. This can be attributed to the subcellular dimensions of the IDEs with smaller pitches and the associated difference in the distribution of the electric field. The ECIS model is not appropriate for the IDEs with a small pitch.
- With the variation of the non-insulated electrode area of the IDEs a higher sensitivity was planned to obtain. This could not be achieved due to the low signals and the high deviations of the normalized data for the individual electrodes. The most meaningful information was obtained for the window with the size of $(1.1 \times 1.1) \text{ mm}^2$. Nevertheless, in the following work the adhesion of different cell lines and the histamine stimulation of U373 cells will be analyzed with the various window sizes to further substantiate the correct choice of the window size in terms of highest sensitivity.
- The measurement of the micromotion enabled the analysis of the motility of cell lines and in the broadest sense the characteristics of the cell-cell and cell-substrate interactions. Again the IDEs monitored different signals due to their different distribution of the electric field.

This chapter shows that due to the different distribution of the electric field various aspects of the cells can be analyzed using different dimensions of the layout of the interdigitated electrodes. It is now important to find out in which cell reactions these different focuses of the electric field have advantages or in which assays the decisive cell reaction cannot be monitored with IDEs with subcellular dimension.

7 Phenotypic assays

To further determine the benefits of the interdigitated electrodes in comparison to the commercially available ECIS electrodes it is necessary to perform several phenotypic assays and to measure the associated impedance change. A phenotypic assay is for instance the analysis of the impact of various substances, like small molecules or peptides, to the phenotype of a cell or an organisms.

This chapter describes assays monitoring the formation of cell monolayers, their analysis and their manipulation by the addition of various substances. For each assay, the advantages and disadvantages of the different electrode layouts are elaborated and evaluated.

First, the time-dependent establishment of a monolayer from initially suspended cells is monitored in two different ways: i) a confluent seeding (adhesion) and ii) a subconfluent seeding (proliferation). In the first option the cell density is chosen to be so high, that the cells are covering the entire surface without further division. The attachment and the spreading of these cells are analyzed and compared for the different electrode layouts. For the second opportunity a much lower cell density is chosen and the focus of the measurement is on cell proliferation.

The different monolayers are then manipulated with various substances. As a first assay the osmotic pressure is varied with the addition of sucrose to the electrolyte. This hyperosmotic pressure changes the cell shape in dependence of the sucrose concentration and can be measured with the impedance. Furthermore, the signal transduction pathways are influenced. With the stimulation of the histamine-1 receptor (H_1R) with histamine an electrode specific impedance signal was observed and analyzed. Additionally, the calcium concentration inside the cells is influenced by calcimycin.

Another assay is the measurement of a monolayer of cardiomyocytes. The beating of these cells can be analyzed based on their shape and their quantity. The frequency of the beating is further manipulated with isoprenaline. As a last part of this chapter the cytotoxicity of bisphenol A and ethanol is investigated. This is performed with a wide range of impedance-based measurements, like migration, micromotion or acute toxicity analyses.

7.1 Monitoring the time course of cell adhesion

As a first assay the adhesion of different cell lines on various electrode layouts was analyzed to give a first impression of the distinct benefits of the electrode types. In general, mammalian cells are anchorage-dependent, which means that if the cells are not anchored to a surface, they will not reproduce. Cells remaining in suspension may even undergo programmed cell death (Hong et al., 2011; Ostuni et al., 2001). Consequently, cells in suspension are settling down and adhering on the electrodes, when they are added to the measurement chamber. The continuous measurement of the impedance monitors the spreading of the cells and the morphology changes in a time range up to ≈ 60 h. The electrodes were often coated with different proteins to facilitate the adhesion and to stabilize the adhered cells. It is possible to use proteins like polylysine providing a polycationic surface which can interact with the anionic site on the cell surfaces (Mazia et al., 1975) and to use fibronectin (Wegener et al., 2000a), which can bind to extracellular matrix proteins such as fibrin or collagen for instance. The adhesion on electrodes can also be stabilized with cross-linked gelatin (Arndt et al., 2004). Furthermore, self-assembled monolayer (SAM) were often utilized in research (Asphahani et al., 2008; Ostuni et al., 2001). These SAMs can be formed spontaneously on the substrate and consist of a head group, a tail and a functional end group. The most common used molecules are alkanethiols with a thiol head group which can adhere on the gold substrate. Due to the interactions of the alkyl chains the molecules are organized with a high internal order. By varying the functional end group, the interaction of SAM with the extracellular proteins can be enhanced or inhibited which influences the adhesion.

In this work no direct coating was used. Before addition of the cell suspension, the electrodes were treated with argon plasma and were incubated with 10 mM cysteine solution. The baseline was recorded before the cell suspension - also in serum-containing medium - was introduced into the wells. The adhesion of MDCK I, MDCK II and NRK cells was monitored with different electrode layouts. The concentration of the cell suspension was chosen to ensure a coverage of the complete surface by the settled cells, without the need of further cell division (450,000 cells/cm²).

7.1.1 Three-dimensional representation of time- and frequency-dependent impedance analysis of cell adhesion

For a demonstration of the whole information which can be gained during the establishment of a cell monolayer the impedance measurement is represented in a three-dimensional manner. The impedance change is monitored in a time- and frequency-dependent manner. It is necessary to note that the frequency and the

impedance are plotted on a logarithmic scale, respectively. For all three cell types, the initially suspended cells were added to the measurement chamber at $t=0$ h in serum-containing medium, leading to an initial value of a cell-free electrode. The thicker black lines in fig. 7.1 - fig. 7.3 highlight the impedance for a cell-free and cell-covered electrode before addition of the cells and at the end of the measurement when a confluent cell layer is established. These spectra were further explained in chapter 6. For every cell type and electrode layout it is obvious that the impedance change is strongly dependent on the monitoring frequency.

In fig. 7.1 the three-dimensional representation of the adhesion of NRK cells on 8W10E electrodes (fig. 7.1 A) and on an IDE 12 (fig. 7.1 B) can be seen.

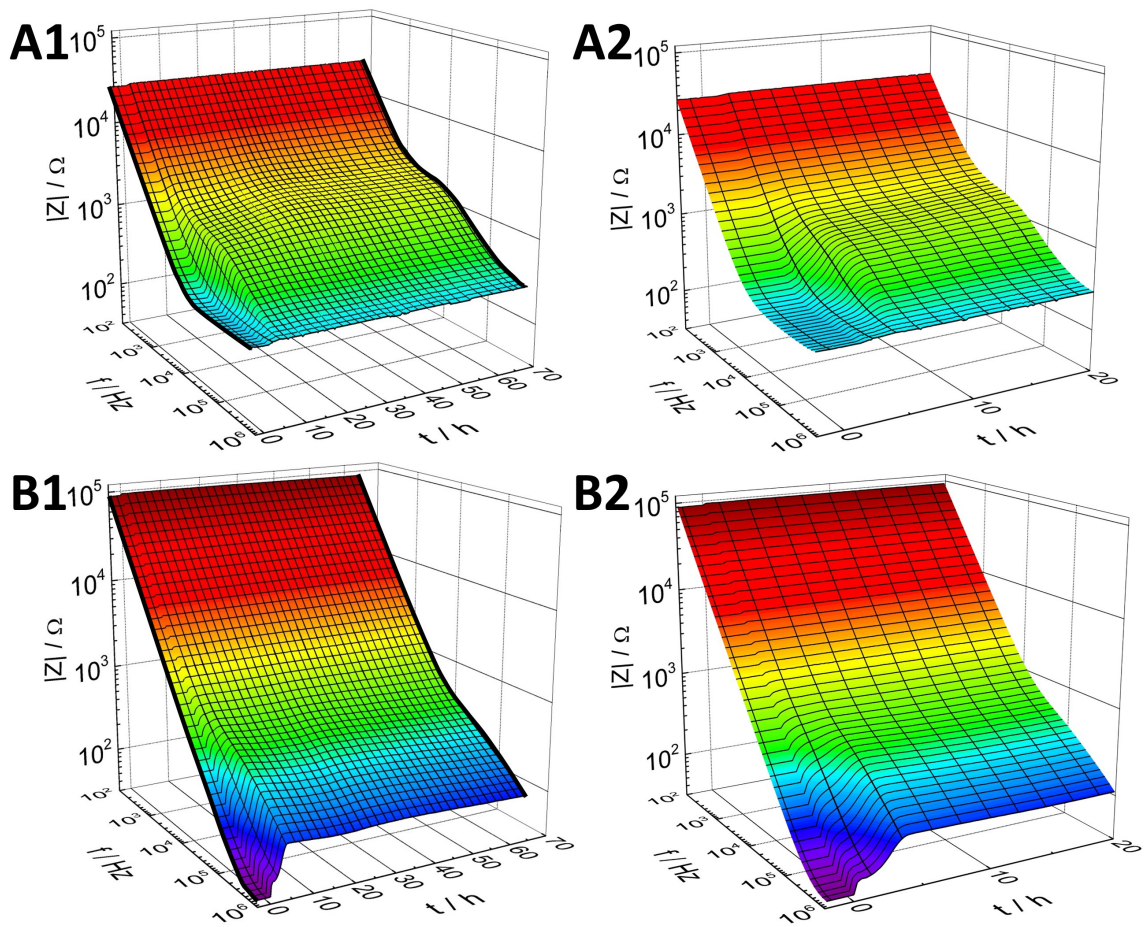


Figure 7.1: Three-dimensional representation of the frequency- and time-dependent impedance change during adhesion of NRK cells on two different electrode types. The cells were added in a serum-containing medium at $t=0$ h with a seeding density of 450,000 cells/cm². The impedance change occurs as a function of the frequency and the time during the establishment of a confluent layer. Two different electrodes were used: **A**: 8W10E with the whole measurement seen in **A1** and with a zoom to the first 20 h in **A2**, and **B**: IDE 12 with **B2** as a zoom of **B1**. The thicker black lines highlight the spectra of the cell-free and the cell-covered electrodes.

In the lower frequency range ($<10^3$ Hz) hardly no change of the impedance is revealed independently of the measurement duration in the case of both electrodes.

In the middle frequency range (from 10^3 Hz to 10^5 Hz) the impedance change varies between the two electrode layouts. For the 8W10E electrodes (fig. 7.1 **A1** and **A2**) the main increase of the impedance is seen within this range. The impedance is rising to half of the maximum impedance value immediately after the cells were added and continues to increase slowly until a constant value is reached after ≈ 25 h. The biggest impedance change occurs at ≈ 16 kHz, which can be seen more precisely in fig. 7.4. The impedance change of the IDE 12 (fig. 7.1 **B1** and **B2**) is not highly pronounced in this range. The bigger the frequency, the higher is the impedance change. Consequently, in the higher frequency range ($> 10^5$ Hz) the IDE 12 shows the highest increase of the time-dependent impedance course which is different to the 8W10E electrodes. The impedance is increasing immediately after the addition and remains nearly unchanged until the end of the measurement (see fig. 7.5). For the 8W10E electrodes the impedance magnitude in this frequency range ($> 10^5$ Hz) is decreasing strongly and nearly no change can be observed at the highest frequencies. The maximum value for the magnitude of the impedance can therefore be recorded much faster with the IDE 12 than with the 8W10E electrodes.

Similarly, the adhesion of MDCK I cells is analyzed in a three-dimensional manner. The impedance change in dependence of the time and the frequency during the attachment and spreading of these cells is shown in fig. 7.2.

The impedance changes of the two electrodes vary widely. The 8W10E electrodes (fig. 7.2 **A1** and **A2**) reveal an increase in impedance over the whole frequency range even at smaller frequencies $< 10^2$ Hz (not shown here), while with higher frequencies ($> 10^5$ Hz) the impedance magnitude is slowly reduced. The main impedance change occurs in a wide frequency range of ≈ 600 Hz - 13,000 Hz. Here, the impedance is increasing in different phases. Directly after the addition of the cells a short maximum is reached, followed by a period of slow increase before a stronger rise occurs at $t \approx 50$ h. The exact curve at the highest impedance change is shown in fig. 7.4. The impedance course of IDE 12 contrasts strongly with this (see fig. 7.2 **B1** and **B2**). Below a frequency of 10^4 Hz the measured impedance was insensitive for cell adhesion, whereas at higher frequencies the impedance is rising and a change over time can be monitored. In the first 15 h a strong increase immediately after addition of the cell suspension with a subsequent decrease of half of the impedance magnitude occurs. This plateau of the value extends to the time at $t \approx 40$ h after addition of the cells, when the impedance increases abruptly and remains at a constant impedance value until the end of the measurement (see fig. 7.5 for the precise course). These frequency- and time-dependent impedance courses illustrate that with the 8W10E electrodes as well as with the IDE 12 a fast detection of the settled cells on the electrodes can be achieved. A big difference of these two electrode types is the measurement of the rise of the impedance at $t \approx 40$ h which is detected as a fast

increase in the case of the IDE12 and a slow increase in the case of the 8W10E electrodes. This indicates that with IDE12 a different part of the cell reaction is monitored as with the 8W10E electrodes.

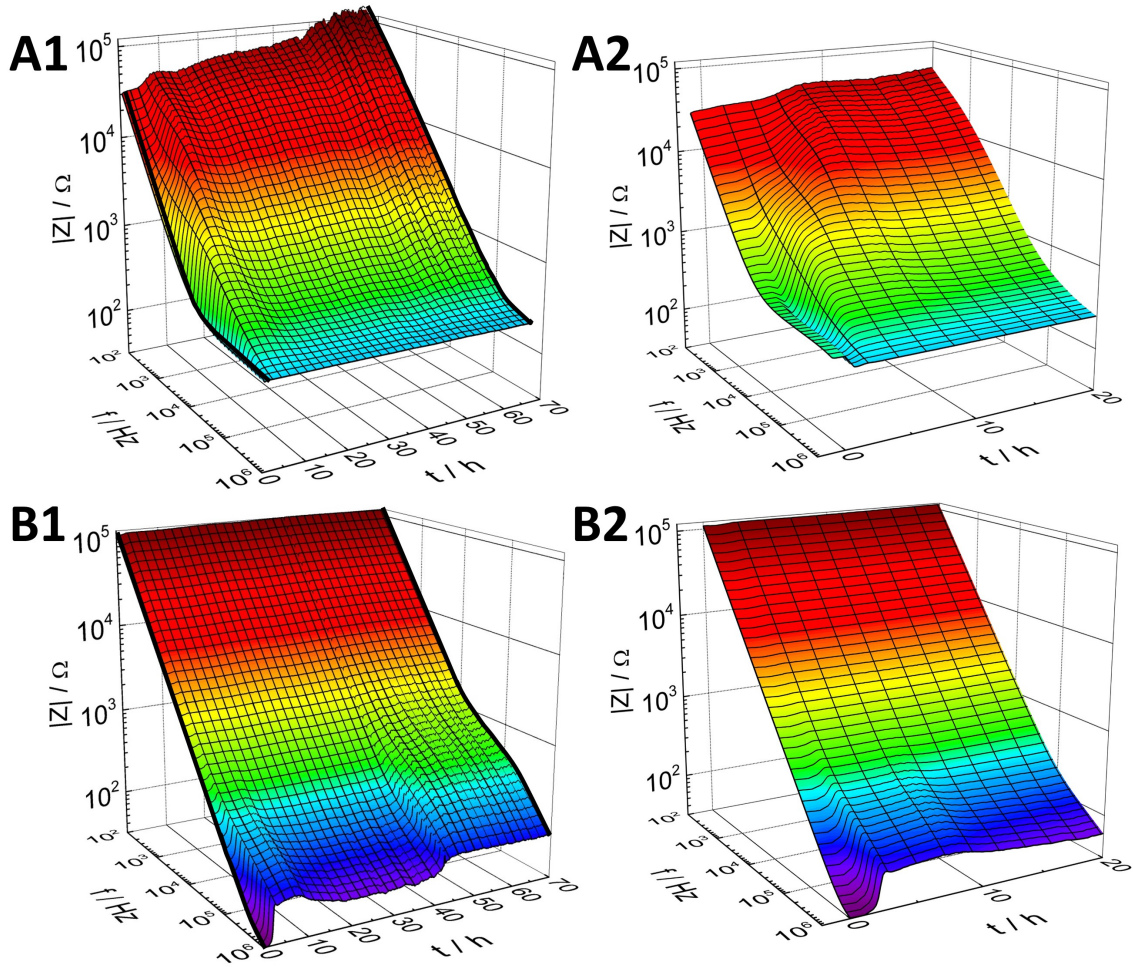


Figure 7.2: Three-dimensional representation of the impedance change in dependence of the frequency and the time during the adhesion of initially suspended MDCK I cells. The cells were added in serum-containing culture medium at $t = 0$ h with a seeding density of 450,000 cells/cm². Two different electrode layouts were used: **A**: 8W10E electrodes with the whole measurement seen in **A1** and a zoom of the first 20 h after seeding in **A2**, and **B**: IDE12 with **B2** as a zoom of **B1**. The thicker black lines represent the spectra of the cell-free and the cell-covered electrodes.

The third three-dimensional representation reveals the adhesion of MDCK II cells cultivated on the 8W10E electrodes and IDE 12 (fig. 7.3).

Similar to the MDCK I cells, the impedance change of the MDCK II cells is seen over a wide range of frequencies for the 8W10E electrodes (fig. 7.3 **A1** and **A2**). In the very low frequency range ($< 10^3$ Hz) a strong short maximum of the impedance is detected at $t \approx 10$ h before a constant value extends to the end of the measurement. In a frequency range $> 10^5$ Hz the measured impedance magnitude is reduced and no significant change is revealed over the whole duration of the measurement. In

the wide frequency range in between (10^3 - 10^5 Hz) a time-dependent change of the measured impedance is monitored. Immediately after the addition of the suspended cells the impedance is shortly increasing before it remains constant until the end of the measurement. The accurate course is revealed in fig. 7.4.

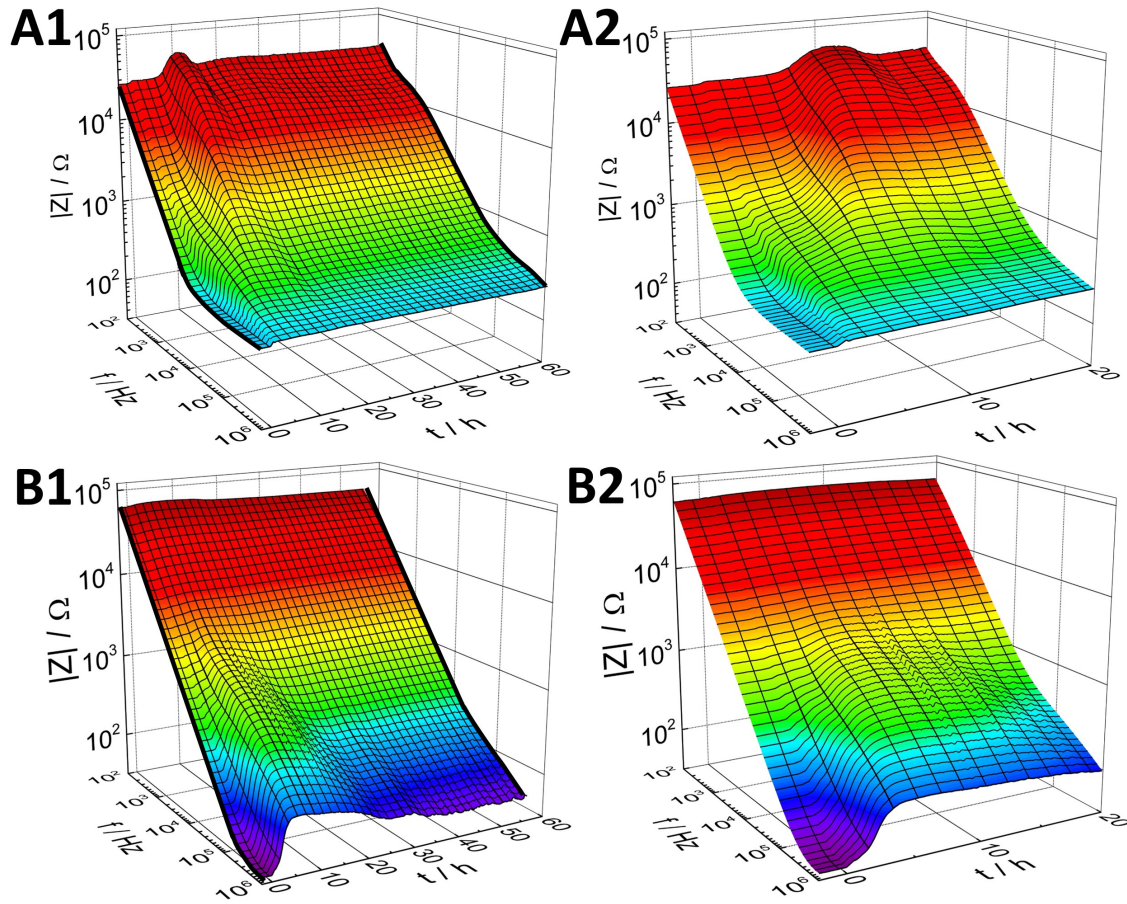


Figure 7.3: Three-dimensional representation of the frequency- and time-dependent impedance during adhesion of MDCK II cells on different electrode types. The cells were added in serum-containing medium at $t=0$ h with a seeding density of 450,000 cells/cm². The impedance is monitored as a function of the frequency and the time during the attachment and spreading of the cells. For the experiment 8W10E (A) and IDE12 (B) were used. In A1 and B1 the whole measurement can be seen, while in A2 and B2 a zoom to the first 20 h after addition of the cell suspension is shown. The thicker black lines highlight the spectra of the cell-free and the cell-covered electrodes.

One difference to the other three-dimensional representations is the possibility to detect an impedance change in the first 20 h even at very low frequencies ($< 10^3$ Hz) which is not possible in the later measurement. Consequently, the sensitivity of the measurement at these frequencies varies over time. The alteration of the sensitivity change of one frequency over time can also be revealed in the case of the IDE 12 (fig. 7.3 B1 and B2). In the range of 10^4 Hz - 10^5 Hz a short increase in impedance can be seen for the first 20 h. After 20 h the impedance decreases and is indistinguishable

from a cell-free electrode. This insensitivity is revealed in the complete frequency range $< 10^5$ Hz in a time over 30 h. In the range $> 10^5$ Hz the strongest impedance change over time is monitored with the sharp immediate increase and the decrease within the first 20 h before a small constant value is reached for the remaining measurement (the exact impedance course is shown in fig. 7.5). Repeatedly, the adhesion of MDCK II cells is monitored more sensitively with IDE12 due to the faster rise of the impedance after cell addition.

The representations of the adhesion show a faster acquisition of the impedance change measured with the IDE 12 in comparison to the 8W10E electrodes and in the case of the MDCK I cells a more clearly detection of changes of the established monolayer. This indicates an advantage of IDE 12 compared to 8W10E electrodes.

7.1.2 Time-dependent analysis of cell spreading by single frequency impedance readings

The attachment and the spreading of different cell types is further analyzed with regard to the precise time-dependent change of the impedance and the capacitance. For each parameter and electrode f_{max} is chosen, respectively. In fig. 7.4, fig. 7.5 and fig. 7.6 the adhesion of MDCK I, MDCK II and NRK cells measured with 8W10E, IDE 20, IDE 12, IDE 10 and IDE 7 is revealed.

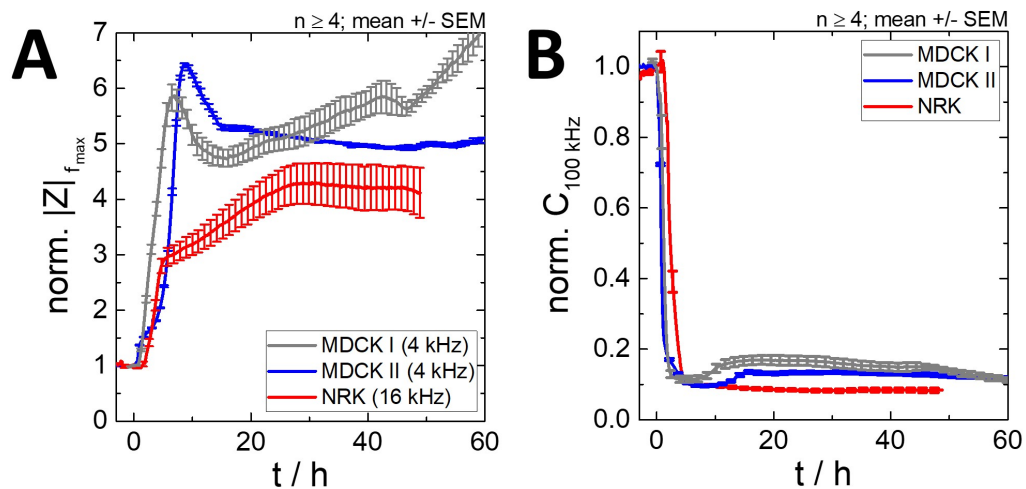


Figure 7.4: Time course of normalized impedance magnitude and normalized capacitance during the adhesion measurement of various cell types cultured on 8W10E electrodes. The cell suspension in serum-containing medium was added at $t = 0$ h with a seeding density of 450,000 cells/cm². Two time-dependent changes are monitored: **A:** impedance magnitude and **B:** capacitance at various frequencies: norm. $|Z|$ at cell-dependent frequencies, norm. C at 100 kHz. All data are normalized to the initial value of a cell-free electrode (8W10E: $|Z|_{4 kHz} = (980 \pm 175) \Omega$ (MDCK), $|Z|_{16 kHz} = (380 \pm 51) \Omega$ (NRK), $C = (37 \pm 12) \text{ nF}$).

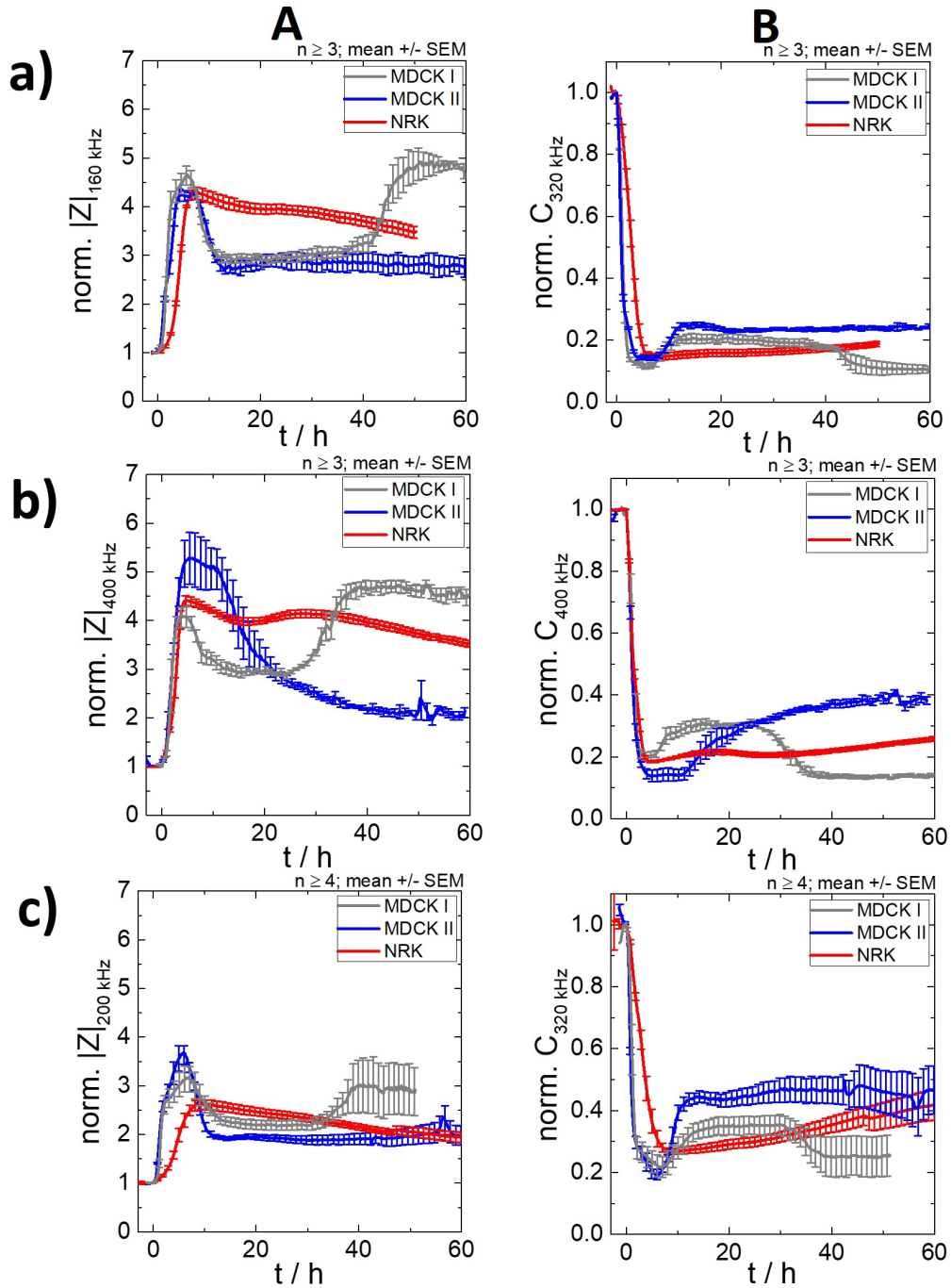


Figure 7.5: Time course of normalized impedance magnitude and normalized capacitance during the adhesion measurement of various cell types cultured on different electrode layouts. The cell suspension in serum-containing medium was added at $t = 0$ h with a seeding density of 450,000 cells/cm². Two time-dependent changes are monitored: **A**: impedance magnitude and **B**: capacitance. Different electrodes are shown at the individual frequency f_{max} : **a**): IDE 20 (norm. $|Z|$ at 160 kHz, norm. C at 320 kHz), **b**): IDE 12 (norm. $|Z|$ and norm C at 400 kHz), **c**): IDE 10 (norm. $|Z|$ at 200 kHz, norm. C at 320 kHz). All data are normalized to the initial value of a cell-free electrode (IDE 20: $|Z| = (107 \pm 6) \Omega$, $C = (57 \pm 7) \text{ nF}$), IDE 12: $|Z| = (45 \pm 2) \Omega$, $C = (16 \pm 2) \text{ nF}$), IDE 10: $|Z| = (108 \pm 11) \Omega$, $C = (13 \pm 3) \text{ nF}$).

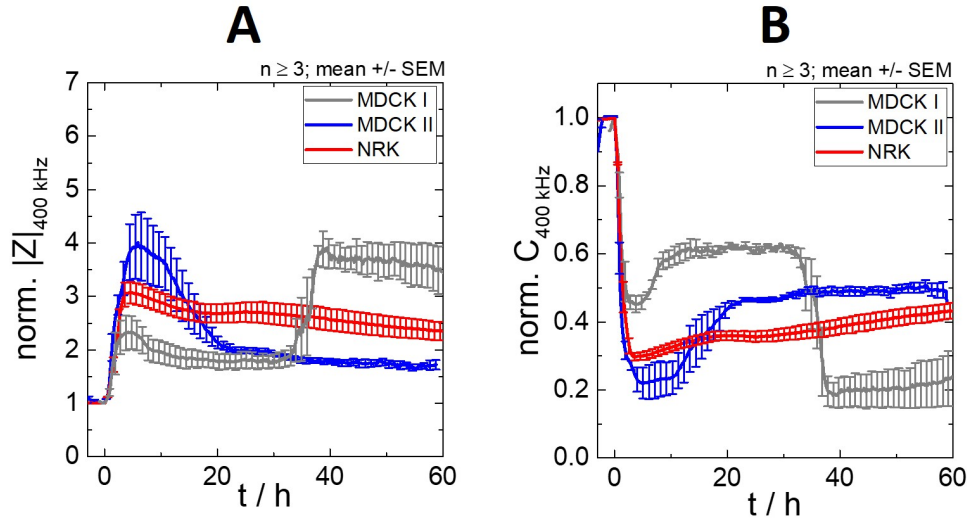


Figure 7.6: Time course of normalized impedance magnitude and normalized capacitance during the adhesion measurement of various cell types cultured on **IDE 7**. The cell suspension in serum-containing medium was added at $t = 0$ h with a seeding density of 450,000 cells/cm². Two time-dependent changes are monitored: **A**: impedance magnitude and **B**: capacitance at 400 kHz, respectively. All data are normalized to the initial value of a cell-free electrode (IDE 7: $|Z| = (35 \pm 2) \Omega$, $C = (23 \pm 4) \text{ nF}$).

Fig. 7.4, fig. 7.5 and fig. 7.6 show the time-dependent adhesion measurement of MDCK I, MDCK II and NRK cells in dependence of the normalized impedance (**A**) and the normalized capacitance (**B**) of various electrode types: 8W10E electrodes (fig. 7.4), IDE 20 (fig. 7.5 **a**)), IDE 12 (fig. 7.5 **b**)), IDE 10 (fig. 7.5 **c**)) and IDE 7 (fig. 7.6).

The time-dependent changes of the impedance and the capacitance of the individual cell lines which are shown at the individual frequency f_{max} will be explained collectively for all electrodes.

The **NRK** cells show a different time course for the impedance change of the individual electrodes. Immediately after the addition of the cells the impedance is increasing strongly in all cases. The impedance of the 8W10E electrodes rises rapidly to a value of $\text{norm. } |Z| = 2.9 \pm 0.1$ at 5.1 h before a slower increase to $\text{norm. } |Z| = 4.3 \pm 0.4$ at 27.6 h occurs which remains constant until the end of the measurement. This first sharp rise can also be seen for the various IDEs with the difference that the maximal impedance value is reached in one step without a second increase. The values for the maxima are in the same range for all IDEs and can be seen at similar time points: $\text{norm. } |Z| = 4.3 \pm 0.1$ at 7.6 h (IDE 20), $\text{norm. } |Z| = 4.41 \pm 0.10$ at 4.7 h (IDE 12), $\text{norm. } |Z| = 2.6 \pm 0.1$ at 8.9 h (IDE 10) and $\text{norm. } |Z| = 3.1 \pm 0.2$ at 4.6 h (IDE 7). During the remaining measurement time the impedance is slightly decreasing for all IDEs. The capacitance changes do not differ much for the individual

electrode layouts. Immediately after the addition the capacitance is declining rapidly to values of norm. $C = 0.101 \pm 0.003$ for 8W10E electrodes, norm. $C = 0.148 \pm 0.001$ for IDE 20, norm. $C = 0.185 \pm 0.004$ for IDE 12, norm. $C = 0.269 \pm 0.010$ for IDE 10 and norm. $C = 0.30 \pm 0.01$ for IDE 7, which were reached after an average time of $t = (5 \pm 1)$ h. It is noteworthy that with a smaller pitch, the minimal values of the capacitance are increasing. Furthermore, with smaller pitches a slight increase of the capacitance after the minimum value is revealed more clearly.

This measurement of the time-dependent adhesion of NRK cells shows that when using the IDEs, the maximum change of the impedance is reached much faster than with the 8W10E electrodes. This means that the attachment of the cells is detected more sensitive with the IDEs compared to the 8W10E electrodes.

For the adhesion of **MDCK II** cells similar time course data have been recorded with the different electrodes. After the addition of the cells the impedance is strongly increasing to a short maximum in all cases before a constant value for the remaining measurement is reached. This constant values are similar with the ones of the second phase in the MDCK I measurement. The heights of the maxima are varying for the electrode types: norm. $|Z| = 6.43 \pm 0.03$ at 8.9 h (8W10E), norm. $|Z| = 4.23 \pm 0.08$ at 6.3 h (IDE 20), norm. $|Z| = 5.3 \pm 0.5$ at 5.6 h (IDE 12), norm. $|Z| = 3.67 \pm 0.2$ at 5.8 h (IDE 10) and norm. $|Z| = 3.9 \pm 0.6$ at 5.7 h (IDE 7). The maximum of the 8W10E electrodes is higher than the ones of the IDEs and is reached ≈ 3 h later. The IDEs reveal maximum values after an average of $t = (5.9 \pm 0.3)$ h, whose intensity cannot be clearly distinguishable within the errors. After a certain time, the impedance decreases to smaller values that represent only a percentage of the maximum value. The normalized impedance values of the saturation and the time duration between the maximum value and reaching saturation are as follows: $\Delta t = 5.8$ h and norm. $|Z| = 5.33 \pm 0.04$ (8W10E), $\Delta t = 6.9$ h and norm. $|Z| = 2.8 \pm 0.2$ (IDE 20), $\Delta t = 23.1$ h and norm. $|Z| = 2.15 \pm 0.05$ (IDE 12), $\Delta t = 5.8$ h and norm. $|Z| = 1.9 \pm 0.1$ (IDE 10) and $\Delta t = 16.3$ h and norm. $|Z| = 1.78 \pm 0.05$ (IDE 7). For the duration of the maximum no clear correlation can be seen comparing all the different electrode layouts, whereas the values of the plateau show a clear trend. The impedance of the 8W10E electrodes has a much higher saturation than the ones of the IDEs. Within the IDEs it is obvious that the smaller the pitch, the lower is the constant value. During the remaining measurement no significant change is obtained.

The capacitance measurements show the inverse time course. Within the first ≈ 15 h a clear decrease with a minimum can be seen before the capacitance is increasing to a higher value which remains constant until the end of the measurement. Measuring with the 8W10E electrodes the rise of the capacitance is not as pronounced as with the IDEs. For the IDEs it applies that with smaller pitch the value of the constant capacitance is higher.

Comparing the time-dependent changes during the adhesion of MDCK II cells it can be said that the IDEs show a much faster impedance and capacitance change than the 8W10E electrodes. The first increase of the impedance or rather decrease of the capacitance to the maximum or minimum, respectively, is reached much faster with the IDEs. Consequently, these electrodes are more sensitive for the attachment of the MDCK II cells compared to the 8W10E electrodes.

The time-dependent impedance course of the adhesion of **MDCK I** cells differs significantly between the 8W10E electrodes and the IDEs. The impedance change is a three-phase process for all electrodes. In the first phase after cell addition at $t = 0$ h the impedance is rising in an abrupt manner to a short maximum (for the IDEs: norm. $|Z| = 3.5 \pm 0.9$ at $t = (5 \pm 1)$ h and for 8W10E electrodes: norm. $|Z| = 5.8 \pm 0.2$ at $t = 6.9$ h) which declines for all electrodes, until a constant value is reached after $t = (12 \pm 2)$ h. This first maximum is revealed faster with the IDEs, but with a smaller maximum impedance value. In the second phase the time courses differ from each other. After the decrease of the maximum the 8W10E electrodes show a slow increase which lasts for $\Delta t = 29$ h. The value achieved after this time is in a similar range as the maximum at $t = 6.9$ h after seeding (norm. $|Z| = 5.8 \pm 0.3$). On the contrary, the impedance measured with the IDEs remains constant in this second phase after the first maximum for $\Delta t = 29.3$ h at a value norm. $|Z| = 3.0 \pm 0.1$ (IDE 20), for $\Delta t = 17.8$ h at a value norm. $|Z| = 2.98 \pm 0.05$ (IDE 12), for $\Delta t = 19.3$ h at a value norm. $|Z| = 2.2 \pm 0.1$ (IDE 10) and for $\Delta t = 23.3$ h at a value norm. $|Z| = 1.8 \pm 0.1$ (IDE 7). Afterwards, in a third phase the impedance is changing again for all electrodes. The 8W10E electrodes monitor a further increase with a steeper, nearly linear rise from norm. $|Z| = 5.6 \pm 0.1$ (at $t = 47.3$ h) to norm. $|Z| = 6.9 \pm 0.2$ (at $t = 58.4$ h). Until the end of the measurement no saturation can be seen. The IDEs obtain a second plateau at $t = (41 \pm 5)$ h after seeding. The rapid increase of the impedance to this second plateau measured with the different IDEs occurs within $\Delta t = (7 \pm 1)$ h and shows an increase of Δ norm. $|Z| = 1.3 \pm 0.4$ (IDE 20), Δ norm. $|Z| = 1.3 \pm 0.3$ (IDE 12), Δ norm. $|Z| = 0.7 \pm 0.7$ (IDE 10) and Δ norm. $|Z| = 1.6 \pm 0.6$ (IDE 7). The individual heights of the saturation which stay constant for the rest of the measurement of the IDEs can be compared in the summary of the different time courses in fig. 7.7 **A** in the following in-depth analysis.

The capacitance measurement reveals also a three-phase process. In the first phase the capacitance is decreasing immediately after the addition of the cells. At around $t = (12 \pm 1)$ h after seeding the minimum is slightly increasing and remains constant for a longer time. The 8W10E electrodes do not show a significant change during the rest of the measurement. On the contrary, the capacitance of the IDEs is changing at $t = (34 \pm 6)$ h after seeding. For all IDEs the capacitance is increasing within $\Delta t = (5.8 \pm 0.9)$ h, whereas the difference is higher, the smaller the pitches are. The

achieved values remain constant for the rest of the measurement. A comparison of the capacitance time courses can be seen in fig. 7.7 **B**.

The various time courses of the cell adhesion and maturation of the MDCK I cells measured with the 8W10E electrodes and the IDEs will be further compared in the following in-depth analysis. The time courses of the impedance (**A**) and capacitance (**B**) change during adhesion and maturation measured with the various electrode types are summarized in fig. 7.7 to get an overview and to enable a direct comparison.

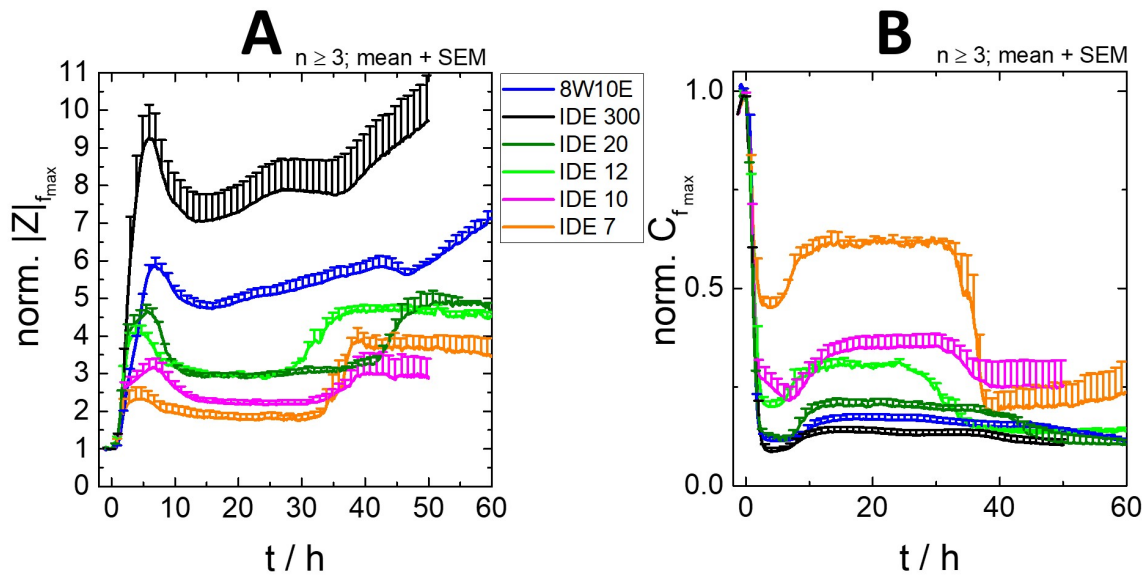


Figure 7.7: Time courses of the normalized impedance and capacitance magnitude during the adhesion of MDCK I cells on different electrode types. The cell suspension was added at $t=0$ h in a seeding density of 450,000 cells/cm² and the adhesion and maturation of the cells was monitored for further 60 h. The time course of the impedance in **A** and of the capacitance in **B** is shown at the specific frequency f_{\max} : for 8W10E at 4 kHz (norm. $|Z|$) and 100 kHz (norm. C), for IDE 300 at 4 kHz (norm. $|Z|$) and 100 kHz (norm. C), for IDE 20 at 160 kHz (norm. $|Z|$) and 320 kHz (norm. C), for IDE 12 at 400 kHz (norm. $|Z|$ and norm. C), for IDE 10 at 200 kHz (norm. $|Z|$) and 320 kHz (norm. C) and for IDE 7 at 400 kHz (norm. $|Z|$ and norm. C). The legend in the middle applies to both graphs. All data were normalized to the initial value of the individual cell-free electrode (8W10E: $|Z| = (980 \pm 175) \Omega$, $C = (37 \pm 12) \text{ nF}$; IDE 300: $|Z| = (1903 \pm 367) \Omega$, $C = (20 \pm 4) \text{ nF}$; IDE 20: $|Z| = (107 \pm 6) \Omega$, $C = (57 \pm 7) \text{ nF}$; IDE 12: $|Z| = (45 \pm 2) \Omega$, $C = (16 \pm 2) \text{ nF}$; IDE 10: $|Z| = (108 \pm 11) \Omega$, $C = (13 \pm 3) \text{ nF}$; IDE 7: $|Z| = (35 \pm 2) \Omega$, $C = (23 \pm 4) \text{ nF}$). The mean with the SEM in positive direction is plotted with $n \geq 3$.

The precise time course has already been explained previously. Looking at the summary in fig. 7.7 **A** it has to be emphasized that the first maximum of the measured impedance is reached much faster with the IDEs ($t = (5 \pm 1) \text{ h}$) than with the 8W10E electrodes ($t = 6.9 \text{ h}$). An exception is the measurement with the IDE 300 (see fig.

7.7) which reaches the first maximum at $t = 6.2$ h which is more in line with the measurement of the 8W10E electrodes. It can be concluded that the measurement with the IDEs with a small pitch is more sensitive to cell attachment and that the IDE 300 resembles more the 8W10E electrodes. This can further be seen in the slow impedance increase measured with the IDE 300 starting at $t = 37.0$ h with a similar slope as with the 8W10E electrodes which starts to increase at $t = 46.6$ h, whereas the IDEs with a small pitch reveal a rapid increase of the impedance at $t = 41.9$ h (IDE 20), $t = 28.0$ h (IDE 12), $t = 35.0$ h (IDE 10) and $t = 32.0$ h (IDE 7). The capacitance measurement underlines the observations of the impedance change (fig. 7.7 B). The 8W10E electrodes and the IDE 300 do not show a significant change in the later measurement (> 30 h), whereas the capacitance of the IDEs is decreasing strongly until a constant value is reached. It is not possible to see a clear trend between the pitch and the value of the plateau and the percentage decrease of the capacitance measured with the IDEs.

In summary it can be said that the IDEs with a small pitch detect the attachment of the cells much faster and that by using those IDEs it is possible to monitor a maturation of the MDCK I in a time > 30 h more clearly in comparison to the 8W10E electrodes and the IDE 300. This maturation of the cell layer in a time > 30 h is further analyzed by microscopic studies.

For these microscopic studies, the MDCK I cells were stained with various dyes at defined points in time after seeding. First, a three-dimensional image of cultivated MDCK I cells is shown at 25 h and 50 h after seeding of the cells (fig. 7.8).

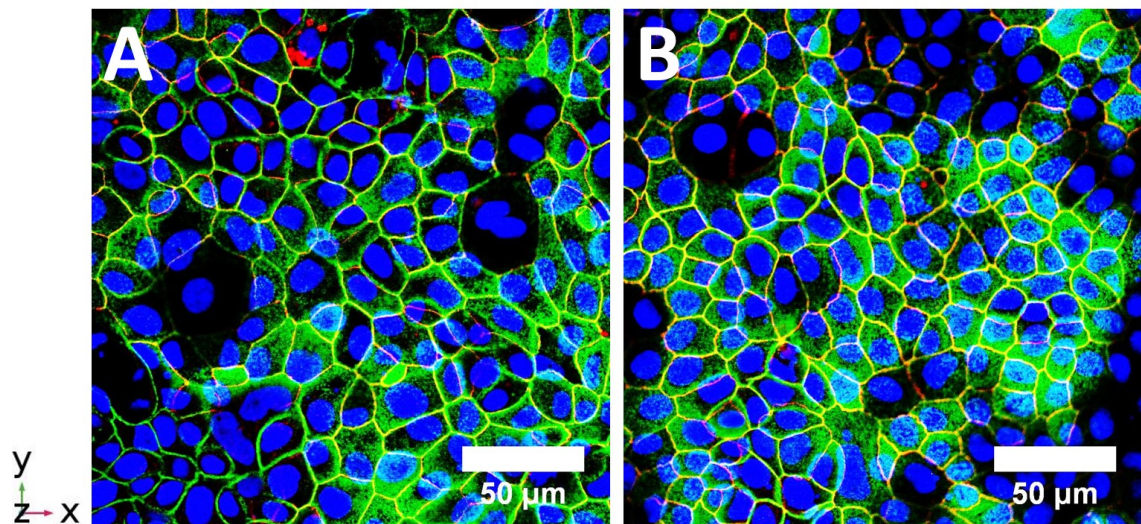


Figure 7.8: Three-dimensional stack of a monolayer of MDCK I cells which is stained with phalloidin alexa-fluor 488 (green), DAPI (blue) and an immunostaining of the ZO-1 protein (red) shown with view in z-direction. The images were taken with CLSM (60x magnification) at two different time points: **A:** 25 h and **B:** 50 h after cell seeding in a density of 450,000 cells/cm². The scale bar represents 50 μm.

For this image the whole cell layer was pictured layer by layer and the individual images were stacked to get a three-dimensional representation which shows all the stained cell components in one image. In fig. 7.8 this stack is shown with view in z-direction. The cell nuclei were stained with DAPI (blue), the actin cytoskeleton with phalloidin alexa-fluor 488 (green) and the tight junctions with an immunostaining of the associated ZO-1 protein (red). This staining was done at 25 h (fig. 7.8 **A**) and at 50 h (fig. 7.8 **B**) after seeding with a seeding density of 450,000 cells/cm². The stained cell nuclei appear blue in the figure. All cell nuclei have a uniform round shape and are evenly distributed over the whole image. Comparing the number of cell nuclei at 25 h and at 50 h no significant difference can be seen. This proves that the cells had built a monolayer after 25 h and do not drastically change the number of cells during the later measurement. With the green fluorescent phalloidin the actin cytoskeleton was stained. This is monitored in both pictures as the small green dots (microvilli) and the actin belt around the cells. With this staining it is seen that the size of the cells is not changing significantly over time. Furthermore, there is no clear trend to see if the microvilli change their distribution. For a better visualization of the actin cytoskeleton a staining with phalloidin alone was repeated at more time points with a direct comparison with NRK cells (see fig. 7.10). The third staining was visualized with red fluorescence of the immunostained tight junction-associated protein ZO-1. Due to the fact that in the three-dimensional image (fig. 7.8) the green and the red fluorescence is overlaid, only the red channel of this image (fig. 7.8) is shown in fig. 7.9.

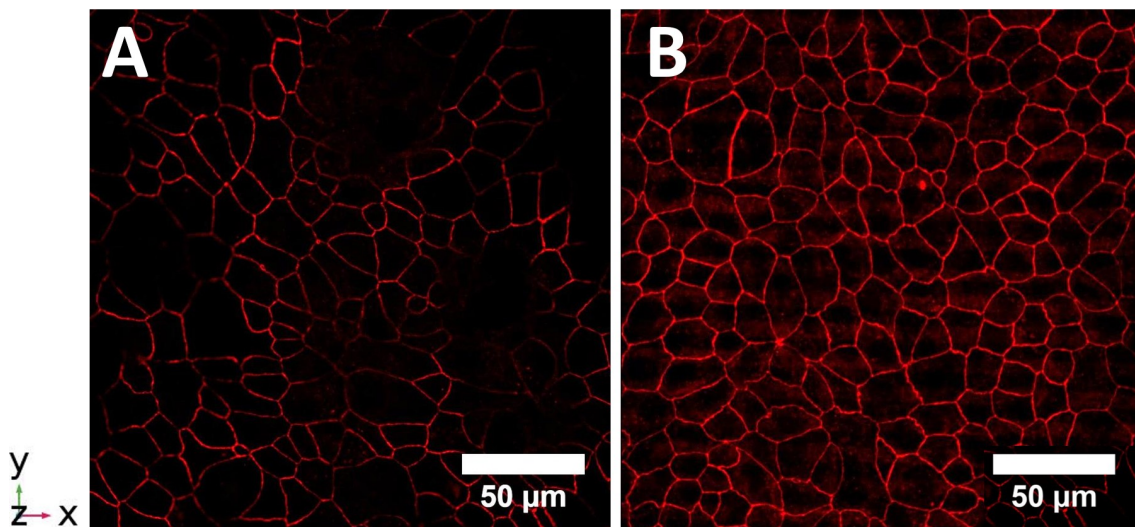


Figure 7.9: Red channel of the three-dimensional stack over the monolayer of MDCK I cells in fig. 7.8 with view in z-direction. The immunostaining of the tight junction-associated protein ZO-1 (red) is visualized. The images were taken with CLSM (60x magnification) at: **A:** 25 h and **B:** 50 h after seeding with a density of 450,000 cells/cm². The scale bar accounts to 50 μm.

Fig. 7.9 shows the red channel of the three-dimensional stack shown in fig. 7.8. The immunostaining of the tight junction-associated protein ZO-1 can be seen. 25 h after seeding a red fluorescence is monitored at very few cell-cell contacts but it is unevenly distributed over the image and no homogeneous formation of tight junctions is revealed (fig. 7.9 **A**). Conversely to this, the red fluorescence shows a uniformly allocation after 50 h (fig. 7.9 **B**). All cell-cell contacts were stained equally red which proves that it will take far more than 25 h before most of the tight junctions were formed.

Additionally to the previously mentioned images, the change of the actin cytoskeleton was analyzed at different time points after seeding in a two-dimensional manner (see fig. 7.10).

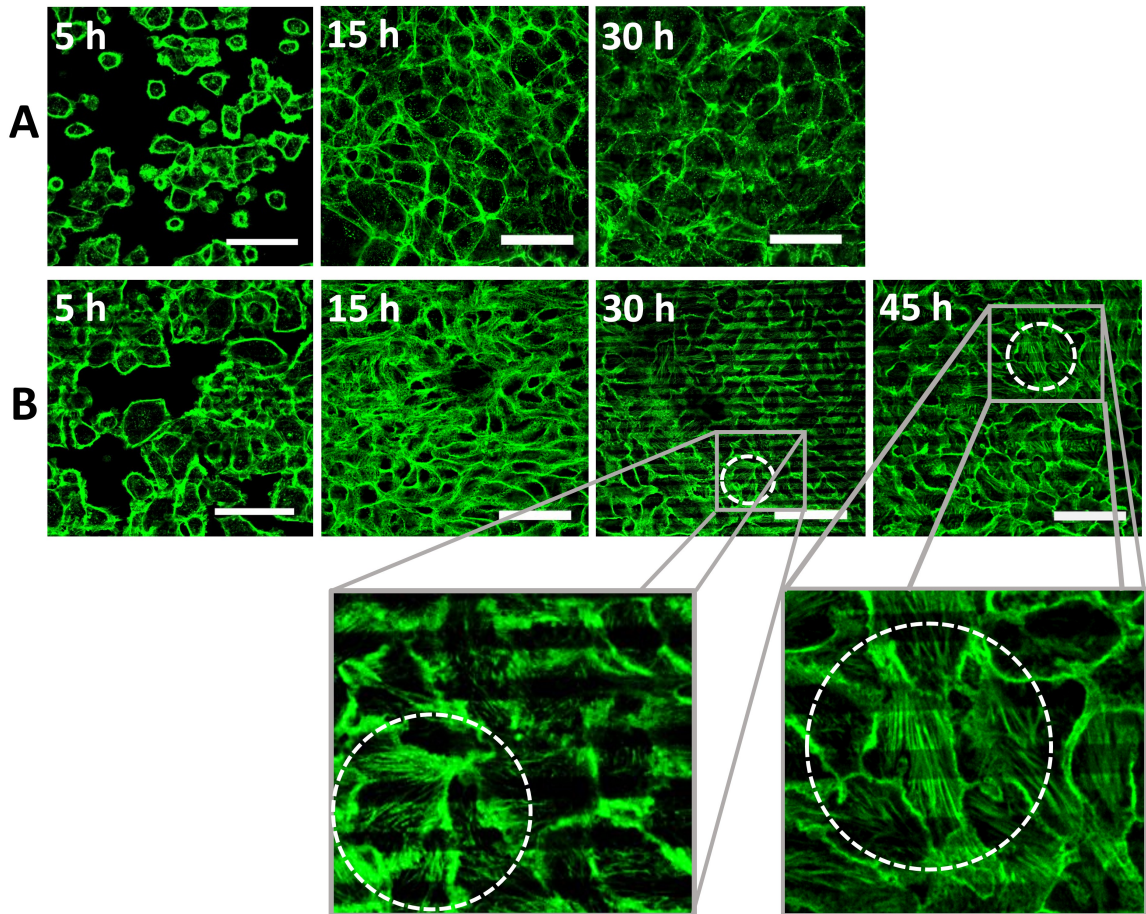


Figure 7.10: Staining of the actin cytoskeleton of two different cell types with phalloidin alexa-fluor 488 at defined points in time after seeding on IDEs with a seeding density of 450,000 cells/cm². **A:** NRK and **B:** MDCKI cells. The images were taken with the CLSM (60x magnification, excitation with 488 nm, detection with 515/30 nm) at 5 h, 15 h, 30 h and in the case of MDCKI cells at 45 h after seeding. The white dotted circles highlight the actin stress fibers. In the gray box a magnification of the highlighted actin fibers can be seen. The scale bar corresponds to 50 µm.

For a comparison NRK cells (fig. 7.10 **A**) and MDCK I cells (fig. 7.10 **B**) were stained at 5 h, 15 h, 30 h and in the case of MDCK I cells 45 h after seeding with a cell density of 450,000 cells/cm². In general, the NRK cells have a greater size than the MDCK I which was already examined in chapter 6. 5 h after the addition of the cell suspension the cells settled down on the electrodes and started to spread. This is seen in the changed cell shape. The cells loose their forms as spheres which they have in suspensions and spread over the electrode area to build a monolayer. Due to the black areas between the cells, it is clear that the electrodes were not fully covered with cells. The area in the images might be greater than in the case of non-treated cells of an impedance measurement, because it is necessary to perform several washing steps during the staining process which detach some of the settled cells. After 15 h the electrodes were fully covered with cells and the cytoskeleton is well-developed. For NRK cells (fig. 7.10 **A**) no significant differences between the staining at 15 h and 30 h can be identified. In the case of the MDCK I cells (fig. 7.10 **B**) actin stress fibers were formed (exemplarily highlighted with white dotted circles) after 30 h and after 45 h. The actin stress fibers are clearly pronounced and distributed throughout the whole cell layer and are highlighted in the magnification in the gray box for the staining at 30 and 45 h.

With the various stainings different aspects of the cell maturation of MDCK I cells at different time points can be analyzed. These maturations are used to explain the measured increase of the impedance > 30 h. With the staining of the cell nuclei it can be shown that the cell number is not significantly changing from 25 h to 50 h after seeding. Consequently, there is no connection of a changing number of cells to the increasing impedance. This is different for the staining of the tight junctions. At 25 h some tight junctions exist but they are not equally distributed over the monolayer. After 50 h the tight junctions are clearly pronounced and distributed over the whole cell monolayer. This formation of the tight junctions can be seen as the reason for the rapid increase of the impedance measured with the IDEs. The staining of the actin cytoskeleton does not provide further insights. The main change of the MDCK I cells over time are the actin stress fibers. Those fibers are visible at 30 h after seeding as well as at 45 h after seeding. Consequently, the staining of the cytoskeleton does not explain the increased impedance in this time period.

Comparing the time courses of the adhesion of different cell types measured with the 8W10E electrodes and IDEs with various pitches, some peculiarities stand out. The first rise of the impedance after addition of the cells for both the MDCK I and the MDCK II cells as well as for the NRK cells is detected faster with the IDEs with a small pitch than with the 8W10E electrodes. The maximum is reached with a few hours time difference. Thus, with these IDEs the initial attachment of cells

can be detected more quickly and sensitively. This suggests a clear advantage of the IDEs with a small pitch over the 8W10E electrodes. Further, it is possible to detect maturation of the MDCK I monolayer in a time > 30 h after seeding with the IDEs with a small pitch more clearly than with the 8W10E electrodes. The stainings give an indication that the formed tight junctions are essential for the rapid increase of the impedance measured with the IDEs. The time courses of the MDCK I cells indicate that the IDE 300 resemble more the 8W10E electrodes than the IDEs with a small pitch. The first increase of the time course measured with the IDE 300 as well as the slow increase > 30 h is very similar to the ones of the 8W10E electrodes. The peculiarities of the IDEs is consequently strongly dependent on the pitch. In summary it can be said that the IDEs with a small pitch have advantages in measuring the adhesion compared to the 8W10E electrodes.

7.1.3 Impedimetric monitoring cell adhesion using IDEs: dependence on active electrode area

It was further investigated whether higher sensitivity can be generated using electrodes with different sizes of the non-insulated electrode area (window). The attachment and mutation of MDCK I, MDCK II and NRK cells was measured with three sizes of the windows of the IDE 10 (fig. 7.11 **A**) and of the IDE 20 (fig. 7.11 **B**). The measurements of the (1.1×1.1) mm² window have been taken from fig. 7.5.

The attachment and spreading of **MDCK I** cells (seen in fig. 7.11 **a**)) shows a different impedance time course for the various window sizes. After the addition of the cells at $t = 0$ h the impedance is increasing immediately, passes through a maximum and remains constant for several hours. This is a general observation for all window sizes of the two electrode types, whereas the highest signal is obtained for the electrodes with the (1.1×1.1) mm² window and the lowest signal for the ones with the (2.0×2.0) mm² window. In the case of the IDE 10 (fig. 7.11 **A, a**)) the impedance of the smallest and the biggest window starts to fluctuate strongly at the same time as the increase with the middle window occurs (≈ 33 h). It can be assumed that the impedances are increasing slightly but due to the high errors, it cannot be confirmed for certain. The measurement with the IDE 20 (fig. 7.11 **B, a**)) with the biggest window also shows a slight increase after ≈ 40 h. Consequently, it is possible to detect a change of the cells at ≈ 40 h with the electrodes with the windows of (0.5×0.5) mm² and (2.0×2.0) mm². However, it is not as obvious as with the electrodes with the window of (1.1×1.1) mm². The associated measured capacitance change of these electrode layouts monitors this assumption more obviously (see appendix A.15 **a**)). In the time > 33 h the capacitance of the IDE 10 is clearly decreasing for the biggest window and also for the smallest window a clear change

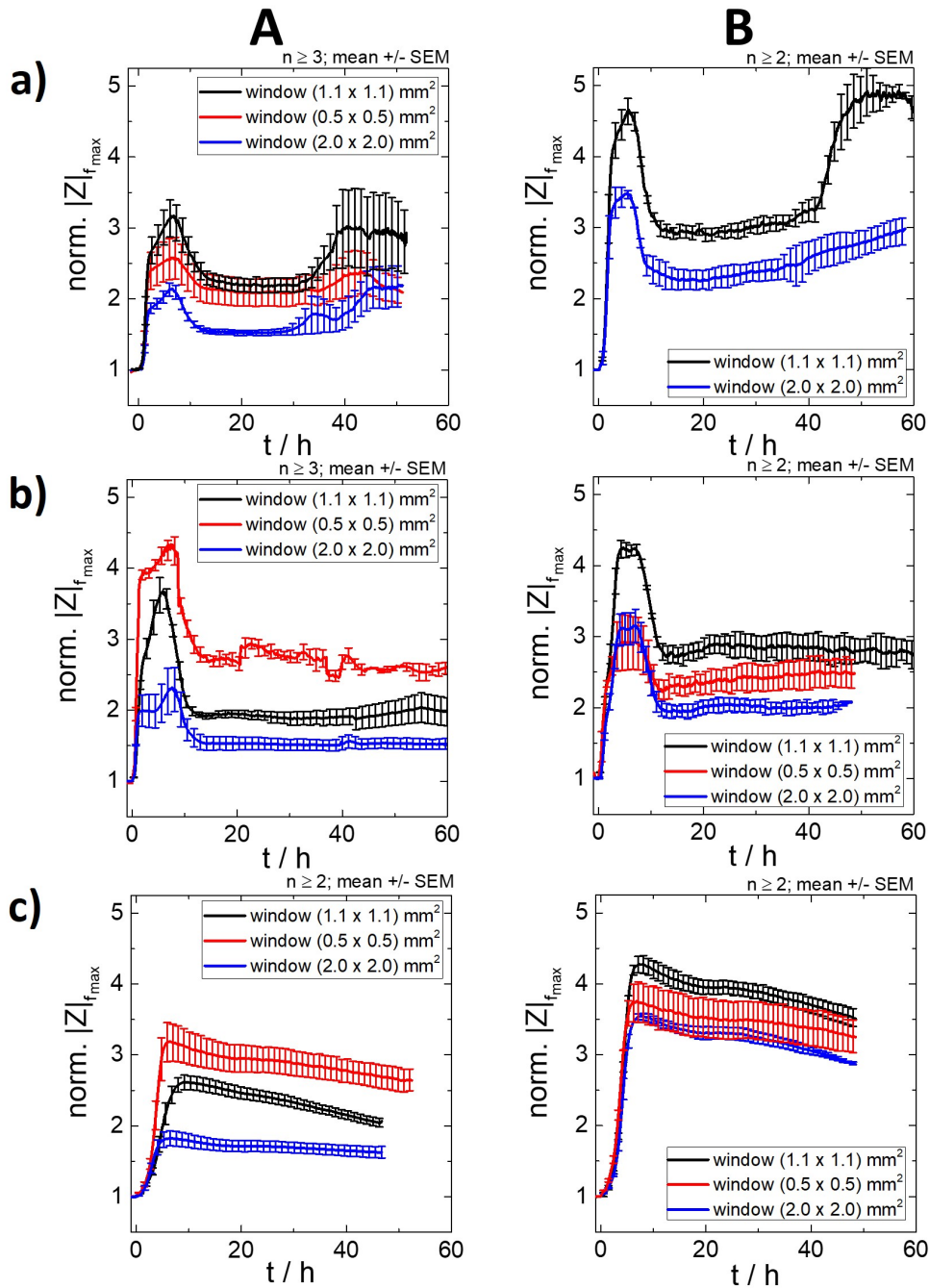


Figure 7.11: Time course of the normalized impedance change during the adhesion of different cell lines on the various non-insulated electrode areas (window) of IDEs. The three different cell lines were added at $t=0$ h with a seeding density of 450,000 cells/cm²: **a)** MDCK I, **b)** MDCK II and **c)** NRK cells. The window sizes were varied for IDE 10 (**A**) and IDE 20 (**B**) and were measured at the individual frequency f_{max} : IDE 10 with (1.1 x 1.1) mm² at 200 kHz, with (0.5 x 0.5) mm² at 320 kHz, with (2.0 x 2.0) mm² at 79 kHz, and for IDE 20 (1.1 x 1.1) mm² at 160 kHz, (0.5 x 0.5) mm² at 200 kHz and (2.0 x 2.0) mm² at 79 kHz. All data were normalized to the initial value of a cell-free electrode (IDE 10: $|Z| = (212 \pm 22) \Omega$ of (0.5 x 0.5) mm², $|Z| = (76 \pm 3) \Omega$ of (2.0 x 2.0) mm²; IDE 20: $|Z| = (310 \pm 54) \Omega$ of (0.5 x 0.5) mm², $|Z| = (68 \pm 5) \Omega$ of (2.0 x 2.0) mm²). mean \pm SEM

can be seen. However, the change of the signal > 40 h for the biggest window of IDE 20 is less pronounced in the capacitance measurement.

Furthermore, the adhesion of the **MDCK II** cells was measured with the electrodes with different windows sizes (fig. 7.11 **b**)). In general, the same impedance curve is revealed for the three different window sizes of the IDE 10 (fig. **A**, **b**)) and the IDE 20 (fig. **B**, **b**)), respectively. Immediately after the seeding at $t = 0$ h the impedance is increasing strongly, shows a maximum and reaches a plateau after $t = (12.5 \pm 0.5)$ h. This value remains constant until the end of the measurement. The difference between the various window sizes is the height of the signal. The measurement of the IDE 10 (fig. **A**, **b**)) shows a greater value, the smaller the window is. Consequently, the highest sensitivity is seen for the electrodes with the window of (0.5×0.5) mm² and the smallest magnitude for the biggest window. The IDE 20 (fig. **B**, **b**)) reveals the highest impedance for the middle window and the smallest one for the window with (2.0×2.0) mm². The electrodes with the window (0.5×0.5) mm² show within the errors the same value for the maximum as the (2.0×2.0) mm², but reaches a higher signal for the plateau lying in the middle of the other windows. The capacitance measurement of this adhesion can be seen in the appendix (fig. A.15 **b**)). All measured capacitances show the same time course with the minimum right after the addition of the cells and the constant value after an average of $t = (12.4 \pm 0.8)$ h. The difference between the windows is repeatedly the height of the signal. In the case of the IDE 10 the measured capacitance is the smaller, the bigger the window is. The measurement with the IDE 20 obtains the biggest magnitude change for the window with (1.1×1.1) mm², whereas the signal cannot be differentiated for the electrodes with the other two windows.

As the last cell line, the adhesion of the **NRK** cells was analyzed (fig. 7.11 **c**)). Parallel to the other two cell lines, all windows show the same impedance change over time. After the addition of the cells the impedance is increasing and is remaining nearly constant. With the IDE 20 (fig. **B**, **c**)) a slight decrease is seen for all window sizes. For the IDE 10 (fig. **A**, **c**)) the smallest window shows the highest impedance magnitude and the biggest window the lowest one. For the IDE 20 the window with (1.1×1.1) mm² reveals the highest impedance magnitude, followed by the smallest one and then the biggest window. The capacitance (see fig. A.15 **c**)) reveals no difference for the electrodes with the smallest and the middle windows in the case of IDE 10, whereas the electrodes with the biggest window has the highest magnitude. The IDE 20 monitors the largest signal change for the middle window and the other two were not distinguishable.

The purpose of this chapter was to investigate whether it is possible to increase the sensitivity of the measurement of the adhesion by varying the non-insulated electrode area of IDE 10 and IDE 20. In the case of the adhesion of the MDCK II and NRK

cells nearly the same time course of the normalized impedance and capacitance for all window sizes of the two electrode types are seen. The only difference is the amount of the impedance which is higher, the smaller the window is in the case of the IDE 10. The capacitance magnitude is inverse, the larger the window, the higher the value. For the measurement of the IDE 20 the highest impedance and the lowest capacitance magnitude can be monitored for electrodes with the middle window size. It can be summarized that for the adhesion of the MDCK II and NRK cells no increased sensitivity and consequently no advantage of the use of the smaller or larger window can be generated. For the measurement of the MDCK I cells with the various window sizes a different time course of the normalized impedance and capacitance is revealed. The clear rapid increase of the impedance at $t \approx 33$ h measured with both electrode types with the window size of $(1.1 \times 1.1) \text{ mm}^2$ cannot be seen in the same way with electrodes with the small and the big window. With these window sizes only a slight increase and fluctuation of the impedance is measured. Also the measurement of the capacitance show only a strong fluctuation and a slow decrease at $t \approx 33$ h. The relatively sharp increase of the impedance, measured with the middle window, can consequently not be revealed with the small and the big window size. In summary, no increased sensitivity can be generated with the variation of the window size. In the case of the adhesion of the MDCK I cells there is even a deterioration of the sensitivity.

7.1.4 Discussion

For the measurement of the adhesion no direct coating was used. Nevertheless, the electrodes were treated with a cysteine solution before the monitoring of the baseline was started. This procedure was done for every assay in this thesis. The cysteine can bind over its thiol groups to the gold electrode surface resulting in a monomolecular layer. It was shown that this treatment can be used for the enhancement of the reproducibility of the electrode/electrolyte interface impedance (Wegener et al., 2000a). The baseline was recorded with serum-containing medium, resulting in a spontaneous and instant adsorption of different adhesive proteins from the medium onto the surface of the electrodes (Wegener, 2010).

In general, when mammalian cells adhere and spread on an electrode surface the overall impedance is altered. The almost spherical cells reach the electrodes and increase the contact area of the basal membrane and the substrate continuously during settlement and spreading. Due to their insulating character, the current from the electrode into the bulk is more and more restricted and consequently, the impedance is increasing (Arndt et al., 2004; Hong et al., 2011). With a time-resolved impedance-based measurement it is possible to monitor this impedance change dur-

ing the complete adhesion of the cells over time.

The three-dimensional representations reveal that the obtained impedance is strongly dependent on the chosen frequency, because at the individual frequency a different fractional contribution of the cell-cell and cell-substrate contacts is dominating the signal (Arndt et al., 2004). In the very low frequency range (depending on the electrode layout, approximately $< 10^2$ Hz) the measurement is very insensitive to monitor the spreading. The impedance is dominated in this range by the rather high impedance of the electric double layer and double layer capacitance of the electrode/electrolyte interface (Arndt et al., 2004; Lee et al., 2014; Wegener et al., 2000a). Besides, the sensitivity is also rather limited in the very high frequency range ($> 10^5$ Hz) in the case of the 8W10E electrodes. Here, the measured impedance is dominated by the sum of: i) resistance of the electrolyte, ii) constriction resistance of the working electrode, iii) all wiring (Arndt et al., 2004). In the middle frequency range the cell impedance is higher than the impedance of the double layer and the impedance change can be monitored over time (Lee et al., 2014). The choice of the frequency f_{max} enables a comparison of the results of the electrode types with each other.

For all cell lines on the various electrode layouts a rapid increase of the impedance is seen immediately after the addition of the cells. This first rise is resulting from the cells settling onto the electrode surface. With ECIS it is possible to measure the presence of a cellular body nearby the electrode surface or even a loose attachment (Wegener et al., 2000a). Consequently, the cells which were immediately settled down change the current and the impedance is strongly increasing (Mamouni and Yang, 2011; Procházka et al., 2019; Wegener, 2010). It can be concluded that in the first increase the formation of cell-substrate junctions are measured (Wegener, 2010). This explanation can further be underlined with the capacitance measurement. The decline of the capacitance at high frequencies can be correlated with the presence of a plasma membrane on the electrode and the associated electrode coverage (Lee et al., 2014; Wegener, 2010). The significant decrease of the capacitance in the first $t = (5 \pm 1)$ h for all cell types and electrodes measured in this work proves that the cells are settling down on the electrodes and are covering nearly the complete electrode surface. Consequently, the cell density was high enough to cover the whole area without any further cell division. Using the IDEs with a small pitch for this measurement it is seen that the initial increase of the impedance is detected much faster with the IDEs than with the 8W10E electrodes. The simulations in chapter 5.3 and 6.1 showed that in the case of the IDEs with a small pitch the main part of the electric field arises in a small volume above the electrodes. Consequently, the space some hundred nm above the electrodes has a bigger influence on the measured signal. When cells settle on these electrodes, the main part of the electric field is

much stronger restricted with a small electrode gap than with 8W10E electrodes. As a result, the impedance measured with the IDEs shows a much faster change than with the 8W10E electrodes. Another explanation for this faster impedance increase is the subcellular dimension of the IDEs. When cells adhere to these electrodes, they cover many more electrodes and gaps than in the case of a large electrode area, like the one of 8W10E electrodes. Consequently, the current is more restricted in the case of electrodes with a subcellular dimension compared to electrodes where the cells cover only a small part of the electrode area. Due to the fact that within the errors no significant difference of the various cell types can be seen it is proven that the first increase or decrease is dependent on the settling and spreading of the cells independently of the cell type. A further proof is the phalloidin staining at 5 h after seeding. The cells were settled down on the electrode and started to spread without building a complete monolayer at this moment.

In the next phase the confluent monolayer was built which could be proven with the phalloidin and DAPI staining. At 15 h and 25 h the electrodes were completely covered with cells which form cell-cell contacts. Due to cell spreading (Mamouni and Yang, 2011) intercellular contacts were established in a time ≥ 10 h (Wegener, 2010). This phase can be seen as a stationary one in which the cells reach confluence (Procházka et al., 2019). It is defined as stationary because cells divide until the growing surface is covered by a single layer. Afterwards, an inhibition of the cell division occurs (Hong et al., 2011) and the proliferation of the cells stops resulting in a constant residual number of cells (Procházka et al., 2019). The mechanical properties of this built cell-cell adhesion can be traced back to desmosomes and adherens junctions which are both of the cadherin type. They hold the intercellular cleft mechanically together but are not strong barriers (Wegener, 2010). This building of the confluent monolayer is obtained in the constant impedance and capacitance values for the NRK, MDCK II and MDCK I cells, independently of the electrode type between 20 h and 40 h after seeding, with the exception of the MDCK I cells measured with the 8W10E electrodes. For the MDCK I cells a slow increase of the impedance is measured with the 8W10E electrodes within this time period. The MDCK I cells build very tight epithelia and it can be concluded that the built intercellular contacts in this period are very tight, resulting in an increasing impedance for this cell type. The constant capacitance values reveal the complete coverage of the electrode surface which is also proven with the phalloidin and DAPI staining. The stained monolayer does not show a significant difference between 15 h and 30 h, and 25 h and 50 h, respectively. The different signal heights of the NRK and MDCK II cells measured with the IDEs can be related to the cell height and was explained in chapter 6.1. In this chapter it was proven that the cell height is decisive for the distribution of the electric field when using IDEs with a small pitch. It was shown that the flatter

the cells, the more dominant is the distribution of the electric field in the intercellular cleft. Due to the fact that the NRK cells are flatter ($h = (3.6 \pm 0.6) \mu\text{m}$ (Parak et al., 1999)) than the MDCK cells ($h = 5 \mu\text{m}$ (Lo et al., 1995)) the intercellular cleft of the NRK cells have a higher influence on the measured impedance than the one of the MDCK II cells. This results in a higher impedance magnitude for the NRK cells than for the MDCK II cells measured with IDEs with a small pitch.

A difference from these stationary phases is the increasing impedance of the MDCK I cells measured with 8W10E electrodes after 45 h. This rise indicates the formation of barrier forming tight junctions. This formation requires completely established cell-substrate contacts and close cell-to-cell annexation which were established through adherens junctions and desmosomes (Wegener, 2010). These tight junctions influence strongly the impedance and increase the signal. In the case of the IDEs the stationary phase is nearly identical for the MDCK I and MDCK II cells before the impedance is increasing rapidly for the MDCK I cells > 30 h. In this period the tight junctions were built. The MDCK I cells grow to very tight epithelia with very strong tight junctions, whereas the MDCK II cells build a more leaky monolayer with weaker tight junctions, seen in the corresponding resistances (Balcarova-Ständer et al., 1984; Richardson et al., 1981). The measurements in this chapter show that the weaker tight junctions of the MDCK II cells are not efficient enough to increase the impedance as significantly as the MDCK I cells. The formation of the tight junctions in a time > 30 h after seeding can be proven with the immunostaining directed against the zonula occludens-1 (short: ZO-1) protein which is a peripheral protein localized at the tight junctions. Furthermore, it is an omnipresent component of the tight junctions in mammalian cells (Arndt et al., 2004; Stevenson et al., 1986) and is located at the cell borders of adjacent cells (Wegener et al., 1998). In the staining performed in this work only very few cell-cell contacts showed a positive staining for ZO-1 at 25 h after seeding, whereas after 50 h a homogeneous distribution at the cell-cell contacts can be seen which proves the formation of tight junctions in this time. Due to the fact that the tight junctions are localized at the apical side of two bordering cells (Wegener, 2010), it is not possible to monitor the complete formation over time with IDEs. With the cell height of the MDCK cells the main part of the electric field is distributed underneath the cells (seen in chapter 6.1). Only when the tight junctions reach a defined strength, the cell-cell contacts are strong enough to significantly change the impedance of the IDEs. With this strong cell-cell contacts the resistance underneath the cells is significantly influenced because the intercellular cleft is directly connected to the space underneath the cells which is filled with electrolyte. Cells with strong cell-cell contacts have a reduced conductivity in the space underneath the cells (Reiss and Wegener, 2015). It was proven in the previous chapters that this space underneath the cells dominates the measured

impedance of the IDEs with a small pitch. When the tight junctions reveal a certain strength, the conductivity underneath the cells is changed strongly which has a significant influence on the measured impedance with the IDEs with a small pitch. This explains the fast increase of the signal to the second plateau which remains constant until the end of the measurement. In contrary to this, the ECIS electrodes monitor the whole cell-cell interactions and display this formation over time with the slowly increasing impedance. A disadvantages of this measurement is, that with the 8W10E electrodes it cannot be said exactly when the tight junctions have been fully formed.

Another aspect analyzed in this chapter was the possibility of increasing the sensitivity by varying the different window sizes. The observation that the electrodes with the different window sizes show nearly the same time course for all cell types prove that the sensitivity cannot be increased with the smaller $(0.5 \times 0.5) \text{ mm}^2$ and the bigger window size $(2.0 \times 2.0) \text{ mm}^2$ in comparison to the middle window size of $(1.1 \times 1.1) \text{ mm}^2$. In the case of the MDCK I cells the sensitivity is even worsened because the increase of the impedance at $t \approx 33 \text{ h}$ can only be seen in a slow increase and strong fluctuation of the impedance measured with the small and big window. The main difference of the measurements with the various window sizes is the distinct impedance and capacitance magnitude. This can be explained with the various influences of the $|Z|_{CPE}$ and R_{bulk} . The impedance of the CPE is influenced by the electrode size (explained in chapter 5). With a smaller electrode size the impedance is shifted to higher values. The impedance of the $(0.5 \times 0.5) \text{ mm}^2$ window is more influenced with the impedance of the electrode/electrolyte interface due to its smaller electrode area, whereas the window with $(2.0 \times 2.0) \text{ mm}^2$ obtains a higher influence of the resistance of the electrolyte relatively to the cell impedance. These various impedance magnitudes do not influence the sensitivity. On average, the window with the size of $(1.1 \times 1.1) \text{ mm}^2$ reveals the highest sensitivity and can monitor the rapid increase of the impedance of the MDCK I cells very clearly. Consequently, this window was chosen for the following experiments. Another advantage of this window is, that the electrode area resembles the one of the 8W10E electrodes which enables a comparison with each other.

In summary, the attachment and spreading of different cell lines could be detected with the various electrodes types. It was found that with IDEs with a small pitch the initial attachment of the cells can be monitored faster and more sensitively than with the 8W10E electrodes. Furthermore, the formation of tight junctions in a confluent monolayer of MDCK I cells was detected more accurately with the IDEs with a smaller pitch. This indicates a clear advantage of the IDEs with a small pitch over the 8W10E electrodes. The IDE300 resemble more the 8W10E electrodes proving that the electrode gap is decisive for the advantages of the IDEs.

7.2 Monitoring cell proliferation using different electrode layouts

A further phenotypic assay is the measurement of the proliferation. In contrary to the adhesion measurement, a cell density of just 10,000 cells/cm² was used which led to a subconfluent seeding of the cells. Consequently, it was possible to measure mainly the spreading and division of the cells. These measurements took much more time to significantly change the impedance or the capacitance and were stopped after 120 h. The proliferation of NRK and MDCK II cells was measured with the 8W10E electrodes, IDE12 and IDE7, both with a non-insulated electrode area of (1.1 x 1.1) mm². Identically to the measurement of the adhesion (chapter 7.1), the electrodes were treated with argon plasma and were incubated with 10 mM cysteine without further coating. For monitoring the baseline and for the cell suspension serum-containing medium was used.

In fig. 7.12 the time-dependent impedance (**A**) and capacitance (**B**) change of the NRK and MDCK II cells is seen measured with the 8W10E electrodes (**a**)), IDE12 (**b**)) and IDE7 (**c**)). In general it is shown, that it took ≈ 40 h to monitor any change of the impedance, whereas the capacitance is slowly decreasing right from the beginning and at ≈ 40 h the decline is getting stronger.

The proliferation of the **NRK** cells measured with all three electrode layouts is monitored in 7.12. After addition of the cells at $t = 0$ h the impedance is not changing significantly and only after $t = 42.5$ h (8W10E electrodes), $t = 37.8$ h (IDE 12) and $t = 36.3$ h (IDE 7) the impedance is strongly increasing (fig. 7.12 **A**). For the different IDEs an individual maximum is reached which remains constant for the rest of the measurement: norm. $|Z| = 4.4 \pm 0.1$ at $t = 68.2$ h (IDE 12) and norm. $|Z| = 2.9 \pm 0.3$ at $t = 74.1$ h (IDE 7). With the measurement of the 8W10E electrodes a maximum of norm. $|Z| = 5.5 \pm 0.3$ at $t = 89.0$ h is passed before a value of norm. $|Z| = 4.6 \pm 0.3$ is reached at $t = 99.7$ h which remains constant. This short maximum with the followed decrease cannot be seen in the capacitance measurement (fig. 7.12 **B**). For all three electrode types the capacitance is slowly decreasing right after the addition of the NRK cells. After an average of $t = (28 \pm 2)$ h the slope of the decline is getting stronger until a minimum of norm. $C = 0.079 \pm 0.006$ at $t = 86.0$ h (8W10E), norm. $C = 0.179 \pm 0.006$ at $t = 67.1$ h (IDE 12) and norm. $C = 0.35 \pm 0.02$ at $t = 72.6$ h (IDE 7) is reached which remains constant for the rest of the measurement. In this measurement it can be seen that the IDE 12 and IDE 7 reveal a faster increase of the impedance and a faster reaching of the impedance maximum or the capacitance minimum, respectively, compared to the ECIS electrodes. Consequently, these electrodes can monitor the initial attachment and spreading of the cells faster than the 8W10E electrodes.

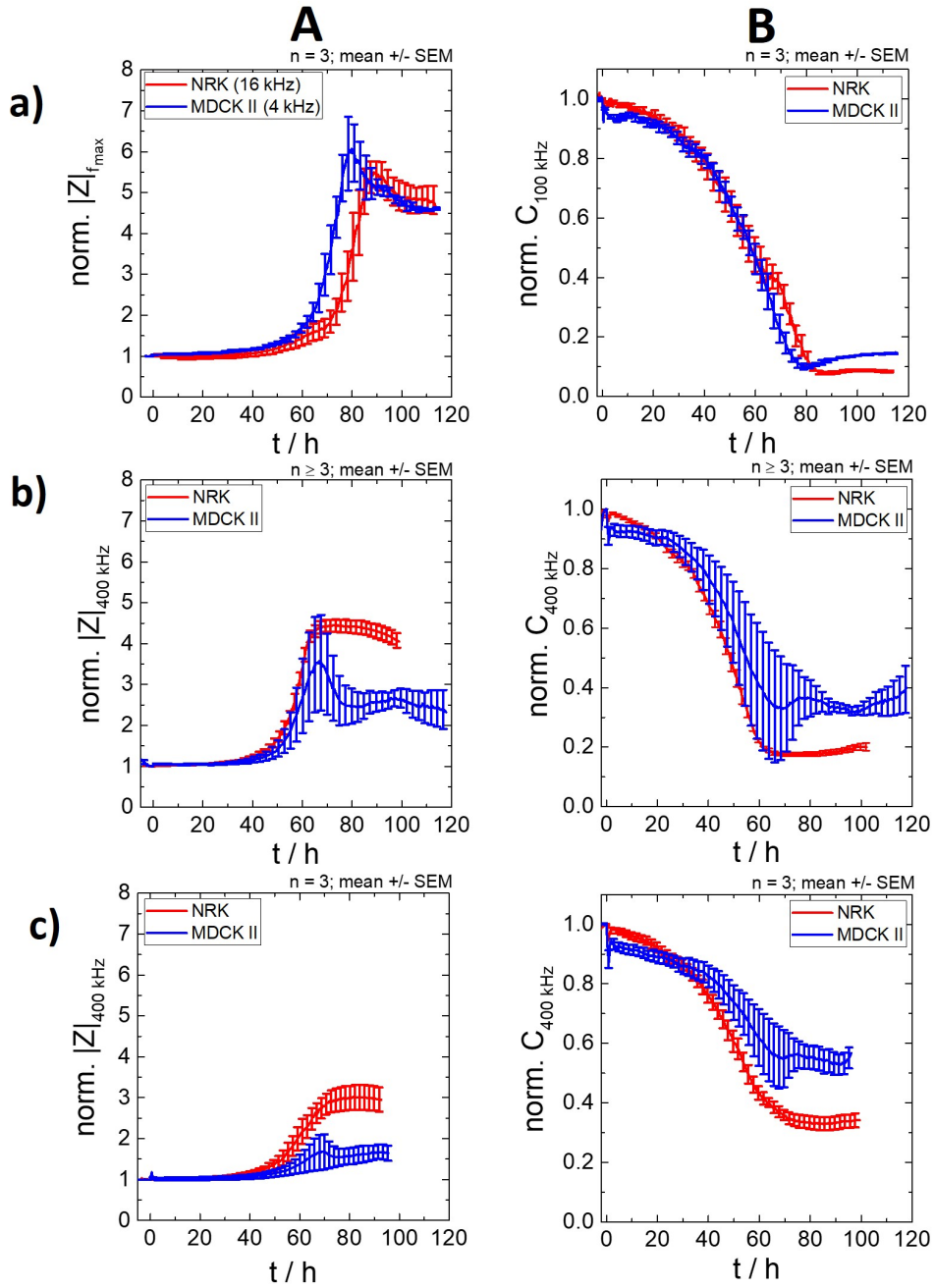


Figure 7.12: Time course of the normalized impedance and capacitance change during the cell proliferation of NRK and MDCK II cells measured with different electrode layouts. The cells were added in a density of 10,000 cells/cm² at $t=0$ h. The representation reveals the normalized impedance (**A**) and the normalized capacitance change (**B**) over time. For the measurement different electrode layouts at individual frequencies were used: **a)** for the norm. $|Z|$ of the 8W10E electrodes at cell specific frequencies (NRK: 16 kHz; MDCK II: 4 kHz) and for norm. C at 100 kHz ($n=3$), **b)** IDE12 at 400 kHz ($n \geq 3$) and **c)** IDE7 at 400 kHz ($n=3$). The data were normalized to the initial value of a cell-free electrode (8W10E electrodes: $|Z|_{4\text{ kHz}} = (911 \pm 28) \Omega$ (MDCK), $|Z|_{16\text{ kHz}} = (359 \pm 42) \Omega$ (NRK), $C = (44 \pm 3) \text{ nF}$; IDE12_{400 kHz} = $(44 \pm 2) \Omega$, $C = (17 \pm 2) \text{ nF}$; IDE7_{400 kHz}: $|Z| = (34 \pm 2) \Omega$, $C = (18 \pm 3) \text{ nF}$). The mean with SEM is plotted.

The time-dependent impedance measurement of the proliferation of **MDCK II** cells shows a similar course for the different electrode types. The addition of the cells at $t = 0$ h does not influence the impedance until it is increasing dramatically at $t = (43 \pm 4)$ h to a maximum of norm. $|Z| = 6.0 \pm 0.8$ at $t = 79.5$ h (8W10E electrodes), norm. $|Z| = 4 \pm 1$ at $t = 66.6$ h (IDE 12) and norm. $|Z| = 1.7 \pm 0.4$ at $t = 68.5$ h (IDE 7) before the impedance is decreasing to a value which remains constant until the end of the measurement. This constant value is reached at different time points after seeding: at $t = 102.4$ h (norm. $|Z| = 4.7 \pm 0.1$) for 8W10E, at $t = 79.2$ h (norm. $|Z| = 2.5 \pm 0.4$) for IDE 12 and at $t = 74.1$ h (norm. $|Z| = 1.6 \pm 0.3$) for IDE 7. Consequently, the 8W10E electrodes show a delayed signal both at the first rise of the impedance and at the maximum compared to the IDE 12 and IDE 7. A further difference of the various electrode layouts is the much higher impedance magnitude of the 8W10E electrodes than of the IDEs. This higher change is also seen in the capacitance measurement (fig. 7.12 B). The constant capacitance value of the 8W10E electrodes is reached after $t = 78.6$ h (norm. $C = 0.10 \pm 0.01$), in contrary to the time point of the IDE 12 at $t = 68.2$ h (norm. $C = 0.3 \pm 0.2$) and of the IDE 7 at $t = 68.4$ h (norm. $C = 0.6 \pm 0.1$). Due to the high errors of the IDE measurement it is difficult to see a clear trend of the capacitance change but a small minimum of the capacitance value can be assumed before a constant value which remains until the end of the measurement is reached.

The measurement of the proliferation of NRK cells as well as of MDCK II cells shows a delayed impedance and capacitance change for the 8W10E electrodes. The initial increase of the impedance and the reaching of the maximum of the impedance and the minimum of the capacitance occurs much faster with the IDEs. These electrodes monitor the attachment and the spreading more quickly and thus more sensitively than the 8W10E electrodes, indicating a distinct advantage of the IDEs.

To enable a direct comparison of the proliferation of the various cell types measured with the 8W10E electrodes, the IDE 12 and the IDE 7 the area under the curve (AUC) was calculated (fig. 7.13). The baseline was defined with $y = 1$ and the absolute area between this line and the individual time courses was calculated in the time period of 0 h - 95 h. AUC was analyzed for the curve of norm. $|Z|$ (fig. 7.13 A) and for norm. C (fig. 7.13 B).

The AUC of the NRK and the MDCK II cells reveals distinct values for the electrode types. In the case of the 8W10E electrodes the impedance of MDCK II cells is increasing faster than of the NRK. However, both impedances level off at a similar value within the error range. This correlates with the higher AUC for the MDCK II than for the NRK cells. These differences converge to each other in the case of the capacitance measurement. The decrease of the capacitance curves for MDCK II and NRK cells are very similar and consequently, the AUC of MDCK II cells shows only a

slightly higher value than of the NRK cells which can nearly be neglected due to the errors. The IDE 12 and IDE 7 obtain the reversed trend. The impedance of the NRK cells is increasing faster than the one of the MDCK II cells and has a much higher saturation resulting in a higher AUC of NRK cells for both the IDE 12 and IDE 7. This trend can also be seen in the curve of the capacitance in which the NRK cells are decreasing with a steeper slope and lower saturation than the MDCK II cells. As a result, the AUC of the norm. C is higher in the case of the NRK cells, but the difference to the lower value of MDCK II cells is not as pronounced as with the norm. $|Z|$.

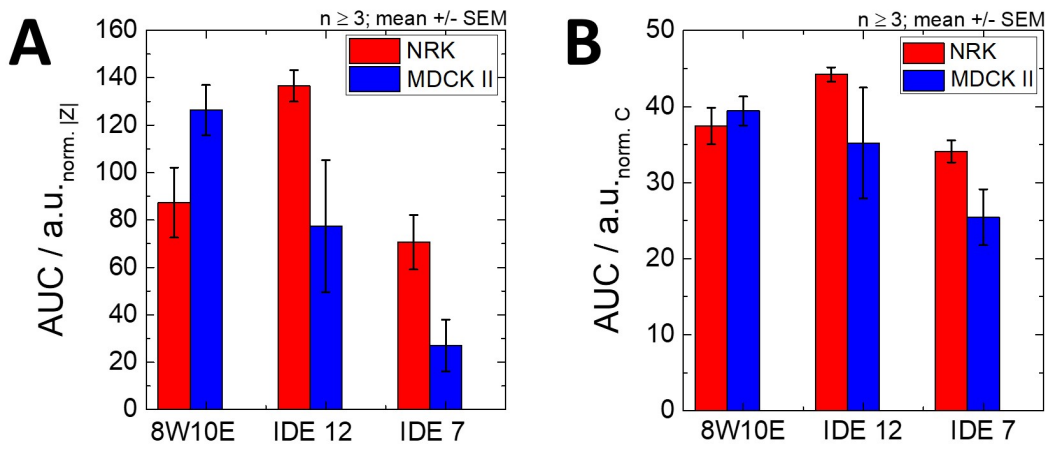


Figure 7.13: Calculation of the area under the curve (AUC) for the time course of norm. $|Z|$ (A) and norm. C (B) of the proliferation measurement in fig. 7.12 measured with 8W10E electrodes, IDE 12 and IDE 7. The baseline was defined as $y = 1$ and the absolute area in a time range of 0 h - 95 h was calculated. The mean with the SEM is plotted ($n \geq 3$).

With this representation of the AUC it is underlined that the NRK cells reveal a higher impedance and a lower capacitance magnitude than the MDCK II cells measured with the IDEs, whereas it is reverse with the 8W10E electrodes.

7.2.1 Discussion

The measurement of the proliferation is associated with the one of the adhesion (see chapter 7.1) with the difference that a cell density of only 10,000 cells/cm² was used (2.22 % of the adhesion). This led to a subconfluent seeding of the cells, and the spreading and the division were analyzed which took much longer time than a confluent seeding. The electrodes were identically to the ones in the adhesion measurement treated with cysteine to enhance the reproducibility of the electrode/electrolyte interface impedance (Wegener et al., 2000a) and were measured with

serum-containing medium resulting in an adsorption of adhesive proteins onto the surface of the electrodes (Wegener, 2010). The proliferation can be divided into different phases: i) initial phase, in which the cells settle down on the electrodes and start to adhere and to spread, ii) the exponential phase, in which cell proliferation occurs and iii) the stationary phase, when confluence is reached (Procházka et al., 2019). The initial phase lasts some hours, during which the cells attach and spread on the electrode. The impedance is not significantly changing in this time range. The number of the seeded cells is so small that the insulating character of those is not decisive enough for a significant restriction of the current (Arndt et al., 2004). The fact that the capacitance is decreasing slowly right from the beginning, proves the high sensitivity of the capacitance for the coverage of the electrode. Even when a fractional part of the electrode is covered with cells, the measured signals are influenced decisively (Lee et al., 2014; Wegener et al., 2000a). In the exponential phase ($\approx 40\text{ h}$ - 80 h) the number of the cells is increasing until it is high enough to cover the electrode and to build intercellular connections like adherens junctions and desmosomes (Wegener, 2010). This cell proliferation is a rise of the cell population due to cell division and cell development (Hong et al., 2011). The cells are further dividing and the impedance and capacitance is strongly influenced due to the growing restriction of the current resulting in a strong increase in the impedance and a steep decrease in the capacitance (Procházka et al., 2019). When the cells reached confluence ($\approx 80\text{ h}$) in the stationary phase, the cells stop to proliferate which leads to a constant residual number of cells (Procházka et al., 2019). The different signal heights of the NRK and the MDCK II cells of the IDEs compared with the 8W10E electrodes is identical with the adhesion measurement and was explained before (see chapter 6). The increase of the impedance and the reaching of the maximum can be detected faster with the IDEs than with the 8W10E electrodes. The same advantage of the IDEs was seen in the adhesion measurement. The simulations in chapter 5.3 and 6.1 proved that with electrodes with a small gap the main part of the electric field is distributed in a volume close to the electrodes. When cells settle down on the electrodes and adhere and spread the electric field is strongly influenced resulting in a faster impedance increase. Due to the subcellular dimension of the IDEs the current is restricted strongly when cells settle down on the electrodes because more electrode gaps are covered. This coverage of the electrode gaps has a stronger influence on the measured impedance than a large electrode area at which the adhered cells cover only a small part of the working electrode.

In summary, it is repeatedly seen that the attachment and spreading of the cells is detected faster with the IDEs with a small pitch compared to the 8W10E electrodes. This higher sensitivity of the IDEs indicates an advantage over the 8W10E electrodes in proliferation measurements.

7.3 Monitoring the impact of non-isotonic media

In this chapter the interdigitated electrodes are analyzed with regard to their advantages or disadvantages for the detection of cell size changes. These changes were induced by non-isotonic osmotic pressure to initiate a cell swelling or shrinking in response to the osmolality of their environment.

Osmosis is a physical phenomenon which is often used for application in food processing or seawater/brackish water desalination (see Cath et al., 2006). It is the net passage of water across a membrane which is permeable for the movement of water but hinders specifically solute molecules or ions to pass (Cath et al., 2006). The movement of water is driven by an osmotic difference across the membrane (Cath et al., 2006; Baumgarten and Feher, 2001). The addition of impermeable extracellular solutes into the supernatant around the cells, increases the osmotic pressure and the cells react as an osmometer. In a hypertonic solution, the cells are shrinking, whereas in a hypotonic solution the cells are swelling (Fullerton et al., 2006).

In this work the concentration of the solutes in the supernatant was increased to induce a hypertonic pressure by adding corresponding amounts of sucrose. For this purpose, two different solutions of sucrose were used: i) 100 mM and ii) 200 mM as an addition to an isotonic solution. Sucrose is a disaccharide which is comprised of the two monosaccharides: glucose and fructose. The structural formula can be seen in fig. 7.14. The conductance of the solutions was adjusted to the one of PBS⁺⁺/glucose (1 g/L) which served as the solvent and as the control. This ensures three iso-conductive buffers with different osmotic pressures which were verified by freezing point depression. The final values of the conductance and the osmolalities can be seen in tab. 4.7 in chapter 4.4.3.3.

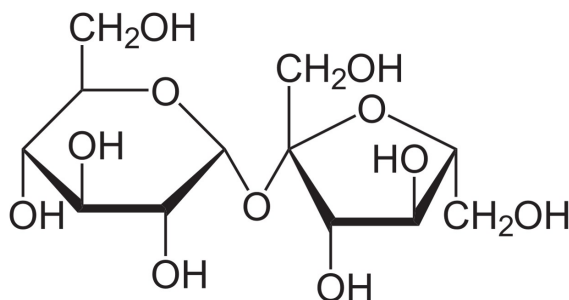


Figure 7.14: Structural formula of sucrose. IUPAC name: β -D-fructofuranosyl α -D-glucopyranoside.

The influence of the hyperosmotic pressure on the measured impedance was analyzed for MDCK II and NRK cells. Both cell types were cultivated on three different IDE layouts: i) IDE 10, ii) IDE 12 and iii) IDE 20 and on 8W10E electrodes to enable a comparison with a commercially available electrode. The use of the 8W10E

electrodes made it possible to calculate the change of the ECIS parameters R_b , α and C_m during the measurement in a time-dependent manner. The parameters were further explained in chapter 3.1.1.

7.3.1 Monitoring the impact of non-isotonic pressure on MDCK II cells

As a first aspect, the influence of hyperosmotic pressure on the impedance of MDCK II cells cultivated on 8W10E electrodes will be analyzed.

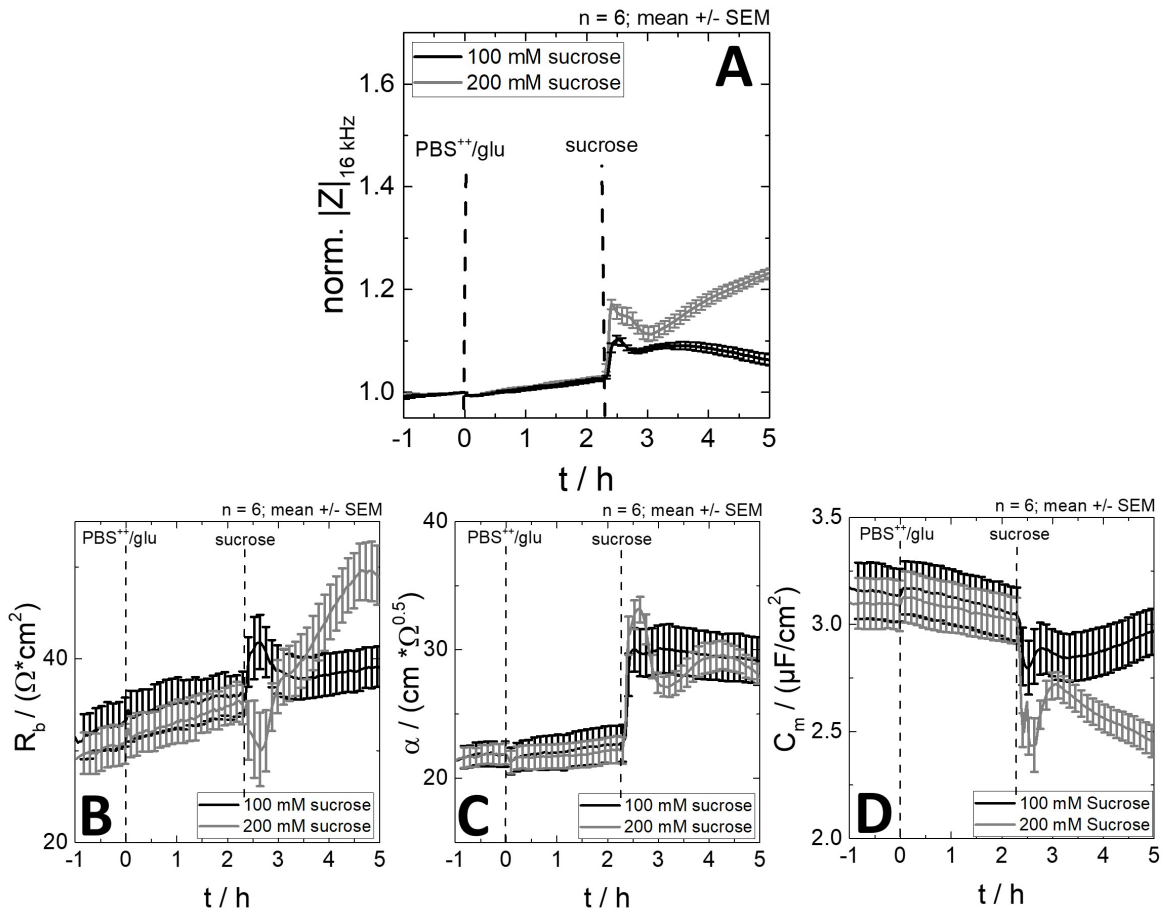


Figure 7.15: Measurement of the time-dependent impedance change of MDCK II cells cultured on 8W10E electrodes due to the influence of a hyperosmotic pressure. The experiment was proceeded on the third day after seeding. The baseline was monitored in isotonic PBS⁺⁺/glu and at $t = 0$ h this isotonic solution of PBS⁺⁺/glu was added as a temperature and volume control. At $t = 2.3$ h the non-isotonic solutions with 100 mM and 200 mM sucrose were added. **A:** shows the impedance time course at 16 kHz. The data are normalized to the initial values before addition ($|Z| = (1552 \pm 112) \Omega$). On the basis of the frequency spectra the three ECIS parameters are calculated, which can be seen in **B:** R_b , **C:** α , **D:** C_m . The mean and the SEM is plotted with $n = 6$.

Fig. 7.15 **A** shows the time-dependent impedance course of MDCK II cells during the addition of the control (PBS⁺⁺/glu) at $t = 0$ h, which was also used to monitor the baseline, and the different non-isotonic solutions at $t = 2.3$ h which changes the osmotic pressure. The impedance does not reveal a significant change after the addition of the control which proves that the volume change of the electrolyte does not affect the osmolality and the measured impedance when a solution is added in the following experiment. Otherwise, the two non-isotonic solutions (100 mM and 200 mM sucrose) are increasing the impedance immediately (for 100 mM to a value of norm. $|Z| = 1.102 \pm 0.009$ and for 200 mM to norm. $|Z| = 1.171 \pm 0.009$) which decreases again in the following 0.5 h (100 mM) and 0.7 h (200 mM), respectively. During the remaining measurement period the impedance for the 100 mM is slowly reduced, whereas it is rising distinctly for the 200 mM. This measurement, performed with the ECIS electrodes, enables the calculation of the change of different parameters in dependence of the time on the basis of the frequency spectra: i) R_b (fig. 7.15 **B**), ii) α (fig. 7.15 **C**) and iii) C_m (fig. 7.15 **D**). After the addition of the control none of the parameters vary significantly, whereas the influence of the osmolality shows a change of the individual parameters. R_b reveals a dip within the first 0.5 h in positive direction with 100 mM and in negative direction with 200 mM sucrose. After reaching the initial value, R_b for 100 mM remains constant, whereas it is rising for 200 mM sucrose. The addition of sucrose increases α which stays constant in the case of the 100 mM sucrose for the rest of the measurement. For 200 mM α fluctuates strongly around the same value as for the smaller concentration. As a last parameter C_m is analyzed. After addition of the two non-isotonic solutions C_m is decreasing showing a small dip in the first 30 min, before it is on the one hand slowly increasing with 100 mM, and on the other hand decreasing with 200 mM sucrose. It can be concluded that the cell-cell contacts were not changing significantly after the addition of 100 mM sucrose because R_b , which represents the resistance of the cell-cell contacts, remains almost constant. The rise of the values of α which show the impedance in the cell-electrode junction must be related either to the changing radius of the cells or the increased resistivity of the electrolyte underneath the cells. Furthermore, the different values of the specific cell membrane capacitance C_m lead to the conclusion that the topography of the membrane is changing. In summary, it is obvious that the osmotic pressure has an influence on the shape of the cells and their corresponding impedimetric characteristics which is measured with 8W10E electrodes.

To enable a comparison of the individual electrode types, MDCK II cells were cultivated on different IDEs and the osmotic pressure was increased identically to the 8W10E electrodes using non-isotonic solutions with 100 mM and 200 mM sucrose.

In fig. 7.16 the normalized impedance changes are seen, measured with IDE 10 (fig. 7.16 A), with IDE 12 (fig. 7.16 B) and with IDE 20 (fig. 7.16 C).

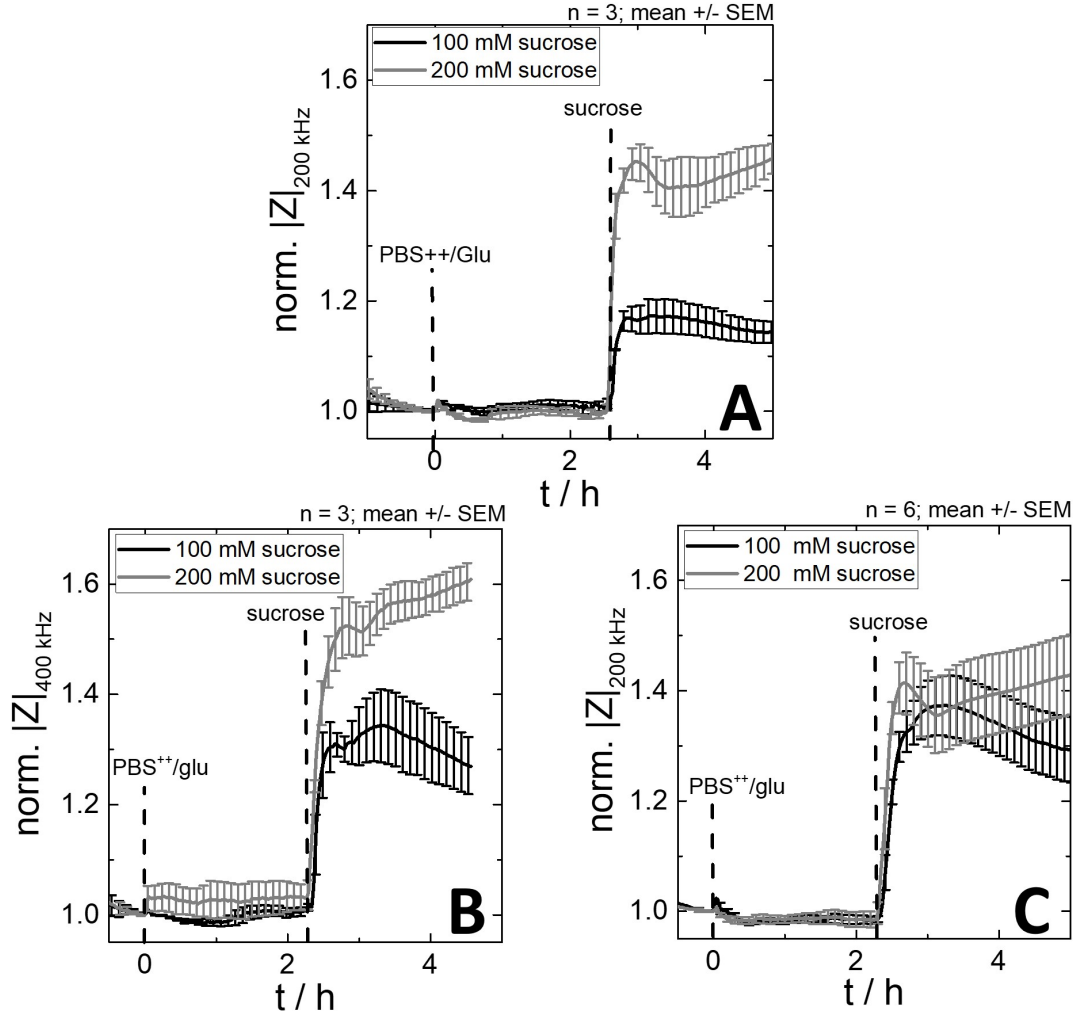


Figure 7.16: Time-dependent change of the normalized impedance of MDCK II cells cultured on different IDE layouts after the addition of a control (PBS⁺⁺/glu) at $t = 0$ h and different non-isotonic sucrose solutions (100 mM and 200 mM sucrose) at $t \approx 2.4$ h. The measurement was performed at the third day after seeding. Different electrodes were used at the individual frequency f_{max} : **A:** IDE 10 at 200 kHz ($n = 3$), **B:** IDE 12 at 400 kHz ($n = 3$) and **C:** IDE 20 at 200 kHz ($n = 6$). All data were normalized to the initial value before addition of the control (IDE 10: $|Z| = (189 \pm 22) \Omega$; IDE 12: $|Z| = (132 \pm 20) \Omega$; IDE 20: $|Z| = (279 \pm 35) \Omega$). The mean with SEM is plotted.

The addition of the control ($t = 0$ h) and the corresponding volume change of the electrolyte shows consistently no influence on the measured impedance. After addition of the non-isotonic solutions the impedance is increasing immediately for all electrodes independently of the concentration. The individual impedances measured with IDE 10 (fig. 7.16 A) and IDE 12 (fig. 7.16 B) reveal a similar course. With 100 mM the impedance is increasing (for IDE 10 to a value of $\text{norm. } |Z| = 1.17 \pm 0.02$ and for IDE 12 to $\text{norm. } |Z| = 1.31 \pm 0.03$) and is staying nearly constant until the end

of the measurement. A slight trend of a decrease is seen but due to the errors this is not clearly. Furthermore, a small shoulder within the first 30 min is revealed, which also can be seen in the impedance course with 200 mM (at norm. $|Z| = 1.45 \pm 0.03$ for IDE 10 and at norm. $|Z| = 1.52 \pm 0.05$ for IDE 12). Here, the short hub is more pronounced and lasts ≈ 1 h, before the impedance is further slowly increasing. The impedance course with 200 mM measured with IDE 20 (fig. 7.16 C) shows a similar trend with the hub in the first hour, the following increase, and the slightly decrease of the impedance after addition of 100 mM. The difference to the other electrodes is the height of the signal change. Both impedance time courses reveal a maximum of norm. $|Z| = 1.41 \pm 0.05$ after addition of the non-isotonic solutions with 100 mM and 200 mM sucrose.

Comparing the results for the MDCK II cells measured with the 8W10E electrodes and the IDEs shows many similarities and differences. All impedances are increasing after the addition of sucrose and in all cases the impedance changes measured with the IDEs are bigger than with the 8W10E electrodes. Consequently, the change in cell shape of MDCK II cells due to the osmotic pressure has a higher impact on the measured impedance of the IDEs compared to the 8W10E electrodes. Another similarity is the higher impedance change of the 200 mM sucrose in comparison to the 100 mM, except for the IDE 20. Moreover, the different curves of the individual electrodes look alike. For the incubation with 100 mM sucrose a small shoulder within the first 0.5 h after addition is monitored before the impedance is slightly decreasing during the remaining measurement. Also for the stimulation with 200 mM sucrose all graphs show a shoulder in the first hour after addition with a following increase of the impedance.

7.3.2 Monitoring the impact of non-isotonic pressure on NRK cells

The influence of osmotic pressure on the impedance was analyzed using NRK cells. These cells were cultivated on 8W10E electrodes and on different IDEs. Three solutions were added: i) isotonic PBS⁺⁺/glu, and non-isotonic solutions with ii) 100 mM and iii) 200 mM sucrose in analogy to the measurement of the MDCK II cells.

In fig. 7.17 A the time course of the impedance change of the NRK cells on the 8W10E electrodes is shown. The addition of the control (PBS⁺⁺/glu) at $t = 0$ h does not change the impedance and proves consistently that the change of the volume of the supernatant has no influence on the measured impedance. The non-isotonic solutions which were added at $t = 2.3$ h cause a decrease of the impedance independently of the concentration. The impedance with 100 mM falls over a small shoulder to a saturation of norm. $|Z| = 0.911 \pm 0.002$ after 1 h, at which it remains constant

until the end of the measurement. With 200 mM the impedance is decreasing to a value of $\text{norm. } |Z| = 0.844 \pm 0.004$ after 0.8 h and is further sinking after 4 h. On the basis of the frequency spectra the changes of the ECIS parameter R_b (fig. 7.17 **B**), α (fig. 7.17 **C**) and C_m (fig. 7.17 **D**) can be calculated over time. The changes during the measurement of the 100 mM sucrose are similar for all three parameters. The values of the parameters are decreasing and showing a saturation after 1.5 h for R_b , after 1.3 h in the case of α and after 0.6 h in the case of C_m . One exception of these courses is the small shoulder in the R_b calculation in the first 0.3 h. The changes of the parameters with an addition of 200 mM is similar in all three cases. The values are strongly decreasing in the first 0.8 h. During the remaining measurement all parameters are sinking slowly without a saturation.

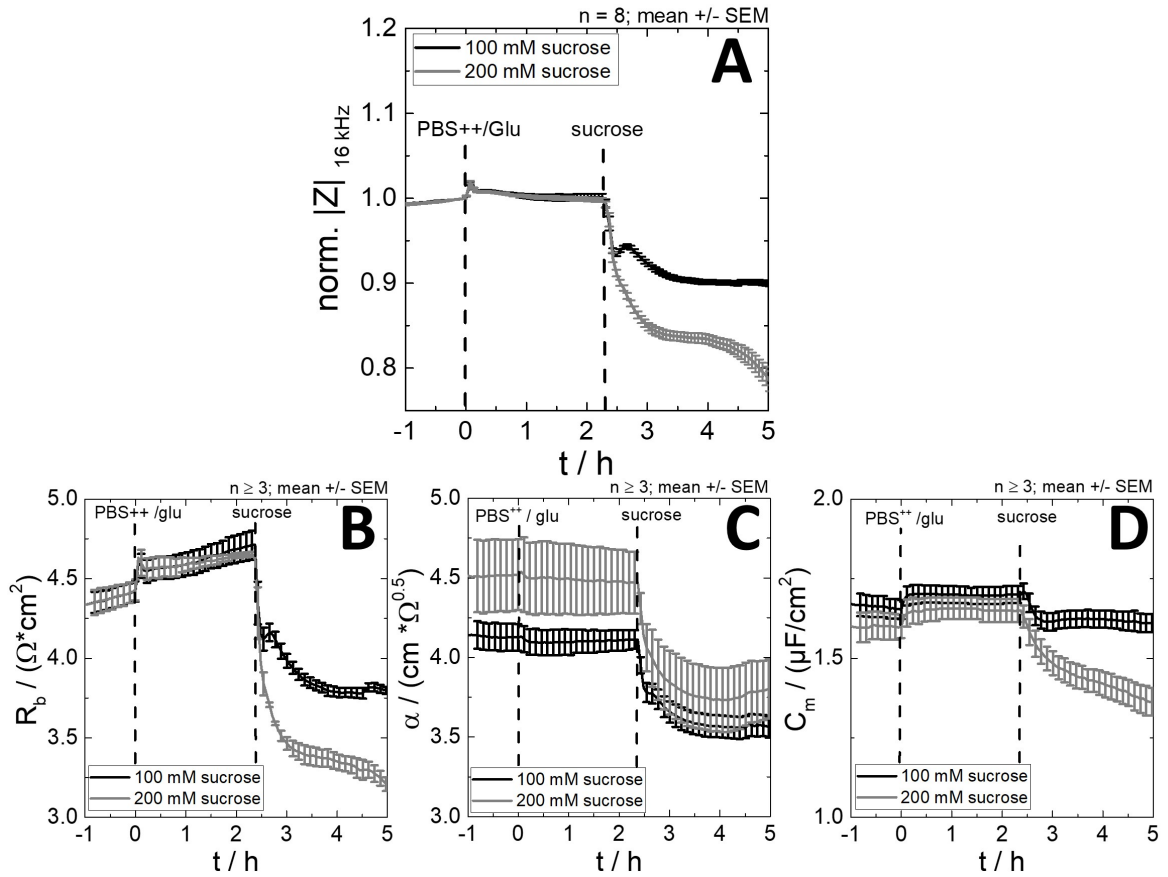


Figure 7.17: Time-dependent measurement of the impedance change of NRK cells cultured on 8W10E electrodes due to the influence of a hyperosmotic pressure. The isotonic control (PBS⁺⁺/glu) was added at $t = 0$ h and the non-isotonic sucrose solutions (100 mM and 200 mM sucrose) at $t = 2.3$ h, respectively. The experiment was performed on the third day after seeding. **A:** reveals the normalized impedance time course at 16 kHz ($n = 8$). The values are normalized to the initial values before addition ($|Z| = (1451 \pm 55) \Omega$). The frequency spectra served as basis for the calculation of the three ECIS parameters ($n \geq 3$), which is seen in **B:** R_b , **C:** α and **D:** C_m . The mean and the SEM is plotted.

The impact of an increased osmotic pressure on the impedance of the NRK cells measured with the 8W10E electrodes is clearly visible in fig. 7.17. All calculated parameters are decreasing, resulting in a reduced impedance of the cell-cell contacts (R_b), the impedance of the cell-electrode junction (α) and the specific cell membrane capacitance (C_m). Consequently, the increased osmotic pressure changes significantly the cell shape of the NRK and the corresponding impedance measured with 8W10E electrodes.

The same experiment was performed with NRK cells cultivated on different IDE layouts (see fig. 7.18).

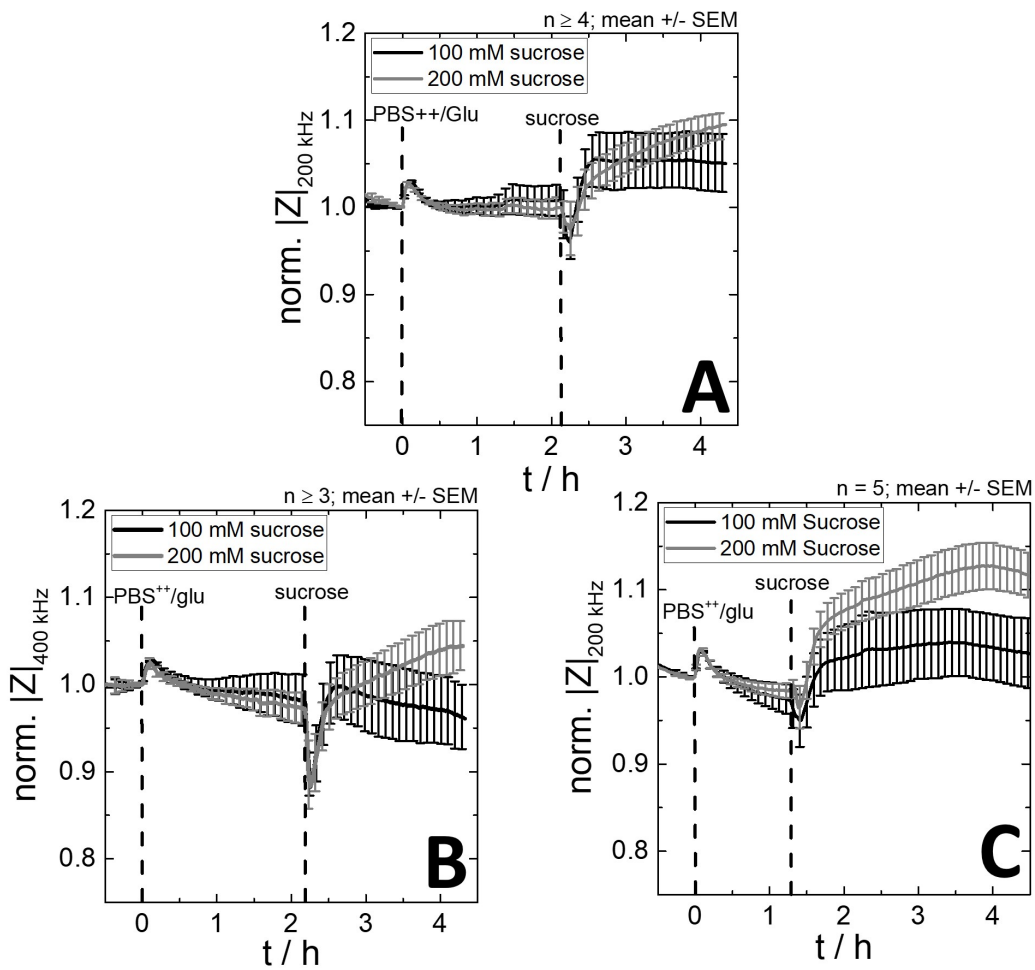


Figure 7.18: Measurement of the time-dependent impedance change due to the influence of an osmotic pressure. NRK cells were cultivated on IDEs and were measured on the third day after seeding. The control (PBS⁺⁺/glu) was added at $t = 0$ h and the non-isotonic solutions (100 mM and 200 mM sucrose) at $t = 2.1$ h (IDE 10 and IDE 12) and at $t = 1.2$ h (IDE 20). All data were normalized to the initial values before addition of the control (IDE 10: $|Z| = (203 \pm 30) \Omega$; IDE 12: $|Z| = (153 \pm 25) \Omega$; IDE 20: $|Z| = (272 \pm 42) \Omega$). For the different IDEs the frequency f_{max} was used: **A:** IDE 10 at 200 kHz ($n \geq 4$), **B:** IDE 12 at 400 kHz ($n \geq 3$) and **C:** IDE 20 at 200 kHz ($n = 5$). The mean with the SEM is plotted.

The time-dependent change of the normalized impedance of the NRK cells for three different IDEs can be seen: i) IDE 10 in fig. 7.18 **A**, ii) IDE 12 in fig. 7.18 **B** and iii) IDE 20 in fig. 7.18 **C**. Again the isotonic control (PBS⁺⁺/glu), added at $t = 0$ h, does not have any impact on the measured impedance for none of the IDEs. The addition of the 100 mM sucrose solution causes a slight increase of the impedance, but within the errors the change is not very expressive. An increase can also be seen due to the impact of 200 mM sucrose. After a small dip immediately after the addition, the impedance is slowly increasing during the remaining measurement starting from the initial value.

Comparing the time-dependent impedance changes of the NRK cells measured with the 8W10E electrodes and the IDEs after addition of non-isotonic solutions reveals clear differences. The impedance measured with the 8W10E electrodes is strongly decreasing after addition of the non-isotonic solutions and the calculated ECIS parameter show a decreased impedance of the cell-cell contacts and of the cell-electrode junctions. Also the specific cell membrane capacitance is decreasing. Contrary to this, nearly no change in the impedance after increasing the osmotic pressure can be seen for the IDEs. There is even a small rise of the impedance of the NRK cells incubated with 200 mM sucrose recognizable. Consequently, the change of the cell shape of the NRK cells as a result of the increase of the osmotic pressure has a significantly different effect on the impedance measured with the 8W10E electrodes and the IDEs.

7.3.3 Discussion

During hyperosmotic pressure cell lines react differently to deal with this stress and each cell line has an individual capacity to handle it (Nakanishi et al., 1988). Also the regulation of the volume change is dependent on the cell line (Baumgarten and Feher, 2001). In general, osmotic pressure can be defined as the required hydrostatic pressure which is needed for the inhibition of the osmotic flow across a barrier (Baumgarten and Feher, 2001; Cath et al., 2006). Most cell membranes have a higher permeability to water than to solutes leading to a cell swelling or shrinking in hypoosmotic or hyperosmotic solutions, respectively (Fullerton et al., 2006). The regulation of the cell volume can lead to a reorganization or deformation of the cytoskeleton (Baumgarten and Feher, 2001). The hypertonic pressure used in this work, leads to dehydration and a corresponding compression of the cell bodies (Sapper et al., 2006). The impedance change due to a hyperosmotic pressure was analyzed for two cell lines: i) MDCK II and ii) NRK cells leading to different results. MDCK II cells have many distinct transport systems from kidney tissues (Roy and Sauve, 1987). Consequently, many different reactions can be measured with a hy-

perosmotic pressure. Among others, the synthesis of sulfated glycosphingolipids in MDCK II cells was increased in hyperosmotic medium (Niimura and Ishizuka, 1990). Furthermore, the K^+ and Cl^- concentrations inside the cells were increasing (Baumgarten and Feher, 2001; Nakanishi et al., 1988; Roy and Sauve, 1987), whereas the membrane potential was not changing (Roy and Sauve, 1987). Additionally, the myo-inositol concentration was rising in parallel to the osmolality (Nakanishi et al., 1988), just to name some influences.

The main part of the ECIS signal is the change in the cell size. In general, MDCK II cells have a low water permeability at the apical side (Simmons and Tivey, 1992). These cells can activate specific ion and amino-acid transport pathways which regulate the volume as a reaction to the hyperosmotic pressure (Roy and Sauve, 1987). Nakanishi et al. tested the influence of an increase of osmolality to 615 mOsmol/kg on MDCK II cells and observed that the cells start to round up and to detach within at time of 24 h. Furthermore, they measured a decreased water content in the cells (Nakanishi et al., 1988). This underlines the cells' shrinking of MDCK II cells. Roy et al. saw as a fact of the addition of a hyperosmotic solution of 475 mOsmol/kg that during this shrinkage the intercellular space of the cells did not change. The anticipated widening of the spaces initiated with the smaller cell sizes did not occur, due to the fact that the cross section of the cells was not reduced. The decreasing cell volume and the shrinkage could only be measured in the declining height of the cells. MDCK II cells were attached to a rigid surface and had strong tight junctions, with the result that only the apical membrane can move freely (Roy and Sauve, 1987). Consequently no influence in the cell-cell contacts occurred.

This all corresponds with the calculated ECIS parameters. R_b , which is the barrier resistance, does not change significantly with the 100 mM due to the fact, that the cell-cell contacts were not changing. With higher concentration R_b is increasing showing that the higher hyperosmotic pressure influences the cell-cell contacts. The parameter α is linked to the current flow in the cleft between the cells and the substrate. It is dependent on the cell radius r_c , the resistivity of the electrolyte in the cleft ρ and the distance between cell and substrate h like following:

$$\alpha = r_c \sqrt{\frac{\rho}{h}} \quad (7.1)$$

With the microscopic analysis of Roy et al. it was shown that the radius was not changing. As an explanation of the increased values in the experiments two opposing aspects must be taken into account: i) the cells were changing their distance to the electrodes due to the shrinking and ii) the resistivity of the electrolyte in the cleft was changing.

The reason for this changes are the tight junctions of the MDCK II cells. These tight junctions close the intercellular diffusion pathway with the result that epithelial cell layers act as a selective permeability barrier which separates two liquid compartments (Wegener and Galla, 1996). In this work the osmolarity of the electrolyte was adjusted by addition of sucrose. It was found that sucrose permeates with $(0.9 \pm 0.2) \cdot 10^{-7}$ cm/s across MDCK II cells (Wegener et al., 2000b). Wegener et al. concluded that due to the limitation of the sucrose permeation across the cell layer, water is drawn out from the cell bodies but also from the water-filled space of the intercellular cleft and the space between the cells and the substrate (Wegener et al., 2001). This transepithelial water transport can be seen for various epithelial cell layers (Reuss, 2001). As a result of the water loss in the space underneath the cells, the distance between the cell and the substrate is decreasing and the immobilization and the ion concentration of the remaining water may be heightened (Wegener et al., 2000b). As seen in equation 7.1 these two effects are contrary. With a decreased cell-substrate distance α is increasing and with an increased ion concentration α is decreasing. This cleft is very small and even small changes in ion concentrations have a huge influence on it. The resulting α is probably a mixture of both effects. The third parameter is the decreasing C_m which symbolizes the capacitance of the cell membrane. C_m is dependent on the topography of the cell membrane. Due to the explanation that the height of the cells is changing, the cell membrane is changing. When the cell is shrinking, the membrane will be more squeezed together which decreases C_m because the current pathway is more restricted. The combination of these three parameter explains the course of the impedance of the 8W10E electrodes.

The principal signal changes measured with the IDEs can also be interpreted with the previous explanations. The increased ion concentration underneath the cells and the decreased cell-substrate distance also influences the measured impedance of the IDEs. Both opposing effects play a role in the results. The difference of the measurement with the IDEs to the 8W10E electrodes is the higher magnitude of the impedance change in the case of the IDEs. It was shown in chapter 6.1 in fig. 6.3 that the cell height has a significant influence on the distribution of the electric field using IDEs with a subcellular dimension. The smaller the cell height is, the higher is the part of the electric field in the intercellular cleft. With the original cell height of $h = 5 \mu\text{m}$ of the MDCK cells (Lo et al., 1995) it was shown in the simulations that the main part of the electric field is distributed underneath the cells, while with decreasing height of the cells, the electric field is increasingly focused on the intercellular cleft. As mentioned previously, the MDCK II cells reduce their cell height as a reaction to the hyperosmotic pressure. Using the IDEs with subcellular dimension this shrinkage means that the focus of the electric field is shifted to the

intercellular cleft. The strong cell-cell contacts of the MDCK II cells have then a higher influence on the measured impedance, resulting in a higher time-dependent impedance increase compared to the 8W10E electrodes.

The time-dependent impedance of the NRK cells shows a completely different course than of the MDCK II cells. The big difference to the MDCK II cells is that since the NRK cells do not form tight junctions only a weak permeability barrier of sucrose exist. Due to this nearly open intercellular cleft the non-isotonic solution flows around the cell body and the water transport, as explained with the MDCK II cells, is not implemented to the same extent. This was also observed with the measurement of 3T3 fibroblasts which do not form tight junctions (Wegener et al., 2001). Wegener et al. calculated a permeation rate of sucrose across these cells of $(1.6 \pm 0.3) \cdot 10^{-5}$ cm/s which is almost a factor of 100 larger than the one of the MDCK II cells (Wegener et al., 2000b). Consequently, the hyperosmotic pressure on the NRK cells causes the shrinkage of the cells. Due to the fact that NRK cells do not have strong cell-cell contacts, those were weakened or even destroyed with the shrinking of the cells. This is seen in the decreasing cell barrier resistance (R_b). The current is less restricted and flow more easily resulting in a lowered impedance. The decrease of C_m does not differ much from the MDCK II cells and can also be explained due to the change of the membrane area and the associated squeezing. The shrunken cells round up more and more and the cleft between the cells and the substrate is becoming bigger, leading to a decrement of α .

The course measured with the IDEs cannot be explained precisely at the current state of knowledge. Due to the subcellular dimension of the electrodes, the main part of the current is flowing underneath the cells. Consequently, the increased ion concentration underneath the cells is influencing the measured impedance strongly and due to the shrinking of the cells there are less cell-cell contacts and the electric field can distribute more easily. The measured impedance is probably a combination of several effects.

To sum it up, it was possible to detect the time-dependent impedance change induced from the influence of a hyperosmotic pressure. Both 8W10E electrodes and IDEs could be used to measure the change of the MDCK II cells. With the IDEs a higher impedance increase can be achieved. Otherwise, it was possible to calculate the ECIS parameters with the 8W10E electrodes and due to this, to further understand the exact process of the shrinkage of the cells. The influence of the hyperosmotic stress to NRK cells could be measured on the one hand very clearly with the 8W10E electrodes. On the other, nearly no change in impedance could be seen with the IDEs. Consequently, IDEs can be used for measurements of the hyperosmotic pressure but the benefit depends strongly on the cell type.

7.4 Monitoring signal transduction cascades

When cells are exposed to a special substance, as for instance a receptor ligand, different signal transduction cascades can be started leading to complex cellular events. This causes, for example, a modulation of the cytoskeleton with the associated changes in the cell shape and volume, cell-substrate junctions and cell-cell interactions which influence the flow of the extracellular and transcellular current. This in turn can be monitored with an impedance measurement. The aim of this chapter is to measure these changes with the IDEs in comparison to the ECIS electrodes. First, the H_1 receptor was stimulated with histamine and secondly, the Ca^{2+} concentration inside the cells was increased with a calcium ionophore.

7.4.1 Impedance-based analysis of the stimulation of the H_1 receptor with histamine

The biggest and most important group of receptor targets in drug discovery represent the G-protein-coupled receptors (GPCRs). These receptors are distributed uniformly in the whole body, for example in the skin, in the lung and in the gastrointestinal tract and can cause smooth muscle contraction, neurotransmission, dilatation of capillaries and many more (Panula et al., 2015). Specific stimulation of these cell surface receptors leads to different effects on the actin cytoskeleton influencing cellular parameters which can be measured by impedance-based cell assays (Verdonk et al., 2006). In this chapter, the H_1 receptor (H_1R) was stimulated with 10 μM histamine (the structural formula is shown in fig. 7.19 A). Histamine is a biogenic amine which acts as a local mediator in the skin, gut and immune system or as a neurotransmitter in the nervous system (Panula et al., 2015). It can bind to different histamine receptors like H_1 , H_2 , H_3 and H_4 whose expression is dependent on the cell type. The U373 cells, used in this chapter, express the H_1 receptor which belongs to the family of the rhodopsin-like G-protein-coupled receptors. When the receptor is activated by histamine, a signal cascade is starting leading to an rise of cytosolic Ca^{2+} which changes the cell morphology (Lieb et al., 2016b). The cascade and the associated change in the cell shape will be explained in more details in the later discussion. The stimulation of U373 cells with histamine and the associated impedance change is shown in fig. 7.19. The control is an addition of L-15 medium to exclude temperature or liquid handling effects on the signal. In none of the measurements a significant influence of the control can be seen leading to the conclusion that the signal is originated from the H_1 receptor stimulation alone. The characteristic impedance courses and the specificity of various histamine H_1 receptor antagonists is widely examined, for example in Lieb et al., 2016a.

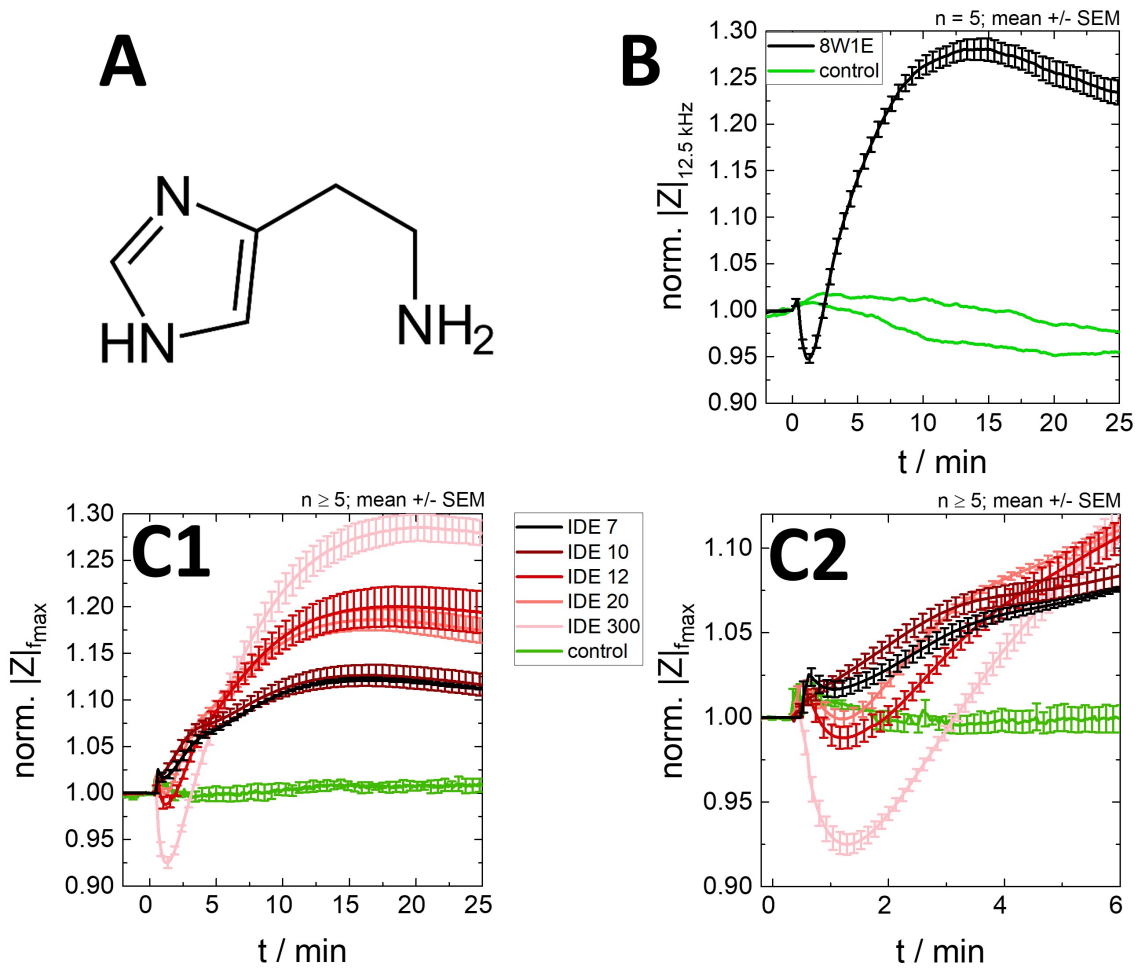


Figure 7.19: Time course of the normalized impedance during stimulation of H_1R expressed by U373 cells with $10 \mu\text{M}$ histamine at $t = 0 \text{ min}$ monitored with different electrode types at the individual f_{\max} on the third day after seeding. The control consists of L-15 medium. **A:** chemical formula of histamine: 2-(1H-imidazol-4-yl)-ethanamin (IUPAC), **B:** 8W1E electrodes with $n = 5$ (12.5 kHz), **C 1:** IDEs with different pitches at f_{\max} with $n \geq 5$: IDE 7 (400 kHz), IDE 10 (316 kHz), IDE 12 (400 kHz), IDE 20 (200 kHz) and IDE 300 (25 kHz), **C 2:** zoom in C1 to the first 6 min of the measurement. The data were normalized to the last value before addition of histamine (8W1E: $|Z| = (5114 \pm 76) \Omega$; IDE 7: $|Z| = (69 \pm 6) \Omega$; IDE 10: $|Z| = (173 \pm 21) \Omega$; IDE 12: $|Z| = (127 \pm 13) \Omega$; IDE 20: $|Z| = (233 \pm 10) \Omega$; IDE 300: $|Z| = (1015 \pm 71) \Omega$) and the mean with the SEM is plotted.

After the addition of $10 \mu\text{M}$ histamine at $t = 0 \text{ min}$ the normalized impedance of the 8W1E electrodes (fig. 7.19 **B**) is decreasing within the first $t = (1.1 \pm 0.2) \text{ min}$ to a value of $\text{norm. } |Z| = (0.947 \pm 0.004)$ before it increases again until a maximum at $t = (13.8 \pm 0.7) \text{ min}$ is seen. After reaching the maximum the signal is slowly decreasing until the end of the measurement. Nearly the same impedance course can be obtained with the IDE 300 (fig. 7.19 **C1** and **C2**). The first decrease after addition has a minimum at $t = (1.29 \pm 0.09) \text{ min}$ and the following maximum is reached after $t = (20.3 \pm 0.6) \text{ min}$. Declining the pitch of the IDEs the signal is changing gradually

(see fig. 7.19 **C1**). For a better visualization, the impedance change of the first 6 min after addition of histamine is magnified (fig. 7.19 **C2**). The dip in the first minutes after addition can clearly be seen with the IDE 300, whereas a much smaller one is monitored with IDE 20 and IDE 12. With the IDE 10 and IDE 7 the dip disappears and a small shoulder at 3 min arises which also can be observed with the IDE 20 and IDE 12. The height of the maxima is also decreasing with declining pitch (precise data can be seen in tab. 7.1).

The histamine stimulation was further analyzed using different non-insulated active electrode areas (windows) of IDE 10, IDE 12 and IDE 20 (fig. 7.20).

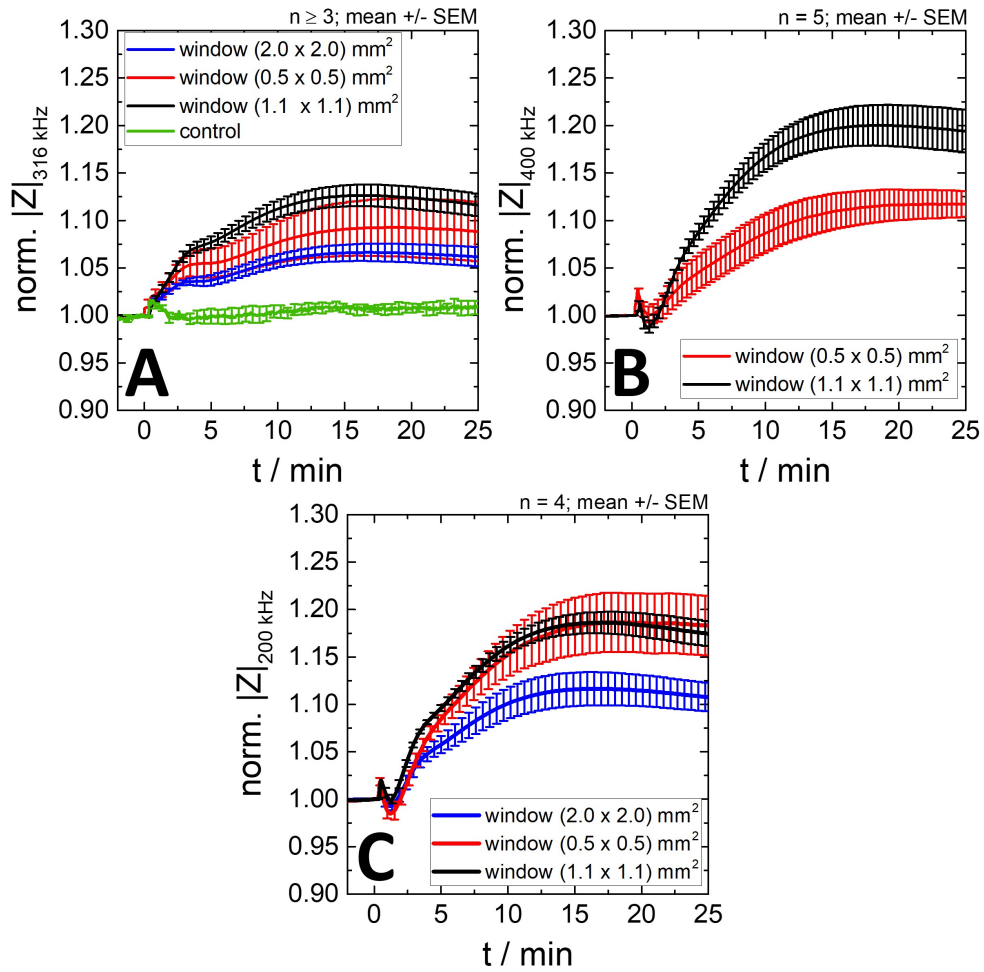


Figure 7.20: Time course of the impedance during the stimulation of H₁R expressed by U373 cells with 10 μ M histamine at $t=0$ min on the third day after seeding. The control consists of L-15 medium. Different IDEs with various sizes of the active electrode areas (windows) at the f_{max} were used: **A:** IDE 10 (316 kHz), **B:** IDE 12 (400 kHz), **C:** IDE 20 (200 kHz). All data were normalized to the last value before addition of histamine (window (0.5 x 0.5) mm²: $|Z| = (623 \pm 15) \Omega$ (IDE 10), $|Z| = (262 \pm 140) \Omega$ (IDE 12), $|Z| = (790 \pm 85) \Omega$ (IDE 20); window (1.1 x 1.1) mm²: $|Z| = (173 \pm 21) \Omega$ (IDE 10), $|Z| = (127 \pm 13) \Omega$ (IDE 12), $|Z| = (233 \pm 10) \Omega$ (IDE 20); window (2.0 x 2.0) mm²: $|Z| = (87 \pm 10) \Omega$ (IDE 10), $|Z| = (100 \pm 6) \Omega$ (IDE 20)). The mean with the SEM is plotted.

For every individual pitch the impedance changes of the electrodes with the different windows have the same trends. The impedance of the IDE 10 (fig. 7.20 **A**) does not show any dip in the first minutes for any window but all time courses show a shoulder at 3min. Increasing the pitch (IDE 12) the dip of the impedance is appearing at both windows (fig. 7.20 **B**) and also the measurement with the IDE 20 reveals a dip of the impedance for every window and a slight shoulder at 4 min (fig. 7.20 **C**). The difference of the electrodes with the various windows is the magnitude of the impedance. The electrodes with the biggest windows (2.0 x 2.0) mm² show the lowest impedance magnitude, whereas the electrodes with the middle window (1.1 x 1.1) mm² reveal the highest one in the case of the IDE 10 and IDE 12. The impedance of the electrodes with the smallest window (0.5 x 0.5) mm² lies in between, with the exception of the IDE 20 with which it is similar to the middle window. The analysis of the single measurements is summarized in tab. 7.1.

Table 7.1: Summary of different parameters of the individual measurements of U373 cells expressing the H₁ receptor which is stimulated with 10 μ M histamine. A distinction is drawn between the different window sizes of the electrode types. The values of $\Delta\text{norm. } |Z|_{\text{max}}$, which is calculated from the initial value to the maximum, and the time points of the minimum (t_{min}) and the maximum (t_{max}) are listed. The data were obtained from fig. 7.19 and fig 7.20.

electrode type	window size / mm ²	t_{min} / min	$\Delta\text{norm. } Z _{\text{max}}$	t_{max} / min
8W1E	-	1.1 ± 0.2	1.28 ± 0.03	13.8 ± 0.7
IDE 7	1.1 x 1.1	-	1.125 ± 0.007	16.1 ± 0.5
IDE 10	0.5 x 0.5	-	1.09 ± 0.04	16 ± 3
	1.1 x 1.1	-	1.14 ± 0.01	17 ± 2
	2.0 x 2.0	-	1.06 ± 0.02	16 ± 1
IDE 12	0.5 x 0.5	1.4 ± 0.3	1.11 ± 0.04	18 ± 4
	1.1 x 1.1	1.3 ± 0.7	1.20 ± 0.05	18 ± 2
IDE 20	0.5 x 0.5	1.2 ± 0.1	1.18 ± 0.08	16 ± 2
	1.1 x 1.1	1.21 ± 0.05	1.19 ± 0.02	16 ± 1
	2.0 x 2.0	1.16 ± 0.10	1.12 ± 0.03	16 ± 1
IDE 300	1.1 x 1.1	1.29 ± 0.09	1.30 ± 0.06	20.3 ± 0.6

The maximal change of the normalized impedance ($\Delta_{\text{norm.}}|Z|_{\text{max}}$) is calculated from the baseline of the measurement to the maximal impedance value. Consequently, the dip of the impedance which is seen for some electrodes, is not included in this calculation of $\Delta_{\text{norm.}}|Z|_{\text{max}}$. The parameters t_{min} and t_{max} represent the time points when the impedance reaches the minimum and the maximum, respectively.

Due to the absence of the impedance dip t_{min} cannot be determined for IDE 7 and IDE 10. Within the errors no significantly different values of t_{min} can be observed for all the other electrode types, including 8W1E electrodes and IDE 300. The values of $\Delta_{\text{norm.}}|Z|_{\text{max}}$ for the 8W1E electrodes and IDE 300, which are not distinguishable within the errors, are bigger than the ones of the IDEs with a smaller pitch. For those IDEs $\Delta_{\text{norm.}}|Z|_{\text{max}}$ is generally higher for the electrodes with the middle window size of $(1.1 \times 1.1) \text{ mm}^2$. The electrodes with the biggest window $((2.0 \times 2.0) \text{ mm}^2)$ show the smallest values, whereas the electrodes with the smallest window $((0.5 \times 0.5) \text{ mm}^2)$ lie in between, with the exception of the IDE 20 with the smallest window laying in the range of the middle one. A further clear difference between the electrode types can be seen for t_{max} . t_{max} is much smaller for the 8W1E electrodes, as the IDEs reach the maximum some minutes later. The biggest difference is measured with the IDE 300 which reaches the maximum $\approx 6 \text{ min}$ later than the 8W1E electrodes.

In summary, it is obvious that the time-dependent curve of the impedance change is strongly determined by the layout of the electrodes. On the one hand, the interdigitated electrodes show a different signal depending on the pitch, on the other hand IDE 300 monitors a comparable signal as the 8W1E electrodes. This proves that dependent on the electrode pitch a different part of the cell reaction can be monitored. The bigger the electrode pitch, the more the whole cell reaction after the stimulation with histamine can be monitored. With a smaller pitch the focus of the measured signal is more on the basal side of the cell.

7.4.2 Monitoring the stimulation of U373 cells with calcimycin

To further analyze the different electrode types calcimycin was used to change the cell morphology. This is also known as calcium ionophore or the antibiotic A-23187 (see structural formula in fig. 7.21 A). It is an ion-carrier and is used to transport cations from a liquid medium into an organic phase (Reed and Lardy, 1972). As a result, it can increase the intracellular Ca^{2+} concentration in intact cells.

The time-dependent change of the normalized impedance for the 8W1E electrodes and the IDE 10 in fig. 7.21 shows a negligible influence of the control solution which contains the solvent (DMSO) in the same concentration as the calcimycin solution.

The measured signal is therefore determined by the impact of calcimycin. The addition of calcimycin to the measurement chamber with the U373 cells cultured on the 8W1E electrodes evokes a dip of the impedance (norm. $|Z| = 0.97 \pm 0.01$) in the first $t = (1.6 \pm 0.1)$ min, followed by an increase without any saturation within the 40 min of the measurement (see fig. 7.21 **B**). The measurement with the IDE 10 reveals a small increase ($t = (1.7 \pm 0.2)$ min) at nearly the same time point as the dip occurs by the 8W1E electrodes before a further rise of the impedance can be seen (fig. 7.21 **C**).

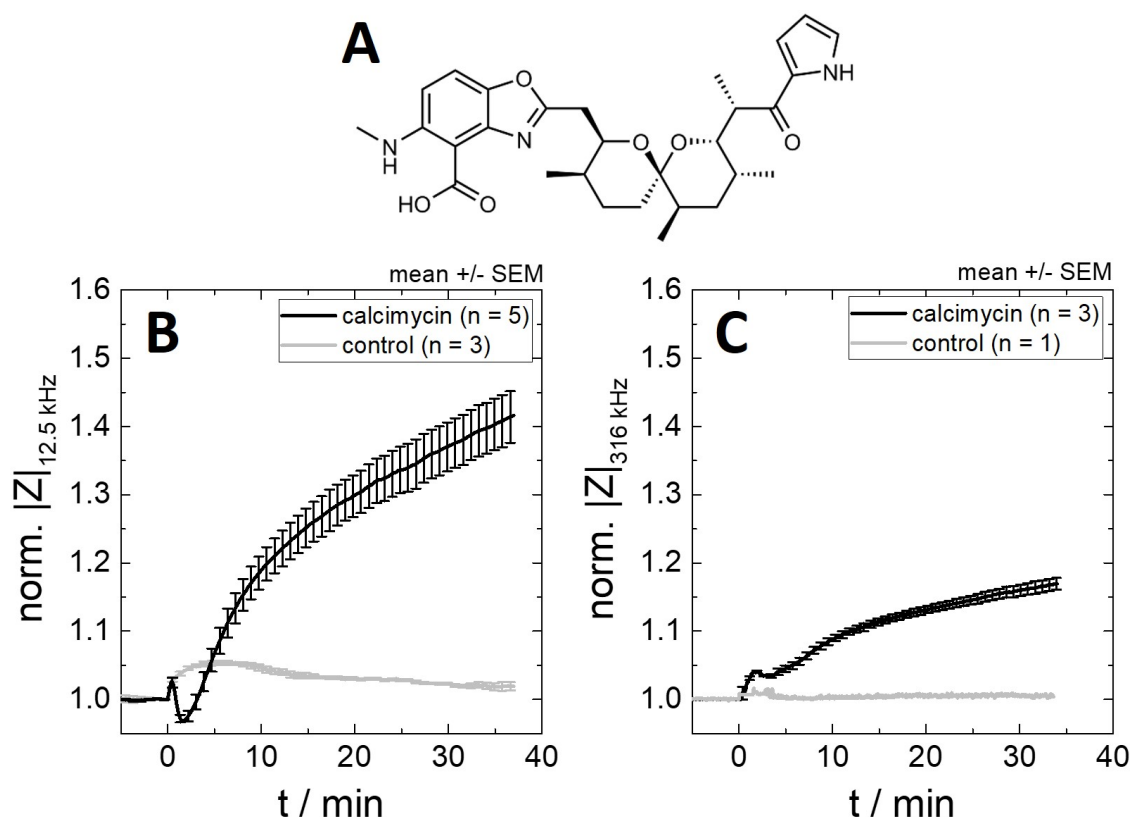


Figure 7.21: Time-dependent impedance change after stimulation of U373 cells at $t = 0$ min with $10 \mu\text{M}$ calcimycin measured with various electrode types. The control contains the same amount of the solvent (DMSO) as the calcimycin solution. U373 cells were stimulated on the third day after seeding. **A**: structural formula of calcimycin, also known as calcium ionophore and antibiotic A-23187, **B**: time-dependent impedance change measured with the 8W1E electrodes (at $f = 12.5 \text{ kHz}$) and **C**: measured with the IDE 10 (at $f = 316 \text{ kHz}$). All data were normalized to the initial value before addition (8W1E electrodes: $|Z| = (4069 \pm 327) \Omega$; IDE 10: $|Z| = (200 \pm 16) \Omega$).

Both graphs resemble the impedance change of the stimulation with histamine in fig. 7.19. Looking at the measurement with 8W1E electrodes, the same magnitude of the dip of the normalized impedance at the same time point after addition and the following increase of the normalized impedance can be seen for both stimulation

measurements. Also with the IDE10 the same short increase and the shoulder of the time-dependent impedance change as with the stimulation with histamine can be seen. This proves that with histamine the intracellular concentration of Ca^{2+} ions is increased and generate those individual impedance time courses.

7.4.3 Discussion

Fast changes in the formation of actin stress fibers can be caused by a direct regulation of second messengers like Ca^{2+} due to classical GPCR signaling pathways or to ionophores. This raised actin polymerization causes a rise in impedance (Verdonk et al., 2006).

Stimulation with histamine

Histamine is an agonist for histamine receptors and induces a signal cascade after binding to these receptors. The exact steps of the signal cascade can be seen in Panula et al., 2015 and Jacoby et al., 2006. In the following only a short overview will be given of the signaling pathway inside the cells.

There exist four known subtypes of histamine receptors: H_1 , H_2 , H_3 and H_4 receptors (Panula et al., 2015). In this work the H_1 receptor, which is G_q -coupled, plays the important role for the measurements with U373 cells. When the receptor is activated by the endogenous agonist histamine, the signal transduction cascade is initiated and the cytosolic Ca^{2+} , the inositol-1,4,5-trisphosphate and diacylglycerol concentrations are increased (Lieb et al., 2016b). An eightfold increase of inositol phosphate in intact cells can be seen within 10 min (Carson et al., 1989). The calcium increase has a maximum at 15-30 s after stimulation and afterwards shows a saturation with a two- to threefold higher concentration than before addition which plays an important role in the regulation of the cell shape (Rotrosen and Gallin, 1986). 4 min after stimulation with 5 μM histamine the cellular Ca^{2+} stores appeared completely depleted (Rotrosen and Gallin, 1986). This raised Ca^{2+} concentration increases the phosphorylation of the 20 kDa myosin light chain, which shows a maximum after 30 s lasting for 90 s before it returns to the basal value after 5 min (Moy et al., 1993). The increased phosphorylation activates the actin cytoskeleton leading to the retraction of the cells and a centripetal tension, mediated due to the interaction of myosin and actin, and the building of F-actin stress fibers (Bischoff et al., 2016). These changes of the cell shape initiated by primarily G-protein activation upon histamine stimulation can be detected with ECIS (Lieb et al., 2016a).

The time courses of the impedance change for the 8W1E electrode (fig. 7.19 B) and for the IDE300 (fig. 7.19 C1) are identical with the measurements of Stolwijk et al. (Stolwijk et al., 2015). The dip of $\Delta|Z|$ in the first two minutes and the later increase within 20 min can be seen for these measurements. On the one hand, no reaction

is monitored under 300 nM, on the other hand the dip occurs with increasing histamine concentration. With an addition of 100 μ M a shoulder at 5 min is monitored (Lieb et al., 2016a; Lieb et al., 2016b). The early transient dip in impedance with the following increase after addition of the agonist is characteristic for a G_q -coupled GPCR (Verdonk et al., 2006). Furthermore, it is known that histamine can induce temporary changes of the barrier properties (Stolwijk et al., 2015). These rapid and transient endothelial barrier disruptions occur maximal 1 min after addition and last under 5 min due to the myosin light chain phosphorylation, among others and lead to a decreased barrier function (van Nieuw Amerongen et al., 1998).

The time courses of the IDEs with lower pitch differ from this. The smaller the pitch is, the less the dip is seen and the more the shoulder at 4 min occurs. The explanation is based on the different penetration depth of the electric field dependent on the electrode gap. In chapter 5.3 it was shown that the main part of the electric field is located in a volume of a few hundred nanometers above the electrodes using IDEs with a small pitch. With the simulation of cells on the IDEs with a small pitch in chapter 6.1 it was further proven that the main part of the electric field is distributed underneath the cells and only a small fraction of the electric field can be located in the intercellular cleft. The use of those IDEs with a small pitch focuses the measurement on the basal side of the cell membrane. Due to the result that the impedance dip cannot be seen for the IDE 7 and IDE 10 it can be concluded that the impedance dip is based on a cell shape change more on the apical side of the cell. With the lowest pitches of IDE 7 and IDE 10 the penetration depth of the electric field is not efficient enough to monitor the whole change of the cell morphology due to the histamine stimulation, whereas with higher pitches like IDE 12 and IDE 20 the dip is more pronounced and the curve approaches the course of IDE 300. The penetration depth of the electric field is consequently more distributed in the intercellular cleft with those higher pitches and the cell shape change on the apical side can be better monitored. The evidence that the penetration depth is decisive for the different course is presented with the IDE 300. This pitch reveals the same impedance change as the 8W1E electrodes showing that not the electrode layout is critical for the detection of the histamine stimulation, but the distance between the electrode fingers and the associated penetration depth. For the shoulder at 4 min no clear explanation can be given right now. In the first 5 min of the stimulation the phosphorylation returns to the basal value and the Ca^{2+} stores are depleted, but the status of the current observations of this work cannot explain this shoulder.

The different impedance magnitudes measured with the electrodes with varied window sizes can be explained with the chosen frequency at which the impedance was measured. The frequency f_{max} of the electrodes with the middle window size of $(1.1 \times 1.1) \text{ mm}^2$ was taken for all windows to enable a direct comparison of the dif-

ferent time-dependent normalized impedance courses. As seen in chapter 6 the electrodes with the various non-insulated electrode areas have a different frequency f_{max} , at which the maximal impedance change occurs, and consequently, different intensities in the impedance can be seen. Due to this fact, only the course of the impedance can be compared. For all windows the same courses dependent on the pitch is seen, which shows that neither an increased sensitivity is achieved nor that a different aspect of the cell is monitored with the varied window size.

Increasing the cytosolic Ca^{2+} concentration with calcimycin

Calcimycin is an ionophore which is able to transport divalent cations, for instance Ca^{2+} , across the cell membrane increasing the intracellular free cytosolic Ca^{2+} concentration (Erdahl et al., 1994; Slaughter and Hobson, 2009). The impedance time course of the stimulation with histamine (fig. 7.19) and with calcimycin (fig. 7.21) shows the same form, the same magnitude and the same time point of the dip and the following increase for the 8W1E electrodes and the increase and the shoulder for the IDE10. Consequently, the increase of Ca^{2+} in the cytosol is sufficient enough to produce the similar ECIS trace as with the histamine stimulation, which proves the importance of the Ca^{2+} for the histamine course. Lieb et al. showed that the increase of intracellular Ca^{2+} alone is able to reveal the same course to those upon the histamine stimulation. The signal of the impedance due to the changed Ca^{2+} concentration can be explained with i) the influence of the actin cortex on the cell morphology and membrane topography and ii) the properties of the Ca^{2+} as a modulator of the cortical actin (Lieb et al., 2016a). Further, this experiment shows that the change of the Ca^{2+} concentration can result in the shoulder in the impedance course of the IDE10.

Application of IDEs in literature

Interdigitated electrodes were not often used in literature for histamine or calcimycin stimulation. There were only some few examples available.

Brischwein et al. invented a screen printed interdigitated Pt electrode with a width and a distance of $\approx 250 \mu\text{m}$, respectively, and analyzed the morphological response of L-929 and HeLa cells. For the stimulation they used $25 \mu\text{M}$ histamine and measured the change of the resistance. The transient dip and the later increase of the resistance change was identical with the typical course of a H_1 receptor activation (Brischwein et al., 2006). This underlines the observation of this work with the bigger pitch of the IDE300 which shows the common course. A different application for the IDEs in this topic was the combination of impedance spectroscopy and live fluorescence microscopy. An optically transparent interdigitated indium tin oxide electrode with a width of $10 \mu\text{m}$ and a spacing of $5 \mu\text{m}$ was invented. The H_1 receptor was stimulated with $100 \mu\text{M}$ histamine and the Ca^{2+} flux and the change of the cell morphology was examined with a fluorescence microscope and the measurement of the impedance.

The timescale of the Ca^{2+} mobilization induced by histamine and the timescale of the decline of the cell-cell adhesion could be brought in line. The microscopy revealed a Ca^{2+} peak with a maximum within the first 60 s after stimulation with histamine. The impedance measurement showed a rapid dip at the same time as the maximum which persisted for a few minutes. Afterwards the values increase for 35 min before they return to the initial value after 80 min (Parviz et al., 2017). This observations with the Ca^{2+} increase at the same time as the dip in impedance underlines the observations and explanation of the measurements in this work that the impedance dip is correlated with the intracellular free cytosolic Ca^{2+} concentration.

In summary, a dip of the time-dependent normalized impedance course could be measured for the IDEs with a higher pitch after stimulation with histamine and calcimycin. For the IDEs with a smaller pitch (IDE 7 and IDE 10) this dip was not present. Based on the simulations in chapter 6.1 and chapter 5.3 it is clear that the penetration depth of the electric field is focused on a volume near the electrodes by using such small pitches. Since the impedance dip cannot be measured with those electrodes with the small pitches, it can be concluded that the cell response is focused on the apical side of the cell after the addition of histamine and calcimycin. With the focus of the electric field underneath the cells with the IDE 10 and IDE 7 those processes on the apical side cannot be detected. This underlines that with IDEs with a small pitch the cell reactions and processes on the basal side of the cells are analyzed. These measurements with histamine and calcimycin prove that with a smaller pitch of the electrodes, the focus can be placed to the basal side of the cells. Consequently, dependent on the electrode pitch various parts of the cells dominate the measured impedance.

7.5 Analysis of the time course of the impedance during adhesion and beating of cardiomyocytes

The IDE 12 and IDE 7 were further tested for their advantages and disadvantages in the measurement of cardiomyocytes. These cells were derived from transgenic mouse embryonic stem cells and have a primary-like cardiac phenotype. In this work the time course of the adhesion, the beating rate and the influence of isoprenaline on the cultivated cells were measured and analyzed. For a possible comparison the 8W1E electrodes served as the commercially available standard.

7.5.1 Monitoring the time course of the cell adhesion of cardiomyocytes on different electrode types

The time course of the adhesion of the cardiomyocytes on the three different electrode types (8W1E electrodes, IDE 12 and IDE 7) were measured for 22 h. The time courses and the corresponding spectra are shown in A.16 and A.17. On the one hand, an increase of the impedance in the spectra and in the time course is revealed for all three electrode types 22 h after seeding the cells (fig. A.16). On the other hand, the capacitance spectra and the time course of the capacitance are decreasing (fig. A.17) after the measured time. This leads to the conclusion that the cells can be detected with all three electrode layouts. Due to the limitation of the measurement device, it was not possible to measure in a frequency range higher than 10^5 Hz with the appropriate time resolution which does not cover the whole range of the impedance increase of the IDEs. The time course of the impedance and the capacitance shows a constant plateau after around 15 h for the IDEs, whereas on the 8W1E electrodes no plateau can be seen but a continuous increase. Within 22 h the cells were not completely adhered and spread on the 8W1E electrodes.

7.5.2 Impedance-based analysis of the beating of the cardiomyocytes cultured on different electrodes

Due to the primary-like cardiac phenotype the cells can contract and relax which changes the measured impedance. This is called beating and is measured in beats per minute, short BPM. As a first analysis, the beats per minute of the cells grown on the three different electrode types were counted. The time points of the counting were varied: i) day 1 after the seeding (after ≈ 24 h) and ii) day 2 after the seeding (after ≈ 48 h). In tab. 7.2 the beating rate of the cardiomyocytes grown on the 8W1E electrodes, the IDE 12 and the IDE 7 are listed with the declaration of the

repetitions. For the IDE 7 no beating of the cells were measured for both days. With the 8W1E electrodes and the IDE 12 it was possible to monitor a beating rate of the cardiomyocytes on day 1 after seeding which was twice as high as on the second day after seeding. On this second day no significant difference between the two electrode types are seen within the error tolerance. The beating rate of the cells fluctuate around 65 BPM for both electrodes types.

Table 7.2: Beating rate (in beats per minute, short: BPM) of the cardiomyocytes grown on various electrode types at different days after seeding. The impedance for each electrode type was measured at a distinct frequency: i) 8W1E at 4 kHz, ii) IDE 12 at 40 kHz and iii) IDE 7 at 40 kHz. The mean with the SD is listed.

day after seeding	beating rate / BPM		
	8W1E	IDE 12	IDE 7
1	140 ± 20 (n = 16)	112 ± 8 (n = 2)	not detectable
2	70 ± 10 (n = 16)	60 ± 10 (n = 11)	not detectable

A further aspect of the beating is the form of the impedance change at different frequencies. To exclude wrong results due to electronic noise of the electrode and the measurement devices, the cell-free electrodes (**a**) were measured at the same frequencies and with the same time resolution as the cell-covered electrodes (**b**). All data were normalized by dividing the measurement by the individual mean value. In fig. 7.22 the measurement of the 8W1E electrodes without cells (fig. 7.22 **a**) and with beating cardiomyocytes on the electrodes (fig. 7.22 **b**) at different frequencies are shown. The cell-free electrodes do not display a big fluctuation (max. Δ norm. $|Z|_{4\text{ kHz}} = 0.003$, max. Δ norm. $|Z|_{40\text{ kHz}} = 0.006$) no matter at which frequency the impedance was measured. Compared to the maximum amplitude of the impedance change of the cell-covered electrodes, these values are only a fraction. This proves that the results are not influenced by the electric noise. The impedance of the cell-covered electrode at 1 kHz is very noisy, albeit a regular increase and decrease of the impedance is observed (max. Δ norm. $|Z|_{1\text{ kHz}} = 0.032$). At 4 kHz the measured impedance shows a regular pattern. This beating is not noisy and a periodical form of every single beat is seen (max. Δ norm. $|Z|_{4\text{ kHz}} = 0.025$). This regular pattern can still be monitored at 40 kHz, even if it is more noisy and smaller (max. Δ norm. $|Z|_{40\text{ kHz}} = 0.011$). Furthermore, the beats do not show the periodical form as at 4 kHz. Different parameter (norm. R, norm. C, norm. Im and the Nyquist plot) were plotted in fig. A.18. All parameters reveal a regular beating at 1 kHz, but the data were too noisy to identify a concrete form. The beats at the norm. R at 4 kHz show a similar form as the norm. $|Z|$, but with a smaller amplitude.

The other parameters display an angular time-dependent impedance course which indicates an electric limitation.

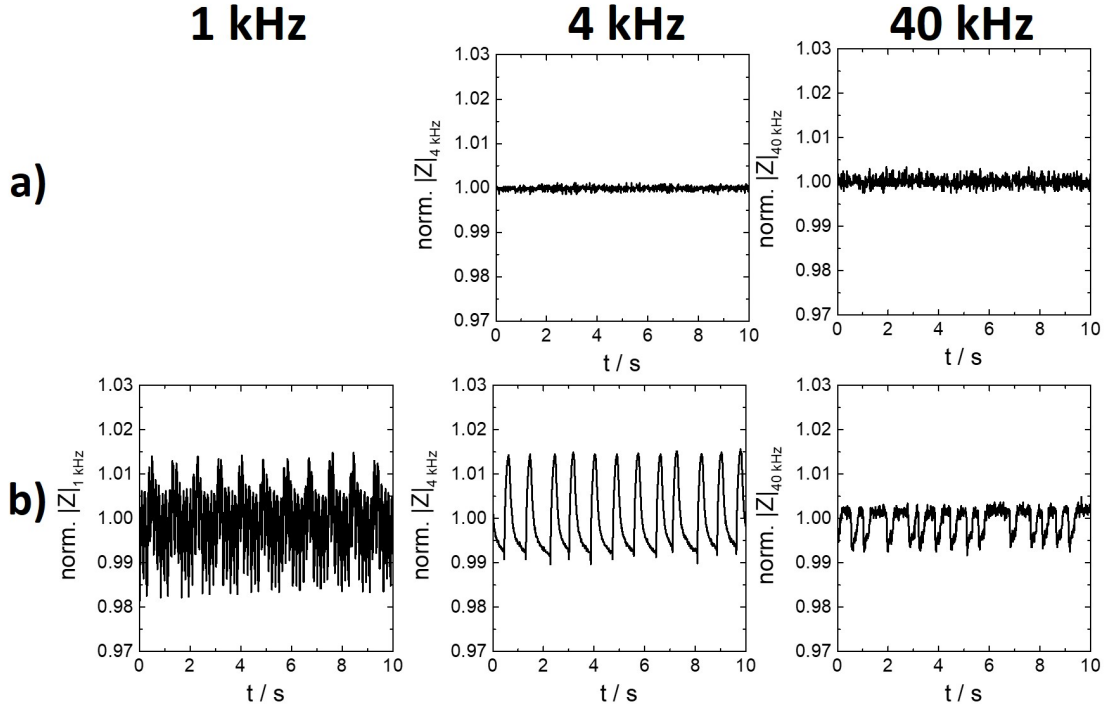


Figure 7.22: Time-dependent impedance change during beating of cardiomyocytes on 8W1E electrodes 48 h after seeding. Different frequencies were shown: i) 1 kHz, ii) 4 kHz, and iii) 40 kHz for the **a)** cell-free electrode and the **b)** cell-covered electrode. All data were normalized dividing the whole measurement by the mean value (cell-free: $|Z| = 7319 \Omega$ (4 kHz), $|Z| = 1762 \Omega$ (40 kHz); cell-covered: $|Z| = 38454 \Omega$ (1 kHz), $|Z| = 19919 \Omega$ (4 kHz), $|Z| = 5797 \Omega$ (40 kHz)).

The beating of the cardiomyocytes can also be analyzed with the IDE 12 and IDE 7. The signals were very noisy and without smoothing no regular impedance change was observed. For this, the Savitzky-Golay smoothing was applied which uses local polynomial to fit small time intervals. All smoothed data were labeled with “10 pts SG smooth”. In fig. A.19 in the appendix the comparison of the raw data and the smoothed ones are visualized. In the raw data of the IDE 12 (fig. A.19 **A1**) a regular impedance increase and decrease can be seen for 40 kHz as well as for 80 kHz, even if it is very noisy. With the high fluctuations of the impedance the beating of the cells cannot clearly be determined. After smoothing with Savitzky-Golay (fig. A.19 **A2**) the individual beats are seen more clearly. Comparing the raw data and the smoothed ones, it can be established that the amplitude and the form of the beats were not influenced with the smoothing. The beating only comes more to the fore. In the case of the IDE 7 (fig. A.19) both, the raw data (**B1**) and the data after smoothing (**B2**), do not reveal a beating.

Fig. 7.23 shows the time-dependent impedance change of the cardiomyocytes on

IDE 12. The impedance of the cell-free electrodes (fig. 7.23 **a**)) reveals a strong fluctuation at 40 kHz and 80 kHz even after smoothing (max. $\Delta \text{norm. } |Z|_{40 \text{ kHz}} = 0.006$; max. $\Delta \text{norm. } |Z|_{80 \text{ kHz}} = 0.024$), whereas with a frequency of 4 kHz nearly no fluctuation can be seen (max. $\Delta \text{norm. } |Z|_{4 \text{ kHz}} = 0.002$). The high fluctuation at 80 kHz is a side-effect of the normalization. The values of the measured impedance are close to the mean value of the whole measurement, which can result in very high values for the calculated normalization. The raw data of the maximum impedance change of the cell-covered electrodes are twice as high as the raw data of the maximum fluctuation of the cell-free electrodes (not pictured). This proves that the high fluctuation with the cell-free electrodes is a side-effect of the calculation of the normalization and that the beating of the cardiomyocytes exceed the electric noise. The cell-covered electrodes (fig. 7.23 **b**)) do not show any regular change in norm. $|Z|$ at 4 kHz, whereas at 40 kHz and 80 kHz a regular normalized impedance increase and decrease can be monitored (max. $\Delta \text{norm. } |Z|_{40 \text{ kHz}} = 0.007$; max. $\Delta \text{norm. } |Z|_{80 \text{ kHz}} = 0.007$). Nevertheless, the beating is very noisy and does not show a distinct form. Furthermore, the amplitude of the beating (max. $\Delta \text{norm. } |Z|_{40 \text{ kHz}} = 0.007$) is much lower than with the 8W1E electrodes (max. $\Delta \text{norm. } |Z|_{4 \text{ kHz}} = 0.025$).

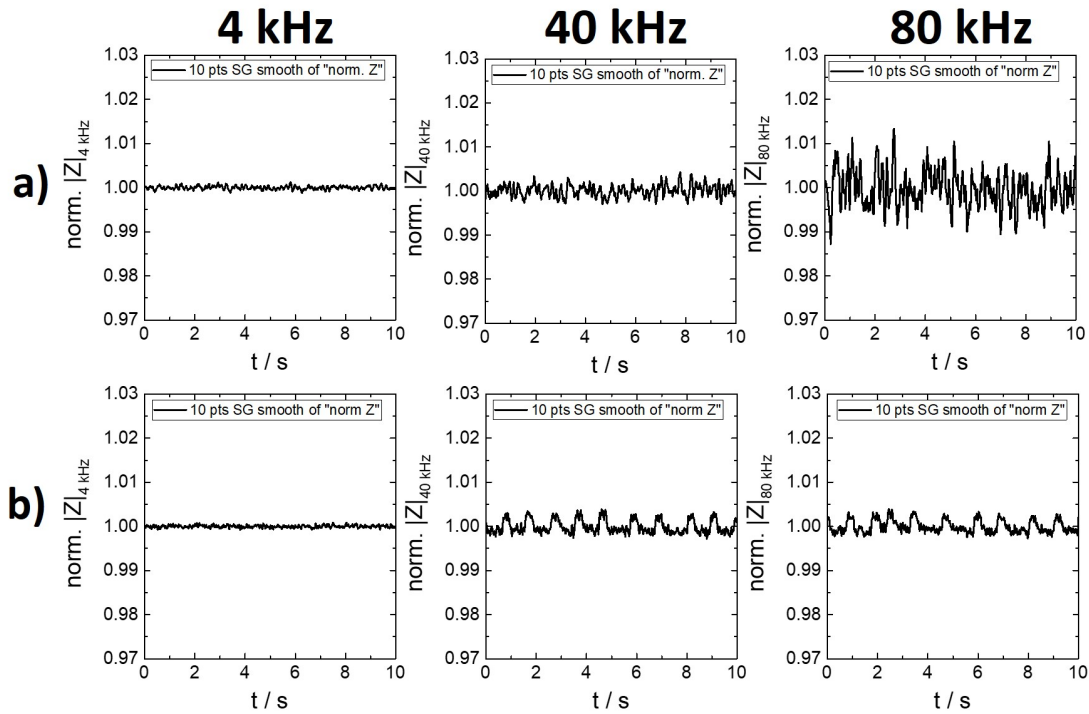


Figure 7.23: Time-dependent change of the impedance during beating of the cardiomyocytes on IDE 12 48 h after seeding. The data were smoothed with the Savitzky-Golay method. Three different frequencies were shown: i) 4 kHz, ii) 40 kHz, and iii) 80 kHz for the **a**) cell-free electrode and the **b**) cell-covered electrode. All data were normalized due division of the whole measurement by the mean value (cell-free: $|Z| = 2695 \Omega$ (4 kHz), $|Z| = 301 \Omega$ (40 kHz), $|Z| = 158 \Omega$ (80 kHz); cell-covered: $|Z| = 4727 \Omega$ (4 kHz), $|Z| = 836 \Omega$ (40 kHz), $|Z| = 594 \Omega$ (80 kHz)).

These observations is also seen by the analysis of different parameters like norm. R, norm. C, norm. Im and the Nyquist plot (see fig. A.20). At 4 kHz no beating can be observed, no matter which parameter is analyzed. At 40 kHz and 80 kHz the norm. R resembles the norm. $|Z|$ with the small noisy and irregular form of the beating. Norm. C and norm. Im have a bigger amplitude, whereas the beating is more noisy and also not very even. The Nyquist plot does not provide further information.

As a third measurement the beats of the cardiomyocytes on the IDE 7 are monitored. In fig. 7.24 a) the cell-free electrodes reveal no fluctuations at 4 kHz, but a strong noisy signal at 40 kHz and 80 kHz, even after the smoothing. This can be attributed to the same reason as for the cell-free electrodes of the IDE 12. Analyzing the cell-covered electrodes (fig. 7.24 b)), the same electric noise at 40 kHz and 80 kHz is seen. No regular pattern of an increase or decrease can be observed which could be significantly distinguished from electric noise. Also the comparison of the raw data of the cell-free electrodes and cell-covered electrodes show no clear difference in the maximum impedance change (not pictured).

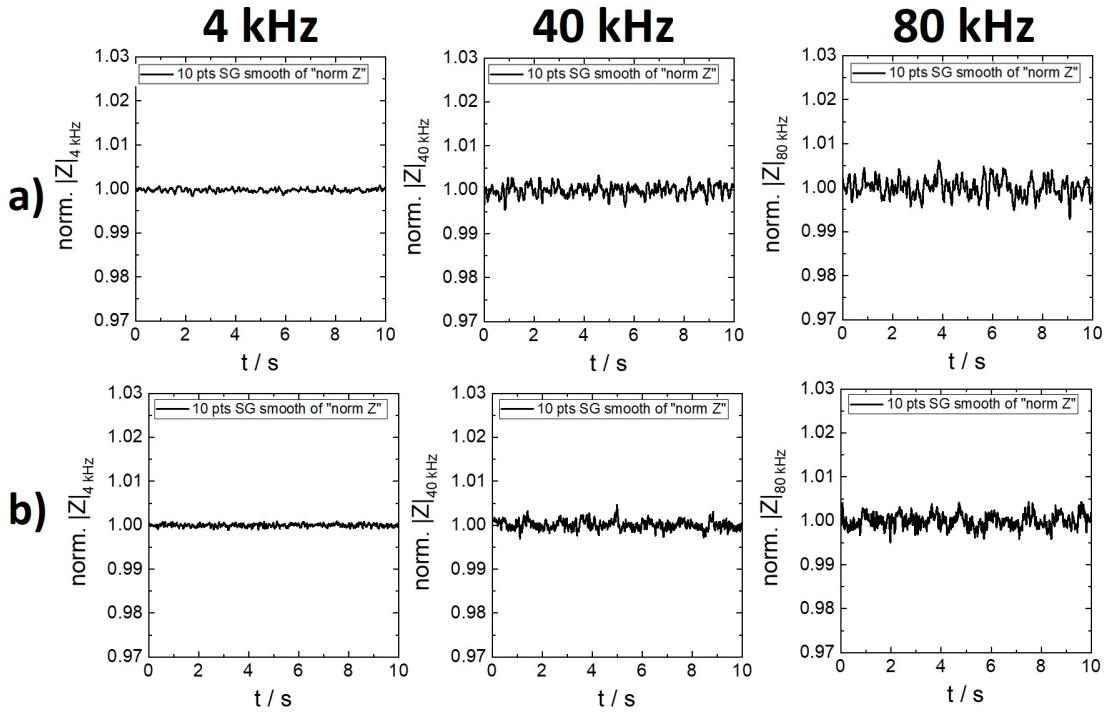


Figure 7.24: Time courses of the change of the impedance during beating of the cardiomyocytes on IDE7 48h after seeding. The data were smoothed with the Savitzky-Golay method. Three different frequencies were shown: i) 4 kHz, ii) 40 kHz, and iii) 80 kHz. **a)** cell-free electrode, **b)** cell-covered electrode. All data were normalized by dividing the whole measurement by the mean value (cell-free: $|Z| = 2986 \Omega$ (4 kHz), $|Z| = 349 \Omega$ (40 kHz), $|Z| = 183 \Omega$ (80 kHz); cell-covered: $|Z| = 3631 \Omega$ (4 kHz), $|Z| = 477 \Omega$ (40 kHz), $|Z| = 287 \Omega$ (80 kHz)).

The beating of the cells can also not be monitored with the analysis of the norm. R, norm. C, norm. Im and the Nyquist plot (see fig. A.21). At 4 kHz no change of any parameter is monitored. At 40 kHz and 80 kHz it is not possible to distinguish the measured signal from the electric noise, independently which parameter is analyzed. Consequently, it is not possible to detect any beating of the cardiomyocytes with the IDE 7.

In summary, the beating of the cardiomyocytes grown on the electrodes can be detected with the 8W1E electrodes and with the IDE 12. The data of the IDE 12 are more noisy and also the amplitude of the beating is only a fraction of the one of the 8W1E electrodes. Furthermore, the beating measured with the IDE 12 does not reveal a distinct form as with the 8W1E electrodes. The measurement with the IDE 7 does not display any difference of the cell-covered electrodes to the electric noise of the cell-free electrodes. Consequently, the IDE 12 are not so good and the IDE 7 are not at all suitable for the analysis of the beating of cardiomyocytes.

7.5.3 Manipulation of the beating rate with isoprenaline

Further, the beating rate was manipulated with 100 nM isoprenaline. This substance is a non-selective β -adrenoreceptor agonist and increases the contraction power and the beating frequency of heart cells. In fig. 7.25 the structural formula and the IUPAC name is shown.

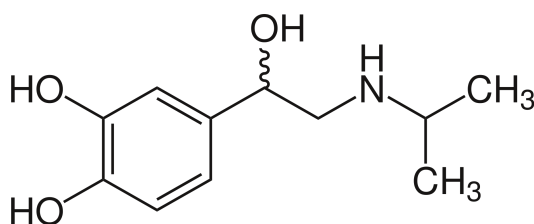


Figure 7.25: Structural formula of isoprenaline (IUPAC name: 4-[1-Hydroxy-2-(isopropylamino)ethyl]-1,2-benzenediol).

Isoprenaline was added and the beating was analyzed at distinct time intervals after the addition. Fig. 7.26 shows the time-dependent change of $\Delta|Z|$ at different time points: i) directly, ii) 5 min, iii) 30 min and iv) 60 min (only for IDE 12) after the addition of isoprenaline. As a control, the beating before the addition is plotted. Furthermore, medium was added in the same volume as the isoprenaline solution and the impedance was monitored 5 min after addition to exclude disturbances of the temperature or volume change. For the measurement with IDE 12 (fig. 7.26 A) and with 8W1E electrodes (fig. 7.26 B) it can be seen, that the medium has no influence on the beating rate. The beating rate cannot be distinguished before

and 5 min after addition of the medium. This proves that temperature and volume changes do not influence the beating of the cardiomyocytes.

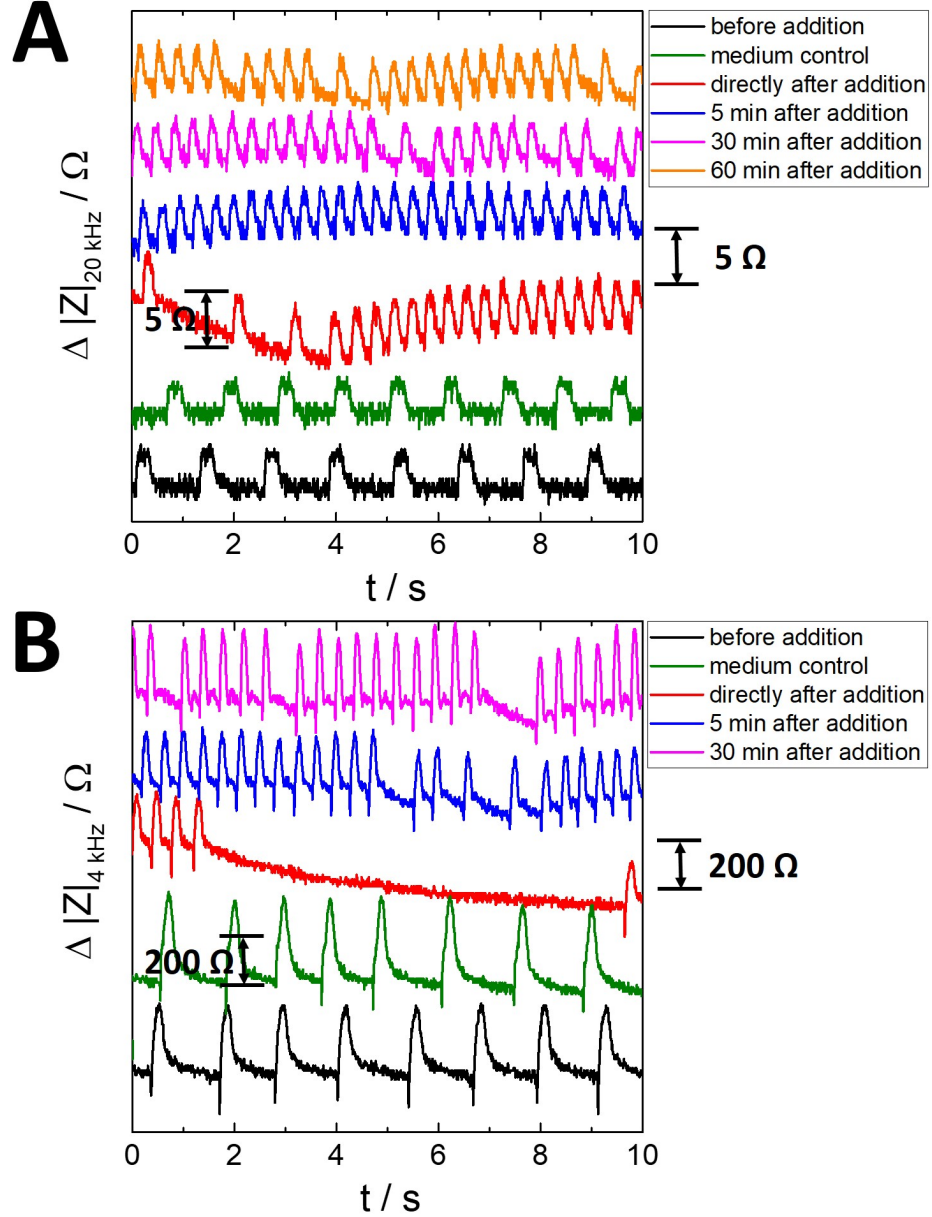


Figure 7.26: Time-dependent change of $\Delta|Z|$ of the beating of the cardiomyocytes at different time points after the addition of 100 nM isoprenaline. The measurement was proceeded with two electrodes at individual frequencies: **A:** IDE 12 (20 kHz), **B:** 8W1E electrodes (4 kHz). The time courses are shifted in y-direction and instead of a y-axis a scale bar of 5Ω (IDE 12) and 200Ω (8W1E electrodes) is added. As a control the measurements before and 5 min after the addition of medium are plotted. $\Delta|Z|$ is calculated due subtraction of the mean value (IDE 12: 1474Ω (before addition), 1522Ω (medium control), 1539Ω (directly after), 1511Ω (5 min after), 1492Ω (30 min after), 1482Ω (60 min after); 8W1E electrodes: 30222Ω (before addition), 25933Ω (medium control), 29790Ω (directly after), 27681Ω (5 min after), 25444Ω (30 min after)).

The big difference of the individual time courses of $\Delta|Z|$ is the increased beating frequency of the cells incubated with isoprenaline. Directly after the addition of isoprenaline some beats are omitted measured with IDE 12 (fig. 7.26 **A**) as well as with 8W1E electrodes (fig. 7.26 **B**). The pattern in both cases is very irregular, but even after 5 min the beating frequency is more regular. The form of the beats matches with the control and shows the regular course. Also after 30 and 60 min (only IDE 12) some irregularities in the beating rate are seen but the beating is clearly increased after addition of isoprenaline.

The raw data of the impedance measurement at different time points after addition of isoprenaline are shown in fig. A.22 in the appendix. In this representation it can be observed, that in the case of the IDE 12 (fig. A.22 **A**) the medium addition does not influence the beating frequency, but the impedance value is increased (from $|Z| = 1474 \Omega$ before addition to $|Z| = 1544 \Omega$ directly after the addition). During the measurement the impedance is decreasing bit by bit until the initial impedance values are reached again after 60 min. A medium control was also measured for the 8W1E electrodes (fig. A.22 **B**), but due to the different initial impedance values of the electrodes it is not possible to plot the data into this graph. For the addition of isoprenaline it can also be seen that the impedance is increasing after addition in the case of the IDE 12 (from $|Z| = 1474 \Omega$ before addition to $|Z| = 1537 \Omega$ directly after the addition) and it is decreasing in the case of the 8W1E electrodes (from $|Z| = 30194 \Omega$ before the addition to $|Z| = 25490 \Omega$ after 30 min). These changing impedance magnitudes are related to temperature and volume effects due to the addition of the solutions. Nevertheless, it has to be emphasized that the beating rate is not influenced by these effects.

The individual beats of the cardiomyocytes can be counted and the beating rate can be calculated for every time point after addition of isoprenaline and the medium control. Analyzing this beating rate it is obvious that 100 nM isoprenaline increases the beating dramatically (see fig. 7.27). After addition, the beating rate with isoprenaline is twice as high as with the added medium control. Measuring the beating rate of the incubation with isoprenaline with the IDE 12 a slight decrease after 60 min can be seen on the one hand, on the other hand the beating of the control is increasing (fig. 7.27 **A**). Due to the small number of repetitions the trends of the changing beating rate during the measurement are not convincing and no further conclusions can be drawn. The beating rate monitored with the 8W1E electrodes shows different values at the different time points (fig. 7.27 **B**). Right after the addition of isoprenaline the beating pattern is irregular and the beats are lower at the beginning than after 5 min and 30 min. Nevertheless, it was only possible to repeat the measurement once. This does not allow any further conclusions to be drawn.

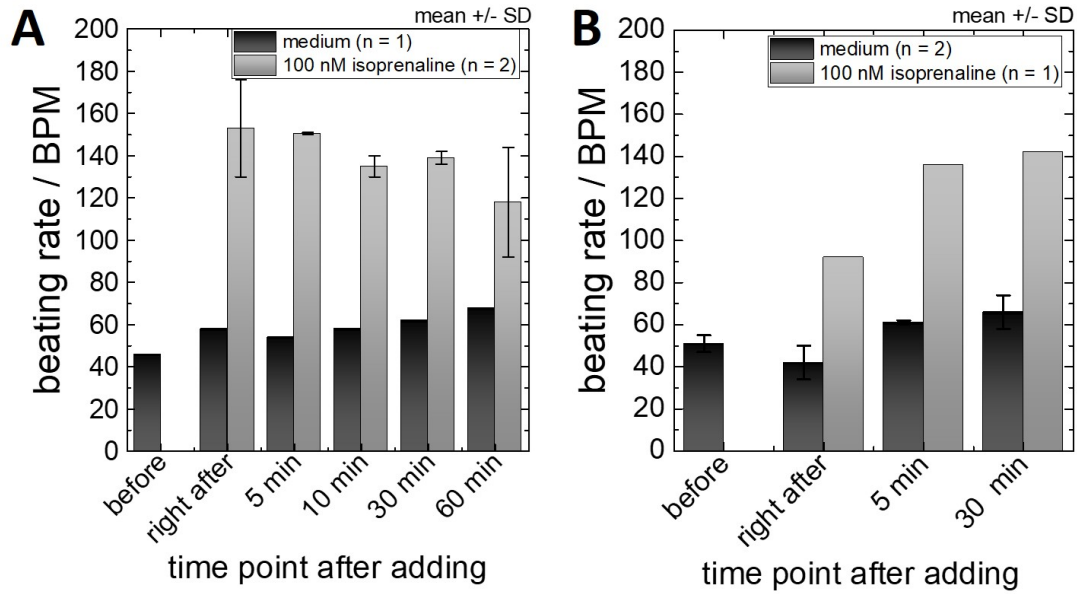


Figure 7.27: Beating rate of the time course in fig. 7.26 with the influence of 100 nM isoprenaline. The beating rate at different time points are determined before or after the addition of isoprenaline or the medium control. **A:** IDE 12 (20 kHz); **B:** 8W1E (4 kHz). The mean with the SD is plotted.

In summary it can be said that the increased beating rate can be measured with the 8W1E electrodes as well as with the IDE 12. The form of the beats is not changing and only the frequency of the beats is increasing.

7.5.4 Discussion

By analyzing the mouse stem-cell derived cardiomyocytes it was possible to monitor the mechanical movement of the spontaneously contracting cells. This beating results from cardiac contractions that are caused by the cardiac action potential involving several ion channels (Li et al., 2016). The myofilaments serve as the contraction actuator and Ca^{2+} ions are essential second messengers (Scott et al., 2013). Bers et al. investigated the exact process: during the action potential, Ca^{2+} ions come into the cell through ion channels which mediates the release of Ca^{2+} from the sarcoplasmic reticulum. This increases the free Ca^{2+} concentration inside the cell. The free Ca^{2+} ions are able to bind to the myofilament protein troponin C and activates the myosin attachment to the actin filament which powers on the contractile machinery. For the relaxation the Ca^{2+} concentration must be decreased again. For this, the ions dissociate from troponin and are transported out of the cytosol. The half-maximal activation needs a concentration of 70 μmol of Ca^{2+} per liter of cytosol (Bers, 2002).

The periodic contractile activity could be monitored with the 8W1E electrodes and the IDE12. This demonstrates the possibility to use the impedance readout to monitor rhythmic contraction and relaxation cycles. Nevertheless, during the first 24 h the beating differentiated from the later measurement. After the adhesion, the cells started sporadic contractions at the beginning, because multiple beating centers were present. Only after a few days a synchronization over the entire well can be seen and the signal became sharper and more regular (Doerr et al., 2015). Abassi et al. also revealed that no consistent beating pattern could be monitored within the first 24 h after seeding. After 48 h the entire monolayer of the mouse cell-derived cardiomyocytes began to beat synchronously. They detected (80 ± 5.7) beats/ min^{-1} (Abassi et al., 2012). This higher beating rate is the result of the higher measurement temperature (37°C) compared to the lower temperature in the present work (34°C) which slow down the contractile activity.

The 8W1E electrodes show a regular pattern of the beating depending on the correct frequency. The sharp and regular form of the beats at 4 kHz after 48 h is similar to typical beating pattern of the same cell type in literature (see for example Himmel, 2013 or Xi et al., 2011). This ensures that the conventional contractility of the cells can be monitored with the 8W1E electrodes. With the IDE12 a regular beating can be revealed. The big difference to the 8W1E electrodes is the irregular beat form and the strong electrical noise. This can be attributed to the focus of the electric field underneath the cells. The monolayer of the cardiomyocytes is beating in a synchronous manner after 48 h but the IDE12 can only detect a small part of the beating cells. The focus of the electric field underneath the cells impeded a detection of the complete contraction of the cells. The measurement with the IDE7 underlines this explanation. In fig. 7.24 no clear periodicity can be revealed. It was proven with the simulations of this electrode gap (see chapter 6.1) that the main part of the electric field is distributed underneath the cells and that the intercellular cleft has only a small influence on the electric field. Consequently, it is not possible to detect any beating with the IDE7 and only very noisy beating with the IDE12 due to their subcellular dimension and the corresponding focus of the electric field underneath the cells.

The beating rate is further manipulated with isoprenaline. It is an agonist for the β -adrenergic receptor activating a GTP-binding protein which in turns leads to the production of cAMP due to the adenylyl cyclase (Bers, 2002). This enables a protein kinase to phosphorylation of many proteins connected to the excitation-contraction coupling (Bers, 2002). The beating rate is consequently raised, while maintaining the amplitude of the beats. In this work the beating rate measured with the IDE12 were increased by $(44.6 \pm 0.9)\%$ and with the 8W1E electrodes by $(46 \pm 6)\%$ after the addition of 100 nM isoprenaline. This is in the same range as the increase of

mouse induced pluripotent stem cell derived cardiomyocytes measured by Jonsson et al.. With a concentration of $0.08 \mu\text{M}$ isoprenaline they monitored a rise of the beating rate from $(170 \pm 9) \text{ min}^{-1}$ to $(315 \pm 16) \text{ min}^{-1}$ which shows an increase by $(53 \pm 6) \%$ (Jonsson et al., 2011). A declaration for the slightly higher beating rate despite the lower concentration can be traced back to the higher temperature (37°C) in comparison to the lower temperature in this work which retards the beating. Consequently, it is possible to measure beating manipulation with the 8W1E electrodes as well as with the IDE 12.

Application of IDEs in literature

A further question is, if interdigitated electrodes are basically not suitable for analyzing the contractility of cardiomyocytes. In literature IDEs are used in some cases for detection of these cells.

Qian et al. used gold IDEs with a width and gap of $5 \mu\text{m}$, respectively, to analyze the influence of different drugs on the growth and contraction of human induced pluripotent stem cell derived cardiomyocytes. They examined norepinephrine which increased the beating rate to 38% at a concentration of 400 nM . Furthermore, the contractility was inhibited with blebbistatin. After addition of $10 \mu\text{M}$ they saw a flat baseline and a static tissue in the microscopic analysis. The beats had a small amplitude and a noisy form which closely resembled the measurement in the present thesis (Qian et al., 2017). This underlines that with a small gap between the electrodes the penetration depth of the electric field is not efficient enough to monitor the whole contraction. Increasing the gap a different beating form can be observed. With interdigitated gold electrodes with a width of $40 \mu\text{m}$ and a gap of $60 \mu\text{m}$ the beating of heart cells of neonatal rats (1-3 days old) were analyzed. The authors wanted to test the cardiotoxicity of doxorubicin, which is a chemotherapeutic agent. A concentration-dependent influence on the amplitude could be seen. With an addition of $20 \mu\text{M}$ the amplitude diminished to 93% , and to 50% with an incubation of $200 \mu\text{M}$. Furthermore, the beating rate was decreased to 99% with $20 \mu\text{M}$, and to 68% with $200 \mu\text{M}$ (Xiao et al., 2010). Further, the design of the IDEs was varied. Hu et al. used gold circles (diameter of $100 \mu\text{m}$) in a row with a regular gap of $35 \mu\text{m}$ between two rows of electrodes. The beating function of human induced pluripotent stem cell derived cardiomyocytes was analyzed after addition of different drugs, for example: i) astemizole, ii) sertindole, iii) cisapride, iv) droperidol or v) isoprenaline (Hu et al., 2015). A similar interdigitated electrode layout with circle-on-line branches with a diameter of $100 \mu\text{m}$ and a gap of $50 \mu\text{m}$ were used to measure dysfunctional models of different drugs. All of these drugs were targeting the excitation-contraction coupling of human induced pluripotent stem cell derived cardiomyocytes. Among others, blebbistatin, which is a myosin inhibitor suppressing the contraction, and isradipine, which inhibits Ca^{2+} ion channels, were tested

(Hu et al., 2018). The same layout with circles in a row of the gold electrodes was used from Gu et al. to evaluate cardiac side-effects of the drugs. The electrodes had a diameter of $70\text{ }\mu\text{m}$ and a gap of $25\text{ }\mu\text{m}$ between the branches. On this layout HL-1 cardiac muscle cells were seeded in different densities and the viability and the electrophysiological activities to cardiac drugs were analyzed. Vinblastin, an anticancer and chemotherapy drug, showed a strong effect on the cell viability (79.83 % decrease after 24 h) and nifedipine, which has effects on the special calcium channels, influenced the beating (86.20 % viability after 24 h) (Gu et al., 2019). A different type of interdigitated electrodes was invented to convert the mechanical contraction of cardiac cells into electrical power due to the piezoelectric effect. The cells of hearts of neonatal rats were seeded on a diaphragm. The interdigitated gold electrodes on one side of the diaphragm had a gap of $80\text{ }\mu\text{m}$ and precluded a direct contact of the cells with the electrodes. It was possible to convert mechanical energy of the beating into electrical energy with a high sensitivity to low-frequency external signal (Choi et al., 2010).

All of these IDEs with bigger dimensions reveal a sharp form of the beats and a high amplitude. The pattern is similar with the conventional measurements. This proves that IDEs can be used for analyzing the contractility of cardiomyocytes, but the dimensions are decisive. If the gap is too small, the penetration depth of the electric field is not efficient enough to monitor the whole beat. This includes the IDEs used in this work. With a gap of $6\text{ }\mu\text{m}$ (IDE 12) the beating can be seen but in an irregular and noisy manner, whereas with a smaller gap of $3\text{ }\mu\text{m}$ (IDE 7) the periodicity of the beating is not visible.

As a consequence it can be concluded that there are no advantages in using IDEs with a subcellular dimension for the analysis of cardiomyocytes because these electrodes are not suitable to measure cardiomyocytes due to the focus of the electric field underneath the cells and the corresponding small penetration depth of the electric field.

7.6 Impedance-based analysis of the cytotoxicity of BPA

As a further aspect it was tested, if the IDEs can be used for cytotoxicity assays. The impact of bisphenol A (BPA) on cultured cells was studied with a whole set of different impedance-based cell assays. The complete study was realized with different ECIS electrodes and the critical ones were repeated with IDE 12.

Bisphenol A (BPA, 4,4'-(propane-2,2-diyl)diphenol) (see fig. 7.28) is one of the most commonly used chemicals worldwide. It is a synthetic organic chemical which is frequently applied as an additive in the production of clear and robust plastics like polycarbonate and resins (Staples et al., 1998). These materials are widely used for plastic consumer products such as drinking bottles, medical equipment, children's toys, as coatings on the inside of many food and beverage cans, and many more.

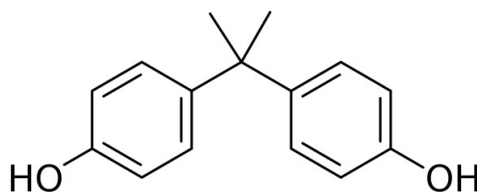


Figure 7.28: Structural formula of bisphenol A, short BPA (IUPAC name: 4,4'-(propane-2,2-diyl)diphenol).

BPA is an endocrine disrupting chemical which mimics estrogen (Bonefeld-Jørgensen et al., 2007). This endocrine disruptor is similar to hormones and can operate at very low concentrations (Schug et al., 2011). Because of its presence in food packaging (even for baby food), concerns about potential health risks have risen significantly and led to new legislation in some European countries limiting its use.

With the use of BPA in industry and households the presence in raw sewage and effluents is constantly growing. Common concentrations of BPA found in waste water near the paper production industry ranges from 28 to 72 $\mu\text{g/L}$ (calculated: 0.12 μM to 0.31 μM) and in proximity to the chemical industry from 2.5 to 50 $\mu\text{g/L}$ (calculated: 0.01 μM to 0.22 μM) (Fürhacker et al., 2000).

A further huge discussion in recent years was the use of BPA as an additive in baby drinking bottles. Due to the necessity of a sterilization step before use, the bottles need to be washed with hot water multiple times (70-100°C). During the sterilization step the free concentration of BPA increases with temperature to average values of 0.12 $\mu\text{g/L}$ at 40°C (calculated: 0.0005 μM) and 1.77 $\mu\text{g/L}$ at 60°C (calculated: 0.008 μM) (Kubwabo et al., 2009). Consequently, the amount of BPA being released into the water at a temperature of 100°C is 15 to 55 fold higher in compari-

son to room temperature (Le et al., 2008).

Since 2016 BPA is added to the list of REACH chemicals and is classified as a substance toxic for the reproductive system. The temporary tolerable daily intake (t-TDI) which is determined by the European Food Safety Authority (EFSA) amounts to 4 µg/kg body weight per day (Gundert-Remy et al., 2017). Consequently, concerns about an excessive exposition and potential resulting diseases have increased in the last years.

Therefore, it was the intention of this chapter to study the impact of BPA on cultured NRK cells with a whole set of impedance-based assays focusing on changes in different cell reactions like i) acute toxicity in equilibrated cell layers, ii) cell micromotion, iii) cell migration and iv) cell proliferation. All assays were measured with the ECIS electrodes and some with the IDE12. These studies were accompanied by a well-established metabolic assay (PrestoBlue) and various stainings (i) EthD-1/CaAM and ii) DAPI). The solid BPA was dissolved in 96 % ethanol and on that account the influence of different ethanol concentrations on the results of the assays was examined additionally. To exclude any impact of ethanol to the cells, the control of 0 µM BPA contained 1.5 % ethanol in every assay, except of the time-dependent impedance change during the proliferation measurement in which 1 % ethanol was added to the control because a higher concentration influenced the proliferation measurement. To compare the various assays and to allow an interpretation of the results, the concentration showing the half maximum effect (EC_{50}) is calculated for every assay using the dose response fitting function.

7.6.1 Analysis of the metabolic activity with a PrestoBlue assay

The influence of BPA on the metabolic activity of NRK cells was measured with a PrestoBlue assay which is based on the reduction of the non-fluorescent resazurin to the fluorescent resorufin in viable cells (Xu et al., 2015a). With the cytotoxicity-dependent change of this fluorescence, the cytotoxicity index (CI) can be calculated which enables conclusions of the harmful impact of a substance:

$$CI = \left(1 - \frac{F_x}{F_0}\right) \cdot 100\% \quad (7.2)$$

F_0 represents the corrected fluorescence intensity of the negative control and F_x is the corrected fluorescence intensity of the corresponding sample. A high value of CI indicates a strong impact on the metabolic activity, whereas a low value represents a negligible one. The calculated cytotoxicity indices were plotted against the added BPA concentrations in a logarithmic manner (see fig. 7.29).

In fig. 7.29 the influence of BPA on the metabolic activity of NRK cells was analyzed

in a concentration range of 0-300 μM BPA after 20 h incubation time. The value of the logarithm of 0 μM BPA was plotted as “ $-\infty$ ”. It can be seen that the lowest concentrations of BPA do not have an effect on the metabolic activity ($\text{CI} = 0\%$), whereas in a concentration range of 30 μM to 140 μM the CI is slowly increasing before reaching a maximum value at concentrations beyond 140 μM . The saturation achieves a CI value of 99.6% which monitors a lethal effect on the cells. The curve was fitted with a dose response equation and an EC_{50} value of $(114 \pm 6) \mu\text{M}$ can be determined.

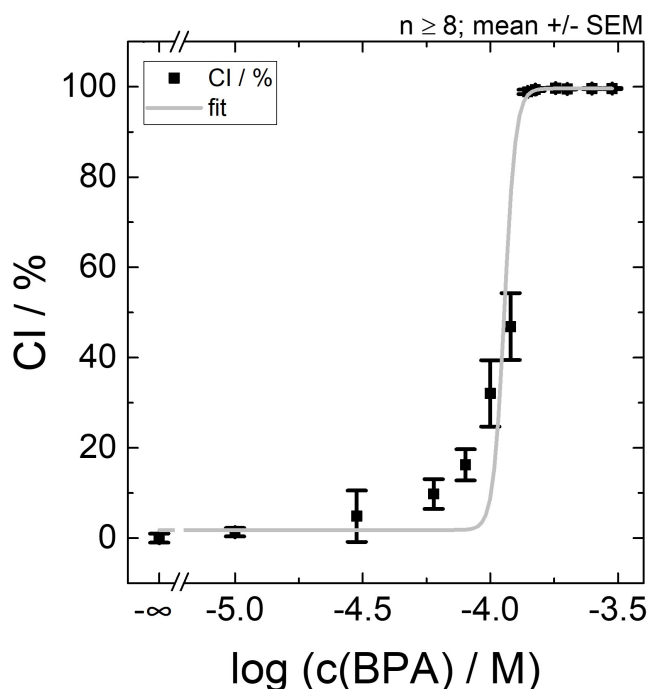


Figure 7.29: The calculated cytotoxicity index (CI) for the analysis of the cytotoxic influence of BPA concentrations (0-300 μM) on the metabolic activity of confluent NRK cells after 20 h incubation time measured with a PrestoBlue assay. The higher the CI, the more the cellular metabolism is affected. The data are fitted with a dose response curve and an EC_{50} of $(114 \pm 6) \mu\text{M}$ can be determined ($n \geq 8$). The mean with the SEM is plotted.

Within the concentration range of 0-300 μM BPA a clear influence on the metabolic activity of confluent NRK cells can be monitored after an incubation time of 20 h. The CI of 0% reveals healthy cells with a high metabolic activity, whereas the CI of 99.6% shows a lethal effect. Those cells have no metabolic activity anymore and are dead. Consequently, in this concentration range (0-300 μM) the BPA influences the NRK cells until a lethal concentration is reached. Based on these results, the concentrations of BPA in the following assays are adjusted to the ones in this assay to analyze the cytotoxicity of BPA in more detail.

7.6.2 Impedance-based analysis of the acute toxicity

Measuring the time-dependent impedance change of confluent NRK cells after the addition of various concentrations of BPA serves as a sensitive readout for the impact of BPA. The measured impedances can show a drop at different time points after addition of BPA. This decrease of the impedance is the basis for the interpretation of the acute toxicity. The faster the impedance is decreasing, the higher is the impact of BPA on the cells and the higher is the acute toxicity of this BPA concentration. This measurement with the confluent NRK cell layer was performed with the 8W10E electrodes (fig. 7.30) and the IDE 12 (fig. 7.31).

In fig. 7.30 **A** the time-dependent course of the normalized impedance measured with the 8W10E electrodes can be seen. The impedances were normalized to the initial value before addition of BPA at $t = 0$ h.

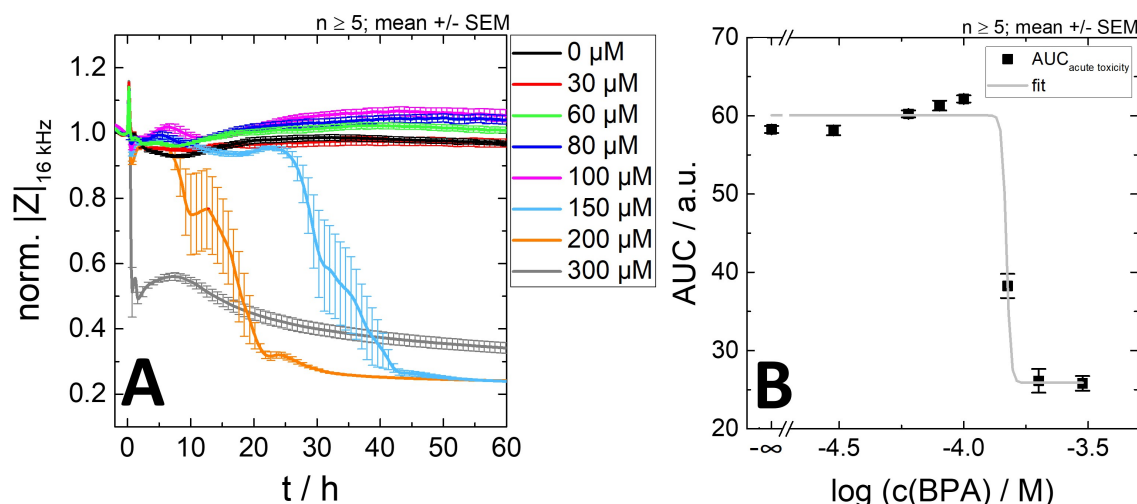


Figure 7.30: Impedance-based measurement of the acute toxicity of BPA on NRK cultivated on the 8W10E electrodes measured at 16 kHz. The solution with 0 μM BPA contains 1.5 % ethanol. **A:** time-dependent change of the normalized impedance after addition of different concentrations of BPA at a time point of $t = 0$ h. The data were normalized to the initial value before adding of BPA ($|Z| = (1524 \pm 47) \Omega$). **B:** calculated area under the curve (AUC) of the normalized impedance with a baseline of $y = 0$ and within the time range of 0-60 h. The data were fitted with a dose response curve and an EC_{50} value of $(148 \pm 13) \mu\text{M}$ can be calculated. The mean ($n \geq 5$) is plotted with the SEM.

Immediately after addition of 300 μM BPA (at $t = 0$ h) a decrease of the normalized impedance is observed, followed by a small increase again before a saturation of $\text{norm. } |Z|_{\min} = 0.34 \pm 0.02$ after around $t_{\min} \approx 20$ h is reached. This decrease of the impedance is also seen delayed with the 200 μM solution after 22 h and for the 150 μM after 43 h. Both curves show a saturation value of $\text{norm. } |Z|_{\min} = 0.250 \pm 0.007$.

It has to be mentioned that the shoulders at 13 h with 200 μM and at 35 h with 150 μM are side-effects of the averaging. The raw data in fig. A.23 **A** show a smooth decrease of the impedance without a shoulder to a value similar to the final value before a short increase of around 6 h occurs. This short increase can only be seen with the averaged data at 22-27 h after addition of the 200 μM (fig. 7.30 **A**). For lower concentrations between 100 μM and 60 μM the normalized impedance shows a short concentration-dependent increase within the first 10 h before it reaches a plateau of $\text{norm. } |Z|_{\text{max}} \approx 1.04 \pm 0.03$. Compared to 30 μM and to the control ($\text{norm. } |Z|_{\text{max}} = 0.98 \pm 0.02$) this represents an increase of the impedance. For a further interpretation the area under the curve (AUC) of the normalized data with a baseline of $y = 0$ and within a time range of 0-60 h was calculated and logarithmically plotted against the concentrations (see fig. 7.30 **B**). The logarithm of 0 μM BPA was plotted as “ $-\infty$ ”. This representation visualizes a higher AUC for 60, 80 and 100 μM BPA in comparison to the lowest concentrations (0 and 30 μM). The AUC values for 200 and 300 μM do not differ significantly and show the smallest values of AUC. After sigmoidal fitting with a dose response curve an $\text{EC}_{50} = (148 \pm 13) \mu\text{M}$ was determined for a measurement time of 60 h.

This experiment was repeated with the IDE 12 to evaluate the utility of an interdigitated structure in cytotoxicity studies. The different concentrations of BPA show a similar impact on the time-dependent change of the normalized impedance measured with the IDE 12 (see fig. 7.31) in comparison to the 8W10E electrodes (fig. 7.30). In fig. 7.31 **A** the normalized impedance course dependent on the time measured with the IDE 12 is monitored for 20 h after the addition of BPA ($t = 0$ h). The highest concentration of BPA (300 μM) causes an immediate decrease of the impedance. Compared to the measurement of the 8W10E electrodes the impedance does not show an additional increase and reaches a minimum of $\text{norm. } |Z|_{\text{min}} = 0.36 \pm 0.02$ after $t_{\text{min}} = 2.5$ h. Consistent to the 8W10E electrodes, the impedance of the cells incubated with 200 μM is decreasing as the second curve, whereas the minimum ($\text{norm. } |Z|_{\text{min}} = 0.34 \pm 0.04$) occurs already after 10 h in the case of the IDE 12. A further difference is the missing short increase which is shown in fig. 7.30. Even in the non-averaged normalized data in fig. A.23 **B** the short increase cannot be seen. The next decrease of the impedance occurs with an incubation of 150 μM after 21 h to a value of $\text{norm. } |Z| = 0.33 \pm 0.04$ (not shown). A relevant difference between the two electrode types is the decreasing impedance after the incubation with 100 μM . The measurement with the IDE 12 shows obviously an impact of the 100 μM BPA on the cells and the impedance is changing substantially, whereas nearly no difference between the 100 μM , 80 μM and 60 μM impedance with the 8W10E electrodes can be distinguished. A further big difference is the increasing impedance of the cells measured with the IDE 12 with an incubation of 60 and 30 μM which differs clearly

from the control measurement. These different trends can be visualized by the values of the calculated area under the curve (AUC) of the normalized impedance which are plotted against the logarithm of the concentrations of BPA (see fig. 7.31 **B**). The baseline of $y=0$ and the time interval of 0-20 h are used. The logarithm of 0 μM BPA is plotted as “ $-\infty$ ”. The values of the AUC are strongly dependent on the concentrations of BPA. The AUC of 30 μM and 60 μM shows a higher value than the control with 0 μM BPA before the values of AUC decrease over the 100 μM and 150 μM to the smallest values for 200 μM and 300 μM . This increased AUC for lower concentrations can also be seen with the 8W10E electrodes. The values for AUC cannot be compared between the electrode types directly due to the different time intervals for the calculation (IDE12: 0-20 h; 8W10E electrodes: 0-60 h). Nevertheless, a value of $\text{EC}_{50} = (156 \pm 23) \mu\text{M}$ using a dose response fit can be determined for the measurement with IDE12 for the first 20 h after addition of BPA.

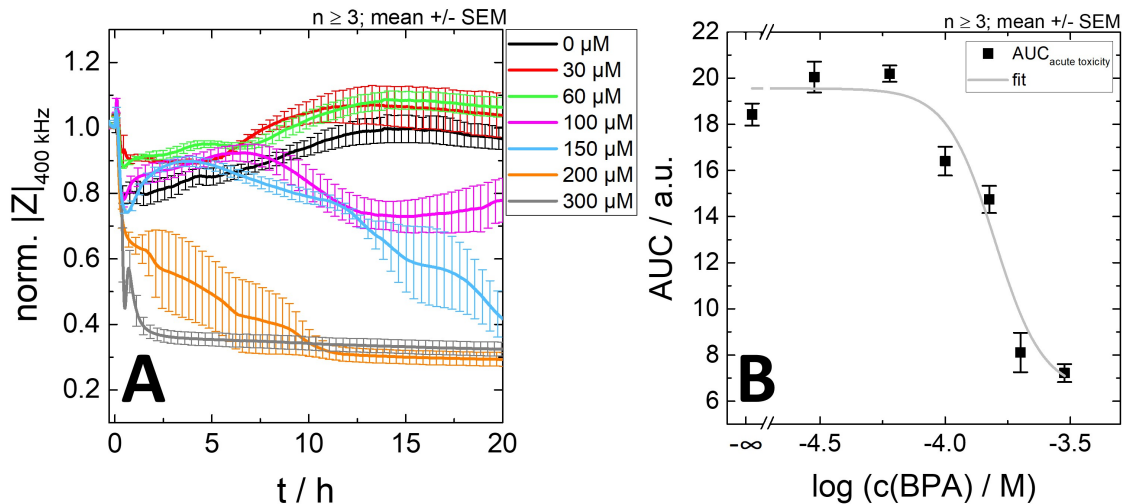


Figure 7.31: Impedance-based measurement of the acute toxicity of BPA on confluent NRK cells grown on IDE12 measured at a frequency of 400 kHz. The solution of 0 μM contains 1.5 % ethanol. **A:** time-dependent change of the normalized impedance after addition of different concentrations of BPA ($t = 0 \text{ h}$). The data were normalized to the initial value before addition of BPA ($|Z| = (167 \pm 16) \Omega$). **B:** calculated area under the curve (AUC) of the normalized data with a baseline of $y = 0$ and in a time range of 0-20 h. It was fitted with the dose response curve and an $\text{EC}_{50} = (156 \pm 23) \mu\text{M}$ can be calculated. The mean ($n \geq 3$) is plotted with the SEM.

For a better overview for the comparison of the two electrode types the values of $\text{norm. } |Z|_{\min}$ and t_{\min} of the saturation for the highest concentrations are compared in table 7.3. It can be seen that the impedance values measured with the IDE12 with all three concentrations and the value for 300 μM measured with 8W10E electrodes do not differ within the errors. Only the values for 150 μM and 200 μM BPA for the 8W10E electrodes show a lower impedance magnitude. The biggest difference of the

electrode types is displayed in the time until the saturation is reached. Even if the trend that the lowest concentration of these three, takes the longest time is existent for both electrode types, the saturation is reached much faster with the measurement of the IDE 12. The impedance is decreasing twice and even ten times faster as with the 8W10E electrodes. This shows that the cell reactions to the impact of BPA is detected much faster with the IDE 12.

Table 7.3: Values for the minima of the impedance after stimulation with the highest BPA concentrations (150 μM , 200 μM , 300 μM) in the acute toxicity assay. The norm. $|Z|_{\min}$ and the t_{\min} are compared for the 8W10E electrodes and the IDE 12.

BPA	8W10E		IDE 12	
concentration	norm. $ Z _{\min}$	t_{\min}	norm. $ Z _{\min}$	t_{\max}
/ μM		/ h		/ h
150	0.253 ± 0.005	43	0.33 ± 0.04	21
200	0.248 ± 0.002	22	0.34 ± 0.04	10
300	0.34 ± 0.03	20	0.36 ± 0.02	2.5

To ensure that the time-dependent impedance changes are initiated by the toxic impact of BPA alone, the effect of ethanol on a confluent monolayer was analyzed with the same experimental preconditions than for the analysis of the acute toxicity.

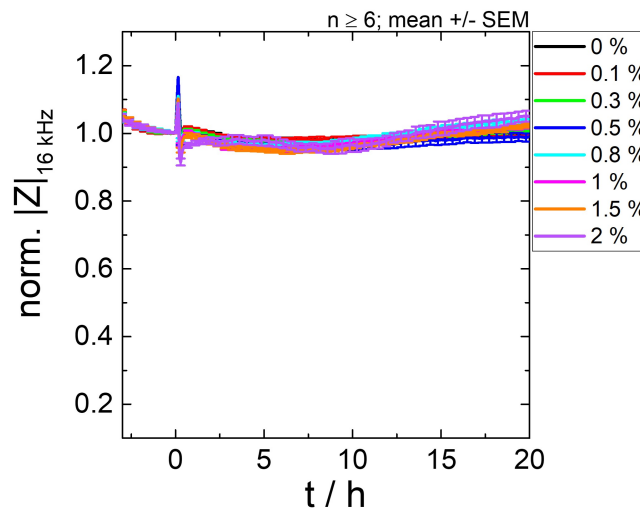


Figure 7.32: Time-dependent impedance measurement of the impact of different ethanol concentrations on a confluent layer of NRK cells grown on 8W10E electrodes at a frequency of 16 kHz. The ethanol solutions were added at $t = 0$ h. The data are normalized to the initial values before addition of ethanol ($|Z| = (11423 \pm 736) \Omega$). The mean with the SEM is plotted with ($n \geq 6$).

The confluent cell layer of NRK cells, grown on the 8W10E electrodes, was incubated with different ethanol concentrations at $t = 0$ h and the normalized impedance was monitored for 20 h (see fig. 7.32). The measurement of the time-dependent impedance change after the addition of ethanol shows no significant change dependent on the different concentrations. Up to a concentration of 2 % ethanol the impedance of the cells are not influenced and cannot be distinguished from the control (0 % ethanol). This measurement proves that ethanol as a solvent has no influence on the measured effect of BPA on the cells in this assay, since a maximum of 1.5 % ethanol was used in the solutions.

In summary, the IDE 12 with the smaller pitch and the corresponding smaller penetration depth of the electric field can monitor the cell responses caused by the toxic effect of BPA on the cells much faster. The EC_{50} value of the IDE 12 is after 20 h already in a size range of the EC_{50} value of the 8W10E electrodes after 60 h. Consequently, it can be concluded that the IDE 12 electrodes are more advantageous than the 8W10E electrodes in this assay due to the much faster detection of the toxic impact of BPA on the cells.

7.6.3 Concentration-dependent micromotion

The confluent cell layer which was incubated for 20 h with the different BPA concentration was further analyzed impedimetrically. The cells in this confluent monolayer are moving in a horizontal and vertical way which can be associated with the fluctuations of the measured impedance. On the basis of these fluctuations the detrended variance of the micromotion can be calculated (explained in chapter 3.1.2.4). The value of the variance can be correlated with the metabolic activity of the cells: the higher the variance, the more motile are the cells and the higher is the metabolic activity of the cells.

In fig. 7.33 the normalized detrended variances of the impedance are shown. The variances are normalized to the values of the 0 μ M BPA (containing 1.5 % ethanol) for each electrode type, since the non-normalized variances of the individual electrodes are not comparable due to the different impedance values of the raw data. The normalized detrended variance of the impedance in fig. 7.33 shows for both electrode types a high dependence on the concentration of the added toxicant. In the case of the 8W1E electrodes (fig. 7.33 A) the variance is decreasing even for the small concentration of 30 μ M, whereas with the IDE 12 (fig. 7.33 B) an increase of the variance is seen for the incubation with 30 μ M in comparison to the control. For higher concentrations the variance is decreasing almost linearly until the values for 200 μ M and 300 μ M BPA are reached. With these concentrations the variance is not changing anymore which indicates a reduced micromotion and a significant

damage of the cells. Fitting the curves with a dose response equation led to an $EC_{50} = (87 \pm 17) \mu\text{M}$ for the 8W1E electrodes and to an $EC_{50} = (90 \pm 14) \mu\text{M}$ for the IDE 12. These comparable EC_{50} values prove that the 8W1E electrodes as well as the IDE 12 are suitable for the measurement of the impact of BPA on the micromotion of NRK cells.

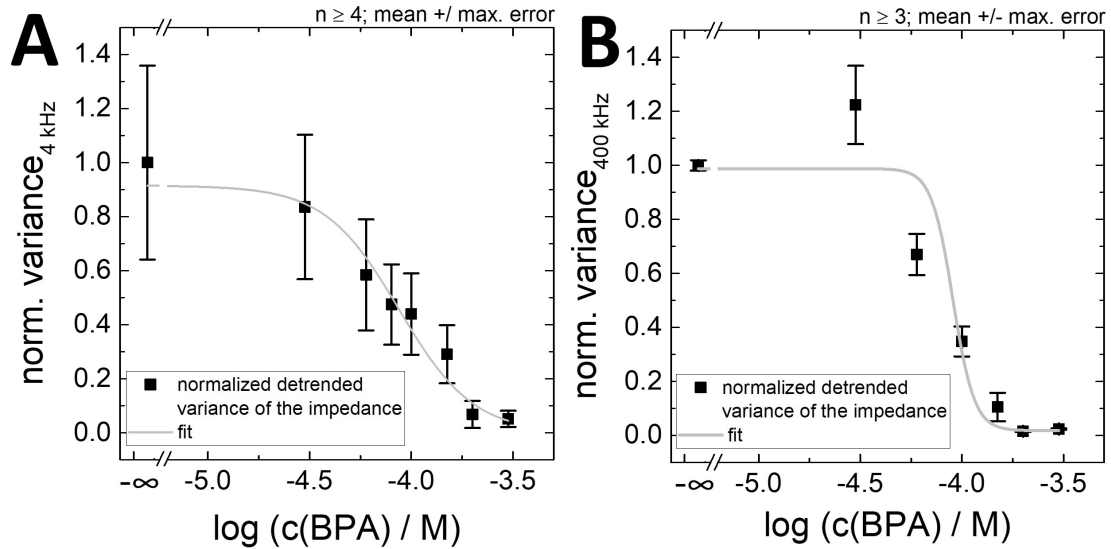


Figure 7.33: Analysis of the BPA concentration-dependent micromotion of NRK cells after 20 h of incubation with different BPA concentrations with the detrended variance of the impedance (calculated with subtraction). **A:** 8W1E electrodes at 4 kHz with $n \geq 4$, **B:** IDE 12 at 400 kHz with $n \geq 3$. The data are normalized to the value of the variance for the $0 \mu\text{M}$, which is plotted as “ $-\infty$ ” (8W1E electrodes: $(1.7 \pm 0.3) \Omega$; IDE 12: $(1.034 \cdot 10^{-4} \pm 1.0 \cdot 10^{-8}) \Omega$). The curves were fitted with a dose response equation and an $EC_{50} = (87 \pm 17) \mu\text{M}$ for the 8W1E electrodes and an $EC_{50} = (90 \pm 14) \mu\text{M}$ for the IDE 12 can be determined. The mean with the max. error is plotted.

To exclude an influence of the solvent (ethanol) to the micromotion of the cells, the micromotion measurement was repeated with different ethanol concentrations. The confluent NRK cell layer grown on 8W1E electrodes was incubated for 20 h with those solutions and the detrended variance of the impedance is calculated similar to the one in fig. 7.33. In fig. 7.34 the calculated variances are normalized to the value of the 0 % ethanol whose logarithm is plotted as “ $-\infty$ ”. For all concentrations of ethanol the normalized detrended variance is in the same range as the control. Within the errors the variance of 1 % is slightly smaller than the others. Nevertheless, the variance of higher concentrations is again in the same range as the control. Consequently, no significant influence of the ethanol up to a concentration of 2 % can be determined. This proves that the impact on the micromotion of the cells with the BPA solutions

is only generated from the BPA, because the maximum concentration of ethanol in the micromotion assay is 1.5 % ethanol.

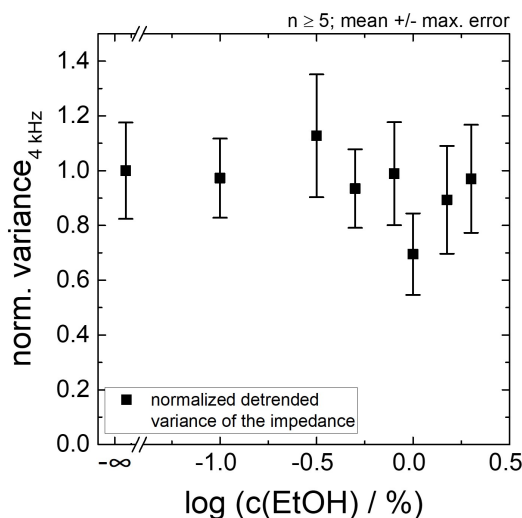


Figure 7.34: Measurement of the impact of different ethanol concentrations on the micromotion of a confluent layer of NRK cells grown on 8W1E electrodes after 20 h of incubation. The detrended variance of the impedance (calculated with subtraction) is analyzed. A frequency of $f = 4$ kHz was used and the data were normalized to the value of 0 % ethanol ($(63 \pm 6) \Omega$) ($n \geq 5$). The mean with the max. error is plotted.

With this micromotion assay no advantage of the 8W1E electrodes over the IDE 12 was found. Both electrodes types generate nearly the same EC_{50} value and show an impact of small BPA concentrations. The only difference is that with IDE 12 the variance is increased with 30 μ M BPA, while it is decreased when measured with the 8W1E electrodes. This difference is explained in the discussion.

7.6.4 Impedance-based analysis of cell migration after wounding

Confluent cell layers can be damaged with a short electrical or voltage pulse and the time to repopulate the damaged area (“wound”) in the monolayer can provide information about cell migration (Bellotti et al., 2015). This wounding method is quantitative and extremely well reproducible (Keese et al., 2004).

For the impedance-based measurement of the cell migration the confluent cell layer was incubated for 24 h with different concentrations of BPA. When a pulse with a few volt was performed, a high voltage is provided over the cell-covered electrode. This results in a voltage drop across the plasma membrane and a sufficient membrane poration. As a consequence, the cells directly grown on the electrodes are dying (Keese et al., 2004) which could be seen in a decreasing impedance. The cells

in the periphery of the electrode are not damaged and start to repopulate the free space of the electrode and thus the impedance increases again. The required time to close the wound is an indication of the toxicity of the BPA concentrations. The more toxic a substance is, the slower the wound is closed and the slower the impedance is increasing. The impact of BPA on the recovery of the cells after wounding was only analyzed for the 8W1E electrodes (see fig. 7.35), because at the time of the measurement the IDEs had not yet been tested for their functionality during wounding.

In fig. 7.35 **A** the time-dependent increase of the impedance during wound closure can be seen.

The wounding (5 V, 40 kHz, 30 s) was performed at $t = 0$ h after an incubation with BPA for 24 h. The data are not normalized because the cells are strongly harmed after 24 h of incubation (see fig. 7.30) and the initial values before wounding differ a lot. After the immediate decrease of the impedance resulting from the wounding the impedance is increasing for some of the BPA concentrations. In the presence of 30 μM and 60 μM the impedance courses are nearly not distinguishable from the control curve. The impedance needs $t_{\text{max}} = 8.29$ h (0 μM , and 30 μM) and $t_{\text{max}} = 9.82$ h (60 μM) to reach the initial value again. The cells in contact to 80 μM BPA need more time to close the wound ($t_{\text{max}} = 13.65$ h), also achieving the impedance value before wounding. With an incubation of 100 μM only a small increase of the impedance after 15 h can be assumed. Beyond 100 μM it is not possible to speak about wound healing because the cells are excessively damaged after 24 h of incubation with BPA and may be dead even before the pulse is applied. As a consequence of this, the impedance is not changing anymore. To calculate the EC_{50} values two different methods were used: i) the area under the curve (AUC) in a time range of 0.2-18.0 h with the baseline defined as the individual first impedance value after wounding for each curve (fig. 7.35 **B**) and ii) the slope at the half maximal change of the impedance after wounding (fig. 7.35 **C**). For the high concentrations (highlighted with *) the slope at $t = 14$ h is calculated. In both cases the values for the lower concentrations do not differ much from the ones of the control (0 μM plotted as “ $-\infty$ ”) within the errors. With an incubation with 80 μM BPA decreased values are seen and with higher concentrations nearly no change is visible. By fitting the curves with a dose response equation an EC_{50} value of (86 ± 2) μM for the AUC and an $\text{EC}_{50} = (84 \pm 3)$ μM for the slope can be determined.

These observations of this cell migration assay agree with the results of the previous assays. With concentrations up to 60 μM no toxic impact on the NRK cells can be measured, whereas with 80 μM an influence is clearly monitored. Cells incubated with concentrations beyond 80 μM for 24 h were damaged excessively.

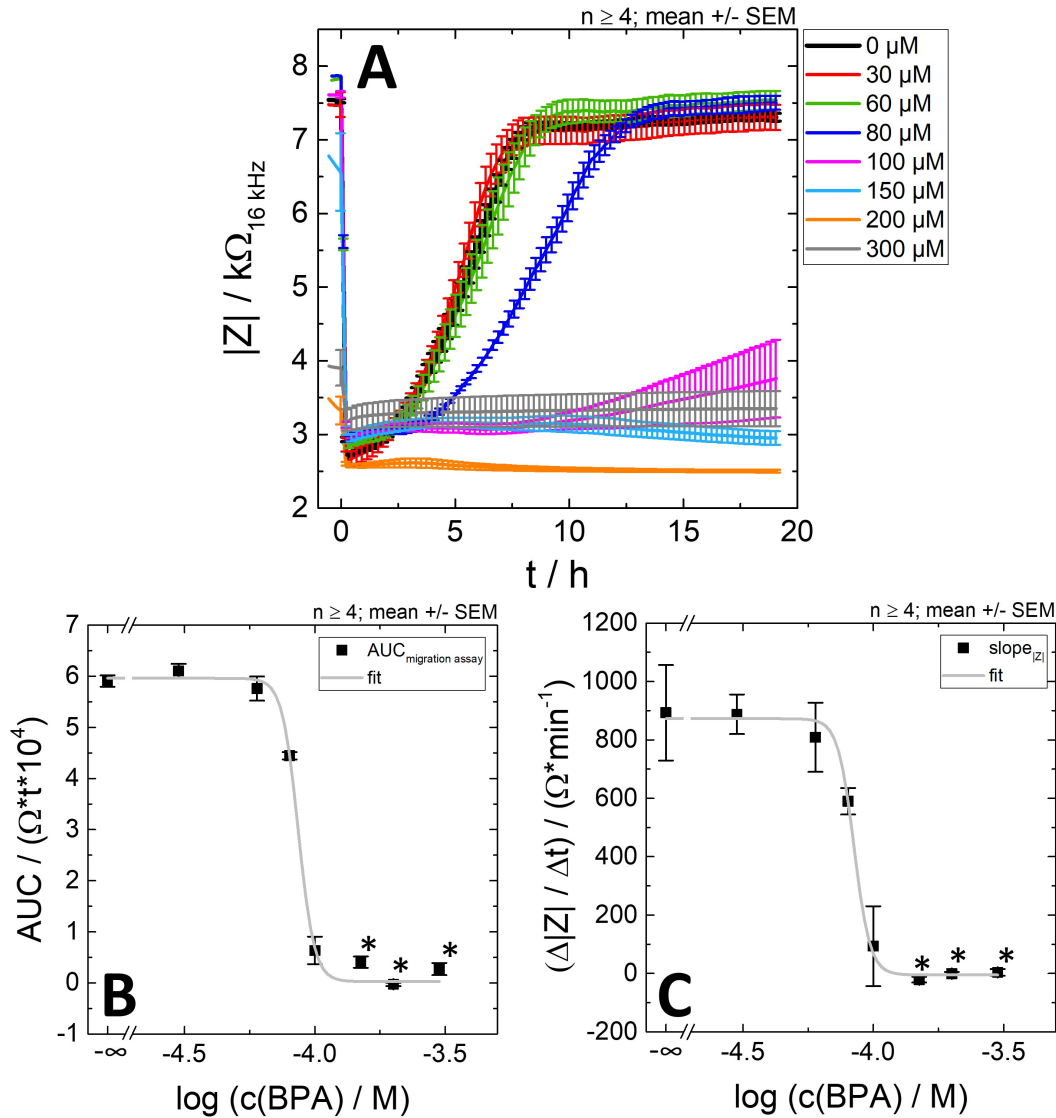


Figure 7.35: Measurement of the wound healing of NRK cells incubated for 24 h with BPA on 8W1E electrodes. With the incubation of 150, 200 and 300 μM BPA wound healing is no longer possible due to the excessive pre-damage of the cells (highlighted with *). **A:** time course of the raw data of cell migration after wounding at $t = 0$ h (5 V, 40 kHz, 30 s) at $f = 16$ kHz. **B:** calculated area under the curve (AUC) of the raw data of the migration assay in a time range of 0.2-18.0 h. The baseline for each curve is the first individual impedance value after wounding. **C:** slope at the half-way recovery time from baseline to plateau. For the high concentrations (highlighted with *) the slope at the time of $t = 14.0$ h was calculated. **B** and **C** are fitted with the dose response curve and an EC_{50} of $(86 \pm 2) \mu\text{M}$ and $(84 \pm 3) \mu\text{M}$ can be determined. The mean with the SEM is plotted with $n \geq 4$.

In fig. 7.36 the migration assay was repeated with the various ethanol concentrations. The time-dependent impedance change after wounding (5 V, 40 kHz, 30 s, $t = 0$ h) at an incubation time of 20 h with ethanol, shows an immediate decrease of the impedance, followed by a recovery of the cells on the electrode and a corresponding

increase of the impedance. Within the errors no clear difference of the individual concentrations can be seen. All impedances increase with a comparable slope to the same impedance values.

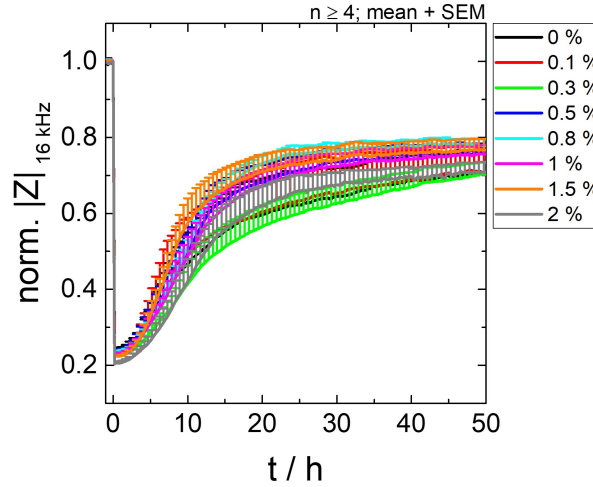


Figure 7.36: Time-course of the normalized impedance during wound healing measured with 8W1E electrodes after wounding (5 V, 40 kHz, 30 s) at $t = 0$ h ($f = 16$ kHz). The cells were incubated with EtOH for 20 h before wounding. The data are normalized to the initial value before wounding ($|Z| = (11577 \pm 762) \Omega$). The mean with SEM in positive direction is plotted ($n \geq 4$).

This proves that ethanol until 2 % does not effect the migration velocity of NRK cells in this assay, because the solutions with BPA contain maximum 1.5 % ethanol.

7.6.5 Time-dependent capacitance change during proliferation

In a different setup, the proliferation of the cells on the 8W10E+ electrodes was measured in the presence of BPA. The time course of the capacitance is a direct parameter for the degree of the electrode coverage (Wegener et al., 2000a). The cells adhered and spread on the electrodes with a subconfluent seeding and the capacitance is decreasing. After 24 h BPA was added and the change of the capacitance was measured (fig. 7.37 A). A decreasing capacitance results from an increasing coverage of the electrodes, whereas the increase of the capacitance after addition of BPA indicates a cell detachment from the electrode. This allows conclusions about the toxic impact of the according BPA concentration.

In the time course of the proliferation measurement (fig. 7.37 A) the capacitance values are normalized to the values of a cell-free electrode. A decreasing normalized capacitance indicates an increasing coverage of the electrode. 24 h after subconfluent seeding of NRK cells ($10,000 \text{ cells/cm}^2$) on 8W10E+ electrodes, BPA was added in the various concentrations which had no significant influence within the errors on

the coverage in a concentration range from 0 (containing 1 % ethanol) to 30 μM . The normalized capacitance of 60 μM shows a similar course, whereas the values are slightly higher than the ones of the lower concentrations. A constant capacitance is observed for concentrations of 80 and 100 μM . This indicates an inhibited proliferation. Concentrations beyond 100 μM lead to a detachment and apoptosis of the cells and the capacitance is consequently increasing. These different impacts on the capacitance is visualized with the values of the norm. C at $t = 89 \text{ h}$ (65 h after addition of BPA) which are plotted against the logarithm of the concentrations of BPA (see fig. 7.37 B). The logarithm of 0 μM BPA is visualized with “ $-\infty$ ”. The incubation with low concentrations (0 and 30 μM BPA) does not affect the coverage of the electrodes and the normalized capacitances have small values. With higher concentrations, higher capacitance values can be seen until a saturation with 150 μM occurs. This indicates that the cells have detached and the values of a cell-free electrode are reached again. Fitting these data with a dose response curve, yields an EC_{50} value of $(86 \pm 6) \mu\text{M}$.

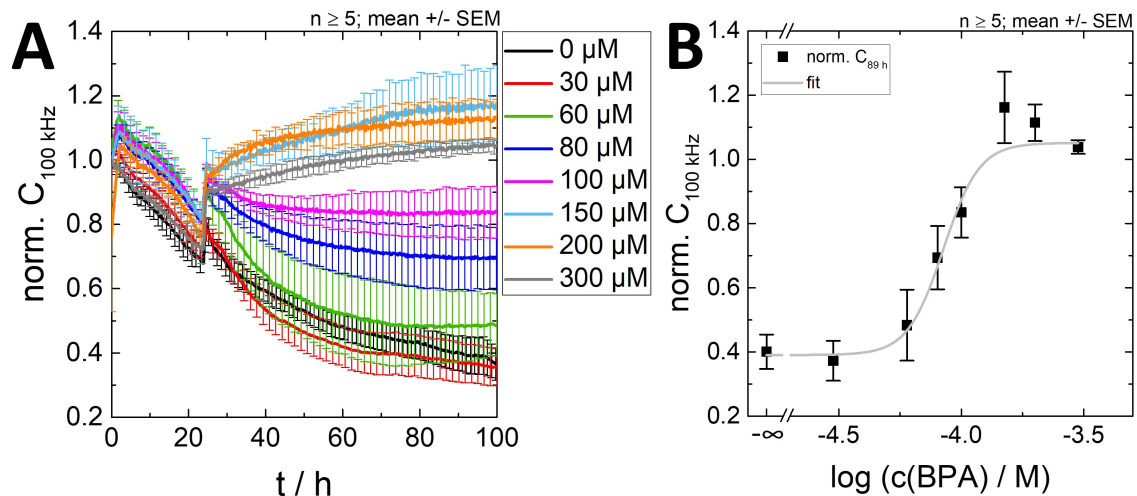


Figure 7.37: Measurement of the time-dependent capacitance change during proliferation of NRK cells in contact to BPA on 8W10E+ electrodes. The cells were seeded subconfluently (10,000 cells/ cm^2) and BPA solutions were added after 24 h. **A:** Time course of the normalized capacitance during cell proliferation at a frequency of 100 kHz. The capacitance is normalized to the initial value of a cell-free electrode ($C = (44 \pm 10) \text{ nF}$). **B:** The norm. C values at $t = 89 \text{ h}$ (65 h after addition of BPA) are plotted against the logarithm of the different BPA concentrations. The logarithm of 0 μM is seen as “ $-\infty$ ”. The data were fitted with a dose response curve and an EC_{50} value of $(85 \pm 6) \mu\text{M}$ can be investigated. ($n \geq 5$; mean \pm SEM).

For this proliferation assay it was also examined, if the solvent ethanol had an influence on the results. The cells were seeded subconfluently (10,000 cells/ cm^2) and after 24 h ethanol in different concentrations was added. In fig. 7.38 A the

time-course of the normalized capacitance change can be seen. When ethanol was added ($t = 24$ h), the capacitance is decreasing with the same velocity than without ethanol. The curve with 1 % ethanol shows slightly higher values, but with respect to the errors a significant difference cannot be proven. The analysis of the norm. C values at $t = 89$ h (65 h after addition) does not generate new information (fig. 7.38 B). No distinct trend can be seen. This proves that the solvent has no influence on the proliferation of the NRK cells in this assay because the BPA solutions in this assay contain maximum 1 % ethanol.

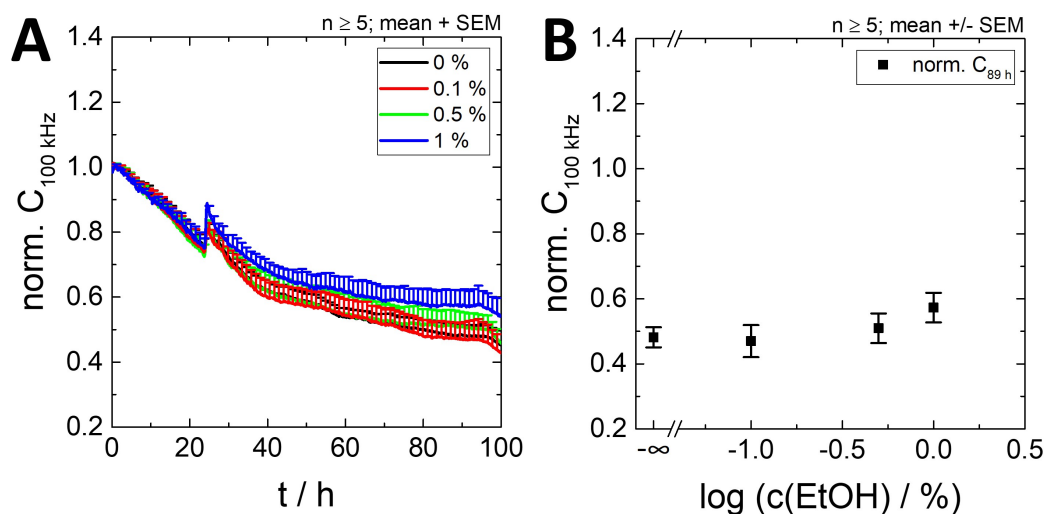


Figure 7.38: Measurement of the influence of different ethanol concentrations on a non-confluent layer of NRK cells grown on various ECIS electrodes. **A:** Proliferation measurement on 8W10E+ electrodes at 100 kHz. The cells were seeded subconfluently (seeding density: 10,000 cells/cm²) and after 24 h ethanol with different concentrations is added. The graph is normalized to the initial value ($n \geq 5$) ($C = (57.9 \pm 7.1)$ nF). **B:** norm. C values of the proliferation after 65 h at 100 kHz ($n \geq 5$). The mean with the SEM in positive direction is plotted in **B** and in both directions in **C**.

With this assay it was repeatedly proven that low concentrations of BPA have no influence on the cell reaction. Beyond a concentration of 80 μ M a toxic impact can be monitored which corresponds to the results of the previous assays.

7.6.6 Staining of the cells after incubation with BPA

To complete the monitoring of the toxicity of BPA a microscopic analysis is performed to determine the impact of the toxicant from another view point. The NRK cells were stained with two dye combinations after 20 h of incubation with different BPA concentrations: i) CaAM/EthD-1 (fig. 7.39 A) and ii) DAPI (fig. 7.39 B).

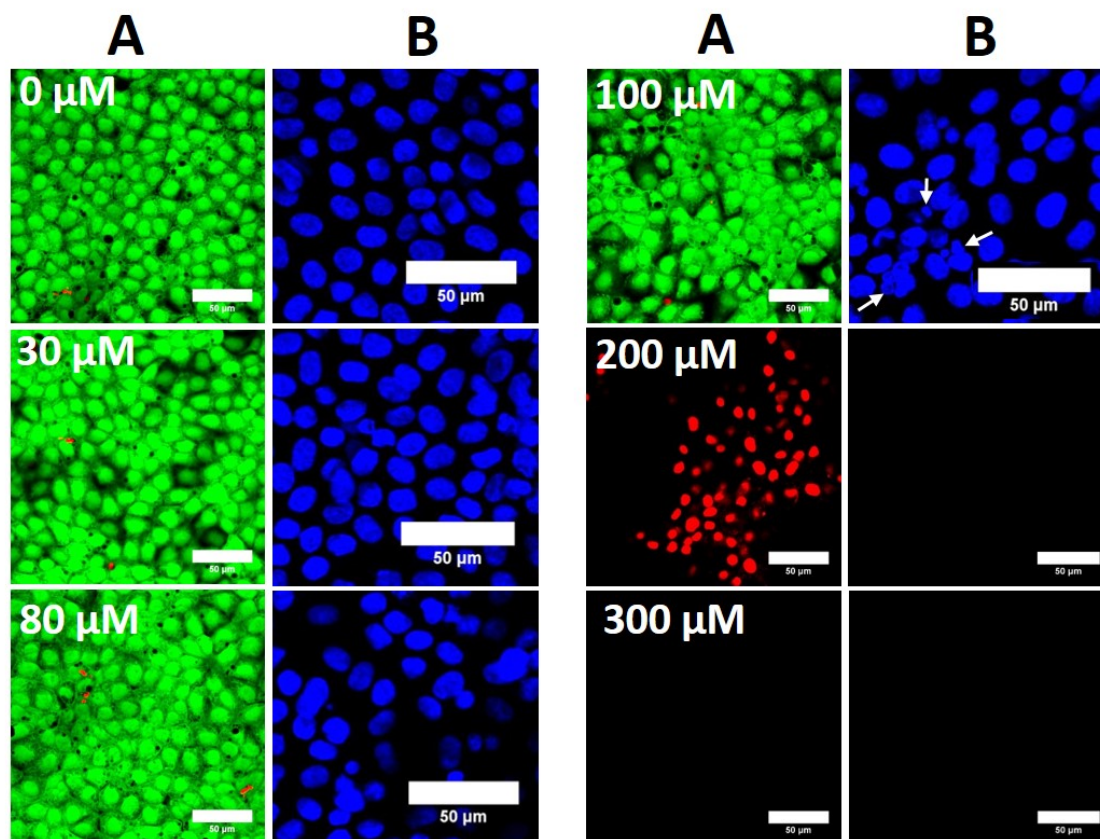


Figure 7.39: Fluorescence images of stained NRK cells after 20 h incubation with different BPA concentrations recorded with the CLSM (60x magnification). **A:** live/dead staining with the dyes CaAM and EthD-1. The healthy cells appear green, the dead cells red. **B:** staining of the cell nuclei with DAPI. The cell nuclei are stained blue. In the image of the 100 μM incubated cells with DAPI the fragmentation of the cell nuclei is highlighted with white arrows. The scale bar represents 50 μm.

In fig. 7.39 the cells incubated with 0 μM (containing 1.5 % ethanol) and 30 μM show an evenly distributed green and blue fluorescence. The cell layer is homogeneous and the cell nuclei have all more or less the same size. The live/dead staining with 80 μM does not show any difference to the lower concentrations. However, an influence of the BPA to the cell nuclei can be seen with the DAPI staining which shows various sizes and a heterogeneous distribution of the cell nuclei. Increasing the concentration of BPA to 100 μM the fluorescence of the live/dead stained cell layer is heterogeneously distributed, but with a complete green fluorescence. Analyzing the cell nuclei, different sizes can be seen. Several small blue dots connected to the big cell nuclei (marked with white arrows) occur. This fragmentation of the cell core shows that the cells are excessively damaged with this concentration after 24 h of incubation. With an incubation of 200 μM only dead red cells can be seen and no stained cell nuclei anymore. The reason for this is the additional washing steps for the DAPI staining. With this washing the strongly damaged cell were washed away. The same is seen for the incubation with 300 μM. Both images show no fluorescence

any more. The cells were detached from the substrate due to the additional washing steps which proves that the cells were completely harmed or even dead. An EC_{50} value of $\approx 100 \mu\text{M}$ can be estimated.

The results of these stainings go hand in hand with the impedance-based measurements. The incubation with small concentrations of BPA (0, 30 and $80 \mu\text{M}$ BPA) have no impact on the fluorescence of the stained cells. Beyond a concentration of $80 \mu\text{M}$ BPA the cells show an excessive damage until a lethal concentrations is reached.

7.6.7 Summary of the cytotoxicity of BPA

For a better overview the EC_{50} values of the previous assays are summarized in fig. 7.40. Three different measurement setups are distinguished: i) without electrodes (w/o electrodes), ii) with ECIS electrodes (8W1E, 8W10E, 8W10E+) and iii) with IDE 12. For all assays NRK cell were used.

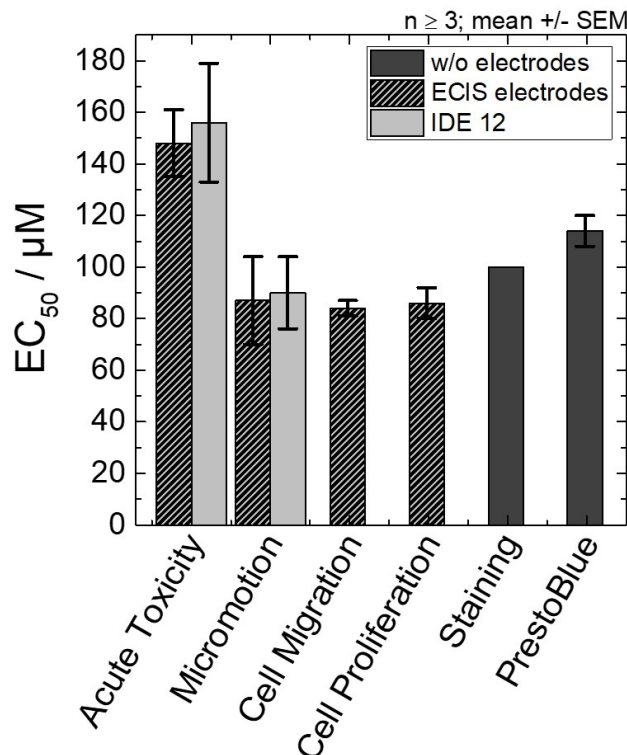


Figure 7.40: Summary of the EC_{50} values reporting on the impact of BPA on different cell reactions of NRK cells determined in various assays. Three measurement setups of the different assays were used: i) without electrodes (w/o electrodes), ii) with ECIS electrodes (8W1E, 8W10E, 8W10E+) and iii) with IDE 12. The mean with the SEM is plotted. ($n \geq 3$) with the exception of the staining ($n = 1$).

The determined EC_{50} values range between $(84 \pm 3) \mu\text{M}$ and $(156 \pm 23) \mu\text{M}$ BPA. A smaller EC_{50} value indicates a lower concentration of BPA which is needed for

the half maximum effect and thereby a higher sensitivity of the measurement setup. The lowest EC_{50} values can be seen for the cell migration and proliferation of the ECIS electrodes and within the errors for the micromotion measurement of the ECIS electrodes and IDE 12. These EC_{50} values are smaller than the ones of the staining and the PrestoBlue assay. The highest EC_{50} values can be monitored for the acute toxicity assay, whereas the EC_{50} value measured with the IDE 12 is slightly higher. Nevertheless, it has to be emphasized that the EC_{50} value of the IDE 12 is calculated out of a measurement time of 20 h. The EC_{50} of the 8W10E electrodes arises from a time of 60 h. Consequently, the measurement of the IDE 12 is significantly more sensitive. The reason of these different EC_{50} values will be explained in the following chapter.

7.6.8 Discussion

Influence of ethanol to the measured signal

It was necessary to analyze, if the solvent has an influence on the results of the toxicity measurements of BPA. The setups of the assays for the impact of ethanol were identical to the BPA measurements to ensure the same preconditions and to exclude side-effects. The applied ethanol concentrations in the control solutions (1.5 % for all assays, except proliferation: 1 %) do not show an impact on the measured impedance in the individual assays within the errors. This proves that all cell reactions and the associated impedance changes were caused only from the toxicity of BPA and not from the solvent.

Concentration-dependent changes of the analyzed parameter

In all measurements a concentration-dependent impact of BPA on the cells can be observed.

The cytotoxicity index determined with the PrestoBlue assay is increasing from a concentration of 30 μ M until a saturation of 99.6 % for concentrations beyond 130 μ M is reached, which indicates a lethal concentration for the cells. This agrees with the assay of the acute toxicity measured with the 8W10E electrodes which shows a high impact of BPA in concentrations higher than 100 μ M, due to the decreasing impedance which indicates cell death. With the highest concentration (300 μ M) the insulating character of the cells is breaking down instantly which implies an immediate destruction of the cells and the cell membranes. Consequently, the current can flow unimpeded and the impedance is decreasing. The impedance of the dead cells incubated with 300 μ M is higher than for the cells incubated with 150 and 200 μ M which suggests that membrane rests or dead cells are still on the electrodes and influence the current flow. For smaller concentrations (200 and 150 μ M) it takes longer for the insulating membrane to break down and for the cells to detach com-

pletely from the electrode. This break down of the membrane can be detected much faster with the IDE 12. At half (150 and 200 μM) or even one-tenth (300 μM) of the time the impedances have reached their minimum measured with the IDE 12 (see tab. 7.3). Besides, the minima are not significantly different measured with the various electrode types. A further difference is that the IDE 12 can reveal a strong influence of 100 μM on the cells. This proves that IDE 12 can monitor the influence of a toxicant to the cells much faster and more sensitive than the ECIS electrodes. As an explanation again the focus of the electric field underneath the cells in the vicinity of electrodes, like IDE 12, can be mentioned and the associated distinct cell parts which can be monitored. Further, the rounding off the cells influences strongly the cleft between the cells and the electrodes. With more rounded cells, the cleft is getting bigger. In the simulations in chapter 5.3 and 6.1 it was explained that with small distances between the electrodes the main part of the electric field is underneath the cells. If the cleft underneath the cells is changing, it has a bigger influence of the signals of the IDE 12 than of the ECIS electrodes. This could lead to a greater influence of the resistance underneath the cells, which has a greater impact on the impedance of the IDE 12. Consequently, the detachment of the cells can be monitored faster with the IDE 12.

The increased impedance of the acute toxicity assay for 60, 80 and 100 μM of 8W10E electrodes and for 30 and 60 μM of the IDEs, which can be seen in fig. 7.30 and fig. 7.31 both in the time course and in the dose-response relation, is attributed to hormesis (Calabrese, 2005; Calabrese and Baldwin, 2003). This effect of overcompensation can also be seen with the analyzed micromotion of the cells incubated with 30 μM measured with IDE 12. The metabolic activity of these cells seems to be enhanced under the influence of small concentrations of BPA. Hormesis only occurs at low concentrations of a toxicant, at which the cells activate their metabolism and for example raise the production of proteins to respond to damage signals with a series of repair processes (Calabrese, 2003; Calabrese, 2008). Consequently, even a small concentration of BPA has an influence on the cells resulting in an increased impedance or increased micromotion.

Looking at the micromotion measurements, the variances of both electrode types show a strong impact at low concentrations except for the increased signal of 30 μM of the IDE 12, which was explained previously. Increasing the concentrations leads to a significant decrease of the variance which is associated with a restricted metabolic activity until no signal can be seen with 200 and 300 μM . This continuous decrease of the variance shows the high sensitivity of this assay which can quantitatively monitor cell motion in the range of nanometer (Giaever and Keese, 1991). Even the smallest concentrations influence the results and can be revealed.

This concentration-dependent impact of BPA on the cells can also be seen with the

migration assay. After the voltage pulse the impedance is dropping to a cell-free impedance value which proves a serious damage of the plasma membrane and the death of the cells. During the closure of the wound the cells can replace the dead cells (Keese et al., 2004). This repopulation of the electrode can be seen in a characteristic increase of the impedance followed by a plateau indicating the end of the cell migration (Gamal et al., 2015). Often the same value as the initial impedance cannot be reached because a small part of the killed cells do not manage to detach from the electrode and the current is partially constrained (Keese et al., 2004). The cells were incubated for 24 h with the BPA before wounding to monitor the toxicity. As seen in the acute toxicity measurement (see fig. 7.30) the cells were strongly harmed during this incubation time and were even dead before the wounding pulse was applied. This is monitored with the different initial impedance values (fig. 7.35) and the associated small impedance change. This characterization is relevant for the highest concentrations of 150, 200 and 300 μM , whose impedance curves do not show any changes after the wounding and consequently, no migration of the cells or a closure of the wound. The cells were damaged too excessively with the BPA concentrations. The cells incubated with 100 μM seem to migrate onto the empty electrode after 15 h. These cells were strongly harmed but can still migrate although a longer time is necessary. This time delay of the wound closure is also present with the incubation of 80 μM . The same value as with smaller concentrations and the control is reached but with 5 h time delay. On the one hand, these BPA concentrations have an influence on the cells, on the other hand they are not high enough to prevent all migration. The lowest concentration of 60 and 30 μM shows the same curve as the control which indicates that these BPA concentrations have no influence on the migration velocity.

The migration measurement was performed only with the 8W1E electrodes since the IDEs had not yet been tested for their wounding functionality at the time of the measurement. Nevertheless, it should be possible to wound the cells on IDEs. As a disadvantage of the IDEs the bigger electrode area should be mentioned and because of that the cells would need much more time to migrate onto the empty electrode area and to close the wound. As a consequence, it would take a much longer time to reach the end of the measurement and to obtain the associated results.

As a last impedance-based assay the proliferation was measured. As mentioned before the capacitance is a parameter for the rate of the electrode coverage (Wegener et al., 2000a). After the addition of the control and 30 μM the capacitance is further decreasing without any influence of the BPA which indicates the further coverage of the electrode. With higher BPA concentration the coverage is more and more restricted. Whereas, the incubation of 60 μM shows only slightly higher capacitance values, the incubation with 80 and 100 μM does not change the capacitance any-

more. BPA harms the cells so strongly that no further proliferation can occur and the attached cells do not grow anymore. With higher concentrations the capacitance is increasing immediately after the addition. This represents the detachment of the cells due to the high impact of BPA.

A different aspect of monitoring the toxicity of BPA was a microscopic analysis of the impact. The concentration-dependent influence on the fluorescence of the cells coincide with the acute toxicity measurement. The staining with the dyes CaAM and EthD-1 for the live/dead images does not show an influence until a concentration of 100 μM . With higher concentrations the cells were dying, as seen in the red fluorescence. With 300 μM the cells were detached, washed away and could not be monitored anymore. This detachment of the cells is a clear indication that the cell membrane collapsed and that the cells were dead. The DAPI staining shows an influence with a concentration from 80 μM on. The cell nuclei are heterogeneously distributed in the image and reveal an impact of BPA. With an incubation of 100 μM a fragmentation of the cell nuclei can be seen. This fragmentation of the cell nuclei shows an excessive damage of the cells. With the highest concentrations of BPA the cells were detached completely and died. This concentration-dependent influence on the measured fluorescence is in agreement with the impedance-based measurements.

Comparison of the various EC_{50} values

The lowest EC_{50} values for the migration and the proliferation with the ECIS electrodes do not deviate significantly from the one of micromotion, whereas the values for acute toxicity are almost twice as high. The EC_{50} value for the PrestoBlue assay and the staining lie in between those values. The high sensitivity of the migration and proliferation measurement can be explained by the metabolic status. The cells are in a metabolically demanding state. They have to form new cell-cell contacts and to proliferate to reduce the holes in the cell layer and therefore, they react more sensitive to minor changes of the metabolism induced by BPA. The sensitivity of the micromotion ranges in a similar size. BPA is added to a confluent cell layer, where the cells do not have to build cell-cell contacts. However, micromotion is very sensitive because the smallest cell movements are analyzed with a high time resolution. Thus, even the smallest influence of a toxicant on the cells is monitored. In the case of the measurement of the acute toxicity, the metabolic activity (PrestoBlue assay) and the images of the staining the impact of BPA was analyzed with a confluent cell layer, 48 h after seeding. Consequently, the cells are not in a metabolically highly demanding process which explains the reduced sensitivity to toxicants. They show effects only for higher concentrations of BPA which directly influence the respiration or the metabolic activity. The cells resist the influence of the high concentration of BPA until the membrane is collapsing and the cells are detaching and dying.

Cytotoxicity of BPA in literature

The EC_{50} values in this work determined in the assays vary in a small concentration range of BPA. In literature many different cytotoxic concentrations are stated depending on the cell type and the setup of the measurement.

Audebert et al. used radio-HPLC to monitor the toxicity of BPA after an incubation of 24 h to three different cell lines. Up to a concentration of 100 μ M a cell viability of $(38 \pm 6) \%$ for HepG2 cells, $(32 \pm 2) \%$ for the ACHN cell line and $(19 \pm 7) \%$ for the LS174T cells could be seen (Audebert et al., 2011). Using the MTS assay a cytotoxicity of $(84.7 \pm 2.1) \%$ on human bronchial epithelial cells could be monitored for concentration of 200 μ M BPA. The authors concluded that the medial inhibitory concentration (IC_{50}) value is $> 200 \mu$ M (George and Rupasinghe, 2018). Furthermore, the cytotoxicity of BPA was established with three different cell types using a sulphorhodamine B assay. It was shown that cytotoxic effects only occur in a range higher than 50 μ g/mL (calculated: 219 μ M). With this assay different IC_{50} values for the cell lines were generated: i) 64.67 μ g/mL for the MCF-7 cells (calculated: 283 μ M), ii) 85.17 μ g/mL for the PC3 cells (calculated: 373 μ M) and ii) 88.48 μ g/mL for 3R3-L1 cells (calculated: 388 μ M) (Hernández-Hernández et al., 2019). In a similar range, the EC_{50} value for a 24 h and a 48 h incubation on daphnia magna were established. The authors used an acute immobilization test to generate an EC_{50} value of 24 mg/L after 24 h (calculated: 105 μ M) and 10 mg/L after 48 h (calculated: 44 μ M) (Chen et al., 2002). A very high EC_{50} was established due to cellular growth and viability assays. With the CHO cells an EC_{50} of $(581.3 \pm 63.6) \text{ mg/L}$ (calculated: $(2545 \pm 279) \mu$ M) was established, whereas the same measurements show an EC_{50} value of $(18.6 \pm 2.2) \text{ mg/L}$ for CAP (calculated: $(81 \pm 9) \mu$ M) and $(14.2 \pm 4.0) \text{ mg/L}$ for hybridoma cells (calculated: $(62 \pm 17) \mu$ M) (Stiefel et al., 2016). Terasaka et al. investigated the 50 % cytotoxic concentration (CC_{50}) with a MTT assay. They found for HL-60 cells a CC_{50} value of 125 μ M, for HSC-2 cell a value of 252 μ M and for HSG cells a value of 258 μ M (Terasaka et al., 2005).

These EC_{50} values are only an incomplete excerpt over different measurement setups. The calculated values range more or less in a same magnitude than the EC_{50} values of this work. The impedance-based values show a slightly higher sensitivity. This monitors clearly that the assays in this work guarantee comparable results and even improve the known data. A further huge advantage was the time-dependent change of the cell behavior during incubation with BPA. Most of the assays in literature are end-point assays and do not allow to draw conclusions about course of the toxicity.

In summary, it was possible to show that BPA has a toxic influence on NRK cells. In a range of 0 μ M to 300 μ M BPA the effect of the toxicant varies from non-influencing to a lethal impact which was analyzed with a whole set of different assays. Both

ECIS electrodes and IDE 12 could be used to generate the concentration of the half maximum effect (EC_{50}) which range from $(84 \pm 3) \mu\text{M}$ to $(156 \pm 23) \mu\text{M}$. Depending on the assay format, different sensitivities were observed. In addition, it was possible to monitor the time-dependent change of the impedance more accurately with the IDE 12 due to the much earlier change in impedance with concentrations beyond $100 \mu\text{M}$ BPA. Consequently, a higher sensitivity of the IDE 12 in comparison to the ECIS electrodes in this assay was demonstrated. This earlier detection of a cell reaction is a clear advantage of the IDEs in comparison to the ECIS electrodes.

8 Use of interdigitated electrodes in emerging impedance-based assays

In the following chapter the use of interdigitated electrodes in emerging impedance-based cell assays is analyzed. In the first case the cell monolayer was manipulated with short electric pulses. This electroporation triggers the intake of fluorescent substances into the cells what can be monitored with CLSM images. The second assay was performed with a three-dimensional cell aggregate, called spheroid. These spheroids were set on the electrodes and their adhesion, outgrowth and the stimulation of the H_1 receptor with histamine was examined.

8.1 *In situ* electroporation

The plasma membrane of living cells shows a highly selective permeability and is therefore the major barrier for the diffusion of big or hydrophilic molecules into the cells (Hapala, 1997). Molecules can be excluded due to their size or polarity. By introducing of structural defects in the membrane, like pores, it is possible for extrinsic substances varying from low-molecular substances to macromolecules to pass the cell membrane, whereas an efficient barrier for others is still existing (Hapala, 1997). This method is called electroporation. It is often used in biotechnological applications to enable the intake of small molecules into cells which do not permeate naturally, for example carbohydrates or nucleic acids (Meldrum et al., 1999).

In general there are two possible electroporation methods: i) cells in suspension and ii) adherent cells. Suspended cells are located between two electrodes which are connected to a generator of high-voltage electric field (Hapala, 1997). The electric pulse of several kV/cm is applied and a permeabilization of the membrane on the place of the largest transmembrane potential gradient took place (Hapala, 1997). A disadvantage of this procedure is that the cells must attach and spread before the newly generated cell properties can be examined (Wegener et al., 2002). Furthermore, anchorage-dependent cells have to be trypsinated before electroporation to get a cell suspension. This tryptic digestion is more invasive for the cells and can influence the results (Zheng and Chang, 1991). In this work the second mode for electroporation

is used. Adherent cells on conductive surfaces like electrodes were electroporated with pulses of some V for a short time (μs to ms) (Stolwijk et al., 2011). A difficulty is to find the optimal voltage value which differs between different cell lines and electrode layouts (Raptis and Firth, 1990; Wegener et al., 2002). On the one hand the voltage has to result in the highest permeability, on the other hand it should maintain the maximal viability of the cells. If the voltage is too high, the electroporation can be irreversible and cytotoxic, including DNA breaks or the production of reactive oxygen species (Meldrum et al., 1999). In this work the electroporation was performed with sinusoidal voltage pulses of different amplitudes and the cells were monitored before and immediately after the pulse. The efficiency of the electroporation was controlled with the uptake of a fluorescent probe (FITC-dextran: fluorescein isothiocyanate dextran) from the extracellular electrolyte. As a comparison the electroporation with the corresponding CLSM images were performed with the 8W1E electrodes and the IDEs with different pitches.

8.1.1 *In situ* electroporation using commercial electrode layouts

First, the electroporation measured with 8W1E electrodes will be discussed. In fig. 8.1 **A** the impedance change measured with the 8W1E electrodes during the electroporation of a confluent layer of NRK cells and the regeneration is shown, while 8.1 **B** reveals a zoom in to the first 35 min after the pulse.

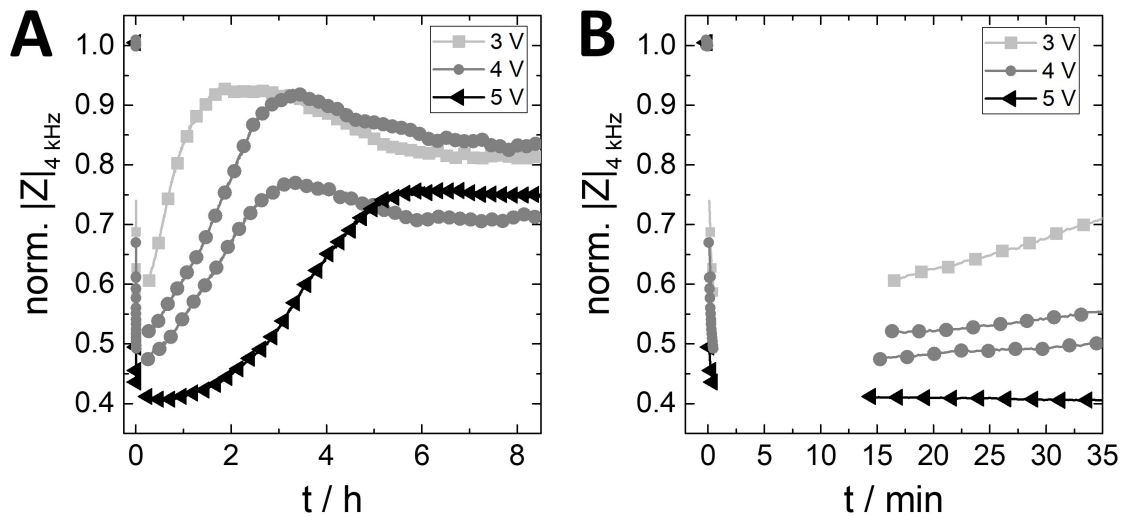


Figure 8.1: Time-dependent change of the normalized impedance after electroporation at $t = 0$ h of NRK cells on 8W1E electrodes at 4 kHz. Voltages of 3 V, 4 V and 5 V (40 kHz, 125 ms) were applied. **A:** time-dependent change of the impedance for 8.5 h, **B:** zoom in to the first 35 min. The values are normalized to the initial value of the cell-covered electrodes before electroporation ($|Z| = (20375 \pm 491) \Omega$). ($n = 1$)

All electroporation pulses were performed at 40 kHz and for 125 ms with varying voltages of 3 V, 4 V and 5 V. The electroporation was executed at the time point of $t = 0$ h what is seen in the decreasing impedance. The higher the voltage, the lower is the value of the norm. $|Z|_{min}$ after electroporation (3 V: norm. $|Z|_{min} = 0.61$; 4 V: norm. $|Z|_{min} = 0.52$ and 0.47, 5 V: norm. $|Z|_{min} = 0.41$). Afterwards, the impedance is increasing gradually again to pre-pulse values forming a saturation which stays constant until the end of the measurement. Depending on the voltage, the time when the maximum is reached is changing. The fastest increase of the impedance to a maximum of norm. $|Z|_{max} = 0.92$ can be seen for the pulse with 3 V after $t = 1.83$ h. The maximum of the impedance with the pulse of 4 V (norm. $|Z|_{max} = 0.92$ and 0.77) is reached after $t = 3.22$ h, whereas the impedance needs $t = 5.97$ h to reach the saturation of norm. $|Z|_{max} = 0.76$ with the pulse of 5 V. Consequently, the higher the voltage, the longer does the impedance need to increase to a saturation value. Nevertheless, it can be seen that in no case the impedance returns to the initial values.

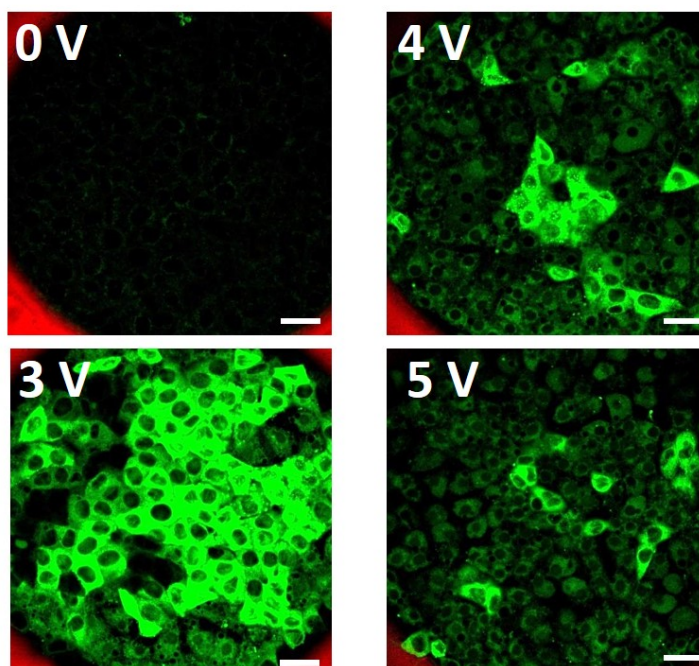


Figure 8.2: Microscopic images of electroporated NRK cells on 8W1E electrodes using a 60x magnification with the CLSM. Due to electroporation the green fluorescent FITC-dextran could pass the cell membrane and enter the cells dependent on the applied voltage. The images of the fluorescence of the cells with the FITC-dextran were monitored with the CLSM. A study of the efficacy of different voltage pulses (0 V, 3 V, 4 V, 5 V at 40 kHz and for 125 ms) was performed. The red fluorescence arises from the photopolymer. The scale bar represents 25 μm .

The efficacy of the electroporation can be controlled with the introduction of a big molecule into the cells (Ghosh et al., 1993). In this work the green fluorescent FITC-dextran (2 MDa and 2 mg/mL) was used which could not enter the cells naturally

due to the size exclusion of the cell membrane. During electroporation with the right magnitude of the voltage pulse the FITC-dextran entered the cells and it was possible to visualize the green fluorescence of the FITC-dextran inside the cells. In fig. 8.2 the electroporated cells with different voltage pulses can be seen. As a control (0 V) the FITC-dextran solution was added to the cells and no pulse was applied. After washing, the cells were imaged and no fluorescence is seen in contrast to the clearly visualized green fluorescence with a pulse of 3 V. The black circles in the middle of the cells are the cell nuclei and the red fluorescence arises from the photopolymer. The cells directly on the electrode show green fluorescence, whereas the cells near to the electrode could not be seen in these images. The cells which were electroporated with 4 V and 5 V display less fluorescence and only some of them are completely green, whereas the image of the cells with 5 V illustrate even less green cells.

The microscopic images illustrates clearly that the FITC-dextran could not enter the cells without any electroporation because after washing no fluorescence was detected for the cells without a pulse (0 V). The proof that the electroporation was working is seen in the image of the cells electroporated with 3 V. After a voltage pulse of 3 V the FITC-dextran passed the cell membrane and entered the cells, seen in the green fluorescent cell cytoplasm. With a pulse of 4 V and 5 V most of the cells did not show proper cytoplasmic fluorescence. This indicates that the membrane was damaged and the fluorophore was washed out. This irreversible damage of the cell membrane was also obvious with the impedance data. With an applied voltage of 5 V the measured impedance needed around 6 h to increase until a saturation was reached. In combination with the images of these cells this illustrates that the cell monolayer was wounded and that the cells were not recovering after the electroporation. The images and the impedance data of the cells pulsed with 4 V lay between the working electroporation with 3 V and the supposed wounding with 5 V. Evidently a mixture of electroporation and wounding occurred with this voltage.

8.1.2 *In situ* electroporation using IDEs

To see, if cell manipulation with electric pulses is accessible with IDEs, the IDE 10, IDE 12 and IDE 20 with confluent NRK cells were used.

The AC voltage pulses were applied for 125 ms at $t=0$ min at the specific frequency f_{max} for each IDE, respectively (IDE 10: 200 kHz, IDE 12: 400 kHz, IDE 20: 200 kHz). The time-dependent change of the impedance for the frequencies f_{max} is shown in fig. 8.3. The impedance changes of the IDE 10 (fig. 8.3 **A**) and the IDE 12 (fig. 8.3 **B**) have a similar course. At the time point of the electroporation ($t=0$ h) the impedance rises briefly, whereas the amount of this increase becomes

smaller, the bigger the pitch is, before it decreases to a voltage-dependent minima (from norm. $|Z|_{min} = 0.924 \pm 0.007$ (2 V of IDE 12) to norm. $|Z|_{min} = 0.72 \pm 0.04$ (7 V of IDE 10)). The higher the applied voltage, the lower are the minima of the impedance which occur around 5 min after electroporation. Afterwards, the impedance is increasing again and reaches nearly the same initial values before electroporation within 20 min, with the one exception of 5 V with the IDE 12. Here, the impedance is decreasing and stays constant over time.

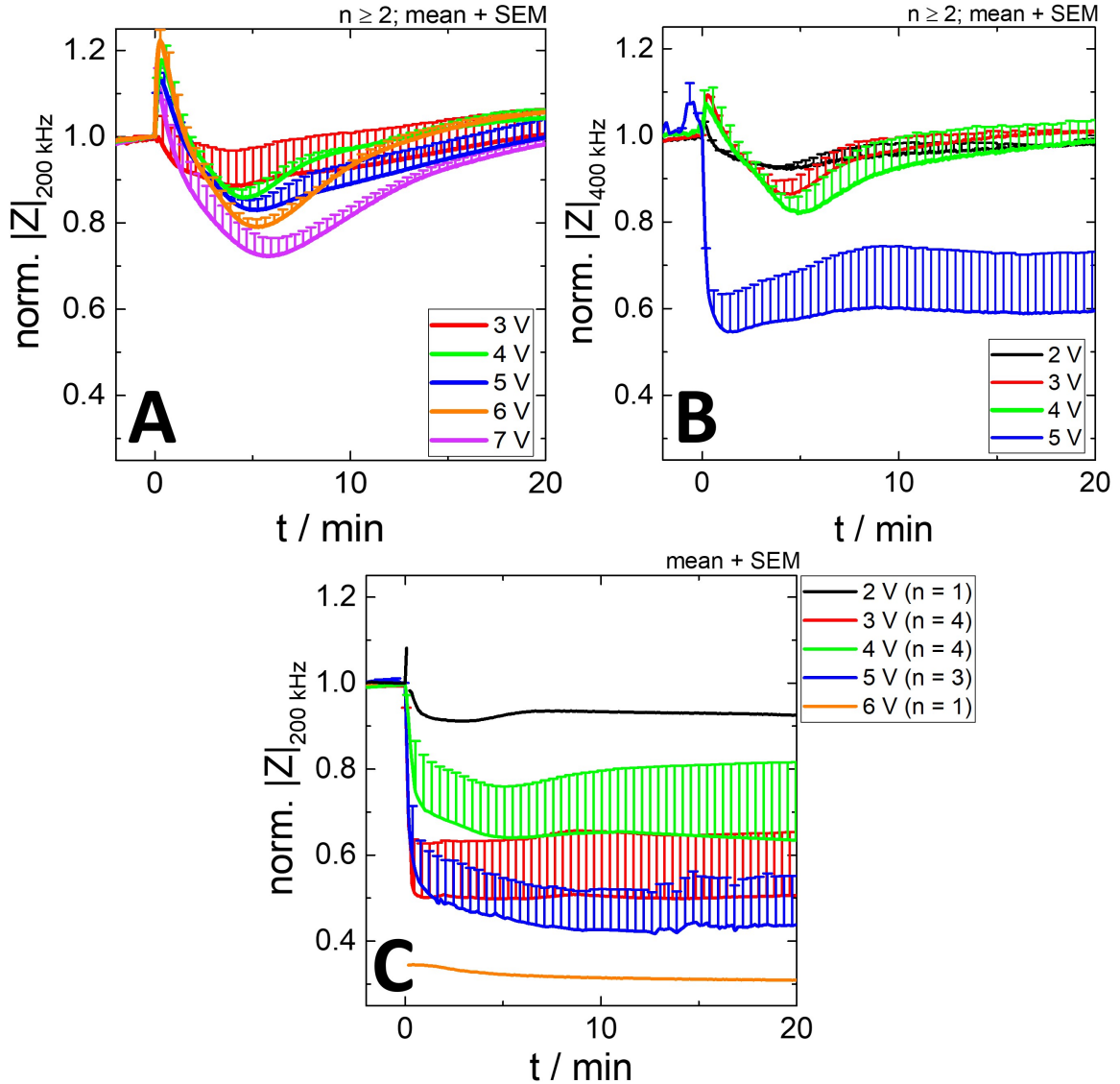


Figure 8.3: Time-dependent change of the normalized impedance after electroporation at $t = 0$ h of NRK cells on different IDEs. Voltage pulses of 2 V, 3 V, 4 V, 5 V, 6 V and 7 V for 125 ms at the specific frequency f_{max} (IDE 10: 200 kHz, IDE 12: 400 kHz, IDE 20: 200 kHz) were applied. The time-dependent impedance change is measured at f_{max} , respectively: **A:** IDE 10 (200 kHz), **B:** IDE 12 (400 kHz), **C:** IDE 20 (200 kHz). The impedance values are normalized to the initial value before electroporation (IDE 10: $|Z| = (244 \pm 46) \Omega$; IDE 12: $|Z| = (186 \pm 21) \Omega$; IDE 20: $|Z| = (383 \pm 49) \Omega$). The mean with the SEM in plus direction is plotted.

The impedance change of the IDE 20 differs from the other two IDEs (see fig. 8.3 C), ipso facto that no increase after electroporation ($t=0$ h) with the different pulses can be seen. The course of 2 V shows no significant change of the impedance after electroporation (norm. $|Z|_{min}=0.93$). The lowest impedance value can be seen for 6 V with a constant value of norm. $|Z|_{min}=0.32$, while the voltage pulses of 3 V, 4 V and 5 V show no distinct trend. The impedance is decreasing to a constant value for all three courses but not in a voltage-dependent manner and does not show any change until the end of the measurement. Within the errors it can be seen that the normalized impedance of the cells which were electroporated with 4 V shows the highest constant value (norm. $|Z|_{min}=0.7 \pm 0.1$) and the one with 5 V the lowest value (norm. $|Z|_{min}=0.43 \pm 0.09$), whereas the one of 3 V lies in between (norm. $|Z|_{min}=0.5 \pm 0.1$).

To proof the efficiency of the electroporation the cells were visualized with the CLSM and the fluorescence was analyzed (see fig. 8.4). The quantity of fluorescent cells and the state of the confluent cell layer is dependent on the applied voltage pulses and vary for every electrode layout.

In fig. 8.4 A the images of IDE 10 are represented which show on the one hand no fluorescence with a pulse of 4 V and 5 V, and on the other hand a nearly evenly distributed monolayer of green fluorescent cells with a pulse of 6 V. Increasing the voltage to 7 V only some cells display a green fluorescence very occasionally. However, the cells do not show smooth borders and seem to be damaged. A similar result is obtained for the IDE 12 (see fig. 8.4 B). With low voltages the cells do not show a bright fluorescence. In the image of the cells electroporated with 2 V it seems that the fluorescent FITC-dextran is attached to the outer surface of the cell membrane, because a diffuse fluorescence around the cells can be seen and no difference between the cell nuclei and the cytoplasm can be made. Consequently, the FITC-dextran was not able to pass the cell membrane. With a pulse of 3 V a small percent of FITC-dextran entered the cells because the black nuclei are visible, even if the fluorescence is not very intense. The most homogeneous distribution of the green fluorescence in the whole monolayer is monitored with a pulse of 4 V. With higher voltage pulses (5 V) the cells do not appear regular in morphology and only rounded cells are seen leading to the conclusion that the cells were dying. The images of the IDE 20 show the same behavior (fig. 8.4 C). With a pulse of 2 V and 3 V only scattered cells express a green fluorescence and with a pulse of 4 V the fluorescence displays a bright and uniform distribution. Increasing the pulse to 5 V leads to less fluorescent cells. Furthermore, the monolayer has huge holes and the borders of the cells look like collapsing cells just leaving rests of the membrane. With the highest voltage pulse of 6 V only small cell rests can be seen.

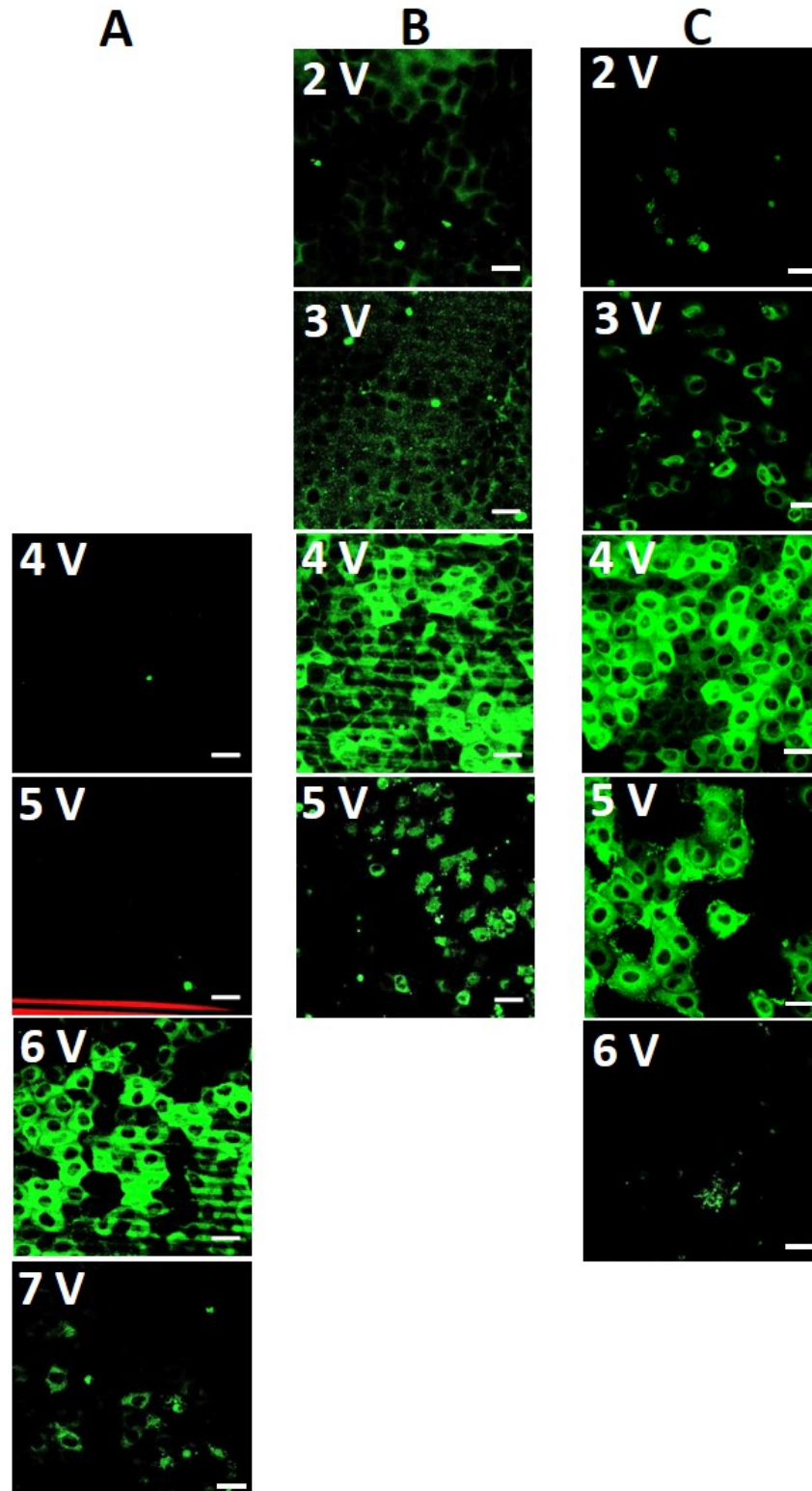


Figure 8.4: Microscopic images of electroporated NRK cells on IDEs using a 60x magnification on the CLSM. Due to electroporation the green fluorescent FITC dextran could enter the cells at the right voltage and could be monitored with CLSM. A study of the efficiency of different voltage pulses (2 V, 3 V, 4 V, 5 V, 6 V, 7 V for 125 ms at the frequency f_{max}) was performed. **A:** IDE 10 (200 kHz), **B:** IDE 12 (400 kHz), **C:** IDE 20 (200 kHz). The scale bar amounts to 25 μm .

Furthermore it was analyzed, if the cells on the whole non-insulated electrode area of the IDEs were electroporated. Fig. 8.5 shows an image of the electroporated cells with the green channel (fig. 8.5 **A**) and the same image with the green and the red channel (fig. 8.5 **B**). The red channel displays the photopolymer which limits the non-insulated electrode area and the green fluorescence which monitors the electroporated cells. With this image it can be shown that cells are electroporated on the whole electrode also near the edge of the insulating photopolymer. On the photopolymer no cells show a green fluorescence, which repeatedly proves that the FITC-dextran can only pass the cell membrane after an voltage pulse and that all cells on the non-insulated electrode area can be electroporated .

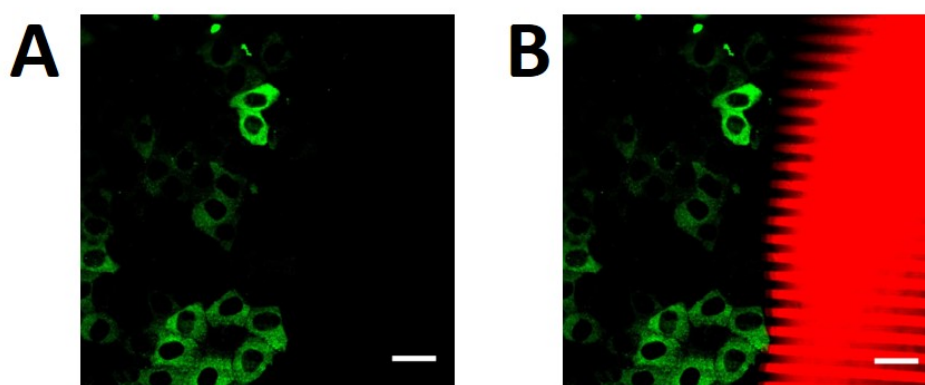


Figure 8.5: Two images of the same field of view of electroporated NRK cells on IDE 10 with a pulse of 6 V (60x magnification with the CLSM) with an analysis of the different color channels. Due to electroporation the green fluorescent FITC-dextran enters the cells after the pulse with 6 V and the fluorescence can be monitored with CLSM. The red area shows the photopolymer which limits the non-insulated electrode area. **A:** green channel, **B:** green and red channel. Only cells on the electrode are electroporated. The scale bar amounts to 25 μm .

This chapter illustrates that the IDEs can be used for the electroporation of NRK cells on condition that an appropriate voltage magnitude is applied. This magnitude is changing for every electrode layout and is essential for a proper electroporation. With lower voltages the membranes are insulating and the FITC-dextran cannot enter the cells. With higher voltages the membranes were damaged and the cells were detached from the electrodes or FITC-dextran was washed out of the cells what can be seen in the missing fluorescence in the images. The most efficient introduction of the FITC-dextran into the cells occurred at 6 V for the IDE 10 (at 200 kHz) and at 4 V for the IDE 12 (at 400 kHz) and IDE 20 (at 200 kHz), respectively. Furthermore, it was shown that the cells on the whole non-insulated electrode area can be electroporated.

8.1.3 Discussion

The efficiency of the electroporation was proven with the intake of the fluorescent FITC-dextran into the cells which occurs with an appropriate voltage amplitude. The brightness of the green fluorescent cells indicates the amount of the introduced dye. The 2 MDa dye is excluded from the nucleoplasm due to the size exclusion of the nuclear pores (20-40 kDa) and consequently, the cell nuclei appear as black circles in the middle of the cells. There are two possible explanations for the introduction of these molecules into the cells: i) pores in the size of nanometers are formed within the membrane and the probes can diffuse into the cells or ii) the electric field initiate the cluster building of the exogenous molecule on the surface of the membrane resulting in an endocytotic uptake (Stolwijk et al., 2011). Right now it is not clear which mechanism is the correct one. Probably it is dependent on the size and the charge of the foreign molecule. Due to the fact that too high voltages lead to irreversible membrane damages, a creation of a dielectric breakdown of the membranes is possible. This is the basis for the formation of pores (Stolwijk et al., 2011). A further hint for the first mechanism is the hydrodynamic diameter of FITC-dextran (2 MDa) of 52 nm (Lebrun and Junter, 1993) and the varying average diameter of the pores from 5 nm to 500 nm which enables the diffusion of the substance (Zaharoff et al., 2008). Furthermore, FITC-dextran (2 MDa) has a diffusion coefficient in water of $D_w = 3.15 \cdot 10^{-7} \text{ cm}^2/\text{s}$ (Lebrun and Junter, 1993). With the assumption that the molecule is only diffusing in one dimension in a direction perpendicularly to the membrane, a maximal diffusion velocity of around $7.9 \mu\text{m}/\text{s}$ can be supposed. Based on the fact that the cell membrane has a thickness of around 4 nm and the pores are large enough for the FITC-dextran to enter, it can be said that the time, when the pores are open, would allow the diffusion of the FITC-dextran into the cells. Furthermore, the control image with no voltage applied shows that the FITC-dextran cannot enter the cells (see fig. 8.2) and after the washing step no fluorescence can be monitored anymore. When a certain voltage is applied, green fluorescence is seen inside the cells, except for the cell nuclei which stand out due to its missing fluorescence. The membrane of the cell nuclei has a high size exclusion and is not electroporated with the voltage pulse. Consequently, the FITC-dextran cannot enter the cell nuclei and remains in the cell cytoplasm. A further hint that the FITC-dextran is inside the cell is the fact that the fluorescence is still visible after several washing steps. In summary it can be said: i) FITC-dextran is too big to diffuse through the intact membrane into the cells and ii) green fluorescence can only occur, if the voltage is high enough to enable the entry of the big molecules into the cell cytoplasm. This can be further proven with the images of the IDEs (fig. 8.4) with the completely missing fluorescence for low voltage amplitudes of the IDE 10 (4 V and 5 V) and a strong reduced fluorescence for the voltage pulses of 2 V

and 3 V for the IDE 12 and IDE 20.

Analyzing the time course of the impedance this efficiency of the intake of the FITC-dextran cannot be explained completely. The higher the applied voltage pulse is, the more pronounced is the impedance drop right after the pulse (with exception of the IDE 20). This effect is often seen in other researches (Ghosh et al., 1993). This large dip of the normalized impedance after electroporation is not resulting from the permeabilization of the membrane and the reclosure. This would only be visible in very short time scales (Stolwijk et al., 2011). The decrease and the slowly increase of the impedance reflects the variation of the cell shape due to the electroporation pulse and the associated effects, like the outflow of molecules from the cytoplasm, the Ca^{2+} influx into the cytoplasm or the transient osmotic imbalance (Stolwijk et al., 2011; Wegener et al., 2002). Nevertheless, the cells can completely recover in a short time (around 1 h) seen in an increasing impedance (Wegener et al., 2002). For the 8W1E electrodes (see fig. 8.1) this impedance recovery time after a voltage pulse of 5 V is almost six times longer. Comparing the time course of the impedance after a voltage pulse of 5 V with the impedance-based analysis of cell migration after wounding measured with 8W1E electrodes (see chapter 7.6.4) a nearly identical impedance time course is seen. In both cases the same voltage at the same frequency is applied to a confluent monolayer of NRK cells and only the time duration of the voltages is different (wounding: 30 s, electroporation: 125 ms). In fig. 7.35 (chapter 7.6.4) the impedance of the control NRK cells need $t = 8.29$ h to recover and to reach the initial impedance after wounding with 5 V (40 kHz, 30 s). In the case of the electroporation the impedance for the cells electroporated with 5 V (40 kHz, 125 ms) reaches a constant value after $t = 5.97$ h. This similar impedance courses indicates that the cells are wounded with the electroporation pulse of 5 V. This can be underlined with the images of the intaken FITC-dextran after a pulse of 5 V. Nearly no fluorescence of the cytoplasm of the cells can be monitored. The reason is that the cell membrane is damaged and the fluorophore is washed out which shows a clear wounding of the cell layer. Consequently, the impedance course and the image show clearly, that the cell monolayer is wounded after an electroporation pulse of 5 V due to the fact that the voltage is too high to maintain the viability of the cells. For an applied pulse of 4 V measured with the 8W1E electrodes it seems to be a mixture of electroporation and wounding. The impedance needs 3.22 h to reach the initial impedance value. This is between the impedance of the 3 V and the 5 V. Also the images show some green cells, whereas the cells with reduced fluorescence dominate indicating a damaged cell membrane and the associated washing out of the fluorescence. Consequently, most of the cells were wounded at this voltage pulse. However, the difference with the impedance and the images of the 5 V shows that not all cells are wounded, but some cells were electroporated. In the case of the IDEs the cells are also dying with

higher voltage pulses which can be seen in the constant impedance values of the 5 V of the IDE 12 and the 6 V of the IDE 20 and the corresponding images in fig. 8.4 showing damaged cells with an irregular morphology. When the applied voltage is too high, the reversibility of the electroporation is not given anymore and the cells are harmed irreversibly (Wegener et al., 2002). This can lead to the following results: i) the cells cannot hold the dye anymore and the fluorescence is reduced. ii) The high voltages can destroy the membrane and necrosis of the cells appears. This is seen for the IDE 20 with 5 V or 6 V with only some cell remnants of the membrane left or with completely detached cells.

On the contrary it was quite possible to perform electroporation without wounding the whole monolayer. The impedance measured with the 8W1E electrodes is recovering after a voltage pulse of 3 V after $t = 1.83$ h and the cells show a homogeneous fluorescence. Consequently, the electroporation is working similar to the literature (for example (Wegener et al., 2002) or (Stolwijk et al., 2011)). The IDEs also show an increase of the impedance directly after the electroporation pulse. This increase of the impedance to the initial values is much faster with the IDE 10 and IDE 12 as with the IDE 20 or the 8W1E electrodes. Even within one electrode type the initial impedance regains slower with higher voltage pulses (Ghosh et al., 1993). The exceptions are the pulses with which the images emphasized the cell death: i) IDE 12: 5 V, ii) IDE 20: 5 V partially and 6 V. The faster recovery of the impedance with lower voltages can be explained due to the fact that the voltage pulses are not efficient enough to enable the intake of the fluorophore which also can be seen in the missing fluorescence in the images. Consequently, the cells are only reacting to the short electric pulse but do not have to suffer a strong cell shape or osmotic imbalance. The longer recovery time for the IDE 20 can occur because this electrode layout has a larger distance between the electrodes and the ratio of the electric field in the intercellular cleft is higher than for the other electrodes (see fig. 6.6 in chapter 6.1). With this higher ratio in the intercellular cleft it is possible to monitor more of the cell shape change and recovery than with the smaller pitches. For the short measured time interval seen in fig. 8.3 it is not possible to say, if and when the impedance reaches the initial values. Comparing this time section with the first 20 min of the 8W1E electrodes (see fig. 8.1 **B**) no clear difference within the errors can be determined.

In the previous chapters it was seen that the focus of the monitoring and detection of the impedance measured with the IDEs was on the basal side and underneath the cells. On this basis it should not be possible to electroporate cells with IDEs with a small pitch. The simulations in chapter 6.1 showed that with the IDEs with a small pitch the main part of the electric field is seen underneath the cells. Nevertheless, with flatter cells, like the NRK cells, a large ratio of the electric field is shifted to

the intercellular cleft and a significant proportion of the electric field reaches the apical membrane side (see fig. 6.3 in chapter 6.1). When now a voltage, for example 5 V, is applied, the ratio of the electric field which reaches the apical side of the cells seems to be enough to enable the electroporation. This would require that the electroporation with IDEs is only possible with flat cells, so that a sufficient ratio of the electric field with the according voltage magnitude reaches the apical membrane side to allow the intake of the fluorophore into the cells. A more detailed explanation cannot be given at this stage of the work, since further tests and simulations are required.

Fig. 8.5 shows a big advantage of the IDEs in electroporation measurements. In this work all cells on the non-insulated electrode area were electroporated homogeneously and the cells on the insulating photopolymer do not show a fluorescence. This non-insulated electrode area of the IDEs ($(1.1 \times 1.1) \text{ mm}^2 \cong 1.21 \text{ mm}^2$) is much bigger than the electrode area of 8W1E electrodes with a diameter of $250 \text{ }\mu\text{m}$ ($\cong 0.05 \text{ mm}^2$). With this higher non-insulated electrode area of the IDEs much more cells can be electroporated than with the 8W1E electrodes. This is a huge advantage, for example in pharmaceutical applications when drugs need to be introduced into as many cells as possible. The non-insulated electrode area of the IDEs can be varied with the method of photolithography. However, it was shown in chapter 6.3 that with a larger size of the non-insulated electrode area the electrical ratios change. Therefore, according to the current state of work, it is not possible to conclude that the non-insulated electrode area can be increased arbitrarily. For this further investigations are necessary.

Electrodes with an interdigitated structure were rather infrequently used in different research groups for electroporation with suspended or adherent cells. In the following some examples of these applications will be explained.

The measurement of suspended cells is seldom done with interdigitated electrodes. Xu et al. invented a printed circuit board to fabricate IDEs with a width of $150 \text{ }\mu\text{m}$ and a gap of $250 \text{ }\mu\text{m}$. The three-dimensional electrode had a thickness of $35 \text{ }\mu\text{m}$. For comparison of the results of these electrodes, planar two-dimensional electrodes (thickness $< 1 \text{ }\mu\text{m}$) with the same pitch were used, made of a conductive (Ti/Au) and an insulating layer ($\text{Si}_3\text{N}_4/\text{SiO}_2$). The suspended cells were added to the measurement chambers and could settle down during a 5 min equilibration time. Plasmids encoding a green fluorescent protein were electroporated into different cell types. Afterwards, the cells were cultured for 24 h before the viability was measured. The authors concluded that the cell survival rate of the cells with the three-dimensional electrodes were higher with a better transfection rate than with the two-dimensional ones (Xu et al., 2015b). A different group used annular interdigitated electrodes

with a width of 100 μm and a gap of 500 μm . The suspended cells were added to the electrodes with a mixture of plasmids or synthetic siRNA and an electric pulse depending on the cell type (between 60 V to 150 V for 0.1 ms to 0.6 ms) was applied. After a cultivation time of 24 h the GFP expressing cells were counted. They were able to achieve a cell viability of 80 % and from these cells a transfection rate of 90 % (Huang et al., 2011).

A further annular interdigitated electrode was used for electroporation of adherent cells with a non-contact method. The round shaped interdigitated gold structure (width: 75 μm and gap: 150 μm) was patterned onto a stamp. This stamp was positioned over the cultivated cells in a distance of 10 μm with microseparations to avoid contact of the cells and the electrode. Different pulses of 100 μs were applied to create an electric field of 1.2, 1.6, 2.0 and 2.2 kV/cm at the surface of the electrode in the presence of FITC-dextran. After 2 h the fluorescence of the cells was analyzed. The authors saw 50 % efficiency of the electroporation for 2.2 kV/cm (García-Sánchez et al., 2012). The group around Yu-Cheng Lin used interdigitated electrodes to electroporate DNA plasmids into adherent cells. First, they apply an electric field to attract DNA plasmids to the gold interdigitated electrodes (width and gap of 100 μm , respectively) with the help of a gold cathode on top of the measurement chamber and the interdigitated electrodes on the bottom of the measurement chamber as an anode. Afterwards, both combs of the interdigitated electrodes were connected and a voltage of 3 V with two pulses with a duration of 20 ms and a frequency of 25 Hz was used to electroporate the DNA plasmids into the adherent cells. With an attractive voltage to the DNA plasmids before electroporation a better distributed fluorescence over the monolayer could be seen (Jen et al., 2004). Furthermore, a microchip with interdigitated gold electrodes (a width and a gap of 100 μm) was invented. The seeded cells were electroporated with a voltage of 1, 2, 4, 6 and 8 V with a duration of 20 ms and at a frequency of 25 Hz. They generated for 8 V a survival rate of 39 % and a transfection rate of 36 % (Lin et al., 2003).

In all of these mentioned applications IDEs with a much higher width and gap than in this work were used. For the adherent cells this has the consequence that it was not possible to generate a homogeneous electric field and that less cells could be transfected in parallel. By using electrodes with a subcellular dimension a homogeneous electric field can be generated and, as seen in this work, the adherent cells can be electroporated in parallel in a largely uniform manner. This applies also to suspended cells. When the pitch is too large, no homogeneous electric field can be generated. Furthermore, in none of these publications a time-dependent measurement of the cell reaction after electroporation was analyzed. This is a huge advantage of the impedance-based measurement for a better understanding of the electroporation process and the corresponding cell reaction.

In summary, it is possible for both the 8W1E electrodes and the IDEs to use electroporation to enable the intake of FITC-dextran into the cells. The properly proceeding electroporation measured with IDEs is resulting in an increase of the impedance, after the first drop, to nearly the initial values within a time duration of < 2 h and a green fluorescence of the cytoplasm. What has become clear through this chapter is that the choice of the applied voltage is essential for a proper electroporation. If the voltage is too low, no intake of the FITC-dextran is possible. With a too high voltage, the cells were wounded seen in the slowly increasing impedance and the washed out fluorophore resulting from the damaged cell membrane. The appropriate voltage magnitude is dependent on the electrode layout. It was also shown that compared to the 8W1E electrodes the IDEs have the major advantage that more cells can be manipulated due to the larger non-insulated electrode area.

8.2 Impedance-based analysis of U373 spheroids

As another emerging assay the adhesion of a three-dimensional spheroid on the electrodes was analyzed. Further conclusions were drawn from the staining and the stimulation of the H_1 receptor with histamine. Spheroids are spherically aggregates of cells varying with the cell number (Hamilton, 1998). The three-dimensional multicell spheroids were often used in biology and cancer research as an *in vitro* model for tumor microregions or micrometastases. It can be seen as the intermediate between monolayer and tumors (Sutherland, 1986). The spherical form and the size of the spheroids (some hundred μm to 1 mm) lead to a decreasing supply of nutrient towards the center of the spheroid. In the center of the spheroid the nutrient concentration drops below a critical level and the cells are dying leading to a necrotic core (Greenspan, 1972; Sutherland, 1988).

8.2.1 Adhesion of spheroids on different electrode types

For measuring the adhesion of spheroids (400 μm in diameter) they were put centrally onto the different electrode types and the settling and the centrosymmetric spreading of the cells were measured. It is shown in fig. 8.6 **A** that the adhered and stained spheroid is smaller than the non-insulated electrode area of the IDE12 which is defined by the photopolymer (seen with the red color). The cells of the spheroids are growing on the electrode and are spreading in a centrosymmetrical way over the photopolymer and even over the leads. The adhered spheroid on the 8W1E electrode in fig. 8.6 **B** is much bigger than the small working electrode in the middle of the image (bright circle). Nevertheless, the spread cells can be seen around the spheroid growing in a centrosymmetrical way.

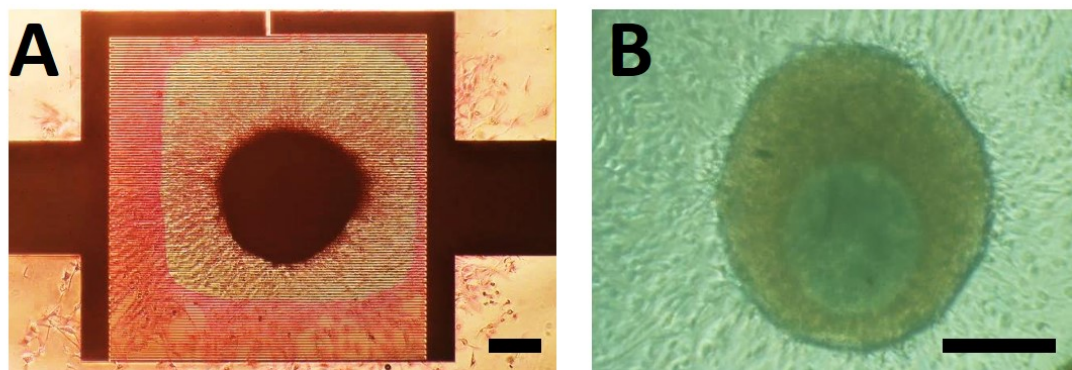


Figure 8.6: Microscopic images of spheroids adhered on the electrodes on the third day after inoculation. **A:** Spheroid adhered on IDE12 after carbol fuchsin staining. **B:** Spheroid adhered on a 8W1E electrode (bright circle) without any additional staining. The scale bar represents 200 μm .

For a three-dimensional visualization of the adhered spheroids, the cells were stained with a live/dead dye (CaAM / EthD-1) (fig. 8.7) and the cell nuclei with DAPI (fig. 8.8). Furthermore, the spheroids were pictured layer by layer and the individual images were stacked along the z-direction resulting in a three-dimensional representation of the spheroids (fig. 8.7 **A**, **B** and 8.8A, B).

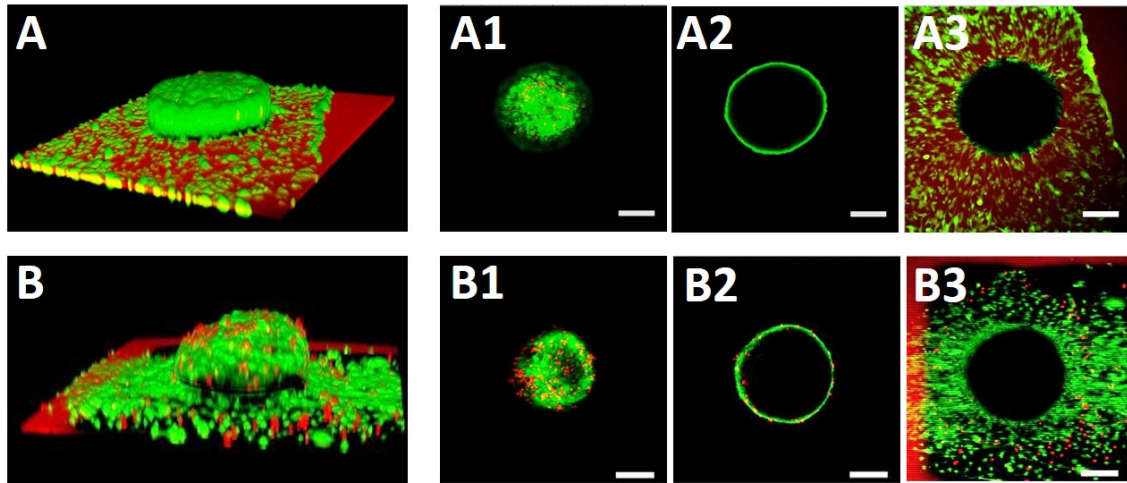


Figure 8.7: Microscopic images of live/dead stained spheroids (dyes: CaAM / EthD-1) adhered on the electrodes on the third day after inoculation in a three-dimensional visualization using the CLSM (10x magnification), **A**: 8W1E electrode and **B**: IDE12. An optical section of the spheroids in z-direction from the top of the spheroids (**A1**, **B1**) over the center of the spheroids (**A2**, **B2**) to the spreading zones (**A3**, **B3**) can be seen. The healthy cells appear green, the dead cells red. The large red fluorescent area is the photopolymer. The scale bars account for 200 μm .

In fig. 8.7 the healthy cells are stained green, whereas the dead cells have a red fluorescence. The larger red fluorescent areas represent the photopolymer which limits the non-insulated electrode area. The image of the adhered spheroid on the 8W1E electrode (see fig. 8.7 **A**) does not show a border of the photopolymer because the spheroid is bigger than the non-insulated electrode area and covers the electrode completely. In the case of the IDE (see fig. 8.7 **B**) the rim of the photopolymer can be seen which shows the larger size of the non-insulated area in comparison to the spheroid. The image of the three-dimensional spheroids can further be analyzed with different optical sections in z-direction: i) in the optical section on top of the spheroids (fig. 8.7 **A1** and **B1**) the healthy cells are distributed in a regular manner and only some dead cells can be seen. ii) In the middle of the spheroid (fig. 8.7 **A2** and **B2**) only a small rim of healthy cells is represented, whereas the center of the spheroid is completely black. iii) The optical section in the area of the spreading zone (fig. 8.7 **A3** and **B3**) shows a distribution of healthy cells on the electrodes. The spheroid in the middle stays black whereas the border of the photopolymer is red in the case of the IDE.

As a second staining the cell nuclei of the same adhered spheroids were stained with

DAPI resulting in a blue fluorescence (see fig. 8.8). In the three-dimensional images (fig. 8.8 **A** and **B**) the cells spread on the electrode around the spheroid can be seen. The images of the different optical sections resemble the ones of the live/dead staining with the regular distribution of the cell nuclei on top of the spheroid (see fig. 8.8 **A1** and **B1**), the blue rim with the black inside of the spheroid (see fig. 8.8 **A2** and **B2**) and the adhered cells with the black spheroid in the middle (see fig. 8.8 **A3** and **B3**).

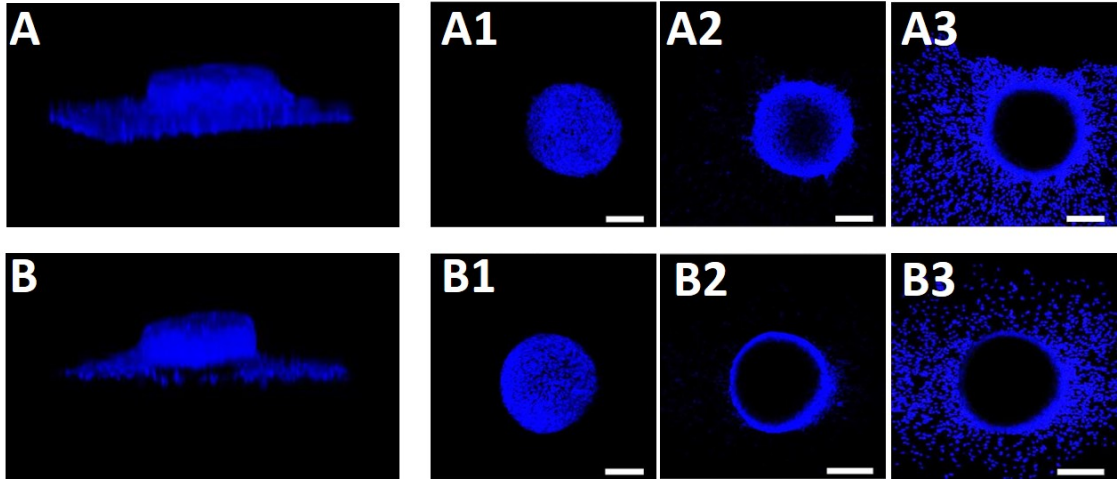


Figure 8.8: Microscopic images of DAPI stained spheroids adhered on the electrodes on the third day after inoculation in a three-dimensional visualization using the CLSM (10x magnification), **A**: 8W1E electrode and **B**: IDE12. The cell nuclei appear blue. An optical section of the spheroids in z-direction from the top of the spheroids (**A1**, **B1**), over the center of the spheroids (**A2**, **B2**) to the spreading zones (**A3**, **B3**) can be seen. The scale bars represent 200 μm .

All in all it can be shown with the microscopic images that the spheroids settled down on the electrodes and adhered in a centrosymmetrical way. This adhesion can also be monitored with impedance-based measurements as described in the following.

In fig. 8.9 the time-dependent change of the normalized impedance during adhesion of the spheroids on different electrode types at the individual frequency f_{max} is shown. After inoculation of the spheroids to the 8W1E electrodes at the time point $t = 0$ h the impedance is increasing immediately (see fig. 8.9 **A**). At $t \approx 12$ h it reaches a maximum (norm. $|Z|_{max} = 4.0 \pm 0.2$) and remains nearly constant until the end of the measurement. The adhesion of the spheroids on IDE 10, IDE 12 and IDE 20 at the individual frequency f_{max} can be seen in fig. 8.9 **B**. After inoculation of the spheroids the impedance is increasing slowly to a maximum after around 35 h and remains at this value. The maxima of the normalized impedance vary dependent on the pitch from norm. $|Z|_{max} = 1.35 \pm 0.03$ (IDE 10) to norm. $|Z|_{max} = 2.7 \pm 0.3$ (IDE 12), over norm. $|Z|_{max} = 2.2 \pm 0.1$ (IDE 20) without a clear dependence of the impedance magnitude to the pitch.

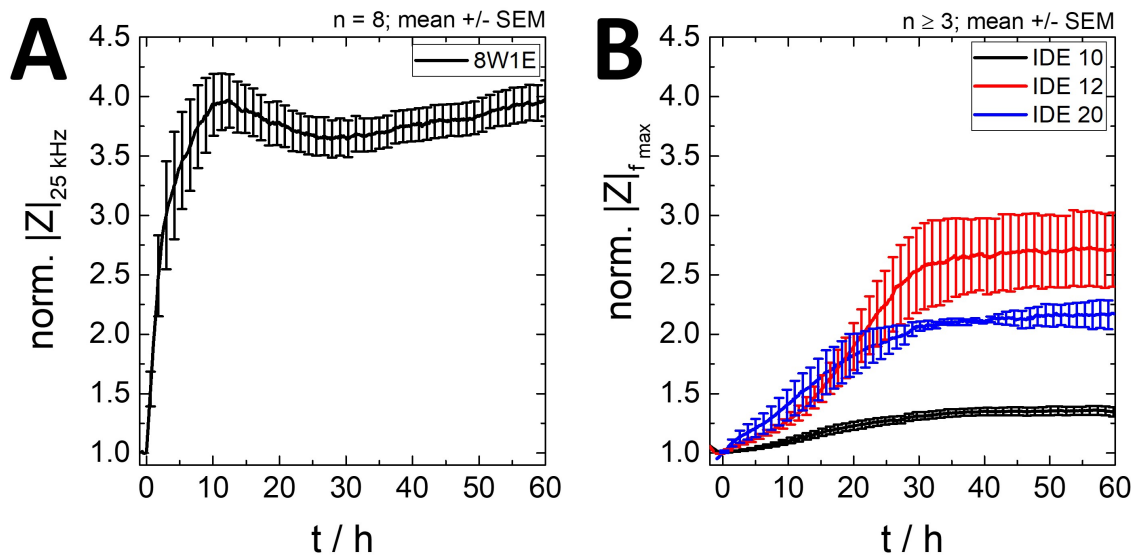


Figure 8.9: Time course of the normalized impedance change during the adhesion of spheroids on different electrode types at the individual frequencies f_{\max} . **A:** 8W1E electrode (25 kHz; $n=8$); **B:** IDE 10 (200 kHz; $n=7$), IDE 12 (400 kHz; $n=3$), IDE 20 (200 kHz; $n=3$). All graphs are normalized to the initial value of a cell-free electrode before inoculation of the spheroid (8W1E: $|Z| = (2202 \pm 127) \Omega$; IDE 10: $|Z| = (123 \pm 15) \Omega$; IDE 12: $|Z| = (50 \pm 6) \Omega$; IDE 20: $|Z| = (110 \pm 12) \Omega$) and the mean with the SEM is plotted.

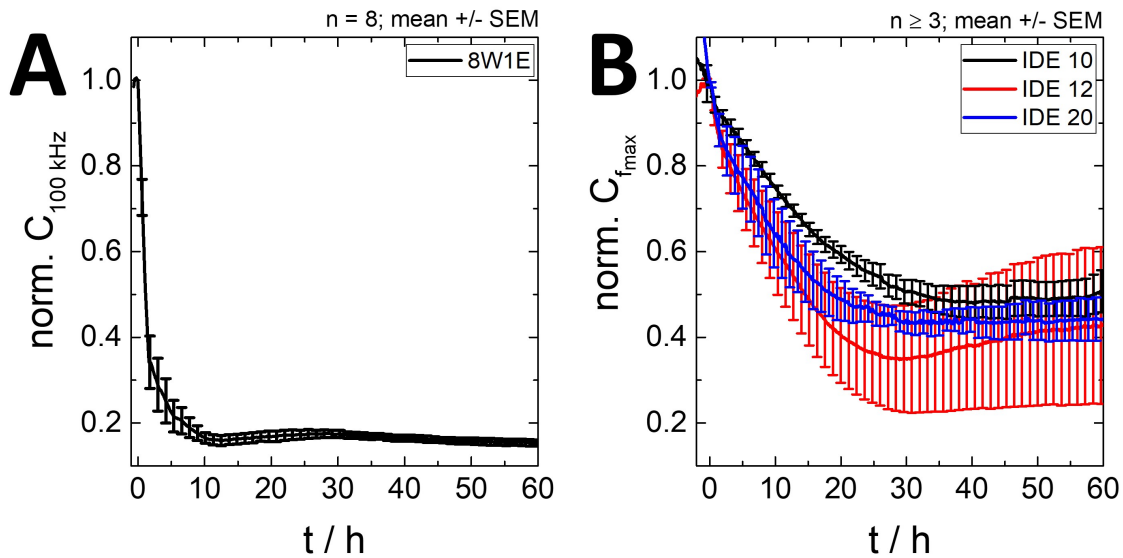


Figure 8.10: Time course of the normalized capacitance change during the adhesion of spheroids on different electrode types at the individual frequencies f_{\max} . **A:** 8W1E electrode (100 kHz; $n=8$); **B:** IDE 10 (400 kHz; $n=7$), IDE 12 (400 kHz; $n=3$), IDE 20 (251 kHz; $n=3$). All graphs are normalized to the initial capacitance value before inoculation of the spheroid (8W1E: $C = (3.0 \pm 0.4) \text{ nF}$; IDE 10: $C = (17 \pm 3) \text{ nF}$; IDE 12: $C = (25 \pm 8) \text{ nF}$; IDE 20: $C = (11 \pm 3) \text{ nF}$) and the mean with the SEM is plotted.

A different parameter of the adhesion which can be analyzed is the time-dependent change of the capacitance at the individual frequencies f_{max} (see fig. 8.10). The normalized capacitance of the 8W1E electrode (fig. 8.10 **A**) shows a rapid decrease after addition of the spheroid at a time point of $t=0$ h to a minimum of $\text{norm. } C_{min} = 0.17 \pm 0.01$ at a time point of $t_{min} = 10.1$ h. This minimum is remaining almost constant until the end of the measurement. Contrary to this, the capacitances of the IDEs (fig. 8.10 **B**) need longer to reach their specific minimum (IDE 10: $t_{min} = 36.7$ h, $\text{norm. } C_{min} = 0.49 \pm 0.04$; IDE 12: $t_{min} = 29.5$ h, $\text{norm. } C_{min} = 0.4 \pm 0.1$; IDE 20: $t_{min} = 31.7$ h, $\text{norm. } C_{min} = 0.44 \pm 0.03$), whereas the values of $\text{norm. } C_{min}$ fluctuate within the errors in the same range and do not significantly change after reaching them.

For a better understanding of the time-dependent impedance and capacitance change the spheroids (illustrated with the blue dotted circles) were placed on different positions of the non-insulated electrode area (symbolized with the yellow dotted squares) of the IDE 300 shown in fig. 8.11. This method should help to appreciate which part of the adhering spheroid was responsible for the changes.

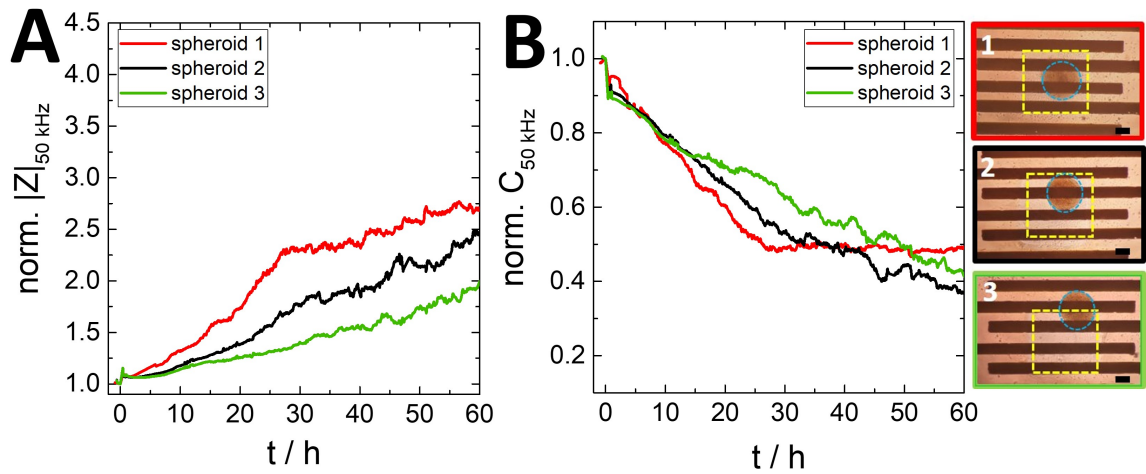


Figure 8.11: Time course of the adhesion of spheroids on IDE 300 with three different positions of the spheroids (illustrated with the blue dotted circles): *spheroid 1* in the center of the non-insulated electrode area (shown with the yellow dotted square), *spheroid 2* near the edge of the photopolymer and *spheroid 3* half over the edge of the photopolymer. **A:** time-dependent normalized impedance (50 kHz) and **B:** time-dependent normalized capacitance (50 kHz). All graphs are normalized to the last value before inoculation of the spheroids ($|Z| = 422 \Omega$, $|Z| = 862 \Omega$, $|Z| = 367 \Omega$; $C = 12.8 \text{ nF}$, $C = 8.7 \text{ nF}$, $C = 15.8 \text{ nF}$). The scale bars amount to $200 \mu\text{m}$ ($n = 1$).

Three different positions of the spheroids on IDE 300 were chosen: i) in the center of the non-insulated electrode area (spheroid 1), ii) near the edge of the photopolymer (spheroid 2) and iii) half over the edge of the photopolymer (spheroid 3). The

impedance of the three different spheroids is increasing with different slopes (see fig. 8.11 **A**) until the non-insulated electrode area was fully covered with cells. The fastest change of the impedance is seen for the spheroid in the center of the non-insulated electrode area. Here, a maximum of $\text{norm. } |Z|_{\text{max}} = 0.3$ after $t = 28$ h is reached which is comparable with the impedance course in fig. 8.9. The closer the spheroids were put to the edge of the photopolymer, the slower the impedance is increasing. Consequently, the spheroid which was put only half on the non-insulated electrode area shows the slowest increase of the impedance. Nevertheless, all three impedance graphs seem to increase until a saturation of around $\text{norm. } |Z|_{\text{max}} \approx 2.5$ is reached. The time-dependent capacitance course (see fig. 8.11 **B**) shows only a constant value for the spheroid which was centrally placed on the non-insulated electrode area. This time course is comparable with the course in fig. 8.10 **B**. In the case of the other spheroids the capacitance is decreasing and no saturation is observed. The various time courses can be explained with the position of the spheroids on the electrode area. The adhering cells are growing in a centrosymmetrical way around the spheroid and thus the position of the spheroid on the electrode area is decisive for the increase of the impedance. Spheroids at the edge of the photopolymer cannot grow radially from the center of the electrode and need much more time to cover the electrode area. The adhering cells of spheroids which are placed centrally on the electrode can cover the electrode area in a radial way resulting in a faster increase of the measured impedance.

For a further interpretation it is necessary to analyze the adhesion of a monolayer of the same cell line as the spheroids (U373 cells) on IDE 10 (see fig. 8.12).

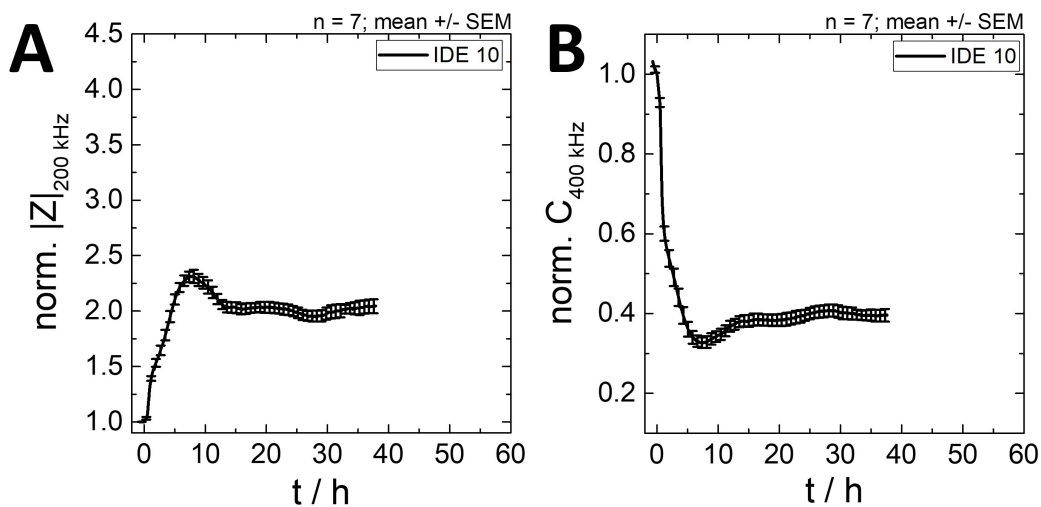


Figure 8.12: Time course of the adhesion of a confluent monolayer of U373 cells on IDE 10. The cells were added at $t = 0$ h with a seeding density of $100,000 \text{ cells/cm}^2$. **A:** normalized impedance (200 kHz) and **B:** normalized capacitance (400 kHz). All graphs are normalized to the initial value before adding of the cells ($|Z| = (117 \pm 8) \Omega$, $C = (12 \pm 4) \text{ nF}$). The mean ($n = 7$) is plotted with the SEM.

The time-dependent normalized impedance is increasing after the addition of the cells to a maximum of norm. $|Z|_{max} = 2.1 \pm 0.1$ at $t_{max} = 7.5$ h and decreases after 6 h to a saturation of norm. $|Z| = 1.91 \pm 0.08$ which remains constant until the end of the measurement (fig. 8.12 **A**). This time course can be confirmed looking at the capacitance (fig. 8.12 **B**). The capacitance is decreasing to a minimum of norm. $C_{min} = 0.33 \pm 0.01$ at a time $t_{min} = 7.3$ h and is increasing within 6 h to a saturation of norm. $C = 0.39 \pm 0.02$ which is alike the value of the capacitance of the spheroids.

Comparing the time courses measured with the IDE10 for the confluent seeded U373 cells (fig. 8.12) and the spheroids (fig. 8.9 **B** and fig. 8.10 **B**), it can be proven that the same capacitance values are reached but at different time points. The constant capacitance value measured for the spheroids is reached ≈ 30 h after inoculation of the spheroid, whereas ≈ 10 after seeding of the cells the saturation is reached for the monolayer. Consequently, the adhering cells of the spheroids are covering the whole electrode area but need more time due to their radial growth around the spheroid compared to the confluent seeded cells.

8.2.2 Stimulating cell-surface receptors

A further aspect of the adhered spheroids which was analyzed was the stimulation of the H_1 receptors with histamine (10 μ M histamine in L-15 medium) seen in fig. 8.13.

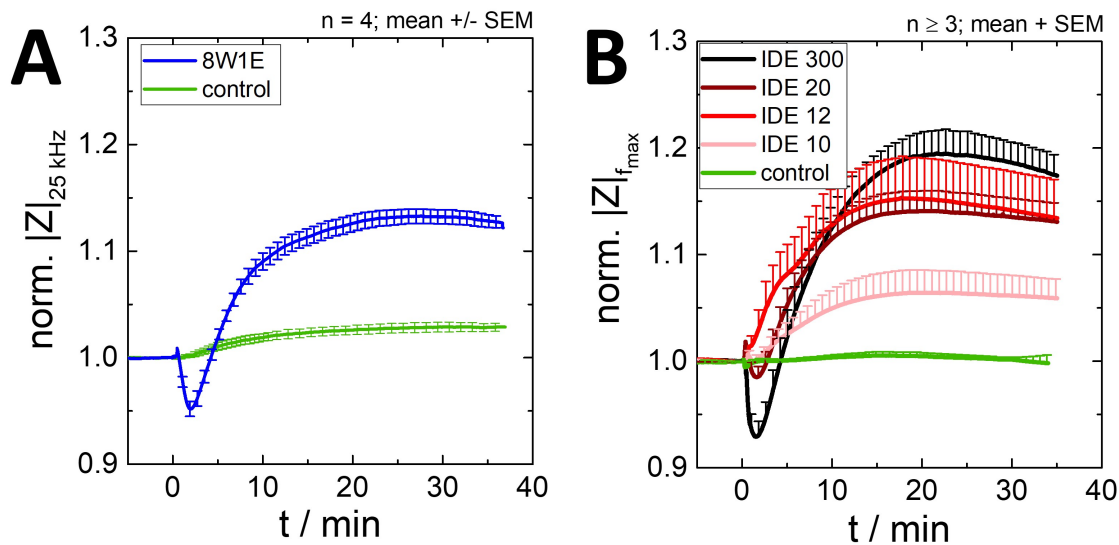


Figure 8.13: Time-dependent change of the impedance after the stimulation of the H_1 receptors of adhered spheroids with 10 μ M histamine in L-15 medium ($t = 0$ h) on the third day after inoculation. As a control the same volume of L-15 medium without histamine was added at $t = 0$ h. **A:** 8W1E electrodes at a frequency of 25 kHz ($n = 4$); **B:** IDEs of different types ($n \geq 3$) at the individual frequency f_{max} (IDE 10: 200 kHz; IDE 12: 400 kHz; IDE 20: 200 kHz; IDE 300: 25 kHz). All data were normalized to the initial value before addition (8W1E: $|Z| = (9589 \pm 690) \Omega$; IDE 300: $|Z| = (1451 \pm 672) \Omega$; IDE 20: $|Z| = (208 \pm 34) \Omega$; IDE 12: $|Z| = (106 \pm 17) \Omega$; IDE 10: $|Z| = (165 \pm 31) \Omega$). The mean with the SEM is plotted, whereas in **B** only the SEM in plus direction is shown.

To enable an interpretation the maximal signal height ($\Delta \text{norm. } |Z|_{max}$) and the time until the maximum is reached (t_{max}) are analyzed and compared with a confluent monolayer of the same cell line (U373) (see chapter 7.4.1). An overview is shown in tab. 8.1.

As a control the same volume of L-15 medium without histamine was added at $t = 0$ h to exclude an influence of temperature or volume changes to the signal. Given the fact that the impedance is not increasing after adding the control, non-specific changes of the impedance can be excluded. The impedance change of the spheroid on the 8W1E electrodes (fig. 8.13 **A**) after histamine addition at $t = 0$ h shows a similar course as the one with the monolayer (see fig. 7.19 in chapter 7.4.1). In the first 5 min the impedance is decreasing before it increases to a saturation of $\Delta \text{norm. } |Z|_{max} = 1.133 \pm 0.007$ at a $t_{max} = (26 \pm 3)$ min. Nevertheless, in comparison with the monolayer ($\Delta \text{norm. } |Z|_{max} = 1.28 \pm 0.03$ at $t_{max} = (13.8 \pm 0.7)$ min) the

impedance takes twice as long to reach a comparably smaller amount. Such a significant time lag measured for the monolayer and the spheroid cannot be seen in the case of the IDEs. Within the errors t_{max} resembles between the monolayer and the spheroids for each IDE layout. Otherwise, $\Delta \text{norm. } |Z|_{max}$ shows in general higher values for the monolayer (see table 8.1). The big difference between the IDE types is the varied time course of the impedance change (see fig. 8.13 B). The IDEs with the smallest pitch (IDE 10) show no decrease at the beginning of the stimulation but an immediate increase of the impedance. The same phenomenon occurs with the IDE 12, whereas a shoulder in the course at around 4 min can be observed. Increasing the pitch the dip at the beginning is getting more distinct. In the case of IDE 20 a decrease of the impedance at the beginning and a shoulder at around 5 min is revealed. The most notable dip occurs with a pitch of IDE 300, whereas also a small shoulder at around 6 min is monitored.

Table 8.1: Values for the H_1 receptor stimulation with 10 μM histamine of the U373 monolayer in comparison to the adhered spheroids on 8W1E electrodes, IDE 10, IDE 12, IDE 20 and IDE 300. $\Delta \text{norm. } |Z|_{max}$ and the t_{max} of the maximal impedance change are compared. The mean with the SEM is listed with $n \geq 3$.

electrode type	monolayer		spheroid	
	$\Delta \text{norm. } Z _{max}$	t_{max} / min	$\Delta \text{norm. } Z _{max}$	t_{max} / min
8W1E	1.28 ± 0.03	13.8 ± 0.7	1.133 ± 0.007	26 ± 3
IDE 10	1.14 ± 0.01	17 ± 2	1.07 ± 0.05	20 ± 3
IDE 12	1.20 ± 0.05	18 ± 2	1.15 ± 0.07	17.7 ± 0.8
IDE 20	1.38 ± 0.02	16 ± 1	1.14 ± 0.04	19 ± 4
IDE 300	1.29 ± 0.03	19 ± 2	1.19 ± 0.04	20.8 ± 0.9

Overall, the stimulation of the H_1 receptor with histamine can be summarized as followed:

- $\Delta \text{norm. } |Z|_{max}$ is higher for the monolayer than for the spheroids.
- t_{max} shows only for 8W1E electrodes a significant difference.
- The time course of the normalized impedance of the IDEs displays a different form. However, the higher the pitch, the more the course is adapted to the one of the 8W1E electrodes.

8.2.3 Discussion

The aim of this chapter was to ascertain, if the adhesion and the spreading of spheroids and the outgrowth of the cells of the spheroid can be monitored with the different electrode layouts and which parts of the adhered and spread spheroids were responsible for the impedance changes during the stimulation of the H_1 receptor with histamine.

With the microscopic images and the different stainings it is clarified that the spheroids are able to settle down on the electrodes and that the cells are adhering and spreading in a centrosymmetrical way around the spheroids. Fig. 8.6 illustrates the reason for the different signals of the electrode types due to the different non-insulated electrode areas. The area of the 8W1E electrodes is much smaller than the adhering spheroid leading to the conclusion that only a small part of the spheroid on the electrode and not the spreading and the outgrowth of the cells around the spheroid can be measured. In contrast, the IDEs have a larger non-insulated electrode area and the outgrowth of the spheroids can be monitored until they grow onto the insulating photopolymer. This is also confirmed in fig. 8.7 **B** with the red fluorescent photopolymer and the adhered spheroid inside the borders of the photopolymer, whereas in the case of the 8W1E electrodes (fig. 8.7 **A**) no border is visualized because the electrode is completely covered with the spheroid.

These images are the basis for the explanation of the impedance and capacitance time courses. The impedance of the 8W1E electrodes is changing immediately after inoculation of the spheroid (fig. 8.9 **A**). The spheroid is settling down on the electrode and the current flow is influenced. Given that $\text{norm. } |Z|$ remains constant after the first increase shows that the further spreading and outgrowth of the cells cannot be measured because of the smaller size of the 8W1E electrodes in comparison to the spheroid. Only the part of the spheroid set directly on the electrode is recorded. This is emphasized with the capacitance measurement (fig. 8.10 **A**) which is a direct parameter to analyze the electrode coverage (Wegener et al., 2000a). The immediate decrease of the capacitance shows that the whole electrode is covered with the spheroid right at the beginning of the measurement and that the further spreading and outgrowth of the cells does not affect the coverage of the electrode and the associated capacitance. This limitation can be avoided with the IDEs with a larger non-insulated electrode area. Due to the smaller size of the spheroids in comparison to the non-insulated electrode area the adhesion and the spreading of the spheroid and the outgrowth of the cells can be seen until the whole electrode area is covered (see fig. 8.9 **B**). This is visualized in the increasing impedance which takes around 30 h to reach a maximum, whereas the adhesion of a confluent monolayer of the same cells displays a saturation after 10 h (see fig. 8.12 **A**). Consequently, it takes longer for the cells of the spheroid to cover the whole electrode area because

the proliferation and the outgrowth only starts from the spheroid and not from the confluent seeded cells. A further proof for this explanation is the retarded reaching of a saturation in the capacitance value of the spheroid (see fig. 8.10 **B**) in comparison to the capacitance of the monolayer (see fig. 8.12 **B**). The impedance of the monolayer monitors a saturation after 15 h, whereas it takes around 35 h for the cells of the spheroid. Nevertheless, within the errors the same capacitance value of the covered electrode areas are revealed. Due to the aforementioned fact that the capacitance is a direct parameter for the electrode coverage, this explains that the seeded monolayer is covering the electrode much faster than the cells of the spheroid. However, in both cases the electrodes are covered completely.

Furthermore, the measurement of the different positions of the spheroids on the electrode area (see fig. 8.11) underlines this explanation. Due to the fact that the adhering cells are growing in a centrosymmetrical way around the spheroid, the position of the spheroid on the electrode is important. The spheroid in the center of the electrode area shows the fastest change in impedance and capacitance because the cells are adhering and spreading in a centrosymmetrical way around the spheroid and the electrode area is covered the fastest. In the case of the spheroid near the edge of the photopolymer or lying over the edge the spreading of just a part of the cells can be detected with the non-insulated electrode area. Half of the spheroid or even less is growing on the electrode without photopolymer and it takes longer to cover the whole electrode. However, it can be implied that the same maximal impedance and capacitance is reached at the end of the adhesion. All these aspects lead to the conclusion that the adhesion of the spheroid can be detected with the IDEs and the 8W1E electrodes, but the spreading and outgrowth of the cells of the spheroid can only be monitored with the IDEs.

The measurement and analysis of the spreading out of a three-dimensional multicellular spheroid has been poorly reported in literature. One of these seldom analysis was performed by the lab of Robitzki et al.. They invented a novel technique for the live monitoring of cell outgrowth from a micro-tumor using a multiwell microelectrode array. This array consists of 9 culture chambers with 42 electrodes per well (diameter of 100 μm and distance between the electrodes of 300 μm) and a counter electrode resulting in a total of 378 electrodes. They analyzed the migration and spreading out of three different tumor cell lines, one of a breast cancer and two from a malignant melanoma cell line. The size of the built spheroids after 10 days ranges from 100-500 μm . The spheroids were placed centrally on the microelectrode array individually in each well and the cell migration was measured over time counting the covered electrodes and measuring the cell density on the electrode. 144 h after inoculation the spheroids were stained with a live/dead staining revealing a high level of vitality. With this high-dense microelectrode array they were able to monitor im-

pedimentally the migration and the outgrowth of three-dimensional spheroids over time and to compare proliferation effects of the three individual cell lines (Jahnke et al., 2019). A particular challenge of this kind of array is the positioning of the spheroid in the center of the well. When additional positioning aids are avoided, there are a lot of difficulties to get and keep the spheroid in place, especially when the arrays are moved, for example from the microscope to the incubator. This problem also occurred mainly with the 8W1E electrodes in this work. On one array there are eight working electrodes, on which the spheroids should be placed, individually. The spheroids were placed by tilting and tapping the entire array. Once a spheroid was placed, it was very difficult to place the next one without removing the first. In the case of the IDEs this was much easier because on one substrate is only one electrode structure. Thus, the second and subsequent spheroids could be placed without affecting the previous ones. This is a huge practical advantage of the IDEs compared to the 8W1E electrodes.

A different aspect of spheroids is the necrotic core which is examined and calculated in different research groups (Drasdo and Höhme, 2005; Greenspan, 1972; Mueller-Klieser, 2000; Sutherland, 1988 and many more). The complicated transport of nutrition or oxygen inside the spheroids leads to hypoxia and necrosis and consequently, to a necrotic core (Bryne and Chaplain, 1996; Hamilton, 1998). This necrotic core is analyzed for example with frozen slices of the spheroids with an immunostaining to show hypoxic regions (Baye et al., 2017). A valid question is, if this necrotic core can be monitored with the impedance-based measurement setup and the staining in this thesis. The z-stack in the center of the spheroid and the spreading zone of the live/dead and the cell nuclei staining (fig. 8.7 and fig. 8.8) shows only the rim of the cells and the inside of the spheroid seems to be black. This is not the evidence for the necrotic core. There are two reasons for the black core of the spheroid in this case: i) it is not possible for the dye to pass the outer cell layers and to penetrate the whole spheroid during the short incubation time. Consequently, only the cells in the outer layers are stained and can be visualized. ii) Even if cells inside the spheroid are stained, the light which is necessary to excite the fluorescence cannot penetrate the whole spheroid. Thus, the inside of the spheroid appears black without any conclusion of the necrotic core. Consequently, it is not possible to draw conclusions about the necrotic core with the staining in this thesis. As a last aspect of the measurement of adhered and spread out spheroids the stimulation of H_1 receptors with histamine is discussed. Histamine is not membrane-permeable and can only diffuse extracellularly into the interior of the spheroid, which only occurs with a long incubation period. It can be concluded that mainly cells in the periphery of the spheroid and the spread out cells are stimulated during the short incubation and measurement time in this work. However, only the change

of the cell shape and the corresponding impedance change of cells on the electrodes can be monitored. With this argument it is possible to explain the delayed t_{max} and the lower value for $\Delta\text{norm.}|Z|_{max}$ of the spheroids measured with the 8W1E electrodes compared to the monolayer (see chapter 7.4.1). Conceptually the same impedance course after the stimulation of the H_1 receptor with histamine can be seen for the spheroid and the monolayer but with a different time resolution. The spheroid is sitting directly on the working electrode of 8W1E electrodes and the cells were outgrown on the insulated substrate. When histamine is added, the reaction of these cells as well as of the cells in the periphery of the spheroid on the stimulus cannot be measured. Nevertheless, histamine slowly diffuses to the cells below the spheroid above the electrode, among others, and stimulates these receptors. This diffusion requires a longer time and consequently the cell shape change of these cells and the corresponding impedance change is delayed. However, histamine is not diffusing completely underneath the spheroid in this measurement time resulting in a much lower impedance signal because only a fraction of the cells get in contact with histamine and only the cells on the electrode are measured.

The measurement of the H_1 receptor stimulation of the adhered and spread out spheroids on the IDEs does not show a huge time delay in comparison to the stimulation of the monolayer (see chapter 7.4.1). The value of $\Delta\text{norm.}|Z|_{max}$ of the spheroids is only a little bit lowered compared to the corresponding values of the monolayer. As shown previously, the non-insulated electrode area of the IDEs is larger than the spheroids and the spreading out of the cells of the spheroid can be monitored with these electrodes. These spread out cells build a monolayer on the electrodes around the spheroid. When histamine is added, this spread out cells were stimulated in the same way as the original monolayer resulting in the same impedance time course. Histamine is barely diffusing underneath the spheroid during the short measurement time and consequently, cannot stimulate these cells completely. Similar to the measured cells underneath the spheroid of the 8W1E electrodes, these cells are also stimulated with a delay but this effect is not seen in the results because the impedance signal of the spread out cells dominates the overall measured impedance signal. Nevertheless, due to the difficult accessibility of the cells below the spheroid less cells contribute to the impedance amount and $\Delta\text{norm.}|Z|_{max}$ is reduced compared to the monolayer.

In summary some observations can be made:

- 8W1E electrodes as well as IDEs can be used for the measurement of the adhesion of single spheroids, but 8W1E electrodes are too small to detect the spreading out of the cells of the spheroid, whereas the IDEs are able to monitor the centrosymmetrical spreading of the cells.

- The necrotic core cannot be visualized with the different stainings because of the slight penetration of the dye and the laser inside the spheroid.
- When stimulating the H₁ receptor with histamine only the cells in the periphery and the spread out cells of the spheroid can be monitored. The IDEs are more advantageous here because spread out cells grow on the non-insulated electrode area compared to the 8W1E electrodes where the spread out cells grow on the insulated substrate.
- The placing of the spheroids is much easier using the IDEs because on one substrate there is only one electrode structure, whereas one 8W1E electrode is on an array with eight electrodes.

In literature the IDEs were usually used to monitor reactions of the spheroids in suspension and not adherent ones.

Ino et al. invented a local redox cycling-based electrochemical chip device with a ring-type interdigitated array (width and gap of 5 μm , respectively). To trap cell aggregates a microwell with a diameter of 430 μm above the electrodes was used. The aim of this work was to analyze the correlation of the differentiation of cardiomyocytes from embryonic stem cells and the activity of alkaline phosphatase. For this, they used three-dimensional cystic embryoid bodies with a diameter of 400 μm and measured the electrochemical responses. The authors were able to detect the gradually decreasing alkaline phosphatase activity during the differentiation of the embryonic stem cells into cardiomyocytes (Ino et al., 2013). Furthermore, IDEs were used to measure in a real-time and label-free manner the formation of spheroids and the influence of an anticancer drug. The spheroids (diameter of 200 μm) were formed on a non-adherent surface of hydrogel with the interdigitated electrodes (width of 150 μm and a gap of 100 μm) below. Impedance spectra were measured every 24 h during the formation of the spheroids and an increase of the impedance can be seen. The second part of the experiment was the addition of the anticancer drug doxorubicin in different concentrations. The impedance spectra show an inhibition of the growth with 50 $\mu\text{g/mL}$ and an apoptosis with 250 $\mu\text{g/mL}$ (Lei et al., 2017). A further application of IDEs was the analysis of the drug efficacy for spheroids. Spheroids of human lung carcinoma cell lines were formed (300 μm in diameter) and attached during impedance measurement to an interdigitated structure with a gap of around 30 μm . Per well 30 spheroids were added because less spheroids were not able to be detected. After the spheroids were entirely attached after 24 h an anticarcinogen drug, cisplatin, was added. To interpret the impedance data a monolayer of the same cell line was treated with the same concentrations of cisplatin. The authors saw that the impedance response of the monolayer was higher and consequently, the drug resistance was lower for the two-dimensional cells than for

the spheroid. They explained the higher drug resistance of the spheroids with the longer time for the inner and outer cells to interact with each other (Wu et al., 2018).

In literature IDEs are rarely used to detect spheroids. In contrary to this work the spheroids were measured on the one hand in suspension. Non-adhesive surfaces were used and the reaction of the whole spheroid was measured. On the other hand, attached spheroids were measured but with a much higher gap and width of the electrodes than in this work. It was only possible to monitor an impedance change with a parallel measurement of 30 spheroids in one well and even therefore no detailed analysis of the adhesion and the adhered and spread out spheroid was possible. The advantage of the measurement setup in this work is a detailed monitoring of the adhesion and stimulation of single adhered spheroids. Furthermore, with the IDEs it is possible to monitor the spreading out of the cells in contrary to the 8W1E electrode. This is a clear advantage of the IDEs.

9 Summary

The aim of this thesis was to analyze and to characterize interdigitated electrodes (IDEs) with subcellular dimensions. The focus was to find out their advantages when used as electrodes in impedance-based cellular assays in comparison to commercially available electrodes. In the assays mainly the following IDEs were used: IDE 20 (width and gap 10 μm), IDE 12 (width and gap 6 μm), IDE 10 (width and gap 5 μm) and IDE 7 (width 4 μm , gap 3 μm).

For a basic characterization the impedance, resistance and capacitance changes of cell-free electrodes were analyzed as a function of the frequency. The IDEs with small pitches showed lower effects of the electrolyte than the IDE 300 (width and gap 150 μm) and the ECIS electrodes which were used as reference values for all assays. With a finite element technique (using COMSOL simulations) it was illustrated that the distribution of the electric field into the electrolyte is strongly dependent on the distance between the electrodes. In the case of the IDEs with a small pitch it was calculated that over 87 % of the electric field was in a small volume above the electrodes within a distance of the size of the electrode gap. Further simulations proved, that additionally to the distance between the electrodes also the cell height and the cell-substrate distance had significant influences on the distribution of the electric field. When the cell-substrate distance was comparatively high (500 nm), the electric field distributed without restriction, resulting nearly in the data of cell-free electrodes. Additionally, it was simulated that with flatter cells, the ratio of the electric field in the intercellular cleft was increasing. With larger cells, the main electric field was seen underneath the cells. On the basis of these simulations it was possible to explain the cell specific frequency-dependent impedance, resistance and capacitance data and the cell micromotions, measured with the different electrode types. With the variation of the non-insulated electrode areas (double and half size) a decreased sensitivity of the frequency spectra was revealed because those electrodes obtain larger fluctuations (especially the ones with the small area) and it was more difficult to distinguish the cell signals for both layouts.

In the measurement of the adhesion and spreading of MDCK I, MDCK II and NRK cells as well as in the proliferation measurement, the IDEs were able to detect the initial attachment of the cells more quickly and sensitively than the 8W10E electrodes. Further, it was possible to reveal different time-dependent impedance

and capacitance courses during adhesion measured with the various electrode types. Most noteworthy was the sudden rise in impedance at ≈ 40 h in the measurement of MDCK I cells with the IDEs. With the staining of the ZO-1 proteins it was indicated that this increase was dependent on the formation of the tight junctions. Due to the small fraction of the electric field in the intercellular cleft in the case of the IDEs, those electrodes were not able to monitor the complete formation of the tight junctions over time like the 8W10E electrodes. Only when a defined strength of the tight junctions were reached the impedance of the IDEs was influenced strongly. As the cells were subjected to an osmotic pressure, the cells shrank and reduced their cell height revealing a changed distribution of the electric field in the case of the IDEs. With the shrunk cells the main part of the electric field was shifted to the intercellular cleft resulting in a higher impedance signal for the MDCK II cells. In the measurement of the H_1 receptor stimulation, the impedance changes measured with the IDEs deviated more and more from those of the 8W10E electrodes and IDE 300, the smaller the pitch became. This proved that with different electrode distances various parts of the cell body and cell reactions can be detected. Another assay was the analysis of cardiomyocytes. The regular contracting and relaxing was well measurable with the 8W1E electrodes, whereas only a low and noisy impedance change was detected with the IDEs. When analyzing the cytotoxicity of bisphenol A and ethanol, the IDEs turned out to analyze the impact of BPA on the cells earlier than the ECIS electrodes. At lower concentrations ($100\text{ }\mu\text{M}$ BPA) it was already possible to observe changes in the impedance of the confluent cell layer, whereas with the ECIS electrodes only a change $\geq 150\text{ }\mu\text{M}$ BPA could be obtained.

Another advantage of the IDEs was found in the electroporation measurements. Using a proper voltage magnitude an introduction of the fluorescent FITC-dextran into the cells was enabled. With the IDEs it was possible to electroporate more cells due to the larger non-insulated electrode area compared to the 8W1E electrodes. Another advantage of the larger non-insulated electrode area of the IDEs was the detectable outgrowth of spheroids. With the ECIS electrodes only the sedimentation of these spheroids could be measured, whereas centrosymmetrical outgrowth of the cells could be monitored with the IDEs.

In summary, the interdigitated electrodes with subcellular dimensions have disadvantages when they are used to detect whole cell reactions, like the beating of the cardiomyocytes. The focus of these electrodes is underneath the cells. They are advantageous when, for example, a rapid detection of the initial attachment of cells or cell responses in a cytotoxicity study are necessary. Moreover, with the larger non-insulated electrode area in comparison to the ECIS electrodes greater areas can be monitored and more cells can be manipulated. For future work, it is important to adapt the dimensions of the electrodes to the effects to be detected.

10 Zusammenfassung

Ziel dieser Arbeit war es, interdigitierte Elektroden (IDEs) mit subzellulären Dimensionen zu charakterisieren und zu analysieren. Ihre Vorteile beim Einsatz als Elektroden in Impedanz-basierten zellulären Assays wurden im Vergleich zu kommerziell erhältlichen Elektroden herausgearbeitet. Der Fokus lag bei den folgenden Elektroden: IDE 20 (Breite und Abstand 10 μm), IDE 12 (Breite und Abstand 6 μm), IDE 10 (Breite und Abstand 5 μm), IDE 7 (Breite 4 μm und Abstand 3 μm).

Für eine grundlegende Charakterisierung wurden die Impedanz-, Widerstands- und Kapazitätsänderungen von zellfreien Elektroden in Abhängigkeit der Frequenz analysiert. Die IDEs mit kleinem Pitch zeigten einen geringeren Einfluss des Elektrolyten als die IDE 300 und ECIS Elektroden, die für alle Assays als Vergleichswerte mitgeführt wurden. Mit einer Finite-Elemente-Technik (COMSOL Simulationen) wurde gezeigt, dass die Eindringtiefe des elektrischen Feldes in den Elektrolyten stark vom Abstand zwischen den Elektroden abhängt. Im Fall der IDEs mit kleinem Abstand wurde simuliert, dass sich über 87 % des elektrischen Feldes oberhalb der Elektroden innerhalb eines Volumens mit der Höhe des Elektrodenabstandes befanden. Weitere Simulationen zeigten, dass neben dem Elektrodenabstand auch die Zellhöhe und der Zell-Substrat-Abstand wesentlichen Einfluss auf die Verteilung des elektrischen Feldes haben. War der Zell-Substrat-Abstand vergleichsweise groß (500 nm), konnte sich das elektrische Feld ungehindert ausbreiten, was nahezu zu den Daten der zellfreien Elektroden führte. Zusätzlich wurde simuliert, dass mit flachen Zellen der Anteil des elektrischen Feldes im interzellulären Spalt zunahm, während bei größeren Zellen der Hauptteil des elektrischen Feldes unterhalb der Zellen zu sehen war. Diese Simulationen dienten als Erklärung für die zellspezifischen frequenzabhängigen Impedanz-, Widerstands- und Kapazitätsdaten, sowie die Zellmikrobewegungen. Bei Variation der nicht-isolierten Elektrodenfläche (doppelte und halbe Größe) wurde eine geringere Sensitivität erreicht, da diese Elektroden Fluktuationen zeigten und die Unterscheidung der Zellsignale erschwert war.

Bei der Messung der Adhäsion von MDCK I, MDCK II und NRK-Zellen sowie bei der Proliferationsmessung konnten die IDEs die initiale Sedimentation der Zellen schneller und empfindlicher erfassen als die 8W10E-Elektroden. Weiterhin wurden unterschiedliche zeitabhängige Impedanz- und Kapazitätsverläufe während der Adhäsion beobachtet, gemessen mit den verschiedenen Elektrodentypen. Am auf-

fallendsten war der schnelle Anstieg der Impedanz der MDCK I-Zellen nach ≈ 40 h, gemessen mit den IDEs. Mit der Färbung der ZO-1 Proteine wurde gezeigt, dass dieser Anstieg von der Bildung der *tight junctions* herrührt. Aufgrund des geringen Anteils des elektrischen Feldes im interzellulären Spalt bei den IDEs waren diese Elektroden nicht wie die 8W10E-Elektroden in der Lage, die vollständige Ausbildung über die Zeit zu überwachen. Erst als eine entsprechende Stärke der *tight junctions* erreicht war, wurde die Impedanz der IDEs stark beeinflusst. Als die Zellen einem osmotischen Druck ausgesetzt wurden, schrumpften diese und verringerten ihre Zellhöhe, was im Fall der IDEs zu einer veränderten Verteilung des elektrischen Feldes führte. Bei den geschrumpften Zellen wurde der Hauptteil des elektrischen Feldes in den interzellulären Spalt verlagert, was ein höheres Impedanzsignal für die MDCK II-Zellen ergab. Bei der Messung der H_1 -Rezeptorstimulation wichen die Impedanzverläufe der IDEs immer mehr von denen der 8W10E-Elektroden und der IDE 300 ab, je kleiner der Elektrodenabstand wurde. Dies bewies, dass mit unterschiedlichen Elektrodenabständen verschiedene Teile des Zellkörpers und der Zellreaktionen detektiert werden konnten. Ein weiterer Assay war die Messung des regelmäßigen Kontrahierens und Relaxierens von Kardiomyocyten, was mit den 8W1E-Elektroden gut messbar war, während mit den IDEs nur eine geringe und stark verrauschte Impedanzänderung zu erkennen war. Bei der Analyse der Zytotoxizität von Bisphenol A stellte sich heraus, dass die IDEs den toxischen Einfluss auf konfluente Zellen früher detektierten als die ECIS-Elektroden. Bei niedrigen Konzentrationen ($100\text{ }\mu\text{M}$ BPA) konnten Änderungen der Impedanz beobachtet werden, während mit den ECIS-Elektroden nur ein Einfluss $\geq 150\text{ }\mu\text{M}$ BPA detektiert wurde. Ein weiterer Vorteil der IDEs konnte bei den Elektroporationsmessungen festgestellt werden. Bei entsprechender Spannungsstärke wurde das Molekül FITC-Dextran in die Zellen aufgenommen. Mit den IDEs war es möglich, aufgrund der größeren nicht-isolierten Elektrodenfläche, im Vergleich zu den 8W1E-Elektroden mehr Zellen zu elektroporieren. Durch diese größere Fläche der IDEs war es außerdem möglich, das Herauswachsen von Sphäroiden zu messen. Mit den ECIS-Elektroden konnte nur die Sedimentation dieser Sphäroide gemessen werden, während mit den IDEs ein zentrosymmetrisches Auswachsen der Zellen beobachtet wurde.

Zusammenfassend lässt sich sagen, dass die IDEs mit subzellulären Dimensionen Nachteile haben, wenn sie zur Detektion ganzer Zellreaktionen, wie dem Schlagen der Kardiomyozyten, eingesetzt werden. Der Fokus dieser Elektroden liegt unterhalb der Zellen. Deshalb sind sie vorteilhaft, wenn eine schnelle Detektion der Sedimentation von Zellen oder der Zellreaktionen notwendig ist. Außerdem können durch die größere nicht-isolierte Elektrodenfläche der IDEs größere Bereiche beobachtet und mehr Zellen manipuliert werden. Für zukünftige Arbeiten ist es wichtig, die Dimensionen der Elektroden an die zu detektierenden Effekte anzupassen.

11 Outlook

The aim of this thesis was to analyze the benefits of interdigitated electrodes. It was important to determine in which kind of cell reaction they show an additional or more sensitive signal change than commercially available electrodes. This knowledge can be used as a basis for the development of a body-on-a-chip system with different layouts of interdigitated electrodes combined with a flow system. These chips are in general microfluidic cell culture chips which can simulate the activities and physiological responses of cell types of an organ or of different organ systems connected with each other.

A scheme of the possible layout is shown in fig. 11.1.

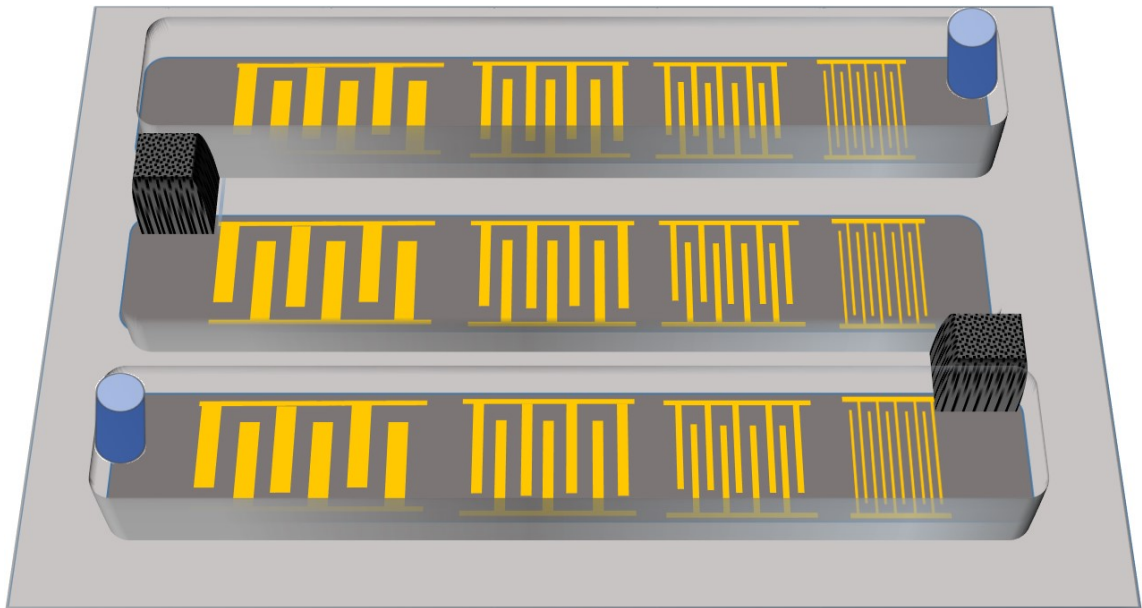


Figure 11.1: Scheme of a body-on-a-chip system with different interdigitated electrode layouts. The chip consists of three different channels with four interdigitated structures, respectively. The channels are linked with each other and can be locked with a removable barrier shown as a black cuboid. With this construction individual cell types can be cultivated in each channel. The blue cylinders reveal the inlet and the outlet of the flow system.

The chip consists of three linked channels with varied electrode layouts, respectively. In the scheme four different pitches are shown for every individual channel. These

pitches cover a huge range of various gaps and widths of the electrodes and consequently, a huge range of various penetration depth of the electric field. On the basis of this thesis, the layouts can be chosen to analyze different aspects of the cell reaction. With the three channels the gained results can be further expanded. They are separated with a removable barrier (seen as black cuboid). These barriers enable the cultivation of individual cell types in the different channels. The cells can be grown without the shear stress due to the flow and the specific medium can be used for each cell type for seeding and feeding. When the cells built a confluent monolayer, the barrier is removed and the channels can be filled with the measurement buffer. For further experiments, the channels are closed strongly with a tight lid defining the reaction volume and a flow system can be plugged. With the flow inlet and outlet (shown in blue cylinder), the substances under investigation are added to the chip. Due to the flow system the substance is pumped through the three channels and comes into contact with the three different cell types successively. The individual pitches monitor the different cell reactions of the cell types.

This chip can be used for further reduction of animal tests. A huge field for the application of body-on-a-chip is actually the development of drugs. Due to the different cell types cultured on one chip which is connected to a flow system, it can be used for tests of effects and side-effects of individual substances. Furthermore, the activity and the toxicity of drugs to human organs can be predicted and causes of diseases and therapeutic approaches can be explored. Furthermore, it is possible to use the chip to test the impedance change of a confluent monolayer during the incubation of suspicious substances. The impact of the xenobiotics like nanoparticles, water pollutants, like ammonia or phenol, or pesticides can be monitored over time.

This will show great advantages over the commercially available end-point experiments, like MTT. With the time-resolved influence of the substances, the operating principle of the harmful impact on the cells can be understood more precisely and the development of countermeasures is simplified.

References

- Abassi, Y. A., Xi, B., Li, N., Ouyang, W., Seiler, A., Watzele, M., Kettenhofen, R., Bohlen, H., Ehlich, A., Kolossov, E., Wang, X., and Xu, X. (2012). Dynamic monitoring of beating periodicity of stem cell-derived cardiomyocytes as a predictive tool for preclinical safety assessment. *British journal of pharmacology*, 165(5):1424–1441.
- Abdullah, A., Dastider, S. G., Jasim, I., Shen, Z., Yuksek, N., Zhang, S., Dweik, M., and Almasri, M. (2019). Microfluidic based impedance biosensor for pathogens detection in food products. *Electrophoresis*, 40(4):508–520.
- An, Y., Jin, T., Zhang, F., and He, P. (2019). Electric cell-substrate impedance sensing (ecis) for profiling cytotoxicity of cigarette smoke. *Journal of Electroanalytical Chemistry*, 834:180–186.
- Arndt, S., Seebach, J., Psathaki, K., Galla, H.-J., and Wegener, J. (2004). Bioelectrical impedance assay to monitor changes in cell shape during apoptosis. *Biosensors and Bioelectronics*, 19(6):583–594.
- Asphahani, F., Thein, M., Veiseh, O., Edmondson, D., Kosai, R., Veiseh, M., Xu, J., and Zhang, M. (2008). Influence of cell adhesion and spreading on impedance characteristics of cell-based sensors. *Biosensors & bioelectronics*, 23(8):1307–1313.
- Astanina, K., Simon, Y., Cavelius, C., Petry, S., Kraegeloh, A., and Kiemer, A. K. (2014). Superparamagnetic iron oxide nanoparticles impair endothelial integrity and inhibit nitric oxide production. *Acta biomaterialia*, 10(11):4896–4911.
- Audebert, M., Dolo, L., Perdu, E., Cravedi, J.-P., and Zalko, D. (2011). Use of the yh2ax assay for assessing the genotoxicity of bisphenol a and bisphenol f in human cell lines. *Archives of toxicology*, 85(11):1463–1473.
- Babuska, I. (1973). The finite element method with lagrangian multipliers. *Numerische Mathematik*, 20(20):179–19.
- Balcarova-Ständer, J., Pfeiffer, S. E., Fuller, S. D., and Simons, K. (1984). Development of cell surface polarity in the epithelial madin-darby canine kidney (mdck) cell line. *THE EMBO Journal*, 3(11):2687–2694.

- Barsoukov, E. and Macdonald, J. R. (2005). *Impedance spectroscopy: Theory, experiment, and applications*. Wiley-Interscience, Hoboken N.J., 2nd ed. edition.
- Baumgarten, C. M. and Feher, J. (2001). Osmosis and regulation of cell volume. *Cell Physiology Source Book*, 3:319–355.
- Baye, J., Galvin, C., and Shen, A. Q. (2017). Microfluidic device flow field characterization around tumor spheroids with tunable necrosis produced in an optimized off-chip process. *Biomedical microdevices*, 19(3):59.
- Bazzoni, G., Martinez-Estrada, O. M., Orsenigo, F., Cordenonsi, M., Citi, S., and Dejana, E. (2000). Interaction of junctional adhesion molecule with the tight junction components zo-1, cingulin, and occludin. *The Journal of biological chemistry*, 275(27):20520–20526.
- Bellotti, M. I., Giana, F. E., and Bonetto, F. J. (2015). Impedance spectroscopy applied to the fast wounding dynamics of an electrical wound-healing assay in mammalian cells. *Measurement Science and Technology*, 26(8).
- Bergveld, P. (1970). Development of an ion-sensitive solid-state device of neurophysiological measurements. *IEEE Transactions of biomedical engineering*, pages 70–71.
- Bergveld, P. (2003). Thirty years of isfetology: What happened in the past 30 years and what may happen in the next 30 years. *Sensors and Actuators B: Chemical*, 88:1–20.
- Bers, D. M. (2002). Cardiac excitation-contraction coupling. *Nature*, 415:198–205.
- Beyer, S., Blocki, A., Cheung, M. C. Y., Wan, Z. H. Y., Mehrjou, B., and Kamm, R. D. (2021). Lectin staining of microvascular glycocalyx in microfluidic cancer cell extravasation assays. *Life (Basel, Switzerland)*, 11(3).
- Bigner, D. D., Bigner, S. H., Ponten, J., Westermarck, B., Mahaley, M. S., Ruoslahti, E., Herschman, H., Eng, L. F., and Wikstrand, C. J. (1981). Heterogeneity of genotypic and phenotypic characteristics of fifteen permanent cell lines derived from human gliomas. *Journal of Neuropathology and Experimental Neurology*, (3):201–228.
- Bischoff, I., Hornburger, M. C., Mayer, B. A., Beyerle, A., Wegener, J., and Fürst, R. (2016). Pitfalls in assessing microvascular endothelial barrier function: impedance-based devices versus the classic macromolecular tracer assay. *Scientific reports*, 6:23671.
- Bohrn, U., Stütz, E., Fleischer, M., Schöning, M. J., and Wagner, P. (2011). Eukaryotic cell lines as a sensitive layer for direct monitoring of carbon monoxide. *physica status solidi (a)*, 208(6):1345–1350.

- Bonefeld-Jørgensen, E. C., Long, M., Hofmeister, M. V., and Vinggaard, A. M. (2007). Endocrine-disrupting potential of bisphenol a, bisphenol a dimethacrylate, 4-n-nonylphenol, and 4-n-octylphenol in vitro: new data and a brief review. *Environmental health perspectives*, 115:69–76.
- Brennan, L. M., Widder, M. W., Lee, L. E. J., and van der Schalie, W. H. (2012). Long-term storage and impedance-based water toxicity testing capabilities of fluidic biochips seeded with rtgill-w1 cells. *Toxicology in vitro : an international journal published in association with BIBRA*, 26(5):736–745.
- Breus, V. V., Pietuch, A., Tarantola, M., Basché, T., and Janshoff, A. (2015). The effect of surface charge on nonspecific uptake and cytotoxicity of cdse/zns core/shell quantum dots. *Beilstein journal of nanotechnology*, 6:281–292.
- Brischwein, M., Herrmann, S., Vonau, W., Berthold, F., Grothe, H., Motrescu, E. R., and Wolf, B. (2006). Electric cell-substrate impedance sensing with screen printed electrode structures. *Lab on a chip*, 6(6):819–822.
- Brockman, J. M., Nelson, B. P., and Corn, R. M. (2000). Surface plasmon resonance imaging measurements of ultrathin organic films. *Annual review of physical chemistry*, 51:41–63.
- Brosel-Oliu, S., Mergel, O., Uria, N., Abramova, N., van Rijn, P., and Bratov, A. (2019). 3d impedimetric sensors as a tool for monitoring bacterial response to antibiotics. *Lab on a chip*, 19(8):1436–1447.
- Bryne, H. M. and Chaplain, A. J. (1996). Growth of necrotic tumors in the presence and absence of inhibitors. *Mathematical Biosciences*, 135:187–216.
- Bu, T., Huang, Q., Yan, L., Zhang, W., Dou, L., Huang, L., Yang, Q., Zhao, B., Yang, B., Li, T., Wang, J., and Zhang, D. (2019). Applicability of biological dye tracer in strip biosensor for ultrasensitive detection of pathogenic bacteria. *Food chemistry*, 274:816–821.
- Bujong, M. R., Yunas, J., Hamzah, A. A., Majlis, Y., Larki, F., and Aziz, N. A. (2015). Design, fabrication and characterization of dielectrophoretic microelectrode array for particle capture. *Microelectronics International*, 32(2):96–102.
- Bullock, J., Pagan-Mercado, G., and Becerra, S. P. (2020). Cell-based assays to identify novel retinoprotective agents. *MethodsX*, 7:101026.
- Butler, D., Goel, N., Goodnight, L., Tadigadapa, S., and Ebrahimi, A. (2019). Detection of bacterial metabolism in lag-phase using impedance spectroscopy of agar-integrated 3d microelectrodes. *Biosensors & bioelectronics*, 129:269–276.

- Buttry, D. A. and Ward, M. D. (1992). Measurement of interfacial processes at electrode surfaces with the electrochemical quartz crystal microbalance. *Chemical reviews*, 92(6).
- Calabrese, E. J. (2003). The maturing of hormesis as a credible dose-response model. *Nonlinearity in Biology, Toxicology and Medicine*, 1:319–343.
- Calabrese, E. J. (2005). Paradigm lost, paradigm found: the re-emergence of hormesis as a fundamental dose response model in the toxicological sciences. *Environmental pollution (Barking, Essex : 1987)*, 138(3):379–411.
- Calabrese, E. J. (2008). Hormesis: Why it is important to toxicology and toxicologists. *Environmental toxicology and chemistry*, 27(7):1451–1474.
- Calabrese, E. J. and Baldwin, L. A. (2003). Hormesis: the dose-response revolution. *Annual review of pharmacology and toxicology*, 43:175–197.
- Carey, T. E., Takahashi, T., Resnick, L. A., Oettgen, H. F., and Old, L. J. (1976). Cell surface antigens of human malignant melanoma: Mixed hemadsorption assays for humoral immunity to cultured autologous melanoma cells. *Proceedings of the National Academy of Sciences of the United States of America*, 73(9):3278–3282.
- Carson, M. R., Shasby S. S., and Shasby, D. M. (1989). Histamine and inositol phosphate accumulation in endothelium: camp and a g protein. *The American Physiological Society*, 89:259–264.
- Cath, T., Childress, A., and Elimelech, M. (2006). Forward osmosis: Principles, applications, and recent developments. *Journal of Membrane Science*, 281:70–87.
- Chan, J., Soraya, G. V., Craig, L., Uddin, S. M., Todaro, M., Huynh, D. H., Abeyrathne, C. D., Kostenko, L., McCluskey, J., Skafidas, E., and Kwan, P. (2019). Rapid detection of hla-b*57:01-expressing cells using a label-free interdigitated electrode biosensor platform for prevention of abacavir hypersensitivity in hiv treatment. *Sensors (Basel, Switzerland)*, 19(16).
- Chen, C. J., Liu, J. T., Chang, S.-J., Lee, M.-W., and Tsai, J.-Z. (2012). Development of a portable impedance detection system for monitoring the growth of mouse 1929 cells. *Journal of the Taiwan Institute of Chemical Engineers*, 43(5):678–684.
- Chen, M.-Y., Ike, M., and Fujita, M. (2002). Acute toxicity, mutagenicity, and estrogenicity of bisphenol-a and other bisphenols. *Environmental Toxicology*, 17:80–86.
- Chinnadayala, S. R., Park, J., Abbasi, M. A., and Cho, S. (2019). Label-free electrochemical impedimetric immunosensor for sensitive detection of igm rheumatoid factor in human serum. *Biosensors & bioelectronics*, 143.

- Cho, Y., Kim, H. S., Frazier, A. B., Chen, Z. G., Shin, D. M., and Han, A. (2009). Whole-cell impedance analysis for highly and poorly metastatic cancer cells. *Journal of Microelectromechanical Systems*, 18(4):808–817.
- Choi, E., Lee, S. Q., Kim, T. Y., Chang, H.-k., Lee, K. J., and Park, J. (2010). Mems-based power generation system using contractile force generated by self-organized cardiomyocytes. *Sensors and Actuators B: Chemical*, 151(1):291–296.
- Cole, K. S. and Curtis, H. J. (1938). Electric impedance of single marine eggs. *The Journal of General Physiology*, pages 591–599.
- Cole, K. S. and Guttman, R. M. (1942). Electric impedance of the frog egg. *The Journal of General Physiology*, pages 765–775.
- COMSOL (2018). *The AC/DC Module User’s Guide*.
- Couniot, N., Flandre, D., Francis, L. A., and Afzalian, A. (2013). Signal-to-noise ratio optimization for detecting bacteria with interdigitated microelectrodes. *Sensors and Actuators B: Chemical*, 189:43–51.
- Curie, J. and Curie, P. (1880). Développement par compression de l’électricité polaire dans les cristaux hémiedres à faces inclinées. *Bulletin de la Société minéralogique de France*, 3(4):90–93.
- Curtis, T. M., Tabb, J., Romeo, L., Schwager, S. J., Widder, M. W., and van der Schalie, W. H. (2009a). Improved cell sensitivity and longevity in a rapid impedance-based toxicity sensor. *Journal of applied toxicology : JAT*, 29(5):374–380.
- Curtis, T. M., Widder, M. W., Brennan, L. M., Schwager, S. J., van der Schalie, W. H., Fey, J., and Salazar, N. (2009b). A portable cell-based impedance sensor for toxicity testing of drinking water. *Lab on a chip*, 9(15):2176–2183.
- Daikuzono, C. M., Delaney, C., Morrin, A., Diamond, D., Florea, L., and Oliveira, O. N. (2019). Paper based electronic tongue - a low-cost solution for the distinction of sugar type and apple juice brand. *The Analyst*, 144(8):2827–2832.
- Das, D., Shiladitya, K., Biswas, K., Dutta, P. K., Parekh, A., Mandal, M., and Das, S. (2015). Wavelet-based multiscale analysis of bioimpedance data measured by electric cell-substrate impedance sensing for classification of cancerous and normal cells. *Physical review. E, Statistical, nonlinear, and soft matter physics*, 92(6):062702.
- de Larco, J. E. and Todaro, G. J. (1978). Epithelioid and fibroblastic rat kidney cell clones: Epidermal growth factor (egf) receptors and the effect of mouse sarcoma virus transformation. *J. Cell. Physiol.*, 94:335–342.

- Deakin, M. R. and Buttry, D. A. (1989). Electrochemical applications of the quartz crystal microbalance. *Analytical chemistry*, 61(20).
- Doerr, L., Thomas, U., Guinot, D. R., Bot, C. T., Stoelzle-Feix, S., Beckler, M., George, M., and Fertig, N. (2015). New easy-to-use hybrid system for extracellular potential and impedance recordings. *Journal of laboratory automation*, 20(2):175–188.
- Drasdo, D. and Höhme, S. (2005). A single-cell-based model of tumor growth in vitro: monolayers and spheroids. *Physical biology*, 2(3):133–147.
- Duc-Nguyen, H., Rosenblum, E. N., and Zeigel, R. F. (1966). Persistent infection of a rat kidney cell line with rauscher murine leukemia viruse. *Journal of Bacteriology*, 92(4):1133–1140.
- Ehret, R., Baumann, W., Brischwein, M., Schwinde, A., Stegbauer, K., and Wolf, B. (1997). Monitoring of cellular behaviour by impedance measurements on interdigitated electrode structures. *Biosensors & bioelectronics*, 12(1):29–41.
- Ehret, R., Baumann, W., Brischwein, M., Schwinde, A., and Wolf, B. (1998). On-line control of cellular adhesion with impedance measurements using interdigitated electrode structures. *Medical & biological engineering & computing*, 36(3):365–370.
- Eldawud, R., Wagner, A., Dong, C., Rojansakul, Y., and Zoica Dinu, C. (2015). Electronic platform for real-time multi-parametric analysis of cellular behavior post-exposure to single-walled carbon nanotubes. *Biosensors & bioelectronics*, 71:269–277.
- Englebienne, P., van Hoonacker, A., and Verhas, M. (2003). Surface plasmon resonance: principles, methods and applications in biomedical sciences. *Spectroscopy*, 17:255–273.
- Erdahl, W. L., Chapman, C. J., Taylor, R. W., and Pfeiffer, D. R. (1994). Ca^{2+} transport properties of ionophores a23187, ionomycin, and 4-bra23187 in a well defined model system. *Biophysical Journal*, 66:1678–1693.
- Évora, A., de Freitas, V., Mateus, N., and Fernandes, I. (2017). The effect of anthocyanins from red wine and blackberry on the integrity of a keratinocyte model using ecis. *Food & function*, 8(11):3989–3998.
- Fallarero, A., Batista-González, A. E., Hiltunen, A. K., Liimatainen, J., Karonen, M., and Vuorela, P. M. (2015). Online measurement of real-time cytotoxic responses induced by multi-component matrices, such as natural products, through electric cell-substrate impedance sensing (ecis). *International journal of molecular sciences*, 16(11):27044–27057.

- Figueiredo, S. A., Vilela, F. M. P., Anjos, T. N. d., Pádua, A. N. F. d., and Fonseca, M. J. V. (2021). Evaluation of cell biomarkers as in vitro photoprotective assays for sunscreen formulations. *Revista de Ciências Farmacêutica Básica e Aplicadas - RCFBA*, 42.
- Fogh, J., Fogh, J. M., and Orfeo, T. (1977). One hundred and twenty-seven cultured human tumor cell lines producing tumors in nude mice. *Journal of National Cancer Institute*, 59(1):222–225.
- Forbes, B. and Ehrhardt, C. (2005). Human respiratory epithelial cell culture for drug delivery applications. *European journal of pharmaceutics and biopharmaceutics : official journal of Arbeitsgemeinschaft fur Pharmazeutische Verfahrenstechnik e.V.*, 60(2):193–205.
- Franklin, M. J., Nivens, D. E., Guckert, J. B., and White, D. C. (1991). Effect of electrochemical impedance spectroscopy on microbial biofilm cell numbers, viability, and activity. *National Association of Corrosion Engineers*, 47(7):519–522.
- Fricke, H. (1924). A mathematical treatment of the electric conductivity and capacity of disperse systems i. the electric conductivity of a suspension of homogeneous spheroids. *Physical Review Journals Archive*, pages 575–587.
- Frutos, A. G. and Corn, R. M. (1998). Peer reviewed: Spr of ultrathin organic films. *Analytical chemistry News & Features*, 1:449–455.
- Fuller, S., von Bonsdorff, C.-H., and Simons, K. (1984). Vesicular stomatitis virus infects and matures only through the basolateral surface of the polarized epithelial cell line, mdck. *Cell*, 38:65–77.
- Fullerton, G. D., Kanal, K. M., and Cameron, I. L. (2006). On the osmotically unresponsive water compartment in cells. *Cell biology international*, 30(1):74–77.
- Fürhacker, M., Scharf, S., and Weber, H. (2000). Bisphenol a: emissions from point sources. *Chemosphere*, 41:751–756.
- Gamal, W., Borooah, S., Smith, S., Underwood, I., Srsen, V., Chandran, S., Bagnaninchi, P. O., and Dhillon, B. (2015). Real-time quantitative monitoring of hipsc-based model of macular degeneration on electric cell-substrate impedance sensing microelectrodes. *Biosensors & bioelectronics*, 71:445–455.
- García-Sánchez, T., Sánchez-Ortiz, B., Vila, I., Guitart, M., Rosell, J., Gómez-Foix, A. M., and Bragós, R. (2012). Design and implementation of a microelectrode assembly for use on noncontact in situ electroporation of adherent cells. *The Journal of membrane biology*, 245(10):617–624.
- George, I., Vranic, S., Boland, S., Courtois, A., and Baeza-Squiban, A. (2015). Development of an in vitro model of human bronchial epithelial barrier to study

- nanoparticle translocation. *Toxicology in vitro : an international journal published in association with BIBRA*, 29(1):51–58.
- George, V. C. and Rupasinghe, H. P. V. (2018). Dna damaging and apoptotic potentials of bisphenol a and bisphenol s in human bronchial epithelial cells. *Environmental toxicology and pharmacology*, 60:52–57.
- Geys, J., Coenegrachts, L., Vercammen, J., Engelborghs, Y., Nemmar, A., Nemery, B., and Hoet, P. H. M. (2006). In vitro study of the pulmonary translocation of nanoparticles: a preliminary study. *Toxicology letters*, 160(3):218–226.
- Ghosh, P. M., Keese, C. R., and Giaever I. (1993). Monitoring electroporabilization in the plasma membrane of adherent mammalian cells. *Biophysical Journal*, 64:1602–1609.
- Giaever, I. and Keese, C. R. (1984). Monitoring fibroblast behavior in tissue culture with an applied electric field. *Proceedings of the National Academy of Sciences of the United States of America*, 81:3761–3764.
- Giaever, I. and Keese, C. R. (1986). Use of electric fields to monitor the dynamical aspect of cell behavior in tissue culture. *IEEE Transactions of biomedical engineering*, BME-33(2):242–247.
- Giaever, I. and Keese, C. R. (1991). Micromotion of mammalian cells measured electrically. *Proceedings of the National Academy of Sciences of the United States of America*, 88:7896–7900.
- Giard, D. J., Aaronson, S. A., Todaro, G. J., Arnstein, P., Kersey, J. H., Dosik, H., and Parks, W. P. (1973). In vitro cultivation of human tumors: Establishment of cell lines derived from a series of solid tumors. *Journal of the National Cancer Institute*, 51(5).
- Greenspan, H. (1972). Models for the growth of a solid tumor by diffusion. *Studies in Applied Mathematics*, (4):317–340.
- Gu, C., Wei, X., Pan, Y., Liang, T., Gan, Y., Gao, K., Qiu, Y., Wan, H., and Wang, P. (2019). High-temporal-range drug-induced cardiac side-effect evaluation using simultaneous hl-1-based impedance and long-term electrophysiology recording systems. *Analytical Methods*, 11(41):5250–5259.
- Gundert-Remy, U., Bodin, J., Bosetti, C., FitzGerald, R., Hanberg, A., Hass, U., Hooijmans, C., Rooney, A., Rousselle, C., van Loveren, H., Wölflé, D., Barizzzone, F., Croera, C., Putzu, C., and Castoldi, A. F. (2017). Bisphenol a (bpa) hazard assessment protocol. *EFSA Supporting Publications*, 14(12):401.

- Guo, R., Wang, S., Huang, F., Chen, Q., Li, Y., Liao, M., and Lin, J. (2019). Rapid detection of salmonella typhimurium using magnetic nanoparticle immunoseparation, nanocluster signal amplification and smartphone image analysis. *Sensors and Actuators B: Chemical*, 284:134–139.
- Guo, X. (2012). Surface plasmon resonance based biosensor technique: a review. *Journal of biophotonics*, 5(7):483–501.
- Hafeman, D. G., Parce, J. W., and McConnell, H. M. (1988). Light-addressable potentiometric sensor for biochemical systems. *Science (New York, N.Y.)*, 240(4856):1182–1185.
- Hamilton, G. (1998). Multicellular spheroids as an in vitro tumor model. *Cancer Letters*, 131:29–34.
- Han, J., Tong, F., Chen, P., Zeng, X., and Duan, Z. (2018). Study of inflammatory factors’ effect on the endothelial barrier using piezoelectric biosensor. *Biosensors & bioelectronics*, 109:43–49.
- Hapala, I. (1997). Breaking the barrier: methods for reversible permeabilization of cellular membranes. *Critical reviews in biotechnology*, 17(2):105–122.
- Hattori, S.-I., Higashi-Kuwata, N., Hayashi, H., Allu, S. R., Raghavaiah, J., Bulut, H., Das, D., Anson, B. J., Lendy, E. K., Takamatsu, Y., Takamune, N., Kishimoto, N., Murayama, K., Hasegawa, K., Li, M., Davis, D. A., Kodama, E. N., Yarchoan, R., Wlodawer, A., Misumi, S., Mesecar, A. D., Ghosh, A. K., and Mitsuya, H. (2021). A small molecule compound with an indole moiety inhibits the main protease of sars-cov-2 and blocks virus replication. *Nature communications*, 12(1):668.
- Hayes, G., Biden, T. J., Selbie, L. A., and Shine, J. (1992). Structural subtypes of the dopamine d2 receptor are functionally distinct: Expression of the cloned d2a and d2b subtypes in a heterologous cell line. *Molecular Endocrinology*, 6(6):920–926.
- Hering, E., Bressler, K., and Gutekunst, J. (2014). *Elektronik für Ingenieure und Naturwissenschaftler*. Springer, Berlin, Heidelberg, 5 edition.
- Hernández-Hernández, K. L., Tapia-Orozco, N., Gimeno, M., Espinosa-García, A. M., García-García, J. A., Araiza-Olivera, D., Sánchez-Bartez, F., Gracia-Mora, I., Gutierrez-Aguilar, M., and García-Arrazola, R. (2019). Exposure to bisphenol a: current levels from food intake are toxic to human cells. *Molecular biology reports*, 46(2):2555–2559.
- Himmel, H. M. (2013). Drug-induced functional cardiotoxicity screening in stem cell-derived human and mouse cardiomyocytes: effects of reference compounds. *Journal of pharmacological and toxicological methods*, 68(1):97–111.

- Homola, J., Yee S. S., and Gaultitz G. (1999). Surface plasmon resonance sensors: review. *Sensors and Actuators B: Chemical*, 54:3–15.
- Hong, J., Kandasamy, K., Marimuthu, M., Choi, C. S., and Kim, S. (2011). Electrical cell-substrate impedance sensing as a non-invasive tool for cancer cell study. *The Analyst*, 136(2):237–245.
- Hu, N., Wang, T., Wan, H., Zhuang, L., Kettenhofen, R., Zhang, X., Zhang, Y. S., Xu, W., Gossmann, M., Bohlen, H., Hou, X., and Wang, P. (2018). Synchronized electromechanical integration recording of cardiomyocytes. *Biosensors & bioelectronics*, 117:354–365.
- Hu, N., Wang, T., Wang, Q., Zhou, J., Zou, L., Su, K., Wu, J., and Wang, P. (2015). High-performance beating pattern function of human induced pluripotent stem cell-derived cardiomyocyte-based biosensors for herg inhibition recognition. *Biosensors & bioelectronics*, 67:146–153.
- Huang, H., Wei, Z., Huang, Y., Zhao, D., Zheng, L., Cai, T., Wu, M., Wang, W., Ding, X., Zhou, Z., Du, Q., Li, Z., and Liang, Z. (2011). An efficient and high-throughput electroporation microchip applicable for sirna delivery. *Lab on a chip*, 11(1):163–172.
- Huerta-Nuñez, L. F. E., Gutierrez-Iglesias, G., Martinez-Cuazitl, A., Mata-Miranda, M. M., Alvarez-Jiménez, V. D., Sánchez-Monroy, V., Golberg, A., and González-Díaz, C. A. (2019). A biosensor capable of identifying low quantities of breast cancer cells by electrical impedance spectroscopy. *Scientific reports*, 9(1):6419.
- Huiszoon, R. C., Subramanian, S., Ramiah Rajasekaran, P., Beardslee, L. A., Bentley, W. E., and Ghodssi, R. (2019). Flexible platform for in situ impedimetric detection and bioelectric effect treatment of escherichia coli biofilms. *IEEE transactions on bio-medical engineering*, 66(5):1337–1345.
- Hulanicki, A., Glab, S., and Ingman, F. (1991). Chemical sensors definitions and classification. *International Union of Pure and Applied Chemistry*, 63(9):1247–1250.
- Ibáñez, C., Md Arshad, M. K., Gopinath, S. C. B., Nuzaihan M N, M., M Fathil, M. F., and Estrela, P. (2019). Gold interdigitated triple-microelectrodes for label-free prognosticative aptasensing of prostate cancer biomarker in serum. *Biosensors & bioelectronics*, 136:118–127.
- Ino, K., Nishijo, T., Kanno, Y., Ozawa, F., Arai, T., Takahashi, Y., Shiku, H., and Matsue, T. (2013). Electrochemical device with interdigitated ring array electrodes for investigating the relationship between cardiomyocyte differentiation from embryonic stem cells and alkaline phosphatase activity. *Electrochemistry*, 81(9):682–687.

- Jacoby, E., Bouhelal, R., Gerspacher, M., and Seuwen, K. (2006). The 7 tm g-protein-coupled receptor target family. *ChemMedChem*, 1(8):761–782.
- Jahnke, H.-G., Mewes, A., Zitzmann, F. D., Schmidt, S., Azendorf, R., and Robitzki, A. A. (2019). Electrochemical live monitoring of tumor cell migration out of microtumors on an innovative multiwell high-dense microelectrode array. *Scientific reports*, 9(1):13875.
- Jasim, I., Shen, Z., Mlaji, Z., Yuksek, N. S., Abdullah, A., Liu, J., Dastider, S. G., El-Dweik, M., Zhang, S., and Almasri, M. (2019). An impedance biosensor for simultaneous detection of low concentration of salmonella serogroups in poultry and fresh produce samples. *Biosensors & bioelectronics*, 126:292–300.
- Jen, C.-P., Wu, W.-M., Li, M., and Lin, Y.-C. (2004). Site-specific enhancement of gene transfection utilizing an attracting electric field for dna plasmids on the electroporation microchip. *Journal of Microelectromechanical Systems*, 13(6):947–955.
- Jeong, S., Lim, J., Kim, J., Kim, M.-Y., and Lee, J.-H. (2019). Label-free electrochemical impedance spectroscopy using a micro interdigitated electrode inside a pcr chip for real-time monitoring. *Microsystem Technologies*, 25(9):3503–3510.
- Jildeh, Z. B., Oberländer, J., Kirchner, P., Keusgen, M., Wagner, P. H., and Schöning, M. J. (2018). Experimental and numerical analyzes of a sensor based on interdigitated electrodes for studying microbiological alterations. *physica status solidi (a)*, 215(15):1700920.
- Jonsson, M. K. B., Wang, Q.-D., and Becker, B. (2011). Impedance-based detection of beating rhythm and proarrhythmic effects of compounds on stem cell-derived cardiomyocytes. *Assay and drug development technologies*, 9(6):589–599.
- Jun, L. Q., bin Djaswadi, G. W., bin Hawari, H. F., and Zakariya, M. (2018). *Science, technology & humanities: reinventing the future*. IEEE, Piscataway, NJ.
- Kandasamy, K., Choi, C. S., and Kim, S. (2010). An efficient analysis of nanomaterial cytotoxicity based on bioimpedance. *Nanotechnology*, 21(37):375501.
- Keese, C. R., Wegener, J., Walker, S. R., and Giaever, I. (2004). Electrical wound-healing assay for cells in vitro. *Proceeding of the National Academy of Science of the United States of America*, 101(6):1554–1559.
- Kenchetty, P., Miura, T., and Uno, S. (2019). Computer simulation for electrochemical impedance of a living cell adhered on the inter-digitated electrode sensors. *Japanese Journal of Applied Physics*, 58(SB):SBBG15.

- Kenchetty, P. and Uno, S. (2020). Impact of width and spacing of interdigitated electrode on impedance-based living cell monitoring studied by computer simulation. *Japanese Journal of Applied Physics*, 59(SD):SDDE02.
- Köhler, A. and Loos, W. (1941). Das phasenkontrastverfahren und seine anwendungen in der mikroskopie. *Die Naturwissenschaften*, 29(4):49–61.
- Koo, Y. and Yun, Y. (2016). Effects of polydeoxyribonucleotides (pdrn) on wound healing: Electric cell-substrate impedance sensing (ecis). *Materials science & engineering. C, Materials for biological applications*, 69:554–560.
- Kubwabo, C., Kosarac, I., Stewart, B., Gauthier, B. R., Lalonde, K., and Lalonde, P. J. (2009). Migration of bisphenol a from plastic baby bottles, baby bottle liners and reusable polycarbonate drinking bottles. *Food additives & contaminants. Part A, Chemistry, analysis, control, exposure & risk assessment*, 26(6):928–937.
- Lai, Y.-T., Chu, Y.-S., Lo, J.-C., Hung, Y.-H., and Lo, C.-M. (2019). Effects of electrode diameter on the detection sensitivity and frequency characteristics of electric cell-substrate impedance sensing. *Sensors and Actuators B: Chemical*, 288:707–715.
- Le, H. H., Carlson, E. M., Chua, J. P., and Belcher, S. M. (2008). Bisphenol a is released from polycarbonate drinking bottles and mimics the neurotoxic actions of estrogen in developing cerebellar neurons. *Toxicology letters*, 176(2):149–156.
- Lebrun, L. and Junter, G.-A. (1993). Diffusion of sucrose and dextran through agar gel membranes. *Enzyme Microbiological Technology*, 15.
- Lee, G. H., Pyun, J.-C., and Cho, S. (2014). Electrical impedance characterization of cell growth on interdigitated microelectrode array. *Journal of nanoscience and nanotechnology*, 14(11):8342–8346.
- Lee, S. Y., Jeong, E.-K., Jeon, H. M., Kim, C. H., and Kang, H. S. (2010). Implication of necrosis-linked p53 aggregation in acquired apoptotic resistance to 5-fu in mcf-7 multicellular tumour spheroids. *Oncology Reports*, 24:73–79.
- Lei, K. F., Lin, B.-Y., and Tsang, N.-M. (2017). Real-time and label-free impedimetric analysis of the formation and drug testing of tumor spheroids formed via the liquid overlay technique. *RSC Advances*, 7(23):13939–13946.
- Levenson, A. S. and Jordan, V. (1997). Mcf-7: The first hormone-responsive breast cancer cell line. *Cancer Research*, 57:3071–3078.
- Li, X., Zhang, R., Zhao, B., Lossin, C., and Cao, Z. (2016). Cardiotoxicity screening: a review of rapid-throughput in vitro approaches. *Archives of toxicology*, 90(8):1803–1816.

- Lieb, S., Littmann, T., Plank, N., Felixberger, J., Tanaka, M., Schäfer, T., Krief, S., Elz, S., Friedland, K., Bernhardt, G., Wegener, J., Ozawa, T., and Buschauer, A. (2016a). Label-free versus conventional cellular assays: Functional investigations on the human histamine h1 receptor. *Pharmacological research*, 114:13–26.
- Lieb, S., Michaelis, S., Plank, N., Bernhardt, G., Buschauer, A., and Wegener, J. (2016b). Label-free analysis of gpcr-stimulation: The critical impact of cell adhesion. *Pharmacological research*, 108:65–74.
- Lieber, M., Smith Barry, Szakal, A., Nelson-Rees, W., and Todaro, G. J. (1976). A continuous tumor-cell line from a human lung carcinoma with properties of type ii alveolar epithelial cells. *International Journal of Cancer*, 17:62–70.
- Liedberg, B., Nylander, C., and Lundstrom, I. (1983). Surface plasmon resonance for gas detection and biosensing. *Sensors and Actuators*, 4:299–304.
- Limonciel, A., Wilmes, A., Aschauer, L., Radford, R., Bloch, K. M., McMorrow, T., Pfaller, W., van Delft, J. H., Slattery, C., Ryan, M. P., Lock, E. A., and Jennings, P. (2012). Oxidative stress induced by potassium bromate exposure results in altered tight junction protein expression in renal proximal tubule cells. *Archives of toxicology*, 86(11):1741–1751.
- Lin, Y.-C., Li, M., Fan, C.-S., and Wu, L.-W. (2003). A microchip for electroporation of primary endothelial cells. *Sensors and Actuators A: Physical*, 108(1-3):12–19.
- Liu, J., Jasim, I., Abdullah, A., Shen, Z., Zhao, L., El-Dweik, M., Zhang, S., and Almasri, M. (2018). An integrated impedance biosensor platform for detection of pathogens in poultry products. *Scientific reports*, 8(1):16109.
- Lo, C. M. and Ferrier, J. (1998). Impedance analysis of fibroblastic cell layers measured by electric cell-substrate impedance sensing. *Physical review. E*, 57(6).
- Lo, C.-M., Keese, C. R., and Giaever, I. (1993). Monitoring motion of confluent cells in tissue culture. *Experimental cell research*, 204:102–109.
- Lo, C. M., Keese, C. R., and Giaever, I. (1995). Impedance analysis of mdck cells measured by electric cell-substrate impedance sensing. *Biophysical Journal*, 69:2800–2807.
- Lovelady, D. C., Richmond, T. C., Maggi, A. N., Lo, C.-M., and Rabson, D. A. (2007). Distinguishing cancerous from noncancerous cells through analysis of electrical noise. *Physical review. E, Statistical, nonlinear, and soft matter physics*, 76(4 Pt 1):041908.
- MacKay, S., Hermansen, P., Wishart, D., and Chen, J. (2015a). Simulations of interdigitated electrode interactions with gold nanoparticles for impedance-based biosensing applications. *Sensors (Basel, Switzerland)*, 15(9):22192–22208.

- MacKay, S., Hermansen, P., Wishart, D., Hiebert, W., and Chen, J. (2015b). *Simulating Electrical Properties of Interdigitated Electrode Designs for Impedance-based Biosensing applications*. IEEE, Piscataway, NJ.
- Male, K. B., Hamzeh, M., Montes, J., Leung, A. C. W., and Luong, J. H. T. (2013). Monitoring of potential cytotoxic and inhibitory effects of titanium dioxide using on-line and non-invasive cell-based impedance spectroscopy. *Analytica chimica acta*, 777:78–85.
- Male, K. B., Lachance, B., Hrapovic, S., Sunahara, G., and Luong, J. H. T. (2008). Assessment of cytotoxicity of quantum dots and gold nanoparticles using cell-based impedance spectroscopy. *Analytical chemistry*, 80(14):5487–5493.
- Male, K. B., Lam, E., Montes, J., and Luong, J. H. T. (2012). Noninvasive cell-based impedance spectroscopy for real-time probing inhibitory effects of graphene derivatives. *ACS applied materials & interfaces*, 4(7):3643–3649.
- Mamouni, J. and Yang, L. (2011). Interdigitated microelectrode-based microchip for electrical impedance spectroscopic study of oral cancer cells. *Biomedical microdevices*, 13(6):1075–1088.
- Matsuo, T. and Esashi, M. Y. (1981). Methods of isfet fabrication. *Sensors and Actuators A: Physical*, 1:77–96.
- Mavrikou, S., Moschopoulou, G., Tsekouras, V., and Kintzios, S. (2020). Development of a portable, ultra-rapid and ultra-sensitive cell-based biosensor for the direct detection of the sars-cov-2 s1 spike protein antigen. *Sensors (Basel, Switzerland)*, 20(11).
- Mazia, D., Schatten, G., and Sale, W. (1975). Adhesion of cells to surfaces coated with polylysine. *Journal of Cell Biology*, 66:198–200.
- Meldrum, R. A., Bowl, M., Ong, S. B., and Richardsonm S (1999). Optimisation of electroporation for biochemical experiments in live cells. *Biochemical and Biophysical Research Communications*, 256:235–239.
- Miyamoto, K.-i., Wagner, T., Mimura, S., Kanoh, S., Yoshinobu, T., and Schöning, M. J. (2011). Constant-phase-mode operation of the light-addressable potentiometric sensor. *Sensors and Actuators B: Chemical*, 154(2):119–123.
- Moraes, M. L., Lima, L. R., Vicentini-Oliveira, J. C., de Souza, A. V. G., Oliveira, O. N., Deffune, E., and Ribeiro, S. J. L. (2019). Immunosensor for the diagnostics of autoimmune hemolytic anemia (aiha) based on immobilization of a monoclonal antibody on a layer of silk fibroin. *Journal of nanoscience and nanotechnology*, 19(7):3772–3776.

- Moy, A. B., Shasby, S. S., Scott, B. D., and Shasby, D. M. (1993). The effect of histamine and cyclic adenosine monophosphate on myosin light chain phosphorylation in human umbilical vein endothelial cells. *The Journal of clinical investigation*, 92(3):1198–1206.
- Mueller-Klieser, W. (2000). Tumor biology and experimental therapeutics. *Critical Reviews in Oncology/Hematology*, 36:123–139.
- Muñoz-Berbel, X., Godino, N., Laczka, O., Baldrich, E., Muñoz, F. Y., and del Campo, J. (2008). Impedance-based biosensors for pathogen detection. In Zourob, M., editor, *Principles of bacterial detection: Biosensors, recognition receptors and microsystems*, pages 341–376. Springer Science and Business Media, New York.
- Nakanishi, T., Balaban, R. S., and Burg, M. B. (1988). Survey of osmolytes in renal cell lines. *The American Physiological Society*, 255:181–191.
- Nguyen, H. H., Park, J., Kang, S., and Kim, M. (2015). Surface plasmon resonance: a versatile technique for biosensor applications. *Sensors (Basel, Switzerland)*, 15(5):10481–10510.
- Niimura, Y. and Ishizuka, I. (1990). Adaptive changes in sulfoglycolipids of kidney cell lines by culture in anisotonic media. *Biochimica et Biophysica Acta*, 1052:248–254.
- Ostuni, E., Chapman, R. G., Liang, M. N., Meluleni, G., Pier, G., Ingber, D. E., and Whitesides, G. M. (2001). Self-assembled monolayers that resist the adsorption of proteins and the adhesion of bacterial and mammalian cells. *Langmuir*, 17(20):6336–6343.
- O’Sullivan, C. K. and Guibault, G. (1999). Commercial quartz crystal microbalances - theory and applications. *Biosensors and Bioelectronics*, 14:663–670.
- Owicki, J. C., Bousse, L., Hafeman, D. G., Kirk, G. L., Olson, J. D., Wada, H. G., and Parce, J. W. (1994). The light-addressable potentiometric sensor: Principles and biological applications. *Annual Review of Biophysics and Biomolecular Structures*, 23:87–113.
- Panula, P., Chazot, P. L., Cowart, M., Gutzmer, R., Leurs, R., Liu, W. L. S., Stark, H., Thurmond, R. L., and Haas, H. L. (2015). International union of basic and clinical pharmacology. xcvi. histamine receptors. *Pharmacological reviews*, 67(3):601–655.
- Parak, W., Domke, J., George, M., Kardinal, A., Radmacher, M., Gaub, H. E., de Roos, A., Theuvsen, A., Wiegand, G., Sackmann, E., and Behrendts, J. C. (1999). Electrically excitable normal rat kidney fibroblasts: A new model system for cell-semiconductor hybrids. *Biophysical Journal*, 76:1659–1667.

- Parekh, A., Das, D., Das, S., Dhara, S., Biswas, K., Mandal, M., and Das, S. (2018). Bioimpedimetric analysis in conjunction with growth dynamics to differentiate aggressiveness of cancer cells. *Scientific reports*, 8(1):783.
- Parviz, M., Gaus, K., and Gooding, J. J. (2017). Simultaneous impedance spectroscopy and fluorescence microscopy for the real-time monitoring of the response of cells to drugs. *Chemical science*, 8(3):1831–1840.
- Petchakup, C., Tay, H. M., Yeap, W. H., Dalan, R., Wong, S. C., Li, K. H. H., and Hou, H. W. (2018). Label-free leukocyte sorting and impedance-based profiling for diabetes testing. *Biosensors & bioelectronics*, 118:195–203.
- Ponten, J. and Magintyre, E. H. (1968). Long term culture of normal and neoplastic human glia. *Acta path. microbiol. scandinav.*, 74:465–486.
- Poole, J. A., Wyatt, T. A., Romberger, D. J., Staab, E., Simet, S., Reynolds, S. J., Sisson, J. H., and Kielian, T. (2015). Myd88 in lung resident cells governs airway inflammatory and pulmonary function responses to organic dust treatment. *Respiratory research*, 16:111.
- Procházka, V., Matějka, R., Ižák, T., Szabó, O., Štěpanovská, J., Filová, E., Bačáková, L., Jirásek, V., and Kromka, A. (2019). Nanocrystalline diamond-based impedance sensors for real-time monitoring of adipose tissue-derived stem cells. *Colloids and surfaces. B, Biointerfaces*, 177:130–136.
- Prozialeck, W. C., Edwards, J. R., Lamar, P. C., and Smith, C. S. (2006). Epithelial barrier characteristics and expression of cell adhesion molecules in proximal tubule-derived cell lines commonly used for in vitro toxicity studies. *Toxicology in vitro : an international journal published in association with BIBRA*, 20(6):942–953.
- Puck, T. T., Cieciura, S. J., and Robinson, A. (1958). Genetics of somatic mammalian cells. iii. long-term cultivation of euploid cells from human and animal subjects. *The journal of experimental medicine*, 108:945–959.
- Qian, F., Huang, C., Lin, Y.-D., Ivanovskaya, A. N., O’Hara, T. J., Booth, R. H., Creek, C. J., Enright, H. A., Soscia, D. A., Belle, A. M., Liao, R., Lightstone, F. C., Kulp, K. S., and Wheeler, E. K. (2017). Simultaneous electrical recording of cardiac electrophysiology and contraction on chip. *Lab on a chip*, 17(10):1732–1739.
- Ramasamy, S., Bennet, D., and Kim, S. (2015). Synthesis of hollow mesoporous ruthenium nanoparticles: evaluation of physico-chemical properties and toxicity. *RSC Advances*, 5(97):79616–79623.

- Raptis, L. and Firth, K. L. (1990). Electroporation of adherent cells in situ. *DNA and Cell Biology*, 9(8):615–621.
- Rawson, J. M. O., Duchon, A., Nikolaitchik, O. A., Pathak, V. K., and Hu, W.-S. (2021). Development of a cell-based luciferase complementation assay for identification of sars-cov-2 3clpro inhibitors. *Viruses*, 13(2).
- Redepenning, J., Schlesinger, T. K., Mechalke, E. J., Puleo, D. A., and Bizios, R. (1993). Osteoblast attachment monitored with a quartz crystal microbalance. *Analytical Chemistry*, 65(23):3378–3381.
- Reed, P. W. and Lardy, H. A. (1972). A23187: A divalent cation ionophore. *The Journal of biological chemistry*, 247(21):6970–6977.
- Reiss, B. and Wegener, J. (2015). Impedance analysis of different cell monolayers grown on gold-film electrodes. *IEEE*, pages 7079–7082.
- Reitingner, S., Wissenwasser, J., Kapferer, W., Heer, R., and Lepperdinger, G. (2012). Electric impedance sensing in cell-substrates for rapid and selective multipotential differentiation capacity monitoring of human mesenchymal stem cells. *Biosensors & bioelectronics*, 34(1):63–69.
- Reuss, L. (2001). Tight junction permeability to ions and water. In Cereijido, M. and Anderson, J., editors, *Tight junctions*, pages 61–88. CRC Press LLC.
- Richardson, J., Scalera, V., and Simmons, N. L. (1981). Identification of two strains of mdck cells which resemble separate nephron tubule segments. *Biochimica et Biophysica Acta*, 673:26–36.
- Rother, J., Pietuch, A., Koll, K., Schladt, T. D., Köhler, O., Schick, I., Tremel, W., and Janshoff, A. (2013). Enhanced motility of alveolar cancer cells induced by cpg-odn-functionalized nanoparticles. *Journal of Nanoparticle Research*, 15(12):675.
- Rotrosen, D. and Gallin, J. I. (1986). Histamine type i receptor occupancy increases endothelial cytosolic calcium, reduces f-actin, and promotes albumin diffusion across cultured endothelial monolayers. *The Journal of cell biology*, 103(6):2379–2387.
- Roy, G. and Sauve, R. (1987). Effect of anisotonic media on volume, ion and amino-acid content and membrane potential of kidney cells (mdck) in culture. *The Journal of membrane biology*, 100:83–96.
- Runfeng, L., Yunlong, H., Jicheng, H., Weiqi, P., Qin Hai, M., Yongxia, S., Chufang, L., Jin, Z., Zhenhua, J., Haiming, J., Kui, Z., Shuxiang, H., Jun, D., Xiaobo, L., Xiaotao, H., Lin, W., Nanshan, Z., and Zifeng, Y. (2020). Lianhuaqingwen exerts anti-viral and anti-inflammatory activity against novel coronavirus (sars-cov-2). *Pharmacological research*, 156:104761.

- Rutten, M. J., Laraway, B., Gregory, C. R., Xie, H., Renken, C., Keese, C., and Gregory, K. W. (2015). Rapid assay of stem cell functionality and potency using electric cell-substrate impedance sensing. *Stem cell research & therapy*, 6:192.
- Sambale, F., Wagner, S., Stahl, F., Khaydarov, R. R., Scheper, T., and Bahnemann, D. (2015). Investigations of the toxic effect of silver nanoparticles on mammalian cell lines. *Journal of Nanomaterials*, 2015(2):1–9.
- Santaguida, S., Janigro, D., Hossain, M., Oby, E., Rapp, E., and Cucullo, L. (2006). Side by side comparison between dynamic versus static models of blood-brain barrier in vitro: a permeability study. *Brain research*, 1109(1):1–13.
- Sapper, A., Wegener, J., and Janshoff, A. (2006). Cell motility probed by noise analysis of thickness shear mode resonators. *Analytical chemistry*, 78(14):5184–5191.
- Schöning, M. J. and Poghossian, A. (2002). Recent advances in biologically sensitive field-effect transistors (biofets). *The Analyst*, 127(9):1137–1151.
- Schug, T. T., Janesick, A., Blumberg, B., and Heindel, J. J. (2011). Endocrine disrupting chemicals and disease susceptibility. *The Journal of steroid biochemistry and molecular biology*, 127(3-5):204–215.
- Schwartz, S. M. (1978). Selection and characterization of bovine aortic endothelial cells. *In vitro*, 14(12):966–980.
- Scott, C. W., Peters, M. F., and Dragan, Y. P. (2013). Human induced pluripotent stem cells and their use in drug discovery for toxicity testing. *Toxicology letters*, 219(1):49–58.
- Simmons, N. L. and Tivey, D. R. (1992). The effect of hyperosmotic challenge upon ion transport in cultured renal epithelial layers (mdck). *European Journal of Physiology*, 421:503–509.
- Singh, K. V., Whited, A. M., Ragineni, Y., Barrett, T. W., King, J., and Solanki, R. (2010). 3d nanogap interdigitated electrode array biosensors. *Analytical and bioanalytical chemistry*, 397(4):1493–1502.
- Slaughter, G. E. and Hobson, R. (2009). An impedimetric biosensor based on pc 12 cells for the monitoring of exogenous agents. *Biosensors & bioelectronics*, 24(5):1153–1158.
- Soule, H. D., Vazquez, J., Long, A., Albert, S., and Brennan, M. (1973). A human cell line from a pleural effusion derived from breast carcinoma. *Journal of the National Cancer Institute*, 51(5).

- Stannes, K. A., Westrum, L. E., Fornaciari, E., Mascagni, P., Nelson, J. A., Stenglein, S. G., Myers, T., and Janigro, D. (1997). Morphological and functional characterization of an in vitro blood-brain barrier model. *Brain research*, 771:329–342.
- Staples, C. A., Dorn, P. B., Klecka, G. M., O’Block, S. T., and Harris, L. R. (1998). A review of the environmental fate, effects, and exposures of bisphenol a. *Chemosphere*, 36(10):2149–2173.
- Stevenson, B. R., Anderson, J. M., Goodenough, D. A., and Mooseker, M. S. (1988). Tight junction structure and zo-1 content are identical in two strains of madin-darby canine kidney cells which differ in transepithelial resistance. *The Journal of cell biology*, 107(6):2401–2408.
- Stevenson, B. R., Siliciano, J. D., Mooseker, M. S., and Goodenough, D. A. (1986). Identification of zo-1: A high molecular weight polypeptide associated with the tight junction (zonula occludens) in a variety of epithelia. *The Journal of cell biology*, 103:755–766.
- Stiefel, F., Paul, A. J., Jacopo, T., Sgueglia, A., Stützle, M., Herold, E. M., and Hesse, F. (2016). The influence of bisphenol a on mammalian cell cultivation. *Applied microbiology and biotechnology*, 100(1):113–124.
- Stojanović, G., Kojić, T., Radovanović, M., Vasiljević, D., Panić, S., Srdić, V., and Cvejić, J. (2019). Flexible sensors based on two conductive electrodes and mwcnts coating for efficient ph value measurement. *Journal of Alloys and Compounds*, 794:76–83.
- Stolwijk, J. A., Hartmann, C., Balani, P., Albermann, S., Keese, C. R., Giaever, I., and Wegener, J. (2011). Impedance analysis of adherent cells after in situ electroporation: non-invasive monitoring during intracellular manipulations. *Biosensors & bioelectronics*, 26(12):4720–4727.
- Stolwijk, J. A., Matrougui, K., Renken, C. W., and Trebak, M. (2015). Impedance analysis of gpcr-mediated changes in endothelial barrier function: overview and fundamental considerations for stable and reproducible measurements. *Pflügers Archiv : European journal of physiology*, 467(10):2193–2218.
- Stolwijk, J. A., Skiba, M., Kade, C., Bernhardt, G., Buschauer, A., Hübner, H., Gmeiner, P., and Wegener, J. (2019). Increasing the throughput of label-free cell assays to study the activation of g-protein-coupled receptors by using a serial agonist exposure protocol. *Integrative biology : quantitative biosciences from nano to macro*, 11(3):99–108.
- Sutherland, R. M. (1986). Importance of critical metabolites and cellular interactions in the biology of microregions of tumors. *Cancer*, 58(8):1668–1680.

- Sutherland, R. M. (1988). Cell and environment interactions in tumor microregions: The multicell spheroid model. *Science*, (240):177–184.
- Tarantola, M., Pietuch, A., Schneider, D., Rother, J., Sunnick, E., Rosman, C., Pierrat, S., Sönnichsen, C., Wegener, J., and Janshoff, A. (2011). Toxicity of gold-nanoparticles: synergistic effects of shape and surface functionalization on micromotility of epithelial cells. *Nanotoxicology*, 5(2):254–268.
- Tarantola, M., Schneider, D., Sunnick, E., Adam, H., Pierrat, S., Rosman, C., Breus, V., Sönnichsen, C., Basché, T., Wegener, J., and Janshoff, A. (2009). Cytotoxicity of metal and semiconductor nanoparticles indicated by cellular micromotility. *ACS nano*, 3(1):213–222.
- Terasaka, H., Kadoma, Y., Sakagami, H., and Fujisawa, S. (2005). Cytotoxicity and apoptosis-inducing activity of bisphenol a and hydroquinone in hl-60 cells. *Anticancer Research*, 25:2241–2248.
- Thangavel, P., Viswanath, B., and Kim, S. (2018). Synthesis and characterization of kaempferol-based ruthenium (ii) complex: A facile approach for superior anticancer application. *Materials science & engineering. C, Materials for biological applications*, 89:87–94.
- Thévenot, D. R., Toth, K., Durst, R. A., and Wilson, G. S. (2001). Electrochemical biosensors: recommended definitions and classification. *Biosensors and Bioelectronics*, 16:121–131.
- Tian, J., Shi, R., Liu, Z., Ouyang, H., Yu, M., Zhao, C., Zou, Y., Jiang, D., Zhang, J., and Li, Z. (2019). Self-powered implantable electrical stimulator for osteoblasts’ proliferation and differentiation. *Nano Energy*, 59:705–714.
- Tornavaca, O., Chia, M., Dufton, N., Almagro, L. O., Conway, D. E., Randi, A. M., Schwartz, M. A., Matter, K., and Balda, M. S. (2015). Zo-1 controls endothelial adherens junctions, cell-cell tension, angiogenesis, and barrier formation. *The Journal of cell biology*, 208(6):821–838.
- Tran, T. B., Nguyen, P. D., Um, S. H., Son, S. J., and Min, J. (2013). Real-time monitoring in vitro cellular cytotoxicity of silica nanotubes using electric cell-substrate impedance sensing (ecis). *Journal of Biomedical Nanotechnology*, 9(2):286–290.
- Turolla, A., Di Mauro, M., Mezzera, L., Antonelli, M., and Carminati, M. (2019). Development of a miniaturized and selective impedance sensor for real-time slime monitoring in pipes and tanks. *Sensors and Actuators B: Chemical*, 281:288–295.
- van Gerwen, P., Laureyn, W., Laureys, W., Hyberegts, G., de Beeck, M. O., Baert, K., Suls, J., Sansen, W., Jacobs, P., Hermans, L., and Mertens, R. (1998).

- Nanoscaled interdigitated electrode arrays for biochemical sensors. *Sensors and Actuators B: Chemical*, 49:73–80.
- van Nieuw Amerongen, G. P., Draijer, R., Vermeer, M. A., and van Hinsbergh, V. (1998). Transient and prolonged increase in endothelial permeability induced by histamine and thrombin. *Journal of the American Heart Association*, 83:1115–1123.
- Venkatesan, G., Dancik, Y., Sinha, A., Kyaw, H. M., Srinivas, R., Dawson, T. L., Bigliardi, M., Bigliardi, P., and Pastorin, G. (2021). Development of novel alternative hair dyes to hazardous para-phenylenediamine. *Journal of hazardous materials*, 402:123712.
- Verdonk, E., Johnson, K., McGuinness, R., Leung, G., Chen, Y.-W., Tang, H. R., Michelotti, J. M., and Liu, V. F. (2006). Cellular dielectric spectroscopy: A label-free comprehensive platform for functional evaluation of endogenous receptors. *Assay and Drug Development Technologies*, 4(5):609–619.
- Wang, L., Yin, H., Xing, W., Yu, Z., Guo, M., and Cheng, J. (2010). Real-time, label-free monitoring of the cell cycle with a cellular impedance sensing chip. *Biosensors & bioelectronics*, 25(5):990–995.
- Wegener, J. (2010). Impedance analysis of cell junctions. In Schmid, G., editor, *Nanotechnology*, pages 2210–2242. Wiley Interscience, Hoboken, NJ.
- Wegener, J. and Galla, H.-J. (1996). The role of non-lamellar lipid structures in the formation of tight junctions. *Chemistry and Physics of Lipids*, 81:229–255.
- Wegener, J., Janshoff, A., and Galla, H.-J. (1998). Cell adhesion monitoring using a quartz crystal microbalance: comparative analysis of different mammalian cell lines. *European Biophysics Journal*, 28(1):26–37.
- Wegener, J., Janshoff, A., and Steinem, C. (2001). The quartz crystal microbalance as a novel means to study cell-substrate interactions. *Cell Biochemistry and Biophysics*, (34):121–151.
- Wegener, J., Keese, C. R., and Giaever, I. (2000a). Electric cell-substrate impedance sensing (ecis) as a noninvasive means to monitor the kinetics of cell spreading to artificial surfaces. *Experimental cell research*, 259(1):158–166.
- Wegener, J., Keese, C. R., and Giaever, I. (2002). Recovery of adherent cells after in situ electroporation monitored electrically. *BioTechniques*, 33(2):348–357.
- Wegener, J., Seebach, J., Janshoff, A., and Galla, H.-J. (2000b). Analysis of the composite response of shear wave resonators to the attachment of mammalian cells. *Biophysical Journal*, 78:2821–2833.

- Wegener, J., Zink, S., Rösen, P., and Galla, H. (1999). Use of electrochemical impedance measurements to monitor beta-adrenergic stimulation of bovine aortic endothelial cells. *Pflügers Archiv : European journal of physiology*, 437(6):925–934.
- Wen, T., Wang, R., Sotero, A., and Li, Y. (2017). A portable impedance immunosensing system for rapid detection of salmonella typhimurium. *Sensors (Basel, Switzerland)*, 17(9).
- Weng, K.-Y., Chang, Y.-J., Ho, C.-Y., Liou, D. U., Huang, Y.-T., Chung, W.-Y., and Chin, T.-Y. (2018). Measurement of impedimetric ratio of blood cells using microfluidic chip with zno nanowires. *Journal of Medical and Biological Engineering*, 38(1):150–158.
- Widder, M. W., Brennan, L. M., Hanft, E. A., Schrock, M. E., James, R. R., and van der Schalie, W. H. (2015). Evaluation and refinement of a field-portable drinking water toxicity sensor utilizing electric cell-substrate impedance sensing and a fluidic biochip. *Journal of applied toxicology : JAT*, 35(7):701–708.
- Wilson, D., Materón, E. M., Ibáñez-Redín, G., Faria, R. C., Correa, D. S., and Oliveira, O. N. (2019). Electrical detection of pathogenic bacteria in food samples using information visualization methods with a sensor based on magnetic nanoparticles functionalized with antimicrobial peptides. *Talanta*, 194:611–618.
- Wu, Q., Liu, Y., Ren, Y., Xu, X., Yu, L., Li, Y., and Quan, C. (2010). Tight junction protein, claudin-6, downregulates the malignant phenotype of breast carcinoma. *European journal of cancer prevention : the official journal of the European Cancer Prevention Organisation (ECP)*, 19(3):186–194.
- Wu, Q., Wei, X., Pan, Y., Zou, Y., Hu, N., and Wang, P. (2018). Bionic 3d spheroids biosensor chips for high-throughput and dynamic drug screening. *Biomedical microdevices*, 20(4):82.
- Xi, B., Wang, T., Li, N., Ouyang, W., Zhang, W., Wu, J., Xu, X., Wang, X., and Abassi, Y. A. (2011). Functional cardiotoxicity profiling and screening using the xcelligence rtca cardio system. *Journal of laboratory automation*, 16(6):415–421.
- Xiao, C. and Luong, J. H. T. (2003). On-line monitoring of cell growth and cytotoxicity using electric cell-substrate impedance sensing (ecis). *Biotechnology progress*, 19(3):1000–1005.
- Xiao, C. and Luong, J. H. T. (2005). Assessment of cytotoxicity by emerging impedance spectroscopy. *Toxicology and applied pharmacology*, 206(2):102–112.

- Xiao, C. and Luong, J. H. T. (2010). A simple mathematical model for electric cell-substrate impedance sensing with extended applications. *Biosensors & bioelectronics*, 25(7):1774–1780.
- Xiao, L., Hu, Z., Zhang, W., Wu, C., Yu, H., and Wang, P. (2010). Evaluation of doxorubicin toxicity on cardiomyocytes using a dual functional extracellular biochip. *Biosensors & bioelectronics*, 26(4):1493–1499.
- Xing, F., Persaud, Y., Pratilas, C. A., Taylor, B. S., Janakiraman, M., She, Q.-B., Gallardo, H., Liu, C., Merghoub, T., Hefter, B., Dolgalev, I., Viale, A., Heguy, A., de Stanchina, E., Cobrinik, D., Bollag, G., Wolchok, J., Houghton, A., and Solit, D. B. (2012). Concurrent loss of the pten and rb1 tumor suppressors attenuates raf dependence in melanomas harboring (v600e)braf. *Oncogene*, 31(4):446–457.
- Xu, M., McCanna, D. J., and Sivak, J. G. (2015a). Use of the viability reagent prestoblue in comparison with alamarblue and mtt to assess the viability of human corneal epithelial cells. *Journal of pharmacological and toxicological methods*, 71:1–7.
- Xu, Y., Su, S., Zhou, C., Lu, Y., and Xing, W. (2015b). Cell electroporation with a three-dimensional microelectrode array on a printed circuit board. *Bioelectrochemistry (Amsterdam, Netherlands)*, 102:35–41.
- Xu, Y., Xie, X., Duan, Y., Wang, L., Cheng, Z., and Cheng, J. (2016). A review of impedance measurements of whole cells. *Biosensors & bioelectronics*, 77:824–836.
- Yao, X., Ye, F., Zhang, M., Cui, C., Huang, B., Niu, P., Liu, X., Zhao, L., Dong, E., Song, C., Zhan, S. Lu, R., Li, H., Tan, W., and Liu, D. (2020). In vitro antiviral activity and projection of optimized dosing design of hydroxychloroquine for the treatment of severe acute respiratory syndrome coronavirus 2 (sars-cov-2). *Clinical Infectious Diseases*, 71(15):732–739.
- Yoshinobu, T., Iwasaki, H., Ui, Y., Furuichi, K., Ermolenko, Y., Mourzina, Y., Wagner, T., Näther, N., and Schöning, M. J. (2005). The light-addressable potentiometric sensor for multi-ion sensing and imaging. *Methods (San Diego, Calif.)*, 37(1):94–102.
- Young, E. F. and Smilenov, L. B. (2011). Impedance-based surveillance of transient permeability changes in coronary endothelial monolayers after exposure to ionizing radiation. *Radiation Research*, 176:415–424.
- Young, W. K. and Hyochoong, B. (2000). *The Finite Element Method Using MATLAB*. CRC Press LLC, New York, second edition.
- Yuqing, M., Jianguo, G., and Jianrong, C. (2003). Ion sensitive field effect transducer-based biosensors. *Biotechnology Advances*, 21(6):527–534.

- Zagórska-Dziok, M., Ziemlewska, A., Bujak, T., Nizioł-Łukaszewska, Z., and Hordyjewicz-Baran, Z. (2021). Cosmetic and dermatological properties of selected ayurvedic plant extracts. *Molecules (Basel, Switzerland)*, 26(3).
- Zaharoff, D. A., Henshaw, J. W., Mossop, B., and Yuan, F. (2008). Mechanistic analysis of electroporation-induced cellular uptake of macromolecules. *Experimental biology and medicine (Maywood, N.J.)*, 233(1):94–105.
- Zernike, F. (1942). Phase contrast, a new method for the microscopic observation of transparent objects. *Physica IX*, (7):686–698.
- Zheng, Q. and Chang, D. C. (1991). High-efficiency gene transfection by in situ electroporation of cultured cells. *Biochimica et Biophysica Acta*, 1088:104–110.
- Zink, S., Rösen, P., Sackmann, B., and Lemoine, H. (1993). Regulation of endothelial permeability by β -adrenoceptor agonists: contribution of β_1 - and β_2 -adrenoceptors. *Biochimica et Biophysica Acta*, 1178:286–298.
- Zinkl, M. (2015). Master thesis: Impedanz-basierte analyse von adhärenzen zellen mit hilfe interdigitierter elektroden subzellulärer dimensionen. *University Regensburg*.
- Zinkl, M. and Wegener, J. (2019). Using animal cells as sensors for xenobiotics: monitoring phenotypic changes by multimodal impedance assays. *Current Opinion in Environmental Science & Health*, 10:30–37.

.

A Appendix

A.1 Supplementary information

A.1.1 Simulation of cell-free electrodes by finite element techniques using COMSOL simulations

Simulation of the electric potential of cell-free IDEs

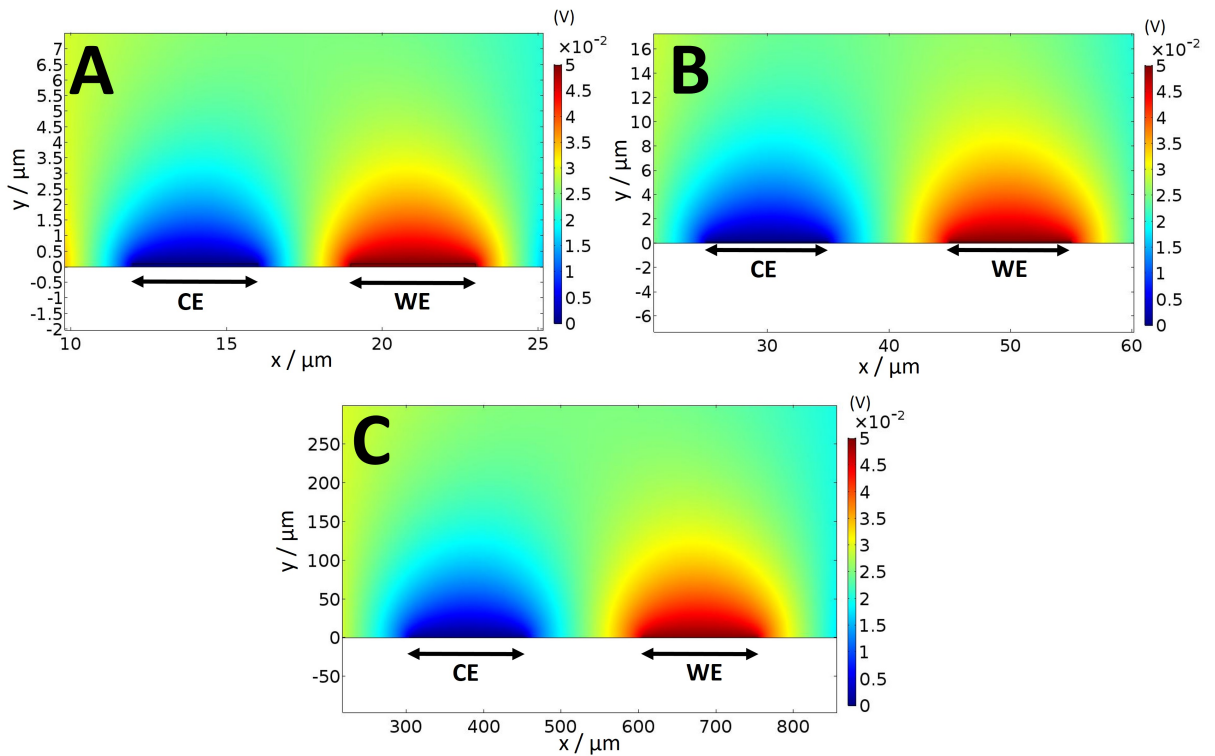


Figure A.1: Two-dimensional cross section of the simulated two dimensional distribution of the electric potential (in V) modeled with different layouts of the cell-free IDEs. The counter (CE) and the working electrodes (WE) are highlighted with black arrows. The simulation was performed with an initial electric potential of $V = 0.05$ V and at different frequencies: **A:** IDE 7 at $f = 400$ kHz, **B:** IDE 20 at $f = 200$ kHz and **C:** IDE 300 at $f = 4$ kHz.

Simulation of the electric field of cell-free IDEs

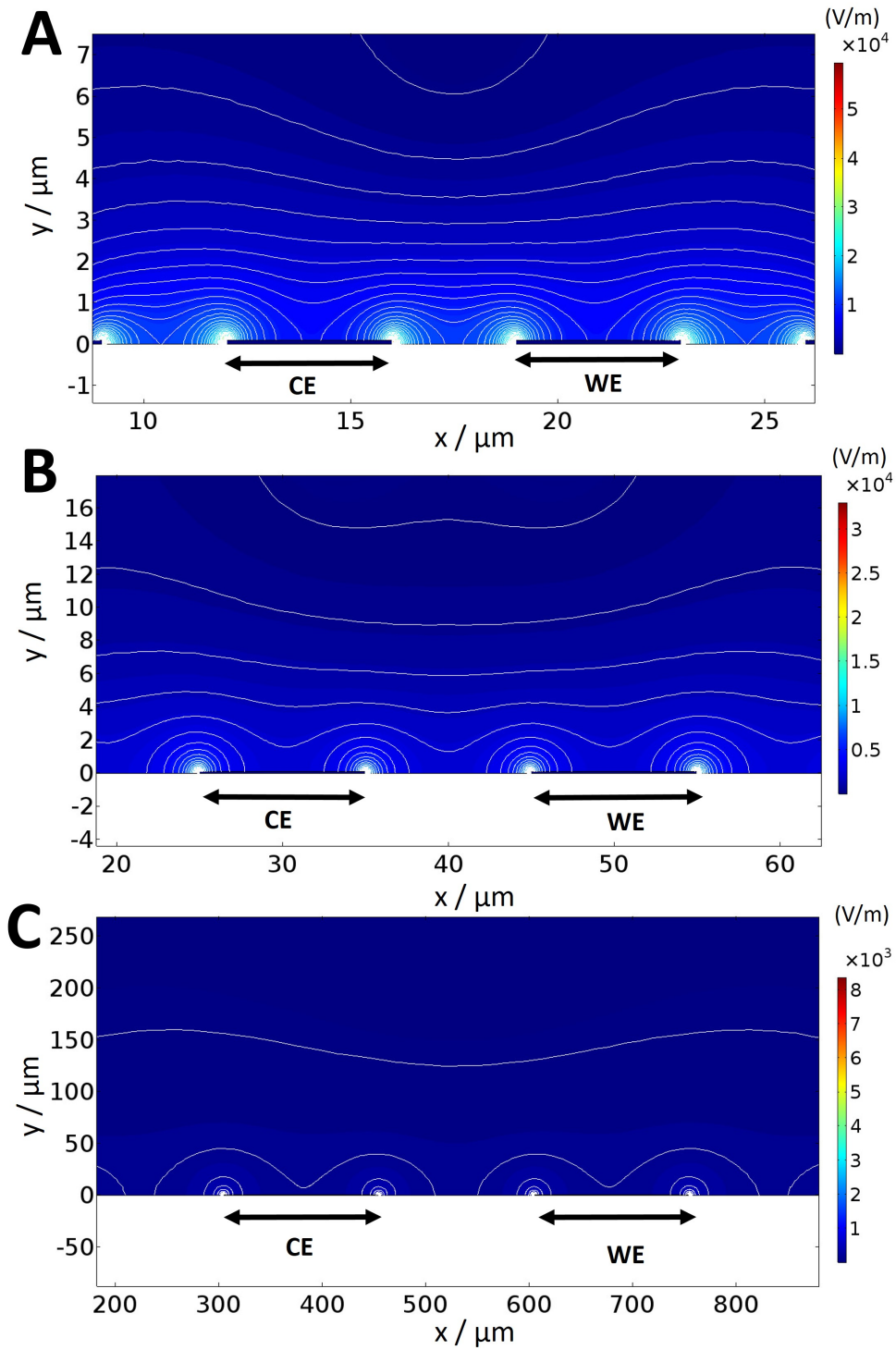


Figure A.2: Two-dimensional cross section of the simulated two dimensional distribution of the electric potential (in V) modeled with different layouts of the cell-free IDEs. The counter (CE) and the working electrodes (WE) are highlighted with black arrows. The simulation was performed with an initial electric potential of $V = 0.05 \text{ V}$ and at different frequencies: **A:** IDE 7 at $f = 400 \text{ kHz}$, **B:** IDE 20 at $f = 200 \text{ kHz}$ and **C:** IDE 300 at $f = 4 \text{ kHz}$.

A.1.2 Measurement of the cell size

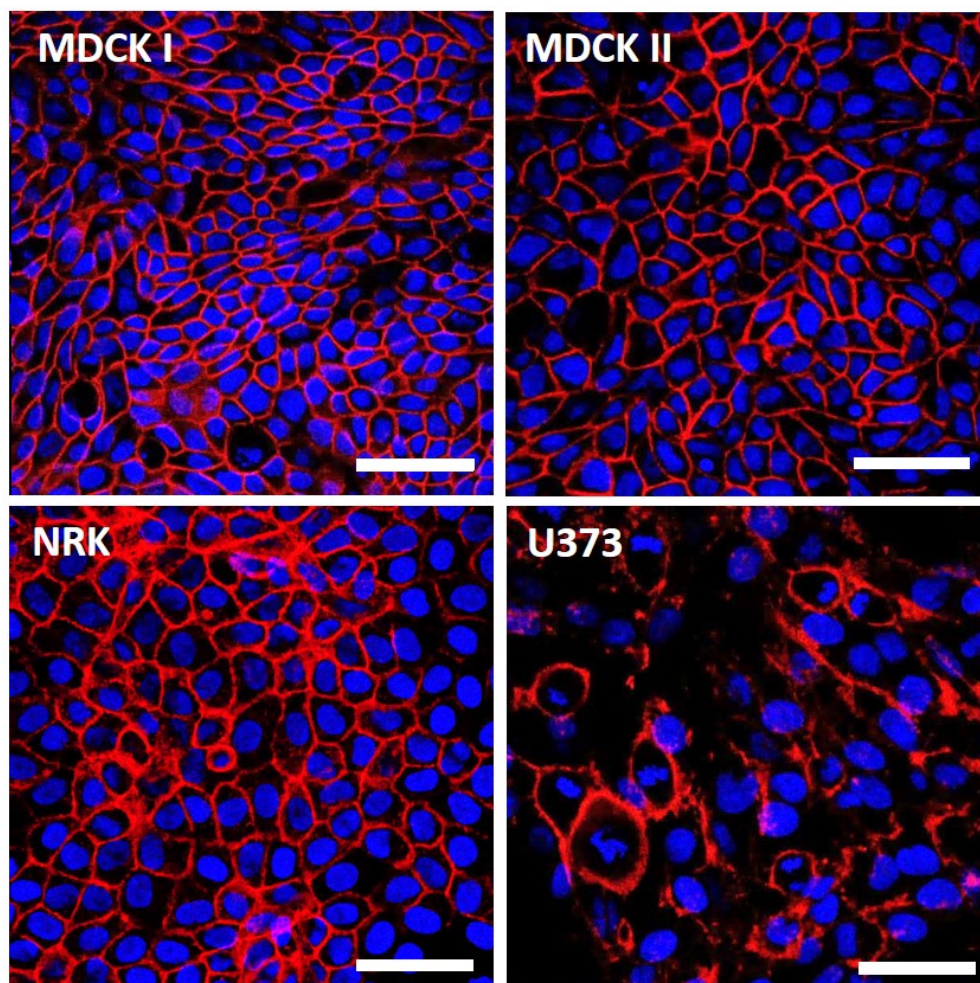


Figure A.3: Four different cell types cultivated on a petri dish. The cells were stained with TRITC phalloidin (red) and DAPI (blue) on the third day after seeding. The images were taken with the CLSM (60x) with a laser with 408 nm and a 450 / 35 nm BP detector for the DAPI staining, and with a laser with 543 nm and a 650 LP detector for the TRITC phalloidin. The sizes of the cells were measured with ImageJ and the area, the radius and the diameter were calculated assuming circular cells. MDCK I (seeding density: 450,000 cells/cm²), MDCK II (seeding density: 450,000 cells/cm²), NRK (seeding density: 450,000 cells/cm²) and U373 cells (seeding density: 100,000 cells/cm²) were seeded. The scale bar represents 50 μm.

A.1.3 Impedance-based comparison of different mammalian cell lines grown on various electrode layouts

Simulating the dielectric properties of adherent cells grown on interdigitated electrodes by finite element techniques

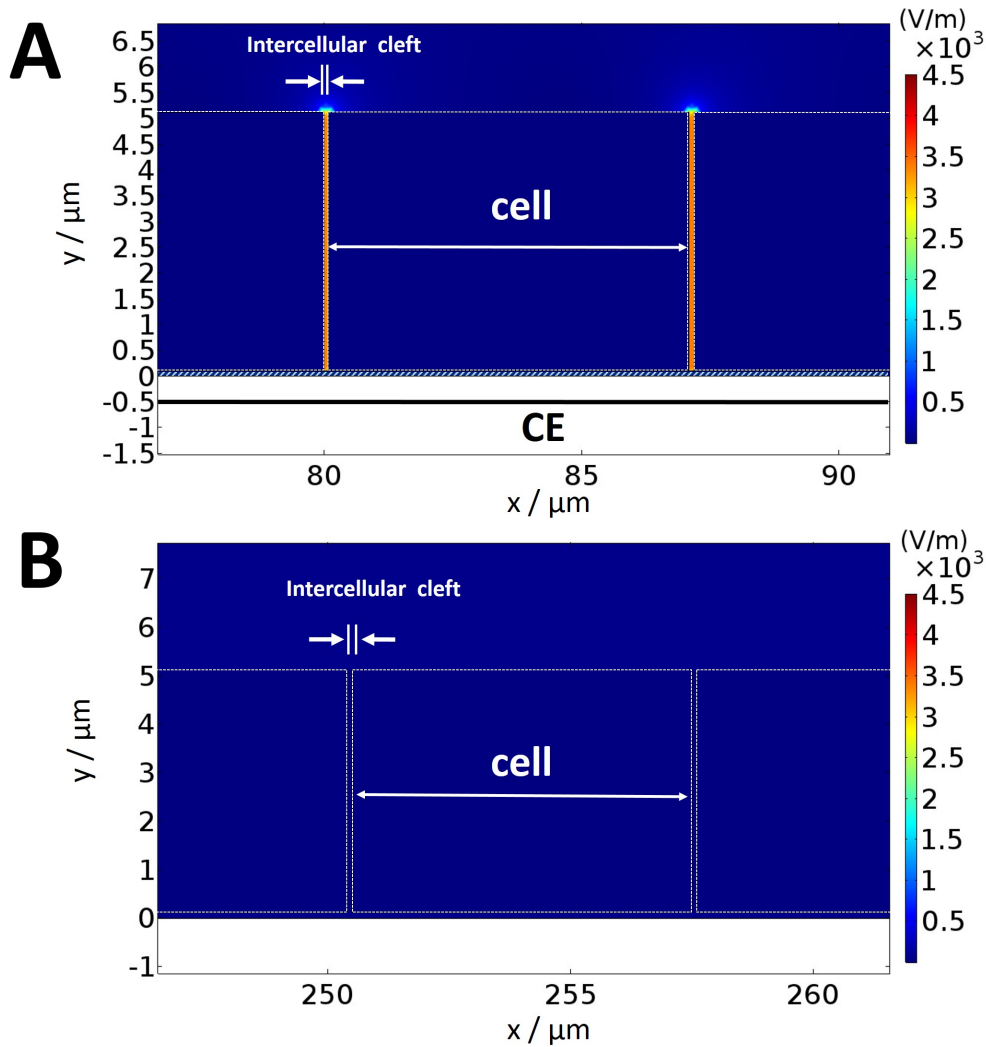


Figure A.4: Representation of the two-dimensional excerpts of the simulated expansion of the electric field in V/m with cells grown on the IDE 300 simulated with an electric potential of $V = 0.05 \text{ V}$ and at a frequency of $f = 4 \text{ kHz}$ (see fig. 6.5). The gap and width of the electrodes are defined to be $150 \mu\text{m}$, respectively. The insulated cells ($h = 5 \mu\text{m}$) are modeled as rectangles with a white dashed border. The height of the cell-electrode distance amounts to 25 nm and the intercellular cleft to 100 nm . This cleft is marked and labeled. The electrodes were highlighted with blue dashes and the width and the location of the electrodes are monitored with black arrows. **A:** excerpt of the simulation of cells grown directly on the electrode, **B:** excerpt of the simulation of cells grown between the counter and the working electrode. **CE:** counter electrode.

Resistance spectra of cell-covered electrodes with different layouts

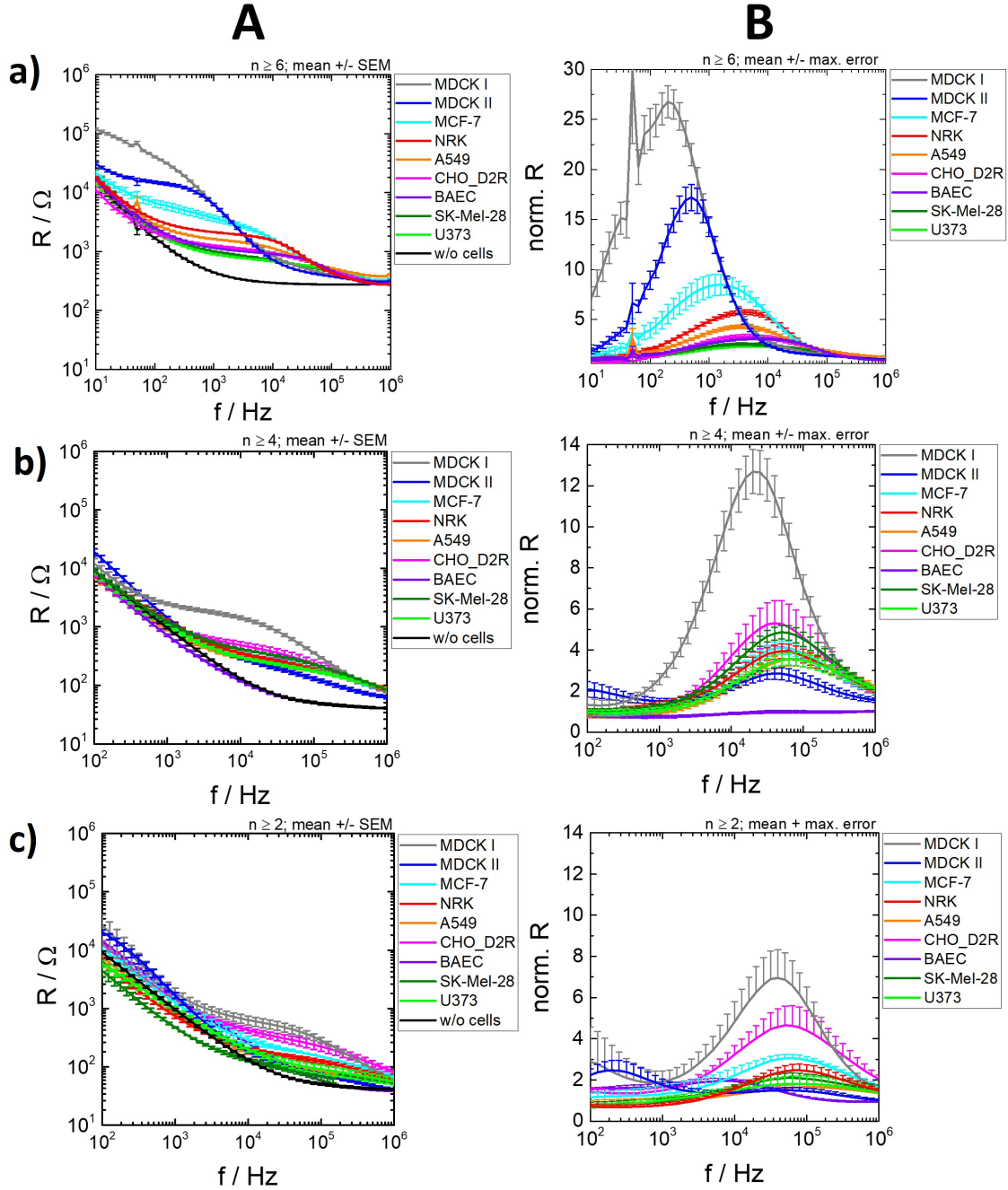


Figure A.5: Resistance spectra in dependence of the frequency of nine different cell lines. The spectra were measured on the third day after cultivation with different electrode types: **a)**: 8W10E electrodes ($n \geq 6$), **b)**: IDE 12 ($n \geq 4$), **c)**: IDE 7 ($n \geq 2$). Two different data representations in dependence of the frequency were chosen: **A**: spectra of the resistance and **B**: norm. R. The mean is plotted with the SEM in **A** and with the max. error in **B**.

Capacitance spectra of cell-covered electrodes with different layouts

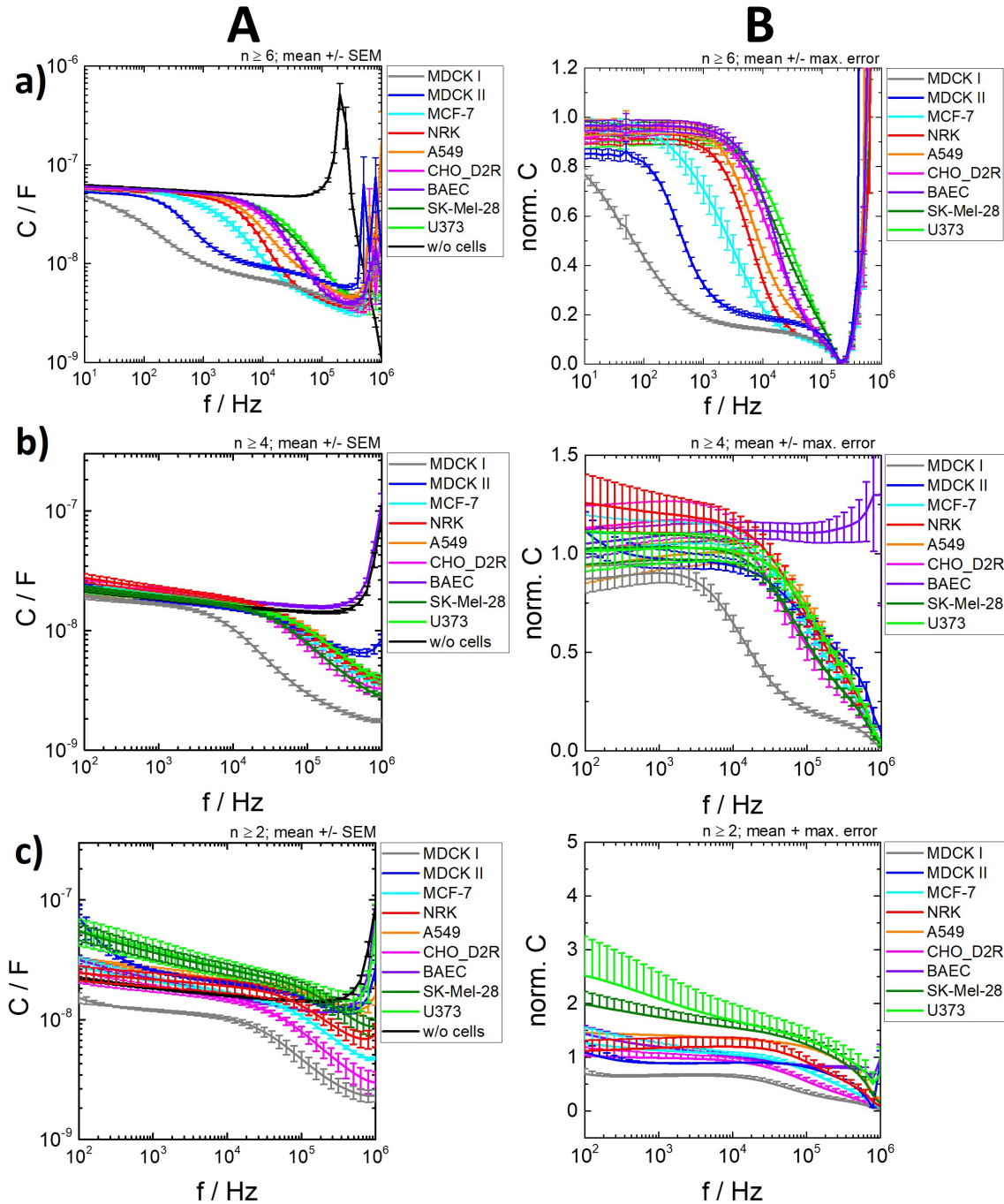


Figure A.6: Capacitance spectra in dependence of the frequency of nine different cell lines on various electrode layouts. The measurement was proceeded on the third day after cultivation. Three different electrode types were used: **a)**: 8W10E electrodes ($n \geq 6$), **b)**: IDE 12 ($n \geq 4$), **c)**: IDE 7 ($n \geq 2$). Two data representations were chosen: **A**: spectra of the capacitance and **B**: norm. C. The mean with the SEM is plotted in **A** and with the max. error in **B**.

Simulated spectra of cell-covered IDE 12 on the basis of the ECIS theory

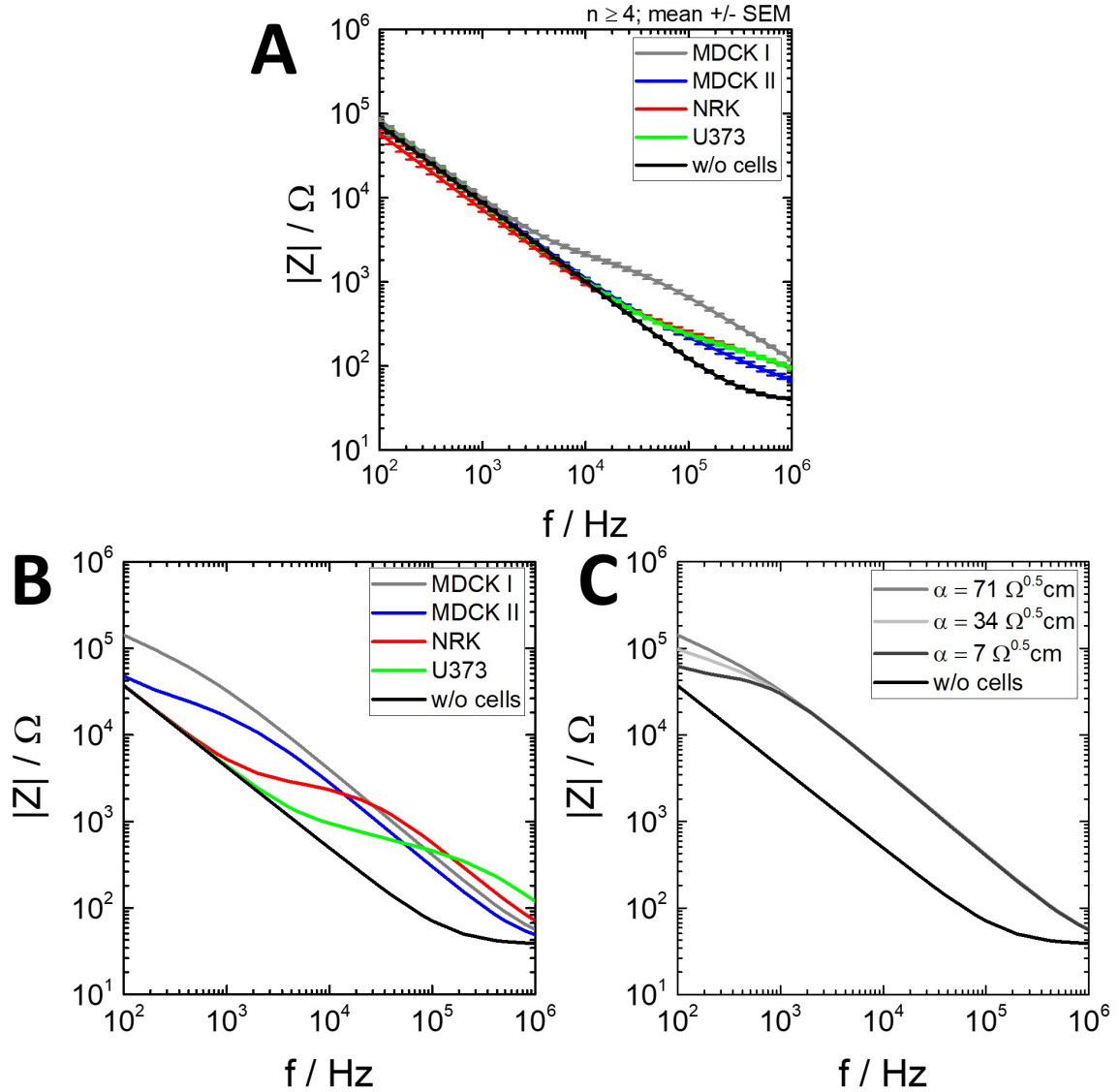


Figure A.7: Comparison of the measured and simulated spectra of an IDE 12. The basis for the simulations was the ECIS theory. **A** shows the measured impedance spectra of the cells (from fig. 6.7 **B**). For the simulation following parameters were used: $WE = CE$, electrode area: 0.003 cm^2 , A of CPE: $2.10 \cdot 10^{-5} \text{ cm}^2$, n of CPE: 0.94 , $R_{\text{bulk}} = 38 \Omega$. In **B** four different cell types were simulated with the following parameter: MDCK I: $R_b = 121 \Omega \text{ cm}^2$, $\alpha = 71 \Omega^{0.5} \text{ cm}$, $C_m = 3.1 \mu\text{F}/\text{cm}^2$; MDCK II: $R_b = 30 \Omega \text{ cm}^2$, $\alpha = 17 \Omega^{0.5} \text{ cm}$, $C_m = 4.4 \mu\text{F}/\text{cm}^2$; NRK: $R_b = 5.1 \Omega \text{ cm}^2$, $\alpha = 4.1 \Omega^{0.5} \text{ cm}$, $C_m = 2.0 \mu\text{F}/\text{cm}^2$; U373: $R_b = 0.9 \Omega \text{ cm}^2$, $\alpha = 3.1 \Omega^{0.5} \text{ cm}$, $C_m = 1.0 \mu\text{F}/\text{cm}^2$. In **C** the MDCK I cells were simulated with the same parameters except α which was varied.

Resistance spectra of four different cell types on various cell-covered IDE layouts

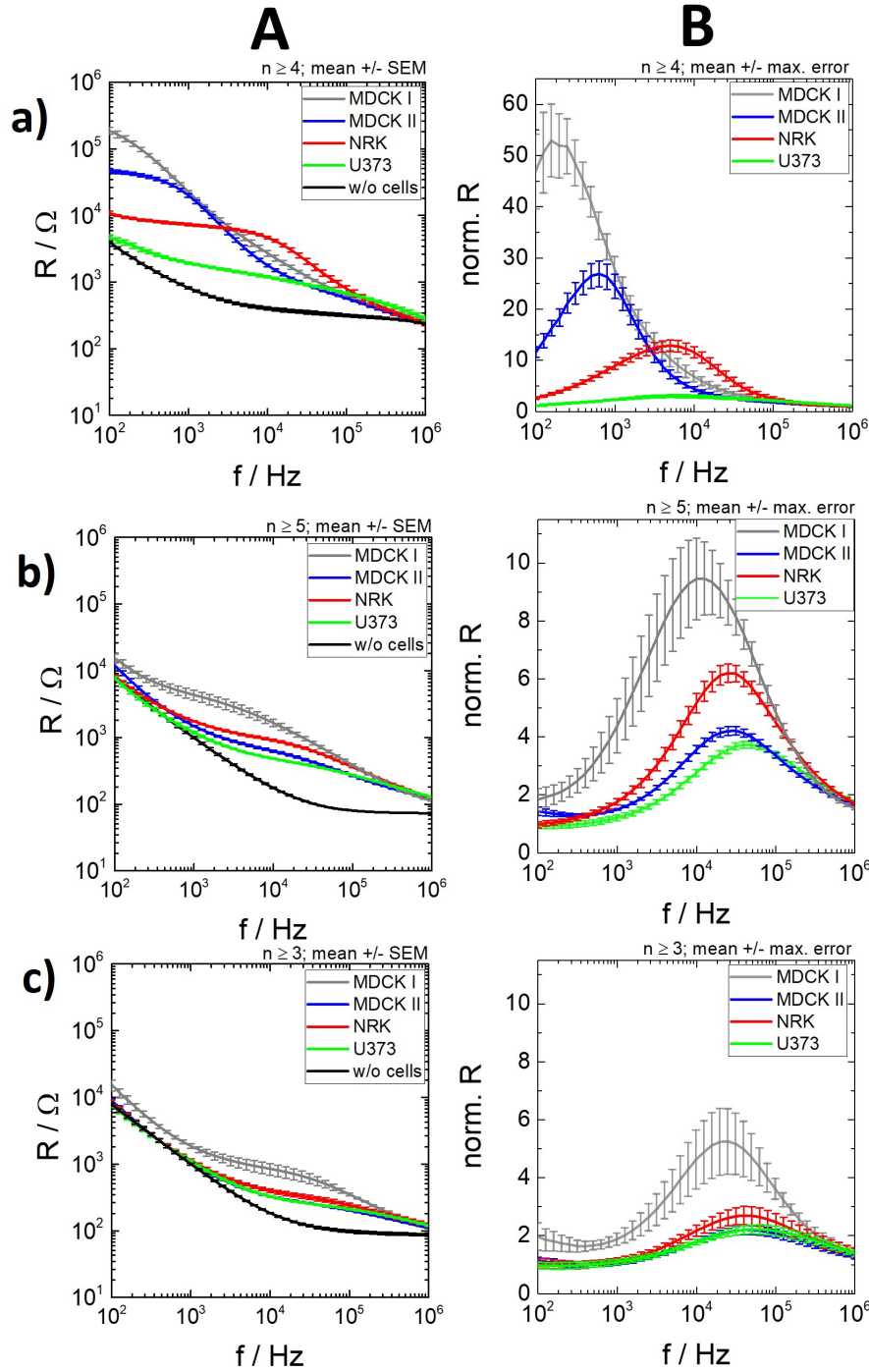


Figure A.8: Resistance spectra in dependence of the frequency of four distinct cell types cultured on three different IDE layouts. The spectra were measured on the third day after cultivation. The IDE layouts used in this experiments were **a)**: IDE 300 ($n \geq 4$), **b)**: IDE 20 ($n \geq 5$) and **c)**: IDE 10 ($n \geq 3$). The resistance spectra (**A**) and the norm. R (**B**) are presented. In the spectra the mean with the SEM is plotted and for norm. R the mean with the max. error.

Capacitance spectra of four different cell types on various cell-covered IDE layouts

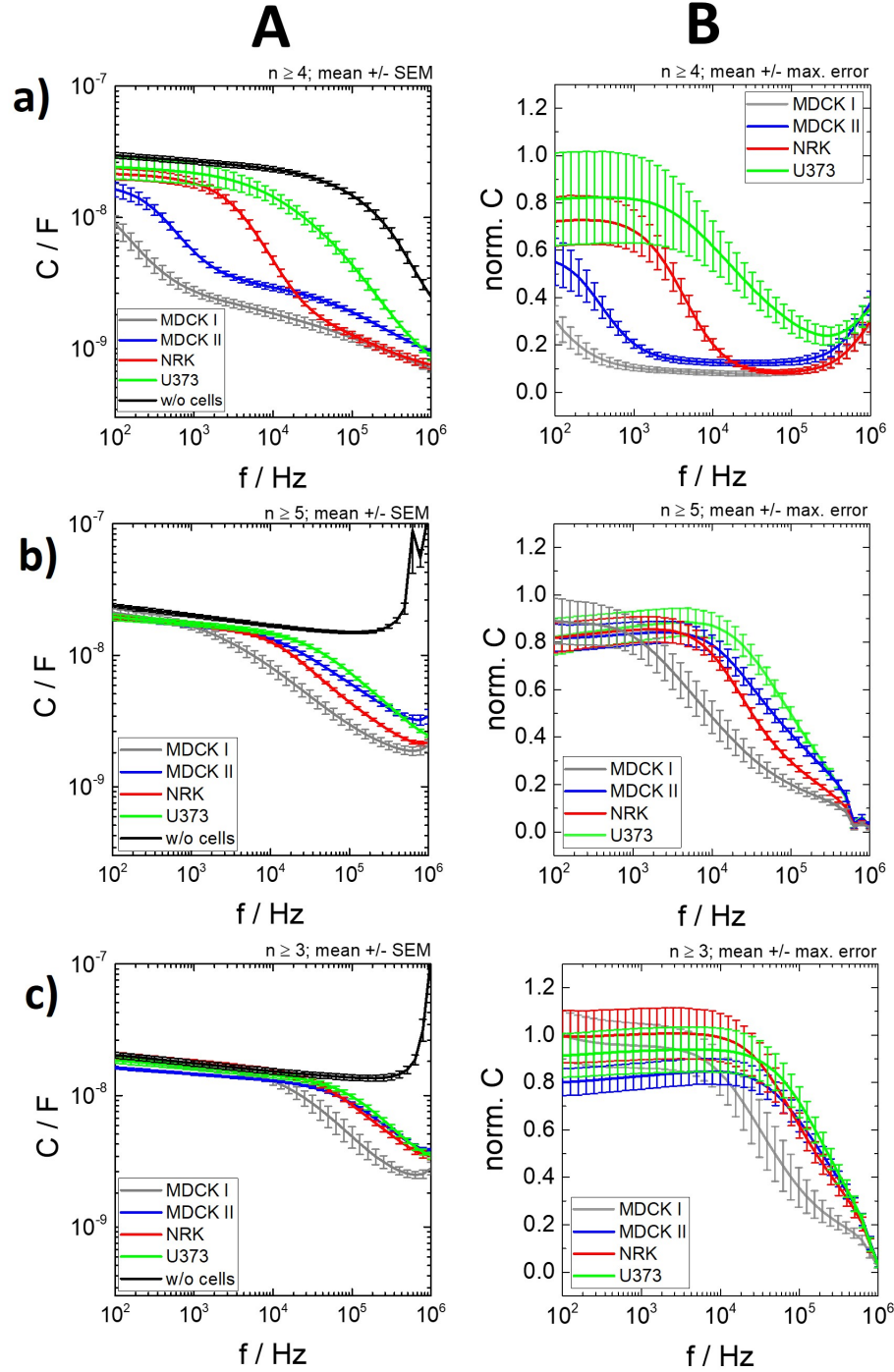


Figure A.9: Capacitance spectra in dependence of the frequency of four different cell types on three various IDE layouts. The measurement was executed on the third day after cultivation. Three different electrode types were used: **a)**: IDE 300 ($n \geq 4$), **b)**: IDE 20 ($n \geq 5$) and **c)**: IDE 10 ($n \geq 3$). The two data representations are: **A**: spectra of the capacitance and **B**: $norm. C$. The mean with the SEM is plotted for the spectra and with the max. error in the case of the $norm. C$.

Calculation of the area under the curve of the norm. $|Z|$

Table A.1: Area under the curve of the norm. $|Z|$. For the calculation norm. $|Z|$ was plotted against $\log(f)$ and the area under the curve with a baseline of $y=0$ was determined. For this calculation the 8W10E electrodes ($n \geq 6$), IDE 300 ($n \geq 4$), IDE 20 ($n \geq 5$), IDE 12 ($n \geq 4$), IDE 10 ($n \geq 3$) and IDE 7 ($n \geq 2$) were used. The mean with the max. error is listed.

cell type	8W10E / a.u.	IDE 300 / a.u.	IDE 20 / a.u.	IDE 12 / a.u.	IDE 10 / a.u.	IDE 7 / a.u.
MDCK I	15.2 ± 0.6	30 ± 4	10.5 ± 1.0	11.0 ± 0.7	6.9 ± 0.8	9.2 ± 1.0
MDCK II	10.8 ± 0.5	18 ± 2	7.0 ± 0.4	5.4 ± 0.4	5.3 ± 0.3	5.0 ± 0.1
MCF-7	10.2 ± 0.6	-	-	5.9 ± 0.2	-	5.0 ± 0.1
NRK	8.5 ± 0.3	15 ± 1	8.4 ± 0.4	5.6 ± 0.4	5.2 ± 0.4	4.4 ± 0.5
A549	7.4 ± 0.3	-	-	5.9 ± 0.4	-	3.6 ± 0.3
CHO_D2R	6.6 ± 0.3	-	-	6.4 ± 0.9	-	6.7 ± 0.9
BAEC	6.5 ± 0.2	-	-	4 ± 3	-	3.9 ± 0.2
SK-Mel-28	5.8 ± 0.2	-	-	6.3 ± 0.5	-	4.0 ± 0.8
U373	5.9 ± 0.2	7.3 ± 0.9	6.7 ± 0.3	5.8 ± 0.4	5.1 ± 0.3	3.5 ± 0.8

Resistance spectra of cell-covered IDEs with various window sizes

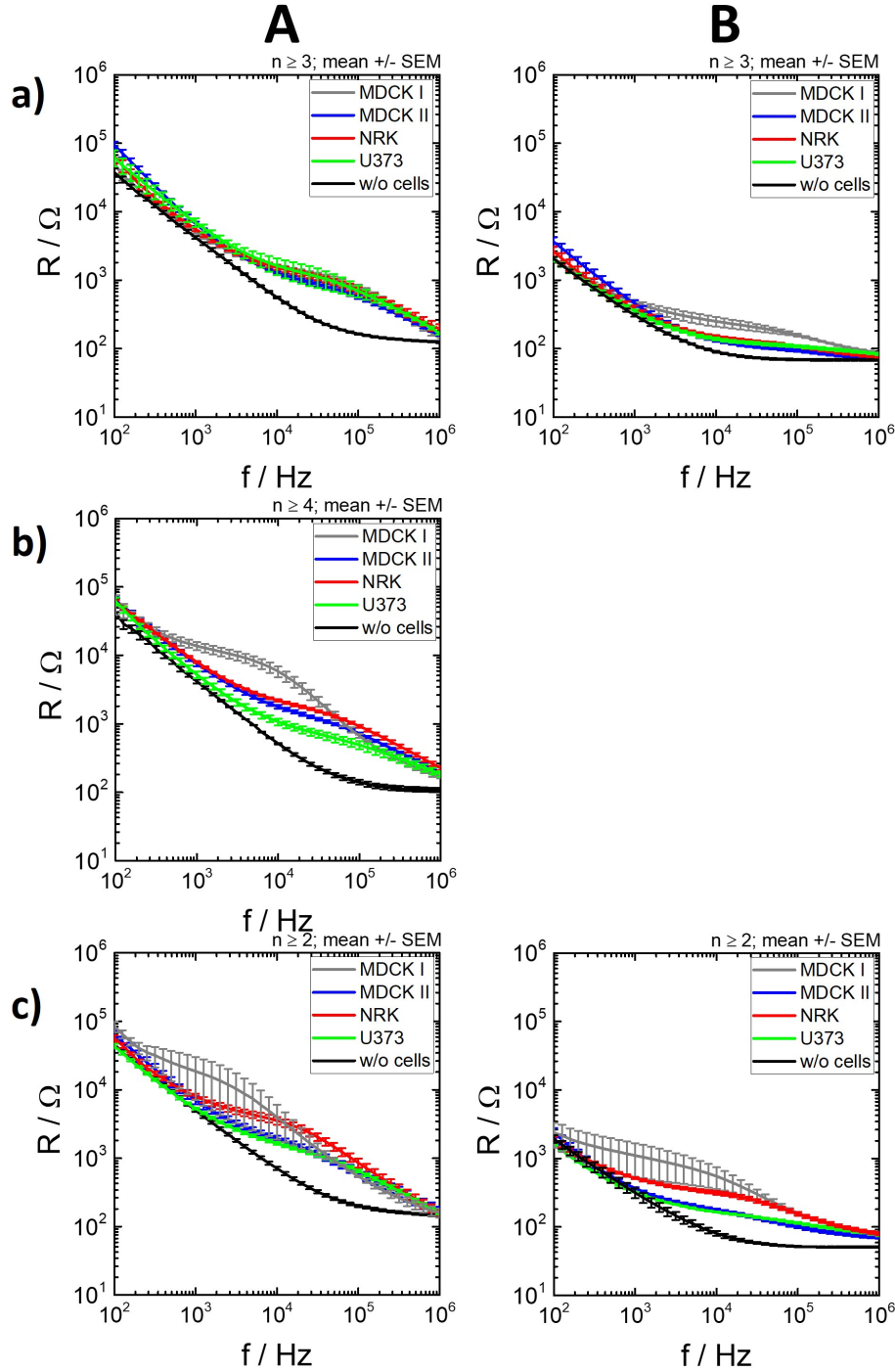


Figure A.10: Resistance spectra in dependence of the frequency of MDCK I, MDCK II, NRK and U373 cells measured with different interdigitated electrodes with various window sizes. The measurement was executed on the third day after seeding. The window sizes of **A**: (0.5 x 0.5) mm² and **B**: (2.0 x 2.0) mm² were used for the IDEs **a**): IDE 10 ($n \geq 3$), **b**): IDE 12 ($n \geq 4$) and **c**): IDE 20 ($n \geq 2$). The mean with the SEM is plotted.

Normalized resistance spectra of cell-covered IDEs with different window sizes

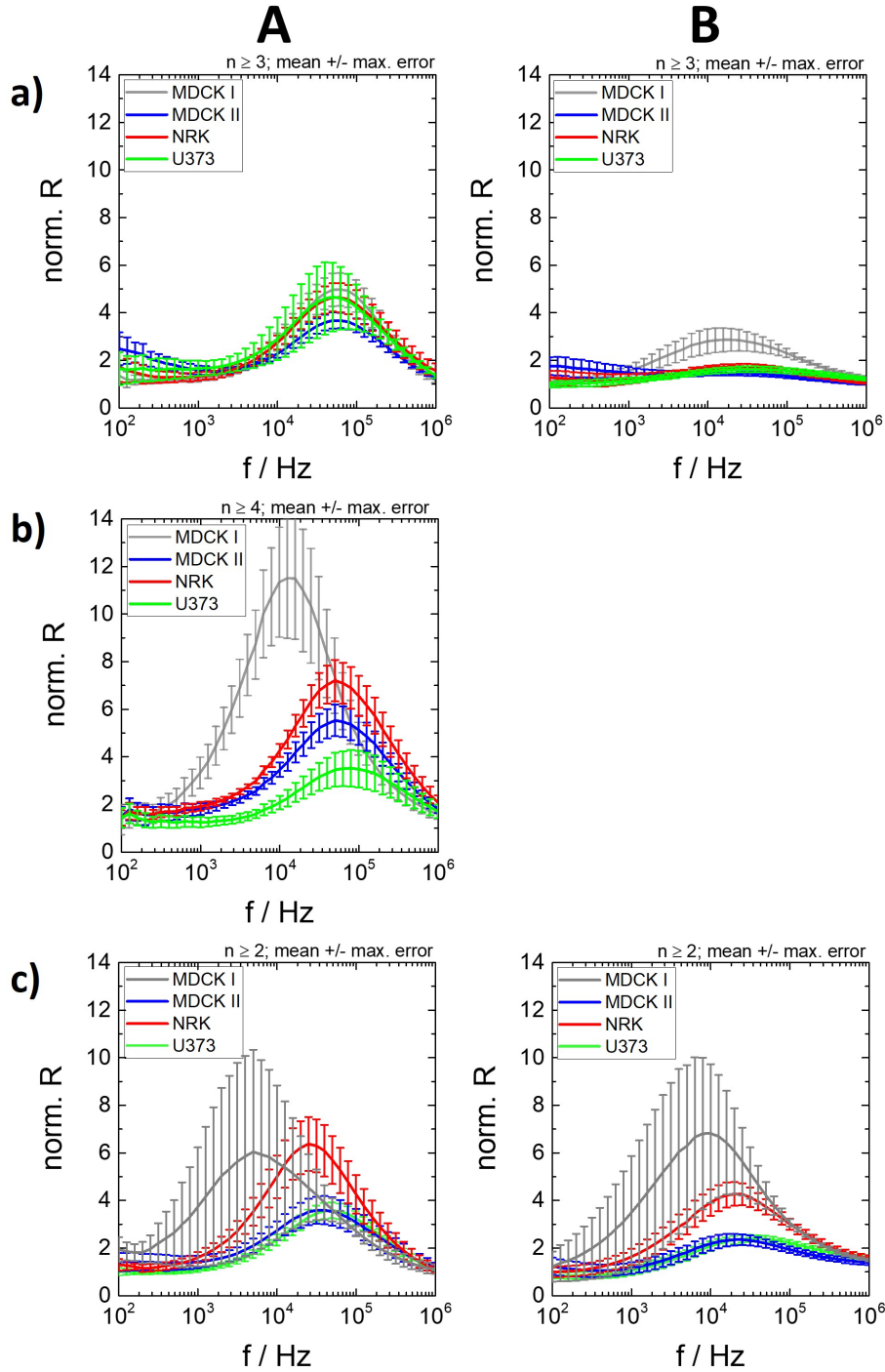


Figure A.11: Norm. R in dependence of the frequency of MDCK I, MDCK II, NRK and U373 cells cultivated on different interdigitated electrodes with various window sizes. The measurement was proceeded on the third day after seeding. The window sizes of **A**: $(0.5 \times 0.5) \text{ mm}^2$ and **B**: $(2.0 \times 2.0) \text{ mm}^2$ were used for the IDEs **a**): IDE 10 ($n \geq 3$), **b**): IDE 12 ($n \geq 4$) and **c**): IDE 20 ($n \geq 2$). The mean with the max. error is plotted.

Capacitance spectra of cell-covered IDEs with various window sizes

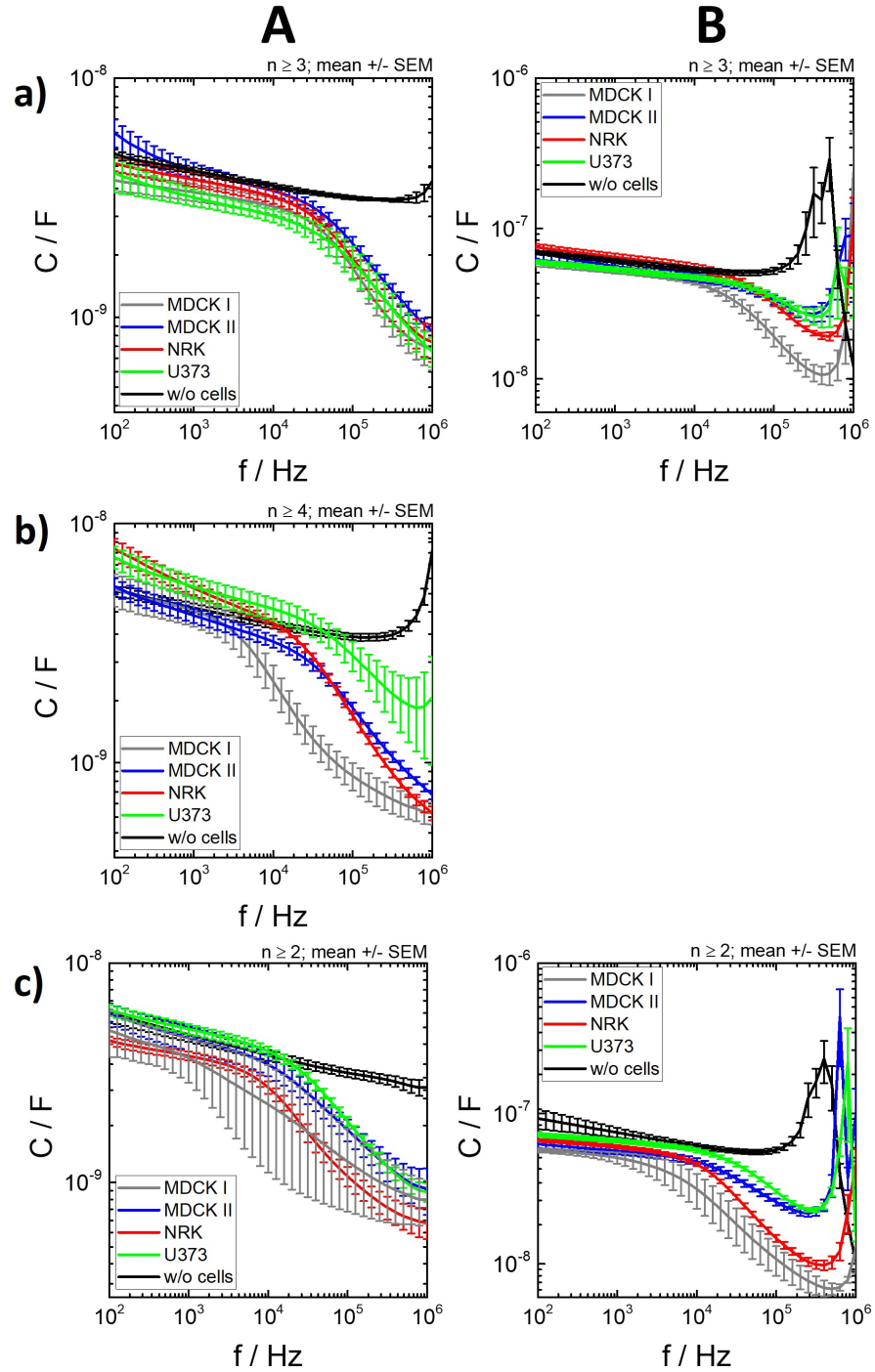


Figure A.12: Capacitance spectra in dependence of the frequency of cell-covered IDEs with various window sizes. MDCK I, MDCK II, NRK and U373 cells were measured on the third day after seeding. The window sizes are defined as **A**: $(0.5 \times 0.5) \text{ mm}^2$ and **B**: $(2.0 \times 2.0) \text{ mm}^2$ for the IDEs of **a)**: IDE 10 ($n \geq 3$), **b)**: IDE 12 ($n \geq 4$) and **c)**: IDE 20 ($n \geq 2$). The mean with the SEM is plotted.

Normalized capacitance spectra of cell-covered IDEs with different window sizes

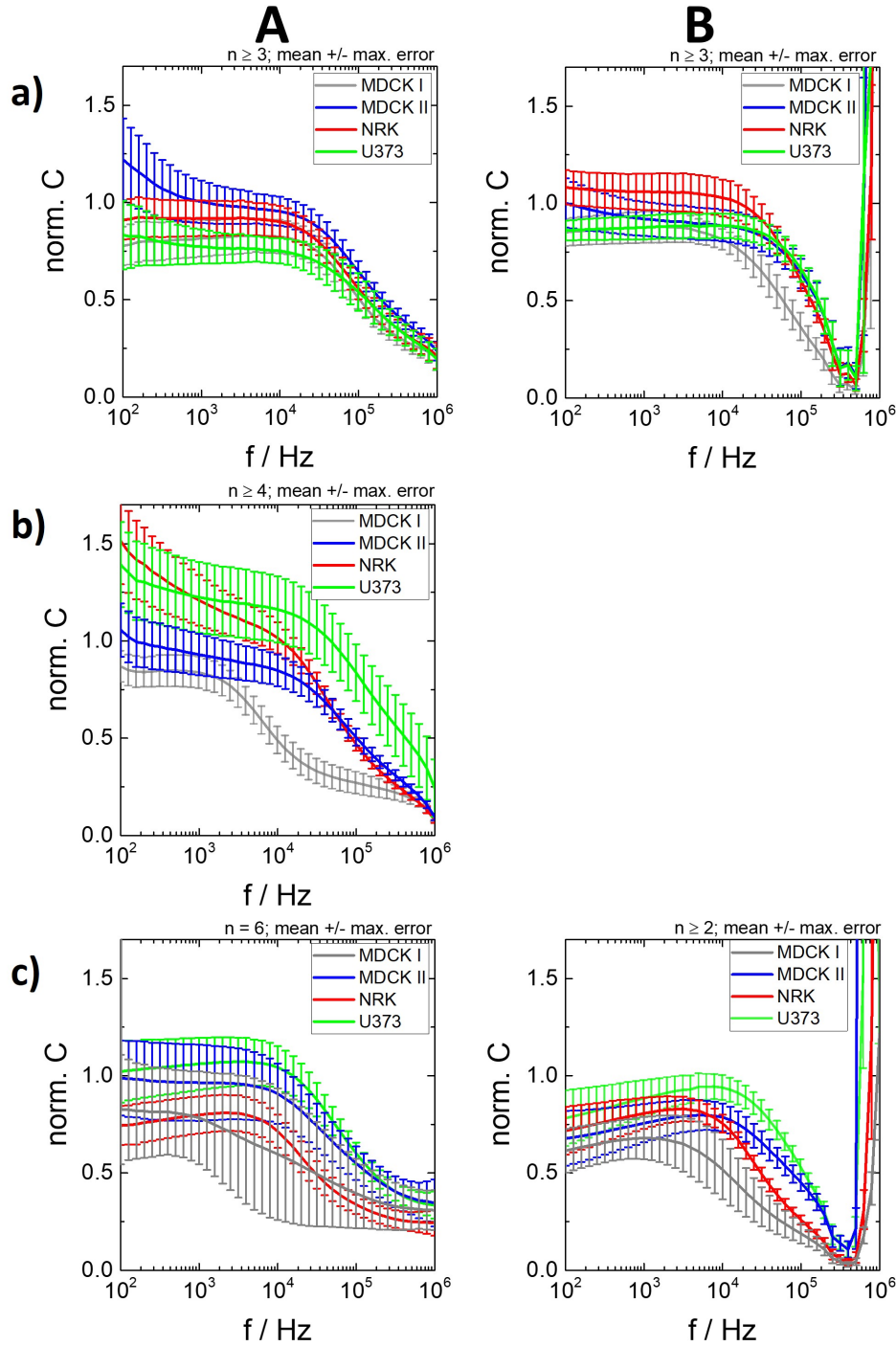


Figure A.13: Norm. C in dependence of the frequency of cell-covered IDEs with different window sizes. For the spectra MDCK I, MDCK II, NRK and U373 were used on the third day after seeding. As the window sizes **A**: $(0.5 \times 0.5) \text{ mm}^2$ and **B**: $(2.0 \times 2.0) \text{ mm}^2$ were chosen. The IDEs used for this experiment are **a**): IDE 10 ($n \geq 3$), **b**): IDE 12 ($n \geq 4$) and **c**): IDE 20 ($n \geq 2$). The mean with the max. error is plotted.

A.1.4 Micromotion measurement of different cell types grown on various electrode layouts

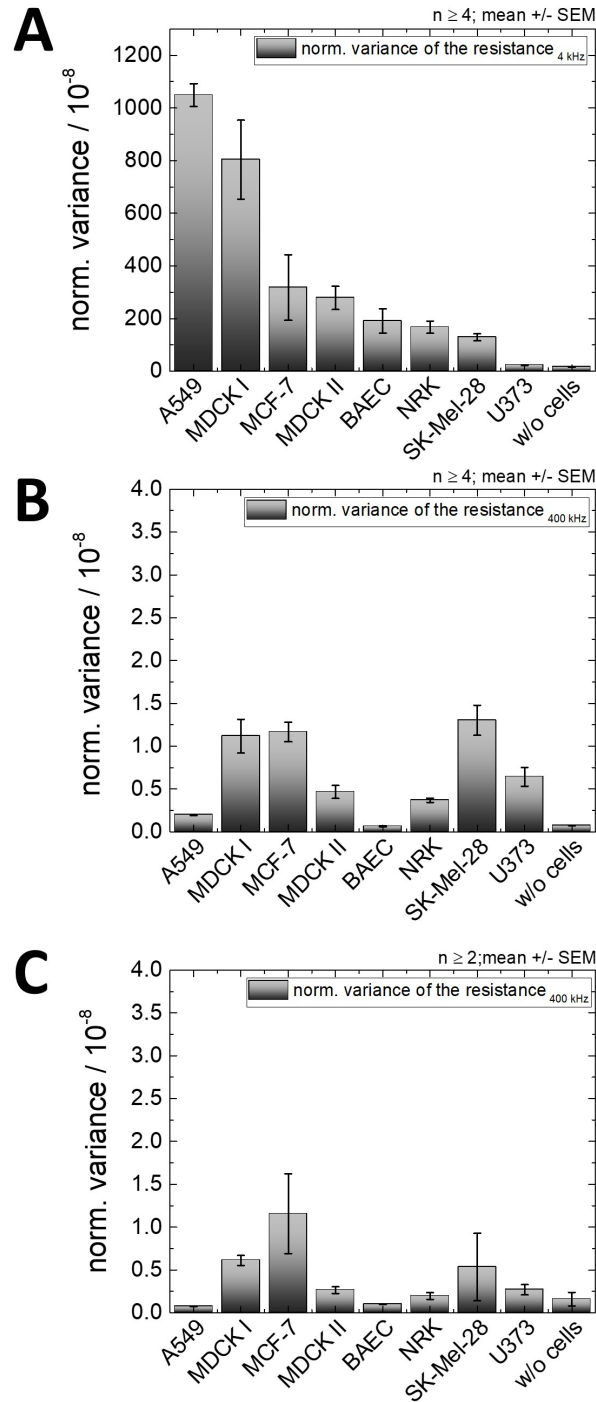


Figure A.14: Data of the detrended variance analysis of the micromotion measurement. The resistance was used and the normalization was done via division. Eight different cell types were cultivated and measured on the third day after seeding. As a control the data of the cell-free electrode were added. For the experiment **A**: 8W1E electrodes ($n \geq 4$) at 4 kHz, **B**: IDE 12 ($n \geq 4$) at 400 kHz and **C**: IDE 7 ($n \geq 2$) at 400 kHz were chosen. The mean with the SEM is plotted.

A.1.5 Monitoring the time course of cell adhesion measurement

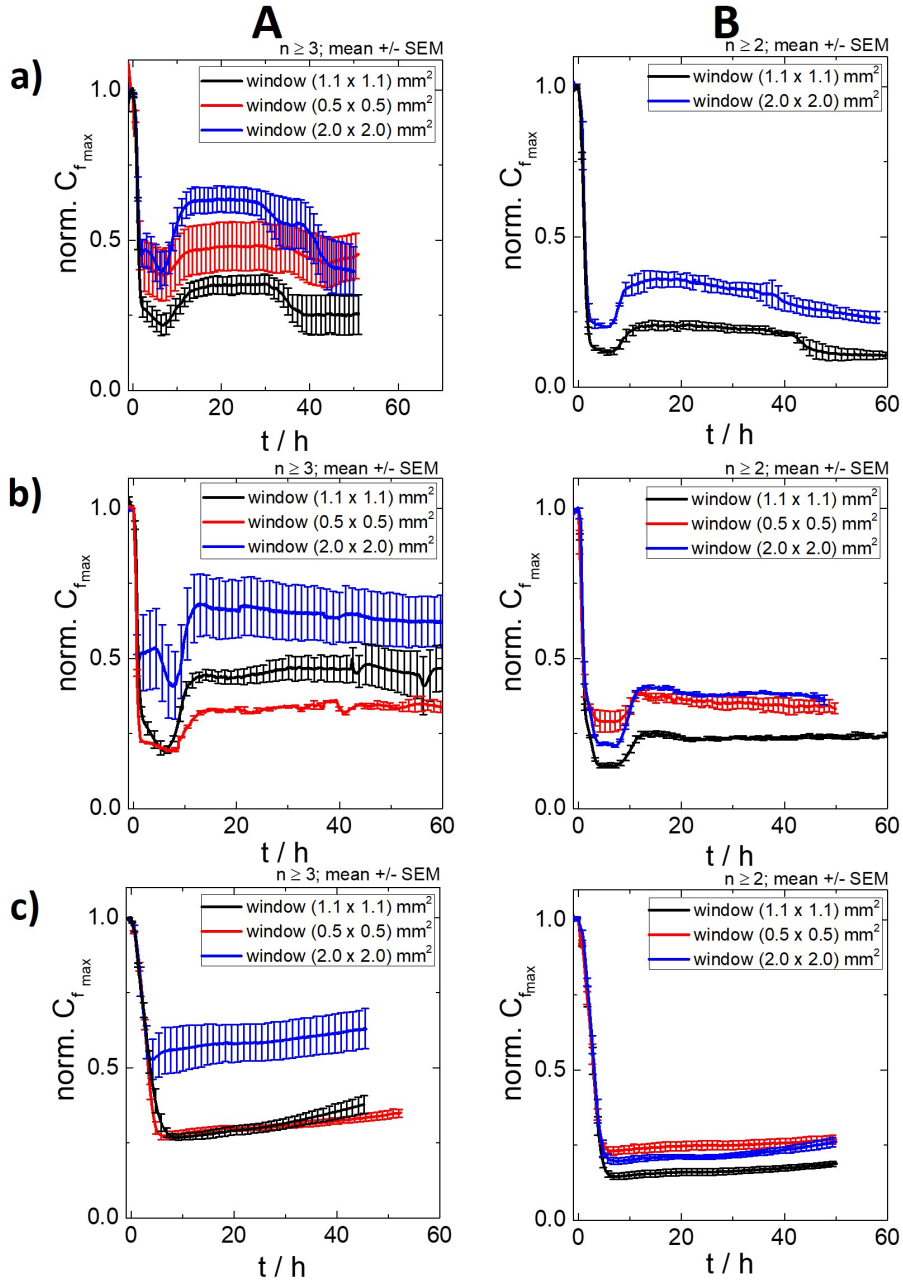


Figure A.15: Time course of the normalized capacitance of the adhesion measurement of three different cell lines **a)**: MDCK I, **b)**: MDCK II, **c)**: NRK cells. Different IDEs were used and the normalized capacitance measured with various window sizes at the frequencies f_{max} is shown: i) the window with $(1.1 \times 1.1) \text{ mm}^2$ at 320 kHz; ii) the window with $(0.5 \times 0.5) \text{ mm}^2$ at 400 kHz; the window with $(2.0 \times 2.0) \text{ mm}^2$ at 126 kHz. The layouts of **A**: IDE 10, **B**: IDE 20 were shown. All data were normalized to the initial value of a cell-free electrode (IDE 10: $C = (13 \pm 2) \text{ nF}$ of $(1.1 \times 1.1) \text{ mm}^2$, $C = (3.5 \pm 0.9) \text{ nF}$ of $(0.5 \times 0.5) \text{ mm}^2$, $C = (53 \pm 4) \text{ nF}$ of $(2.0 \times 2.0) \text{ mm}^2$; IDE 20: $C = (17 \pm 3) \text{ nF}$ of $(1.1 \times 1.1) \text{ mm}^2$, $C = (3.0 \pm 0.7) \text{ nF}$ of $(0.5 \times 0.5) \text{ mm}^2$, $C = (57 \pm 7) \text{ nF}$ of $(2.0 \times 2.0) \text{ mm}^2$). The mean with the SEM is plotted.

A.1.6 Analysis of the time course of the impedance during adhesion and beating of cardiomyocytes

Impedance change during the adhesion of cardiomyocytes

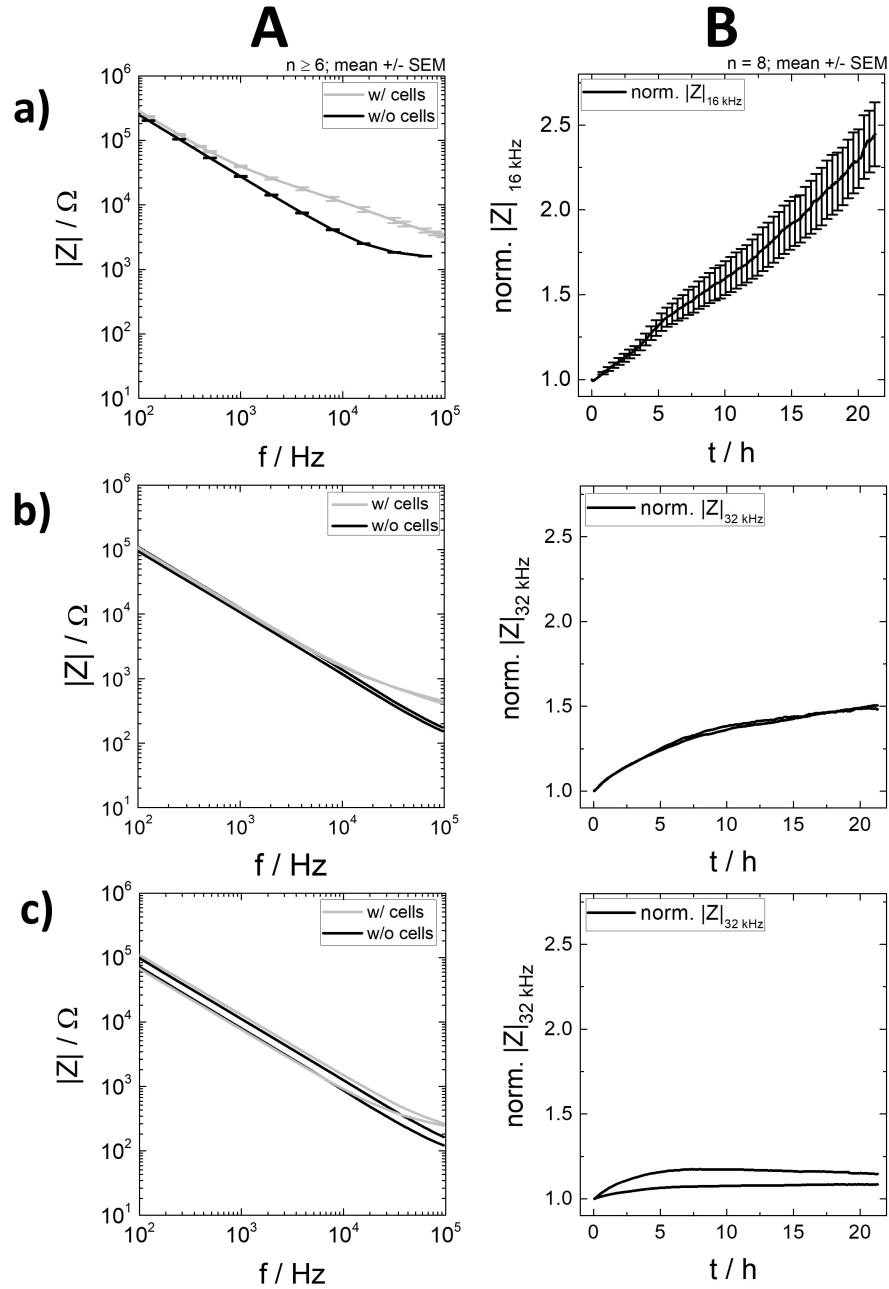


Figure A.16: Impedance change during the adhesion of cardiomyocytes on different electrode types. **A:** impedance spectra of the cell-free and cell-covered electrodes 21 h after seeding, **B:** time course of the impedance change during the adhesion. The graphs are normalized to the initial value of a cell-free electrode (8W1E electrodes: $|Z| = (3454 \pm 194) \Omega$, IDE 12: $|Z| = 488 \Omega$, $|Z| = 499 \Omega$; IDE 7: $|Z| = 341 \Omega$, $|Z| = 496 \Omega$). **a):** 8W1E electrodes at 16 kHz. The mean with the SEM is plotted ($n \geq 6$); **b):** IDE 12 at 32 kHz ($n = 2$), **c):** IDE 7 at 32 kHz ($n = 2$).

Capacitance measurement during the adhesion of cardiomyocytes

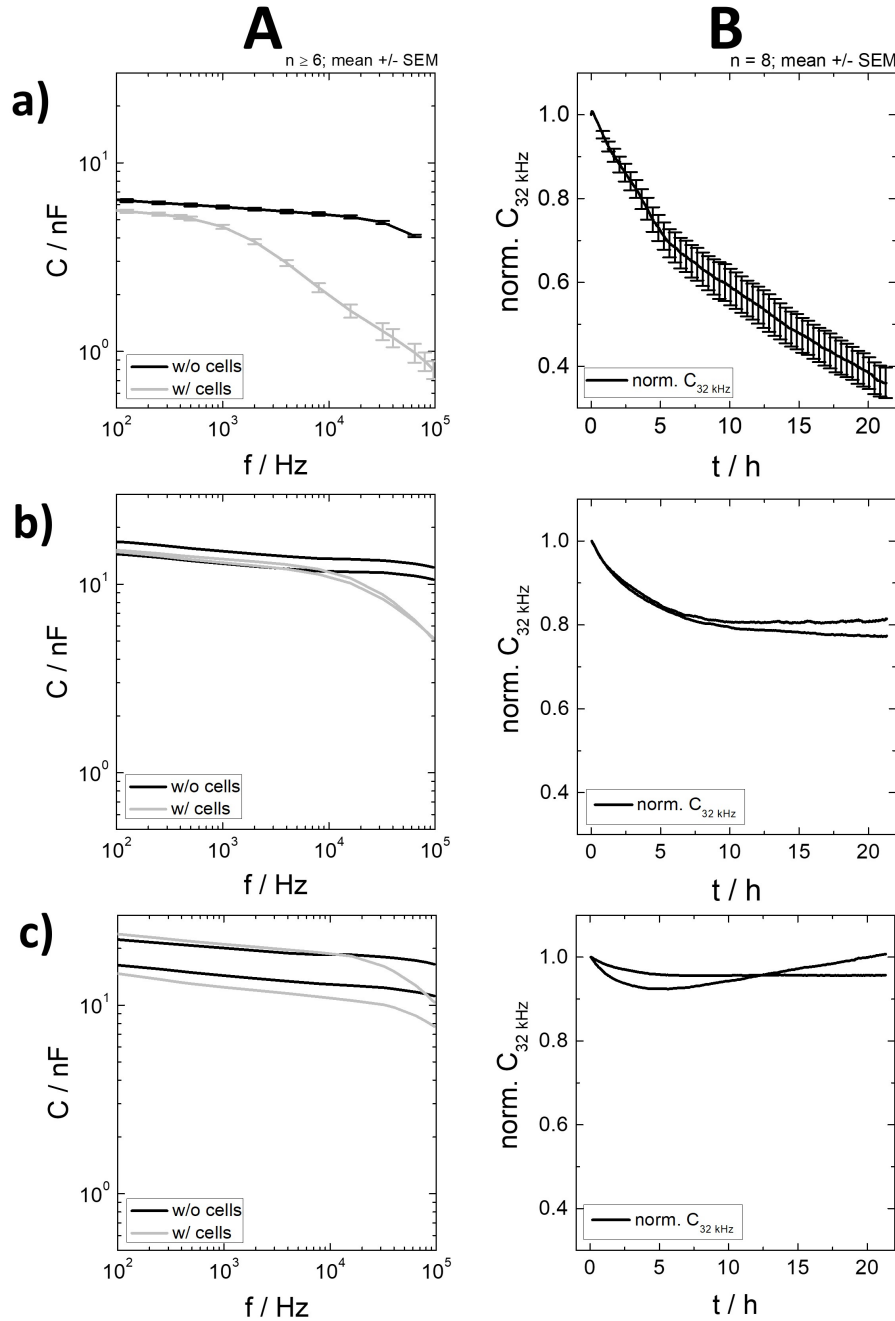


Figure A.17: Capacitance change during the adhesion of cardiomyocytes on different electrode types. **A:** capacitance spectra of the cell-free and cell-covered electrodes 21 h after seeding and **B:** the time course (at 32 kHz) of the capacitance during the adhesion of cardiomyocytes. The graphs are normalized to the initial value of a cell-free electrode (8W1E electrodes: $C = (2.4 \pm 0.1) \text{ nF}$, IDE 12: $C = 10.8 \text{ nF}$, $C = 10.8 \text{ nF}$; IDE 7: $C = 10.5 \text{ nF}$, $C = 15.9 \text{ nF}$). The mean with the SEM is plotted with the individual declaration of the number of repetitions. **a):** 8W1E electrodes. The mean with the SEM is plotted ($n = 8$). **b):** IDE 12 ($n = 2$), **c):** IDE 7 ($n = 2$).

Beating of cardiomyocytes measured with 8W1E electrodes

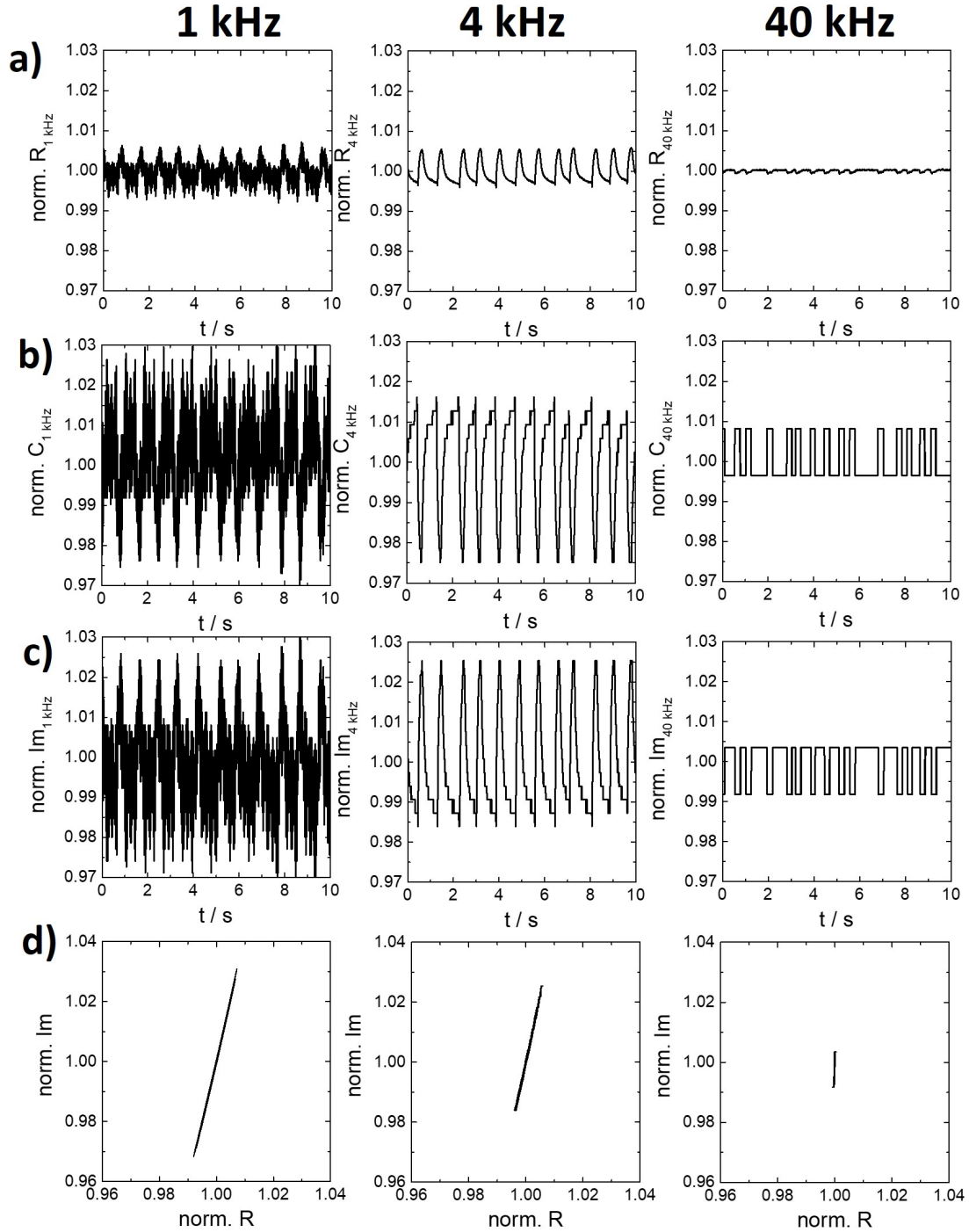


Figure A.18: Time-dependent beating of the cardiomyocytes on 8W1E electrodes with different parameter. **a):** $\text{norm. } R$, **b):** $\text{norm. } C$, **c):** $\text{norm. } \text{Im}$ and **d):** Nyquist plot at different frequencies. **A:** 1 kHz, **B:** 4 kHz, **C:** 40 kHz. All data are normalized by dividing all measuring points by the mean value of each individual measurement ($\text{norm. } R$: $R = 29234 \Omega$ (1 kHz), $R = 14540 \Omega$ (4 kHz), $R = 3440 \Omega$ (40 kHz); $\text{norm. } C$: $C = 6.4 \text{ nF}$ (1 kHz), $C = 2.9 \text{ nF}$ (4 kHz), $C = 8.5 \text{ nF}$ (40 kHz); $\text{norm. } \text{Im}$: $\text{Im} = 24982 \Omega$ (1 kHz), $\text{Im} = 13616 \Omega$ (4 kHz), $\text{Im} = 4665 \Omega$ (40 kHz)).

Comparison of the time-dependent course of norm. $|Z|$ of cardiomyocytes on IDE 12 and IDE 7 before and after smoothing

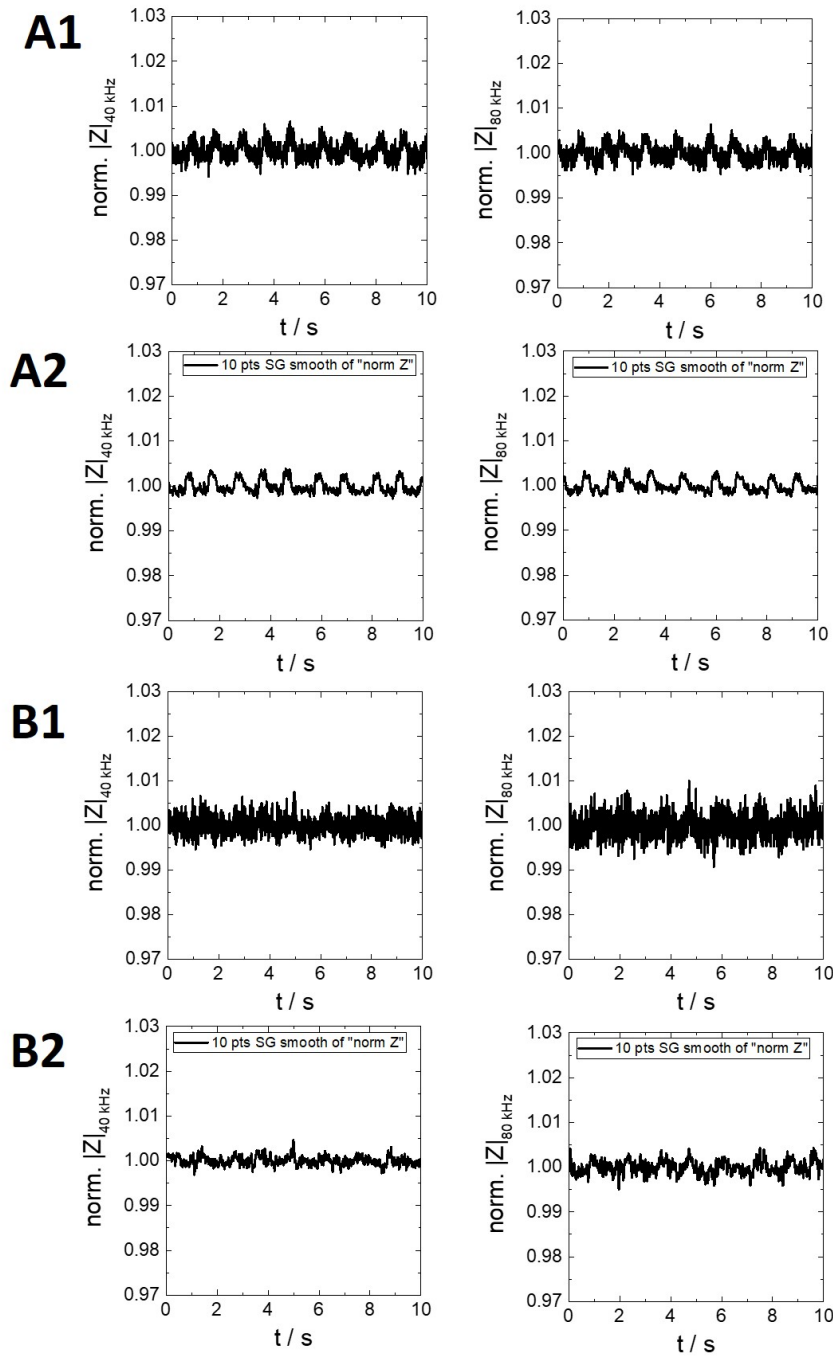


Figure A.19: Comparison of the time-dependent impedance measurement of cardiomyocytes grown on IDE 12 and IDE 7 before and after smoothing the data. For the smoothing the Savitzky-Golay method was used with 10 pts. The norm. $|Z|$ of the electrodes **A**: IDE 12 at 40 kHz and 80 kHz and **B**: IDE 7 at 40 kHz and 80 kHz are analyzed. In **A1** and **B1** the raw data of the measured norm. $|Z|$ can be seen, whereas in **A2** and **B2** the smoothed data are monitored. All data are normalized by division by the mean value of the individual measurement: IDE 12: 836 Ω (40 kHz), 594 Ω (80 kHz); IDE 7: 472 Ω (40 kHz), 287 Ω (80 kHz).

Beating of cardiomyocytes measured with IDE 12

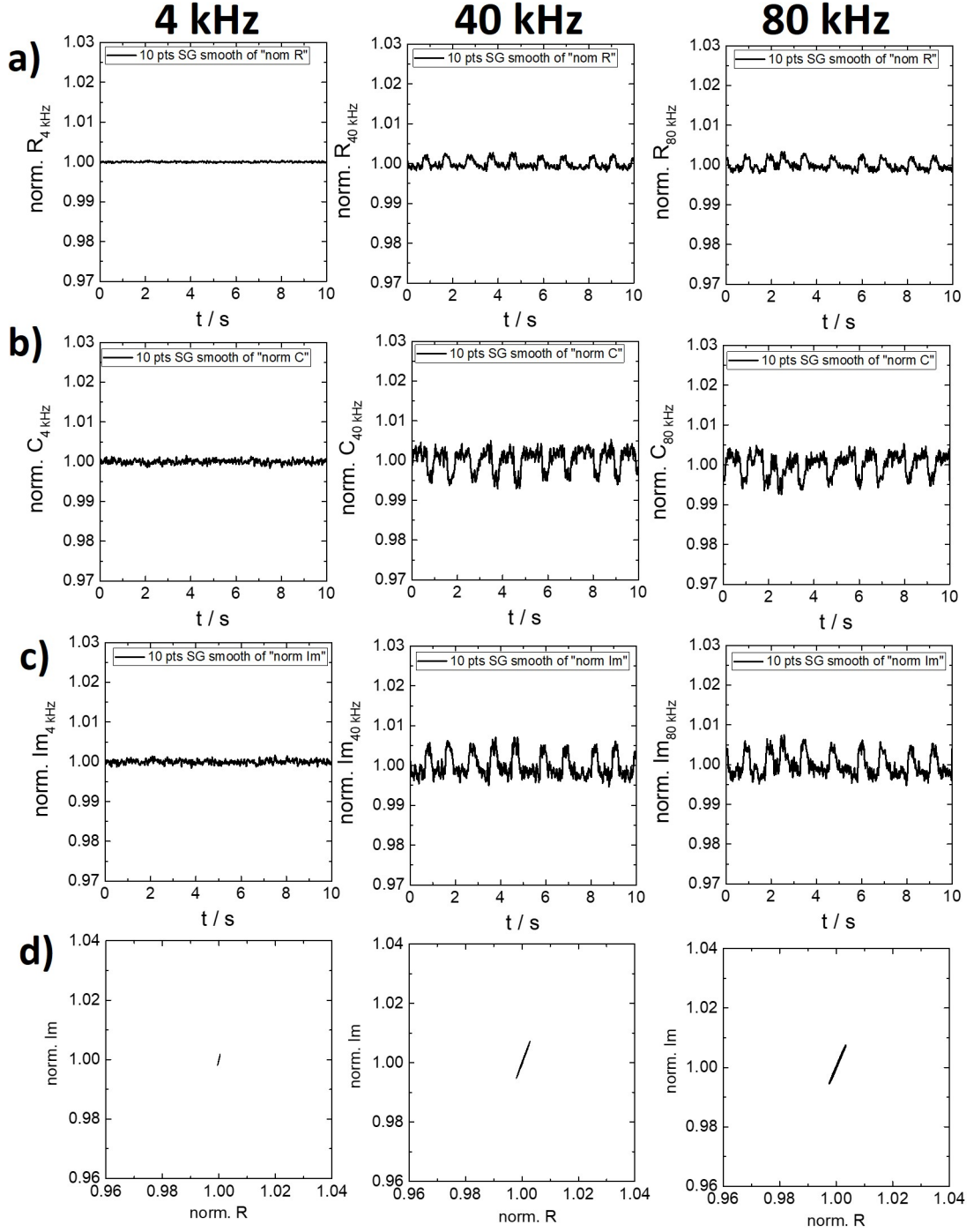


Figure A.20: Time-dependent beating of the cardiomyocytes on IDE 12 with different parameter after smoothing with the Savitzky-Golay method. **a)**: $\text{norm. } R$, **b)**: $\text{norm. } C$, **c)**: $\text{norm. } \text{Im}$ and **d)**: Nyquist plot at different frequencies. **A:** 4 kHz, **B:** 40 kHz, **C:** 80 kHz. All data are normalized by division by the mean value of every individual measurement ($\text{norm. } R$: $R = 3661 \, \Omega$ (4 kHz), $R = 731 \, \Omega$ (40 kHz), $R = 549 \, \Omega$ (80 kHz); $\text{norm. } C$: $C = 13.3 \, \text{nF}$ (4 kHz), $C = 9.8 \, \text{nF}$ (40 kHz), $C = 8.8 \, \text{nF}$ (80 kHz); $\text{norm. } \text{Im}$: $\text{Im} = 2991 \, \Omega$ (4 kHz), $\text{Im} = 406 \, \Omega$ (40 kHz), $\text{Im} = 226 \, \Omega$ (80 kHz)).

Beating of cardiomyocytes measured with IDE 7

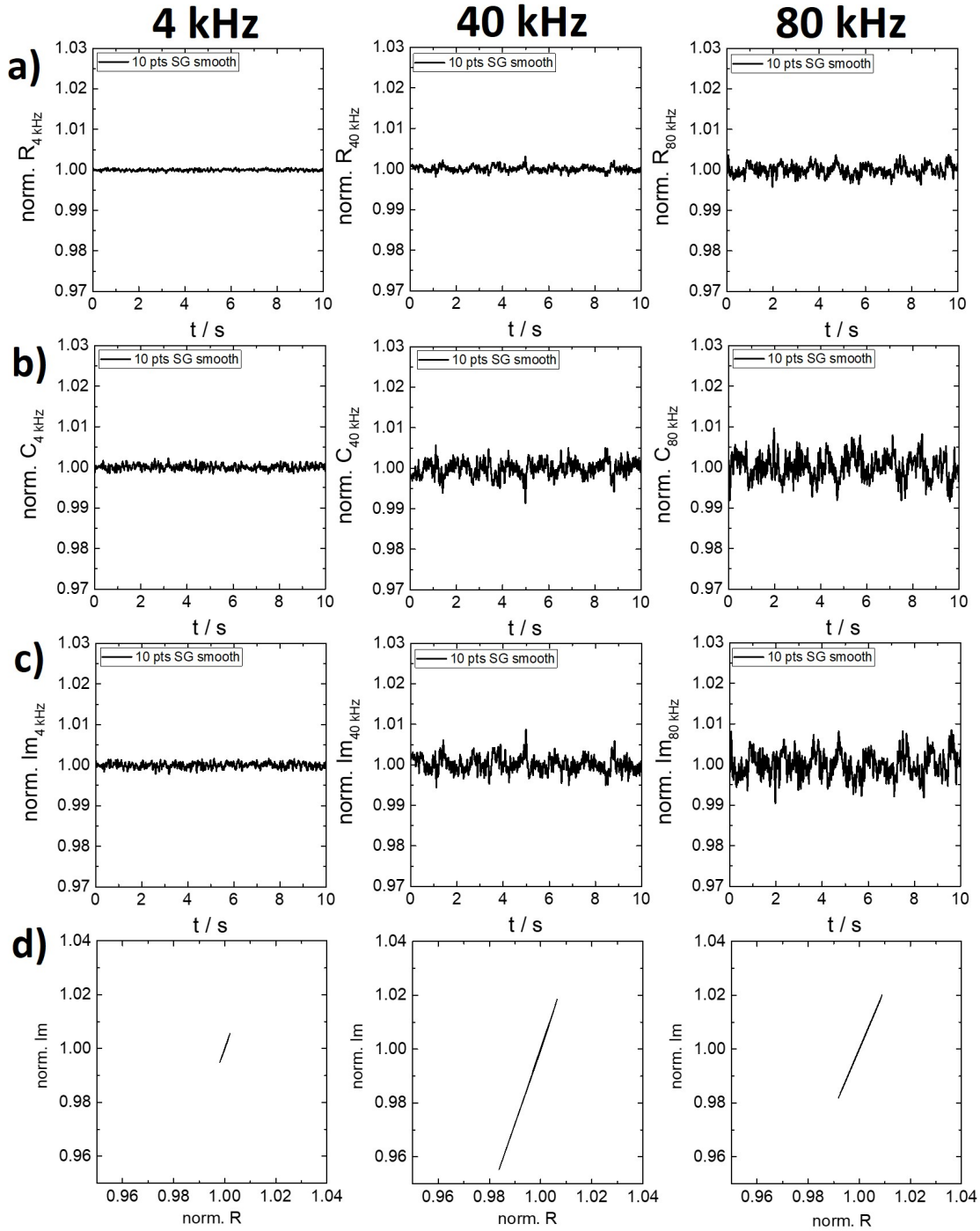


Figure A.21: Time-dependent beating of the cardiomyocytes on IDE 7 with different parameter after smoothing with the Savitzky-Golay method. **a)**: $\text{norm. } R$, **b)**: $\text{norm. } C$, **c)**: $\text{norm. } \text{Im}$ and **d)**: Nyquist plot at different frequencies. **A:** 4 kHz, **B:** 40 kHz, **C:** 80 kHz. All data are normalized by division by the mean value of every individual measurement ($\text{norm. } R$: $R = 3132 \Omega$ (4 kHz), $R = 477 \Omega$ (40 kHz), $R = 287 \Omega$ (80 kHz); $\text{norm. } C$: $C = 21.7 \text{ nF}$ (4 kHz), $C = 15.7 \text{ nF}$ (40 kHz), $C = 20.1 \text{ nF}$ (80 kHz); $\text{norm. } \text{Im}$: $\text{Im} = 1837 \Omega$ (4 kHz), $\text{Im} = 254 \Omega$ (40 kHz), $\text{Im} = 99 \Omega$ (80 kHz)).

Manipulation of the beating rate with isoprenaline

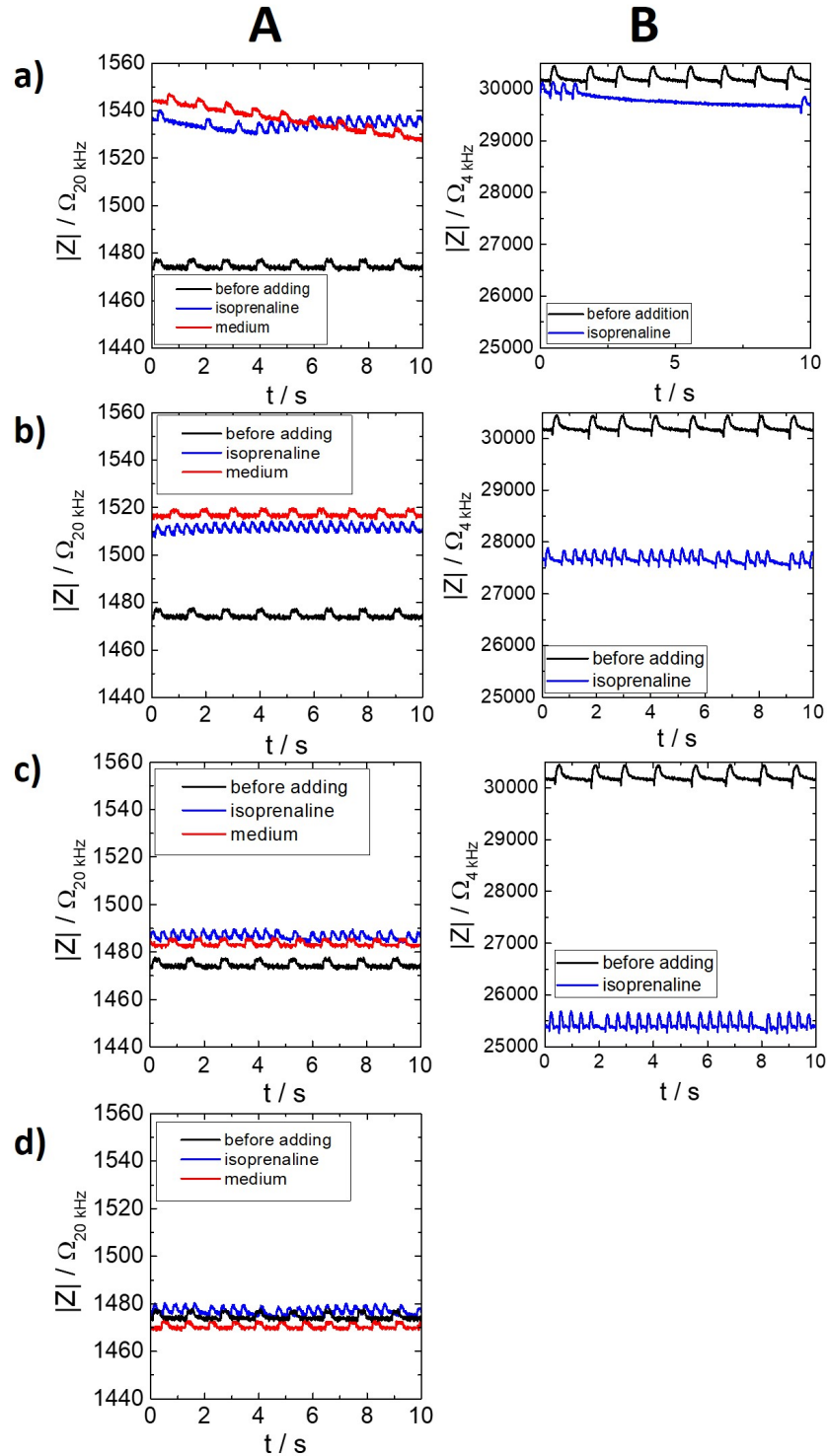


Figure A.22: Time courses of the impedance change during beating of the cardiomyocytes in dependency of the addition of 100 nM isoprenaline. As a control the beating before addition and with the addition of medium are plotted. The impedance time course was measured at different time points: **a)** directly, **b)** 5 min, **c)** 30 min and **d)** 60 min after the adding of isoprenaline. **A:** IDE 12 (20 kHz), **B:** 8W1E electrodes (4 kHz).

A.1.7 Impedance-based analysis of the cytotoxicity of BPA

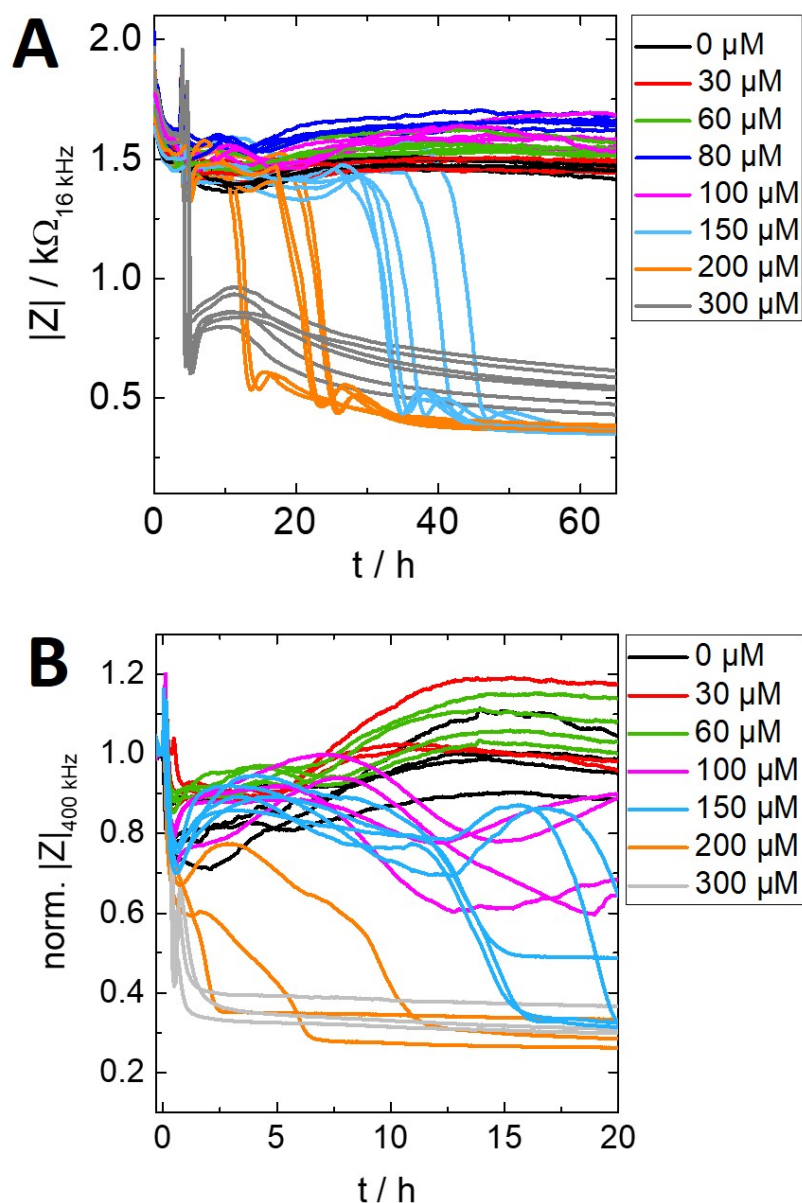


Figure A.23: Time course of the impedance of the acute toxicity measurement of BPA on NRK cells. At the time point $t=0 \text{ h}$ BPA in different concentrations is added. **A:** Raw data of the 8W10E electrodes, **B:** normalized data of the IDE 12. The data were normalized to the initial value of $|Z|$ before adding the BPA ($|Z| = (167 \pm 16) \Omega$).

A.2 Abbreviations and symbols

%	percent
°	degree
°C	centigrade
∇	nabla operator
Δ	delta
α	alpha, cell-substrate interaction
γ	conductivity
ϵ_0	permittivity of vacuum
ϵ_r	relative permittivity
φ	phase angle, phase shift
π	Archimedes' constant, osmolality
ρ	resistivity of the electrolyte in the cleft, charge density
σ	Warburg impedance, electrical conductivity
ω	angular frequency
Ω	ohm
μ_0	permeability of vacuum
μF	microfarad
μg	microgram
μL	microliter
μm	micrometer
μm^2	squaremicrometer
μM	micromolar
μs	microsecond
8W1E	eight wells one electrode
8W10E	eight wells ten electrodes
8W10E+	eight wells ten electrodes, interdigitated
A	area, Ampere, amplitude
A₁	initial value
A₂	final value
A_{El}	electrode area
A549	adenocarcinomic human alveolar basal epithelial cells
AC	alternating current
ACHN	human kidney adenocarcinoma cells
AOD	alcohol oxidase
Au	gold
AUC	area under the curve
BAEC	bovine aortic endothelial cells
BEAS-2B	human bronchial epithelium cells
BLMVEC	bovine lung microvessel endothelial cells
BP	band pass

BPA	bisphenol A
BPAEC	bovine pulmonary artery endothelial cells
BPM	beats per minute
BSA	bovine serum albumine
BSC	kidney cells from cercopithecus aethiops
C	capacitor, capacitance
c_0	velocity of an electromagnetic wave in vacuum
Ca^{2+}	calcium ion
CaAM	calcein acetoxymethyl ester
cAMP	cyclic adenosine monophosphate
CaKi1	human kidney clear cell carcinoma cells
CAP	CEVEC's amniocyte production
CC_{50}	50 % cytotoxic concentration
CdS	cadmium sulfide
CdSe	cadmium selenide
CdTe	cadmium telluride
CE	counter electrode
CFU	colony forming unit
CHO_D2R	chinese hamster ovary cells transfected with dopamine 2 receptor
CI	cytotoxicity index
Cl^-	chloride ion
CLMS	confocal laser scanning microscope
CLS	Cell Lines Service
cm	centimeter
cm^2	square centimeter
C_m	specific cell membrane
CNT	carbon nanotubes
CO_2	carbon dioxide
CPE	constant phase element
Cr	chrome
d	cell-electrode distance
D	displacement
$\text{D2}_L\text{R}$	dopamine 2 receptor in the long variant
D_r	remanent displacement
D_W	diffusion coefficient in water
DAPI	4', 6-diamidino-2-phenylindole dihydrochloride
DC	direct current
dI	infinitesimal small steps of the current
dI_m	current through the cell layer
dI_n	current from the electrode
DMEM	dulbecco's modified eagle's medium

DMSO	dimethyl sulfoxide
DNA	deoxyribonucleic acid
DSMZ	Deutsche Sammlung von Mikroorganismen und Zellkulturen
dV	change of the potential
DVA	detrended variance analysis
d_x	time constant
e	Euler's number
E	electric field, electric field strength
EBSS⁻⁻	earle's balanced salt solution without Ca ²⁺ and Mg ²⁺
EBSS⁺⁺	earle's balanced salt solution with Ca ²⁺ and Mg ²⁺
E.coli	escheria coli
EC₅₀	half maximal effective concentration
ECIS	electric cell-substrate impedance sensing
EDTA	ethylenediaminetetraacetic acid
EFSA	European Food Safety Authority
EIS	electrochemical impedance spectroscopy
ELISA	enzyme linked immuno sorbent assay
et al.	et alii, et aliae
EthD-1	ethidium homodimer
f	frequency
F₀	fluorescence intensity of the negative control
F_x	fluorescence intensity of the corresponding sample
FCS	fetal calf serum
(Fe(CN)₆)^{-3/-4}	ferrocyanide ion
Fe₂O₃	ferric oxide
FET	field-effect transistor
FITC	fluorescein isothiocyanate dextran
g	gram, gravitational field, gap
GFP	green fluorescent protein
glu	glucose
GPCR	G-protein-coupled receptor
GTP	guanosinetriphosphate
h	hour, cell height, distance between substrate and cell
H⁺	proton
H₁, H₂, H₃, H₄	histamine receptors
H₂O	water
hH1R	human histamine 1 receptor
HDFa	human dermal fibroblasts, adult
HELA	human cervical cancer cells from Henrietta Lacks
HEMA	normal human primary epidermal melanocytes
HepG2	liver hepatocellular carcinoma cells

HEPES	4-(2-hydroxyethyl)-1-piperazineethane-sulfonic acid
HL-60	human leukemia cells
HLA-B	human leukocyte antigen
HMEC-1	human dermal microvascular endothelial cells
HPLC	high-performance liquid chromatography
HSC-2	hematopoietic stem cells
HSG	human cervix carcinoma cells
HUVEC	human umbilical vein endothelial cells
Hz	hertz
i	imaginary number
I	current
I₀	applied current, Bessel function of order zero
I₁	Bessel function of order one
IP₃R	inositol-1,4,5-trisphosphate receptor
I(t)	AC current
I₂	iodine
IC₅₀	medial inhibitory concentration
IDE	interdigitated electrode
IgH-2	iguana heart cells
Im(Z)	imaginary part
IUPAC	International Union of Pure and Applied Chemistry
ISFET	ion-sensitive field-effect transistor
j	imaginary unit
J	current density
J_E	externally generated current density
K⁺	potassium ion
KCl	potassium chloride
kDa	kilodalton
kg	kilogram
KH₂PO₄	potassium dihydrogen phosphate
kHz	kilohertz
KI	potassium iodide
L	liter, inductor
l	cell length
LAPS	light-addressable potentiometric sensor
LP	long pass
LS174T	human Caucasian colon adenocarcinoma
max	maximum
MCF-7	michigan cancer foundation-7
MDa	megadalton
MDCK I	madin-darby canine kidney cells, strain I
MDCK II	madin-darby canine kidney cells, strain II

MEM-Eagle	minimum essential medium eagle
MFT	multi-frequency measurement/time
mg	milligram
Mg²⁺	magnesium ion
MHz	megahertz
min	minute, minimum
mL	milliliter
mm	millimeter
mm²	squaremillimeter
mM	millimolar
MnO	manganese (II) oxide
mOsmol	milliosmole
MTT	3-(4,5-dimethylthiazol-2-yl)-2,5-diphenyltetrazolium bromide
ms	millisecond
mV	millivolt
N	number of repetitions
Na²⁺	sodium ion
NaCl	sodium chloride
NaHCO₃	sodium hydrogen carbonate
NaH₂PO₄	sodium dihydrogen phosphate
Na₂HPO₄	disodium hydrogen phosphate
nF	nanofarad
ng	nanogram
nm	nanometer
nM	nanomolar
norm.	normalized
NP	nanoparticle
NRK	normal rat kidney cells
O₂	oxygen
p	pitch
P	polarization vector
PBS⁻⁻	phosphate buffered saline without Ca ²⁺ and Mg ²⁺
PBS⁺⁺	phosphate buffered saline with Ca ²⁺ and Mg ²⁺
PC3	human prostate cancer cells
PFA	paraform aldehyde
pg	picogram
ppm	parts per million
P/S	penicillin/streptomycin
PSA	prostate-specific antigen
Q_j	point current source
QCM	quartz crystal microbalance

QD	quantum dot
R	resistance, resistor
R_b	resistance of cell-cell contacts
R_{bulk}	resistance of the bulk
r_c	cell radius
$R_{contact}$	contact resistance
R_d	detrended sum
R_{lead}	lead resistance
R_s	circuit resistor
$\text{Re}(Z)$	real part
RE	reference electrode
REACH	Registration, Evaluation, Authorization, Restriction of Chemicals
rpm	revolutions per minute
RT	room temperature
RTC	rapid time collection
s	second, slope
SAM	self-assembled monolayer
SE	standard error
SG	Savitzky-Golay
sin	sinus
siRNA	small interfering ribonucleic acid
SK-Mel-28	human malignant melanoma cells
SPR	surface plasmon resonance
SWCNT	single-walled carbon nanotube
t	time
TEER	transepithelial electrical resistance
TRITC	tetramethylrhodamine isothiocyanate
U	voltage
U_0	applied voltage
$U(t)$	AC voltage
UV	ultra violet
U373 MG	human glioblastoma astrocytoma cells
V	scalar electric potential, volt
V_a	externally applied voltage
(v/v)	volume concentration
J	current density
Vol.	volume
w	width
(w/v)	mass concentration
X	reactance
Z	impedance

$ Z $	complex impedance
Z_m	specific impedance of the cell layer
Z_n	specific impedance of cell-free electrode
Z_N	impedance of cell-free electrode
Z_Z	impedance of cell-covered electrode
Z_{total}	specific impedance for a cell-covered electrode
ZnS	zinc sulphide
ZO-1	zonula occludens-1

A.3 Materials and instrumentations

8-well ECIS arrays	Applied BioPhysics, Troy, USA
8-well ECIS station	Applied BioPhysics, Troy, USA
96-well PS-microplate	Greiner Bio-One GmbH, Frickenhausen, Germany
Alexa Fluor 488 phalloidin	Invitrogen, Darmstadt, Germany
Argon Plasma Cleaner	PDC 32G-2, Harrick Plasma Inc., Ithaca, NY, USA
Autoclave DX-45	Systec, Wetztenberg, Germany
BPA	Sigma Aldrich, Munich, Germany
Bunsen burner for cell culture	IBS Tecnomara GmbH, Fernwald, Germany
Buerker hemocytometer	Marienfeld-Superior, Lauda-Königshofen, Germany
Calcimycin	Sigma Aldrich, Munich, Germany
Carbolfuchsin	Sigma Aldrich, Munich, Germany
Cell culture flask	25 cm ² , Greiner, Kremsmünster, Austria
Cell culture incubator	Thermo Fisher Scientific Inc, Waltham, USA
Cell culture medium	(DMEM, MEM Eagle), Sigma Aldrich, St. Louis, USA
Cell culture plate 96-well	Sarstedt, Nümbrecht, Germany
Centrifuge	Heraeus 1-SR, Thermo Fisher Scientific Inc., Waltham, USA
Centrifugation tube	Cellstar® centrifuge tubes, Greiner Bio-One, Kremsmünster, Austria
Cryovial TPP	Sigma Aldrich, Munich, Germany
DAPI	Sigma Aldrich, Munich, Germany

D-galactose	Merck, Darmstadt, Germany
D-glucose	Sigma Aldrich, Munich, Germany
DMSO	Carl Roth GmbH, Karlsruhe, Germany
EBSS⁺⁺	Sigma Aldrich, Munich, Germany
EBSS⁻⁻	Gibco, Life Technologies GmbH, Darmstadt, Germany
ECIS 1600R	Applied BioPhysics, Troy, USA
ECIS array holder	Applied BioPhysics, Troy, USA
ECIS impedance analyzer	Applied BioPhysics, Troy, USA
ECIS Z instrument	Applied BioPhysics, Troy, USA
EDTA	Merck KGaA, Darmstadt Germany
Electrode holder	machine shop, University Regensburg, Germany
Elma clean	Hans Schmidbauer GmbH, Singen, Germany
EthD-1	Biotrend Chemikalien GmbH, Köln, Germany
Ethanol	Merck, Darmstadt, Germany
FCS	Sigma Aldrich, Munich, Germany
FITC-dextran	Sigma Aldrich, Munich, Germany
Foil	(Ink Jet Films, Folex, Seewen, Switzerland
Frequency generator	Type 33120A, Hewlett Packard-Agilent, Böblingen, Germany
Glass ring	workshop, University Regensburg, Germany
Glutardialdehyde	Merck KGaA, Darmstadt, Germany
Ham's F-12	Sigma Aldrich, Munich, Germany
HEPES	Carlo Roth GmbH, Karlsruhe Germany
I₂	Merck KGaA, Darmstadt, Germany
Incubator	Ultima® II, Revco® , Thermo Fisher Scientific, Waltham, USA and Galasy 48S, New Brunswick Scientific, Fisher Scientific, Schwerte, Germany and CO ₂ group MMM Group, Munich, Germany and Modell C170, Binder, Tuttlingen, Germany

Interdigitated electrodes	DropSens, Metrohm GmbH Co. KG, Filderstadt, Germany; Fraunhofer EMFT, Munich, Germany
Impedance analyzer	SI-1260, Solartron Instruments, Farnborough, UK
Isoprenalin	Sigma Aldrich, Munich, Germany
KI	Merck KGaA, Darmstadt, Germany
LabVIEW software	National Instruments, Austin, USA
Laminar air flow hood	Thermo Fisher Scientific Inc, Waltham, USA
Latex Gloves	Carl Roth GmbH, Karlsruhe, Germany
Leibovitz L-15 medium	Gibco, Life Technologies GmbH, Darmstadt, Germany
Lexan® plate	GE, Munich, Germany
L-glutamine	Biochrom KG, Berlin, Germany
Liquid nitrogen tank	GC-BR2150 M, German-Cryo GmbH, Jüchen, Germany
Live dead kit L3224	Invitrogen GmbH, Karlsruhe
Microscope Lens EC Epipla-Neofluar	Zeiss, Jena, Germany
Microscope Nikon Diaphot	Nikon Instruments Europe, Amstelveen, Netherland
Microscope Nikon Eclipse 90i	Nikon Instruments Europe, Amstelveen, Netherland
Microscope Nikon SMZ	SMZ 1500 C-DSD230 CMONikon Instruments Europe, Amstelveen, Netherland
NaCl	VWR International GmbH, Ismaning, Germany
NaOH	Merck KGaA, Darmstadt, Germany
Osmometer	Osmomat 030, Gonotec, Berlin, Germany
Oven	Heraeus, Thermo Scientific,Electron LED GmbH T6, Hanau, Germany
Parafilm	Pechinery Plastic Packaging, Chicago, USA
Paraformaldehyde	Sigma Aldrich, Munich, Germany
PBS⁻⁻	Sigma Aldrich, Munich, Germany
PBS⁺⁺	Sigma Aldrich, Munich, Germany
Penicillin/streptomycin	Sigma Aldrich, Munich, Germany
Petri dish	Sarstedt, Nümbrecht, Germany

Pipettes (10, 200, 100 µL)	Brand GmbH, Wertheim, Germany
Pipette Tips	Sarstedt, Nümbrecht, Germany
Positive photoresist	AZ® -ECI3027, Microchemicals, Ulm, Germany
PrestoBlue® solution	Invitrogen, Darmstadt, Germany
Printer	Sure Color P400, Epson, Suwa, Japan
Relay for ECIS array	Applied BioPhysics, Troy, USA
Relay for IDE	machine shop, University Regensburg, Germany; Fraunhofer EMFT, Munich, Germany
Silicone glue	Master fix Aquarium Silikon, Bauhaus, Regensburg, Germany
Sodium hydroxide	Fisher Chemical, Schwerte, Germany
Sodium dihydrogen phosphate	Sigma Aldrich, Munich, Germany
Sputter coating device	Balzers sputter coater SCD 050, Bal-Tec, Pfäffikon, Switzerland
Spin coater	model WS-650-23B, Laurell Technologies Corporation, North Wales, USA
Sterile filter	TPP® , Sigma Aldrich, Munich, Germany and Sarstedt, Nümbrecht, Germany
Sucrose	Sigma Aldrich, Munich, Germany
Tecan Reader Sunrise	Tecan GmbH, Crailsheim, Germany
TI-Prime	MicroChemicals GmbH, Ulm, Germany
Triton-X-100	Sigma Aldrich, Munich, Germany
Trypsin	Sigma Aldrich, Munich, Germany
Ultrasonic Bath RK 255 H	Bandelin Electronic GmbH & Co. KG, Berlin
UV illumination device	isel® UV illumination device nr. 2, Elterfeld, Germany
UV blocking black dye inkjet ink	Matte Slot, Harke Group, Mühlheim, Germany
Water bath	Julabo, type TW12, Seelbach, Germany
Weighting instrument	Mettler-Toledo, Columbus, USA

A.4 Curriculum Vitae



Personal Information

Name	Maria Zinkl
Date of birth	21.02.1992
Place of birth	Weiden in der Oberpfalz
Nationality	German

University Studies and School Education

since 03/16	Doctoral Student for a PhD in science (Dr. rer. nat.) University of Regensburg, Germany PhD thesis: „ <i>Impedance-based Analysis of Adherent Cells using Interdigitated Electrodes of subcellular dimensions</i> “ Lab: Prof. Dr. J. Wegener Institute of Analytical Chemistry, Chemo- und Biosensors
10/13 – 09/15	Master of Science in Chemistry University of Regensburg, Germany Master thesis: <i>Impedanz basierte Analyse von adhärenenten Zellen mit Hilfe interdigitierter Elektroden subzellulärer Dimension</i> Lab: Prof. Dr. J. Wegener Institute of Analytical Chemistry, Chemo- und Biosensors
05/11 – 09/13	Bachelor of Science in Chemistry University of Regensburg, Germany Bachelor thesis: <i>2D-Luminiscent Sensor for Visualization of H₂O₂</i> Lab: Prof. Dr. J. Wegener Institute of Analytical Chemistry, Chemo- und Biosensors
09/02 - 05/11	University-entrance Diploma (Abitur) Ortenburg Gymnasium, Oberviechtach, Germany

A.5 Danksagung

Als erstes möchte ich mich bei allen bedanken, die mich in der Zeit dieser Doktorarbeit, aber auch während meines kompletten Studiums unterstützt haben. Ohne euch wäre dies alles nicht möglich gewesen.

Ein besonders großer Dank geht natürlich an meinen Doktorvater Prof. Dr. Joachim Wegener, der mich die ganze Promotionszeit über auf eine hervorragende Weise betreut und mich immer unterstützt hat. In jeder Situation hattest du stets eine zündende Idee, die meine Forschung weiter vorantrieb. Außerdem hattest du immer ein Ohr für kleinere oder größere Probleme und fandest immer die richtigen Worte um mich neu zu motivieren. Du hast jeden Scherz mitgemacht und hast damit erreicht, dass die Stimmung bei uns im Arbeitskreis einmalig war. Joe, herzlichen Dank für Alles. Es ist nicht möglich, von einem besseren Doktorvater betreut zu werden!! DANKE!!

Außerdem möchte ich mich herzlich bei Herrn PD Dr. Hans-Heiner Gorris bedanken für die freundliche Übernahme der Zweitkorrektur.

Ein weiterer Dank geht an Herrn Apl. Prof. Dr. Rainer Müller für die Bereitschaft als Drittprüfer zu Verfügung zu stehen.

Des Weiteren möchte ich mich herzlichst bei unserem Arbeitskreis bedanken! Es wird kaum eine andere Arbeitsstelle geben, bei der eine so gute Stimmung geherrscht hat. Man durfte jeden um Hilfe fragen und bekam sofort Unterstützung, egal ob beim "Passagäiern", "Inkubäiern" oder "Desinfizäiern". Besonders bedanken möchte ich mich bei unseren TAs Barbara und Nadja, die mich vor allem am Ende meiner Arbeit unterstützt haben. Außerdem hatten wir alle gemeinsam stets unseren Spaß, sei es bei den täglichen Kaffeetreffen, der Schottland-Rundreise oder dem jährlichen Kanuausflug und dem Bierbrauen. Es war mir eine große Ehre euer Schimmelbeauftragter zu sein.

Zudem möchte ich mich bei dir bedanken Götzi, dafür, dass du mir die Zellkultur und die Impedanzmessungen während meiner Masterarbeit beigebracht hast. Dieses Grundwissen war definitiv nützlich für meine Promotionszeit.

Außerdem gilt mein Dank meiner Praktikantin Saphia Azzam, die im Rahmen ihrer Bachelorarbeit und ihres Forschungspraktikums mich bei den Arbeiten an der BPA

Studie unterstützt hat.

Des Weiteren gilt mein Dank den Quersties. Durch euch wurde meine Studiumszeit einfach unvergesslich. Noch oft denke ich an unsere gemeinsamen Urlaube zurück und die vielen gemeinsamen Erinnerungen, die sich während der letzten 10 Jahre angesammelt haben. Ich hoffe, unsere Freundschaften halten noch weit über die Studiumszeit.

Ein weiterer Dank gilt Susi, die während der Schreibzeit stets an meiner Seite war.

Zudem möchte ich mich bei meiner langjährigen Laborkollegin Lisa bedanken. Vielen Dank, dass ich dich immer um Rat fragen durfte und die Stimmung in unserem Labor immer super war. Egal, ob es um Krisenmanagement, persönliche Anliegen oder seelische Unterstützung ging, warst du immer für mich da. Auch während gelegentlichen Starthilfen deines Autos kamen wir uns näher. Du bist der beste Beweis, dass aus Kollegen Freunde werden können.

Natürlich hab' ich dich nicht vergessen, Flo. Wir haben mittlerweile unsere ganze Studiumszeit inklusive Promotion miteinander verbracht. Das sind jetzt schon unfassbare 10 Jahre. Es war immer eine Spitzenzeit und du hast mich immer verstanden wie kein anderer, meistens auch ganz ohne Worte. Ein Prost auf unsere gemeinsame Zeit als "Bierdimpfl" des Arbeitskreises und auf das nächste gemeinsame Jahrzehnt, in dem wir gemeinsam "umatriscern" werden. Danke für alles!

Ich will auch dir danken, Steffi. Mittlerweile sind wir über 22 Jahre befreundet und du hast mich stets in all meinen Entscheidungen unterstützt und hattest immer ein offenes Ohr für meine Probleme. Vor allem hast du mich in der letzten Phase des Schreibens stets motiviert. Danke für die gemeinsame Zeit!

Außerdem möchte ich meinen Brüdern Thomas und Wolfgang danken, die sich durch diese Arbeit gequält und sie korrigiert haben. Vor allem dir, Thomas, vielen Dank dafür!

Mein größtmöglicher Dank geht aus tiefstem Herzen an meine Eltern. Ohne eure Hilfe wäre weder mein Studium noch meine Promotion zu bewerkstelligen gewesen. Eure finanzielle und vor allem mentale Unterstützung werde ich euch nie vergessen. VIELEN DANK!!

A.6 Eidesstattliche Erklärung

Ich erkläre hiermit an Eides statt, dass ich die vorliegende Arbeit ohne unzulässige Hilfe Dritter und ohne Benutzung anderer als der angegebenen Hilfsmittel angefertigt habe. Die aus anderen Quellen direkt oder indirekt übernommenen Daten und Konzepte sind unter Angabe des Literaturzitats gekennzeichnet.

Weitere Personen waren an der inhaltlich-materiellen Herstellung der vorliegenden Arbeit nicht beteiligt. Insbesondere habe ich hierfür nicht die entgeltliche Hilfe eines Promotionsberaters oder anderer Personen in Anspruch genommen. Niemand hat von mir weder unmittelbar noch mittelbar geldwerte Leistungen für Arbeiten erhalten, die im Zusammenhang mit dem Inhalt der vorgelegten Dissertation stehen.

Die Arbeit wurde bisher weder im In- noch im Ausland in gleicher oder ähnlicher Form einer anderen Prüfungsbehörde vorgelegt.

Ich versichere an Eides statt, dass ich nach bestem Wissen die reine Wahrheit gesagt und nichts verschwiegen habe.

Datum, Ort

Maria Zinkl